RILEM Bookseries

Niki Kringos
Björn Birgisson
David Frost
Linbing Wang *Editors*

Multi-Scale Modeling and Characterization of Infrastructure Materials

Proceedings of the International RILEM Symposium Stockholm, June 2013

Springer

Multi-Scale Modeling and Characterization of Infrastructure Materials

RILEM BOOKSERIES
Volume 8

RILEM, The International Union of Laboratories and Experts in Construction Materials, Systems and Structures, founded in 1947, is a non-governmental scientific association whose goal is to contribute to progress in the construction sciences, techniques and industries, essentially by means of the communication it fosters between research and practice. RILEM's focus is on construction materials and their use in building and civil engineering structures, covering all phases of the building process from manufacture to use and recycling of materials. More information on RILEM and its previous publications can be found on www.RILEM.net.

For further volumes:
http://www.springer.com/series/8781

Niki Kringos · Björn Birgisson · David Frost
Linbing Wang
Editors

Multi-Scale Modeling and Characterization of Infrastructure Materials

Proceedings of the International RILEM Symposium Stockholm, June 2013

Springer

Editors
Niki Kringos
KTH Royal Institute of Technology
Stockholm
Sweden

David Frost
Georgia Institute of Technology
Savannah
Georgia
USA

Björn Birgisson
Royal Institute of Technology (KTH)
Dept. Civil and Architectural Engineering
Div. Soil- and Rock Mechanics
Stockholm
Sweden

Linbing Wang
Virginia Tech
Blacksburg
Virginia
USA

ISSN 2211-0844 ISSN 2211-0852 (electronic)
ISBN 978-94-007-6877-2 ISBN 978-94-007-6878-9 (eBook)
DOI 10.1007/978-94-007-6878-9
Springer Dordrecht Heidelberg New York London

Library of Congress Control Number: 2013937204

Preface

Every year, society makes large efforts on building and maintaining new transport infrastructure. The importance of a sustainable, well-functioning and long-term environmentally friendly infrastructure network goes, however, far beyond the financial costs alone. A thriving transport infrastructure network also functions as a driving force for further economic growth and helps in attracting new ventures, making it also of importance for a prosperous and innovative society.

The micro- and nano-modification of infrastructure materials and the associated multi-scale characterization and simulation has the potential to open up whole new uses and classes of materials, with wide-ranging implications for society. The use of multi-scale characterization and simulation brings the ability to target changes at the very small scale that predictably effect the bulk behavior of the material and thus allowing for the optimization of material behavior and performance.

Under the auspices of the RILEM Technical Committee on Nanotechnology-Based Bituminous Materials 231-NBM and the Transport Research Board (TRB) Technical Committee on Characteristics of Asphalt Materials AFK20, the International RILEM Symposium on Multi-Scale Modeling and Characterization of Infrastructure Materials was held at KTH Royal Institute of Technology in Stockholm, Sweden on June 10-12, 2013.

The Symposium aimed at bringing together key researchers from various disciplines to present their findings and ongoing research in this field in a focused environment with extended discussion times. It resulted in a collection of excellent papers that reach from asphalt to cement, from chemistry to mechanics and from nano- to macro-scale. As such, the Proceedings of this event give a good impression of the width and depth of the currently ongoing efforts of developing more sustainable infrastructure materials. It also highlights the great potential that lies ahead of us to go towards a shared multi-disciplinary vision for developing the infrastructure materials of the future.

The organizing committee is grateful to the international experts that helped in giving detailed reviews of the submitted papers and to the authors to contribute towards out-of-the-box thinking that is needed for a sustainable infrastructure. We hope that this book will serve as a comprehensive reference, as an insight into

currently ongoing research efforts and as an inspiration for new research ideas to enhance the long-term performance of infrastructure materials from a fundamental perspective.

Stockholm, March 2013

Niki Kringos
Björn Birgisson
David Frost
Linbing Wang

Contents

Fracture Toughness Testing Aspects for Assessing Low Temperature Behaviour of Bituminous Binders

Moises Bueno[1,2], Martin Hugener[1], and Manfred N. Partl[1,3]

[1] Road Engineering/Sealing Components Laboratory, Empa,
Swiss Federal Laboratories for Material Science and Technology, Ueberlandstr. 129,
CH-8600 Duebendorf, Switzerland
[2] School of Civil Engineering, UCLM,
Universidad de Castilla-La Mancha, Avda. Camilo José Cela,
s/n 13071 Ciudad Real, Spain
[3] Highway and Railway Engineering, KTH Royal Institute of Technology,
Brinellvägen 23, SE-10044 Stockholm, Sweden
{Moises.Bueno,Martin.Hugener,Manfred.Partl}@empa.ch

Abstract. Thermal cracking of asphalt roads usually occurs in cold regions and areas with frequent temperature changes. Hence, a complete comprehensive understanding about the behaviour of bituminous binders at very low temperatures is required for predicting the performance of the asphalt road. Since conventional methods have not shown reliable results evaluating polymer modified binders, the fracture toughness test (FTT) has been developed as an alternative method for the determination of the low temperature behaviour. This work presents a complementary study where the influence of different parameters on the results in the experimental FTT procedure is analysed. It is shown that preparation and conditioning of the beams before the test can have a significant effect on the fracture temperature. In order to achieve repetitive results in the assessment of different types of binders, the experimental procedure has been improved.

Keywords: Fracture toughness test, low temperature behaviour, polymer modified bituminous binder, thermal cracking, asphalt road.

1 Introduction

Thermally induced cracking of asphalt pavement may occur in cold regions (low temperature cracking) as well as in areas which experience large extremes in daily temperatures (thermal fatigue cracking) [1]. The risk of cracking is increased by numerous imperfections and defects that are common in pavement structures due to either construction or a combination of aging and traffic-induced distress. It is around these imperfections that thermal stresses concentrate allowing crack initiation and/or crack propagation. Under repetitive loading, the micro-cracks can grow and, eventually, merge to large cracks transverse or perpendicular to the

N. Kringos et al. (Eds.): *Multi-Scale Model. & Charact. of Infrastruct. Mater.*, RILEM 8, pp. 1–12.
DOI: 10.1007/978-94-007-6878-9_1

driving direction. Once water enters these cracks, freeze-thaw cycles will quickly cause a total deterioration of the trafficked surface course reducing its service life and increasing cost for maintenance or early pavement repair [2].

When the pavement cools, the asphalt binder slowly transforms from a viscoelastic ductile into an elastic brittle material. Since, asphalt pavements start to experience cracks when reaching the brittle state, efforts in this study were concentrated on the understanding of the binder's fracture behaviour in this case. Final fracture properties of an asphalt mixture depend directly on the behaviour of the binder, hence, it would be useful to consider the fracture properties of the binder for specification purposes [3]. The conventional assessment of the low temperature properties of bituminous binders is often insufficient and repeatedly results in costly misjudgements and damaged roads. Because the standardized test method "Fraass breaking point" [4] shows a low reproducibility, in particular with special and polymer-modified binders, the search for an alternative test method was initiated. Some years ago, the determination of the flexural creep stiffness with the bending beam rheometer (BBR) was proposed [5]. As this is a creep test, the expectations have only partly been satisfied. It is objected that the BBR test stays in a viscoelastic domain of behaviour and therefore it is not able to accurately predict low temperature failure, except for unmodified bitumen [6].

Fracture toughness provides a measure of resistance to failure in the presence of severe tensile constraints and sharp cracks. As this property is independent of sample size and geometry, it is generally considered useful for initial type testing and specification verification [7]. This is particularly true for notched specimen fracture tests at low temperatures. Thus, a fracture toughness test was developed as possible alternative test method for the determination of this property [3]. Recent results from an international round robin test carried out between eight different laboratories (including Empa) have shown that this test is a promising tool for characterising the low temperature behaviour of bituminous binders [8]. Nevertheless, more experimental studies have to be carried out to improve the feasibility of this test defining the influence of the different operational parameters on the results. The present work shows a complementary study evaluating the effect of different materials to create the notch, analysing the repeatability of the improved test method. Furthermore, some points in the experimental procedure before the test have been studied and checked in order to enhance the accuracy of the technique.

2 Experimental

2.1 Materials

In order to study the influence of the experimental steps on the method, two bituminous binders with different characteristics have been used (Table 1). Samples were provided by commercial suppliers, thus, details related to binder formulation and modification (i.e. polymer type and percentage or wax content) are unknown.

Table 1 Properties of the bituminous binders

Binder Type	Penetration [11]	Softening point Ring and ball method [12]	Characteristics
Bitumen 35/50 [9]	42 mm	57.2 °C	Neat bitumen
PmB 25/55-65 [10]	48 mm	92.5 °C	Polymer and wax modified bitumen

2.2 Test Procedure for the Determination of the Fracture Toughness Test (FTT)

The fracture toughness test (FTT) is defined in the European technical specification CEN/TS 15963:2010 [13], which has been approved for provisional application. It is based on a three point bending test where the test sample is a beam with a thin notch in the middle. The test is carried out in a temperature controlled cooling bath.

After the beam has been conditioned at the test temperature in a cooling bath, it is properly placed on the bending rig with the notch facing downwards and aligned with the loading shaft. Next, a vertical loading is applied with a constant displacement rate of 0.01 mm/s on the middle of the upper side of the sample until failure occurs. The force is recorded versus displacement at different test temperatures (Fig. 1). The fracture toughness temperature (T_{FTT}) of a bituminous binder is defined as the temperature at which the displacement at maximum force is 0.3 mm (Fig. 2).

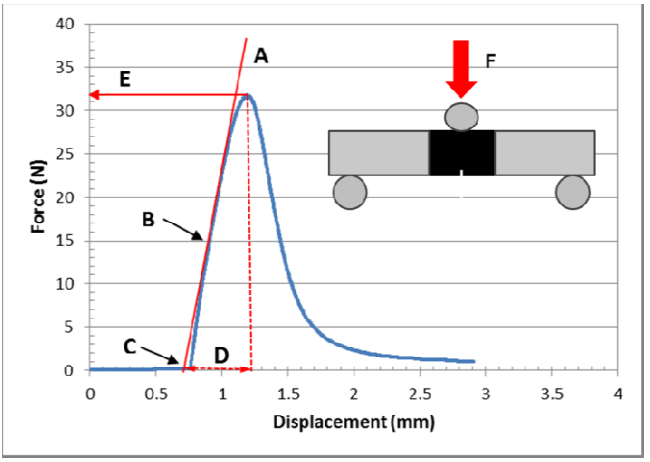

Fig. 1 Displacement curve from a fracture toughness test and scheme of bending rig. (A) Tangent at the (B) inflection point of force versus displacement, (C) zero point and (D) displacement at (E) maximum force.

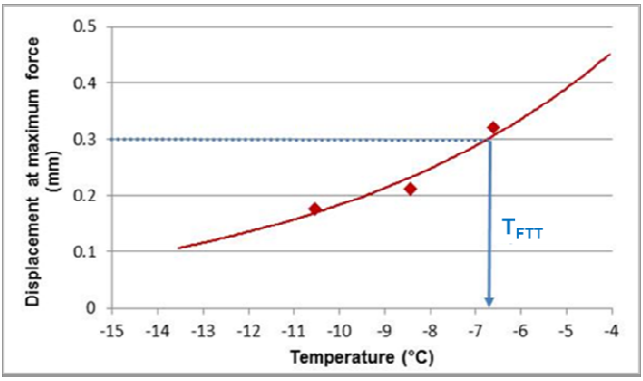

Fig. 2 Calculation of the fracture toughness temperature (T_{FTT})

A more detailed description of the experimental procedure can be found in the technical specification [13] in order to achieve a complete understanding of the fracture toughness test.

2.3 Equipment

In this work a loading system (Instron® 1122, UK), has been used to apply the bending at constant deflection speed. A 0.5 kN load cell (MTS, Switzerland) and a LVDT transducer (HBM, Germany) have been separately installed for the measurement of the force and the deflection. Data acquisition is accomplished with a Spider 8 System and Catman® software (HBM, Germany). Following the standard [13], the bending rig is placed inside a liquid bath with ethanol as cooling fluid, being circulated between the cooling unit (Huber miniStat® cc2, Germany) and the test bath at test temperature.

3 Results and Discussion

3.1 Specimen Preparation

Preparation and conditioning of the samples are important steps in testing the behaviour of bituminous binders and have direct influence on the accuracy and repeatability of the test results. For example, an irregular assembling or an inaccurate demoulding before testing can cause distortion or even break of the beams. For these reasons, specific aspects of sample preparation have been investigated in more detail and suggestions from the practical experience for improving the experimental procedure are presented and discussed in the next sections.

- **Mould Assembling**

An aluminium mould designed and manufactured by IFSTTAR (Nantes, France) assembled by different parts (Fig. 3) is used to prepare a series of ten beams at the same time. A fundamental point to consider is the adhesion between the aluminium inserts and the binder. Before every experiment, inserts have to be cleaned with toluene and afterwards with a degreasing solvent like acetone to remove any traces of oily residues present in toluene, which is produced by distillation of crude oil. In some cases, this procedure was not sufficient and the fracture occurred at the bitumen aluminium interface and not at the notch within the bitumen. Therefore, the surfaces of the aluminium inserts in contact with the bitumen have been roughened to ensure a better adhesion. After this treatment no failure at the aluminium bitumen interface was observed.

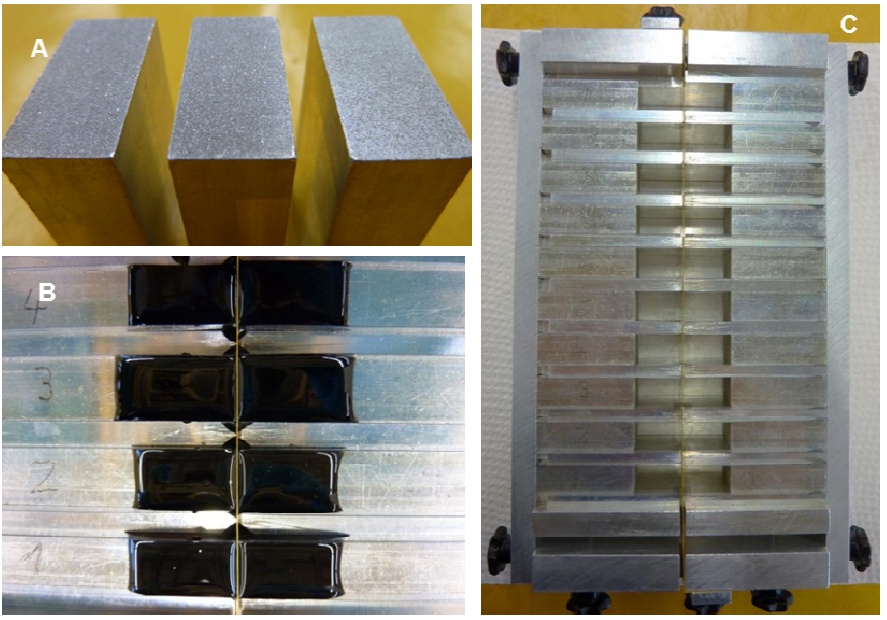

Fig. 3 (A) Roughened surface of the aluminium inserts, (B) binder specimens after pouring and (C) empty assembled mould with silicone film in the middle to form the notch

Following specifications, to prevent sticking of the bituminous binder to the different parts of the mould, plastic films (typically transparency foils) are fixed with an anti-sticking agent (Molykote® Multilub, USA) on the aluminium side spacers and on the bottom. Sometimes, just after the heating of the mould and prior to fill it, the plastic films are undulated or partially removed from the spacers. At this point, the proper adhesion between spacers and films has to be visually checked to assure a regular shape of the specimens.

- **Notch Creating**

The geometry of the notch is crucial for the fracture initiation. The narrower the notch, the more concentrated is the stress for the crack initiation at the notch. In the technical specification, a double PTFE-film of 0.025 mm thickness is processed. A double film layer is needed to make sure there is no major resistance between them when they are separated during the test. To prevent the bitumen to penetrate between the films the same anti-sticking agent Multilub is used. The PTFE-film is very soft and flexible and therefore not easy to handle. For this reason some alternative materials for the film have been tried (Table 2) and compared to the original PTFE-film.

For this study four fracture toughness tests were carried out with the same neat binder bitumen 35/50 at the same test temperature (T=-6.5°C) but varying the film material used to create the notch. The results are presented in Table 2 and plotted in Fig. 4. It can be observed that the averages of the displacement at maximum force related to each test vary between 0.25-0.37 mm depending on the tested material. However, the standard deviations are similar in all tests.

Table 2 Influence of the film material to create the notch on the repeatability

				Fracture Toughness T = -6.5°C	
Ref.	**Materials**	**Manufacturer**	**Thickness**	**Displacement**	**Stand. Dev.**
A	**PTFE Film**	Goodfellow (UK)	0.025mm	0.34 mm	0.03 mm (10%)
B	**Metal Film**	h+s Präzisionsfolie (Germany)	0.030 mm	0.37 mm	0.04 mm (10%)
C	**Coated Silicone Paper**	Hexis (Germany)	0.150 mm	0.33 mm	0.03 mm (10%)
D	**Coated Silicone Paper**	Unknown	0.080 mm	0.25 mm	0.04 mm (14%)

The results in Fig. 4 show the importance of the film material to create the notch. The thinner silicone paper D can be discarded due to its lower displacements compared to other materials and even to the other tested silicone paper C. This shows clearly, that not all silicone papers are equivalent and give the same results. This could be due to a different chemical composition of the silicone coating or the different thickness. However, the thickness of the silicon paper D with 0.080 mm is closer to the thickness of the PTFE-film (0.025 mm) compared to silicone paper C (0.150 mm). Another reason to select a material is its handling during the specimen preparation. In case of the metal film (B), despite of presenting comparable results to the others materials, some operational difficulties in the demoulding phase were encountered. Because it is rather strong, it cannot be torn by hand but has to be pre-cut with a scissor. Even then, it needs more power to separate the test beams form the mould and despite careful handling, some specimens have been destroyed during the demoulding process.

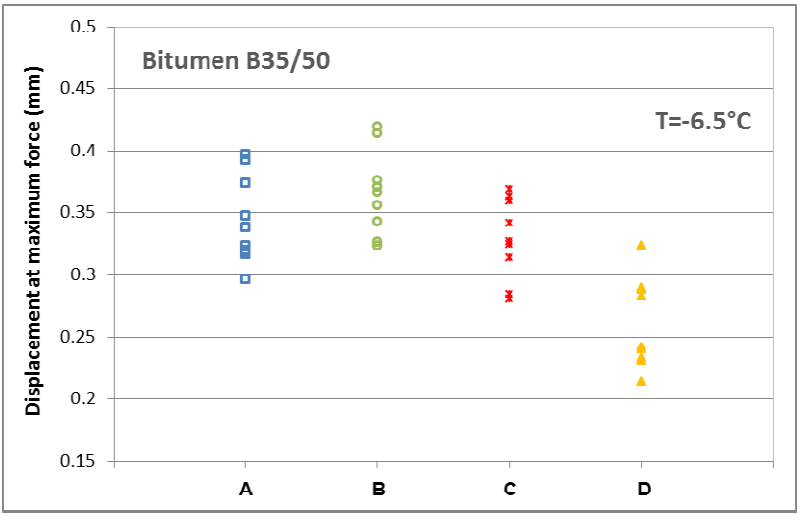

Fig. 4 Influence of the film material to create the notch on the repeatability

The silicone paper C and the PTFE film give comparable results although the paper is considerably thicker than the other materials and the created notch becomes approximately 0.300 mm (2x0.150 mm) instead of 0.050 mm, as recommended by the specifications. Nevertheless, compared to the PTFE film, the silicone paper is much easier to handle due to its higher stiffness. For these practical reasons, further testing has been carried out with the silicone paper C.

- **Demoulding Time and Temperature**

Following the specifications of the standard, just prior to demoulding, the mould containing the test specimens has to be cooled in a cooling chamber or a liquid bath to stiffen the test specimens so that they can be readily demoulded without distortion or breaking. A temperature of -20°C during 10 min is recommended by the technical specification. However, this time can significantly vary depending on the binder to test and the applied cooling temperature. For example, harder binders have to be cooled shorter during a period not longer than 10 min inside the freezer at around -15°C to avoid breakage. On the other hand, soft binders need more than 20 min or a lower temperature for correct demoulding. Due to the difficulty in defining general conditions for binders of different properties, these suggestions related to the workability of binder could be included in the technical specification to ease the experimental procedure.

- **Conditioning Time Before Testing**

Before the test, the specimens have to reach the testing temperature. According to the technical specification they are conditioned at the test temperature in the cooling bath for 60 min. When the FTT is done at several temperatures it may be necessary to have longer time between demoulding and testing. In the time between demoulding and conditioning the demoulded test specimens shall be stored on a flat surface at a temperature which is low enough to prevent creep of

the bitumen (between 2-7°C like in a laboratory fridge). However, it has to be considered that a thermal shock can occur when a beam is put in the bath at very low temperatures caused by internal stresses affecting its structure. Therefore, a progressive step-wise cooling could be superior. On the other hand, excessive conditioning in the alcohol bath at low temperatures could cause unwanted physical hardening, increasing the stiffness of the material as a consequence of wax crystallization and asphaltene aggregation [14].

The influence of the conditioning time and the possible physical hardening on the test was studied on the polymer and wax modified binder PmB 25/55-65 at -18°C. Ten specimens from the same mould were tested with three different temperature conditioning procedures: the first set was tested after three hours of progressive cooling (one hour at -12°C, at -15°C and finally at the test temperature of -18°C), the second after one hour at the test temperature and the third after four hours at -18°C.

Figure 5 shows, that for this binder no significant influence of the thermal conditioning on the results was observed. A progressive cooling or a sudden change in the temperature of the beam has no major effect on the fracture behaviour. Nevertheless, comparing the results after one hour and four hours, there is some indication that one hour of temperature equilibrium is not enough for a complete thermal homogenization of the beam. More studies on additional binders should be carried out to give a closer look at this aspect on the low temperature performance. It is possible that more temperature sensitive binders give different results.

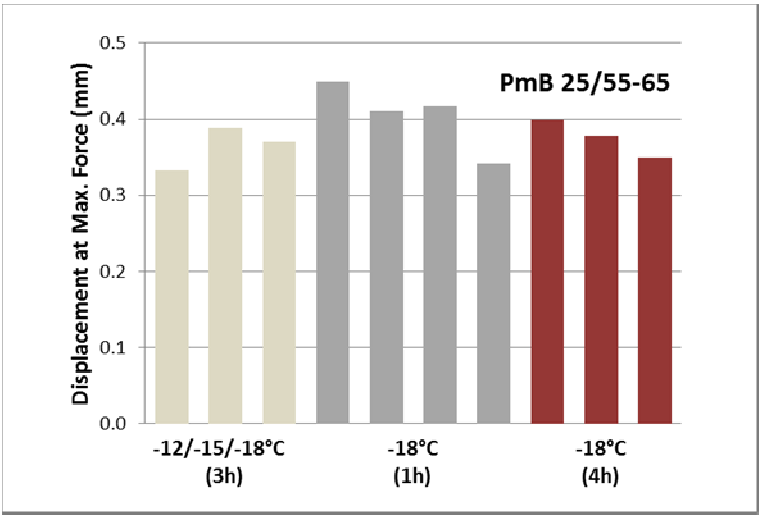

Fig. 5 Effect of the thermal conditioning procedure on fracture toughness test for three sets of specimens

- **Observation of the Fracture Plane**

The resulting fracture plane should be perpendicular to the longitudinal axis of the beam otherwise the results cannot be considered reliable. Different examples of fracture surfaces are presented in Fig. 6, from flat and quite curved fractures to complete distorted fractures. It has been observed that a centred alignment is necessary in order to achieve a plane fracture. Therefore, a mark on the inserts and/or the bending rig would be helpful to align the beam accurately in horizontal direction.

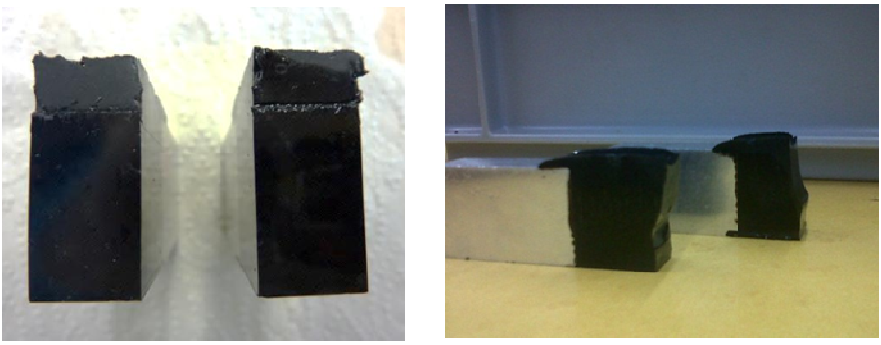

Fig. 6 Detail of different types of fracture surfaces: Flat fracture surface (left) and distorted fracture surface (right).

Furthermore, although the obtained maximum force coincides with the onset of the crack propagation, it is suggested keeping the applied load until total fracture to get a flat surface fracture. Usually, this fact can be reflected in the decreasing of the force to a value below 0.5 N.

3.2 Repeatability of FTT

The Fraass breaking point test is sometimes rejected due to its low repeatability, in this sense an analysis has been carried out to study the repeatability of the FTT. For the study, three test series of ten specimens were carried out with the PmB 25/55-65 using the Hexis® silicone paper to create the notch. All experimental parameters like conditioning time and demoulding temperature were kept constant. Specimens of test A and B were prepared form the same sample container and tested consecutively, whereas test C, coming from a different container, was tested five months earlier. Figure 7 presents the displacements at maximum force for different temperatures and Table 3 the obtained fracture toughness temperatures including average values and standard deviations.

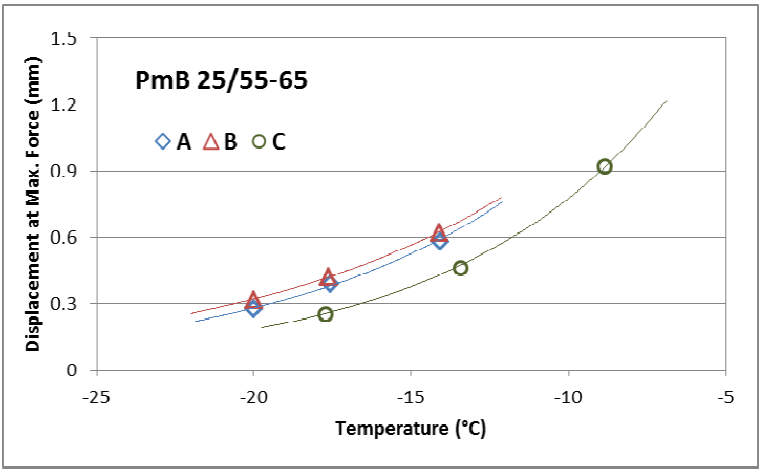

Fig. 7 FTT repeatability study using PmB 25/55-65 binder

Table 3 Results of the FTT repeatability study

PmB 25/55-65	**T_{FTT} (°C)**
Test A	-19.9
Test B	-18.9
Test C	-15.9
Average T_{FTT} (°C)	-18.3
Std. Dev. (°C)	2.1
Rel. Std. Dev.	**11.3%**

In Fig.7 it can be observed that tests A and B present quite similar results in contrast to test C, which shows shorter displacement values at maximum force at approximately the same testing temperature.

Taking into account that a polymer modified binder has been used a deviation of 11% is acceptable. However a maximum difference of 4 °C between fracture toughness temperatures obtained from identical binders would reflect that this study should be analysed in more detail. Especially, the sample preparing procedure (heating, homogenization, cooling), which is the main difference between test A, B, and C, if the homogeneity of the two tested samples is not questioned, could be the reason for this deviation.

4 Conclusions

In this work, to extrapolate to the surface road performance, the practical procedure of the fracture toughness test to assess low temperature behaviour of

bituminous binders has been studied in more detail. After some optimization of the experimental procedure, incorporating suggestions to improve it, this test has shown promising results. Practical reasons and results which are similar to the PTFE-film suggest that silicone paper can be recommended as material to create the notch in the beams. Concerning the temperature conditioning procedure prior to testing, no significant effect has been observed neither with respect to the time the sample stays at the testing temperature nor the way how the specimen was cooled from +5°C to the test temperature for the modified binder investigated. Attending to the analysis of repeatability, good results have been achieved when the samples were prepared from the same container in the same way. However, the deviations were larger when the samples were taken from a different binder batch with slightly different preparation procedure. In order to find a better understanding and assure the reliable of the results, more studies should be carried out to evaluate the repeatability of the fracture toughness test in different cases (influence of binder viscosity, ageing state as well as nature and content of the modifiers) and operational parameters (type of liquid in the cooling bath).

Acknowledgments. This study has been supported by the Swiss Federal Road Office (FEDRO). The corresponding author thanks to the Administration of Science and Technology of Castilla-La Mancha (Spain) for the postdoctoral fellowship co-financed by European Social Funds within the framework of the Regional Plan of Scientific Research, Technological and Innovation Development (PRINCET).

References

[1] Isacsson, U., Zeng, H.: Relationships between bitumen chemistry and low temperature behavior of asphalt. Construct. Build. Mater. 11(2), 83–91 (1997)
[2] Lee, N.K., Morrison, G.R., Hesp, S.A.M.: Low temperature fracture of polyethylene-modified asphalt binders and asphalt concrete mixes. J. Assoc. Asph. Pav. Technol. 64, 534–574 (1995)
[3] Hoare, T.R., Hesp, S.A.M.: Low-temperature fracture testing of asphalt binders regular and modified systems. Transp. Res. Rec. 1728, 36–42 (2002)
[4] CEN 12593, Bitumen and bituminous binders. Determination of the Fraass breaking point, European Committee for Standardization CEN, Brussels (2007)
[5] CEN 14771, Bitumen and bituminous binders. Determination of the flexural creep stiffness. Bending Beam Rheometer (BBM), European Committee for Standardization CEN, Brussels (2005)
[6] Eckmann, B., Mazé, M., Le Hir, Y., Harders, O., Gauthier, G.: Checking low temperature properties of polymer modified bitumen. Is there a future for the Fraass breaking point? In: Proceedings of 3rd Eurobitume Congress, Vienna, Austria (2004)
[7] Hesp, S.: Development of a fracture mechanics-based asphalt binder test method for low temperature performance prediction. Final report for Highway IDEA Project 84 (2004)

[8] Chailleux, E., Scholten, E., Blomberg, T., Hugener, M., Gallet, T., Büchler, S., Lancaster, I.M., Jones, A., Mouillet, V., Lorino, T.: Round robin test of the fracture toughness test for the low temperature properties of bituminous binders. In: Proceedings of 5th Eurasphalt and Eurobitume Congress, Istanbul, Turkey (2012)
[9] CEN TS15963, Bitumen and bituminous binders. Determination of the fracture toughness temperature by a three point bending test on a notched specimen, European Committee for Standardization CEN, Brussels (2010)

Evaluating the Representative Volume Element of Asphalt Concrete Mixture Beams for Testing in the Bending Beam Rheometer

Crystal Rae Clendennen and Pedro Romero

Department of Civil and Environmental Engineering,
The University of Utah, Salt Lake City, UT 84108
crystalclen@gmail.com, romero@civil.utah.edu

Abstract. This work uses three asphalt concrete mixtures with decreasing nominal maximum aggregate size (NMAS) to evaluate the validity of using the bending beam rheometer (BBR) to obtain flexural creep modulus of asphalt concrete mixture beams. Flexural creep modulus of asphalt pavement is an important property used to give insight into the cold property behaviors of the pavement. Previous research has indicated that asphalt mixtures can be tested using small beam samples (12.7-mm x 6.35-mm x 127-mm) in the BBR. Given that some of the dimensions are smaller than the aggregate used in the mixture there is a concern that significant errors would be introduced due to the influence of these larger aggregate, thus the test is not being conducted on the representative volume element (RVE). This paper evaluates this concern. To accomplish this, three mix designs with NMAS, 12.5-mm, 9.5-mm, and 4.75-mm were developed and tested in the BBR. The two smaller mixtures were developed to be scaled equivalents of the 12.5-mm NMAS with similar volumetric parameters and gradation shapes but with decreased ratio of NMAS to beam width and NMAS to beam thickness. This approach is meant to imitate the development of an RVE while maintaining the beam size of 12.7-mm width x 6.35-mm thickness x 127-mm length. A series of experiments using the BBR were performed to calculate the creep modulus of the asphalt mixture beams. Through statistical analysis it was found that creep modulus data obtained from the BBR testing come from a normal distribution with statistically equal variances across different sample groups. This means that the large aggregate mixtures resulted in no more variability than the smaller aggregate mixtures. Consequently, creep modulus data from asphalt mixture beams collected using the BBR could be used to predict the thermal properties of asphalt mixtures. Thus, based on these results, it is concluded that the small beam samples can be tested in the BBR as they meet the minimum RVE requirements.

N. Kringos et al. (Eds.): *Multi-Scale Model. & Charact. of Infrastruct. Mater.,* RILEM 8, pp. 13–30.
DOI: 10.1007/978-94-007-6878-9_2

1 Background

In freeze areas of the US and Canada many notice the premature deterioration of asphalt pavements during the cold months. This is due to improper design of the asphalt mixture to withstand these changes in temperature. The road surfaces crack leading to water intrusion and accelerated damage. Highway agencies spend billions of dollars on maintenance and repair of pavement structures due to this accelerated damage [1]. Many highway agencies are striving to find an effective way to maximize the service life and facilitate improvements of low temperature performance in asphalt concrete pavements. Performance testing of asphalt concrete mixtures is one way to address this issue.

There are many tests that have been developed to determine the cold properties of asphalt concrete mixtures. Perhaps the most common test may be the Indirect Tensile Test (IDT) [2]. The IDT determines the creep compliance of asphalt concrete mixtures and uses visco-elastic principles to predict the stresses caused by thermal gradients [3]. Through years of use and research the IDT has been greatly improved and standardized to ensure accurate results. Standardized protocols have been integrated to predict the actual asphalt pavement performance from IDT results [4]-[6]. Two other tests that have been developed to evaluate low temperature asphalt pavement properties are Thermal Stress Restraint Specimen Test (TSRST) [7]-[9], and the Disc-Shaped Compact Tension (DC(T)) Test [10]-[13]. Many researchers have investigated the applicability of these tests, while these tests have many positive features; none of them have gained popularity. Aside from research projects, none of these tests have been adopted for regular mixture testing for either design or control of the low temperature properties of asphalt mixtures. In fact, as of this writing, no highway agency has adopted any mixture test to control the quality of asphalt mixtures based on their potential for thermal induced cracking. Some reasons that a standard low temperature test has not been adopted include the amount of material needed, the cost and size of the testing equipment and refrigeration units, the complexity of data analysis or interpretation, the training of laboratory staff, and possibly others.

In 2005 Zofka and Marasteanu [14]-[17] and again in 2009 Ho and Romero [18] proposed a simple, fast, relatively inexpensive, and highly repeatable method of testing small beam specimen (12.7-mm x 6.35-mm x 127-mm) using the bending beam rheometer (BBR) customarily used for performance grading (PG) of asphalt binders. Through this research the creep compliance of the asphalt mixture can be used to control low temperature properties in a way comparable with the IDT. Ho and Romero also showed that these results can easily be used to predict thermal stresses during field construction [19], [20].

These studies have demonstrated that small asphalt mixture samples can be used to obtain mechanical properties and predict mixture behavior. Still this

approach of testing small asphalt concrete beams is met with skepticism. Critics are concerned with the beam size in relation to the maximum aggregate size. These critics are hesitant to accept that these measurement samples are in fact the RVE of the material. Velásquez et al. conducted a study to determine the effect of beam size on the creep modulus of asphalt mixtures at high, intermediate, and low temperatures [21]. In that work the beam sizes were increased to see if the size of the beams had an effect on the creep compliance. For the smallest size, the BBR was used but for the subsequent larger sizes equipment designed for the purpose of the research was designed. Velásquez concluded that the creep compliance was affected by the beam size at high and low temperatures, although Velásquez also concluded that the cold temperature fluctuation could be due to ice build up on the measurement devices and the beams themselves. This rationalizes concerns of not only beam size to maximum aggregate size ratio but also the call for proper equipment and standardization of testing.

This work addresses the concern of small beam size to aggregate size ratio through a different approach. In this work three equivalent mixtures with decreasing nominal maximum aggregate size (NMAS) were analyzed. The three different mixtures were evaluated to ensure that the mixtures were in fact equivalent by comparing the volumetric parameters and the gradations. An alternative validation was done by visually analyzing scanned images of the three mixes at the optimum asphalt content. The BBR measurements were collected from the three groups and the variances of the data groups were proven to be equal using Bartlett's Test. Bartlett's Test relies on the data being normally distributed and tests based on empirical distribution function (EDF) statistic confirmed this.

2 Representative Volume Element

The Representative Volume Element or RVE is a certain volume of the composite material that has been determined through calculation and laboratory testing to represent the global properties of the material. Traditionally an RVE is selected by starting with a sample whose smallest dimension is of nominal maximum aggregate size (NMAS); the samples are tested and the sample size is increased accordingly to obtain a normalized variability. The intent of determining if the RVE is met is to ensure that all individual materials of a composite are present for testing. For example, if we have a composite material consisting of aggregate, air, and binder, we want an RVE that contains all three components in enough quantities so that when tested, the response is dependant on all components. Take the two-dimensional example of the X-ray tomography image in Figure 1, When the representative area element (RAE) is very small the % Aggregate can vary from 0% to 100%. As the area is increased the fluctuations in % Aggregate abate and when the fluctuations stabilize this area is the RAE of the sample.

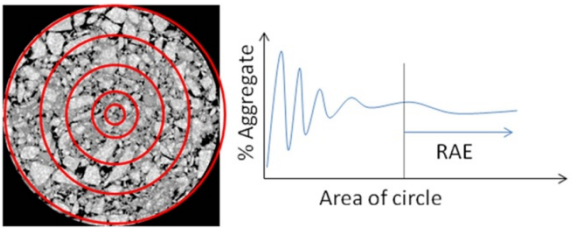

Fig. 1 X-Ray Tomography Image for RVE Conceptualization

It would be meaningless to have an RAE or RVE that has only binder and air, or binder and aggregate when there are three components to the composite. Having a volume that is not representative of the whole composite material would results in extreme fluctuations in variability of results obtained through any testing. A sample volume consisting of only air and binder would result in a very different creep modulus, for example, than a volume consisting of only binder and aggregate. Conceptually, if the variability of measured results from sample to sample is stable then the minimum requirement of the RVE has been met.

Composite theory states that in composite materials having spatial disorder with no microstructural periodicity (e.g., asphalt concrete mixtures) the determination of any stress, strain, or energy field can be measured as an average over the given domain [22]-[23]. Therefore the stress or strain recorded as part of any analysis is not the actual value experienced by a specific component but rather an average or bulk property over the given section. The question asked then is whether this averaging is done over the entire domain that includes all heterogeneities or whether it is influenced by localized phenomenon. This answer depends on the property being measured and the shape of the sample. The size of the domain that satisfies these averaging requirements is the RVE [24].

It is customary in developing the RVE to increase the size of the analyzed volume until a statistical stability is reached. As an example, consider a chain with three components: a large steel link, a medium copper link, and a small iron link as shown in Figure 2. Consider the case where a small sample of this composite material at the length shown in Figure 2 is tested in the laboratory for its elongation. Depending on the location of the sample size, the percent steel in the sample can vary between 0% (no steel) and 100% (all steel). The resulting measured elongation of this sample might result in large fluctuations depending on whether some lengths contain steel while others do not. This sample length does not represent all elements of the chain; the length represented in Figure 2 is not the RVE of this composite material. However, as the sample length is increased, the fluctuations in measured elongation due to variations in steel content greatly abate. In this case, the length at which the elongation function stabilizes is the minimum size needed to overcome the domain of small scale heterogeneity. This domain is the RVE. In general, the RVE ensures a given accuracy of the estimated property obtained by spatial averaging of the stress, strain, or energy fields in the given domain [25]. The length in Figure 3 contains all three components no matter

where on the composite structure this length is obtained. This length is the RVE (representative length element in this example).

Now consider for a moment if the sampling size must remain constant and the exact same chain were then reduced in size as in Figure 4. Now the sample size that was rejected in Figure 2 is acceptable as the RVE of the composite material. All elements of the composite material are present and the properties obtained (elongation) are representative of the composite material. If the reduction process is carried a step farther then more individual elements of the original composite fit within the constant sampling domain (Figure 5).

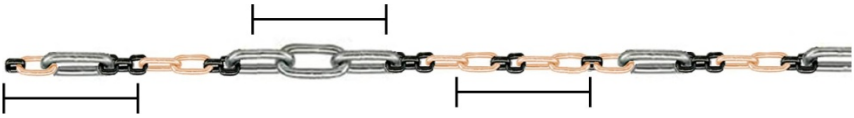

Fig. 2 Composite Chain with Non-Representative Length

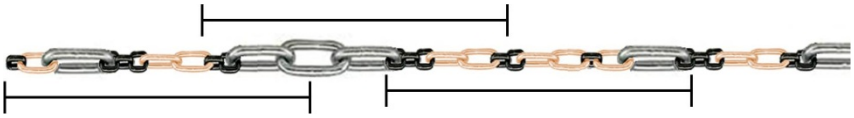

Fig. 3 Composite Chain with RVE Length

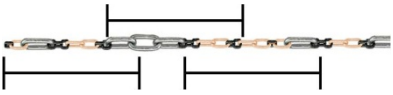

Fig. 4 Composite Chain Reduced to 45% Original Size

Fig. 5 Composite Chain Further Reduced

This is the approach used in this work. The size of the beams used in the BBR are 12.7-mm x 6.35-mm x 127-mm. Although the span of the beam sufficiently encompasses enough material to represent the mixture properties; the main concern is regarding the largest aggregate sizes to smallest beam dimension ratio. For the 12.5-mm mixture this ratio is about 1 for the width of the beam and 2 for the thickness of the beam. This means that one aggregate could take up either of these dimensions entirely as seen in Figure 6.

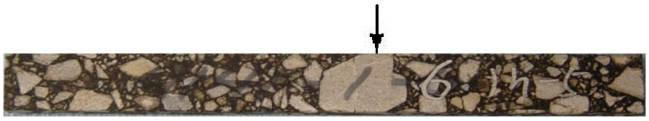

Fig. 6 Example Beam with Large Aggregate Particle

This could be a problem if the desired property being evaluated were strength, but the property that the BBR measures is flexural creep modulus, which is averaged over the gage length of the composite material. This gage length is the length

of the beam, not the width or the thickness. Therefore, in theory, it is valid to use the BBR to test mixture beams to obtain flexural creep modulus.

This work sets out to prove that the results from the BBR testing meet the RVE requirement by showing that the variance from the mixtures containing large (12.5-mm) aggregate particles is the same as the variances from the mixtures containing smaller (9.5-mm, 4.75-mm) aggregate particles. The mixtures have the same volumetric parameters (volume fraction of components) as shown, both by physical, and visual measurements.

3 Materials and Procedures

The hypothesis of this work is that the large aggregate size (12.5-mm) in the mixture does not cause an increase in variability of the creep modulus results from the BBR testing. This is proven by demonstrating that the variability of the larger mixture is equivalent to the variability of the smaller NMAS mixture. If the variability is consistent then the hypothesis is supported, but if the variability is greatly affected then the hypothesis must be rejected.

In this research hot mix asphalt was used with a 12.5-mm NMAS mix as the standard mix. The performance grade (PG) 64-34 binder was selected for use because it has low temperature tolerance and is a relatively soft binder that will allow large movements when tested. The aggregate is of high quality quartz with very low absorption, this allows for easier modification of the mix design. Asphalt concrete was chosen as a good composite material to illustrate the hypothesis because it is a material with spatial disorder and no microstructural periodicity.

Volumetric Parameters

A voids analysis is very important while developing a gradation and mix design. It is important to understand the volumetric parameters of compacted asphalt concrete mixtures for both mix design and construction control. Many mix design methods (including the Superpave mix design method, preferred by many department of transportations (DOTs) and government agencies require the volumetric parameters to be within certain ranges. These parameters help standardize asphalt concrete mix designs and achieve certain desirable properties. The percent voids in the mineral aggregate (VMA), is a measure of the space available in the aggregates for the addition of the asphalt cement. The voids filled with asphalt are called VFA and the total voids of the mix are called the VTM. Figure 7 depicts the components of the compacted asphalt mixture and the corresponding equations to calculate the volumetric parameters of the mixture.

As the NMAS of a mixture decreases the specific surface area of the mix increases therefore, more asphalt is required to maintain a constant apparent film thickness (AFT) [26]. The film thickness is referred to as apparent because within the mixture a film thickness cannot truly be measured, it can only be estimated. Although the AFT can only be estimated it can be used to generalize comparisons between mixtures. For example an aggregate with a much smaller AFT will not have the same response as aggregate with a larger AFT as is illustrated in Figure 8.

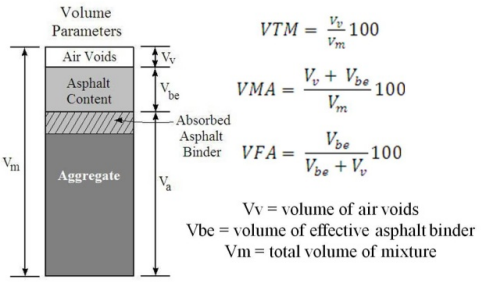

Fig. 7 Components of Compacted Mixture with Equations

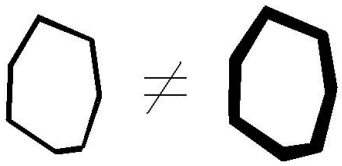

Fig. 8 Unequal Film Thickness on Aggregate

0.45 Chart Theory and Gradation

The 0.45 power chart is a common tool for Superpave gradation design. The horizontal scale is a 0.45 power function of the sieve size and the vertical scale is the percent of aggregate passing the corresponding sieve. The maximum density line on the 0.45 power chart represents a gradation of spheres of different sizes that create a mixture that has maximum theoretical density. This maximum density line is a straight line from the origin to the NMAS of the mixtures. This line represents the gradation or particle size distribution that results in the highest level of packing, thus the highest bulk density. For example, Figure 9 shows the space between large aggregate represented by theoretical spheres. The space between these large spheres is then filled with the next largest sphere size, then the next size of spheres fill the resulting spaces, then smaller spheres in the space around the those spheres, continuing into infinity into theoretical maximum density, leaving no space or voids. Decreasing the NMAS would merely shift the maximum density line to the left of the chart but still result in the same level of packing as the larger NMAS max density line that is to the right.

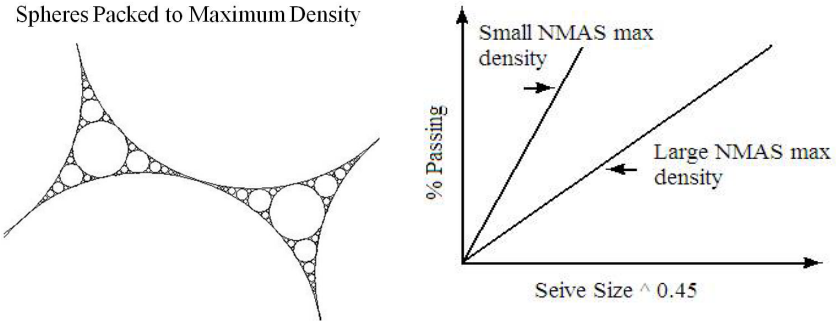

Fig. 9 Theoretical Maximum Density Example

Voids play an important role in asphalt mixture performance. There has to be enough voids in the mix to support the asphalt binder which is the glue, essentially, to keep the aggregate together. Too many voids and the mix will rut and too few voids and the mix will crack when placed in the field. An S shaped curve with respect to the maximum density line has been the preferred shape for Superpave gradation mix designs. This shape has shown good performance when used in conjunction with certain volumetric parameters.

The mixtures used in this work had NMAS of 12.5-mm, 9.5-mm, and 4.75-mm. The goal was to use the 12.5-mm aggregate gradation as the model and scale the gradation curve to the other two respective NMAS sizes. The goal was not to merely eliminate the larger particles but have actual mixes with equivalent volumetric parameters and similar gradation shapes. The shape of each gradation curve was kept similar with respect to the maximum density line as seen in Figure 10.The gradations and the volumetric properties of the mixtures used in this work are shown in Figure 11.

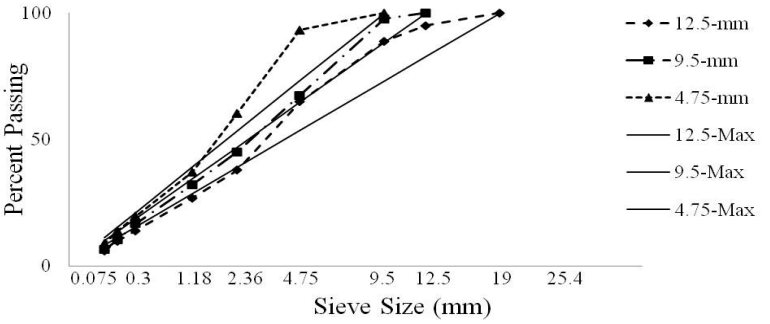

Fig. 10 0.45 Power Chart Depicting the Three Gradations Used for This Research

Mixture Design			
Seive Size (mm)	12.5-mm	9.5-mm	4.75-mm
	Percent Passing (%)		
19	100	100	100
12.5	95	100	100
9.5	89	97.8	100
4.75	65	67.5	84.9
2.36	38	45.2	60.4
1.18	27	32.2	37.3
0.3	14	16.8	19.8
0.149	10	10.6	14
0.075	6.2	6.6	9

Volumetric Properties				
NMAS (mm)	Asphalt Content	VTM	VMA	VFA
4.75	6.5	4	17.19	79.05
9.5	6.2	4	16.70	78.44
12.5	6	4	16.38	78.03

Fig. 11 Mixture Designs and Volumetric Properties for the 12.5-mm, 9.5-mm, and 4.75-mm NMAS

In theory similar shaped 0.45 gradations imply similar aggregate structure within the composite [27]. As the NMAS is reduced the amount of fines and therefore aggregate surface area increases. To match the VFA of the two developed mixes to the standard 12.5-mm mix, the binder content had to increase. This resulted in an increase in the VMA, but held the VFA constant. The goal was to keep the VFA and VTM constant, ensuring that proportionally the same amount of binder was present resulting in the same apparent film thickness on the particles. The gradation and binder content was adjusted several times through trial and error to accomplish similar gradation shape and volumetric parameters. A similar 0.45 gradation shape VMA, VTM, and VFA ensured that the mixes were essentially scaled equivalents of each other.

Bending Beam Rheometer

For this work a standard bending beam rheometer manufactured by Cannon Instrument Company was used. The BBR applies a constant load to the midpoint of a simply supported prismatic beam of, traditionally, asphalt binder. The BBR measures the deflection at the midpoint due to a constant force applied at this midpoint. This BBR system consists of a loading frame within a temperature controlled bath and a computer controlled automated data acquisition unit. The bath uses ethylene glycol as the cooling medium as required in AASHTO T313. The Cannon BBR can maintain temperatures from ambient air to -36° ± 0.03° Celsius. To perform a test, a beam is placed in the bath and loaded with a constant force of 450 grams. As the beam creeps, the deflection at the midpoint is measured. This equipment is capable of measuring at multiple times to determine the visco-elastic properties of the material. For this work the flexural creep modulus at 60 and 120 seconds was recorded for analysis. The flexural creep modulus controls the thermal stresses and is related to the damage that occurs to asphalt concrete called thermal fatigue cracking. Figure 12 shows a picture of the Cannon BBR and a diagram of the BBR simply supported beam mechanism within the temperature controlled bath.

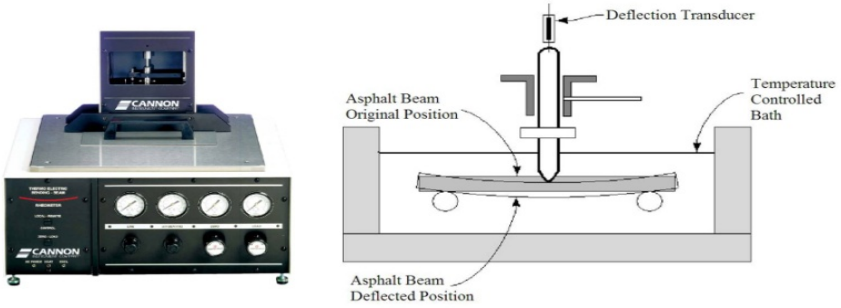

Fig. 12 Bending Beam Rheometer and Simply Supported Beam Diagram

Ho and Romero determined that twenty realizations for any one particular sample were enough to accurately represent the population composite [18]. In that study it was found that twenty samples were needed to stabilize the fluctuation in variability. Ho and Romero determined that to evaluate the variance, the minimum replicate of asphalt mixtures beams should be at least fifteen. Therefore, for this work, twenty beams cut from the same sample ensured that the properties of the mixture were accurately represented. Therefore at least twenty beams were tested from each compacted mixture. The mixture "pucks" were of standard 150-mm diameter and were compacted using a gyratory compactor. The air voids within a puck are known to have a gradient distribution, where on the edges the voids may be slightly higher than in the middle of the puck. Therefore, testing 20 beams from each sample normalizes the variability that this gradient introduces. Using a lapidary saw, these pucks were cut into blocks, after which, the volumetric parameters were measured. These blocks were frozen to reduce excess heat developed when cutting into the small beams. A standard tile saw was used to cut the blocks into beams. For more detailed, step-by-step sample preparation, please refer to Romero and Ho's work [18] - [20],

4 Homoscedasticity

Homoscedasticity, or homogeneity of variances, is where there are equal variances across samples. The hypothesis throughout this work is that all three mixtures resulted in the same variability in creep modulus. If the mixtures of these three NMAS have the same variability and volumetric properties, as discussed earlier, then it is true that for these NMAS the small beams of size 12.7-mm x 6.35-mm x 127-mm are the RVE and the data collected from the BBR can be used as descriptive properties of these mixtures. Before a test on the homogeneity of variances could be performed, it was desirable to determine the distribution of the data sets. We assume that the sample creep moduli of the asphalt mixtures are drawn from a normal distribution. Graphical analysis showed that the creep moduli fit the normal distribution well, see Figure 13; tests based on empirical distribution function (EDF) statistics also confirmed this [28]. These tests were the Kolmogorov-Smirnov D test, Kuiper V test, Cramer-von Mises W^2 test, Watson U^2 test, and the Anderson-Darling A^2 test. With a confidence level of 99%, all sample sets were found to be of a normal distribution. Outliers were not evaluated because the data sets were a good fit to the normal distribution when all the data points were included for each sample set as well as when the data sets were trimmed. Therefore, no data was excluded from any statistical test for the purposes of this research.

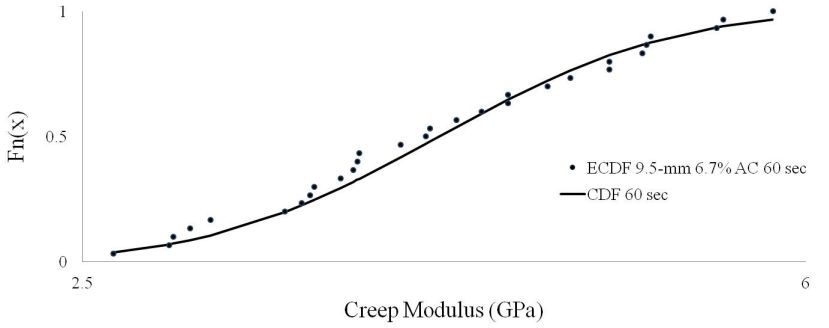

Fig. 13 Creep Modulus Empirical Cumulative Distribution Function (ECDF) and Cumulative Distribution Function (CDF) for the 9.5-mm mixture at 6.7% Asphalt Content (AC) and 60 seconds of Loading

The three NMAS groups were developed for this research to explore possible sources of variability with respect to aggregate size. If the variances of the three NMAS are equal then we know that the size of the aggregate does not affect the variability of the data and we can conclude that for the 12.5-mm NMAS the small beam of size 12.7-mm x 6.35-mm x 127-mm is in fact a representative volume element (RVE). The most robust method to evaluate for homoscedasticity is Levene's test. But if there is strong evidence that the data do in fact come from a normal distribution, then Bartlett's test has better performance [25]. Because the tests based on EDF statistics confirmed that all our data sets are of normal distribution, the Bartlett's test was selected to prove homogeneity of variances. The variable used in Bartlett's test is defined as:

$$T = \frac{(N-k)\ln\left(s_p^2\right) - \sum_{i=1}^{k}(N_i - 1)\ln\left(s_i^2\right)}{1 + \left(\frac{1}{3(k-1)}\right)\sum_{i=1}^{k}\left(\frac{1}{N_i - 1}\right) - \frac{1}{N-k}}$$

Where N is the total sample size, s_i^2 is the variance of the *i*th group, N_i is the sample size of the *i*th group, k is the number of groups, and s_p^2 is the pooled variance. The pooled variance is a weighted average of the group variances.

With significance level α the variances are judged to be unequal if

$$T > X^2_{(1-\alpha,k-1)}$$

Where $X^2_{(1-\alpha,k-1)}$ is the upper critical value of the chi-square distribution, with $k-1$ degrees of freedom. If $T < X^2_{(1-\alpha,k-1)}$ we fail to reject the null hypothesis and the mixtures have statistically equal variances. Through Bartlett's test the three sample groups fail to reject H_0. This supports our hypothesis that with the NMAS of 12.5-mm and small beam of dimensions 12.7-mm x 6.35 mm x 127-mm no more variability is introduce than for the 9.5-mm or 4.75-mm NMAS mixtures with the same beam size. Since the mixture with NMAS of 12.5-mm has

aggregate that is larger than the smaller dimensions of the beam it can be extended that when measuring the global properties of the mixture such as stress or strain the aggregate size does not have an effect on the variance of the sample group. Because the variability of the sample groups remains constant the test is not adversely affected by the large aggregate. It can be extended further that the smaller NMAS with increased number of aggregate in the small size beams do not increase the variability either.

Six other groups were developed by mixing binder sweeps of the optimum asphalt content +0.5% and -0.5% for each mixture. The null hypothesis was tested utilizing the Bartlett's test for all sample groups. This included the three optimum mixtures with asphalt content +0.5% and -0.5% with each of those 9 mixtures having creep modulus readings taken at 60 seconds and 120 seconds recorded as separate data sets. This resulted in 18 total sample groups. Bartlett's test fails to reject H_0; therefore, all 18 sample groups have statistically equal variances. Figure 14 shows the creep modulus data for the three NMAS mixtures at the optimum AC and the Bartlett's test used to prove homoscedasticity. A summary of all data can be found in Figure 17.

H_0:	$\sigma^2_{12.5NMAS} = \sigma^2_{9.5NMAS} = \sigma^2_{4.75NMAS}$							
H_A:	The three samples variances are heterogeneous							
Group	12.5 NMAS Creep Modulus at 60 sec. (GPa)		9.5 NMAS Creep Modulus at 60 sec. (GPa)		4.75 NMAS Creep Modulus at 60 sec. (GPa)		k=3	
	2.94	4.38	5.08	7.1	4.64	6.35		
	3.17	4.43	5.12	7.11	4.79	6.47		
	3.27	4.57	5.28	7.16	5.03	6.55		
	3.82	4.76	5.7	7.18	5.2	6.62		
	3.94	4.78	5.77	7.2	5.22	6.67		
	4.03	4.97	6.08	7.44	5.24	6.72		
	4.04	4.97	6.27	7.56	5.29	6.77		
	4.06	4.99	6.61	7.73	5.43	6.81		
	4.09	5.23	6.73	7.75	5.56	6.84		
	4.1	5.31	6.74	8.31	5.6	6.88		
	4.13	5.79	6.77	8.57	5.66	6.9		
	4.16	5.81	6.82	8.78	5.76	6.98		
	4.22		6.85	8.83	6.07	7.06		
			7.1		6.31	7.64		
					6.31			
N_i	25		27		29		$N = \sum N_i$	81
s_i^2	0.5392		1.0586		0.6269			
$s_p^2 = \frac{\sum_{i=1}^{k}(N_i - 1)\, s_i^2}{N - k}$							0.7438	
$B = (N-k)\ln(s_p^2) - \sum_{i=1}^{k}(N_i - 1)\ln(s_i^2)$							3.3346	
$C = 1 + \left(\frac{1}{3(k-1)}\right)\sum_{i=1}^{k}\left(\frac{1}{N_i - 1}\right) - \frac{1}{N-k}$							1.0258	
$T = B/C$	3.2508				$X^2_{(\alpha=0.05,2)}$		5.991	
Conclusion: $T < X^2_{(\alpha=0.05,2)}$, we fail to reject H_0								

Fig. 14 Bartlett's Test on Creep Modulus of the Three Different NMAS Mixtures at Optimum AC

5 Scaled Mixtures

For this work to be valid the three mixtures must be 'scaled equivalents' of each other. While volumetric measurements and 0.45 power chart shapes show this to be true, an additional visual examination was done. For this visual approach, the asphalt pucks were cut into blocks exposing the aggregate of the mixtures. These blocks were then scanned into images to digitally analyze the skeletal make-up of the mixes. The images were digitally scaled according to the physical ratios of the mixtures' NMAS with respect to each other. After digitally scaling, the images of the mixtures were visually indistinguishable. To be sure that these scaled mixtures were equivalent, the images were randomly divided into thirteen equally sized sections and the aggregate in each section was counted. If the number of aggregate in each scaled image is statistically equivalent then this further supports the assumption that the mixtures are scaled equivalents of each other.

Most of the literature can agree that the aggregate or fines passing the 0.075-mm sieve is filler and does not interact directly with the larger aggregate. Although this filler does affect some properties of the mix, for the purposes of this visual analysis, it will not be considered to affect the skeleton of the mixture. This mineral filler has an upper limit requirement of all passing the 0.6-mm sieve. Consequently, any aggregate larger than the 0.6-mm sieve could be contributing to the structural integrity of the asphalt mixture. Greene theorized that the dominant aggregate size range (DSAR) is the interactive range of particle sizes that form the primary structural network of aggregates, and for the 12.5-mm mix only particle sizes greater than 1.18-mm can be considered coarse enough to provide the particle interlock necessary to resist permanent deformation [30]-[31]. For the purposes of this visual analysis we will solely be concerned with the aggregate sizes that directly contribute to the skeleton of the mixture. This includes all aggregate larger than the 0.6-1.18 mm range. Conveniently this range of aggregate size is the smallest range that the eye can clearly see in a scanned image.

At a mid-point in the beam cutting process, each block of the optimum mixtures was scanned. The scanned images of the optimum asphalt content mixtures for the 12.5-mm, 9.5-mm, and 4.25-mm were scaled to 50%, 66%, and 100% original size, respectively; this can be seen in Figure 15. This scaling is based on the US customary measurements where the 4.75-mm = 0.25 inch NMAS, 9.5-mm = 0.375 inch NMAS, and 12.5-mm = 0.5 inch NMAS. The 0.5 inch NMAS is two times the size of the 0.25 inch NMAS and the 0.375 inch NMAS is one and one-half times the size of the 0.25 inch mix. Using the 0.25 inch mix at 100% to scale from, we scale $\frac{0.25\ inch\ mix}{0.50\ inch\ mix} = {}^{1}/_{2}$ x 100% = 50% and $\frac{0.25\ inch\ mix}{0.375\ inch\ mix} = {}^{1}/_{1.5}$ x 100% = 66%. An alternative scaling scheme could be to increase the 4.75-mm mixture x 200% and the 9.5-mm mixture x 150% and keep the 12.5-mm mixture x 100% but this scheme resulted in issues with the image clarity. The resolution of the scanned images was not high enough to support this kind of magnification. Thirteen areas of equal size and random location were selected

from each scaled image and the aggregate was counted for each area. Figure 16 depicts how an area from each mixture was cropped and magnified. This was done for all 13 areas. Any aggregate visually identifiable within a given area was tallied. If the number of aggregate counted within each area of the three mixtures was the same we can further confirm that the two smaller NMAS mixtures are in fact scaled equivalents of the 12.5-mm NMAS mix because the solids in the volume fraction images are roughly the same. The tallied aggregate were, in fact, statistically equivalent.

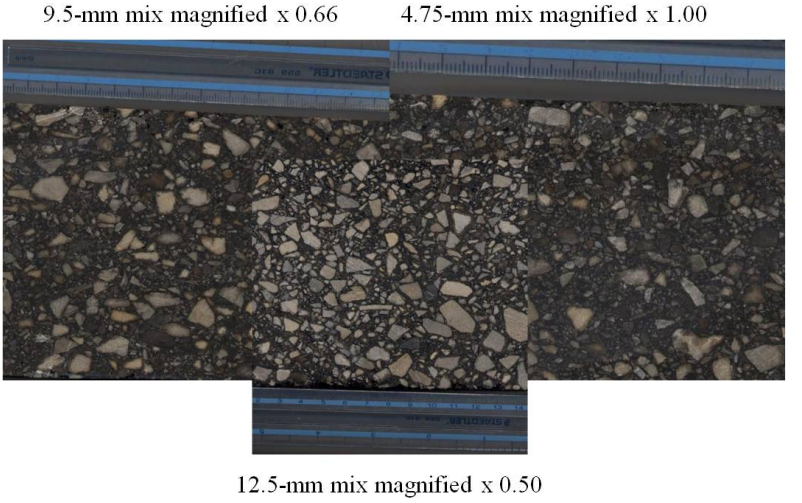

Fig. 15 Scanned and Scaled Images of Mixtures for Visual Equivalence Evaluation

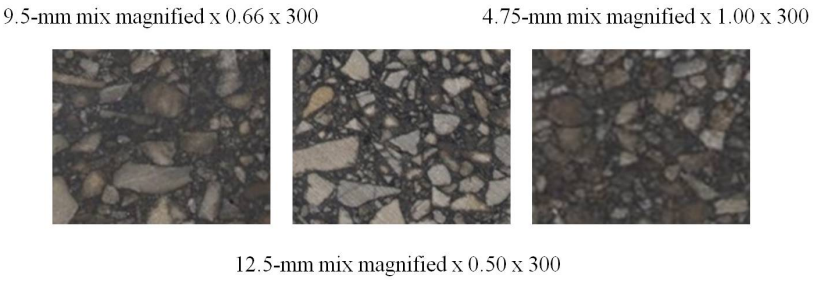

Fig. 16 One Area from Each Mixture Magnified to 300% of Scaled Image

6 Summary and Conclusions

The importance of keeping cost down while maintaining technicality is a paramount key in developing any test, standard, or specification. Most DOTs as well as research laboratories utilize the BBR and are very familiar with the operation of

the BBR. This machine can produced same day results pertaining to a mixture being put into use. That is to say, a test could be conducted on the same day as a pavement is being laid and thus give accurate, affordable, simple, repeatable, essential information about the mixture being laid. This essential information could raise awareness about inconsistencies of mixtures form day to day during the road construction, or show deviations from a mixture specification established prior to construction. Utilizing the BBR could potentially achieve this.

In this work it has been shown that three mixtures of descending NMAS can be created to evaluate if the size of the large particles affect the variability of the results obtained from BBR measurements. The results show that in utilizing the BBR to test asphalt concrete mixtures, NMAS as large as 12.5-mm do not introduce any excess variability than a smaller NMAS of 9.5-mm or 4.75-mm at the sample dimension recommended for use in the BBR (12.7 mm x 6.35 mm x 127-mm). Therefore, the 12.5-mm NMAS can be used with confidence in the BBR at the specified beam size. Let it be stressed that one puck of standard dimensions of 150-mm diameter and 100-mm height can yield close to 40 samples within dimensional tolerances. This can be achieved with a simple lapidary saw, freezer, and tile saw [18], [20].

Summary of Observations

- The sample groups in this work were found to be of normal distributions with statistically equal variances.
- Within a constant area, the 4.75-mm mixture was found to have twice the amount of solids as the 12.5-mm mixture and the 9.5-mm mixture was found to have one and a half times as many solids as the 12.5-mm mixture.
- Large aggregate taking up the entire width and/or thickness dimensions of the beams do not create outliers within the data sets because the gage length is the *length* of the beam when determining the flexural creep modulus.
- It is simple to obtain flexural creep modulus of small asphalt mixture beams using the BBR.

Conclusions

Based on this work, it is concluded that using the BBR to test mixtures could be a viable answer to getting fast, inexpensive, and crucial information about a mixture for quality control as well as incorporating parameters for cold temperature properties.

Recommendations

Based on the results from this and other similar studies, it is recommended that work be conducted to implement the BBR as a performance based test to control the low temperature properties of asphalt concrete mixtures used in cold climates. It is also recommended to use a similar approach of scaling mixtures to determine the RVE of small samples being testing in other equipment.

Summary of Data

	Data Set								
	1	2	3	4	5	6	7	8	9
NMAS (mm)	12.5	12.5	12.5	12.5	12.5	12.5	9.5	9.5	9.5
Asphalt Content (%)	6	6	5.5	5.5	5	5	5.7	5.7	6.2
Time Measured (seconds)	60	120	60	120	60	120	60	120	60
Creep Modulus Range (Gpa)	2.94-5.81	2.29-4.81	1.73-5.28	1.29-4.41	1.27-5.24	0.93-4.29	6.33-8.71	5.40-7.51	5.08-8.83
Average (Gpa)	4.40	3.51	3.77	3.07	2.99	2.36	7.68	6.57	6.95
Standard Deviation (Gpa)	0.734	0.577	0.897	0.820	0.791	0.666	0.630	0.618	1.03
Number of Samples	25	25	25	25	34	34	23	23	27

	Data Set								
	10	11	12	13	14	15	16	17	18
NMAS (mm)	9.5	9.5	9.5	4.75	4.75	4.75	4.75	4.75	4.75
Asphalt Content (%)	6.2	6.7	6.7	6	6	6.5	6.5	7	7
Time Measured	120	60	120	60	120	60	120	60	120
Creep Modulus Range (GPa)	4.43-7.82	2.65-5.84	2.07-4.86	4.21-6.30	3.45-5.30	4.64-7.64	3.91-6.58	3.95-6.76	3.19-5.56
Average (GPa)	6.09	4.23	3.43	5.29	4.42	6.17	5.25	5.17	4.25
Standard Deviation (GPa)	0.933	0.884	0.777	0.609	0.526	0.791	0.719	0.715	0.607
Number of Samples	27	30	30	22	22	29	29	26	26

Fig. 17 Basic Information on Data Sets

References

[1] Marasteanu, M., Zofka, A., Turos, M., Li, X., Valasques, R., Buttlar, W., Paulino, G., Braham, A., Dave, E., Ojo, O., Bahia, H., Willioams, C., Bausano, J., Gallistel, A., McGraw, J.: Investigation of Low Temperature Cracking in Asphalt Pavements. National Pooled Fund Study 776. Report MN/ RC 2007-43 Minnesota Department of Transportation (October 2007)

[2] American Association of State Highway and Transportation Officials. Standard Test Method for Indirect Tensile (IDT) Strength of Bituminous Mixtures. Standard Specifications for Transportation Materials and Methods of Sampling and Testing T 322. AASHTO, 29th edn., (2009)

[3] Roque, R., Hiltunen, D.R., Butlar, W.G.: Thermal Cracking Performance and Design of MIxutres Using Superpave. Journal of the Association of Asphalt Paving Technologist 64, 718–735 (1995)

[4] Lytton, R., Uzan, J., Fernando, E.G., Roque, R., Hilunen, D., Stoffels, S.: Development and Validation of Performance Prediction Models and Specifications for Asphalt Binders and Paving Mixes. SHRP Report: SHRP-A-357, Washington, D.C. (1993)

[5] Buttlar, W.G., Roque, R.: Determination and Evaluation of the Strategic Highway Research Program Measurement and Analysis System for Indirect Tensile Testing at Low Temperature. In the Journal of Transportation Research Board No. 1454, 163–171 (1994)

[6] Roque, R., Hiltunen, D.R.: Use of Canadian SHRP Test Sections to Evaluate the SHRP Indirect Tensile Creep and Failure Test for Control of Thermal Cracking. In: Proceedings of the Canadian Technical Asphalt Association, vol. XXXIX, pp. 441–464 (1994)

[7] American Association of State Highway and Transportation Officials. Standard Method for Testing Asphalt Mixtures Using the Thermal Stress Restrained Specimen Test (TSRST). Provisional Standard TP10, 2000 Edition (2000)

[8] Jung, D., Vinson, T.S.: Low Temperature Resistance of Asphalt Concrete Mixtures. Asphalt Paving Technology, Journal of the Association of Asphalt Paving Technologists 62, 54–92 (1993)

[9] Monismith, C.L., Secor, G.A., Secor, K.E.: Temperature Induced Stresses and Deformations in Asphalt Concrete. Journal of the Association of Asphalt Paving Technologist 34, 248–285 (1965)

[10] Wagoner, M.P., Buttlar, W.G., Paulino, G.H.: Disk-Shaped Compact Tension Test for Asphalt Concrete Fracture. Society for Experimental Mechanics 45(3), 270–277 (2005)

[11] American Society of Testing and Materials. Standard Test Method for Determining Fracture Energy of Asphalt Aggregate Mixtures Using the Disk-Shaped Compacte Tension Geometry. D731307-07

[12] Charmot, S., Romero, P.: Fracture Energy Evaluation of Cold In-Place Recycling Mixtures. In: Loizos, Parti, Scarpas, Al-Qadi (eds.) Advanced Testing and Characterization of Bituminous Material, Two Volume Set (ATCBM 2009), pp. 1123–1130 (May 2009) ISBN 978-0-415-55854-9

[13] Charmot, S., Romero, P.: Assessment of Fracture Parameters to Predict Field Cracking Performance of Cold In-Place Recycling Mixtures. Paper 10-1773 Journal of the Transportation Research Board No. 2155, 34–43 (2010)

[14] Zofka, A., Marasteanu, M.O., Li, X., Clyne, T.R., McGraw, J.: Simple Method to Obtain Asphalt Binders Low Temperature Properties from Asphalt Mixtures Properties. Journal of the Association of Asphalt Paving Technologists 74, 255–282 (2005)

[15] Zofka, A.: Investigation of Asphalt Concrete Creep Behavior Using 3-Point Bending Test. University of Minnesota, Minneapolis (2007)

[16] Zofka, A., Marasteanu, M., Turos, M.: Investigation of Asphalt Mixture Creep Compliance at Low Temperatures. Journal of Road Materials and Pavement Design 9, 269–286 (2008)

[17] Zofka, A., Marasteanu, M., Turos, M.: Determination of Asphalt Mixture Creep Compliance at Low Temperatures Using Thin Beam Specimens. Journal of the Transportation Research Board, No. 2057, 134–139 (2008)

[18] Ho, C.H., Romero, P.: Using Asphalt Mixture Beams in the Bending Beam Rheometer: Experimental and Numerical Approach. Paper 091027, accepted for publication in the Journal of Road Materials and Pavement Design (2010)

[19] Ho, C.H., Romero, P.: Asphalt Mixture Beams Used in Bending Beam Rheometer for Quality Control. Paper 12-1273 Journal of the Transportation Research Board. Issue 2268/2012, 92–97 (2012)

[20] Romero, P., Ho, C.H., Van Frank, K.: Development of Methods to Control Cold Temperature and Fatigue Cracking of Asphalt Mixures. Utah Department of Transportation Research Division, Report No. UT-10.08 (May 2011)

[21] Velásquez, R., Labuz, M., Marasteanu, M., Turos, M.: Effect of Beam Size on the Creep Stiffness of Asphalt Mixtures at Low Temperatures. In: Loizos, Parti, Scrapas, Al-Qadi (eds.) Advanced Testing and Characterization of Bituminous Materials, Two Volume Set (ATCBM 2009), ch. 31, pp. 313–322 (May 2009) ISBN 978-0-415-55854-9

[22] Du, X., Ostoja-Starzewski, M.: On the scaling from statistical to representative volume element in thermoelasticity of random materials. Networks and Heterogenous Media 1(2), 259–274 (2006)

[23] Ostoja-Starzewsky, M.: Materials Spatial Randomness: From Statistical to Representative Volume Element. Probabilistic Engineering Mechanics 21(2), 112–132 (2006) ISSN 0266-8920

[24] Hashin, Z.: A Variational Approach to the Theory of Elastic Behavior of Multiphase Materials. Journal of the Mechanics and Physics of Solids 11(2), 127–140 (1963)

[25] Kanit, T., Forest, S., Galliet, I., Mounoury, V., Jeulin, D.: Determination of the Size of the Representative Volume Element for Random Composites: Statistical and Numerical Approach. International Journal of Solids and Structures 40, 3647–3679 (2003)

[26] Christensen, Jr., D.W., Bonaquist, R.F.: Volumetric Requierments for Superpave Mix Design. Transportation Research Board, Washington, D.C., NCHRP Report 567 (2006), http://onlinepubs.trb.org/onlinepubs/nchrp/nchrp_rpt_567.pdf

[27] Goode, J.F., Lufsey, L.A.: A New Graphical Chart for Evaluating Aggregate Gradations. In: Proceedings of the Association of Asphalt Paving Technologist, January 29-31, vol. 31, pp. 176–207 (1962)

[28] D'Agostino, R.B., Stephens, M.A. (ed.) Goodness-of-Fit Techniques. Statistics: a Series of Textbooks and Monographs, vol. 68. Dekker, New York (1986)

[29] Zar, J.H.: Biostatistical Analysis, 4th edn. Prentice Hall (1999)

[30] Greene, J., Kim, S., Choubane, B.: Accelerated Pavement Testing of a HMA Gradation-Based Evaluation Method. State of Florida Department of Transportation, State Materials Office. FL/DOT/SMO/10-539 (December 2010)

[31] Kim, S., Roque, R., Guarin, A., Birgisson, B.: Identification and Assessment of the Dominant Aggregate Size Range (DASR) of Asphalt Mixture. Journal of the Association of Asphalt Paving Technologists 75, 789–814 (2006)

Consideration of Grain Size Distribution and Interfacial Transition Zone in the Prediction of Elastic Properties of Cementitious Composites

Francois Duplan[1,2], A. Abou-Chakra[1], A. Turatsinze[1], G. Escadeillas[1], S. Brule [2], and F. Masse [2]

[1] Université de Toulouse; UPS, INSA; LMDC (Laboratoire Matériaux et Durabilité des Constructions), 31 077 Toulouse, France
[2] Menard, 91 620 Nozay, France

Abstract. The purpose of the current article is a micromechanical-based model predicting the elastic properties of cementitious composites exhibiting low elasticity moduli. The model is generalized to composites made of a matrix in which are embedded various spherical concentric inclusions of different radi and properties.

For a given type of aggregate, the grain size distribution is divided into 1 000 discrete elements which volume fractions are determined by linear interpolation.

The following input data needs to be known: the elastic properties, the volume fractions of each phase, and the grain size distribution of each aggregate type. The effective elastic properties of the composite are obtained thanks to a loop-type computation of the analytical model described in this article.

The direct application of this model allows a comparison between experimental and predicted elastic moduli of cement-based mortars made of natural sand and lightweight aggregates.

Variables Index

Aggregate type

f_g : total volume fraction of aggregate in composite

Grain size distribution

r_k : radius

Δ_d : diameter interval

p_k : density function for percentage passing of $r_k \pm \Delta d$

Properties of phase i,g with k-number diameter

f_i^g : volume fraction of phase i for aggregate type g

r_i^g : radius of phase i for aggregate type g

N. Kringos et al. (Eds.): *Multi-Scale Model. & Charact. of Infrastruct. Mater.,* RILEM 8, pp. 31–44.
DOI: 10.1007/978-94-007-6878-9_3

k_i^g : bulk modulus of phase i for aggregate type g

μ_i^g : shear modulus of phase i for aggregate type g

$\underline{\underline{\underline{\underline{A}}}}_i^g$: localization tensor of phase i for aggregate type g

$A_i^{sph,g}$: spheric localization tensor mean of phase i for aggregate type g

$A_i^{dev,g}$: deviatoric localization tensor mean of phase i for aggregate type g

Macroscopic elastic properties of composite

k^{hom} : effective bulk modulus of composite

μ^{hom} : effective shear modulus of composite

1 Introduction

The homogenization of the linear elastic properties for cementitious composites has a long history of using micromechanics. By defining a representative elementary volume (REV) composed of inclusions and of a matrix, models based on Eshelby's solution (Eshelby 1957) are able to predict the effective behavior of the composite material when elastic, geometric properties and volume fractions of composite phases are known.

(Herve and Zaoui 1993) proposed a model suitable for n-layered spherical inclusions. It allows the consideration of various spherical phases, but they are taken into account as adherent and concentric phases. This geometry does not match with the physiognomy of cementitious composites incorporating various types of aggregates. Furthermore, this modelling method does not take into account grain size distribution of inclusions. It is well known that aggregate size distributions have an impact on elastic properties of cementitious composites (Zheng and Jin 2011).

Another approach was made by (Li et al. 1999) for concrete composed of one-type of aggregate and considered as a tri-phase composite made of aggregates, interfacial transition zone (ITZ), and cement paste. In their work, the authors calculated the composite effective bulk modulus thanks to the Christensen-Lo approximation (Christensen and Lo 1979), which is based on the self-consistent scheme. On the other hand Poisson's ratio was calculated thanks to the series mixture law. They made the comparison between numerical and experimental results from (Stock et al. 1979), with only one aggregate type.

The present contribution is based on the approach of (Li et al. 1999), but both elastic properties are calculated by applying the Mori-Tanaka (or mean field) estimate, and using two aggregate types for lightweight mortars (sand and expanded clay aggregates). The proposed model considers not only relative volume of each phase but also takes into account aggregate size distributions thanks to a two-step homogenization:

In the first step, an unitary REV is defined for each type and diameter of aggregate, and the localization tensors and volume fractions of each phase is calculated (as shown in figure 1),

In the second step, the effective properties of the composite are calculated thanks to the volume fractions and localization tensors from the first step, and the elastic properties of the corresponding phases.

This entire method, from the determination of REV dimensions to calculation of localization tensors, is described explicitly. Strains and stresses fields are developed as in (Herve and Zaoui 1993) and (Sanahuja 2008), and their averages corresponding to localization tensors are calculated as in (Sanahuja 2008).

The comparison of experimental and model-predicted results shows that they are in good agreement.

2 Model Theory

2.1 Reasoning

Actual generalized model is made of various aggregate types noted as g, which each has n-1 inclusions surrounding it and noted as i. Furthermore, letter k specifies the rank into grain size distribution.

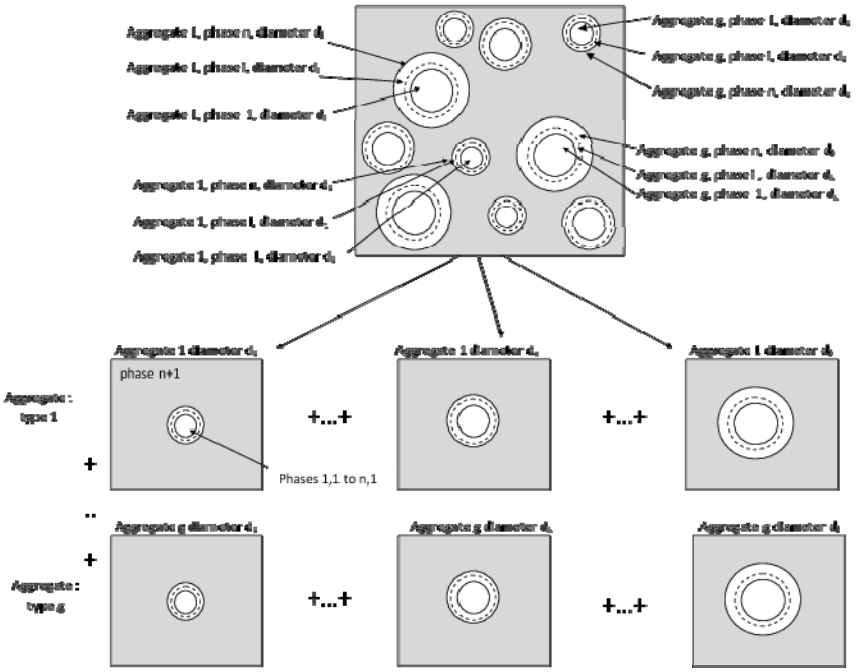

Fig. 1 Decomposition of cementitious composite into unitary REVs

As a matter of fact, grain size distribution of each aggregate type is divided into 1 000 sieves sizes of radius r_k and fraction p_k, such as in figure 2. Discretisation into 1 000 elements is made because when divided into a lower number of elements, it shows a slight influence on numerical results.

2.2 *Unitary REV Definition*

The REV of a typical inclusion with a single ITZ is described in figure 3 . The ITZ thickness is taken as a constant for each type of aggregate, as various authors such as (Scrivener and Nemati 1996) have concluded that it does not vary with aggregates size, at least for gravel or sand aggregates.

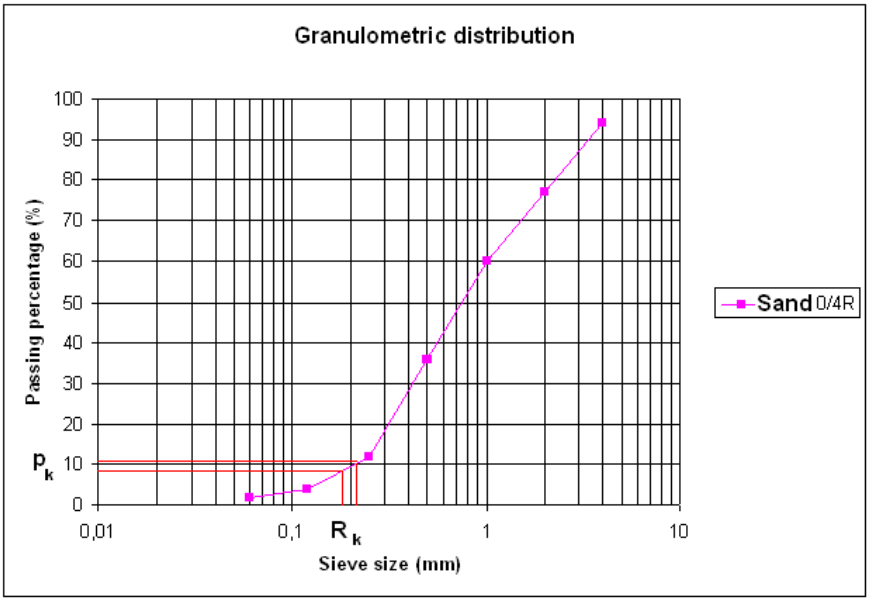

Fig. 2 Grain size distribution discretisation

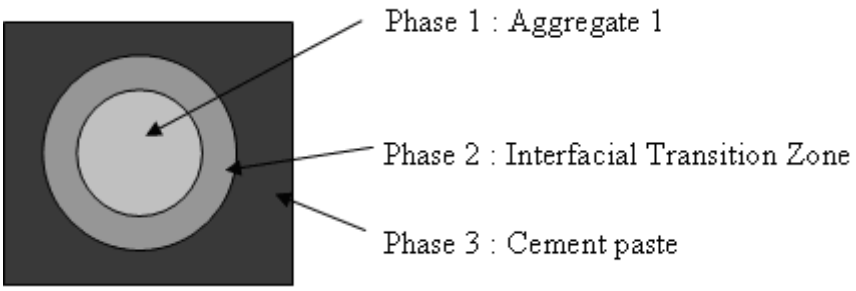

Fig. 3 Representative Elementary Volume

Each phase is defined by its external radius R_i, its shear modulus μ_i and its bulk modulus k_i , as seen in variables index. Figure 4 shows a single ITZ, but (Herve and Zaoui 1993) proved that even with n layers, average strains and stresses (and so the localization tensors) can still be calculated.

The radi and relative volumes used for modeling REVs were first determined according to equations 1 to 2 :

$$r_2 = r_1 + e_{itz} \tag{1}$$

$$r_3 = r_{2,max} = \frac{r_1}{f_g^{1/3}} \tag{2}$$

If condition $r_3 \geq r_{2,max}$ was respected, the ITZ and cement paste volume fractions were calculated as in equations 3 and 4 :

$$f_2 = \frac{r_2^3 - r_1^3}{r_{2,max}^3} \tag{3}$$

$$f_3 = 1 - f_1 - f_2 \tag{4}$$

If the past condition was not respected, the ITZ is "too thick" ; its thickness is reevaluated according to equations 5 and 6, and the volume fractions according to equations 7 and 8.

$$r_2 = r_{2,max} = \frac{r_1}{f_1^{1/3}} \tag{5}$$

$$e_{itz} = r_2 - r_1 \tag{6}$$

$$f_2 = 1 - f_1 \tag{7}$$

$$f_3 = 0 \tag{8}$$

2.3 Calculation of Spherical Localization Tensors

When subjected to an hydrostatic pressure implying an E_0 macroscopic strain to material, strains in all phase are strictly radial, and do only depend on radius, as in equation 9:

$$u_{r,i}(r) = F_i r + \frac{G_i}{r^2} \tag{9}$$

With

$u_{r,i}$: radial displacement in phase i

r : distance from REV to center

F_i , G_i : constants

Stresses can be expressed thanks to Hooke's law, as in equations 10 and 11 :

$$\sigma_{rr,i} = 3k_i F_i - \frac{4\mu_i G_i}{r^3} \tag{10}$$

$$\sigma_{\theta\theta,i} = -\sigma_{\varphi\varphi,i} = 3k_i F_i + \frac{2\mu_i G_i}{r^3} \tag{11}$$

With

$\sigma_{rr,i}$: radial stress

$\sigma_{\theta\theta,i}$, $\sigma_{\varphi\varphi,i}$: orthoradial stresses

There are two boudaries conditions :

nullity of displacement at center of REV : $G_1 = 0$

imposed displacement at n+1 phase external radius : $F_{n+1} = E_0$

With equations from interfacial continuity, which are two for each phase, an isostatic system is obtained, independently of the number of cocnentric phases.

Scalar means of spherical localization tensors are calculated from phase 1 to phase n. Spherical tensor A_1^{sph} of phase 1 is calculated with equation 12 ; equation 13 describes how to calculate this tensor for the union of phases from center to phase i (noted $A_{1\to i}^{sph}$).

Equation 14 describes how to evaluate the tensor of phase i knowing its one for union of phases 1 to i-1.

$$A_1^{sph} E_0 = F_i \tag{12}$$

$$A_{1\to i}^{sph} E_0 = F_i + \frac{G_i}{r_i^2} \tag{13}$$

$$A_i^{sph} E_0 = \frac{A_{1\to i}^{sph} - (\frac{r_1}{r_i})^3 A_{1\to i-1}^{sph}}{1 - (\frac{r_1}{r_i})^3} \tag{14}$$

2.4 Calculation of Deviatoric Localization Tensors

When subjected to simple shear , strains and stresses in phases are both radial and ortho-radial, as in equations 15 and 16 :

$$u_{r,i}(r) = A_i r - \frac{6\nu_i}{1-2\nu_i} B_i r^3 + 3\frac{C_i}{r^4} + \frac{5-4\nu_i}{1-2\nu_i}\frac{D_i}{r^2} \tag{15}$$

$$u_{\theta,i}(r) = -u_{\phi,i}(r) = A_i r - \frac{7-4\nu_i}{1-2\nu_i} - 2\frac{C_i}{r^4} + 2\frac{D_i}{r^2} \tag{16}$$

With

$u_\theta(r,i)$: ortho-radial displacement in phase i

A_i, B_i, C_i, D_i : constants

Thanks to Hooke's law, stresses can be calculated as in equations 17 and 18 :

$$\sigma_{rr,i} = A_i\mu_i + \frac{3\nu_i\mu_i B_i r^3}{1-2\nu_i} + \frac{-12C_i}{r^5} + \frac{D_i(-10+2\nu_i)}{r^3(1-2\nu_i)} \tag{17}$$

$$\sigma_{\theta\theta,i} = -\sigma_{\varphi\varphi,i} = A_i\mu_i - \frac{3\nu_i\mu_i B_i r^2}{1-2\nu_i} + \frac{8C_i}{r^5} + \frac{D_i(2+2\nu_i)}{r^3(1-2\nu_i)} \tag{18}$$

There are two boudaries conditions :

nullity of displacement at center of REV : $C_1 = D_1 = 0$

imposed displacement at n+1 phase external radius : $A_{n+1} = E_0 \qquad B_{n+1} = 0$

With equations from interfacial continuity, which are four for each phase, an isostatic system is obtained, independently of the number of concentric phases.

Scalar means of deviatoric localization tensors are calculated, same as for their spheric parts, from phase 1 to phase n.

Deviatoric tensor of phase 1 is calculated with equation 19 ; equation 20 describes how to calculate this tensor for the union of phases from center to phase i (noted $A^{dev}_{1\to i}$). Equation 21 gives the expression of phase i tensor knowing its one for phases 1 to i-1.

$$A_1^{dev} E_0 = A_1 - \frac{21B_1 r_1^2}{5(1-2\nu_1)} + \frac{4D_1(4-5\nu_1)}{5(1-2\nu_1)r_1^3)} \tag{19}$$

$$A_{1\to i}^{dev} E_0 = A_i - \frac{21B_i r_i^2}{5(1-2\nu_i)} + \frac{4D_i(4-5\nu_i)}{5(1-2\nu_i)r_i^3)} \tag{20}$$

$$A_i^{dev} E_0 = \frac{A_{1\to i}^{dev} - (\frac{r_1}{r_i})^3 A_{1toi-1}^{dev}}{1-(\frac{r_1}{r_i})^3} \tag{21}$$

2.5 *Effective Properties Calculation Based on Mori-Tanaka Estimate*

According to (Mori and Tanaka 1973), strains in matrix are those of the effective medium. Indeed, localization tensor of the matrix is different from the inclusions ones, as shown in equations 22 to 24.

$$\underline{\underline{A}}_{n+1,k}^{g} = \underline{\underline{I}}_d \tag{22}$$

$$A_{n+1,k}^{sph,g} = 1 \tag{23}$$

$$A_{n+1,k}^{dev,g} = 1 \tag{24}$$

Means of spheric localization tensors are used for calculation of bulk modulus, as in equation 25 while deviatoric ones are used for homogenization of shear modulus as in equation 26.

$$k^{hom} = \frac{\sum_{g=1}^{l}\sum_{k=1}^{1000}\sum_{i=1}^{n+1} p_k^g f_g f_{i,k}^g k_{i,k} A_{i,k}^{sph,g}}{\sum_{g=1}^{l}\sum_{k=1}^{1000}\sum_{i=1}^{n+1} p_k^g f_{i,k}^g A_{i,k}^{sph,g}} \tag{25}$$

$$\mu^{hom} = \frac{\sum_{g=1}^{l}\sum_{k=1}^{1000}\sum_{i=1}^{n+1} p_k^g f_g f_{i,k}^g \mu_i A_{i,k}^{dev,g}}{\sum_{g=1}^{l}\sum_{k=1}^{1000}\sum_{i=1}^{n+1} p_k^g f_{i,k}^g A_{i,k}^{dev,g}} \tag{26}$$

3 Experimental Mixes

Various cementitious composites were investigated, with aggregates volumes and properties varying. Tested composites included mortar and lightweight mortar. For each mortar, we tried to maintain the Water/Cement (W/C) ratio constant (so that the cement paste elastic properties remain unchanged) and adjusted it with rheology-modifying admixtures in order to maintain slump between 18 and 22 cm.

In order to consider the effective W/C ratio of the cement paste, the water absorption of aggregates was taken into account : 1.9 % for sand.

The mortars compositions are given in tables 1 and 2 ; their elastic moduli were tested according to the European standard Rilem CPC8,72 (Rilem 1972).

Table 1 Sand mortars

Relative sand volume (%)	0	20	40	62
Cement (kg/m^3)	639	510	372	242
Water (kg/m^3)	670	511	402	254
Sand (kg/m^3)	0	532	1065	1644
Filler (kg/m^3)	358	285	215	135
Viscosity agent	12	10	0	0
Super-plasticizer (kg/m^3)	0	0	0	4.73

The lightweight aggregates were pre-saturated before mixing according to their data-sheet. Their absorbed water (5 minutes water absorption) does not figure in the compositions of table 2. Lightweight mortars were obtained by substitution of sand by expanded clay aggregates from the mortar containing 62% of sand volume.

Table 2 Lightweight mortars

Lightweight aggregate substitution rate (%)	0	30	60
Cement (kg/m^3)	242	242	242
Water (kg/m^3)	254	254	254
Sand (kg/m^3)	1644	1562	1397
Filler (kg/m^3)	135	135	135
Lightweight aggregates (kg/m^3)	0	222	444
Super-platicizer (kg/m^3)	4.73	7.20	7.20
Viscosity agent (kg/m^3)	0	1.06	1.06

4 Comparison of Predicted and Measured Elastic Moduli

4.1 Input Data

Grain Size Distributions
The grain size distribution of sand and lightweight aggregates is defined by sieve sizes and passing percentages as shown in table 3.

Table 3 Grain size distributions

Sieve size (mm)	Passing (%)
0.06	0
0.30	20
0.80	50
2.20	80
4	100

Sieve size (mm)	Passing (%)
0.06	0
1	28
2	56
3.10	82
4	100

Properties of sand ITZ
(Mindess 1989) observed that the ITZ thickness varies between 50 and 100 μm, and its elastic properties vary between 40 and 60% of cement paste ones ;

(Hu and Stroeven) observed that the ITZ thickness is usually under 10 μm.

(Bentz and Garboczi 1999) observed that the ITZ thickness is about half of the median size of cement particles.

The first observation from (Mindess 1989), when compared to our own SEM observations and measurements, seemed too large for studied composites. We made the final assumption of an ITZ thickness of 5 μm, with a 50% Young's modulus of cement paste one.

Properties of lightweight aggregates ITZ
Thanks to Scanning Electron Microscopy observations, the expanded clay aggregate's ITZ was identified as inexistent, as shown in figure 4. According to (Ke et al. 2010), the high porosity of aggregates allow the cement paste to penetrate their surface and guarantees the model hypothesis of continuity for displacements and stresses. For computation of those aggregates REVs, no ITZ was taken into account.

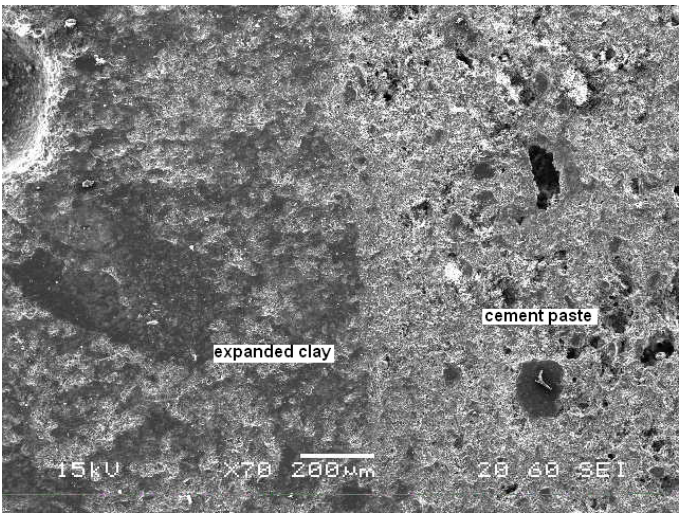

Fig. 4 Lightweight aggregate in cement paste

Properties of aggregates

Young's modulus of sand was taken as silicium's one (107 GPa), our sand being silicious.

For lighter aggregates from same production, (Ke et al. 2010) found by inverse modeling their Young's modulus to be between 8 and 12 GPa, and Poisson's ratio to be around 0,2. We chose a 12.5 GPa modulus and a 0.2 Poisson's ratio.

Poisson's ratio of sand, cement paste and sand ITZ were taken as in (Simeonov and Ahmad 1995).

All phases elastic properties are summarized in table 4 :

Table 4 Sand mortars phases elastic properties

Phase	Young's modulus (GPa)	Poisson ratio
Sand	107	0.15
Sand ITZ	3.5	0.3
Lightweight aggregate	12.5	0.2
Cement paste	7	0.25

4.2 Results

Figure 6 shows experimental and predicted results for sand and lightweight mortars.

For 0% of sand, material is uniphasic ; its measured properties were used for the computation of the cement paste properties. For 20 and 62% of sand volume, relative error is under 5%.

For 40% of sand volume, relative error is up to 19%. This point does not match with the curve general trend. This can be explained by the use of a viscosity modifying admixtures in the other mixes to guarantee the workability, stability and homogeneity of the fresh mixes. The mortar with 40% of sand volume did not contain either of those viscosity-modifying admixtures. In such conditions one should notice that the computed properties of cement paste are somewhat impacted by the effect of the viscosity agent, which has a slight but inherent consequence when modelling the properties of admixtures-free cementitious composites.

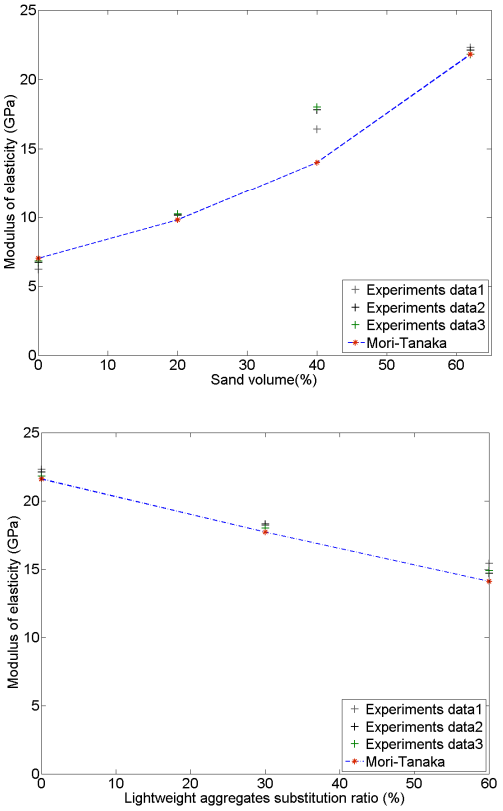

Fig. 5 Young's moduli prediction

For lightweight aggregates, relative error is under 4 %.

Conclusion and Prospects

The relative errors obtained are mainly under 5% , which is very satisfying knowing the experimental dispersion and the difficulty of identifying the actual

properties of phases such as sand grains, lightweight aggregates or ITZ. The use of this model might also be extended to others types of cementitious composites, geomaterials or bituminous composites, ...

Similar tools will be applied to self-consistent scheme in a following contribution in preparation. Furthermore such a specific estimate is expected to be more efficient to evaluate linear elastic properties of porous composites.

In an ongoing program, linear elastic behavior of phases is to be changed into elasto-plastic behavior as in (Abou et al. 2008), so that the micromechanics-calculated localization tensors can be exploited for finite element computations at macroscopic and large infrastructure scales. The comparison between those simulations and in-situ full-size testing of Controlled Modulus Columns (also called soil strengthening rigid inclusions) will be used to validate the model.

Acknowledgement. We would like to thank Menard company for their financial support and showing great interest in our work.

References

(Abou et al. 2008) Abou-Chakra, A., Cormery, F., Shao, J., Kondo, D.: A micromechanical model of elastoplastic and damage behavior of a cohesive geomaterial. International Journal of Solids and Structures 45(5), 1406–1429 (2008)

(Bentz and Garboczi 1999) Bentz, D., Garboczi, E.: Engineeering and Transport Properties of the Interfacial Transition Zone in Cementitious Composites. RILEM Publications SARL, ENSCachan (1999)

(Christensen and Lo 1979) Christensen, R., Lo, K.: Solutions for effective shear properties in three phase sphere and cylinder models. Journal of Mechanics and Physics Solids 27, 315–330 (1979)

(Eshelby 1957) Eshelby, J.: The determination of the elastic field of an ellipsoidal inclusion and related problems. Proceedings Royal Society 241, 376–396 (1957)

(Herve and Zaoui 1993) Herve, E., Zaoui, A.: N-layered inclusion-based micromechanical modelling. International Journal of Engineering Science 31(1), 1–10 (1993)

(Hu and Stroeven) Hu, J., Stroeven, P.: Properties of the interfacial transition zone in model concrete. Interface Science 12, 389–387 (2004)

(Ke et al. 2010) Ke, Y., Ortola, S., Beaucour, A., Dumontet, H.: Identification of microstructural characteristics in lightweight aggregate concretes by micromechanical modelling including the interfacial transition zone. Cement and Concrete Research 40(11), 1590–1600 (2010)

(Li et al. 1999) Li, G., Zhao, Y., Pang, S.: Four phase sphere modelling of effective bulk modulus of concrete. Cement and Concrete Research 29, 839–845 (1999)

(Mindess 1989) Mindess, S.: Interfaces in concrete. Materials Science of Concrete I, 163–180 (1989)

(Mori and Tanaka 1973) Mori, T., Tanaka, K.: Average stress in matrix and average elastic energy of materials with misfitting inclusions. Acta Metallurgica 21, 1605–1609 (1973)

(Rilem 1972) Rilem. Rilem cpc8-tc14: Modulus of elasticity of concrete in compression. Materials and Structures 6(30) (1972)

(Sanahuja 2008) Sanahuja, J.: Impact de la morphologie structurale sur les performances mécaniques des matériaux de construction: application au plâtre et à la pâte de ciment. Phd Thesis, Annex C

(Scrivener and Nemati 1996) Scrivener, K., Nemati, K.: The percolation of pore space in the cement paste/aggregate interfacial zone of concrete. Cement and Concrete Research 26, 35–40 (1996)

(Simeonov and Ahmad 1995) Simeonov, P., Ahmad, S.: Effect of transition zone on the elastic behavior of cement based composites. Cement and Concrete Research 25(1), 165–176 (1995)

(Stock et al. 1979) Stock, F., Hannantt, D.J., Williams, R.I.T.: The effect of aggregate concentration upon the strength and modulus of elasticity of concrete. Magazine of Concrete Research 31(109), 225–234 (1979)

(Zheng and Jin 2011) Zheng, J., Jin, X.: Numerical method for predicting young modulus of concrete with aggregate shape effect. Journal of Materials in Civil Engineering 23, 1609–1615 (2011)

Multi-scale Characterization of Asphalt Mastic Rheology

Ebrahim Hesami, Ali N. Ghafar, Björn Birgisson, and Niki Kringos

Division of Highway and Railway Engineering, Transport Science Department,
KTH Royal Institute of Technology, Sweden

Abstract. Understanding the influence of the fundamental parameters on asphalt mastic rheology is an important step towards improving the quality of asphalt mixtures. Due to the size of fillers and the sensitivity of the rheological behaviour of mastic, it is not always possible to study the effect of all parameters at one scale. Hence in this study, a theoretical framework is established for calculating the relative viscosity of asphalt mastics as a function of its filler concentration. Furthermore, a new test protocol is introduced for measuring the viscosity of asphalt mastic at higher temperatures and different filler concentrations. To characterize the fillers and their agglomeration and distribution inside solid mastics, X-ray tomography, laser scattering, scanning electron microscopy, BET and Helium Pycnometery were utilized. To characterize the energy dissipation potential of the mastics under cyclic loads, as a function of their fillers, the dynamic mechanical analyzer was utilized. The research shown in this paper further investigated the various dominant parameters related to fillers and bitumen in mastics and relate them to the workability and resulting mechanical properties and developed an overall framework to connect different scales. The developed characterization protocols have the potential to allow the asphalt engineers to design their hot and warm asphalt mixtures on a more fundamental and thus sustainable basis.

1 Introduction

Asphalt mixtures are complex composite materials build up from a mixture of aggregates, bitumen, fillers and additives. As such, the end performance of asphalt mixtures entirely depends on its component's properties, their interaction with to each other and the surrounding environment. Variation in the quantity and quality of the components is, unfortunately, quite normal and has a significant effect on the material's long term performance. Understanding the effect of the individual material components is thus essential for correctly designing asphalt mixtures to meet desirable structural and surface requirements [1-5]. In addition to the base components, there are many other parameters which can be controlled that have a high impact on the ultimate performance of asphalt mixtures.

N. Kringos et al. (Eds.): *Multi-Scale Model. & Charact. of Infrastruct. Mater.,* RILEM 8, pp. 45–61.
DOI: 10.1007/978-94-007-6878-9_4

Being a composite material, also means that the way the mixture is handled and constructed has a large impact on the resulting behavior. In the case of hot mix asphalt (HMA), this means that the material will be heated initially when mixing the components to ensure that the mastic viscosity is reduced sufficiently to coat the aggregates. Then, upon the time of paving, the mixture is heated up again to ensure sufficient workability and compactability. The relationship between the chosen temperatures and the material properties will thus affect the resulting mixture properties. In the case of warm mix asphalts, the use of additives and their interaction with the fillers and bitumen is chosen today, rather arbitrarily and is uncoupled to the short term workability and the long term sustainability demands.

Currently, most mastic parameters are chosen mainly based on experience and measurements of the viscosity of the bitumen only. Yet many parameters have a significant influence, such as aggregate size distribution, filler size distribution, filler agglomeration, mastic viscosity and physicochemical interaction between the aggregates and the asphalt mastic. Studying the influence of all these parameters also means that several scales need to be investigated.

As viscosity of asphalt mixture is a complex phenomenon, for predicting and/or measuring the workability and optimizing the long term field response of asphalt mixtures it is crucial to clearly understand the effect of all the dominant parameters and be able to measure them. To do so, in this research the asphalt mastic phase (i.e. the filler-bitumen mixture) has been identified as an important phase that can be linked to the bitumen level as well as the asphalt mixture level. For the bitumen-mastic connection, the effect of the bitumen viscosity, the filler properties and the filler-bitumen interaction are important aspects to consider. For the mastic-asphalt concrete mixture the mastic properties (from the previous scale), the aggregate properties and the interaction between the two are important. The latter, though part of the overall research project, will not be treated in this paper.

2 Research Aim

In this paper, focus is placed on determining the fundamental parameters which have influence on the rheology of asphalt mastics and evaluating their effect. To do so, first a theoretical framework is established for calculating the relative viscosity of asphalt mastics as a function of its filler concentration. Then, a new test protocol is introduced for measuring the viscosity of asphalt mastic at higher temperatures and different filler concentrations. Subsequently, the results obtained from this viscometry tests are utilized for evaluating the theoretical framework. To be able to understand the underlying mechanism of the measured mastic behavior, the physical properties of the fillers were measured and compared with their corresponding mastic viscosity. To investigate the agglomeration of filler particles after mixing with bitumen, a detailed X-Ray CT analysis is performed. Finally, to

investigate the energy dissipation of the mastic under cyclic loading after cooling down, a new test set-up was developed utilizing the dynamic mechanical analyzer.

3 Theoretical Framework

According to the basic theory, the viscosity of any material can be calculated by dividing the applied shear stress by shear strain rate (equation 1).

$$\eta = \frac{\tau}{\dot{\gamma}} \tag{1}$$

The relationship of shear stress and shear rate for a Newtonian material is linear. For non-Newtonian material this relationship is non-linear, so calculating the viscosity of non-Newtonian material can be a more challenging task. Asphalt mastics at elevated temperatures behave as non-Newtonian suspensions in which bitumen plays the medium role and fillers are act as particles. Suspensions behave differently at varying particle concentration levels, due to a change in the flow profile of the suspension due to presence of particles, causing the non-linear behavior.

In addition to the particle concentration, as mentioned earlier, there are several other parameters that can affect the viscosity of suspensions. Most of the theories which are available for calculating the viscosity of suspension are restricted to certain assumptions and are not necessarily able to model the behavior of mastic at the relevant range of filler concentrations. For this reason a framework was established, based on available theoretical models, to be able to calculate the viscosity of the mastic from dilute to high concentrated suspensions [6].

This framework divides the suspension viscosity behavior into two general regimes: the hydrodynamic and the frictional regime (figure 1) [7]. In the *hydrodynamic* regime, at lower filler concentrations, particles are positioned far from each other, forming thus a so-called dilute suspension. At higher concentration, particles come into a closer position but still do not have any direct filler-filler contact. In the *frictional* regime fillers come into direct content and make a network of filler-filler contacts. In this regime the frictional force is dominant.

As is illustrated in figure 1, in the hydrodynamic regime there are two models that can asymptotically model the mastic relative viscosity, which is the viscosity of the mastic at each concentration divided by viscosity of the neat bitumen. The Einstein formulation (equation 2) and the Frankel formulation (equation3) can be used for lower and higher filler concentration, respectively. Yet there is a gap between the low and high concentrations, which is not covered either by Einstein nor by the Frankel equation. For this zone a transition equation (equation 6) was created to be able to connect the lower filler concentrations to the higher filler concentrations.

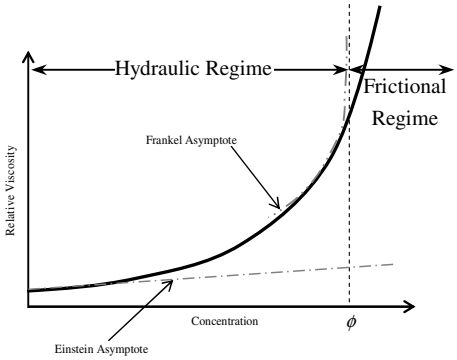

Fig. 1 Relative viscosity versus concentration bounded by two asymptotes

$$\eta_r = 1 + k\phi \tag{2}$$

$$\eta_r = C' \left\{ \frac{\left(\frac{\phi}{\phi_{max}}\right)^{\frac{1}{3}}}{1 - \left(\frac{\phi}{\phi_{max}}\right)^{\frac{1}{3}}} \right\} \tag{3}$$

$$h = 2r \left[\left(\frac{\phi}{\phi_{max}}\right)^{\frac{1}{3}} - 1 \right] \tag{4}$$

$$h_r = \frac{h}{r} \tag{5}$$

$$\eta_r = C \left(\frac{1}{h_r}\right)^n \tag{6}$$

where η_r is the relative viscosity, k is the Einstein constant, ϕ is the filler concentration, C' is the Frankel constant, ϕ_{max} is theoretical maximum concentration which there is no any free binder in the mastic, r is the is the average weighted radius of the particles, C and n are transition constants and h_r is the average distance between filler grains.

As the fillers come into contact, they form frictional interactions which gets activated upon shearing of the mixtures. So by using the concept of primary and secondary aggregate structures, equation 7 was defined for calculating the relative viscosity of the mastics in this regime.

$$\eta_r = \left(\frac{\delta}{r} - h_r\right) N_c C_1 \tag{7}$$

where δ is the adsorbed asphalt layer thickness, the term of (δ/r-h_r) shows the strength of contact. N_c is the number of particles and it shows the number of contacts which are producing the friction force and C_1 is the friction coefficient of the whole particles structure [7].

4 New Protocol for Measuring the Viscosity of Asphalt Mastics

After establishing and testing the framework it was necessary to measure the viscosity of asphalt mastic at elevated temperature for a wide range of filler concentrations. Considering that such measurements should be able to clearly identify the effect of various parameters, the robustness, reliability and repeatability of the test should be assured. It was therefor decided to develop a standardized protocol in which the dominant parameters are clearly defined.

The *temperature* is certainly an important parameter, which has a significantly effect on viscosity values. In two stages in the developed test protocol temperature plays an important role: during the filler and bitumen mixing and during the actual measurement. The latter one is more often controlled than the first, but since asphalt mastic is a history dependent material, the entire handling and temperature treatment should be controlled as much as possible. Furthermore, during the mixing process, an optimum temperature is needed to provide suitable bitumen viscosity. So, all mastic samples were mixed at the same temperature (140˚C), to reduce the temperature effect of the mixing procedure. This temperature was chosen such that it would be appropriate for mixing the bitumen and fillers at all percentages. Mixing of the bitumen with the fillers was done with a mechanical high shear mixer.

Due to the influence of particle size on the viscosity of mastic, it is important to have a good control on the homogeneity of the filler size. To make sure for all samples that the filler size distribution is the same and segregation does not have any effect on the filler size, sufficient amount of filler for all samples were collected and stirred to ensure a representative filler distribution. Then, the filler was divided into different portions for the mastic samples. At that point filler was placed in the oven for 24 hours to get completely dry and also heated up to the mixing temperature.

Because of the importance of the volumetric characteristics of the fillers and bitumen, the amount of filler content was calculated by volume instead of weight. The weight of volume for a specific concentration was calculated by measuring the density of the fillers and the bitumen at the temperature at which the mastic viscosity will be measured. For calculating the concentration of filler a volumetric calculation was made:

$$\phi = \frac{V_F}{V_b + V_F} \tag{8}$$

Where V_F is the volume of filler and V_b is the volume of bitumen.

Adding filler to the bitumen is an action which seems simple, but can also affect the rate of agglomeration. Agglomerated particles make a bigger artificial particle that can act as coarser filler. For this reason, the adding procedure of the fillers to the bitumen was also standardized as much as possible to avoid introducing additional variables into the mixtures.

Air pockets or enclosed bubbles are an unfortunate reality from the mixing process and can have a significant effect on the viscosity. Air bubbles can be introduced into the mastic during the filler adding into mastic mixing process. Therefore, to prevent adding air bubbles into the mix, the filler was gradually spread in the bitumen during the mixing. The mastic was kept in an oven at 140˚C for 2 hours to give the samples time to release any remaining air bubbles. To ensure a homogeneous mixture, the mastic was mixed again at the relevant test temperature before pouring mastic into the cup of the viscometer.

Deciding on the appropriate viscometer cylinder geometry is quite challenging since various geometries are available on the market, but for converting the measured torque and velocity to the correct shear stress and shear rates, some considerations must be made. First of all, some of these geometries are suitable for Newtonian material and others for non-Newtonian. The theoretical equations for calculating shear stress and shear rate usually are based on the assumption that the material moves instantly with the inner cylinder. This means that the system should not have any slipping on inner and outer cylinder wall. The zero shear, or plug, zone is also a non-negligible phenomenon that can occur for some stiffer mastic or for very low shear rate test.

To satisfy all the above conditions, a rotational co-axial viscometer was utilized. This viscometer was found to be able to apply the accurate range of shear stress at different magnitudes for measuring the mastic viscosity with a varying range of viscosity, relevant for mastics. Due to varying flow behaviour of the tested mastics with the different filler concentration, accurate measurement should be possible when mastics display a different type of behaviour such as Bingham flow, shear thinning or thixotropy. For this reason a viscometer was chosen, able to use different geometries and procedures. The geometry and the gap between inner and outer cylinder were chosen very carefully to avoid the influence of the boundaries on the measurements.

The DIN standard (3219:1993(E)) gives the geometry of inner rotor for Newtonian materials (figure 2-c). In this standard, the converting equations are based on the assumptions of dealing with a Newtonian material. As such, the shear stress gradient in the gap between inner and outer cylinder is considered linear, there is no plug zone and no slippage on the wall of inner and outer cylinder. From these assumptions, the limitations of using the cylindrical rotor are considerable.

Bitumen is in principle a Newtonian material. But, when increasing the filler concentration, mastic starts to behave more non-Newtonian. From the particular filler concentration that this behavior is noted, the use of the cylindrical rotor to measure the viscosity is no longer appropriate. This, firstly, because of a boundary bias which starts to occur at that point, and secondly, because the penetration of

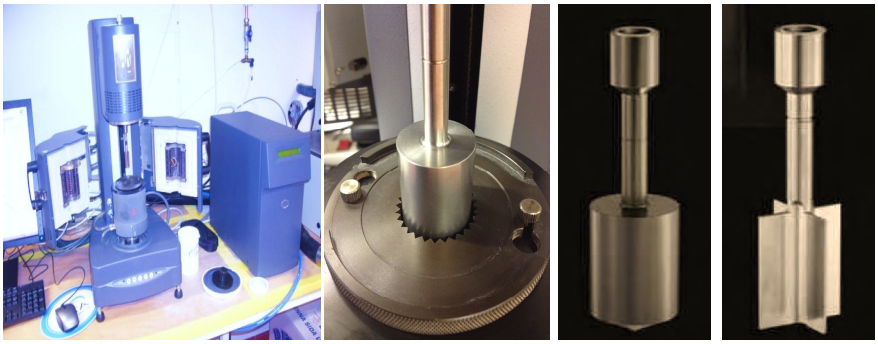

(a) (b) (c) (d)

Fig. 2 a) The TA Rheometer (viscometer), b) grooved cup, c) cylindrical rotor and d) vane shaped rotor

the inner cylinder or rotor becomes more difficult for stiffer mastics. Lastly, slippage on the wall of the inner cylinder must be prevented, the risk of which becomes quite high for the cylindrical geometry at the higher concentration. For these reasons, a vane shaped rotor (figure 2-d) was chosen in this study for the higher filler concentration. The range of filler concentration for using the two rotors can vary from one type of mastic to the other and it is highly depended on the filler size. From the tested mastics, however, most of the mastics showed that around 20% filler concentration can be a suitable boundary for shifting from cylindrical rotor to a vane shaped rotor.

As mentioned earlier, bitumen is a visco-elastic material and its rheological behaviour is highly depended on the temperature. So, maintaining the accurate temperature during the measurement is crucial. The test temperature can be designed according to the aim of the test. There are, however, some limitations for choosing the test temperature when testing mastics. According to Stokes' law the speed of sedimentation of particles inside a liquid is a function of the weight of the particle and the viscosity of the liquid. Hence, the combination of higher temperature and longer testing time may increase the risk of filler sedimentation. On the other hand, if the testing temperature is too low, the viscosity result may not be representative of or relevant for the viscosity behaviour of bituminous mastic, especially for modified bitumen. To deal with this issue all mastic viscosity measurement were done at 100˚C.

5 Material Selection

In this research, for studying the effect of different fillers and filler concentrations, an extensive laboratory program was performed. The fillers were selected to enable the study of a range of parameters, such as filler chemistry, surface area and particle shape on the viscosity of the mastic. Hence, three different types of mineral fillers were selected; two silica based filler (M10 and M600) and fly ash. For

all samples presented in this paper, a standard 70/100 bitumen from Nynas was used. Silica based fillers have a completely different angular shape compared to the rounded fly ash particles. M10 and M600 are both from silica based mineral. M600 is, however, much finer than M10, having thus a much higher surface area and, consequently, behaving very differently in terms of bitumen-filler interaction and agglomeration. The mastic samples were prepared with different filler content ranging from 5% to 50% or more, depending on stiffening effect of the filler on the bitumen.

6 Filler Fundamental Properties

To analyze the characteristics of the selected fillers scanning electron microscopy (SEM), laser scattering, BET (Brunauer, Emmett and Teller theory) and helium absorption were used to determine shape, size distribution, specific surface area and density, respectively.

Figure 3 shows examples of pictures captured by SEM from all fillers. As figure 3-a and 3-b show, M10 and M600 have similar angular shapes, however due to their different size the particle interaction is different, leading to a varying agglomeration. Figure 3-c and 3-d shows this difference. Fly ash filler, figure 3-e and 3-f, has a round shape particle that makes it completely different from the two other fillers in terms of shape.

Laser scattering is one of the possible methods for measuring the size and size distribution of particles with diameter less than 2 mm. In Figure 4 the size distribution of the three fillers measured by laser scattering is shown.

The phenomenon of physical adsorption of gases was taken up the BET to determine the specific surface area of fillers. Measurement of specific surface area of M10, M600 and fly ash by Micromeritics Gemini 2360 Surface Area Analyzer gave 0.93, 4.0 and 1.5 m^2/g respectively (Table 1). To determine the density of the fillers, their weight was determined by an accurate scale and their volume by a Helium Pycnometer. According to test results from the Helium Pycnometer the densities 2.79, 2.75 and 2.41 kg/cm^3 were obtained for M10, M600 and fly ash respectively (Table 1).

7 Filler Agglomeration in Asphalt Mastics

The filler phase in asphalt mixture gradation is most often noted as the mineral particles which have an average diameter below 63 µm (or 73 µm in American standards). From figure 4, however, it can be seen that a wide filler size range was measured, which may affect the mastic rheological behavior. Additionally, it is interesting to know to what extend the fillers form clusters after they are mixed in the bitumen.

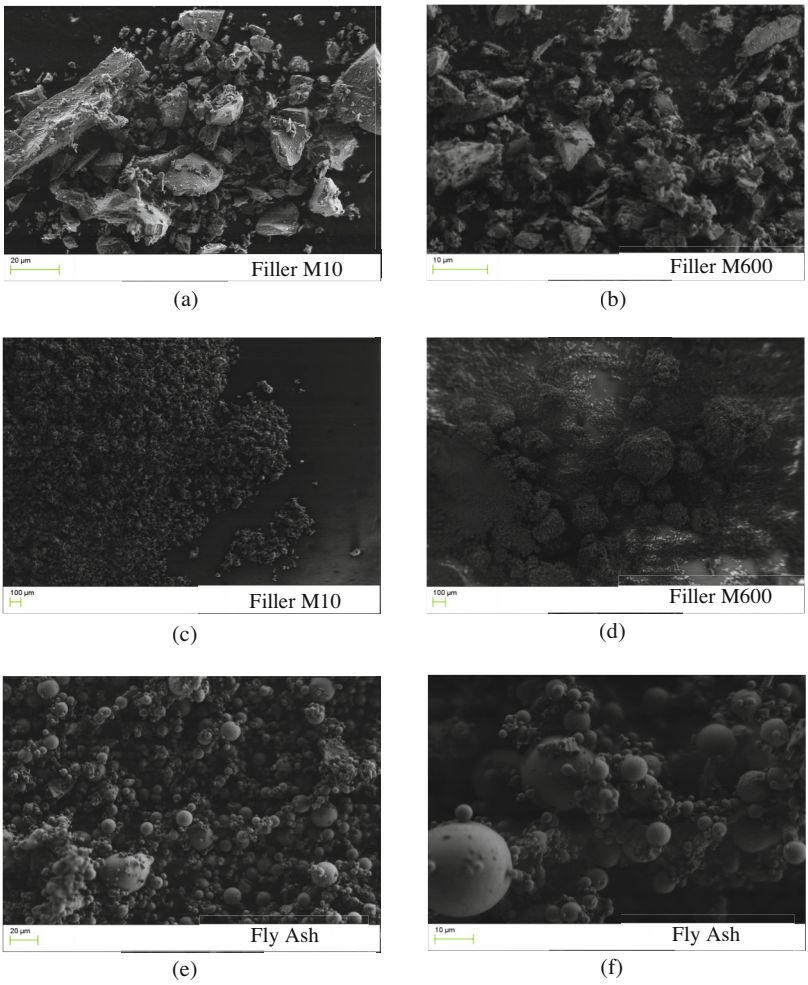

Fig. 3 SEM photograph of fillers, a) M10, b) M600, C & d) comparison agglomeration between M10 & M600, e & f) fly ash

To study if the particles agglomerate in the bitumen and how much this agglomeration would affect the actual filler gradation, X-ray computed tomography was used to scan the mastic samples. The 3D X-ray images were then analyzed to measure the volume and size of the filler inside the bitumen mastic and represented in a sieve-size graph to compare to the original filler before mixing. Several samples were prepared with bitumen 70/100 and 30% filler (M600) volumetrically and poured into specially designed silicone molds (figure 5). The sample size is important for the necessary resolution of the scans, so the size of the mold was chosen small enough for the X-rays to be able to capture the fillers as much as possible with good accuracy and big enough to provide suitable data for

the statistical analyzing, Figure 6. To avoid erroneous conclusions due to resolution issues, the measured mineral volumes were calculated and compared to be equal to the actual amount as measured from the sample preparation.

The X-Ray image sieve analyses showed a different size of fillers compared to what was measured at the filler's dry stage. As can be seen from the graph, the filler gradation shifted to the right side (coarser side) of the dry filler gradation curve, which indicates the amount of filler agglomeration inside the samples, Figure 6. As can be seen from the graph, the agglomeration is really significant which means that the actual filler concentration will be quite different from what the mastic is originally designed for, had the filler distributed evenly. From the analyses it was also found that the distribution of the fillers within the mastic was not homogeneous and, as can be easily seen with the bear eye in Figure 5, part of the larger filler particles seem to sediment toward the bottom of the sample.

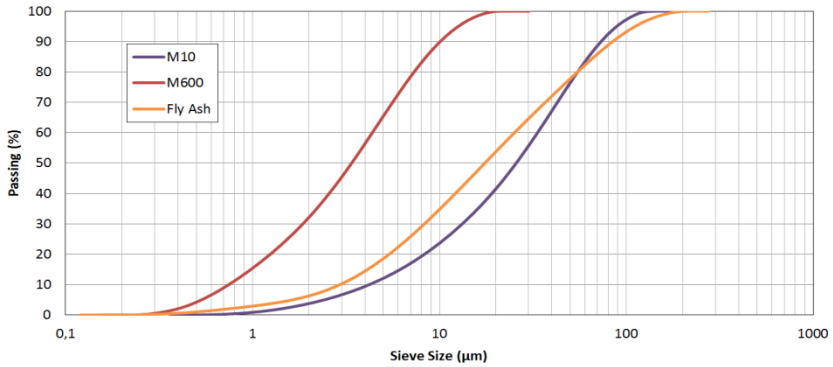

Fig. 4 Filler size distribution for M10, M600 and fly ash

Table 1 BET and Helium Pycnometer results

	M600	M10	Fly Ash
Specific surface area (m^2/g)	4.0	0.93	1.5
Density (kg/cm^3)	2.75	2.79	2.41

8 Viscosity Result Utilizing New Protocol and Framework Validation

To measure the viscosity of the mastics and relate them to the filler properties, several asphalt mastic samples were prepared. In both sample preparation and testing steps of the viscometry, the presented protocol was followed. Figure 7 shows an example of the viscosity result for mastics at different filler concentrations. This figure shows the relationship between shear stress and shear rate for

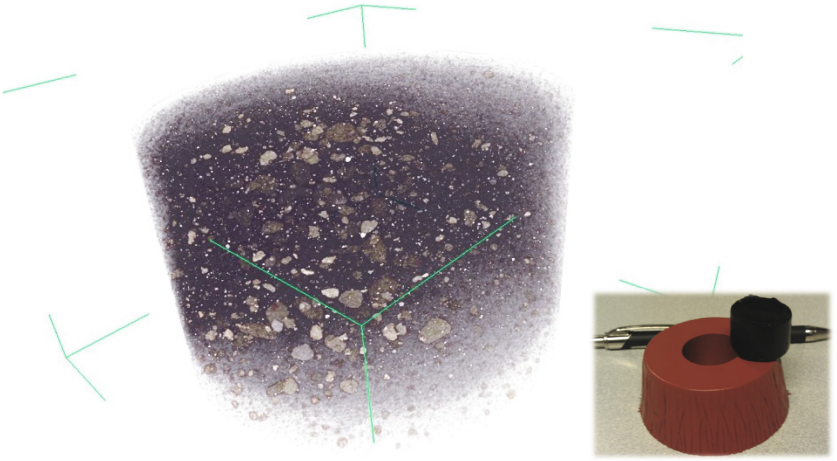

Fig. 5 Illustration of filler agglomeration, M600, and actual scanned specimen & its silicon mold

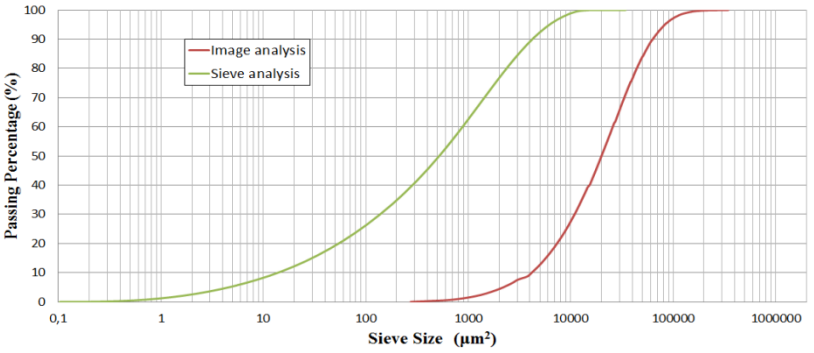

Fig. 6 M600 gradation before and after mixing

mastic with filler M600. As can be seen from the graphs, a clear increase of the viscosity of the mastics as a function of filler percentage was measured.

Figure 8 shows the relationship between relative viscosity and filler concentrations at 1.5(1/s) shear rate for three different mastics. The relative viscosity of each filler concentration was calculated by dividing the viscosity of mastic with that particular concentration by the viscosity of the neat bitumen. Figure 8 shows the final viscometry result for all the filler concentrations (from 5% to 50%). It is important to note, however, that for each curve two type of rotor geometry were used. As it discussed earlier for mastics with filler concentration lower than certain concentration (about 20%), the cylindrical inner rotor was used; and for higher than that concentration the vaned rotor was used. In all cases a good connection between the transfer point of these rotors was found in the measurement.

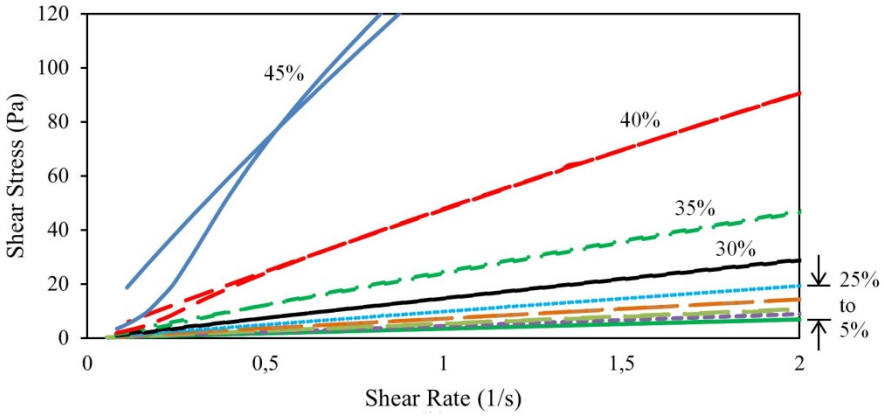

Fig. 7 An example of viscosity results, shear stress vs. shear rate for mastic M600 at different filler concentrations

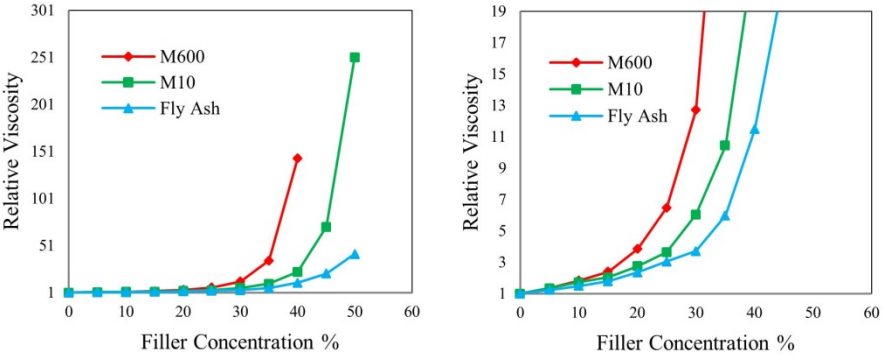

Fig. 8 Relative viscosity of mastics at 100 C and 1.5 1/s shear rate with combination of cylindrical and vaned rotor (left: complete graphs, right: focused on lower concentrations)

From the measurements the highest relative viscosity for a certain filler concentration was seen with the M600 filler, which is the finest filler with a high surface area and angularity, followed by the mastics with M10 and fly ash fillers. From the first two mastics it can be concluded that with the same mineralogy, but increasing surface area, viscosity will increase. The comparison between the viscosity result of the mastics containing M10 and fly ash shows the effect of shape of filler. The spherical particle of fly ash inside the bitumen under shear stress are rotating and rolling more easily, giving less resistance to flow compare with angular particle of M10.

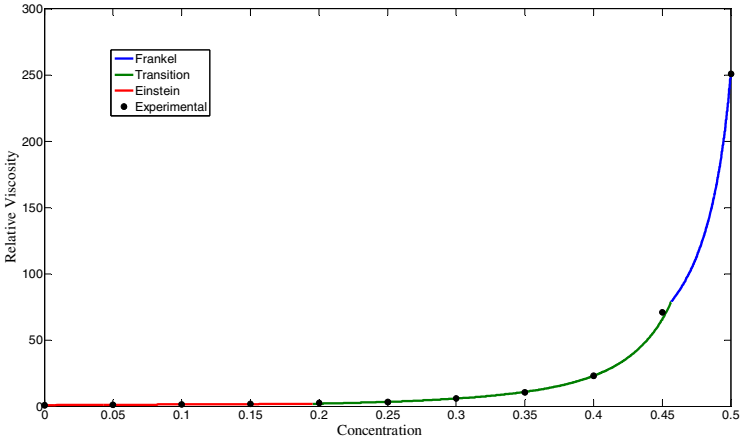

Fig. 9 Fitting the framework into the experimental results

Figure 9 shows that a good agreement between the experimental result and the developed theoretical framework was found. The fitted framework is able to capture all experimental results quit well; however still makes use of fitting parameters which are presented in table 2. From this it can be noted that a clear distinction can be made between the mastics and that the framework can uniquely describe the behavior of the mastics over a wide range of concentrations. While the fitting factors shows same trend, finding the physical explanation for these factors is the aim of the ongoing project.

Table 2 Fitting parameters

Fitting Parameters	M 10	M 600	Fly Ash
Φ_m	0.5	0.4	0.6
C'	2.8	3.5	3.6
C	1.5	1.4	1.5
n	1.5	1.7	1.8
K	7.8	8.8	5.1

9 Energy Dissipation of Asphalt Mastic

To investigate the mechanical property of the mastics as a function of the varying filler types and concentrations, the ability of the mastics to dissipate energy is an important property to characterize the mastics. To be able to measure this it is important to vary the train rates in a controlled manner and to create a uniform stress field inside the materials. For this, a new test set-up is being developed that

will enable the loading of mastic samples under a uniform stress and strain field and measure their ability to dissipate energy. For this, a DMA Q800 set-up (Figure 10-a) is being utilized and a special sample holder is developed that allows for the required stress and strain fields. In order to increase the accuracy of the sample preparation and reduce the effects of stress concentration on the corners of the rectangular cross section, the standardly available film tension clamp was modified by designing and appending two external parallel ring & plates (Figure 11-a). Consequently the shape of the specimens was changed to a cylindrical shape. Furthermore, in order to mold the specimens with accurate dimensions, a silicon rubber mold and a fixture were designed and built as Figure 11.

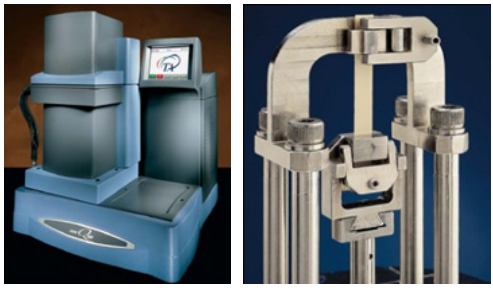

(a) (b)

Fig. 10 Apparatus for measuring energy dissipation, a) DMA Q800, b) film tension clamp

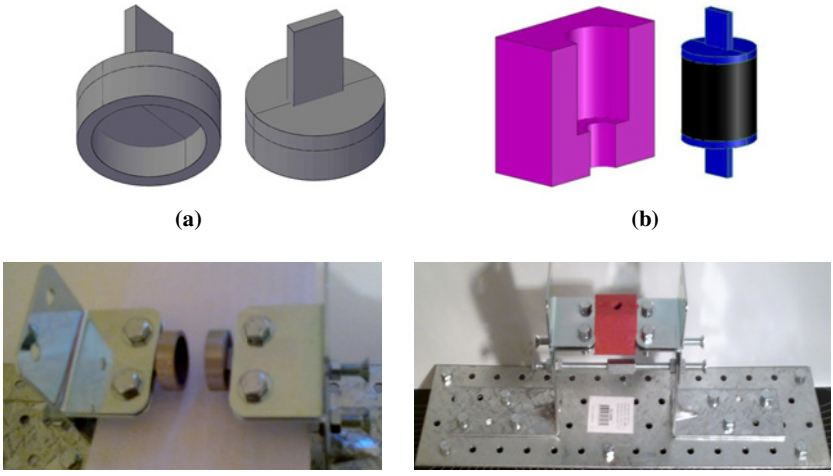

(a) **(b)**

(c) **(d)**

Fig. 11 a) external parallel ring & plate, b) silicon rubber mold, c) ring & plate in the fixture and d) whole set up

The test is currently still under development, but some preliminary test results are shown in Figure 12. In this graph the displacement versus time is plotted for mastics with different concentrations of fillers. The applied stress field was intended to be a haversine in the tension domain. From the initial analyses it showed that the applied force-field is not yet as needed for the mastic test as is therefore not further shown here. Nevertheless, from the initial results one can see that the test is able to have a first indication of the behavior of mastics, and that the effect of the different filler particles is visible from the test. The development of this test will be further worked upon in the current research project, which will allow for a detailed analyses of the mastic behavior under varying (operational) temperatures and will be linked to its rheology behavior at 100 Celsius. From this the effect of the particle size, distribution and interaction will become clear and will allow for an optimizes mastic design, taking into account the workability of the mastic and the long term performance under the service stress-strain and temperature conditions.

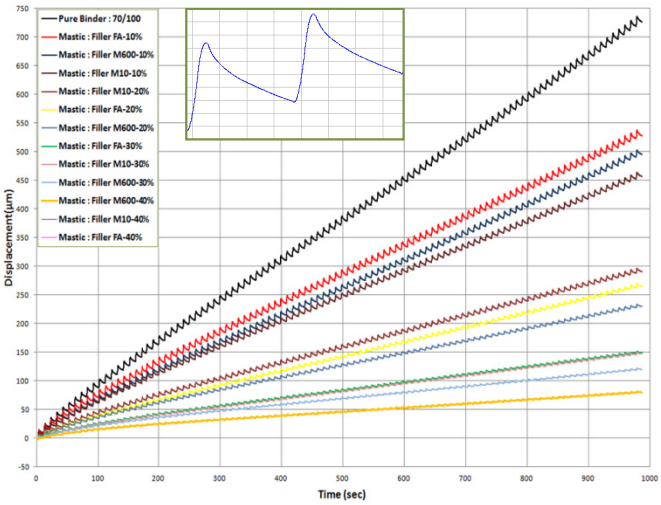

Fig. 12 Comparison of Displacement-Time curves for mastics with different concentration of filler M10, M600 and Fly Ash

10 Conclusion

In this study, theoretical and experimental techniques were utilized for evaluating the effect of fillers on the rheology of asphalt mastics. A theoretical framework was established that is capable of calculating the viscosity of asphalt mastics at different filler concentrations in two hydrodynamic and frictional regimes. The framework was extensively validated and a new protocol to measure the actual

viscosity of mastics with different concentrations at higher temperatures was developed. To have a reliable and reputable test the relevant parameters that can affect the viscometry were standardized. To study the effect of the different properties of filler on mastics rheology, three different types of fillers were selected that enable the systematic study of a range of parameters, such as filler chemistry, surface area and particle shape on the rheology of the mastic.

From the measurements it was found that, as M600 is much finer than M10, the M600 has more internal interaction between the particles and showed more agglomeration in the unmixed situation. X-ray tomography also showed that the filler inside the bitumen does not have the same gradation as unmixed. The filler gradation inside the mastic is shifted entirely to the coarser part of graph, which shows the effect of filler agglomeration. The mastic with the finer filler, M600, showed the highest value of viscosity for each concentration, followed by M10 and Fly ash. Fly ash and M10 almost have the same size, however due to the spherical shape of the fly ash particle it showed a lower viscosity compared to M10. The viscometry result also showed that the mastic with higher filler concentration is not Newtonian anymore. So for measuring the viscosity of mastic with higher filler concentration (more than 20%), a vaned rotor was used. Initial measuring of the energy dissipation of asphalt mastics showed that mastics with higher filler concentration have lower visco-elastic energy dissipation potential under dynamic loading. Partly this could be due to the diminished amount of visco-elastic binder (i.e. the bitumen), since the volumes are kept the same. Other reasons for this could be the non-visco-elastic particle-particle interactions at higher concentrations and the increase of bitumen-filler interaction. The mastic energy dissipation test is, however, still under evaluation and not too many conclusions can yet be drawn from its current results. In the continuation of this research, the test will however serve as an important step in linking the production stage behavior of the mastics with the actual long-term field performance.

References

1. Delgadillo, R., Bahia, H.: Effects of temperature and pressure on hot mixed asphalt compaction: field and laboratory study. Journal of Materials in Civil Engineering 20(6), 440–448 (2008)
2. Yildirim, Y., Solaimanian, M., Keunedy, T.: Mixing and Compaction Temperatnres for Superpave Mixes. Association of Asphalt Paving Technologists 69, 34–71 (2000)
3. Bennert, T., Reinke, G., Mogawer, W., Mooney, K.: Assessment of Workability and Compactability of Warm-Mix Asphalt. Transportation Research Record 2180, 36–47 (2010)
4. Gudimettla, J., Cooley, L., Brown, E.: Workability of Hot-Mix Asphalt. Transportation Research Record 1891, 229–237 (2004)
5. Tayebali, A., Malpass, G., Khosla, N.: Effect of mineral filler type and amount on design and performance of asphalt concrete mixtures. Transportation Research Record 1609, 36–43 (1998)

6. Hesami, E., Jelagin, D., Birgisson, B., Kringos, N.: Towards a New Experimental and Numerical Protocol for Determining Mastic Viscosity. In: Scarpas, A., Kringos, N., Al-Qadi, I., Loizos, A. (eds.) 7th RILEM International Conference on Cracking in Pavements. RILEM Bookseries, vol. 4, pp. 103–114. Springer, Heidelberg (2012)
7. Hesami, E., Jelagin, D., Kringos, N., Birgisson, B.: An empirical framework for determining asphalt mastic viscosity as a function of mineral filler concentration 35, 23–29 (2012)
8. Kim, Y.R.: Modeling of Asphalt Concrete, 1st edn. Mc Graw Hill, Raleigh (2009)
9. Lee, K.W., Mahboub, K.: Asphalt Mix Design and Construction: Past, Present, and Future, 1st edn. American Society of Civil Engineers, Reston (2006)

Integrating Physicochemical and Geochemical Aspects for Development of a Multi-scale Modelling Framework to Performance Assessment of Cementitious Materials

Yogarajah Elakneswaran and Tetsuya Ishida

Department of Civil Engineering, University of Tokyo, Japan

Abstract. A robust and reliable model has been required to take into account the fundamental physicochemical and geochemical reactions resulting due to detrimental effects during the service-life of concrete structures. A multi-scale model developed by Concrete Laboratory at the University of Tokyo is extended in this study by coupling geochemical code PHREEQC with the model. The newly developed multi-scale modelling framework capable of addressing physiochemical and geochemical processes in cementitious materials such as hydration of cement particles, pore structure formation, multi-species transport, activity effect, ionic interaction with cement hydrates, etc. In addition, it provides a better understanding of the underlying mechanisms, which govern the degradation of cementitious materials. The model predictions for composition of cement hydrates and porosity are quantitatively compared with experimental results obtained in the literature. The capability of the model in evaluating the performance of cementitious materials in various aggressive environments is addressed. The simulation results predict the spatial and time variation of solid phases, pore water compositions, pore structure properties, etc. Thus the developed multi-scale framework can potentially be applied to assess long-term durability of concrete infrastructures.

1 Introduction

The deterioration of cementitious materials in concrete structures is causing concern over the world today. The long-term service life of infrastructures can be achieved through improved quality control materials, methods, and design and construction practices. A detailed knowledge is essential on these aspects, and this knowledge need to be incorporated into models for understanding the phenomena and hence for predicting the actual service life of the structures. There are number of models have been developed to provide much information on the degradation behaviour of concrete [1-5]. Further, many reports have been published on multi-species transport and coupling the transport with geochemical models [3-5]. However, the developed models unable to predict the hydration and microstructure properties of cementitious materials with time, and they need a

N. Kringos et al. (Eds.): *Multi-Scale Model. & Charact. of Infrastruct. Mater.,* RILEM 8, pp. 63–78.
DOI: 10.1007/978-94-007-6878-9_5

large amount of experimental data as the input to the model. A multi-scale simulator, which was developed in Concrete Laboratory at the University of Tokyo Japan, can predict the state of the concrete from its birth to entire life [1]. Figure 1 shows a schematic representation of the multi-scale simulator for materials and structures [1]. Physicochemical states of substances in nano-micro levels are greatly associated with macroscopic characters of concrete composites. The simulator is able to predict the performance of concrete structures in aggressive environments. For very accurate prediction however, additional mechanisms and processes affecting the performance should also be incorporated into the multi-scale simulator. The main objective of this study is development of a model, which can precisely predict the long-term performance of cementitious materials in various environments. Durability concrete code DuCOM, which is the main part of the multi-scale simulator [1], and geochemical transport code PHREEQC, which is designed to perform variety of geochemical calculations including equilibrium between minerals and solution, ion exchanges, surface complexes, solid solution, and gases, [6-7] will be used to achieve this purpose. The developed model will consider not only the hydration of cement particles and the transport of multi-species into cementitious materials but also the chemical interaction of multi-species with cement phases simultaneously. Further, the model is capable of predicting spatial and time variation of physical and chemical properties of the materials as well as determining the chemical degradation due to

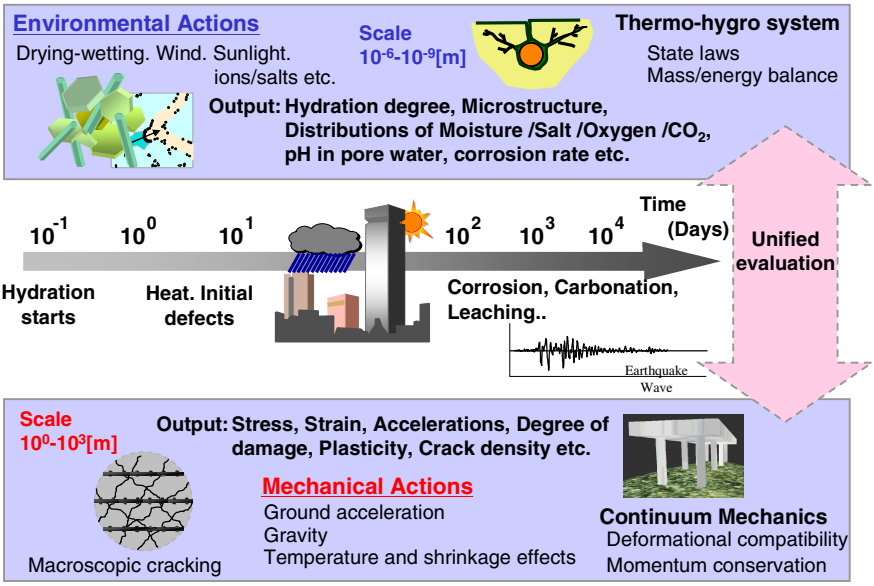

Fig. 1 Multi-scale scheme and lifespan simulation for materials and structures [1]

ingress of detrimental ions. The basic theory behind the ionic transport and geochemical reactions, framework of the model, and coupling procedures of DuCOM and PHREEQC will be presented briefly in this paper. In order to evaluate the model, some of simulation results will be compared with experimental data available in the literature. Further, the coupled model is applied to evaluate the long-term performance of cementitious materials in various aggressive environments.

2 Description of the Model

PHREEQC has been integrated with other programs to perform geochemical calculation. The new IPhreeqc module is designed for coupling of PHREEQC with other programming languages [8]. IPhreeqc module can easily interface with other programming languages and PHREEQC can run without reading or writing files. The data can transfer between PHREEQC and other program through internal computer memory. This kind of process has merits on calculation time and programming because IPhreeqc preserve computed results between time steps rather than redefining PHREEQC for each time step. IPhreeqc provides direct access to geochemical processes in PHREEQC through a library.

It has been proved that DuCOM can predict hydration, pore structure formation, ionic transport in cementitious materials, etc. very well [1]. However, the current DuCOM system cannot perform geochemical reactions simultaneously with above calculations. On the other hand, PHREEQC can perform geochemical and speciation calculation. Further, it can do the same kind of calculation in cementitious materials also [4-5]. However, it cannot predict the hydration or pore structure formation in cementitious materials. In addition, it needs a lot of parameters such as physical and chemical properties (amount of cement hydrates, pore solution composition, etc.) as input to the model. Therefore, DuCOM needs to be coupled with PHREEQC to perform wide range of calculation and for the prediction of cementitious materials in aggressive environments. In this section, set of equations that need to be solved for finite element analysis and coupling procedures are briefly described.

2.1 Governing Mass Balance Equation

The transport of ions into concrete is due to advection and diffusion. The ions are free to move in the liquid medium or bound to solid phase. The governing equation in this phenomenon can be expressed as follows [1-2]:

$$\frac{\partial(\phi \cdot S \cdot C_{ion})}{\partial t} + divJ_{ion} - Q_{ion} = 0 \tag{1}$$

where Φ = porosity; S = degree of saturation of porous media; C_{ion} = concentration of an ion in pore solution; J_{ion} = total flux of an ion; and Q_{ion} = sink term.

In Equation 1, the first term represents the rate of change in total amount of ion per unit time and volume, the second term gives the total flux due to both diffusion and advection, and the last term called the sink or source term which represents the rate of removed or precipitated ions by reactions. The Equation 1 is to be solved for numerical analysis of ionic ingress into concrete. It is considered that the transport of ions in gel and capillary pores. Therefore, porosity, Φ, is the sum of gel and capillary porosities.

2.2 Transport of Multi-species

The ions in a solution have an effect from the co-existing ions. Thus, diffusion coefficients of cations, anions, and neutral species in a solution have different values. However, most of the models to calculate the ionic transport into concrete assume the same diffusion coefficient for all the species. Diffusive flux of ions considering concentration and electrical potential gradients, and chemical activity effects in porous media can be expressed as follows (Nernst-Plank equation) [9]:

$$J_{ion} = -\phi \cdot S \cdot \left(\frac{D_{ion}}{\Omega} \cdot \delta\right) \cdot \left[\frac{\partial \ln(\gamma_{ion})}{\partial \ln(C_{ion})} + 1\right] \frac{\partial C_{ion}}{\partial x} - \phi \cdot S \cdot \frac{F}{RT} Z_{ion} C_{ion} \left(\frac{D_{ion}}{\Omega} \cdot \delta\right) \frac{\partial \psi}{\partial x} + \phi \cdot S \cdot u \cdot C_{ion} \quad (2)$$

where D_{ion} = *d*iffusion coefficient of an ion (m^2/s); δ = constrictivity; Ω = tortuosity; R = ideal gas constant (J/mol.K); T = absolute temperature (K); = Faraday's constant (C/mol); Z_{ion} = ion valance*;* and u = velocity of an ion transported by bulk movement of solution (m/s).

Diffusion coefficient of an ion, D_{ion}, in free water is expressed by [1-2]:

$$D_{ion} = R \cdot T \cdot \frac{\lambda_{ion}}{z_{ion}^2 \cdot F^2} \quad (3)$$

$$\lambda_{ion} = \lambda_{ion\_25} \cdot \exp\left\{-1700\left(\frac{1}{T} - \frac{1}{298}\right)\right\} \quad (4)$$

where λ_{ion} = conductivity of an ion (Sm^2/mol); and λ_{ion_25} = conductivity of an ion at 25°C (Sm^2/mol).

In Equation 2, the first and second terms are due to chemical and electrical potential gradients respectively while the third term represents the advection. The activity coefficients, *γ,* are calculated according to the extended Debye-Huckel [7]:

$$\log \gamma_{ion} = -\frac{A z_{ion}^2 \sqrt{I}}{1 + B a_{ion} \sqrt{I}} + b_{ion} I \quad (5)$$

where A and B are temperature dependent coefficients, and a_{ion} and b_{ion} are ion-specific fit parameters. Ionic strength, I, can be described as:

$$I = \frac{1}{2}\sum_{i=1}^{n} c_i z_i^2 \tag{6}$$

The electrical potential gradient is caused by different mobilities of ions in the solution. If there is no electrical current;

$$\sum_i J_i \cdot Z_i = 0 \tag{7}$$

The zero-charge flux permits to determine the electrical potential gradient as a function of other term in Equation 2.

2.3 Thermodynamic Modelling

This model is used to define the amount the pure phases that can react reversibly with an aqueous phase to achieve equilibrium. The pure phases will dissolve or precipitate to achieve the equilibrium or will dissolve completely. Thermodynamic modelling has been used in cement system for various purposes such as (i) calculation of stable phases based on the solution composition, (ii) to model the influence of the initial composition on the final resulting stable phases, (iii) to simulate the changes with hydration, (iv) to integrate with transport model for understanding the interaction with environment [10]. The equilibrium reactions are expressed by mass-action equations [7]. In general, pure-phase equilibrium can be written as:

$$K_p = \prod_i (\gamma_i c_i)^{n_{i,p}} \tag{8}$$

where K_p = thermodynamic equilibrium constant for the phase p; γ_i = activity coefficients of ion i; c_i = concentration of ion i; and $n_{i,p}$ = stoichiometric coefficient of ion i in the phase p. The thermodynamic equilibrium constant, K_p, at a given temperature T can be expressed as:

$$K_p = \exp\left(-\frac{\Delta_r G_T^0}{RT}\right) \tag{9}$$

Where $\Delta_r G_T^0$ is the standard Gibbs energy of reaction at temperature T:

$$\Delta_r G_T^0 = \sum \Delta_f G_{T,products}^0 - \sum \Delta_f G_{T,reactants}^0 \tag{10}$$

Here $\Delta_f G_T^0$ is the Gibbs free energy of formation for a species at a given temperature T. Explanations on basic principles of the thermodynamic calculations

and chemical reactions are as given in textbooks [6-7]. The sink term in Equation 1 is considered as the rate of dissolved or precipitated ions due to geochemical reactions. The composition of equilibrating solution provides the information about the stability of the products. Comparing ion activity product (IAP) with solubility products gives the degree of over or under saturation of solids with respect the equilibrated solution. When IAP is greater than solubility product or equilibrium constant, the ions in the solution start to precipitate. The amount of precipitated or dissolved ions can be given as the difference of ions in IAP and in equilibrium. The rate of precipitated or dissolved ions can be written as follows:

$$\frac{\partial q_{ion}}{\partial t} = \frac{\partial q_{ion}}{\partial C_{ion}} * \frac{\partial C_{ion}}{\partial t} \tag{11}$$

For pure thermodynamic equilibrium, q_{ion} has a linear relationship with free concentration (C_{ion}). Therefore, sink term can be expressed as follows:

$$Q_{ion} = \frac{\partial q_{ion}}{\partial t} = K * \frac{\partial C_{ion}}{\partial t} \tag{12}$$

2.4 Framework of Coupled Model

A multi-scale numerical framework is proposed to predict the long-term performance of cementitious materials in various aggressive aqueous environments. In this study, DuCOM is coupled with IPhreeqc (hereafter call PHREEQC) using FORTRAN programming language to solve multi-species reactive transport problems in cementitious materials. The coupled model retains all the capabilities of both DuCOM and PHREEQC, and it can be used not only for multi-species reactive transport but also other purposes. A basic framework of DuCOM system coupled with PHREEQC is shown in Figure 2. DuCOM consists of several sub-models, which work together and are interlinked. PHREEQC has incorporated into DuCOM as a model to perform speciation and geochemical calculation after hydration and microstructure computation as well as in each ionic model. It is known that PHREEQC perform variety of calculation, but in the coupled model DuCOM performs hydration, pore structure, multi-ionic transport calculation whereas PHREEQC performs only speciation and geochemical calculations. Therefore, each sub-model in the framework satisfies the governing equation (Equation 1) for FEM calculation through continuous iterations. Each gauss point in the finite element of DuCOM is represented by a single batch reactor for PHREEQC that contains minerals and solution elements, and PHREEQC performs speciation and geochemical calculations. The necessary data to satisfy the governing equation are transferred to DuCOM from PHREEQC through the coupling. The coupling provides the internal data transfer between DuCOM and PHREEQC while they are running concurrently. Therefore, either DuCOM or PHREEQC neither writes nor reads files for coupling. At the beginning of each time step, hydration and microstructure properties are computed

in DuCOM and computed cement hydrates and porosity together with ionic concentrations are passed to PHREEQC. The input of ionic concentration is the preceding step of equilibrated concentration of ions from the last model ("K equilibrium and transport model" in Figure 2). In coupled model, PHREEQC has included in each ionic model and thus it uses the free concentration of ion as the input in the respective ionic model. Figure 3 shows the conceptual approach for data exchange between DuCOM and PHREEQC at each time step. The figure illustrates that the ions in pore solution (Such as $[Na^+]$, $[K^+]$, $[Ca^{2+}]$, etc.) are equilibrium cement hydrates (such as [C-S-H], [CH], [Aft], [Afm], etc.) before "SO_4 equilibrium and transport model". The same values of concentration of ions and cement hydrates are given to PHREEQC in "SO_4 equilibrium and transport model" as input parameters. However, free concentration of sulphate (C_{SO4}^{2-}) in the governing equation (Equation 1) is the degree of freedom to solve FEM. Therefore, the equilibrated sulphate concentration ($[SO_4^{2-}]$) before "SO4 equilibrium and transport model" is given as sink term ($Q_{SO4}^{2-}=\Phi*S*\{[C_{SO4}^{2-}] - [SO_4^{2-}]\}$) to the "$SO_4$ equilibrium and transport model". The degree of freedom (C_{SO4}^{2-}) is modified in FEM calculation using the sink term to satisfy the governing equation (Equation 1) for sulphate ion. Once the governing equation is satisfied, the output values equilibrated concentration of pore solution ($[Na^+]$', $[K^+]$', $[Ca^{2+}]$', etc.) and cement hydrates ([C-S-H]', [CH]', [Aft]', [Afm]') of "SO4 equilibrium and transport model" are given to next model ("OH equilibrium and transport model") as input parameters for PHREEQC in that model. These processes are continued until the last model ("K equilibrium and transport model" in Figure 2). The output of values of "K equilibrium and transport model" is given to "Hydration computation model" in the following step (see Figure 2). These steps of calculations are continued until total time. It can be seen that the output of PHREEQC in one model is passed to following model as the input of PHREEQC. However, free concentration of ion (C_{ion}) are calculated in DuCOM according to the governing equation, and therefore PHREEQC uses the determined free concentration of ion for the calculation instead of output of PHREEQC in the previous model. This approach yields to perform PHREEQC calculation during iteration loop and required output values from PHREEQC is transferred to DuCOM via sink term in the governing equation. The amounts of dissolved and precipitated phases are passed to hydration and microstructure models, which update mineral composition and porosity and use them in the following time step. The main advantage of the current coupled system is the complete coupling between a full suite of geochemical reactions and multi-ionic transport. The coupled model does not need physical or chemical properties in advance as the input data to the model. Therefore, input parameters for the coupled model are the same as the input of DuCOM. The coupled model described here can be used to predict hydration of cement particles, multi-ionic transport, and geochemical reactions in cementitious materials simultaneously. This strong coupling of geochemical processes with physical properties provides more information regarding the long-term performance of cementitious materials in aggressive environments.

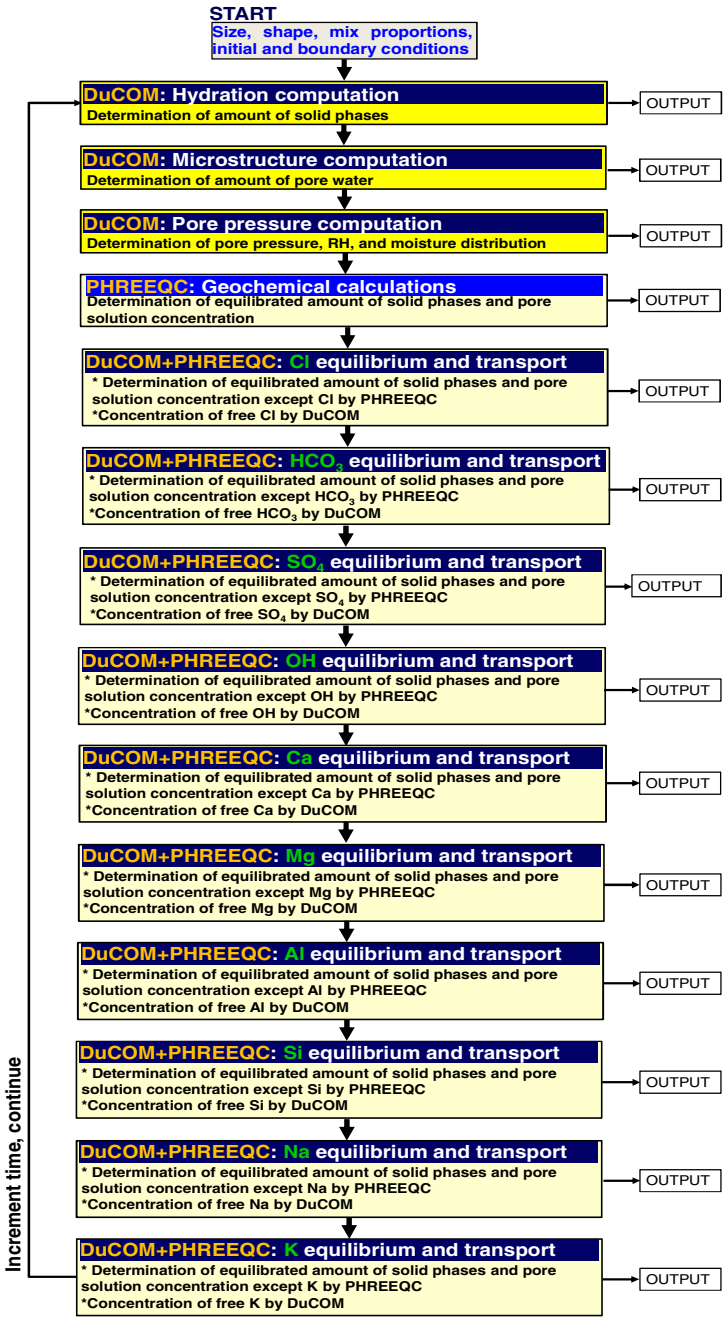

Fig. 2 Framework of coupled DuCOM and PHREEQC. PHREEQC has incorporated into the system as a model after hydration and microstructure computation as well as in each ionic transport model.

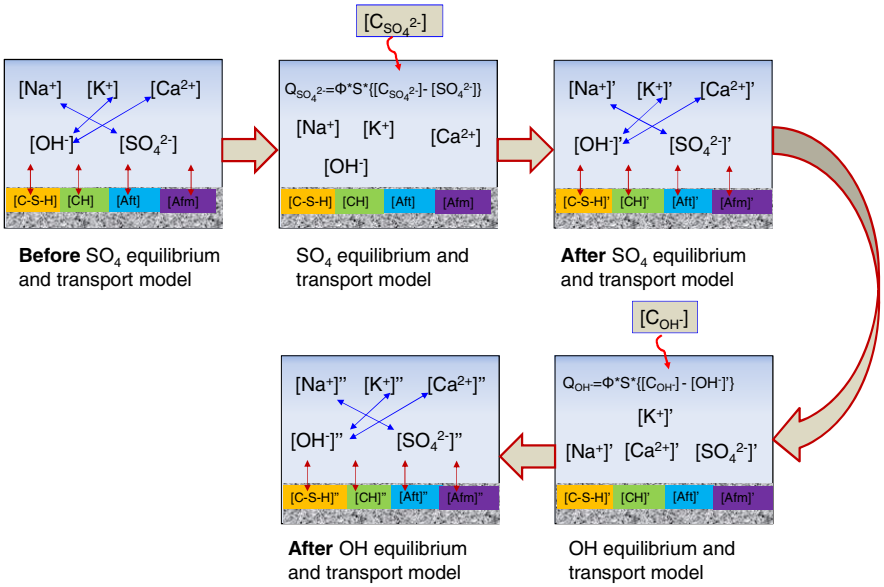

Fig. 3 Conceptual coupling of DuCOM with PHREEQC at each time step

3 Simulation Results and Discussions

3.1 Verification of the Coupled Model: Composition of Cement Hydrates and Porosity

The validity of the coupled model was established by comparing simulated results from the model with published data. Various simulations have been carried out with the proposed model. It provides many details such as the hydration of cement particles, microstructure formation, pore solution concentration, ionic profiles during the transport, mineralogical distributions, etc. as a function of time and depth. In here, the coupled model was used to predict hydration of cement particles and the formation of porosity. The hydration and microstructure formation computations in the coupled model have been described in detail elsewhere [1]. The simulation result for hydrating Ordinary Portland Cement (OPC) with water to cement ratio (W/C) of 0.5 is shown in Figure 4. Beside some un-hydrated clinker, Calcium Silicate Hydrates (C-S-H), Ettringite (Aft), and monosulfate are the main phases in the hydrated OPC. It can further be seen that the formation of monosulfate correlates with the disappearance of ettringite. Ettringite is completely changed to monosulfate at later age (after one days of hydration). The amount of C-S-H and portlandite continues to slowly increase with time. However, the formation of monosulfate does not change with time. The simulated hydrated products are compared with experimental observations.

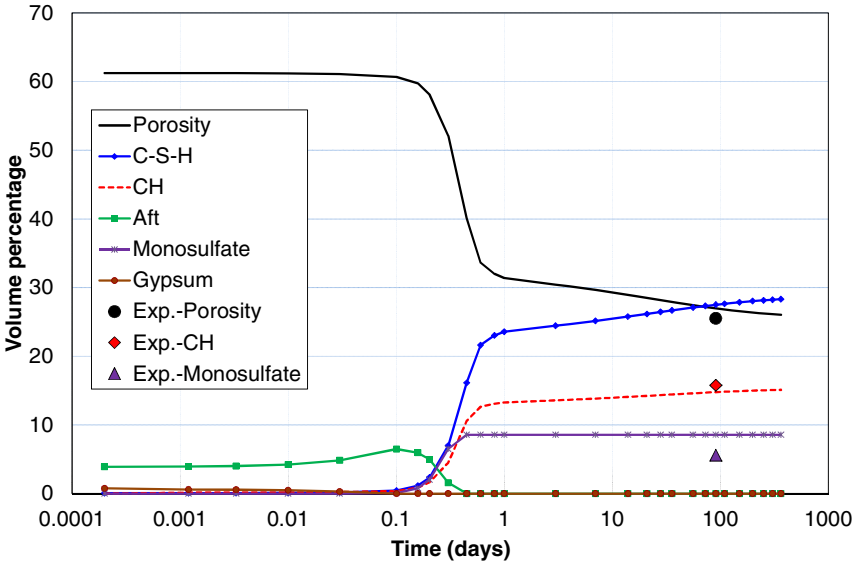

Fig. 4 Hydrates and porosity changes as function of hydration time for OPC with W/C of 0.5(Lines represent the simulated results while marks show the measured data [4] after 91 days of hydration)

Table 1 Input parameters for simulation

Material	OPC concrete
Mineralogical analyses of OPC (%) By Bougue method	
-Alite	52.06
-Belite	22.45
-Aluminate	9.67
-Ferrite	8.82
-Gypsum	3.87
Composition of alkalis (%)	
-Na_2O	0.26
-K_2O	0.38
Characteristics of concrete mixtures	
-W/C	0.5
-Coarse aggregates (kg/m^3)	1035.0
-Fine aggregates (kg/m^3)	803.0
Specimen thickness	10 cm
Curing period and condition	28 days sealed curing
Exposure period	20 years
Temperature	20°C

The XRD Rietveld analysis in the hydrated OPC samples which cured until 91 days showed the same kind of phases as simulated one [4]. The comparison of experimentally determined portlandite and monosulfate with the simulated results are shown in Figure 4. The simulated results agree well with experimental observation. However, quantitative comparison on C-S-H cannot be performed because it is an amorphous phase and hence cannot be determined with XRD Rietveld analysis. In order to determine the total (gel and capillary) porosity in hydrated OPC, Mercury Intrusion Porosimetry (MIP) and nitrogen gas adsorption were used [4]. Very good agreement is obtained between experimentally determined and simulated porosity after hydration of 91 days for OPC sample (Figure 4).

3.2 Application of the Model

The performance of cementitious materials in seawater and sulphate environments was evaluated the using coupled model. The required input parameters for the simulation are tabulated in Table 1. In the simulation, one side of the concrete was considered to be contact with exposure solution of seawater or sulphate solution and the other side was free. A one-dimensional multi-ionic transport coupled with geochemical reactions was considered. The hydration products are dominated by C-S-H (with CaO to SiO_2 ratio of 1.6), portlandite, ettringite, monosulfate, and gypsum. In addition to these hydrates, other phases expected to form under these environment have also been included. However, hydrogarnet phase did not consider in the simulation. The used thermodynamic properties of various minerals and aqueous species were collected from the BRGM database (THERMODDEM) [11]. As for the multi-ionic transport, the main ions in pore solution and exposure solution such as Na^+, K^+, SO_4^{2-}, Ca^{2+}, OH^-, Mg^{2+}, Al^{3+}, H_2SiO4^{2-}, and HCO_3^- were considered. Porosity and pore structure modification due to precipitation or dissolution of minerals have not considered in the simulation. It will be included in the future.

Table 2 Composition of seawater

Ion	Concentration (mM)
Na^+	485
Cl^-	566
K^+	10.6
Ca^{2+}	10.7
Mg^{2+}	55.1
SO_4^{2-}	29.3
pH	8.2

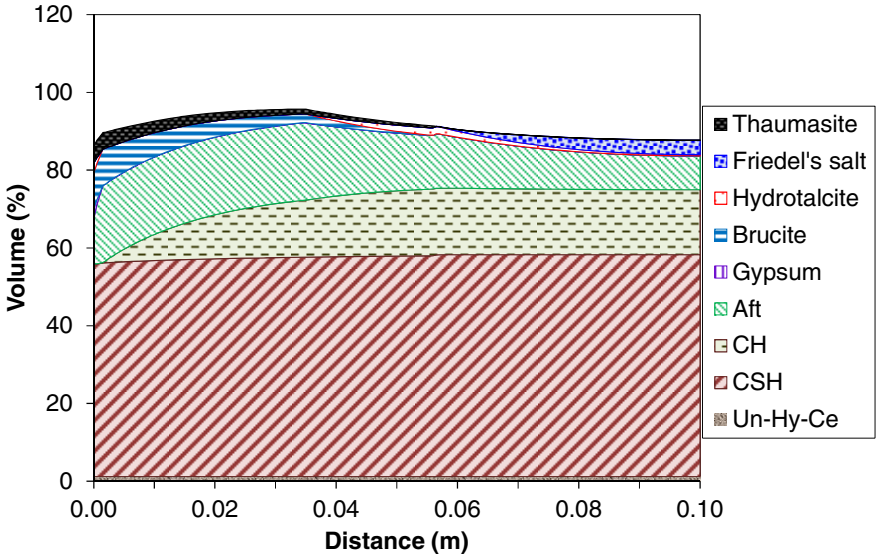

Fig. 5 Representation of the distribution of phases after 20 years of seawater ingress

3.2.1 Evaluating the Performance of Cementitious Materials in Seawater Environment

Cementitious materials in seawater environment can be subjected to various kinds of physical and chemical attack. The main chemical attacks are chloride ingress and sulphate attack. The chemical attack that cementitious materials experience in seawater environment is more complex than those occurring in sulphate-bearing groundwater or sodium sulphate due to the presence of other ions. In addition to chloride ingress and sulphate attack, physicochemical changes are taking place due to magnesium transport, carbonic acid attack, and leaching. The coupled model was applied to investigate the alteration of cement hydrates during seawater transport. It is considered that OPC concrete was in contact with seawater for 20 years and the necessary input parameters for the simulations are given in Table 1. The chemical composition of seawater adopted for the simulation is tabulated in Table 2. The simulation result of mineralogical evolution in terms of volume percentage for 20 years of seawater transport is shown in Figure 5. As indicated in the figure, the left-hand side of the figure corresponds to the exposure surface which in contact with seawater solution. The figure indicates that the reorganization of cement hydrates due to seawater ingress and equilibrium between solids and solution. As can be seen in Figure 5, sulphate and magnesium bearing products are dominated close to the boundary surface. The main hydrated product, C-S-H, is stable during 20 years of seawater ingress. However, complete dissolution of portlandite was observed near to exposure surface and leaves calcium and hydroxyl ions in the pore solution. The disappearance of monosulfate

inside of cement matrix can also be observed in the figure. The dissolved ions from portlandite and monosulfate have contributed to the formation of secondary ettringite in the presence of diffused sulphate ions. Magnesium ions in the pore solution can result in the production of brucite and hydrotalcite, and the formation of brucite enhances the deficiency of portlandite. The penetration of chloride forms Friedel's salt and observes deeply inside of concrete. The reason for the disappearance of Friedel's close to exposed surface is the consumption of aluminates for the formation of ettringite. It can be expected that the formation of thaumasite as displayed in Figure 5. Thaumasite may form from the reaction between sulphates and calcium silicates in the presence of carbonates [12]. A very small amount of gypsum is produced close to exposed surface. It has been experimentally observed the formation of ettringite, brucite, and a mixture of chloroaluminate (possibly Friedel's salt) and monosulfate for OPC mortar stored for 32 weeks in seawater [13]. Further, the absence of gypsum was observed [13]. The field concrete structures fully submerged in seawater shows the same kind of products near to exposed surface [14]. It can be inferred that the coupled model capable of addressing the actual phenomena. This indicates that the important physicochemical and geochemical reactions have taken into account in the coupled model.

3.2.2 Long-Term Performance of Cementitious under Sulphate Attack

The coupled was applied to investigate the degradation process under sulphate attack. The input parameters for the simulation are the same as described before except the concentration of exposure sulfate solution that is 0.1 mol/l SO_4^{2-} with 1.83 mmol/l HCO_3^-. The mineralogical profiles in terms of volume percentage in OPC concrete exposed to sulphate solution for 20 years are shown in Figure 6. As can be seen in Figure 6, sulphate and magnesium bearing products are dominated close to the boundary surface. When sulphate ions penetrate into cement matrix, several reactions are taking place [15]. Sulphate ions react with portlandite and monosulfate to form ettringite and gypsum. The leached ions from portlandite and monosulfate have resulted in the formation of ettringite in the presence of transported sulphate ions. When portlandite is not available, calcium silicate hydrate dissociates into silica gel and releases calcium for the formation of ettringite or gypsum. This dissolution process is controlled by the equilibrium between solid phases and pore solution and the solution conditions controlling the saturation of calcium in pore solution. These processes can clearly be seen in Figure 6. A similar phenomenon is usually observed for cementitious materials exposed to sulphate solution in laboratory or field conditions [3]. The simulation result indicates that C-S-H is stable within the time frame of 20 years in the Na_2SO_4 environment (Figure 6-A). In order to understand the presence of magnesium ions in the exposure solution on the simulation results, the simulation with mixture of sodium, magnesium, bi-carbonate, and sulfate ions was

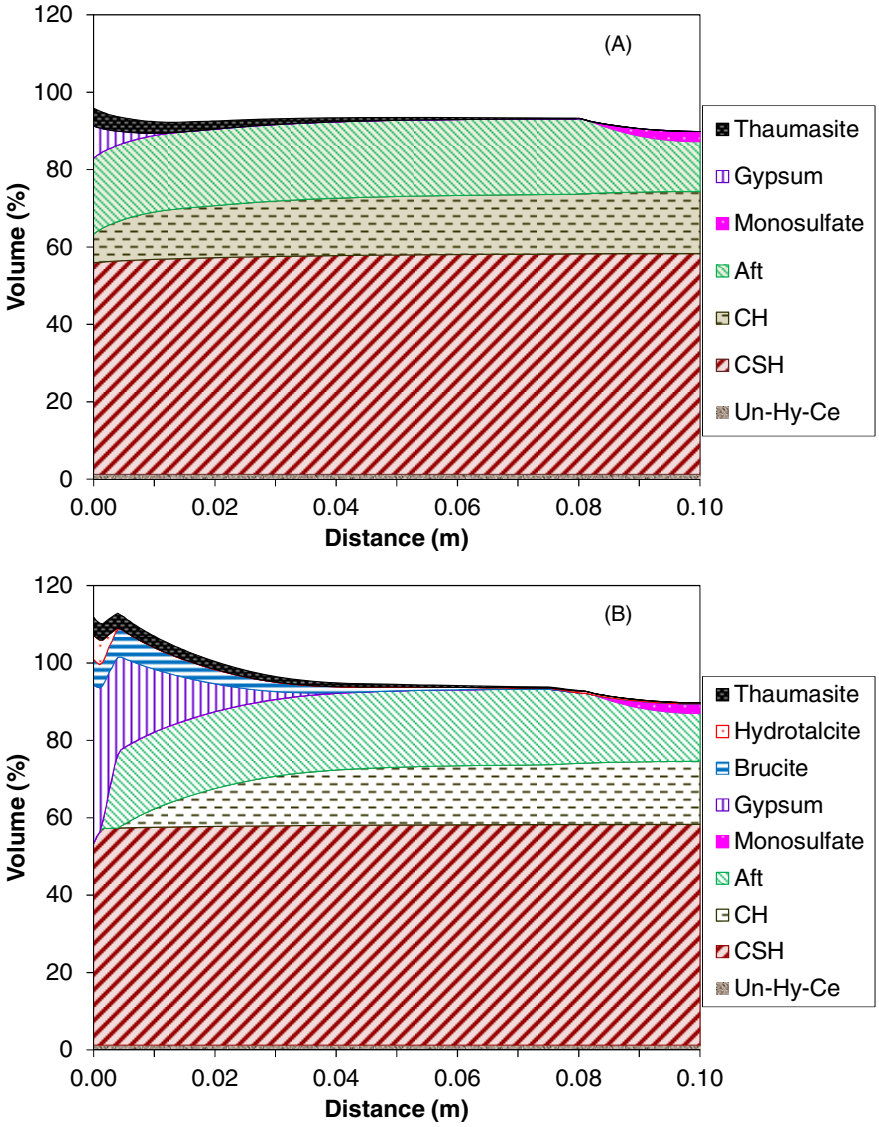

Fig. 6 Representation of the distribution of phases after 20 years of (A) 0.1 mol/l Na_2SO_4 ingress and (B) mixture of 0.05 mol/l Na_2SO_4 and 0.05 mol/l $MgSO_4$

performed. The concentrations of sulfate and bi-carbonates ions are the same as the concentration in Na_2SO_4 solution. In comparison with solids formed in Na_2SO_4 environment (Figure 6-A), Mg bearing products such as brucite and hydrotalcite are formed when the same OPC concrete in contact with the mixture of sodium, magnesium, bi-carbonate, and sulfate ions (Figure 6-B). It is important to note that complete dissolution of portlandite and ettringite, and decalcification of C-S-H

near the exposure surface was observed (Figure 6-B). The dissolution and precipitation of cement hydrates will alter the microstructure. The dissolution and decalcification increase porosity, in turn, increase transport of sulphate ions that produces more sulphate bearing phases which fills the pore space. Thus, the degradation of cement matrix depends on the relative rates of dissolution of cement hydrates and transport of sulphate ions. Figure 6-B indicates that the volume of the solid products near the boundary due to both dissolution of cement hydrates and ingress of sulphate is higher than the initial bulk volume of cement matrix. This may induce cracking of concrete and thus, enhances further transport of ions and lead to progress of damage. Porosity and pore structure modification due to the dissolution and precipitation of the solid phases have not included in the current model. This may have an effect on the transport of multi-species into cementitious materials. This aspect will be taken into account in a future work.

4 Concluding Remarks

In this study, a coupled physicochemical and geochemical model is developed for assessing the cementitious materials in aggressive environments. DuCOM and PHREEQC are used for the development of such a multi-scale computational platform. Coupling both models provides an accurate numerical tool to solve multi-species transport problems together with a comprehensive set of geochemical reactions. In contrast to existing models, the coupled model does not require physical or chemical properties of the materials in advance as input parameters because those are calculating automatically in the model. The coupled model allows predicting the spatial and time variation of minerals compositions, pore water concentrations, and other hydration and pore structures properties. Some of simulation results have been compared with published experimental data. The coupled model is applied to evaluate long-term performance of cementitious materials in seawater and sulphate solution environments. The modelling results have compared with other modelling approaches and laboratory and field observations reported in the literature. It can be inferred that the modelling results capable of capturing the actual occurring phenomena in the aggressive environments. The detail verification for short and long-term performance of cementitious materials in aggressive environments has considered to gain more confidence in the computational platform.

References

1. Maekawa, K., Ishida, T., Kishi, T.: Multi-scale modelling of structural concrete. Taylor & Francis (2009)
2. Ishida, T., Iqbal, P.O., Anh, H.O.: Modelling of chloride diffusivity coupled with non-linear binding capacity in sound and cracked concrete. Cement and Concrete Research 39, 913–923 (2009)

3. Marchand, J., et al.: Theoretical analysis of the effect of weak sodium sulphate solutions on the durability of concrete. Cement & Concrete Composites 24, 317–329 (2002)
4. Elakneswaran, Y., et al.: Multi-ionic transport in cementitious materials with ion-cement hydrates interactions. PhD thesis, Hokkaido University, Japan (2009)
5. Hosokawa, Y., et al.: Development of a multi-species mass transport model for concrete with account to thermodynamic phase equilibrium. Materials and Structures 44, 1577–1592 (2011)
6. Parkhust, D.L., Appelo, C.A.J.: A computer program for speciation, batch-reaction, one-dimensional transport and inverse geochemical calculations, USGS report (1999)
7. Appelo, C.A.J., Postma: Geochemistry, groundwater and pollution. CRC Press Taylor & Francis Group (2009)
8. Charlton, S.R., Parkhurst, D.L.: Modules based on the geochemical model PHREEQC for use in scripting and programming languages. Computers & Geosciences 37, 1653–1663 (2011)
9. Appelo, C.A.J., Wersin, P.: Multicomponent Diffusion Modelling in Clay Systems with Application to the Diffusion of Tritium, Iodide, and Sodium in Opalinus Clay. Environmental Science & Technology 41, 5002–5007 (2007)
10. Lothenbach, B.: Thermodynamic equilibrium calculations in cementitious systems. Materials and Structures 43, 1413–1433 (2010)
11. Blanc, P., et al.: Chemical model for cement-based materials: Temperature dependence of thermodynamic functions for nanocrystalline and crystalline C-S-H phases. Cement and Concrete Research 40, 851–866 (2010)
12. Richardson, M.G.: Fundamentals of durable reinforced concrete. Spon press, Taylor & Francis group (2002)
13. Santhanam, M., Cohen, M., Olek, J.: Differentiating sea-water and groundwater sulfate attack in Portland cement mortars. Cement and Concrete Research 36, 2132–2137 (2006)
14. Neville, A.: Properties of concrete. Peason Education, Essex (2000)
15. Sarkar, S., et al.: Numerical simulation of cementitious materials degradation under external sulfate attack. Cement & Concrete Composites 32, 241–252 (2010)

Investigation on Mechanical Properties of Bituminous Materials through 2D/3D Finite Element Numerical Simulations

Fateh Fakhari Tehrani[1,2], Fatima Allou[2], Joseph Absi[1], and Christophe Petit[2]

[1] Groupe d'Etude des Matériaux Hétérogènes - Équipe Matériaux Minéraux de Grande Diffusion, Centre Européen de la Céramique, 12, rue Atlantis, 87068 Limoges Cedex, France
[2] Groupe d'Etude des Matériaux Hétérogènes - Équipe Génie Civil et Durabilité, Université de Limoges, boulevard Jacques Derche, 19300 Egletons, France
e-mail: {fateh.fakhari-tehrani,fatima.allou,joseph.absi, christophe.petit}@unilim.fr

Abstract. The main objective of this work is to evaluate the influence of a modeling in two and three dimensions (2D, 3D) on the dynamic modulus of bituminous materials based on finite elements method (FEM). The dynamic modulus of the matrix and the elastic properties of aggregates were used as input parameters into the FEM model. The aggregate skeleton of composites was generated randomly. In order to construct numerical master curve of bituminous material this model was subjected to various frequencies loading.

The numerical results were compared to the analytical values of the complex modulus obtained by the Generalized Self-Consistent Scheme (GSCS) and a satisfactory agreement was obtained. Moreover, the 2D numerical results are situated below the 3D results, and both are placed below the experimental results. The observed gap highlights the weakness of 2D models to consider interlock between aggregates and to describe behaviors of materials which are highly influenced by heterogeneities in terms of mechanical properties.

Keywords: Numerical simulation, Mastic, Mortar, Dynamic modulus, Micromechanical model.

1 Introduction

An asphalt mixture is a complex heterogeneous material composed of a viscoelastic binder combined with an elastic skeleton of granular and containing a given percentage of air voids. The mechanical behavior of such heterogeneous material is very complex and one must take into account the geometry of the microstructure, and the mechanical behavior of the different phases.

Dynamic modulus is one of the fundamental engineering properties used to describe the viscoelastic behavior of bituminous materials (Pellinen 2001). There are

N. Kringos et al. (Eds.): *Multi-Scale Model. & Charact. of Infrastruct. Mater.,* RILEM 8, pp. 79–87.
DOI: 10.1007/978-94-007-6878-9_6

many available methods to obtain the dynamic modulus of bituminous composites. The most reliable one is through direct laboratory test on asphalt mixture specimens at different temperatures and loading frequencies. However, it is difficult to measure dynamic modulus in laboratory testing under extreme conditions of temperatures and loading frequencies and it is more costly and time-consuming than other method.

On the other hand, empirical models such as Hirsch's model (Hirsch 1962) and Witczak's model (Bari and Witczak 2001) used in the Mechanistic-Empirical-Pavement Design Guide (MEPDG), have been developed to estimate the dynamic modulus of asphalt mixtures as a function of binder properties and volume filling rate. Empirical regression modeling work has been developed by Witczak and his co-workers over nearly 30 years. In the first version of Witczak's model, 29 mixtures with 87 data points were used. Later, this model was periodically modified to take into account additional experimental data and to include newly adopted material parameters in the asphalt mixtures; such as the asphalt binder complex shear modulus and the phase angle. In the latest version of Witczak's model, as improved by Bari and Witczak (Bari and Witczak 2001), 346 mixtures and 7400 data points were used. These empirical models can satisfactory estimate dynamic modulus, only under the associated specific conditions, and it is complicated to establish a universal relationship which can be applied for several asphalt mixtures types.

Di Benedetto et al (Di Benedetto et al 2004) performed a large number of complex modulus tests at different temperatures and frequencies to establish the links between the linear viscoelastic behavior of asphalt binders and those of bituminous mixes. They used the 2S2P1D rheological model (Olard and Di Benedetto 2003) to simulate linear viscoelastic properties of both bituminous binder and mixes. They concluded that the mix complex modulus can be efficiently predicted from the binder complex modulus.

Chailleux et al (Chailleux and al 2011) used the complex modulus of bituminous mixtures to estimate secant modulus using the indirect test (IT) performed in stress controlled mode. In this study, the behavior law of bituminous mixture was identified in the form of a generalized Maxwell model derived from the measurement of the complex modulus of the bituminous mixture.

During the past two decades, micromechanical models have been introduced to predict properties of asphalt mixtures and mastics from mechanical properties and volume fractions of individual constituents. (Lytton 1990); (Buttlar and Roque 1996); (Buttlar et al. 1999); (Li and al 1999); (Shashidhar and Shenoy 2002); (Huang and al 2007); (Shu and Huang 2008); (You and Buttlar 2006). The generalized self-consistent model (GSCS) (Christensen and Lo 1979); (Christensen and Lo 1986) is recognized among the high sophisticated micromechanical model. This latter is based on a three-phase model: an inclusion is embedded in a finite matrix, which in turn is embedded in an infinite equivalent medium of the composites. Buttlar et al (Buttlar and al. 1999) used this model to predict the stiffness of mastic, with satisfactory results. Shashidhar and Shenoy (Shashidhar and Shenoy

2002) simplified the GSCS equations and they then applied the percolation theory in the GSCS model.

However, most of micromechanical models would be expected to underestimate the stiffness of asphalt mixtures, as aggregate interlock is not captured in these approaches. In order to overcome the limitations of micromechanical models, some authors have employed numerical simulation, using either computer generated microstructures or imagining techniques.

The primary objective of our study is to present a numerical micromechanical modeling based on the finite element method and using a digital biphasic models in two or three dimensions for predicting the dynamic modulus of asphalt materials such as, mastic and mortar. Then, the obtained values will be compared to those obtained with the simplified GSCS model and experimental results. The secondary objective was to study the impact of 2D/3D consideration of the digital models on the modulus values of mastic or mortar composites. Moreover, the effects of various parameters such as Poisson's ratio of asphalt binder and the elastic modulus of aggregates on the predicted dynamic modulus of bituminous material constitute a part of our future tasks.

2 Materials and Experimental Results

Two kinds of bituminous materials were studied (mastic and mortar). They were simulated as a biphasic media composed of matrix and inclusions. The main difference between the numerical models of mastic and mortar is their mechanical properties. For small deformations ($\varepsilon = 10^{-4}$), the matrix has a linear viscoelastic behavior (Olard 2003). In this work, the generalized Maxwell model was used to describe the viscoelastic behavior of the matrix. In the case of mastic, the matrix is considered as a bitumen 50/70. The considered matrix for mortar is the mastic presented by Delaporte (Delaporte and al. 2005) composed of limestone filler and bitumen grade 50/70. The experimental master curves of bitumen and mastic are presented in Figure 1.

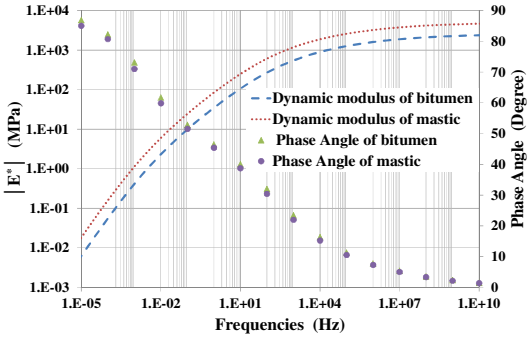

Fig. 1 Dynamic modulus and phase angle master curves of bitumen (50/70) and mastic 30% ($T_{Reference}$= 10°)

The asphalt mortar contains asphalt mastic with 30% of volume filler concentration and fine fractions of sand with maximum particle size of 2 mm. The measured dynamic modulus value of asphalt mastic was then used as an input in the micromechanical model developed in this study to predict the |E*| value of asphalt mortar.

3 Numerical Simulation

3.1 Generation of Microstructure in 2D and 3D

In general, the commercial finite element codes such as ABAQUS cannot construct random microstructures in heterogeneous media. Therefore, it is necessary to generate these microstructures using another software. The MOA program (French acronym of Random Object Generator), developed in our laboratory in C++ language, can generate randomly inclusions of various shapes within a container in the form of a parallelepiped or cylinder in 3D, or in the form of a rectangle in 2D.

The generated objects can be circular or polygonal in 2D, and spherical or polyhedral in 3D. It is also possible to generate separate or not separate objects. In the case of separate objects, a minimum distance between them is imposed by the user. This possibility allows us to numerically imbed aggregates within the matrix. It is also possible to consider an intersection between the objects and the outer surface of the container. Examples of patterns generated by M.O.A. are shown in Figure 2.

The generated files can be written in various formats (STEP, IGES) and then imported into the ABAQUS software. The matrix and inclusion phases were constructed by successive Boolean operations.

3.2 Mechanical Property of Each Phase

For the matrix, different models have been developed and proposed to obtain the complex modulus of bituminous materials. In this study, two models were used: 2S2P1D (2Springs, 2 Parabolic, 1 Dashpot) model (Olard and Di Benedetto 2003);

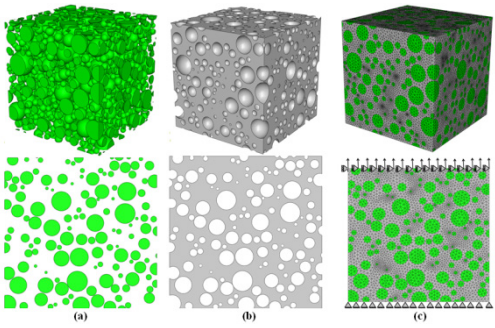

Fig. 2 Two and three-dimensional asphalt mastic microstructural model: (a) aggregates, (b) bitumen, and (c) finite element meshed model

(Di Benedetto et al 2004) and Generalized Maxwell model to determine the mechanical properties of asphalt binder and mastic.

The inclusions (aggregates) have linear isotropic elastic properties. Their moduli were measured in the laboratory through ultrasonic technique method, and were determined from the measured transverse and longitudinal propagation velocity. The average values are 60GPa for the Young's modulus, and 0.2 for Poisson's ratio υ. In order to overcome the effect of aggregate angularity on the result, the generated inclusions are simplified as spherical.

4 Results and Discussions

4.1 Validation of Numerical Results by Analytical Model (GSCS Micromechanical Model) and Experimental Measurements

The numerical predicted dynamic modulus of asphalt mastic was compared to analytical results. The GSCS micromechanical model of Christensen and Lo (Christensen and Lo 1979); (Christensen and Lo 1986) and simplified by Shashidhar and Shenoy (Shashidhar and Shenoy 2002) was used.

The corresponding constitutive equation is:

$$A\left(\frac{G_c}{G_m}\right)^2 + B\left(\frac{G_c}{G_m}\right) + C = 0 \tag{1}$$

Where A, B and C are model parameters which depend on the Poisson ratio of matrix and the volume fraction of inclusions. G_c and G_m are the shear modulus of composite and matrix respectively.

Figure 3 presents the comparison between numerical, analytical and measured dynamic moduli of mastic. It is observed that both the values predicted from 2D and 3D models or calculated analytically and also the measured dynamic modulus followed the general trend of the dynamic modulus of mastic. However the 2D model shows a lower predicted dynamic modulus than the 3D model which is close to the analytical values of the GSCS model. The relative difference between

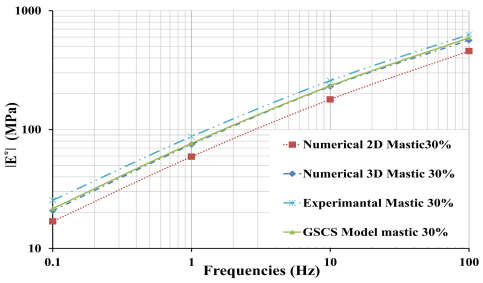

Fig. 3 Numerical, analytical and experimental master curves of mastic 30% $T_{reference}$=10°

the values obtained in 2D and 3D for mastic has been calculated to be almost 25% over the entire considered frequency range. In addition, it is observed that the complex modulus was underestimated by numerical methods compared to experimental measurements.

4.2 *Influence of Filling Rate*

To evaluate the influence of volume filling on 2D and 3D modeling, numerical master curves for 3 filling rates (21%, 35% and 42%) are presented in Figure 4a. The relative difference between the results obtained by 2D and 3D models were also calculated. These results are presented in Figure 4b.

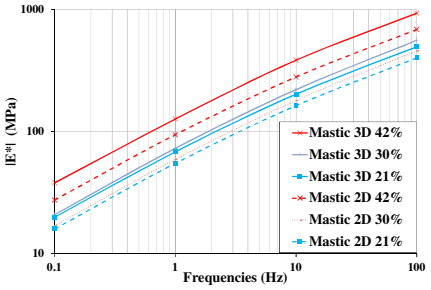

(a)

Fig. 4 (a) Master curves of mastic in 2D and 3D for different filling volume

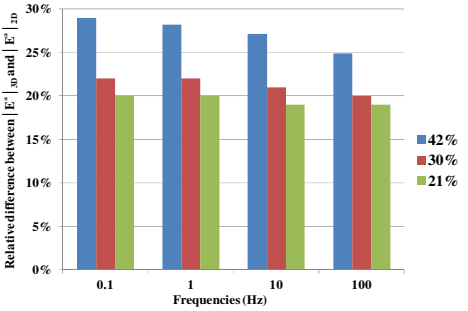

(b)

Fig. 4 (b) Relative difference between results obtained in 2D and 3D for mortar at different filling volume

Several effects were observed. Firstly, when filling rate increases, the impact of transition from a 3D model to a 2D model is more significant. This trend is verified over the entire frequency range. Moreover, it was found that for the same filling rate, higher frequencies have a lower influence on the results of transition from a 3D model to a 2D model. However when the filling rate decreases the frequency variation indicate a smaller relative difference between the results obtained by 2D and 3D models. These results show that increased heterogeneity leads to an increase in the influence of the transition from 2D to 3D modelling.

4.3 Influence of Transition from Mastic to Mortar

To investigate the influence of the stiffening of the matrix by passing from mastic to mortar on different bituminous composites, the predicted master curves of mastic and mortar with a 30% filling rate were calculated. Presented in figure 5 the predicted master curves of mastic and mortar, each of which has a filling rate of 30%. The purpose is to investigate the influence of stiffening within the matrix. In fact, for a given filling rate, the complex modulus of the considered material is influenced by 2D or 3D digital model and by the mechanical properties of the matrix. The properties of the aggregate are unchanged. If we compare results of the complex modulus obtained in 2D and 3D, for the mastic, and next for the mortar, we can observe a relative difference of 25% in the first case, which decreases to 16% in the second. The matrix of the mortar has a higher rigidity than that of the mastic. In conclusion, the transition from 3D to 2D modeling presents less influence on the results for the mortar, than those obtained for the mastic. This trend was observed over the entire studied frequency range. According to these results, we can estimate that a reduction of heterogeneity between the properties (moduli contrast) of the inclusions and matrix, can reduce the impact of the transition from 3D to 2D modeling.

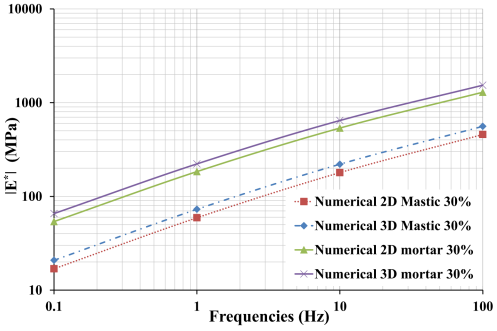

Fig. 5 Master curves of mastic and mortar in 2D and 3D

5 Summary and Conclusions

In this study, 2D and 3D micromechanical FE models were developed to predict the dynamic modulus of asphalt mastic and mortar from its constituent properties (i.e., aggregate, binder and mastic properties).

The models were built using software (M.O.A) which is able to generate randomly the microstructures in 2D and 3D finite volumes. With this software, a user can choose different microstructure parameters, such as microstructure dimensions, shape of the objects, and distance between the objects.

In this approach, two types of heterogeneity are highlighted: the geometrical heterogeneity (volume filling) of the model in 2D or 3D, and mechanical heterogeneity which is explained by the difference in mechanical properties between the

matrix and the inclusions. According to the results, a decrease in the geometrical heterogeneity causes a decrease in the difference between the results obtained in 2D and 3D.

On the other hand, for different bituminous composite materials, decreasing the moduli contrast between matrix and inclusions reduces the difference between the results in 2D and 3D. For example, at frequency loading of 100Hz, the moduli contrast between aggregate and matrix ($E_{aggregates}/E_{matrix}$) decreases from 223 to 99 respectively for asphalt mastic and mortar.

References

Bari, J., Witczak, M.W.: New Predictive Models for Viscosity and Complex Shear Modulus of Asphalt Binders: For Use with Mechanistic–Empirical Pavement Design Guide. J. Trans. Res. Rec. 2001, 9–19 (2007)

Buttlar, W.G., Bozkurt, D., Al-khateeb, G.G., Waldhoff, A.S.: Understanding asphalt mastic through micromechanics. Trans. Res. Rec. 1681, 157–169 (1999)

Buttlar, W.G., Roque, R.: Evaluation of empirical and theoretical models to determine asphalt mixtures stiffnesses at low temperature. Assoc. Asph. Pav. Tech. 65, 99–141 (1996)

Chailleux, E., De la Roche, C., Piau, J.M.: Modeling of complex modulus of bituminous mixtures measured in tension/compression to estimate secant modulus in indirect tensile test. J. Mater. Struc. 44, 641–657 (2011)

Christensen, R.M., Lo, K.H.: Solutions for effective shear properties of three phase sphere and cylinder models. J. Mech. Phy. Solids 27, 315–330 (1979)

Christensen, R.M., Lo, K.H.: Solution for effective shear properties of three phase sphere and cylinder models. J. Mech. Phy. Solids 34, 639–639 (1986)

Delaporte, B., Dibenedetto, H., Sauzéat, C., Chaverot, P.: Linear viscoelatic properties of mastics: results from a new annular shearing rheometer, and modelling. In: International Conference on Bearing Capacity of Road Railways and Airfields (2005)

Di Benedetto, H., Olard, F., Sauzéat, C., Delaporte, B.: Linear viscoelastic behaviour of bituminous materials: from binders to mixes. J. Road. Mater. Pav. Des. 5, 163–202 (2004)

Hirsch, T.J.: Modulus of elasticity of concrete affected by elastic moduli of cement paste matrix and aggregate. J. Am. Conc. Inst. 59(3), 427–452

Huang, B., Shu, X., Li, G., Chen, L.: Analytical modeling of three-layered HMA mixtures. Inter. J. Geomec. 7, 140–148 (2007)

Li, G., Li, Y., Metcalf, J.B., Pang, S.S.: Elastic modulus prediction of asphalt concrete. J. Mater. Civ. Eng. 11, 236–241 (1999)

Lytton, R.: Materials property relationships for modeling the behavior of asphalt aggregate mixtures in pavements. Inter. Memo. Strat. High. Res. Prog., Washington, DC (1990)

Olard, F.: Comportement thermomécanique des enrobés bitumineux à basse température relation entre les propriétés du liant et de l'enrobé. PHD thesis. ENTPE-INSA, Lyon (2003)

Olard, F., Di Benedetto, H.: General "2S2P1D" model and relation between the linear viscoelastic behaviours of bituminous binders and mixes. Road Mater. Pav. Des. 4, 185–224 (2003)

Pellinen, T.K.: Investigation of the use of dynamic modulus as an indicator of hot mix asphalt performance. PHD thesis. Arizona state University, Tempe, Arizona, USA (2001)

Shashidhar, N., Shenoy, A.: On using micromechanical models to describe dynamic mechanical behavior of asphalt mastics. J. Mech. Mater. 34, 657–669 (2002)

Shu, X., Huang, B.: Dynamic modulus prediction of HMA mixtures based on the viscoelastic micromechanical model. J. Mater. Civ. Eng. 20, 530–538 (2008)

You, Z., Buttlar, W.G.: Micromechanical modeling approach to predict compressive dynamic moduli of asphalt mixture using the distinct element method. Trans. Res. Rec. 1970, 73–83 (2006)

Challenges While Performing AFM on Bitumen

Hartmut Fischer[1], Lily D. Poulikakos[2], Jean-Pascal Planche[3], Prabir Das[4], and James Grenfell[5]

[1] TNO Technical Sciences, De Rondom 1 Eindhoven 5612 AP The Netherlands, hartmut.fischer@tno.nl
[2] EMPA Swiss Federal Laboratories for Materials Science and Technology, Überlandstrasse 129, 8600 Dübendorf, Switzerland
[3] WRI, 365 North 9th Street, Laramie, WY 82072, USA
[4] KTH Royal Institute of Technology Division of Highway and Railway Engineering, SE-10044 Stockholm, Sweden
[5] University of Nottingham, University Park, Nottingham, NG7 2RD, UK

Abstract. Using modern microscopic techniques such as atomic force microscopy (AFM) has added significant knowledge on the microstructure of bitumen. The advantages of AFM are that it requires relatively simple sample preparation and operates under ambient conditions. As the use of AFM is becoming more widespread and useful the RILEM technical committee (TC) on nano bituminous materials NBM 231 has conducted a round robin study on this method, the results with respect to reproducibility, repeatability or accuracy limits are presented elsewhere. However, the execution of good quality AFM experiments especially on bitumen is still a challenging task. Sample extraction and preparation are very crucial and attention should be paid to obtain homogenous samples with a sufficient thickness and no surface contamination. The preparation should include a high temperature treatment to provide a smooth homogenous surface. Annealing/resting of the sample has to be sufficiently long, at least 24 h under ambient temperatures to ensure the formation of a (meta)stable micro-structure. Imaging should be done using non-contact (Tapping) mode with stiff cantilevers (resonance frequency ~300 kHz) with a minimum amount of damping as possible.

1 Introduction and Motivation

Bitumen, the residue from the vacuum distillation of petroleum oil is a continuum and complex system of many different organic components such as conjugated polyaromatic and polynuclear ring systems, as well as saturated cyclic and aromatic hydrocarbons containing heteroatoms and linear or branched saturated hydrocarbons (wax) [1].

It is now widely accepted, that bitumen is not a homogenous, single phase system, but contains crystalline parts and displays also a partitioning into domains with a size of several microns to tenth of microns depending on the source of crude oil with different mechanical properties. The present knowledge on the

N. Kringos et al. (Eds.): *Multi-Scale Model. & Charact. of Infrastruct. Mater.,* RILEM 8, pp. 89–98.
DOI: 10.1007/978-94-007-6878-9_7

microstructure of bitumen has been formed using modern microscopic techniques such as atomic force microscopy (AFM) or cryo-SEM and environmental SEM [2, 3]. AFM especially is gaining in popularity for examining bitumen samples [4-11]. The advantage of AFM is that it requires relatively simple sample preparation and operates under ambient conditions. While operated in the simplest mode, the contact mode, only imaging of the surface topology is possible. However, sticky substrates like bitumen generate difficulties for the operation of AFM in contact mode. More recent developed imaging techniques also allow the imaging of a dynamic interaction of the probe tip with the substrate material [12]. Here, in addition the probe is actuated and the damping of the vibrations of the probe while being in close contact with the substrate is registered and used as a feed-back signal. Also and especially in case of sticky and/or soft substrates like bitumen, the difference in phase of the actuated vibration and of the registered response, the phase signal, can indicate areas which differ in stiffness and tackiness. Such phase images of bitumen indicate that this material mixture is not a perfectly homogeneous mixture of hydrocarbons and that not all the hydrocarbons are mutually soluble at room temperature. Previous research has shown that the wax content in bitumen can appear in the form of a type of bee structure with three identifiable phases [7-9]. Lu et al. [12] have studied the effects of time, temperature and thermal cycling on wax crystallisation in bitumen. Using various characterisation techniques, it was shown that non-waxy bitumens displayed no structure or crystals [8, 9, 11]. Also it was shown that the morphology of the crystals was highly dependent on crystallisation temperature and temperature history. The samples that they investigated indicated that bitumen wax usually melted at temperatures lower than 60°C [14-16]. Understanding of the thermal changes is important for the understanding of the behavior of bitumen containing asphalt pavements and as input for multi-scale models describing the behavior of asphalt pavements.

As the use of AFM is becoming more widespread and useful in the scientific community [4-11], the RILEM technical committee (TC) on nano bituminous materials NBM 231 has conducted a round robin study on this method, the results with respect to reproducibility, repeatability or accuracy limits are reported in a separate contribution [22]. The main objective of this paper is to discuss and to highlight critical points and challenges experienced while performing AFM experiments on bitumen samples.

2 Materials

In this investigation four types of materials were used with designations Bit-A, Bit-B, Bit-C and Bit-D.

Table 1 lists the standard material properties provided by the suppliers who are members of the TC. Bit-A contains no wax, Bit-B and Bit-C contain natural wax and Bit-D contains 3% synthetic wax obtained by the Fischer-Tropsch process

(Sasobit 1596).The determined amount of wax fraction can differ depending on the method used. As shown in Table 1, the wax content using EN 12606 part 1 [17] can be quite different in comparison to the wax content using DSC. DSC measures the amount of fraction that crystallizes or melts under the test conditions. This amount is usually higher than the wax content measured by any other EN standard. Table 1 also indicates that the EN method results in some wax content even for non-waxy bitumen such as Bit-A.

Table 1 Standard material properties

Desig.	source	Bitumen	Pen	Soft. Point	DSC wax	EN wax	Dyn. Vis @ 60°C	Kin. Vis. @ 135°C	Fraass point
			[0.1mm]	[°C]	[%]	[%]	Pa.s	[mm^2/s]	[°C]
Bit-A	Venezuela	70/100	91	46.2	0	0.3(1)	168(1)	342(1)	-15(1)
Bit-B	NN	70/100	86	46.4	6.2	1.7	96	181	-16
Bit-C	Kuwait Export Crude	70/100	82	45.8	NN	1	163	399	-15
Bit-D	Venezuela	70/100 Wax mod	50	78	4.5	NN	NN	257	-14

(1) Average values not on exactly the same sample
(2) Using the EN method, some wax content is obtained even for non-waxy bitumen
(3) For natural wax 121 J/g and for synthetic wax 250 J/g was used to calculate wax%
(4) NN=Not Known

However, since Bit-C showed the richest microstructure and most transitions as determined by DSC [22] in the range of temperatures accessible by the AFM setups, the examples and challenges discussed and shown in this contribution were limited to this type of bitumen.

3 Methods

3.1 Sample Preparation, Homogenisation and Conditioning

One of the most important parts of this contribution is the discussion of the sample preparation technique. Since bitumen shows ageing due to oxidation and/or steric hardening, the sample preparation as well as the extraction of a representative sample out of bulk material needs attention. Bitumen as a binder will also collect dust particles etc. with time if not stored in a strictly dust free environment. Dust and other particle contamination may be collected, especially at the surface and

will hence disturb/alter the surface pattern as observable by AFM. Therefore, melting of an extracted bead of the bitumen at elevated temperatures is recommended (Figure 1a and 1b) followed by a spreading with a spatula which removes at the same time the outermost surface and thus also all the contaminations at the same time (Fig. 1c). Attention should be paid, that a sufficient thickness of the sample (100-500 microns) is left over to exclude surface driven and directed structuring effects [18].

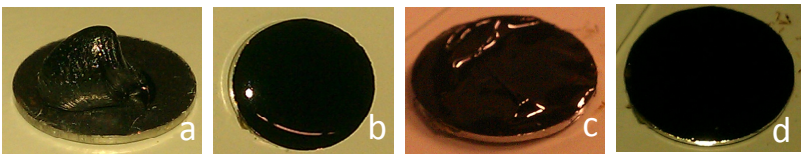

Fig. 1 Preparation of the AFM samples a) bead on holder, b) flown and completely wetted sample after exposure to 100 °C for 5 min, c) removal of top layer and contamination, d) reflow at 100 °C and smooth surface ready for inspection

The method used in this investigation follows an earlier described DSC testing procedure [2, 14-16, 19]. Approximately 15 mg of binder is placed in a conductive sample holder. The sample holder is placed horizontally on a hot plate, 110 – 130°C to let the binder level-out for 15 minutes. Afterwards this sample holder is left to cool covered to prevent dust pick-up, still keeping it horizontally. Thereafter, the sample holder is left horizontally and covered to prevent dust pick-up, for at least 24-26 hours, at 25°C prior to recording the tests. In our test, the removal of the top layer was not yet performed, however, this will be done and recommended for future experiments.

3.2 Testing

The testing procedure also follows the DSC testing procedure closely as the microstructure of the sample is dependent on its thermal history. The tests can be conducted at variable temperatures or at constant temperature. The sample on the magnetic holder is placed in the AFM apparatus and conditioned at 25°C for 5 min. Then it was cooled from 25°C to - 30°C at 10 K/min where it was left for 5 minutes to equilibrate at the isothermal temperature. The measurement phase starts at -30 at 10 K /min. In case variable temperature capability is available then it is recommended to image at 0°C, 15°C, 25°C and thereafter at 5 K intervals (i.e., 30°C, 35°C, 40°C, 45°C …) until no micro-structure is observed (Figure 2).

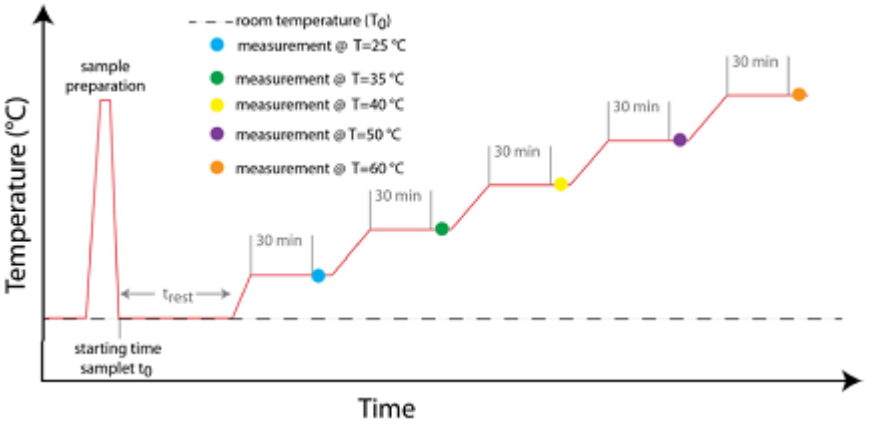

Fig. 2 Protocol of the thermal history during sample preparation and execution of the temperature dependent AFM experiments on bitumen within the round robin study performed in the RILEM TC NBM 231 [19, 20]

4 Results and Discussion

In principle AFM imaging of bitumen can be straightforward, provided that reasonably stiff cantilevers (~40 N/m) are used operating in TappingMode™ with a possible minimum of damping of the amplitude signal. Such imaging can result in very clear pictures allowing the identification of three distinct phases shown in Fig 3.

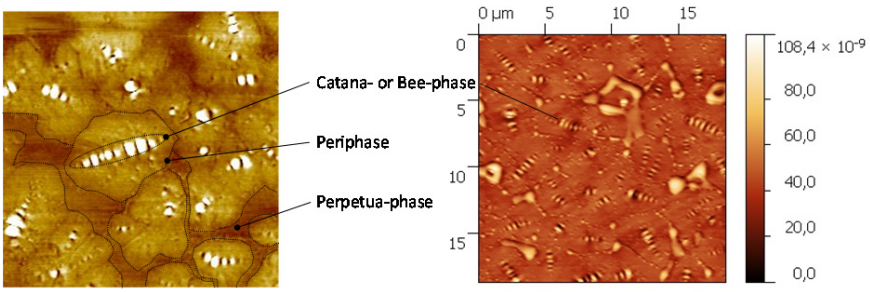

Fig. 3 Identification of the microstructure of bitumen using AFM (scale of the left picture 10 x 10 microns)

Most useful for the discrimination of the different features observable while exploring the microstructure of bitumen is phase contrast imaging. As explained already briefly above, this AFM method refers to the recording of the phase shift signal in intermittent-contact operation. The phase shift can be thought of as a "delay" in the oscillation of the cantilever as it moves up and down in *and* out of contact with the sample. The phase signal in soft materials is sensitive to viscoelastic

properties and adhesion forces, with little participation of elastic properties, but also reflects topographic differences (differences in slope). This is because the phase is really a measure of the energy dissipation involved in the contact between the tip and the sample. Since bitumen is an excellent binder with high stickiness and adhesiveness, the use of very stiff cantilevers with high operation frequencies (around 300 kHz) is preferable to avoid too long and too intense contact of the substrate with the probe resulting in material transfer from the substrate to the probe. Such effects can still occur and are observable by a shift in the resonance frequency of the probe used and in unclear images due to the changes in probe size (i.e. adhered matter).

Other phenomenons observed frequently for bitumen and occurring at ambient and low temperatures is isothermal physical hardening, a molecular restructuring of the asphalt over a long period of time [14]. Netzel et al.[15,16] reported that the phenomenon of hardening in asphalts may also be related to the change in the amount and the thermal event temperature of the crystalline wax fraction with time and possibly kinetically controlled spinodal decomposition of the system. These authors have shown that the formation of the crystalline waxes in asphalt at room temperature as measured using NMR continues for many months. Also DSC experiments showed substantial differences in the amount of crystallised detectable material if different procedures concerning thermal history (annealing time before cooling and the rate of heating of the samples) of the samples under investigation were used [15]. Waxy, paraffinic material will be frozen in the amorphous state during the cooling cycle and, subsequently, during the heating cycle crystallises when the temperature exceeds the glass-transition temperature (T_g). When the heating temperature reaches and exceeds the T_g region as during storage and annealing at ambient temperatures, the methylene carbon segments of the *n*-alkane chains have sufficient mobility to rearrange to an all-*trans* conformation, which is a necessary condition for the onset of crystallisation [15]. Consequently, very different images can be obtained depending on the preparation conditions and the time of isothermal ageing or annealing (fig. 4).

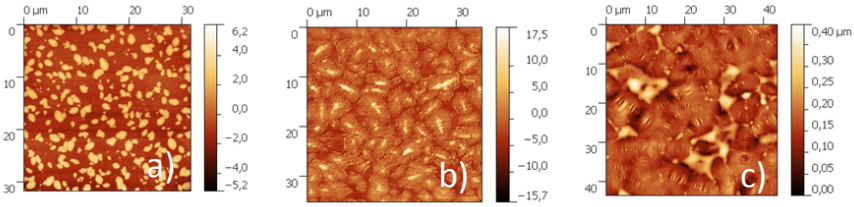

Fig. 4 AFM phase contrast mode images of Bit-C as a function of time of annealing (ambient temperature) after preparation of the sample, a) immediately after cooling, b) 24 hrs. after preparation and c) 1 month after preparation

A melting/dissolution of the crystallites as observable by AFM can now be attributed to exotherm features (gradually melting) observable while performing thermal analysis (Fig. 5).

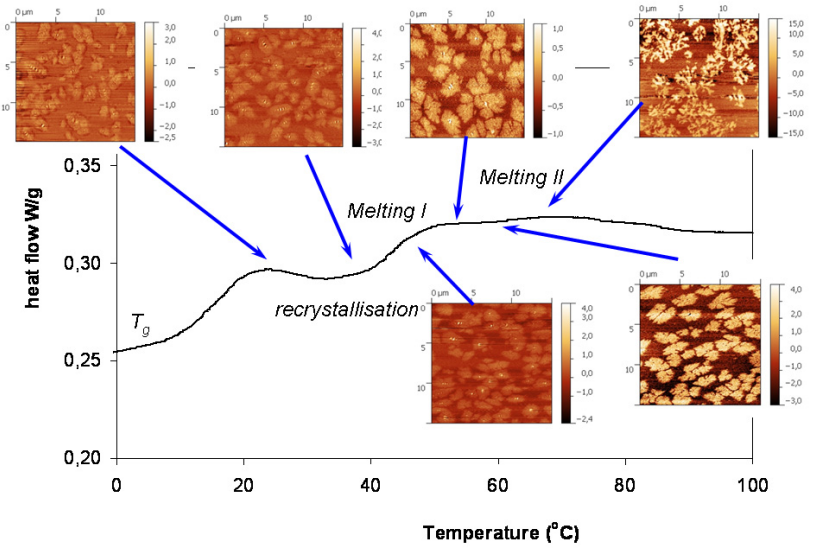

Fig. 5 AFM phase contrast mode images of Bit-C as a function of temperature and corresponding DSC heating curve [19]

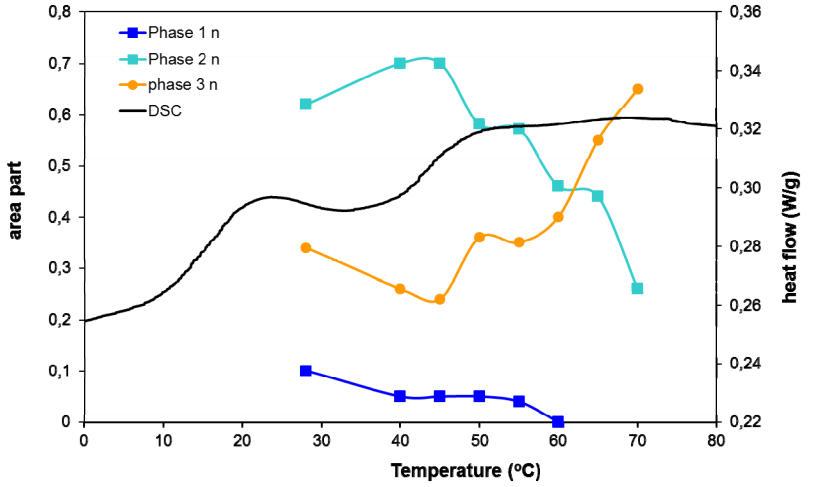

Fig. 6 Plot of the area in the AFM phase contrast pictures attributed to the different phases present within the micro-structure of bitumen (Bit-C; Q8 70-100) and the corresponding DSC heating scan. The change in area contribution of the different phases indicates the transformations taking place in the bitumen as a function of temperature.

Image analysis provides information about the development of the areas covered by the different phases in time. For this, the phase angle signal of the pictures obtained at different temperatures were extracted from the pictures and plotted as area intensity against temperature by using 1D statistical functional analysis [21]. A plot of the relative areas of the three distinguishable phases after deconvolution of the graphs representing areal intensity of the pixels with respect to temperature of the investigation is shown in figure 6.

While linking the thermal events occurring upon heating as displayed by the DSC data to the changes in the formation of microstructure on the surface of a bitumen sample, some information concerning the temperature dependency of the mechanical behaviour of bitumen may be gained.

5 Conclusions

AFM is a versatile instrument able to provide new and interesting insights into the micro-structure of bitumen and the dynamics of structure formation upon heating. A combination of the results obtained from imaging in phase contrast mode as a function of temperature and the transitions indicated in a corresponding DSC heating curve makes it possible to link changes in the observed surface structures to physical transitions occurring mainly in the bulk. The results support the current theory that bee-structures are related to the crystallization of waxy materials at the bitumen surface as a warm sample is cooled. However, the execution of good quality AFM experiments especially on bitumen is still a challenging task. From the round robin experiments for AFM conducted by the RILEM TC NBM 231 in which five laboratories four from Europe and one from USA participated the following conclusions can be drawn:

- Sample extraction and preparation are very crucial and attention should be paid to obtain homogenous samples with a sufficient thickness and no surface contamination
- The preparation should include a high temperature treatment to provide a smooth homogenous surface
- Annealing/resting of the sample has to be sufficiently long, at least 24 hrs. under ambient temperatures to ensure the formation of a (meta)stable microstructure
- Imaging should be done using non-contact (Tapping) mode with stiff cantilevers (resonance frequency ~300 kHz) with a minimum amount of damping as possible.

Acknowledgments. The authors would like to thank the members of RILEM technical committee NBM 231 for their cooperation and input and Nynas and Q8 for supplying the materials. Credit is addressed to N. Kringos (KTH) for discussions and Will Grimes and Troy Pauli at WRI for running experiments. Additionally, Manfred Partl's support of this technical committee is greatly appreciated.

References

[1] Read, J., Whiteoak, D.: The Shell Bitumen handbook, 5th edn (2003) ISBN: 97807277322002003; Edited by R. Hunter

[2] Gaskin, J.: On Bitumen Microstructure and the Effects of Healing. PhD Thesis submitted to the University of Nottingham (2012)

[3] Poulikakos, L.D., Partl, M.N.: Investigation of porous asphalt microstructure using optical and electron microscopy. J. Micros. 240, 145–154 (2010); Corrigendum. J. Micros. 245, 10 (2012)

[4] Loeber, L., Sutton, O., Morel, J., Valleton, J.-M., Muller, G.: New direct observations of asphalts and asphalt binders by scanning electron microscopy and atomic force microscopy. J. Micros. 182, 32–39 (1996)

[5] Masson, J.-F., Leblond, V., Margesson, J.: Bitumen morphologies by phase-detection atomic force microscopy. J. Micros. 221, 17–29 (2006)

[6] Masson, J.-F., Leblond, V., Margesson, J., Bundalo-Perc, S.: Low-temperature bitumen stiffness and viscous paraffinic nano and micro-domains by cryogenic AFM and PDM. J. Micros. 227, 191–202 (2007)

[7] de Moraes, M.B., Pereira, R.B., Simão, R.A., Leite, L.F.M.: High temperature AFM study of CAP 30/45 pen grade bitumen. J. Micros. 239, 46–53 (2010)

[8] Pauli, A.T., Grimes, R.W., Beemer, A.G., Turner, T.F., Branthaver, J.F.: Morphology of asphalts, asphalt fractions and model wax-doped asphalts studied by atomic force microscopy. Int. J. Pav. Eng. 12, 291–309 (2011)

[9] Schmets, A., Kringos, N., Pauli, T., Redelius, P., Scarpas, T.: On the existence of wax-induced phase separation in bitumen. Int. J. Pav. Eng. 11, 555–563 (2010)

[10] Das, P.K., Jelagin, D., Birgisson, B., Kringos, N.: Atomic Force Microscopy to Characterize the Healing Potential of Asphaltic Materials. In: Bellito, V. (ed.) Atomic Force Microscopy - Imaging, Measuring and Manipulating Surfaces at the Atomic Scale, pp. 209–230. Intech, Croatia (2012)

[11] Das, P.K., Jelagin, D., Birgisson, B., Kringos, N.: Micro-Mechanical Investigation of Low Temperature Fatigue Cracking Behaviour of Bitumen. In: Scarpas, A., Kringos, N., Al-Qadi, I., Loizos, A. (eds.) 7th RILEM International Conference on Cracking in Pavements. RILEM Bookseries, vol. 4, pp. 1281–1290. Springer, Heidelberg (2012)

[12] Lu, X., Langton, M., Olofsson, P., Redelius, P.: Wax morphology in bitumen. J. Mat. Sci. 40, 1893–1900 (2005)

[13] Zhong, Q., Innis, D., Kjoller, K., Elings, V.: Fractured polymer/silica fiber surface studied by by tapping AFM. Surf. Sci. 290, 688–692 (1993)

[14] Claudy, P., Letoffe, J.M., Rondelez, F., Germanaud, L., King, G., Planch, J.-P.: Prepr. Am. Chem. Soc., Div. Fuel Chem. 37, 1408 (1992)

[15] Netzel, D.A., Turner, T.F., Forney, G.E., Serres, M.: Am. Chem. Soc. Div. Polym. Chem., Prepr. 38, 829 (1997)

[16] Netzel, D.A.: Transp. Res. Rec. 1638, 23 (1998)

[17] European Standard EN 12606-1. Bitumen and bituminous binders-determination of the paraffin wax content-part 1:method by distillation

[18] Fischer, H.R., Dillingh, E.C., Hermse, C.G.M.: On the interfacial interaction between bituminous binders and mineral surfaces as present in asphalt mixtures. Appl. Surf. Sci. 265, 495–499 (2013)

[19] Materials and Structures: Recommendation for Performing DSC and AFM on Bitumen

[20] Nahar, S., Schmets, A., Fischer, H., Dillingh, B.: The microstructure of bitumen in relation to healing potential, Final report Infraquest project No. 2011-059 (2012)
[21] Fischer, H.R., Dillingh, E., Hermse, C.: On the microstructure of bituminous binders. Int. J. Pav. Eng. (2012) (submitted)
[22] Soenen, H., Besamusca, J., Fischer, H.R., Poulikakos, L.D., Planche, J.-P., Das, P.K., Kringos, N., Grenfell, J., Chailleux, E., Lu, X.: Recommendations for Performing DSC and AFM on Bitumen, and Result of round robin tests using DSC and AFM on bitumen. To be submitted to Mat. Struct. (2013)

A Preliminary Numerical Study on ITZ in Cementitious Composites

Yun Gao[1], Geert De Schutter[1], Guang Ye[2], and Mingzhong Zhang[2]

[1] Magnel Laboratory for Concrete Research, Department of Structural Engineering, Ghent University, Belgium
{yun.gao,geert.deschutter}@ugent.be
[2] Microlab, Faculty of Civil Engineering and Geosciences, Delft University of Technology, The Netherlands
{g.ye,m.zhang}@tudelft.nl

Abstract. In this paper, two prevailing numerical models of cementitious hydration, i.e., the vector type model HYMOSTRUC3D and the pixel type model CEMHYD3D have been employed to simulate the microstructure of aggregate-ITZ-bulk paste. Specifically, a ternary blended system consisting of Portland cement-blast furnace slag-limestone filler is studied. Results indicate that the simulated phase compositions from both models agree well with afore-measured values by BSE-SEM image analysis method. ITZ differs much from bulk paste, i.e., higher porosity and lower anhydrous fraction. Besides that, the capillary pore connectivity and relative diffusivity of ITZ and bulk paste are estimated, while some significant differences can be detected about the corresponding values from the two numerical models.

1 Introduction

For composite materials, interfaces often play an important role in overall properties. Cementitious composites, i.e., concrete, comprised of small and large aggregates bonded by cementitious paste, see many kinds of interfaces. Among them, the specific zone in the vicinity of aggregate, i.e., the interfacial transition zone (ITZ), is thought to be of paramount importance [1-4]. Due to the higher porosity, ITZ is usually considered to facilitate the transport of aqueous and species, which is harmful to concrete durability when subjected to aggressive environments [5-10]. Therefore, ITZ often has to be considered separately from bulk paste. Nevertheless, in most cases, researchers have to utilize empirical or fitting parameters about ITZ for analytical or numerical calculations [11-13]. In this regard, some quantitative information about ITZ microstructure can be quite beneficial.

In recent 20 years, the numerical simulation technique has been applied much often on cementitious materials. At the microscale, numerical models to simulate the hydration process have been developed, such as the vector type HYMOSTRUC3D and the pixel type CEMHYD3D, which take distinct kinetics

N. Kringos et al. (Eds.): *Multi-Scale Model. & Charact. of Infrastruct. Mater.,* RILEM 8, pp. 99–108.
DOI: 10.1007/978-94-007-6878-9_8

and stoichiometry into account [14-19]. In this study, the numerical simulation of ITZ microstructure is carried out by utilizing both HYMOSTRUC3D and CEMHYD3D. In particular, a ternary blended system consisting of Portland cement-blast furnace slag-limestone filler is focused. Two objectives are expected. The first one is to investigate the feasibility of the two models in simulating ITZ of the ternary blended system; the second one is to compare results from the two models, which can be beneficial when researchers need to compare parameters of ITZ acquired from different models.

2 Model

2.1 HYMOSTRUC3D

As a pioneering integrated model of the vector type, HYMOSTRUC3D, which was developed by van Breugel, has obtained considerable enhancements so far [14, 17, 20-22]. Within HYMOSTRUC3D, cementitious particles are simulated as polysized spheres, the three-dimensional structure is determined by particle coordinates and sizes, i.e., sphere centroids and diameters. The rate of hydration and the formation of inter-particle contacts are modeled as a function of particle size distribution, chemical composition, water binder (w/b) ratio and reaction temperature. During the hydration process, two rate controlling kinetics are imposed on particles, i.e., phase boundary at early stages and diffusion controlled at later stages.

For the current ternary blended system, Portland cement particles firstly react with water, which produces calcium silicate hydrate (CSH) and calcium hydroxide (CH). The produced CH acts as one of the reactants for the pozzolanic reaction of blast furnace slag. Limestone filler is seen as inert. Hydration products can be inner CSH, outer CSH and CH. The CSH phase is supposed to grow in a concentric-wise way, while the CH phase is assumed to be randomly located as spheres in pore solutions. When one CH particle is fully embedded in hydrating particles, its position has to be re-located. More details can be found elsewhere [21-25].

2.2 CEMHYD3D

The pixel type CEMHYD3D developed by Bentz is an important integrated hydration model for cementitious materials as well [15, 16]. Within CEMHYD3D, particles are addressed in terms of arrays of pixels (voxels). A set of cellular-automata rules are then applied to the initial microstructure to model the chemical reactions for all of the major phases. During hydration cycles, each pixel can be occupied by undissolved reactants, diffusing ions or precipitating products. In version 3.0, CEMHYD3D has incorporated blast furnace slag and limestone filler as cementitious binders. Specifically, blast furnace slag pixels are assumed to undergo the pozzolanic reaction with the produced calcium hydroxide from the hydration of Portland cement. As for limestone filler, a minor transformation is suggested, i.e., from monosulfoaluminate (AFm) to monocarboaluminate (AFmc). More details can be found [26].

3 Simulation

3.1 Materials

Chemical compositions and physical properties of ordinary Portland cement (cement), blast furnace slag (slag), and limestone filler (filler) are indicated in Table 1. The cumulative particle size distributions of cementitious binders are shown in Fig. 1. The mix proportion for the blended system in mass ratio is designed as 6:2:2 for cement:slag:filler, with w/b ratio of 0.4.

Table 1 Chemical composition and physical properties of binders

Chemical composition and physical properties	Cement	Slag	Filler
Calcium oxide (CaO, %)	63.37	41.83	----
Silica (SiO_2, %)	18.90	36.32	0.80
Alumina (Al_2O_3, %)	5.74	10.72	0.17
Iron oxide (Fe_2O_3, %)	4.31	0.21	0.10
Magnesium oxide (MgO, %)	0.89	8.97	0.50
Potassium oxide (K_2O, %)	0.73	0.37	----
Sodium oxide (Na_2O, %)	0.47	0.27	----
Sulfur trioxide (SO_3, %)	3.34	0.94	----
Calcium carbonate ($CaCO_3$, %)	----	----	98.0
Insoluble residue (IS, %)	0.41	0.25	----
Loss on ignition (LOI, %)	1.51	0.76	----
Blaine fineness (m^2/kg)	353	469	753
Specific density (kg/m^3)	3120	2896	2650

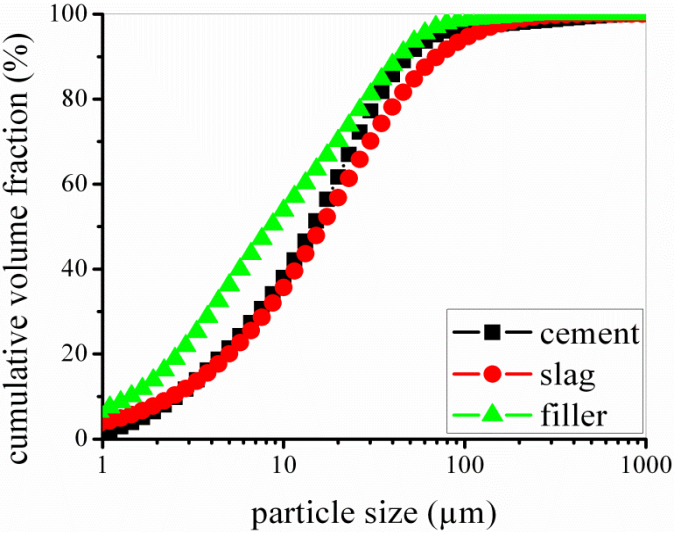

Fig. 1 Cumulative particle size distributions of cementitious materials

3.2 Implementations

Several kinds of mechanism have been proposed to interpret ITZ, which mainly include wall effect and bleeding. In the current simulation, the wall effect mechanism is followed. In particular, the wall effect assumes that large cementitious particles are not able to pack in the vicinity of aggregate as often as small particles due to contact incompatibility. Then, within the zone dominated by small grains, a higher w/b ratio is resulted. In computer implementation, aggregates are represented by rigid boundaries, on which solid particles are not allowed to inter-overlap initially. It should be noted that, some other factors can influence ITZ as well, such as the aggregate content and air voids. Therefore, for the sake of simplicity, the current simulation is targeted on the case of low aggregate content. It is believed that, if any, effects of these additional factors can be reduced. A corresponding mortar with 10% vol. aggregate content was thus casted and analyzed by means of the BSE-SEM method. Experimental details have been published elsewhere [25]. Some results are adopted for comparisons later.

In a recent study, HYMOSTRUC3D has been extended to simulate ITZ, where the local w/b ratio and water transport were taken into account [25]. The extended HYMOSTRUC3D is thus applied. As for CEMHYD3D, the version 3.0 is followed [26]. Ten numerical tests have been implemented for each model. Examples of simulated three-dimensional microstructure based on HYMOSTRUC3D and CEMHYD3D are shown in Fig. 2 and Fig. 3. Within the visualization of CEMHYD3D, the color index for phases is set in such a way, i.e., pores: 0; cement: 1-9; slag: 10-12; cement hydration products: 13-19; slag hydration product: 20-21; $CaCO_3$: 26. It can be observed that, the wall effect is well interpreted in such implementations. At the contact zone between aggregate and paste, the initial water content is much higher. After 56 days' curing, hydration products at the contact zone decrease the porosity remarkably. Some quantitative characterizations on ITZ are presented in Section 5.

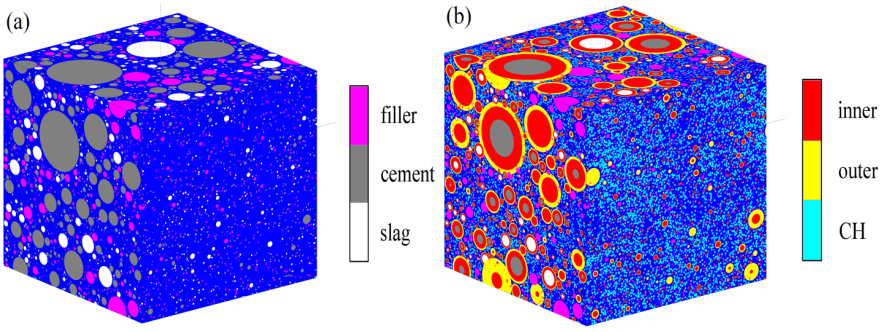

Fig. 2 Simulated microstructure of aggregate-ITZ-bulk paste by HYMOSTRUC3D (a) on mixing; (b) 56 days, where front and back faces represent rigid aggregates, symbols inner and outer denote inner and outer CSH

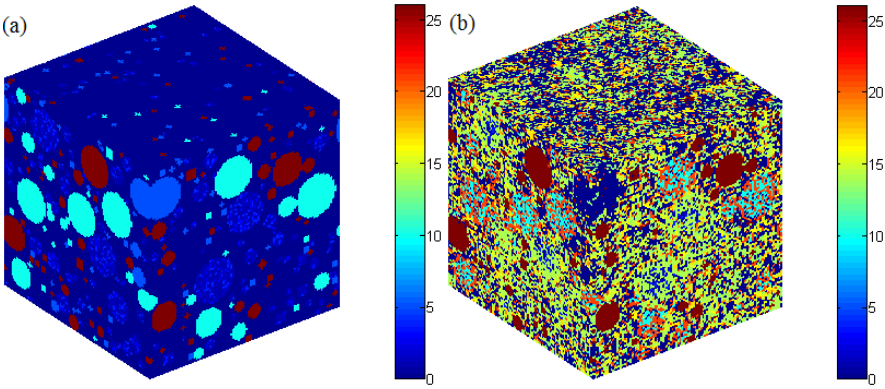

Fig. 3 Simulated microstructure of aggregate-ITZ-bulk paste by CEMHYD3D (a) on mixing; (b) 56 days, where top and bottom faces represent rigid aggregates

4 Results and Discussions

4.1 Quantification of Microstructure

With the simulated microstructure, composition profiles as the distance from aggregate surface can be calculated. As shown in Fig. 4, anhydrous fraction increases as the distance from aggregate surface increases, while porosity sees an opposite trend. Both models show similar results.

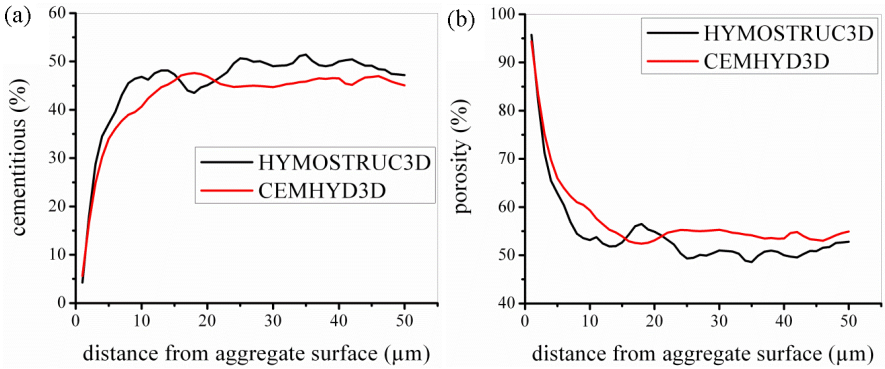

Fig. 4 Examples of simulated composition profiles as distance from aggregate surface on mixing (a) anhydrous; (b) porosity

The overall profiles with regard to hardened aggregate-ITZ-bulk paste are indicated in Fig. 5. As observed, simulation results agree well with the BSE-SEM measurement. Besides that, no apparent boundary can be detected to differentiate ITZ. Referred from past researches, the ITZ extent was around the median size of cementitious particles [6]. Herein, the median size of cement, slag and filler is 16.727 μm, 18.550 μm and 9.775 μm, respectively. In a rough calculation, the median size of cementitious binder equals, i.e., 16.727×57%+18.550×21%+9.775×22%, 15.5 μm, where variables 57%, 21% and 22% are volume fractions of cement, slag and filler. As examined from Fig. 5, it is feasible to set the ITZ extent to be 15 μm. As for bulk paste, it is defined to be the remaining matrix left by ITZ and aggregate, i.e., the zone between 15-μm and 50-μm away from aggregate surface. Thereafter, the average values of anhydrous fraction and porosity can be obtained for ITZ and bulk paste. Results are listed in Table 2. As compared, ITZ possesses lower anhydrous fraction and higher porosity. Some details about ITZ are shown in Fig. 6.

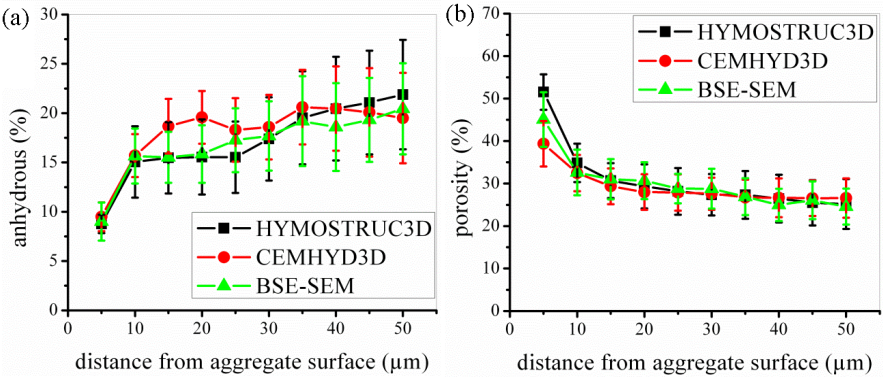

Fig. 5 Composition profiles (w/b=0.4, 56 days) as distance from aggregate surface averaged at successive 5-μm strips (a) anhydrous; (b) porosity

Table 2 Average values of anhydrous fraction and porosity for ITZ and bulk paste (w/b=0.4, 56 days)

Model	ITZ (0-15μm)		Bulk paste (15-50 μm)	
	Anhydrous (%)	Porosity (%)	Anhydrous (%)	Porosity (%)
HYMOSTRUC 3D	13%	39%	19%	27%
CEMHYD3D	15%	34%	20%	27%

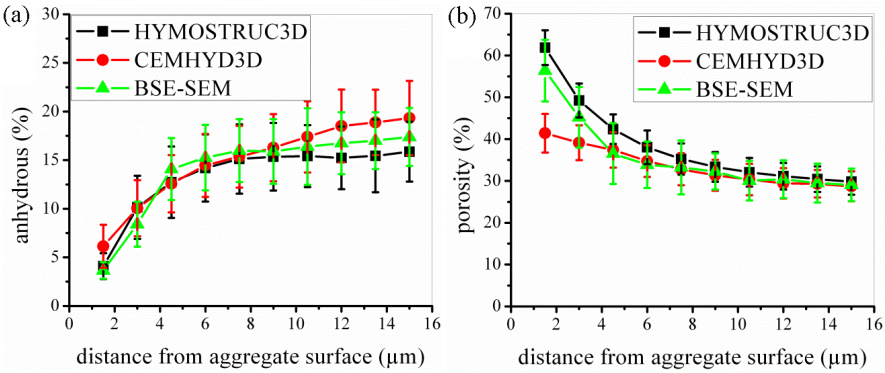

Fig. 6 Composition profiles (w/b=0.4, 56 days) as distance from aggregate surface averaged at successive 1.5-μm strips (a) anhydrous; (b) porosity

4.2 *Connectivity and Diffusivity*

To characterize ITZ in a more profound manner, the relevant pore connectivity and relative diffusivity are calculated as well. Thus, the conventional burning algorithm is utilized to calculate the pore connectivity, while the lattice Boltzmann method is imposed on estimating the relative diffusivity, as schematically illustrated in Fig. 7 and Fig. 8. For more details on the burning algorithm and the lattice Boltzmann method, references are available [26-30]. It should be noted that, the three-dimensional microstructure simulated from HYMOSTRUC3D has also to be digitized. For the sake of comparison, the resolution of 1 μm is set, which is the same in CEMHYD3D. In addition, the scale of bulk paste is also taken as same to ITZ, i.e., 15-30 μm from aggregate surface.

1	0	1	1	0	0	1	1	0	0
1	1	0	0	0	1	0	0	1	0
0	1	1	0	1	1	1	1	1	1
1	0	1	0	1	0	1	0	1	1
1	1	0	0	0	0	1	1	1	1
0	0	0	1	0	0	0	0	0	0
0	0	1	1	0	0	1	0	1	1
1	1	0	0	1	0	0	0	1	0
1	1	1	1	1	1	0	1	0	0
1	1	1	0	1	0	1	0	1	0

Fig. 7 Burning algorithm for the calculation of pore connectivity where voxels occupied by 0 denote pores

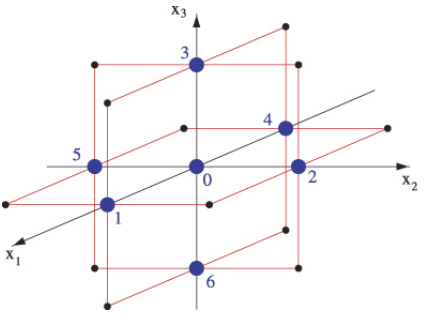

Fig. 8 Schematic illustration of lattice Boltzmann method (D3Q7) for the calculation of relative diffusivity

The pore connectivity is defined by Eq. 1.

$$\kappa = \frac{P_c}{P_t} \tag{1}$$

where κ denotes pore connectivity; P_c and P_t are connected porosity and total porosity, respectively. Results of pore connectivity are listed in Table 3 for the designed mortar (w/b=0.4, 56 days).

Table 3 Pore connectivity of ITZ and bulk paste based on the burning algorithm

Model	ITZ	Bulk paste
HYMOSTRUC3D	98.82%	97.65%
CEMHYD3D	84.19%	74.57%

As for relative diffusivity (D/D_0), it is defined as the ratio of the ionic diffusivity in the material of interest relative to their value in bulk water, as stated by Eq. 2.

$$\frac{D}{D_0} = \frac{w}{w_0} \tag{2}$$

where D and D_0 denote ionic diffusivity in heterogeneous medium (simulated microstructure) and homogeneous medium (bulk water), respectively; w is the ionic flux in simulated microstructure, and w_0 is the ionic flux in bulk water. Upon given initial and boundary conditions, the iteration is processed until a steady state in the lattice Boltzmann method algorithm. Calculation results are listed in Table 4 for the designed mortar (w/b=0.4, 56 days).

Table 4 Relative diffusivity of ITZ (D_{ITZ}) and bulk paste (D_{bulk}) based on the lattice Boltzmann method

Model	D_{ITZ}/D_0	D_{bulk}/D_0	D_{ITZ}/D_{bulk}
HYMOSTRUC3D	0.128	0.080	1.6
CEMHYD3D	0.04	0.025	1.6

It can be noted that, pore connectivity calculated from HYMOSTRUC3D is larger than the value from CEMHYD3D. Similar phenomenon also exists in relative diffusivity. It is believed to be originating from some intrinsic treatments during the hydration process in vector and pixel type models. In particular, positions of spherical particles in HYMOSTRUC3D are fixed. As hydration proceeds, though the growth of particles will cause the occurrence of some overlapping among particles, the overall continuous pathway of pores almost does not get interrupted. Nevertheless, in CEMHYD3D, upon random walk, positions of reacting phases are moving. The hydration process is largely influenced by the

water distribution. During hydration, the overall continuous pathway of capillary pores probably gets blocked. Such difference is reflected in terms of the pore connectivity and relative diffusivity.

5 Concluding Remarks

In this paper, a ternary blended system consisting of Portland cement-blast furnace slag-limestone filler is designed, and the relevant microstructure of aggregate-ITZ-bulk paste has been simulated by two prevailing numerical models, i.e., HYMOSTRUC3D and CEMHYD3D. Some quantitative characterizations are carried out. Results indicate that the ITZ extent is acknowledged to be around the median size of cementitious particles, and ITZ possesses higher porosity and lower anhydrous fraction. Besides that, the pore connectivity and relative diffusivity calculated from HYMOSTRUC3D are larger than their counterparts from CEMHYD3D. Such difference is attributed to the intrinsic different treatments within hydration algorithm, which should be kept in mind when some simulated results from different types of models are under comparison.

References

[1] Scrivener, K.L., Pratt, P.L.: Characterization of interfacial microstructure in 'Interfacial transition zone in concrete'. In: Maso, J.C. (ed.), pp. 3–17. E & FN Spon, London (1996)
[2] Scrivener, K.L., Bentur, A., Pratt, P.L.: Quantitative characterization of the transition zone in high strength concretes. Adv. Cem. Res. 1, 230–237 (1988)
[3] Breton, D., Carles-Gibergues, A., Ballivy, G., Grandet, J.: Contribution to the formation mechanism of the transition zone between rock-cement paste. Cem. Conc. Res. 23, 335–346 (1993)
[4] Ollivier, J.P., Maso, J.C., Bourdette, B.: Interfacial transition zone in concrete. Advn. Cem. Bas. Mat. 2, 30–38 (1995)
[5] Prokopski, G., Halbiniak, J.: Interfacial transition zone in cementitious materials. Cem. Concr. Res. 30, 579–583 (2000)
[6] Scrivener, K., Crumbie, A.K., Laugesen, P.: The Interfacial Transition Zone (ITZ) Between Cement Paste and Aggregate in Concrete. Interface Sci. 12, 411–421 (2004)
[7] Gao, J.M., Qian, C.X., Liu, H.F., Wang, B., Li, L.: ITZ microstructure of concrete containing GGBS. Cem. Concr. Res. 35, 1299–1304 (2005)
[8] Delagrave, A., Bigas, J.P., Ollivier, J.P.: Influence of the interfacial transition zone on the chloride diffusivity of mortars. Adv. Cem. Based Mater. 5(3-4), 86–92 (1997)
[9] Shane, J.D., Mason, T.O., Jennings, H.M.: Effect of the interfacial transition zone on the conductivity Portland cement mortars. Am. Ceram. Soc. 83(5), 1137–1144 (2000)
[10] Principallo, A., Breugel, K.V., Levita, G.: Influence of the aggregate on the electrical conductivity of Portland cement concretes. Cem. Concr. Res. 33, 1755–1763 (2003)
[11] Yang, C.C., Su, J.K.: Approximate migration coefficient of interfacial transition zone and the effect of aggregate content on the migration coefficient of mortar. Cem. Concr. Res. 32, 1559–1565 (2002)

[12] Zheng, J.J., Zhou, X.Z.: Percolation of ITZ in concrete and effects of attributing factors. Mater. Civil Eng. 19, 784–790 (2007)
[13] Sun, G.W., Zhang, Y.S., Sun, W.: Multi-scale prediction of the effective chloride diffusion coefficient of concrete. Constr. Build. Mater. 25, 3820–3831 (2011)
[14] van Breugel, K.: Simulation of Hydration and Formation of Structure in Hardening Cement-Based Materials. PhD Thesis, Delft University of Technology (1991)
[15] Bentz, D.P., Garboczi, E.J.: A digitized simulation model for microstructural development. In: Mindess, S. (ed.) Advances in Cementitious Materials, pp. 211–226. American Ceramic Society, Westville (1989)
[16] Bentz, D.P.: Three-dimensional computer simulation of Portland cement hydration and microstructure development. J. Am. Ceram. Soc. 80(1), 3–21 (1997)
[17] Koenders, E.A.B.: Simulation of volume changes in hardening cement-based materials. PhD Thesis, Delft University of Technology (1997)
[18] Garboczi, E.J., Bentz, D.P.: Modelling of the Microstructure and Transport Properties of Concrete. Constr. Build. Mater. 10(5), 293–300 (1996)
[19] Garboczi, E.J., Bentz, D.P.: Multiscale Analytical/Numerical Theory of the Diffusivity of Concrete. Advn. Cem. Bas. Mat. 8(2), 77–88 (1998)
[20] Ye, G.: Experimental Study and Numerical Simulation of the Development of the Microstructure and Permeability of Cementitious Materials. PhD Thesis, Delft University of Technology (2003)
[21] Zhou, J.: Performance of Engineered Cementitious Composites for Concrete Repairs. PhD Thesis, Delft University of Technology (2010)
[22] Nguyen, V.T.: Rice husk ash as a mineral admixture for Ultra High Performance Concrete. PhD Thesis, Delft University of Technology (2011)
[23] van Breugel, K., Koenders, E.A.B., Ye, G., Lura, P.: Modelling of Transport Phenomena at Cement Matrix—Aggregate Interfaces. Interface Sci. 12, 423–431 (2004)
[24] Ye, G., van Breugel, K.: Simulation of connectivity of capillary porosity in hardening cement-based systems made of blended materials. Heron 54(2/3), 161–182 (2009)
[25] Gao, Y., De Schutter, G., Ye, G., Huang, H.L., Tan, Z.J., Wu, K.: Characterization of ITZ in ternary blended cementitious composites: experiment and simulation. Accepted for publishing Constr. Build. Mater. (2013)
[26] Bentz, D.P.: CEMHYD3D: A Three-Dimensional Cement Hydration and Microstructure Development Modeling Package. Version 3.0. NISTIR 7232, http://ciks.cbt.nist.gov/~garbocz/NISTIR7232/
[27] Bentz, D.P., Garboczi, E.: Percolation of phases in a three-dimensional cement paste microstructural model. Cem. Concr. Res. 21, 325–344 (1991)
[28] Alvarez-Ramirez, J., Nieves-Mendoza, S., Gonzalez-Trejo, J.: Calculation of the effective diffusivity of heterogeneous media using the lattice-Boltzmann method. Phys. Rev. E 53(3), 2298–2303 (1996)
[29] Zhang, M., Ye, G., van Breugel, K.: Microstructure-based modeling of water diffusivity in cement paste. Constr. Build. Mater. 25, 2046–2052 (2011)
[30] Zhang, M., He, Y., Ye, G., Lange, D.A., van Breugel, K.: Computational investigation on mass diffusivity in Portland cement paste based on X-ray computed microtomography (μCT) image. Constr. Build. Mater. 27, 472–481 (2012)

Improvement of the Test Method for Determining Moisture Damage Resistance

Haleh Azari[1] and Alaeddin Mohseni[2]

[1] AASHTO Advanced Pavement Research Laboratory, Washington DC, USA
[2] Pavement Systems, Inc., Washington DC, USA

Abstract. The aim of this paper is to evaluate a new practice for determining resistance of asphalt mixtures to moisture damage. The conditioning involves application of vacuum to fully saturate the mixtures followed by application of cyclic load to create damage using the internal pore pressure. The test specimens are either 150-mm Semicircular Bend (SCB) or 100-mm indirect tensile (IDT) specimens. The mechanical performance test referred to it as Incremental Repeated Load Permanent Deformation Test (iRLPD) is a damaged based test, as opposed to modulus- or strength-based tests. The level of the load in iRLPD test is high enough to cause micro-damages yet low enough not to fail the specimens. Since iRLPD test is not destructive, the test is conducted on the same set of specimens before and after conditioning, hence the sample to sample variability is eliminated. The parameter of the test is the Minimum Strain Rate (MSR) ratio, which is the ratio of the MSR after conditioning to the MSR before conditioning. For moisture resistant mixtures MSR ratio is close to 1 and for the moisture susceptible mixtures the MSR ratio is greater than 1. The results of the study have shown that the combination of vacuum saturation and load conditioning proposed in this study is very effective in creating moisture damage similar to the damage caused by the passing of a heavy tire over a saturated pavement. It is also demonstrated that the iRLPD test is very sensitive to the damage due to moisture.

1 Introduction

The AASHTO T 283 test method also known as modified Lottman [1] is frequently used for the evaluation of moisture susceptibility of asphalt concrete mixtures. The basic concept of the T283 test is to compare the indirect tensile strength of dry specimens and those exposed to saturation, freezing, and thawing. The ratio of average tensile strength of the conditioned and dry specimens, known as tensile strength ratio (TSR) determines the resistance of the mixture to moisture damage. For the laboratory mixed-laboratory compacted specimens a minimum TSR of 0.80 is recommended for correlation with field performance. The method

N. Kringos et al. (Eds.): *Multi-Scale Model. & Charact. of Infrastruct. Mater.,* RILEM 8, pp. 109–125.
DOI: 10.1007/978-94-007-6878-9_9

is used for testing the specimens prepared as part of the mixture design, for the plant control process, and for cores taken from the pavement.

Despite its popularity, AASHTO T 283 test is known to have high variability and sometimes even provide erroneous results. Within the NCHRP 9-26A project, the AASHTO Materials Reference Laboratory (AMRL) conducted an interlaboratory study (ILS) in which precision estimates of the test were developed by determining the allowable difference between test results that are measured in one laboratory (d2s repeatability) and the allowable difference between test results measured in different laboratories (d2s reproducibility) [2]. In the study, TSR data from over 60 different laboratories on two mixtures with expected different levels of moisture susceptibility were collected. The statistical analysis of the ILS data gave a clear indication of the variability of the test. Based on the ILS results, d2s repeatability and d2s reproducibility statistics of the TSR results were reported as 10% and 25%, respectively, which indicate high probability of false-negative or false-positive decisions regarding the resistance of a mixture to moisture damage.

The causes of variability and the possible reasons for the discrepancies of AASHTO T283 test results have been looked at as part of the NCHRP 9-26A study [2] and several other studies [3 through 12]. A list of shortcomings of the T 283 test and some possible solutions identified from these studies are as follows:

1. The AASHTO T 283 test is very time-consuming, it takes five full days from the time the specimens are prepared to the time the strength test is conducted. For a practical mixture design evaluation and for an efficient quality control process, the departments of transportation (DOT) would prefer to condition, and conduct the mechanical test in the shortest time possible.
2. Some components of moisture conditioning, which are the main contributors to the long duration of the test, might not be even necessary. Among these are freezing the specimens for 16 hrs and placing the specimens in 60°C water bath for 24 hrs; yet, the extent to which heat and freeze contribute to the moisture damage in the field is not clear. Very often moisture damage happens during rainy seasons when temperature is rather mild. Stuart [3] expresses that freeze-thaw and thermal cycling are unrelated to stripping and it is unknown if they truly represent in service conditions. He states that these processes may be useful if they result in rupture of asphalt films.
3. Some other components of moisture conditioning might not be long enough to be effective. Stuart [4] emphasizes on the importance of vacuum saturation process in moisture conditioning since it brings the core in a saturated state, which should be its worst condition. However, an application of short period of 5 to 10 minutes of vacuum at 10-26 in. Hg may not be sufficient to pull the water into the pores of specimens. A longer period of vacuum suction may have more significant impact on creating moisture damage. Kandhal and Rickards [5] showed that in four different case studies of stripping in asphalt pavements, the asphalt pavement was nearly 100 % saturated with water, which is higher than the saturation level that is recommended in AASHTO T 283.

4. Part of the reason for the large variability of the test is specimen-to-specimen variability, since the unconditioned specimens (tested dry) are different from the conditioned specimens (tested wet). The specimen to specimen variability, which is inherent to the gyratory compacted specimens, adds significantly to the overall variability of the test. The T 283 mechanical test has the disadvantage of being destructive, which makes it impossible to test the same set of specimens before and after conditioning. It is preferable to reduce the specimen-to-specimen variability by conducting the mechanical test on the same set of specimens before and after conditioning. Several researchers have explored use of non-destructive tests such as indirect resilient modulus or dynamic modulus test for detecting moisture damage [6, 7, and 8]. However, the results of the NCHRP 9-13 study have indicated that indirect resilient modulus test is not as effective as indirect tensile strength test in discriminating between moisture resistant and moisture susceptible mixtures [8]. This might be due to low load level in the resilient modulus test, which might not fully engage the mixture's components for detecting moisture damage.
5. A step that possibly contributes to the variability of the T283 test method is mechanically testing the moisture conditioned specimens while they are still wet. In Section 11.2 of AASHTO T 283, it is recommended to remove the specimens from water bath and place it in the testing machine to conduct the tensile strength test. It is possible that during mechanical testing, the pore pressure induced by the water in the micro-pores may result in increased strength of the material. This could be the reason for occasional higher wet strength than dry strength of the T 283 specimens, which is shown as the wet to dry tensile strength ratio of greater than 1. In a report by Technical Research Centre of Finland it is also argued that the incompressibility of water in the pores of an asphalt specimen and the flow resistance of water in the pore volume substantially increases durability of a water-saturated asphalt structure during rapid loadings [9].
6. The strength test of T 283 could be a major source of discrepancy with the field results. Many researchers have argued that a cyclic load which can simulate the pumping action of traffic load is a better test than loading the specimens with a constant rate [5]. NCHRP Project 9-34 considered the use of a modified environmental conditioning system (ECS) with dynamic complex modulus testing [7]. However, dynamic modulus due to its low level of loading, could not consistently detect the level of moisture damage.
7. Another factor in high variability of the test might be non-uniform moisture conditioning due to the shape and size of the specimens. Kringos et al [10] have demonstrated that water does not uniformly reach the critical zone of the 6"- diameter specimens of T283, where load is being applied. The thinner 4"–diameter specimens have shown significantly improved accessibility to moisture and therefore, are more uniformly conditioned.
8. In addition to achieving better uniformity in moisture conditioning, small specimens can be easily cored from pavement.

9. Although pore pressure from application of repeated load on saturated pavement is known to be an important factor in weakening of the adhesive bonds within asphalt mixtures [11], the cyclic load pore pressure is not included in the T 283 conditioning process. Roque et al. [12], suggested cyclic pore pressure conditioning (CPPC) and repeated load conditioning (RLC). Although RLC was able to effectively induce damage, the method was found to be impractical because of issues regarding the identification of proper load level to achieve damage without fracture during RLC.

In this study, there would be focus on alternatives to the components of T 283 test method to overcome the above mentioned shortcomings of the test and to develop an improved AASHTO test method for more accurate and less time consuming determination of moisture damage susceptibility of asphalt mixtures.

1.1 Goal and Objectives

The goal of the proposed work is to improve to accuracy and precision of the AASHTO T283 test method and at the same time to reduce the total testing time. The objectives of the study are to select effective specimen shape and size, to devise an efficient and practical conditioning process, and to utilize a sensitive mechanical test that can distinguish between moisture sensitive and moisture resistant mixtures.

1.2 Scope of Work

The scope of the study project will encompass the following tasks:

- Investigate various specimen geometries and specimen sizes for improved moisture accessibility
- Evaluate various conditioning methods to improve moisture conditioning and reduce conditioning time
- Examine the effect of incorporating pore pressure in moisture conditioning
- To investigate the damage-based incremental repeated loading approach for testing the same set of specimens before and after conditioning.

2 Experimental Plan

For the experiments in this study, a moisture susceptible mixture was provided by the Wyoming DOT. Following the mix design information, aggregate filler was substituted with hydrated lime to prepare a moisture resistant mixture. Four other mixtures, known to be moisture resistant from previous projects, were also used in the study. Table 1 and Table 2 provide the mixtures description, specimen IDs, and the number of specimens of various types (IDT and SCB specimnes, see next section for description) conditioned using different conditioning schemes. Using the mixtures, various factors for improving the moisture damage test were explored.

Table 1 IDT specimens from WY mixture and 4 other mixtures tested in the study

IDT Specimen Diameter	Mixture	Specimen No	Conditioning Method							Grand Total
			Mist (40°C, 40psi)	Mist (40°C, 60psi)	Mist 40°c, 40 psi	Vacuum 1 Hr @ 15mm Hg	Vacuum 15 min @ 25mm Hg	Vacuum 30 min @ 15mm Hg	Vacuum 4 Hrs @ 15mm Hg	
100mm	Florida	FL33	5							5
	Limestone	LS45	4							4
	New Jersey	NJ16	5							5
	Sandstone	SS02	5							5
	Wyoming w/ lime	WY4L	4							4
		WY5L							5	5
		WY6L		5						5
		WY11L				5				5
	Wyoming w/ no lime	WY1N	4							4
		WY2N							5	5
		WY3N		5						5
		WY7N						5		5
		WY8N					4			4
150mm	Wyoming w/ no lime	WY1N			4					4
		WY2N							4	4
		Grand Total	27	10	4	5	4	5	14	69

2.1 Exploring Specimen Shape and Size

The shape and size of specimens are important factors for both moisture conditioning and mechanical testing. From a conditioning stand point, the specimens should have sufficient accessibility to moisture from all sides and should be able to become saturated uniformly, especially at the critical zone where load is applied. From a mechanical stand point, since tension is the dominant mode of failure in moisture damaged mixtures, the specimens should be suitable for either tension or indirect tension type of loading. For the T 283 test, the specimens are compacted into either 150-mm diameter x 95-mm thick or 100-mm diameter x 63.5-mm thick cylinders. The distance to the core of these specimens seems to be too large to be uniformly conditioned in the specified vacuum level and timing. In addition, since the specimens are as-compacted out of the gyratory mold, they are relatively sealed. In this study, use of smaller size specimens which are cut from larger gyratory compacted specimens was explored.

Table 2 SCB specimens from WY material tested in the preliminary study

Mixture	Specimen No.	Conditioning Method							Grand Total
		Mist	Vacuum 30 min @ 15mm Hg+Mist	T283	Vacuum 1 Hr+ Soak 12 Hr+ Dry	Vacuum 1Hr + Soak 3 Hr	Vacuum 30 min @ 15mm Hg	Vacuum 4 Hr @ 25mm Hg	
Wyoming w/lime	WY9L	2	1			2			5
	WY10L	1	2	2		1			6
	WY4L				8				8
	WY5L	2						2	4
Wyoming w/ no lime	WY7N	1	1	2		2			6
	WY8N	2	2	1		1			6
	WY9N			1					1
	WY3N	3						3	6
	Grand Total	11	6	6	4	10	2	5	48

Three specimen size/shape combinations were investigated. Figure 1 shows the schematics of the evaluated specimen shapes. The specimens explored include 100-mm diameter x 28-mm thick and 150-mm diameter x 38-mm thick circular disks and 150-mm diameter x 38-mm thick semi-circular disks. The disks are referred to as indirect tensile (IDT) specimens and the semi-circular disks are referred to as Semi-Circular Bend (SCB) specimens. Other advantages of the smaller size specimens are that more replicates can be obtained from a gyratory compacted specimen and they can be conveniently cored from the pavement.

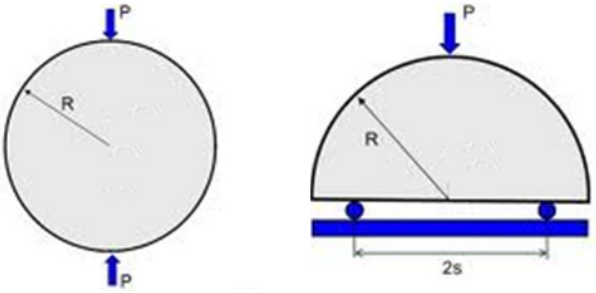

Fig. 1 Schematics of IDT and SCB specimens

2.2 Exploring the Mechanical Test

There are two disadvantages with the tensile strength test specified in AASHTO T 283 as the mechanical performance test. The first disadvantage is its constant rate

of loading. To better simulate the cyclic loading that occurs in the field, it is preferred to use a repeated load test. The second disadvantage of the test is that tensile strength test is a failure test; therefore, it is not possible to test the same specimen before and after conditioning. Several researchers have explored the use of non-destructive tests such as dynamic modulus and resilient modulus [5, 6] tests; however, these tests did not consistently detect the level of moisture damage in the specimens. The reason may be due to the fact that the load level in modulus-based tests is not high enough to engage the aggregate structure and show the internal damage due to moisture.

To overcome the shortcomings of the T283 mechanical test, a repeated load test, referred to as Incremental Repeated Load Permanent Deformation Test (iRLPD) is proposed. As opposed to modulus or strength based tests, iRLPD is a damaged-based test. The loading of the iRLPD resembles to that of the field; it is high enough to engage the components of the mixture and cause damage, yet low enough not to fail the mixture.

The iRLPD test has been successfully used for measuring both high temperature permanent deformation and fatigue resistance of asphalt mixtures in previous studies [13, 14, and 15]. The test is conducted by the Asphalt Mixture Performance Tester (AMPT) servo-hydraulic loading machine or can be conducted using any other servo-hydraulic systems that are used for performing dynamic modulus, flow number, and fatigue tests. Similar to flow number test, the load application of iRLPD includes 0.1 sec. of loading followed by 0.9 sec. of unloading.

Figure 2 shows the output of a typical repeated load test, when the sample is subjected to cyclic load until it reaches a failure. The top portion of the graph shows permanent strain versus number of cycles and the bottom portion of the graph shows the change in permanent strain per cycle (rate of change in strain). Figure 2 also shows the three stages of the test: primary stage, secondary stage,

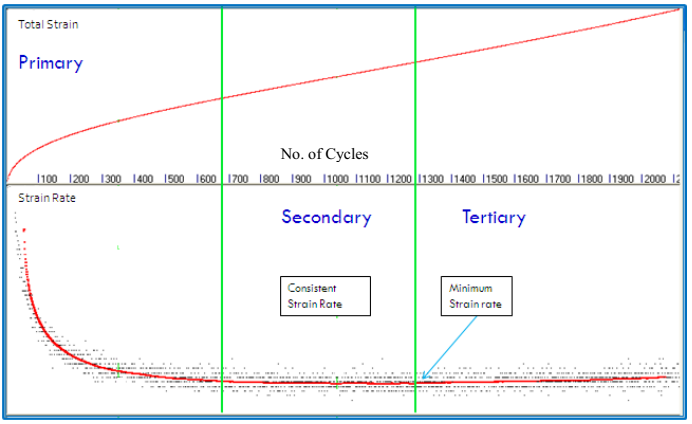

Fig. 2 Output of repeated load test; graph shows the primary, secondary, and tertiary stages of the test

and the tertiary stage. During the primary stage, the change in strain per cycle is very large and the strain is primarily affected by recoverable viscoelastic effects, internal damage due to micro-cracks, and consolidation at the contact points. Throughout the secondary stage the change in strain per cycle is rather consistent but slightly decreasing. The strain growth in this stage is primarily permanent and due to micro-cracks developed within the entire specimen. The final stage of the test is tertiary stage where micro-cracks develop into cracks, mainly in the critical tensile stress location. This is shown by the increase in strain per cycle.

The secondary stage of the repeated load test is of special interest since the strain rate at this stage is rather consistent. The strain measured in the secondary stage is permanent and related to the development of damage in terms of micro-cracks in the mixture. Figure 3 shows that during the secondary stage of the test, the load application has been interrupted and restarted in several increments while the strain rate at the end of each increment, also referred to as minimum strain rate (MSR), has not significantly changed. This indicates that MSR is a material property and can be used as a parameter for indicating internal damage. Since MSR is rather consistent during the secondary stage, the test may be conducted on the same specimen before and after moisture conditioning and any increase in the MSR would represent the increase in damage due to moisture conditioning. For this reason, iRLPD is a good mechanical test for determining moisture damage. The ratio of the MSR after conditioning to the MSR before conditioning would be used as the measure of moisture damage.

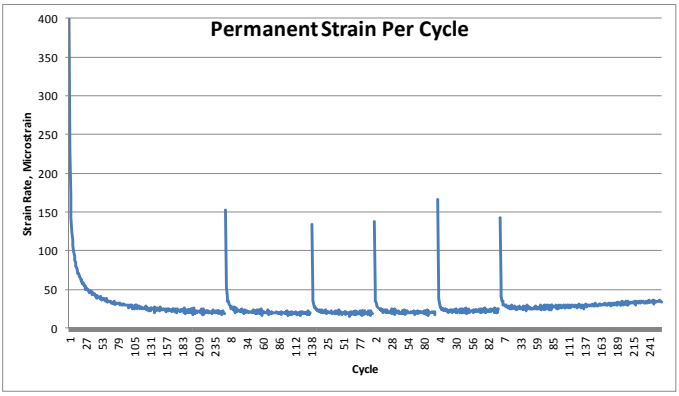

Fig. 3 Six Repeated load test increments; graph shows that strain rate at the end of the first five test increments (minimum strain rate=MSR) remains the same; in the last increment material goes to failure as indicated by increase in strain rate

The iRLPD test conditions for the moisture damage determination are as follows:

- Test temperature was room temperature (23°C) and was kept constant during the entire test.

- Specimens were tested using iRLPD protocol prior to moisture conditioning. Several increments, each consisting of 300-cycles at loading configuration of 0.1 second load and 0.9 second unload were applied to each specimen. The stress was increased for each consequent increment until MSR of around 10 microstrain was reached. The stress at this increment is the test stress level which engages the aggregate structure but would not fail the specimens. This stress level was used on all specimens of the same material. The screen shot of the iRLPD test before moisture conditioning is shown in the left side of Figure 4.
- Specimens were moisture conditioned either using MIST or vacuum of different duration and suction.
- Some specimens were subjected to another increment of 300-cycle iRLPD test at the test stress level after moisture conditioning while the material was still wet to cause pore-pressure damage.
- Specimens were dried using Core-Dry until the weight was within 2 grams of the original weight.

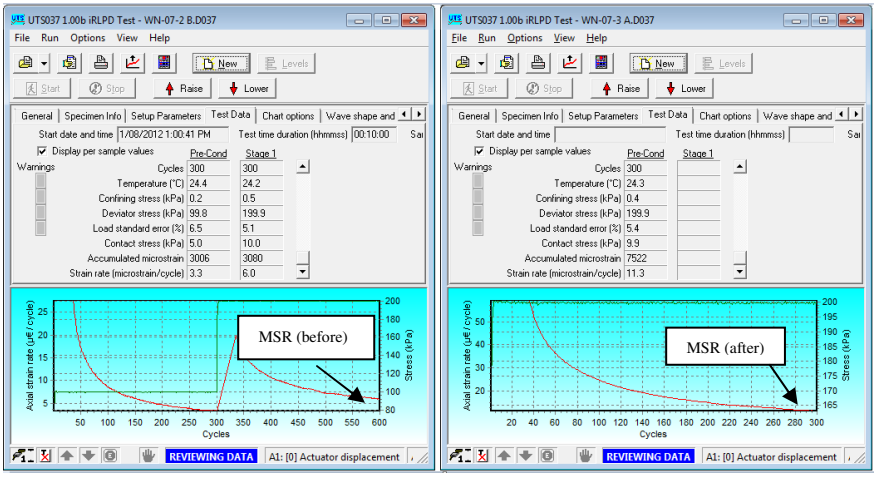

Fig. 4 Screen shots of strain rate measurements before and after conditioning; minimum strain rate (MSR) of before conditioning is measured at the end of the test increment (left) providing MSR around 10 microstrain /cycle conducted before conditioning MSR of after conditioning is measured at the end of the test increment conducted after conditioning (right)

- Specimens were subjected to another increment of 300-cycle iRLPD test at the test stress level after being dried. The right side of Figure 4 shows the screen shot of the iRLPD test after conditioning.
- MSR ratio was calculated as MSR-after divided by MSR-before conditioning. MSR ratio of around one indicates no significant change in damage before and after conditioning and MSR ratio >1 indicates increase in damage after conditioning due to moisture damage.

2.3 Effectiveness of Components of Moisture Conditioning

To overcome the disadvantages of the existing moisture conditioning processes, a new conditioning procedure is proposed in this study. The new process involves application of vacuum saturation to fully saturate micro-pores of asphalt mixtures followed by mechanical loading of the specimens using an increment of iRLPD test. This is intended to simulate the effect of pore pressure when heavy loads pass through a saturated pavement. The optimum components of the proposed conditioning procedure were determined by exploring different levels of the components shown in Table 1and Table 2. The results of the proposed conditioning procedure were also compared with those from AASHTO T283 and those from a new device called Moisture Induced Stress Tester (MIST), which forces water through the samples in cyclic motion [16].

3 Experimental Results

Figure 6 through Figure 10 show the results of the iRLPD test on various sample shapes and sizes, conditioned according to various conditioning schemes. Each test result presented represents an average of the results from testing at least 2 replicates; see Table 1 and Table 2 for the number of specimens tested at each conditioning scheme. The following observations are made:

3.1 Effectiveness of iRLPD Test

Figure 5 shows the average MSR ratios of various mixture types. As indicated from the figure, MSR of the moisture resistant mixtures (Florida, Limestone, New Jersey and Sandstone) remained unchanged after conditioning since MSR ratio is about 1. The MSR ratio of the moisture sensitive WY mixture was around 1.5, however, by adding lime to the WY mixture the MSR ratio decreased to about 1.25 (moisture damage was reduced). This showed the effectiveness of the iRLPD test method and its parameter (MSR) in measuring moisture damage.

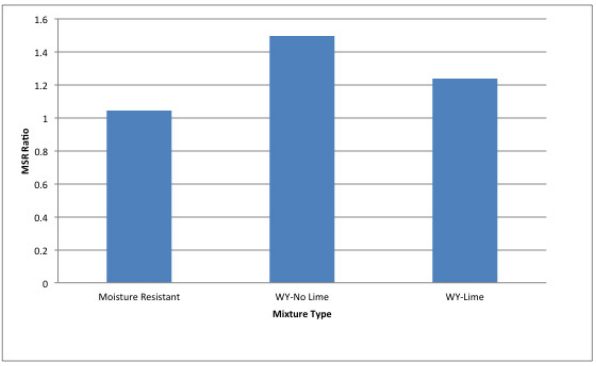

Fig. 5 MSR ratios of moisture sensitive and moisture resistant mixtures

3.2 *Effect of Sample Shape and Size*

Figure 6 shows the average MSR ratios of SCB and 100-mm and 150-mm IDT specimens for moisture sensitive WY mixture tested according the iRLPD protocol. The moisture sensitive Wyoming mixtures were exhibiting MSR ratios of 1.9, 1.6, and 1.2 using SCB, 100mm and 150-mm IDT specimens, respectively. This indicates that the 100-mm IDT and 150-mm SCB specimens showed better distinction between moisture resistance and moisture susceptible mixtures than the 150-mm IDT specimens. The reason for the SCB and 100-mm IDT specimens being more responsive to the moisture conditioning than the 150-mm IDT specimens is probably due to the increased accessibility of the critical zone (area with high tensile stress) of these specimens. Another advantage of using smaller size specimens is that they require smaller loads to produce tensile stress, which is desirable due to the limited load capacity of the AMPT machine. Therefore, 100-mm IDT and 150-mm SCB specimens are selected for further evaluation in the proposed procedure.

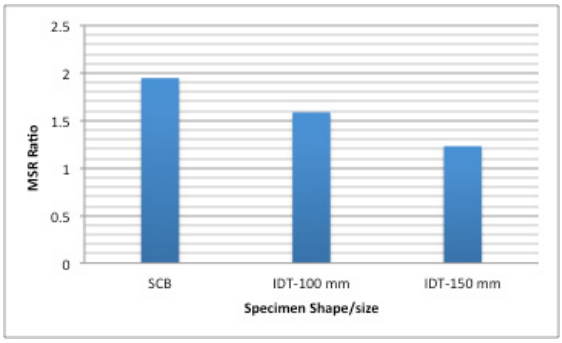

Fig. 6 MSR ratios of SCB and 100-mm and 150-mm in diameter IDT specimens

3.3 *Effect of Various Conditioning Scenarios*

Effect of vacuum saturation. Vacuum saturation provides a fast and effective means of pulling water into the micro-pores of the asphalt mixture. Figure 7 shows the MSR ratios of the specimens conditioned with MIST alone and specimens that were first vacuumed for 30 min. at 25 mm Hg and then conditioned with MIST. As indicated from the figure, MIST conditioning has resulted in substantial damage to the specimens (MSR ratio of 1.8); however, 30 min. of vacuum saturation prior to MIST caused an increase in MSR ratio of the moisture sensitive WY mixture (MSR ratio of 1.9).

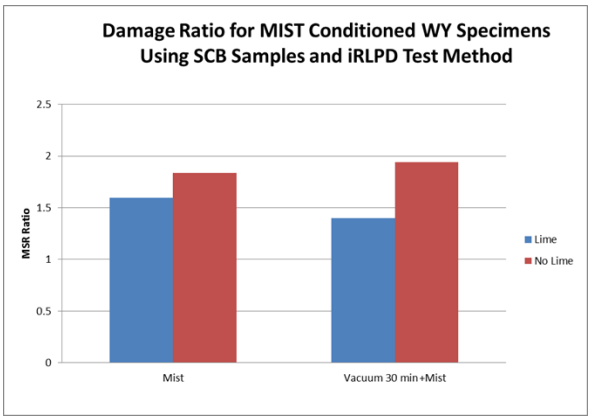

Fig. 7 MSR ratios of moisture resistance and moisture sensitive WY mixtures conditioned by MIST alone and by vacuum saturation plus MIST

Effect of vacuum duration. Figure 8 shows the effect of vacuum duration at the absolute vacuum of 15 mm-Hg on MSR ratios. As this figure shows, increasing the duration of vacuum resulted in increase in MSR ratios which shows increase in moisture damage. Duration of 30 min. at 15-mm-Hg was found to provide complete saturation of the 100-mm IDT and 150-mm SCB specimens.

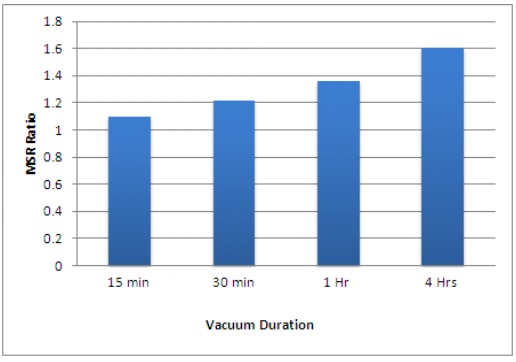

Fig. 8 Change in MSR ratios due to change in vacuum duration

Effect of vacuum Level. Figure 9 shows the effect of vacuum Level on MSR ratios. As indicated, for vacuum duration of 30 minutes, increasing the level of absolute vacuum from 25 mm-Hg to 15 mm-Hg has resulted in increased MSR ratios implying increase in moisture damage.

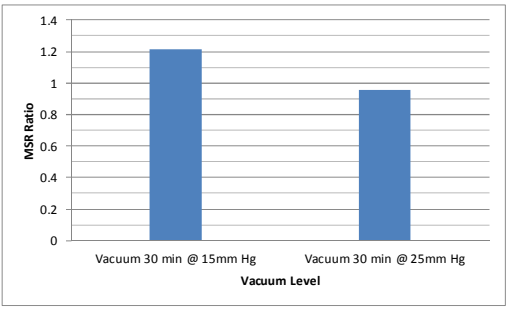

Fig. 9 Change in MSR ratios due to change in vacuum level

Effect of load conditioning. The moisture entrapped in micro-pores of the saturated specimens can cause significant pore pressure under repeated loading which would result in eventual weakening of the adhesive bonds within the mixture. This simulates the pumping action of heavy vehicle on a saturated pavement surface. The MSR of the specimens subjected to repeated load as part of conditioning was compared to the MSR of the specimens not subjected to load conditioning. Figure 10 shows the MSR values before conditioning, as part of load conditioning, and after load conditioning. All specimens were subjected to vacuum saturation of 15-mm Hg for 30 minutes. The "Not Load Conditioned" specimens were then dried and tested to determine "After" MSR. The "Load

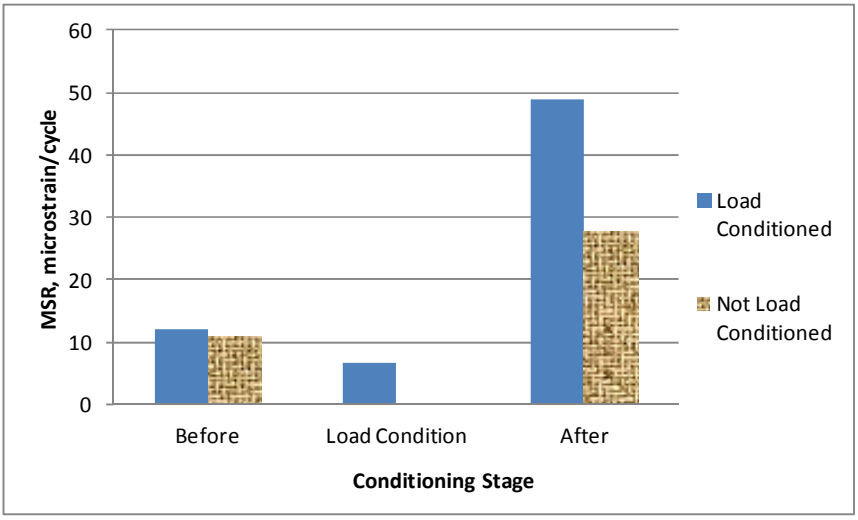

Fig. 10 Comparison of the MSR of the specimens mechanically loaded and those that were not mechanically loaded as part of moisture conditioning

Conditioned" specimens were subjected to 300 load cycles at the test stress level to develop pore pressure damage, then dried and tested again to determine "After" MSR. It was observed that when the saturated specimens were subjected to repeated load as part of load conditioning, MSR dropped drastically (usually to less than half), signifying the increased strength of the material due to pore pressure. However, after drying the specimens, the load conditioned specimens showed a larger increase in MSR than those that were not mechanically conditioned, signifying damage due to pore pressure.

3.4 Comparison of T 283 and the Proposed Conditioning Scheme

Figure 11 shows the comparison of the MSR ratios of the SCB specimens conditioned according to the AASHTO T 283 scheme and using the procedure proposed in this study (vacuum saturation plus load conditioning). The figure shows that the SCB specimens conditioned according to T283 drastically failed in the mechanical testing (MSR ratio of 9). This could be due to embrittlement of the specimens from prolonged conditioning in the 60°C water bath. Figure 12 shows the SCB specimens conditioned according to AASHTO T283 at the left and those conditioned according to the proposed conditioning scheme at the right. As indicated from the figure T283 conditioning was too severe for the SCB specimens. This indicates that smaller sized specimens would require less intense conditioning process than T 283 which may result in significant time saving.

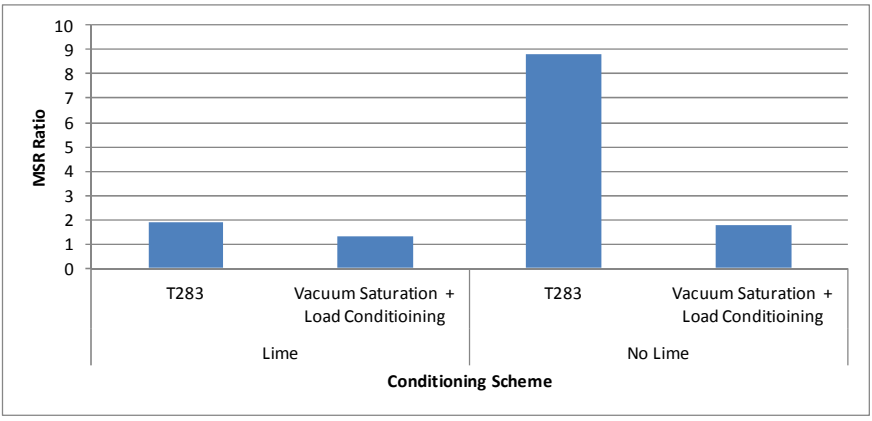

Fig. 11 Comparison of the MSR ratios of the AASHTO T283and Vacuum/load Conditioned WY Specimens

Fig. 12 AASHTO T283 (left) and Vacuum/load Conditioned WY Specimens (right)

4 Summary and Conclusion

In summary, incremental repeated load test made possible testing a sample before and after conditioning; thus, sample to sample variability is reduced. Therefore, the main effect on the mixture from moisture damage would be more pronounced. The Minimum Strain Rate (MSR) parameter showed very high sensitivity to the moisture induced damage since it is insensitive to any micro damages that do not result in property changes.

It was indicated that the long conditioning process of T 283 is not required for causing moisture damage. A shorter conditioning process can be used if the mechanical test is sensitive to the caused damage, if the specimens are small and accessible to moisture from all sides, and if the components of moisture conditioning process are effective.

Smaller specimens are preferable over the T283 specimens for moisture damage determination. This is for several reasons. First, a better distinction between MSR of moisture susceptible and moisture resistant mixtures were obtained using smaller sized specimens. Second, more test replicates can be obtained from a single gyratory compacted specimens. Third, a lower load level is required to test the smaller specimens, which is desirable when there is limitation with the loading machine. Fourth, which is the most important reason; small size specimen can be easily cored from the field.

Two conditioning processes showed effectiveness in causing moisture damage while keeping the specimens intact. The conditioning process proposed in this study involving 30 min. of vacuum suction at 15 mm Hg followed by a 300-cycle increment of repeated load using a hydraulic testing machine induced notable damage to the moisture sensitive mixture of WY. Similarly, the Moisture Induced Sensitivity Test (MIST) conditioning device at 40ºC and 40 Psi induced notable

damage to the WY mixture; however, adding 30 min of vacuum at 15 mm Hg before applying MIST, showed an increased induced damage. This indicates that vacuum saturation and mechanical loading are the two important factors for moisture conditioning process. The mechanical loading of the saturated specimens, as part of the conditioning process, would accelerate the weakening of the cohesive and adhesive bonds within the mixtures. Therefore, less vacuum level and duration are needed to cause moisture damage.

And finally, drying the conditioned specimens before mechanical test would reveal the true weakening of the mixtures as a result of moisture conditioning. Lower MSR values were observed from testing wet specimens than those specimens that were dried. This was because the water that is present in the mixture's pores increases the resistance of the material to the applied load.

References

[1] AASHTO Standard Specifications for Transportation Materials and Methods of Sampling and Testing (Part 2-Tests), 32th edn. American Association of State Highway and Transportation Officials, Washington, DC (2012)

[2] Azari, H., Kringos, N., Scarpas, A.: Precision Estimates of AASHTO T 283 and Identification of Parameters Causing Variability in HMA Moisture Resistance Test Results. NCHRP Web Document 166 (2010)

[3] Stuart, K.D.: Moisture Damage in Asphalt Mixtures: A-State-of-the-Art Report. Federal Highway Administration (FHWA) Report FHWA/RD-90-019, McLean, Virginia (1990)

[4] Stuart, K.D.: Evaluation of Procedures Used to Predict Moisture Damage in Asphalt Mixtures. Federal Highway Administration (FHWA) Report FHWA/RD-86/091, McLean, Virginia (1986)

[5] Kandhal, P., Rickards, I.: Premature Failure of Asphalt Overlays from Stripping: Case Histories. Asphalt Paving Technology 70, 301–351 (2002)

[6] Bausano, J., Williams, R.C.: Transitioning from AASHTO T283 to the Simple Performance Test Using Moisture Conditioning. Journal of Materials in Civil Engineering 21(2) (2009)

[7] Solaimanian, M., Bonaquist, R., Tandon, V.: Improved conditioning and Testing Procedures for HMA Moisture Susceptibility. NCHRP Report 589, Transportation Research Board, National Research Council, Washington, DC (2007)

[8] Epps, J., Sebaaly, P., Penaranda, J., Maher, M., McCann, M., Hand, A.: NCHRP Report 444: Compatibility of a Test for Moisture-Induced Damage with Superpave Volumetric Mix Design (2000)

[9] Laukkanen, K., Halonen, P., Pyy, E.: Resistance of asphalt mixture to freeze - thaw-cycles and combined effect of water and loadings, Finnish Transport Agency, P.O. Box 33, Helsinki FI-00521 Finland (2012), http://worldcat.org/isbn/9789522551627

[10] Kringos, N., Azari, H., Scarpas, A.: Micro-Scale Finite Element Analysis of Moisture Infiltration in the Modified Lottman test. 43 Transportation Research Record, Journal of the Transportation Research Board 2(2127) (2009)

[11] Birgisson, B., Roque, R., Page, G., Wang, J. (2007), Development of New Moisture-Conditioning Procedure for Hot-Mix Asphalt. Transportation Research Record, Journal of the Transportation Research Board 2001 (2001)
[12] Roque, R., Isola, M., Chun, S., Zou, J., Koh, C., Lopp, G.: Effects of Laboratory Heating, Cyclic Pore Pressure, and Cyclic Loading on Fracture Properties of Asphalt Mixture. Florida Department of Transportation Report, Research Management Center, 605 Suwannee Street Tallahassee, FL, 32399 (2012)
[13] Azari, H., Mohseni, M.: Incremental Repeated Load Permanent Deformation Testing of Asphalt Mixtures. In: Report No. 12-4381, Transportation Research Board 91th Annual Meeting (2012)
[14] Azari, H., Mohseni, M.: Effect of Short-Term Conditioning and Long-Term Aging on Permanent Deformation Characteristics of Asphalt Mixtures. Accepted for publication, AAPT Journal (2013)
[15] Azari, H., Mohseni, M.: Permanent Deformation Characterization of Asphalt Mixtures Using Incremental Repeated Load Testing. Accepted for publication, Transportation Research Board 92th Annual Meeting (2013)
[16] http://instrotek.com/material-testing/laboratory-products/mist/

Mode II Cracking Failure in Asphalt Concrete by Using a Non-conserved Phase Field Model

Yue Hou[1,*], Lei Zhang[2], Pengtao Yue[3], Troy Pauli[4], Fengyan Sun[5], and Linbing Wang[6]

[1] Virginia Tech Transportation Institute, Blacksburg, VA 24061
hyue@vt.edu
[2] Research Institute of Highways (RIOH), China
[3] Department of Mathematics, Virginia Polytechnic Institute and State University, Blacksburg, VA 24061, USA
[4] Western Research Institute, Laramie, WY 82072
tpauli@uwyo.edu
[5] National Center for Material Service Safety, University of Science and Technology, Beijing, China
[6] The Via Department of Civil and Environmental Engineering, Virginia Polytechnic Institute and State University, Blacksburg, VA 24061, USA

Abstract. Cracking failure in asphalt concrete has always been one of the most serious problems in pavement structures. Classical fracture mechanics is the most widely used method to analyze the initiation and propagation of cracks. In this paper, a new modeling and computational tool the phase-field method is proposed for modeling the Mode II cracking failure in asphalt concrete. This method describes the microstructure using a phase-field variable which assumes one in the intact solid and negative one in the crack region. The Mode II fracture toughness is modeled as the Mode II surface energy stored in the diffuse interface between the intact solid and crack void. To account for the growth of cracks, a non-conserved Allen-Cahn equation is adopted to evolve the phase-field variable. The energy-based formulation of the phase-field method handles the competition between the growth of surface energy and release of elastic energy in a natural way: the crack propagation is a result of the energy minimization in the direction of the steepest descent. Both the linear elasticity and phase-field equation are solved in a unified finite element frame work, which is implemented in the commercial software COMSOL. It was discovered that the crack propagation in phase-field agrees very well with the Griffith criterion.

Keywords: Mode II cracking failure; Asphalt concrete; Phase field modeling; Non-conserved.

* Corresponding author.

N. Kringos et al. (Eds.): *Multi-Scale Model. & Charact. of Infrastruct. Mater.,* RILEM 8, pp. 127–138.
DOI: 10.1007/978-94-007-6878-9_10

1 Introduction

Cracking failure in asphalt concrete is one of the most serious problems that may lead to pavement failure, which may be caused by traffic overloading, thermal loading, and material internal structure changes due to many complex factors. The cracking dynamics of asphalt concrete and asphalt mixture has always been a challenging issue for pavement engineers (Peterson et al. 2009). Generally, current research of the asphalt cracking failure is focused on the Mode I cracking, which is caused by compressive or tensile loading. The Strategic Highway Research Program (SHRP) was the first to realize the importance of the fracture properties of asphalt material (Anderson et al. 1994). However, there are two problem uncovered considering the progress in the Mode I cracking analysis: first is that although the cracking caused by tensile loading has been investigated, the cracking caused by shear loading that is the pure Mode II cracking failure mechanism of asphalt concrete has not been well studied. Actually the excessive shear loading is very usual in the circumstances such as sudden braking of a vehicle; another problem is that till now, most of the analyses of fractures in asphalt concrete are still based on the Classical Fracture Mechanics (CFM) (Griffith 1921), which needs to clearly depict the crack front conditions and thus may be very complicated. In order to simulate concisely, a new mathematical tool phase-field method is employed for analysis.

The Phase-Field Method (PFM) was originally proposed by Cahn and Hilliard for the spinodal decomposition in phase transition (Cahn et al. 1958). In this model, a phase-field variable is introduced to identify difference phases, based on which a free energy functional is constructed. The whole system evolves toward the direction which minimizes this free energy. In fracture, the phase field variable is used to identify the unbroken solid and the fully broken phase inside the crack. The system is driven by the chemical potential, which is the variation of the free energy with respect to the phase-field variable. Due to the non-conserved nature of crack growth, the Allen-Cahn dynamics has dominated the phase-field modeling of fractures. For example, Kuhn et al. (2010) adopted a non-double-well potential in his Allen-Cahn formulation and still captured the onset of crack propagation correctly. Song et al. (2007) used the phase-field method to investigate the effect of electric field on the crack propagation in a ferroelectric single crystal.

In this paper, the development of an Allen-Cahn phase-field model that can be implemented in the commercial software COMSOL is presented. The model was validated using the two-dimensional simulations of Mode II cracking and comparison with the Griffith theory and experimental results. The ultimate goal is to simulate the crack propagation in asphalt concrete under complex loading conditions, which occurs in reality.

2 Theoretical Model

Landau-Ginzburg Free Energy

In our model, the phase field method uses a phase-field variable ϕ to describe the microstructure surface, where the phase-field variable is set as $\phi = -1$ for the broken phase and $\phi = +1$ for the intact phase, and a diffuse interface separates the two phases. Following Yue et al. (2010), the total free energy in the system can be written in the Landau-Ginzburg form as:

$$F = \int_{\Omega} (f_{gr} + f_{loc} + f_{el}) dV, \tag{1}$$

where

$$f_{gr} = \frac{1}{2}\lambda |\nabla \phi|^2 \tag{2}$$

is the gradient energy density,

$$f_{loc} = \frac{\lambda}{4\epsilon^2}(1-\phi)^2(1+\phi)^2 \tag{3}$$

is the local free energy (double-well potential) which has two minima at the two bulk phases, and f_{el} is the elastic energy. Here λ is the mixing energy density; and ϵ controls the interface thickness. The relationship between λ and ϵ is given as (Yue et al. 2006)

$$\lambda = \frac{3\gamma\epsilon}{\sqrt{8}}, \tag{4}$$

where γ is the surface energy. In facture simulations, $\gamma = \frac{G_c}{2}$, where G_c is the Mode II fracture energy, which is a material parameter. For convenience of further derivation, we denote the summation of the gradient energy, local free energy and the elastic energy of the system as the total energy potential Ψ.

Consider the crack in asphalt concrete occurs at low temperature, it is simplified as a linear elastic material in this research. Consequently, the elastic energy density can be expressed as

$$f_{el} = \frac{E(\phi)}{2(1+\nu)}\left(\frac{\nu}{1-2\nu}(\varepsilon_{ii})^2 + \varepsilon_{ik}\varepsilon_{ik}\right), \tag{5}$$

where $E(\phi)$ is the elastic modulus and ν is Poisson's ratio. Based on the work of Wise et al. (2004), we express $E(\phi)$ as

$$E(\phi) = E + (E - E_0)h(\phi), \tag{6}$$

where E and E_0 are the elastic moduli of the intact material and the broken phase respectively, and

$$h(\phi) = -\frac{1}{4}\phi^3 + \frac{3}{4}\phi + \frac{1}{2} \tag{7}$$

is an interpolation function that satisfies $h(-1) = 0$, $h(1) = 1$, and $h'(-1) = h'(1) = 0$. It should be noted that the elastic modulus in broken phase (which is physically a vacuum) should be zero and the Poisson's ratio is undefined. However, to avoid numerical singularity in elasticity calculations, we assume that $E_0 = 0.01E$ and $\nu = 0.3$ that is phase-independent throughout the calculation domain.

Elasticity

In a Lagrangian system, the infinitesimal strain tensor $\boldsymbol{\varepsilon}$ is obtained by

$$\varepsilon = \frac{1}{2}(\nabla \mathbf{u} + (\nabla \mathbf{u})^T), \tag{8}$$

where $\mathbf{u}$ is the displacement field. According to Hooke's law, the elastic stress is given by

$$\sigma_{ik} = \frac{E(\phi)}{1+\nu}(\varepsilon_{ik} + \frac{1}{1-2\nu}\delta_{ik}\varepsilon_{ii}). \tag{9}$$

Note that in our simulation, for simplicity asphalt concrete is considered as linear elastic material for convenience. The reader may modify equation (9) to adopt the visco-elastic property according to the Generalized Maxwell mode. The stress satisfies the force balance

$$\nabla \cdot \boldsymbol{\sigma} = 0, \tag{10}$$

which is eventually used to determine the displacement field. This elasticity part is handled by the structural analysis module in COMSOL.

Phase-field model

After we obtain the elastic energy, we can plug it into the phase-field model. Considering the fact that the volume of the crack phase grows during crack propagation, the following non-conserved Allen-Cahn equation is adopted:

$$\frac{\partial \phi}{\partial t} = -M\psi \tag{11}$$

where M is the mobility parameter that controls the propagation in asphalt and ψ is the chemical potential

$$\psi = \frac{\delta F}{\delta \phi} = -\nabla \cdot \lambda \nabla \phi + \frac{\lambda}{\epsilon^2}(\phi^2 - 1)\phi + \frac{\partial f_{el}}{\partial \phi} \tag{12}$$

The mobility parameters is usually expressed as $M = \chi\varepsilon^2$ where χ is called the mobility tuning parameter which reflects the propagation speed. Note that $\frac{\partial f_{el}}{\partial \phi}$ is simply

$$\frac{\partial f_{el}}{\partial \phi} = h'(\phi)\frac{E}{2(1+\nu)}\left(\frac{\nu}{1-2\nu}(\varepsilon_{ii})^2 + \varepsilon_{ik}\varepsilon_{ik}\right) \tag{13}$$

Weak form of Equation (11) is needed for the calculation in COMSOL. From Equation (11) and (12), we get

$$\frac{\partial \phi}{\partial t} = \lambda\chi\left(-\nabla\cdot\epsilon^2\nabla\phi + (\phi^2-1)\phi + \frac{\epsilon^2}{\lambda}\frac{\partial f_{el}}{\partial \phi}\right) \tag{14}$$

Multiplying Equation (14) by the test function $\tilde{\phi}$ and then integrating over the computational domain, we get the weak form

$$\int_\Omega \frac{\partial \phi}{\partial t}\tilde{\phi}d\Omega = \int_\Omega -\lambda\chi\left(-(\nabla\cdot\epsilon^2\nabla\phi)\tilde{\phi} + (\phi^2-1)\phi\tilde{\phi} + \frac{\epsilon^2}{\lambda}\frac{\partial f_{el}}{\partial \phi}\tilde{\phi}\right)d\Omega \tag{15}$$

Using Divergence Theorem, this equation can be further expressed as

$$\int_\Omega \frac{\partial \phi}{\partial t}\tilde{\phi}d\Omega = \int_\Omega -\lambda\chi\left(\epsilon^2\nabla\phi\cdot\nabla\tilde{\phi} + (\phi^2-1)\phi\tilde{\phi} + \frac{\epsilon^2}{\lambda}\frac{\partial f_{el}}{\partial \phi}\tilde{\phi}\right)d\Omega + \int_{\partial\Omega} -\lambda\chi(\epsilon^2\nabla\phi\cdot\vec{n}\tilde{\phi})ds \tag{16}$$

Consider a stable situation of crack which means no flux across the boundary and thus the natural boundary condition is adopted

$$\nabla\phi\cdot\vec{n} = 0 \tag{17}$$

such that the surface integral on $\partial\Omega$ vanishes. Consequently, Equation (17) is simplified to

$$\int_\Omega \frac{\partial \phi}{\partial t}\tilde{\phi}d\Omega = \int_\Omega -\lambda\chi\left(\epsilon^2\nabla\phi\cdot\nabla\tilde{\phi} + (\phi^2-1)\phi\tilde{\phi} + \frac{\epsilon^2}{\lambda}\frac{\partial f_{el}}{\partial \phi}\tilde{\phi}\right)d\Omega \tag{18}$$

which is the equation that we input to COMSOL for solution.

3 Results

Generalized Eshelby tensor and J - integral in Phase-field

In phase-field, the total energy potential is denoted as $\Psi = \Psi(\varepsilon_{ij}, x_i)$ and the potential gradient is then obtained as shown in equation (19) based on the chain rule

$$\nabla\Psi = \frac{\partial\Psi}{\partial\varepsilon}\nabla\varepsilon + \frac{\partial\Psi}{\partial\phi}\nabla\phi + \frac{\partial\Psi}{\partial\nabla\phi}\nabla\nabla\phi + (\frac{\partial\Psi}{\partial x})_{expl} \tag{19}$$

where the explicit derivation of Ψ is given as as (Kim et al. 2003)

$$(\frac{\partial\Psi}{\partial x})_{expl} = \frac{\partial}{\partial x_k}\Psi(\varepsilon_{ij}, x_i)\big|\varepsilon_{ij} = const., x_m = const.\ for\ m \neq k \tag{20}$$

The configurational force balance gives

$$\nabla \cdot \boldsymbol{b} + \boldsymbol{g} = 0 \tag{21}$$

where $\boldsymbol{b}$ is the generalized Eshelby tensor given as (Kuhn et al. 2010)

$$\boldsymbol{b} = \boldsymbol{\Psi 1} - \nabla\mathbf{u}^{\mathrm{T}}\sigma - \frac{\partial\boldsymbol{\Psi}}{\partial\nabla\phi}\nabla\phi \tag{22}$$

and $\boldsymbol{g}$ is the configurational body force term shown as(Kuhn et al. 2010)

$$\boldsymbol{g} = \frac{\frac{\partial\phi}{\partial t}}{M}\nabla\phi - (\frac{\partial\Psi}{\partial x})_{expl} \tag{23}$$

The traditional method to describe the cracking is by using the *J* – integral (Rice 1968) shown as

$$J = \int_{\partial\Omega}(f_{el}dy - \mathbf{T}\nabla\mathbf{u}^{\mathrm{T}}dS) \tag{24}$$

where f_{el} is the elastic strain energy in equation (5) and *dS* is the length increment along the given path $\partial\Omega$ shown in Figure 1. $\mathbf{T} = \boldsymbol{\sigma}\cdot\hat{n}$ is the traction vector, where $\hat{n}$ is the unit vector normal to $\partial\Omega$. In phase-field *J* integral is obtained by the contour integration of the generalized Eshelby tensor as

$$J = \int_{\partial\Omega}\boldsymbol{b}\cdot\hat{n}\,dS \tag{25}$$

Kuhn et al. (2010) split the generalized Eshelby tensor in equation (22) to two parts as the elastic energy part and the gradient energy part. In our formulation, we denote them as

$$\boldsymbol{b}^{el} = f_{el}\mathbf{1} - \nabla\mathbf{u}^{\mathrm{T}}\sigma \tag{26}$$

and

$$\boldsymbol{b}^{gr} = f_{gr}\mathbf{1} - -\frac{\partial \boldsymbol{\Psi}}{\partial \nabla \phi}\nabla\phi = \left(\frac{\lambda}{4\epsilon^2}(1-\phi)^2(1+\phi)^2 + \frac{1}{2}\lambda|\nabla\phi|^2\right)\delta_{ij} - \frac{\partial \boldsymbol{\Psi}}{\partial \nabla \phi}\nabla\phi \tag{27}$$

Based on equation (21) and integrate the configurational force over the body, we have

$$\int_\Omega \boldsymbol{g}\, dV = -\int_\Omega \nabla \cdot \boldsymbol{b}\, dV \tag{28}$$

According to the Divergence Theorem, we rewrite the integral of the divergence of Elshelby tensor b as a contour integral on the boundary, which is

$$\int_\Omega \nabla \cdot \boldsymbol{b}\, dV = \int_{\partial\Omega} \boldsymbol{b}\hat{\mathrm{n}}\, dS = \int_{\partial\Omega} \boldsymbol{b}_{el}\hat{\mathrm{n}}\, dS + \int_{\partial\Omega} \boldsymbol{b}_{gr}\hat{\mathrm{n}}\, dS \tag{29}$$

Note that equation (28) reflect *J* – integral. We then divide the energy density and split the calculation domain into two parts as shown in Figure 1:$\Gamma = \Gamma_1 + \Gamma_2 + \Gamma_3 + \Gamma_4$. Note that$\Gamma_1, \Gamma_2, \Gamma_3$ and Γ_{BA} makes a closed contour integration. And thus we have

$$J^{el} = \int_{\partial\Omega} \boldsymbol{b^{el}} \cdot \hat{n}\, ds = \int_{\Gamma_1} \boldsymbol{b^{el}} \cdot \hat{n}\, ds + \int_{\Gamma_2} \boldsymbol{b^{el}} \cdot \hat{n}\, ds + \int_{\Gamma_3} \boldsymbol{b^{el}} \cdot \hat{n}\, ds + \int_{\Gamma_4} \boldsymbol{b^{el}} \cdot \hat{n}\, ds = \int_{\partial\Omega:A\to B} \boldsymbol{b^{el}} \cdot \hat{n}\, ds + \int_{\partial\Omega:B\to A} \boldsymbol{b^{el}} \cdot \hat{n}\, ds \tag{31}$$

And similarly

$$J^{gr} = \int_{\partial\Omega} \boldsymbol{b^{gr}} \cdot \hat{n}\, ds = \int_{\partial\Omega:A\to B} \boldsymbol{b^{gr}} \cdot \hat{n}\, ds + \int_{\partial\Omega:B\to A} \boldsymbol{b^{gr}} \cdot \hat{n}\, ds \tag{32}$$

Since in the internal crack, the elastic energy and stress vanished, it can be seen that elastic part shown in equation (31) is then only consists the contour integral $B \to A$, which means $\int_{\partial\Omega} \boldsymbol{b^{el}}\hat{n}\, ds = \int_{\partial\Omega:B\to A} \boldsymbol{b^{el}}\hat{n}\, ds$ where the phase-field variable $\phi = 1$. It degenerates to the normal situation as we expect. For the gradient energy, it vanishes on $\partial\Omega: A \to B$ and thus the equation (31) can be simplified as

$$\int_{\partial\Omega} \boldsymbol{b^{gr}}\hat{n}\, ds = \int_{\partial\Omega:A\to B} \boldsymbol{b^{gr}}\hat{n}\, ds \tag{33}$$

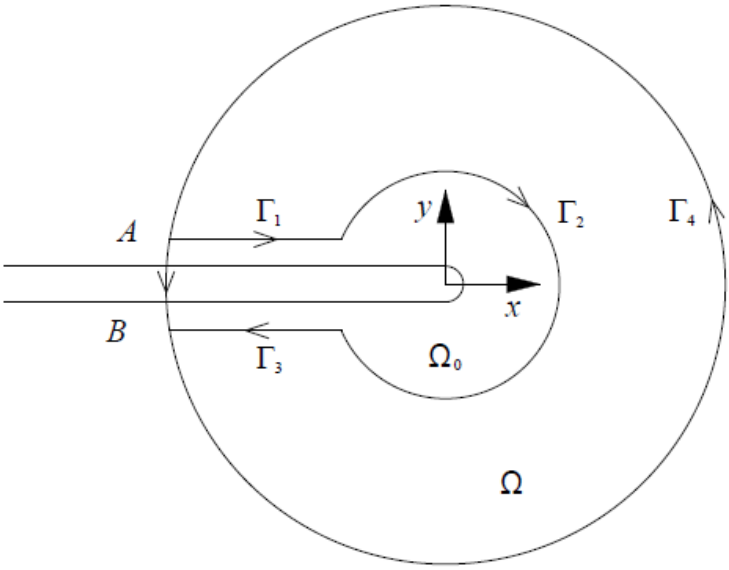

Fig. 1 ϕ contour in the integration domain in Mode II cracking

To solve the integral of the gradient part on $\Omega: B \to A$, we consider the one-dimensional situation of equation (27) and obtained the result based on the contributions of Yue et al. (2004), which reads

$$\gamma = \int_{-\infty}^{+\infty} \{\frac{\lambda}{4\epsilon^2}(1-\phi)^2(1+\phi)^2 + \frac{1}{2}\lambda(\frac{d\phi}{dx})^2\} \tag{34}$$

where γ is the Mode II surface energy. The elastic energy has been totally transformed to the surface energy. Note that we have two new surfaces generating during the crack process so$G_c = 2\gamma$ where G_c is the Mode II fracture energy and the criterion for the crack begins to propagate in phase-field is $J \geq G_c$, which demonstrates that our theory is fundamentally agrees with the Griffith's theory.

Simulation results

Consider a homogeneous model of asphalt concrete and use a two-dimensional finite element model to simulate the cracking process in COMSOL under shear loading. A fixed Eulerian mesh is used to describe the internal interfaces between the intact solid and crack void. The mesh refines adaptively at the interface, as shown in Figure 2, to resolve the ϕ profile across the interface. As we can see, a double – notch exist on both edges. And then two edges will move in the opposite direction so that shear stress will make the initial crack propagate.

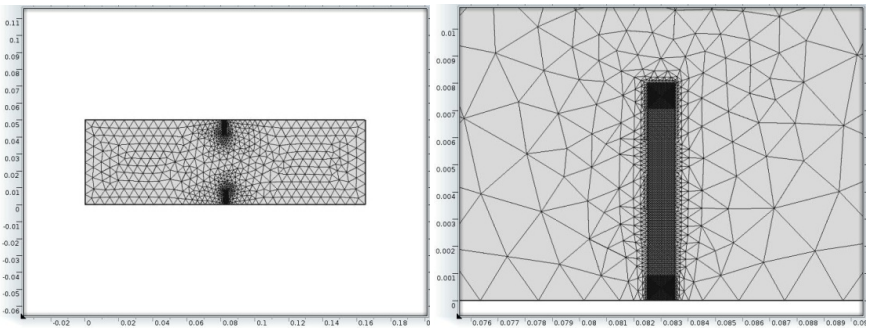

Fig. 2 (a) Unstructured triangular mesh generated by COMSOL with interfacial refinement (b) Magnified view of crack

We consider plane strain and the computational domain is a rectangular with length 0.165m and width 0.05m. We then choose the interfacial thickness $\epsilon = 0.0004\,m$ and the initial crack length $a = 0.008\,m$. Because of the diffuse nature of the phase-field method, we need to impose a finite crack width, which we use W =0.001 m in this simulation. The finest mesh size is set to be $\Delta x = \frac{1}{33}W$ (i.e., $\epsilon \approx 6.6\Delta x$) which sufficiently resolves the diffuse interface (Yue et al. 2010, 2006).

Figure 2 shows that shear movement happens on top and bottom boundaries where the velocity is 0.0002 m/s. The elastic modulus is set as 3450MPa.

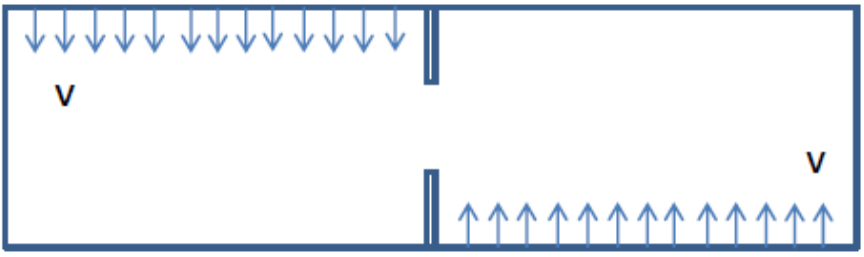

Fig. 3 Opposite movements happens on top and bottom boundaries

Crack propagation at different time instants is shown in Figure 5. It can be clearly seen that crack propagates by applying the boundary moving condition while there is a diffuse interface between the crack phase and the intact phase. It should be noted that ϕ may not be exactly in [-1, 1] in the simulations. However, the deviation is always less than 3%, and therefore can be neglected. Limited by our computational power, we use a relatively coarse mesh which may smooth out the possible crack branching as shown in results of Spatschek *et al.* (2007). It should be noted that under the current force loading condition, the crack propagation is unstable once it starts.

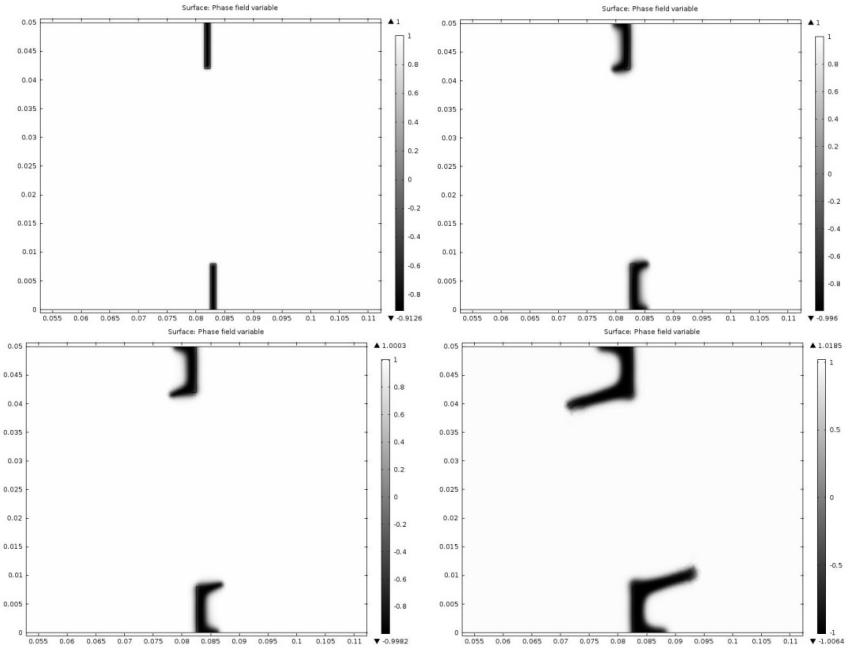

Fig. 4 Magnified view of crack propagation. The snapshots are taken at t=0, 15 Δt , 20 Δt and 60 Δt where the time step interval $\Delta t = 0.01$s is the time step used in the simulation. $\gamma = 100\, J/m^2$ (Braham et al., 2009).

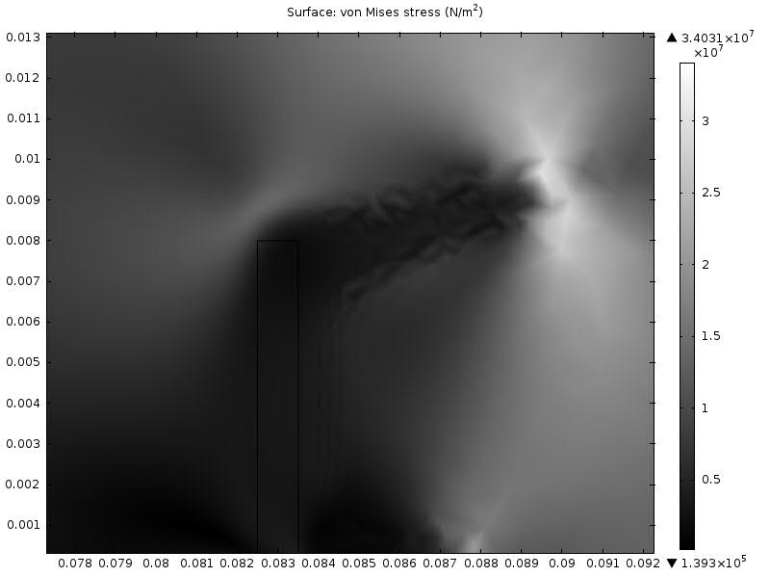

Fig. 5 Magnified view of von Mises stress distribution near crack tip at t=30 Δt

As expected, there is a stress concentration at the crack tip, as shown in Figure 5. The stress contours resemble the conclusions in Song et al. (2007). In the region near the crack tip, the von Mises stress is much larger than that in the intact regions in front of the crack. Immediately above and below the crack, the stress is much lower than the average, since the elastic energy has been released to create new fracture surface area. This observation is in agreement with the classical fracture mechanics. The crack direction is bend bout not almost straight along the *x*-axis, which is reasonable since the shear loading will significantly affect the corresponding kink angle.

4 Summary

In this paper, we present a non-conserved phase field model for mode II cracking in asphalt concrete. The shear simulation on the two-notch asphalt concrete system is conducted. The crack propagation process can then be captured by using the appropriate material property parameters. During the cracking process, the elastic energy is transformed to form the two new surfaces. Overall, the Phase-field model is capable of simulating Mode II fracture in asphalt concrete with reasonable accuracy and presents a promising and innovative method for modeling the low-temperature cracking of asphalt concrete for better quantitative understanding.

Acknowledgement. The paper presented here was performed under the Asphalt Research Consortium Project. The authors would like to express their sincere gratitude to FHWA for funding and the project panel for advising. The authors would also like to thank Mr. Rui Sha for participating in the asphalt cracking experiments.

References

1. Anderson, D.A., Christensen, D.W., Bahia, H.U., Sharma, M.G., Antle, C.E., Button, J.: Binder Characterization and Evaluation. Strategic Highway Research Program (SHRP) A-369, National Research Council (1994)
2. Cahn, J.W., Hilliard, J.E.: Free Energy of a Nonuniform System. I. Interfacial Free Energy. Journal of Chemical Physics 28, 258–267 (1958)
3. Griffith, A.A.: The phenomena of rupture and flow in solids. Philosophical Transactions of the Royal Society of London, Seria A 221, 163–197 (1921)
4. Kim, J.-H., Paulino, G.H.: Mixed-mode J-integral formulation and implementation using graded elements for fracture analysis of nonhomogeneous orthotropic materials. Mechanics of Materials 35, 107–128 (2003)
5. Kuhn, C., Muller, R.: A continuum phase field model for fracture. Engineering Fracture Mechanics 77, 3625–3634 (2010)
6. Peterson, C., Buttlar, W., Braham, A.: Mixed-mode cracking in asphalt concrete. Advanced Testing and Characterization of Bituminous Materials 2, 785–795 (2009)

7. Rice, J.: A path independent integral and approximate analysis of strain concentration by notches and cracks. Journal of Applied Mechanics 35, 379–386 (1968)
8. Song, Y.C., Soh, A.K., Ni, Y.: Phase field simulation of crack tip domain switching in ferroelectrics. Journal of Physics D: Applied Physics 40, 1175–1182 (2007)
9. Spatschek, R., Muller-Gugenberger, C., Brener, E., Nestler, B.: Phase field modeling of fracture and stress-induced phase transitions. Physical Review E 75, 06611 (2007)
10. Wise, S.M., Lowengrub, J.S., Kim, J.S., Johnson, W.C.: Efficient phase-field simulation of quantum dot formation in a strained heteroepitaxial film. Superlattices and Microstructures 36, 293–304 (2004)
11. Yue, P., Feng, J., Liu, C., Shen, J.: A diffuse-interface method for simulating two-phase flows of complex fluids. Journal of Fluid Mechanics 515, 293–317 (2004)
12. Yue, P., Zhou, C., Feng, J., Ollivier-Gooch, C.F., Hu, H.H.: Phase-field simulation of interfacial dynamics in viscoelastic fluids using finite elements with adaptive meshing. Journal of Computational Physics 219, 47–67 (2006)
13. Yue, P., Zhou, C., Feng, J.: Sharp-interface limit of the Cahn-Hilliard model for moving contact lines. Journal of Fluid Mechanics 645, 279–294 (2010)

Asphalt Internal Structure Characterization with X-Ray Computed Tomography and Digital Image Processing

Ibrahim Onifade, Denis Jelagin, Alvaro Guarin, Bjorn Birgisson, and Nicole Kringos

Department of Transport Science (TSC)
Division of Highway and Railway Engineering
KTH Royal Institute of Technology
Brinellvägen 23, SE-100 44 Stockholm, Sweden
onifade@kth.se

Abstract. In this paper, detailed study is carried out to develop a new workflow from image acquisition to numerical simulation for the asphalt concrete microstructures. High resolution computed tomography scanned images are acquired and the image quality is improved using digital image processing techniques. Non-uniform illumination is corrected by applying an illumination profile to correct the background and flat-fields in the image. Distance map based watershed segmentation are used to segment the phases and separate the aggregates. Quantitative analysis of the micro-structure is used to determine the phase volumetric relationship and aggregates characteristics. The result of the quantitative analysis showed a very high level of reliability. Finite Element simulations were carried out with the developed micro-mechanical meshes to capture the strength and deformation mechanisms of the asphalt concrete micro-structure. From the micro-mechanical investigation the load transfer chains, higher strength characteristics and high stress localization at the mastic interface between adjacent aggregates was shown.

Keywords: X-ray computed tomography, digital image processing, finite element method, image based modeling.

1 Introduction

Asphalt concrete (AC) is a heterogeneous material which consists of mastic (binder and fines), aggregates and air-voids. The distribution of the air-voids in the matrix, the interaction between the aggregates and the mastic, and the properties of the aggregates and the mastic plays a vital role in determining the mechanical behavior of the asphalt concrete. Mainly, the aggregate properties determine the strength characteristics, the mastic determines the durability characteristics and the air-void is related to the rate of moisture damage and rutting in the asphalt concrete. The behaviour or response of the AC is highly dependent on the temperature and rate of loading. At low temperatures, it exhibits the characteristics of an elastic material

N. Kringos et al. (Eds.): *Multi-Scale Model. & Charact. of Infrastruct. Mater.,* RILEM 8, pp. 139–158.
DOI: 10.1007/978-94-007-6878-9_11

while at high temperatures above the glass transition temperature, the response is viscoelastic.

The micro-structure of AC is very complicated and it is defined by the gradation of aggregates, the orientation and number of contacts of aggregate particles, the properties of aggregate-binder interface, the voids structure, the chemical constituent of the bitumen, the texture of the stones, the adhesion between aggregates and mastic among others. [Wang, 2010]. Understanding the complex mechanical interaction that exists between the constituents of the asphalt concrete requires a reliable way to characterize the AC micro-structure.

In this context, mastic is referred to as the mixture of binder and fines. The main content of the binder is bitumen which is obtained from the fractional distillation of crude oil. The bitumen is made up of complex chains of hydrocarbon which makes it difficult to model the material using it's true chemical constituent. The hydrocarbon chains are very sensitive to changes in the environment (temperature), the rate of application of external forces or loads can also lead to a possible rearrangement of the chemical structure of the material. To overcome this difficulties, the mastic is usually represented using springs and dashpots to model the rate dependent response of the material. The Prony series, which is made up of springs and dashpots connected in series is used to model the mastic behavior in this study. In this study, the aggregates are considered as a linear elastic material and, as such, the parameters required for modeling the aggregates behavior are the Young's Modulus, the Poisson's ratio and the density.

Under loading condition, there may exist a rearrangement of the internal structure of the asphalt concrete mixture depending on the magnitude and duration of loading. The most important aspects to consider in the modeling are the contact between adjacent aggregates and the interface between the aggregate and the surrounding mastic. The morphological properties (shape, angularity and texture) determines the load transfer between aggregate particles at contact and the bonding at the interface between the mastic and aggregate particles. These properties are captured using the X-ray CT and quantified using an image processing software (Avizo).

In the past, the micro-structure of the AC has been simplified or over-idealized. Bazant et al. [Z.P. et al., 1990] and Schlangen and van Mier [Schlangen and van Mier, 1992] have represented the aggregates as rigid spherical particles while others Wittmann et al. [Wittmann et al., 1985] and Wang et al. [Wang et al., 1999] have used algorithm to generate a random micro-structure image of the asphalt concrete micro-structure. Most of these past investigations were based on 2D analyses of the asphalt concrete micro-stucture due to the complexities in generating or accurately representing the 3D micro-structure of asphalt concrete.

New techniques show a possible way to capture the micro-structure of the AC to generate models for numerical simulation, one of which is X-Ray Computed Tomography (CT). There has been a number of recent attempts to use X-Ray CT to investigate the internal structure of AC and to investigate its impact on the AC mechanical properties. Coleri et al. [Coleri et al., 2012b] used the X-ray CT to study the changes in AC micro-structure using full-scale test sections and Heavy Vehicle Simulator (HVS) loading, and X-ray CT images taken before and after HVS testing.

Coleri et al. [Coleri et al., 2012a] also used the X-ray computed tomography (CT) and digital image processing to generate the internal micro-structure of the asphalt mixtures and study the effectiveness of 2D and 3D models for the simulation of the shear frequency sweep at constant height (FSCH) test. Zelelew [Zelelew and Papagiannakis, 2011] used automated digital image processing (DIP) algorithm called Volumetrics based Global Minima (VGM) thresholding algorithm for processing asphalt concrete (AC) X-ray computed tomography (CT) images. The thresholding algorithm utilizes known volumetric properties of AC mixtures as the main criterion for establishing the air-mastic and mastic-aggregate gray scale boundary thresholds. Bhasin et al. [Bhasin, 2011] used X-ray CT images to study the 3-dimensional distribution of the mastic in asphalt composites. You et al. [You et al., 2012] developed a three-dimensional (3D) micro-structure-based computational model to predict the thermo-mechanical response of the asphalt concrete using a coupled thermo-viscoelastic, thermo-viscoplastic, and thermo-viscodamage constitutive model. You et al. [You et al., 2008] studied the dynamic modulus from the stress-strain response under compressive loads for two-dimensional 2D and three-dimensional 3D micro-structure-based discrete element models of asphalt mixtures. Masad et al. [Masad et al., 2005] developed an approach for constitutive modeling of the viscoplastic behavior of asphalt mixes and measured the micro-structure damage with X-ray computed tomography and image analysis techniques. However, very limited amount of work has been done so far for 3D image-based modeling of AC while some studies only considered the distribution of the aggregates and the mastic phase [You et al., 2012]

The air-voids, mastic and aggregates phase are considered in this study. The interface between the mastic phase and the aggregate phase is challenging to model when considering the mechanics of the mastic phase which is highly anisotropic. Further research is required to adequately understand the interaction at the boundary between the mastic and the aggregates. However, the spatial location of the contact points between adjacent aggregates is determined in this study and referred to as the contact geometry.

2 Objectives and Scope

The present study is aimed at developing the workflow from image acquisition to simulation for accurate characterization of the AC micro-structure. The main objectives of this study are to develop procedures for: (1) Segmentation of the three different phases in AC and determination of their volumetric relationship. (2) Determination of air-voids phase distribution with depth. (3) Determination of aggregates particle size gradation and distribution. (4) Determination of the distribution of contact zones between aggregates. (5) Micromechanical simulation using finite elements method (FEM).

The steps involved in this study are summarized in Figure 1

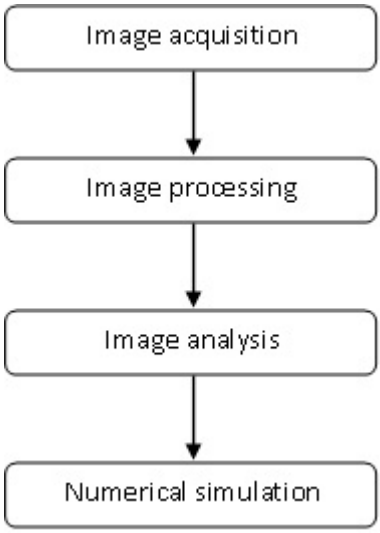

Fig. 1 Process workflow

3 Experimental Data and Scanning Procedure

In this study, the KTH X5000 CT X-ray scanner is used to obtain the detailed microscopic structure of the porous asphalt concrete core sample for further visualization, characterization and analysis. The X5000 CT scanner is a seven-axis universal x-ray imaging system designed for the inspection of large objects. It can accommodate a variety of part shapes, sizes and weights. It can produce X-ray intensities of up to 450kV.

The asphalt concrete core sample with a diameter of 100mm and a height of 80mm as shown in Figure 2 is scanned. The sample is scanned at an energy intensity of 225kV without beam filtration. The scanning resolution is 1949 x 1799 with a slice thickness of 59microns and a total of 1932 slices.

The x-ray scanning process includes sample preparation, warming-up the scanner, pre-scan settings, scanning, detector calibration and CT calibration. Beam hardening artifact is manifested in CT images with brighter edges than the center of the image. Beam hardening artifact reduces the quality of the scanned image and hence affects the phase segmentation results.

There are a number of possible techniques to reduce the beam hardening in the scanned image which includes the use of X-ray beam that is energetic enough to ensure that beam hardening is negligible, use of filters, increased exposure time among others [Ketcham and Carlson, 2001]. In this study, the beam hardening artifact is corrected using the background and flat field correction feature in Avizo Fire. The flat field is computed using the *bkgimg* command in Avizo which computes a background image from a gray level image and a binary mask (or no mask for all pixels of the image) using second order polynomial. The intensities of the 3D input image are then scaled according to the normalized intensities of the flatfield images.

Fig. 2 Porous asphalt concrete sample used in the present study

The input image gets brighter at pixels where the flatfield is dark and vice versa. In this way non-uniform illumination is compensated for [Avizo, 2009]. Other digital image processing and analysis is also performed using Avizo Fire application.

4 Digital Image Processing (DIP)

Image processing mainly involves editing and enhancement of digital image with the aim of improving the quality of the image or to extract relevant information. DIP is also used for the identification and segmentation of the different phases in the AC micro-structure.

The different techniques used in improving the quality of the acquired image include contrast enhancement, illumination correction and filtering to reduce noise in the image. Avizo background and flat field correction tool is used to correct non-uniform illumination in the acquired CT image. Non-uniform illumination correction helps to achieve improved segmentation results especially when the threshold based segmentation is used.

Filters are mainly used to reduce noise and thereby improve image quality. Different types of filters are used in image processing depending on the expected result or outcome. It is important to note that the nature of the mastic makes the segmentation process of the asphalt concrete sample a little cumbersome. Considering the fact that the mastic is a mixture of bitumen and fines, the threshold based segmentation becomes difficult as part of the mastic is identified as aggregates. This is as a result of the CT attenuation of the constituents materials in the asphalt concrete mix. Image filtering can be used to overcome this problem and thus improve the image segmentation results. Non-local means filter is used in this study to reduce the noise in the image and help improve segmentation as it smoothens regions inside objects while preventing smoothening near the edges.

Segmentation is the process of separating pixels with the same gray level value from those pixels with a different value. This is a very important step in AC image

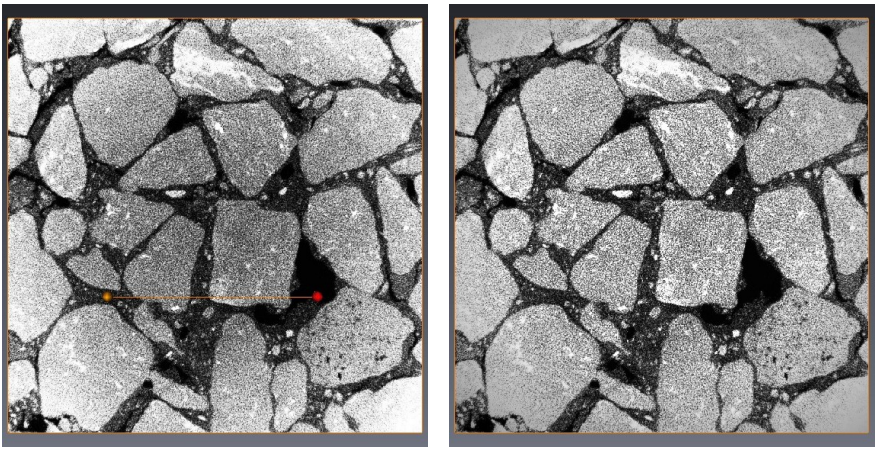

Fig. 3 a). Acquired image with beam hardening present b). Beam hardening corrected image of Asphalt concrete

processing as it is used to separate the constituents of the AC mixture. A good image resolution and contrast between the gray levels is essential for a good segmentation result. Figure 4(a) is the magnitude of the gradient showing the weak and strong edges in the image and Figure 4(b) is the plot of the grayscale along the probe line. The weak edges are variations in density in the same phase while the strong edges represent transition between adjacent phases. The magnitude of the gradient is obtained from the first derivate of the grayscale value in the x and y directions. The equations for calculation of the gradients and the magnitude are shown in equations 1 to 4.

$$(\nabla f) = [G_x^2 + G_y^2]^{\frac{1}{2}} \tag{1}$$

$$\overrightarrow{(\nabla f)} = \alpha(x,y) = tan^{-1}(\frac{G_x}{G_y}) \tag{2}$$

where

$$\frac{\partial f}{\partial x} = G_x = \frac{1}{2}(f(x+1,y) - f(x-1,y)) \tag{3}$$

$$\frac{\partial f}{\partial y} = G_y = \frac{1}{2}(f(x,y+1) - f(x,y-1)) \tag{4}$$

In 3D, one of the major challenge in processing and modeling of the AC micro-structure is the separation of the individual aggregates. Improperly separated aggregates can be seen as one big interconnected mass of stone and quantitative analysis of this interconnected stones does not give any meaningful result. Performing numerical analysis with such improperly segmented 3D micro-structure image does not simulate the behavior of the 3D mix under loading conditions. The 3D model

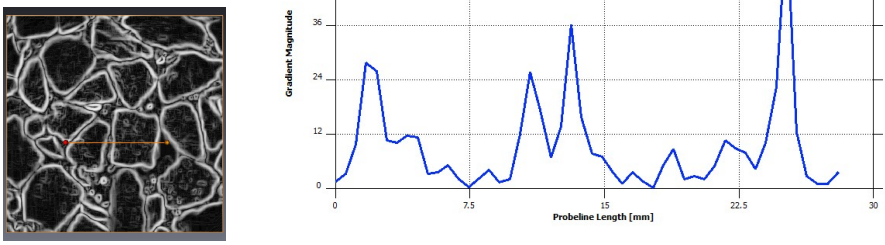

(a) (b)

Fig. 4 a). Gradient of the magnitude result showing edge of objects in the image b). Variation of gradient magnitude along probe line

Fig. 5 Phase segmented image

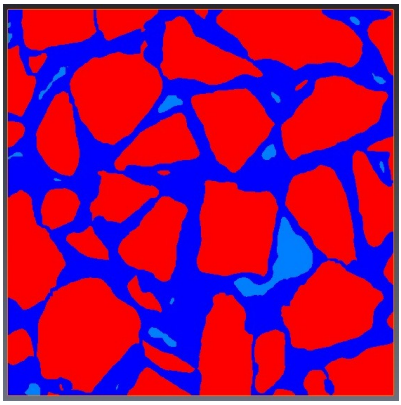

becomes too stiff and rarely deform under normal load conditions. Hence, the interaction between the aggregate and the binder is not well captured and accounted for.

To overcome this problem, different methods were employed for segmentation of the AC micro-structure. The distance-map based watershed segmentation technique gave the most satisfactory result. This method separates the aggregates in the 3D image, determines the contact point between aggregates and also create a region for mastic phase between the interface of two adjacent aggregates.

In this study, the air-void phase is segmented using basic thresholding operation since the gray intensity levels for the air-voids are quite distinct from those of the mastic and aggregates. The aggregate phase is segmented and separated using the distance-map and watershed segmentation and the mastic phase is obtained by subtracting the air-void phase and the aggregate phase from the full mask of the scanned sample. Figure 5 shows the phase-segmented AC image.

5 Digital Image Analysis and Results

After phase segmentation of the AC sample, image analysis is carried out so as to extract pertinent quantitative information. In this study, the interactive measure features of Avizo fire is used for the image analysis. The results of interest from the individual analysis of the aggregates are the Volume in 3D, Area in 3D, Feret diameter (length and width in 3D), and orientation of the aggregates. A sub-volume of $60mm \times 60mm \times 40mm$ was analyzed and the results presented in this section. For accurate aggregates size analysis, the bounding box dimensions can be used for aggregate characterization.

The volume in 3D of an object X is defined by the relationship in Equation 5 for a continuous case but estimated using Equation 6 for a discrete case. The volume is the number of pixels in region X multiplied by the volume of a voxel.

$$V(X) = \int_{R^3} (I(x,y,z)\, dxdydz) \tag{5}$$

$$V(X) = \sum_{i,j,k} I(x_i, y_j, z_k) \tag{6}$$

where
$I(x_i, y_j, z_k)$ = the intensity of the pixel of coordinates x_i, y_j, z_k
$I(x_i, y_j, z_k) = 1$ if the pixel lies within the object X and 0 otherwise

In order simplify the AC micro-structure, aggregate particles with length less than 2.34mm are considered as part of the mastic. The total number of aggregates in the sample after the clean-up is 403 stones. The distribution of the length of the stones is shown in Figure 6 and the distribution of the width in Figure 7. The 3D volume distribution of the stones is shown in Figure 8.

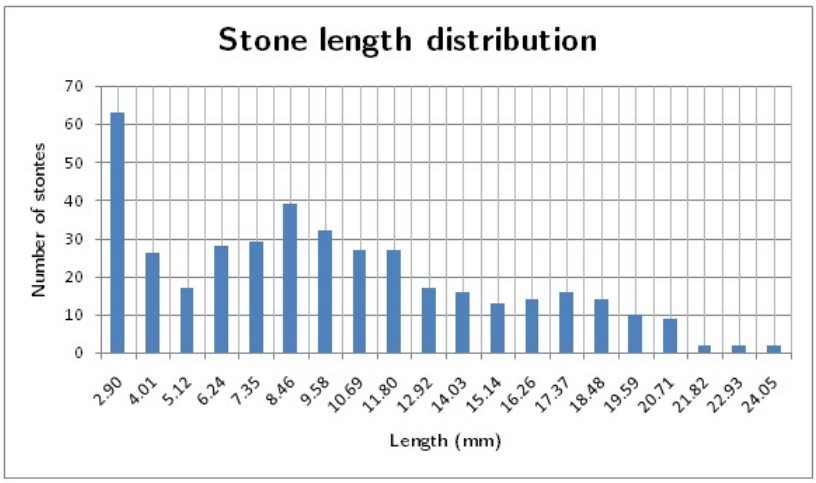

Fig. 6 Distribution of length of stones in the sample

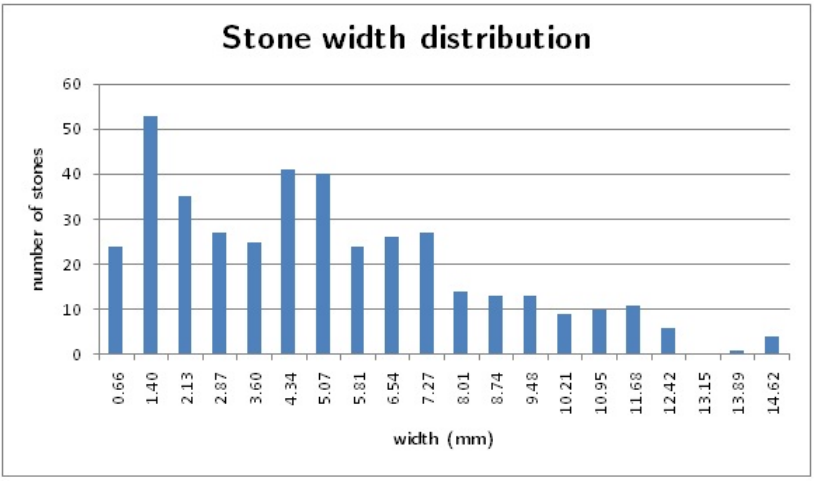

Fig. 7 Distribution of width of stones in the sample

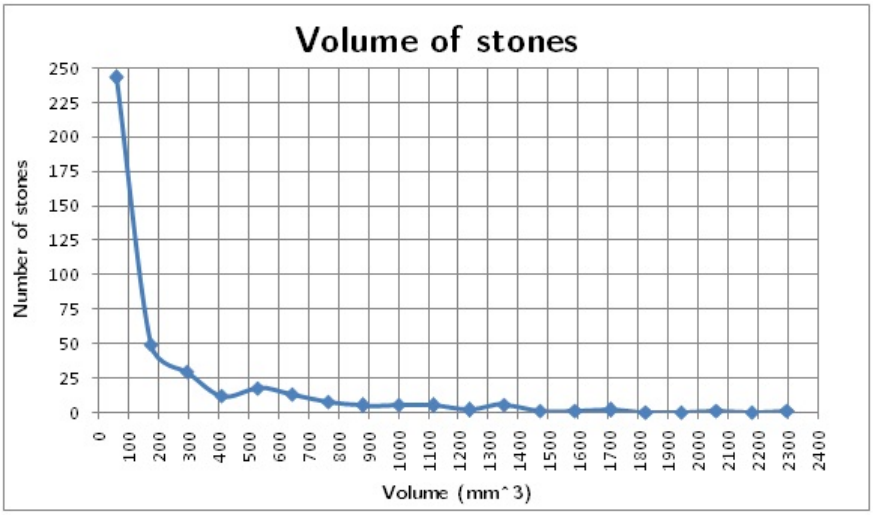

Fig. 8 Volume distribution of stones

Table 1 shows the result of the volumetric analysis of the AC sample. The result shows that the total volume of aggregates in the analyzed sample is 91109mm^2, the total volume of mastic is 36373mm^2 and the total volume of air-voids is 16468mm^2. The percentage volume of the aggregates, mastic and air-voids in the analyzed sample are 63.3%, 25.3% and 11.4% respectively. Table 2 shows the statistical relationship for the area, volume, length and width of the aggregates. Statistical relationship can be used to correlate the AC mix behaviour with geometric properties of the

Table 1 Phase Volumetric relationship

Volume	mm^3	% volume
Aggregates	91109	63.3
Mastic	36373	25.3
Air-voids	16468	11.4
Total volume of sample	143951	100

Table 2 Statistical analysis for aggregates

	$Area3d(mm^2)$	$Volume3d(mm^3)$	$Length3d(mm)$	$Width3d(mm)$
Min	1.74	0.08	2.34	0.30
Max	1221.86	2355.04	24.60	14.99
Mean	215.41	226.08	9.72	5.05
StdDev	235.10	354.75	5.37	3.26
Sum	86809.01	91109.19	3917.45	2034.24

stones. The relationship also gives relevant information that can be used to study asphalt mix design reliability and the micro-structure variability.

Distribution of the air-voids with depth is obtained by calculating the 2D area of air-voids per slice. The 2D area of air-voids is then calculated for each slice along the depth of the sample. Figure 9 shows the variation of the air-voids with sample depth. A practical application of the air-voids distribution is the assessment of compaction in AC sample. The variation of the air-voids can be used as a quality control measure to check the uniformity and adequacy of compaction effort on AC pavements. It can also be used as a tool to assess the condition of existing AC pavements.

It can also be used to examine crack initiation and propagation in AC mixtures. The distribution of the air-voids can be captured in the x, y and z coordinates before the application of mechanical load on the AC sample. After loading, the variation of the air-voids distribution can be used together with other related information to accurately determine the micro-structure evolution as a result of loading.

The contact between adjacent aggregates is captured using a combination of digital imaging techniques. The watershed lines and the aggregate mask used for the segmentation of the aggregate phase is used to determine the location of contacts between aggregates. It is interesting to find out that the air-voids distribution is inversely proportional to the contacts area distribution. It is worthy to note that the processed sample is a porous asphalt sample that have undergone aggregates segregation as a result of clogging. We have more fine particles at the top of the sample and more coarse particles at the bottom. There are more inter-particle contacts and less air-voids at the bottom of the sample. In the same sense, there are more air-voids at the top of the sample and less contacts between the fine aggregates. Figure 10 shows the contact area distribution of the sample.

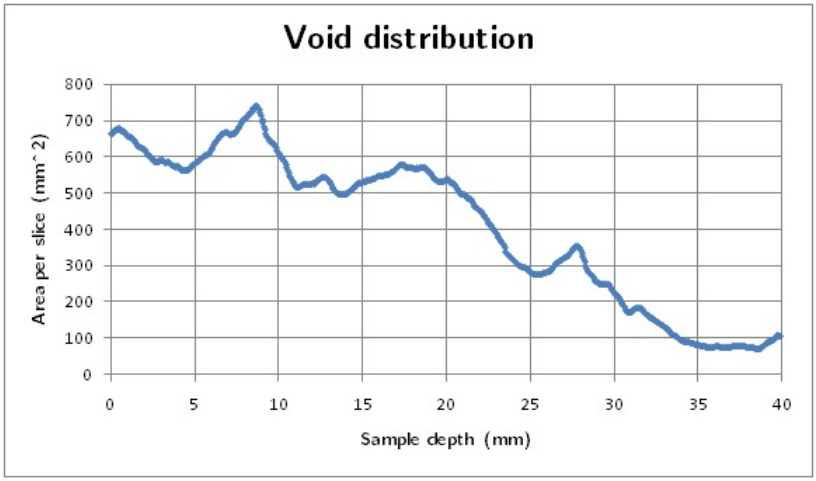

Fig. 9 Density distribution of air-voids with depth

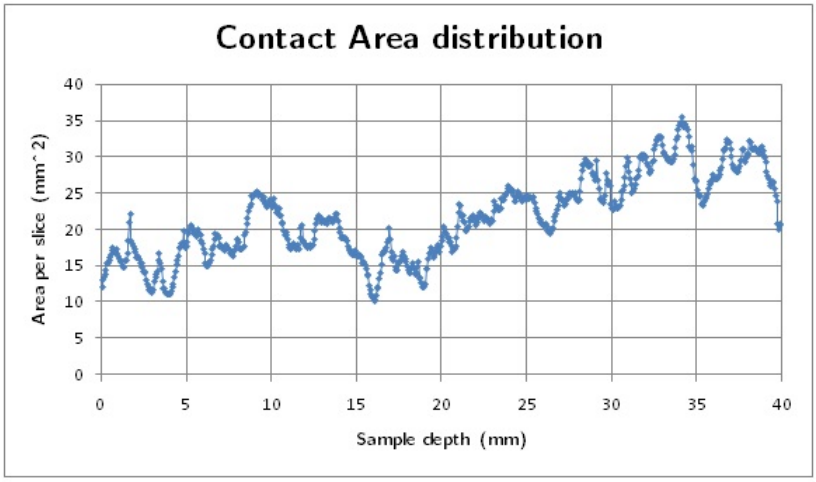

Fig. 10 Stone contact areas with depth

6 Surface and Mesh Generation

The segmented image of the AC microstructure is imported into Simpleware for surface generation and mesh construction. The air-void, mastic and aggregates phases are assigned a grey level of 1, 2 and 3 respectively for identification.

During surface generation, the sample is resampled to simplify the surface and reduce the number of elements generated during the mesh generation. Scanning at

high resolutions helps to capture the pertinent microstructure details and may be suitable for computer visualization. However, this high resolution images are not suitable for finite element analysis as it will take a lot of computer resources to process and run finite element analysis on them. The tweak is to be able to reduce the number of triangles that make up the surface without losing important geometric information.

The surface generated from the acquired image with a resolution of 59microns consists of 98Million triangles before resampling. A comparative study was carried out to determine what amount of resampling will be allowed without loosing considerable amount of details. Figure 11 shows the change in the volume of the different phases with respect to change in resampling resolution. From the study, a resampling resolution of 400micron was considered suitable. After resampling to a resolution of 400microns, the number of triangles was reduced to 12.4M which is about 12.6% of the original amount of triangles.

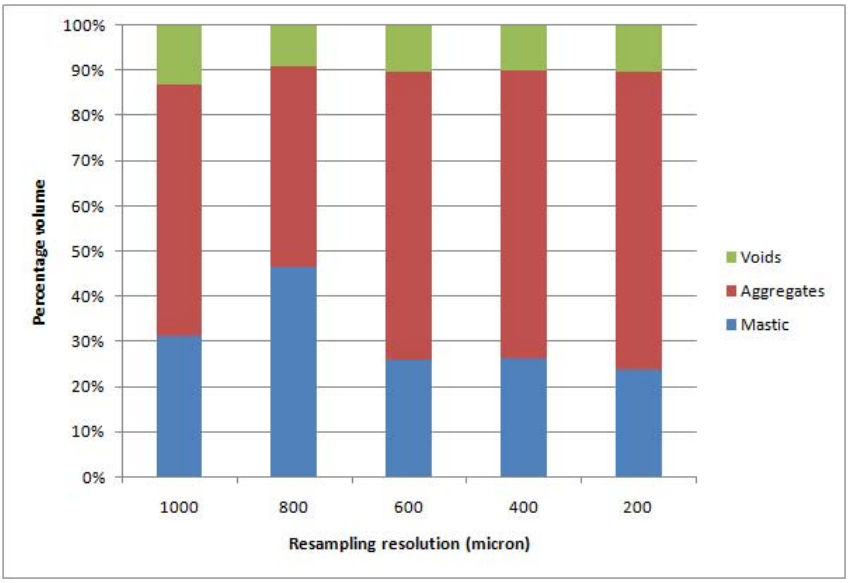

Fig. 11 Comparative study of resampling resolution

Due to limited computer power, a subsample of $30mm \times 30mm \times 30mm$ was taken for mesh generation and transfer into Finite Element (FEM) application for numerical simulation. The mesh was generated using the FE+ grid utility of simpleware. The resulting amount of tetrahedral mesh generated for the $30mm \times 30mm \times 30mm$ sub-volume is 254,000 tets. Simpleware can be used to define the interface and contact between different phases during the mesh generation. These information can be useful for further study of the aggregate-binder interaction in the AC matrix.

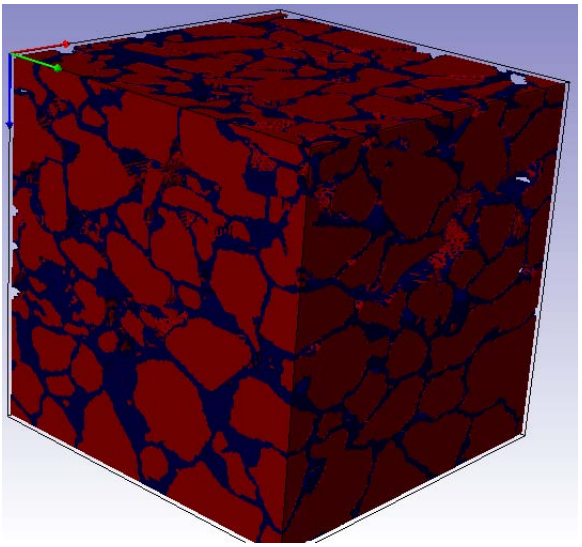

Fig. 12 Surface regeneration of 60x60x60mm AC sample

7 Micromechanical Finite Element (FE) Analysis

In this study, numerical simulation is carried out to investigate the behaviour of the AC microstructure under the action of mechanical loading. Three dimensional (3D) uniaxial compression FEM analysis was carried out on a geometry extracted from the AC microstructure, which is made up of two stones connected with mastic to show local stress and strain distributions. The same uniaxial compression analysis is then carried out on the $30mm \times 30mm \times 30mm$ meshed geometry. It was assumed that there is stress continuity at the interface between the mastic and aggregates as the mechanics of stress transfer between such interface is still under study. The numerical simulation is carried out using COMSOL Multiphysics.

7.1 Material Parameter

In this study, the aggregates is considered as a linear-elastic material while the mastic is considered as a linear-viscoelastic material. The material parameters required to model the elastic behaviour of the aggregates are the Young's modulus, Poission ratio and the density of the aggregates.

The time-dependent mastic property is considered using the Boltzmann superposition principle 7. The maxwell model in the form of a Prony series is used to model the rate dependent behavior of the mastic. The Maxwell model is represented by a series of viscous damper and elastic strings to simulate the viscous and elastic behavior respectively as shown in 13. A 5-leg/chain viscoelastic Maxwell model is used in this study. The viscoelastic model parameters required to model the mastic

behavior are the relaxation time (η_m), the relaxation modulus (E_m), the instantaneous shear modulus (G_0). The time-temperature dependence is modeled using the Williams-Landel-Ferry (WLF) shift function to obtain the shift factors(a_T) at different temperatures.

$$\sigma(t) = \int_0^t E(\xi(t) - \xi(\tau)) \frac{\partial \varepsilon(\tau)}{\partial \tau} d\tau \tag{7}$$

From equation 7, $E(\xi(t) - \xi(\tau))$ is the relaxation modulus at the reduced time $(\xi(t) - \xi(\tau))$ and the reduced time is defined by equation 8. The expression for the WLF shift function is shown in equation 9. From equation 9, T is the selected temperature, T_0 is the reference temperature, C1 and C2 are material constants.

$$\xi = \int_0^t \frac{1}{a_T} dt \tag{8}$$

$$log(a_T) = \frac{-C1 * (T - T_0)}{C2 + (T - T_0)} \tag{9}$$

The viscoelastic material parameters used to model the time-dependent behavior of the mastic was obtained from [You et al., 2012]. The material parameters were obtained from DSR test with a loading time of 1000sec and at a reference temperature of 20°C. The creep behavior has been presented as creep compliance data in [You et al., 2012]. The creep compliance data was converted into relaxation spectrum shown in Table 3 for modeling the mastic material behavior in COMSOL. The Laplace-Transform domain was used to convert the creep compliance data to stress relaxation functions using equations 10 to 12 .

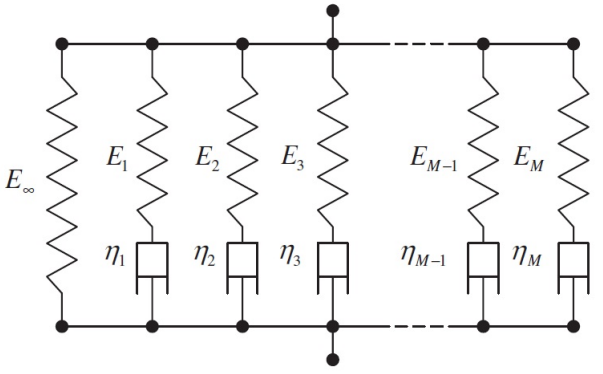

Fig. 13 Prony series

Table 3 Viscoelastic relaxation model parameters

M	$\eta_m(s)$	$E_m(MPa)$
1	0.1	20.7
2	1	46.2
3	10	52.8
4	100	53.5
5	1000	53.6

$$\tilde{G}(s)\tilde{J}(s) = 1 \tag{10}$$

where s = Laplace variable

$$\tilde{G}(s) = G_\infty + \sum_{i=1}^{n} \frac{s\rho_i G_i}{s\rho_i + 1} \tag{11}$$

$$\tilde{J}(s) = J_\infty + \sum_{k=1}^{m} \frac{\lambda_k}{s\lambda_k + 1} \tag{12}$$

7.2 Three-Dimensional (3D) Uniaxial Compression

Uniaxial compression simulation is used to investigate the stone breakage and polishing during compaction. The 3D geometry is extracted from the AC microstructure and it consists of two (2) aggregates interconnected with mastic. A uniaxial compressive displacement of 0.01mm is applied at one end of the model with the other end restrained as shown in Figure 14. The mastic is modeled as linear-viscoelastic material and the aggregates as linear elastic material. The material parameters used to model the viscoelastic behaviour of the mastic is shown in 3. The Young's modulus is selected from the work of [You et al., 2012] and considered to be 25GPa, the poisons ratio is 0.25 and the density is 4000kg/m3.

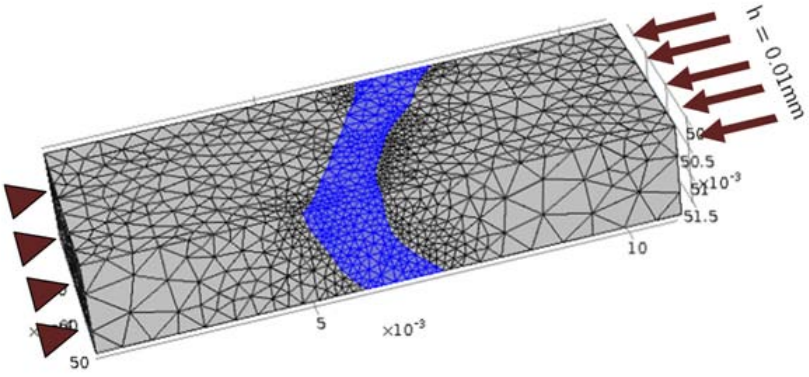

Fig. 14 3D uniaxial compression model

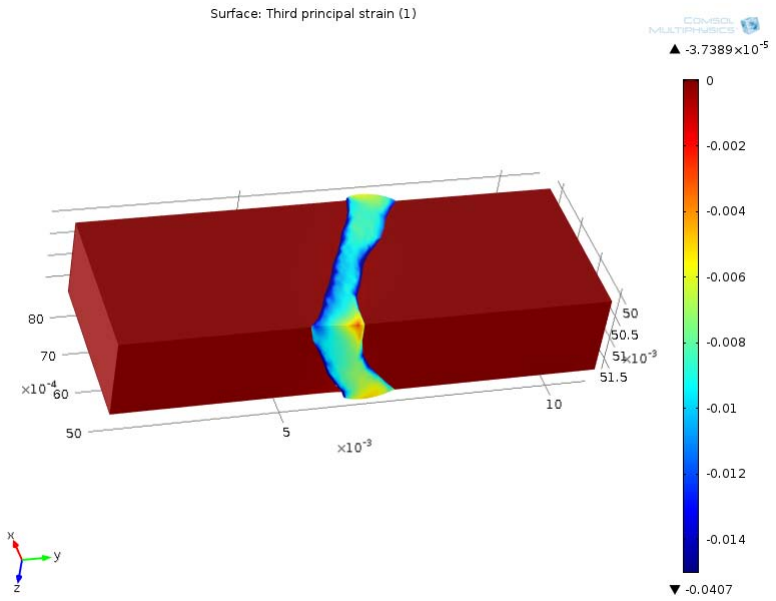

Fig. 15 Compressive strain distribution in x-direction

Figures (15) shows the strain distribution in the 3D model. It can be seen that compressive strains are localized in the binder with a maximum strain of 4.07%. High compressive strains are developed close to the aggregate-mastic interface and at regions with small mastic thickness.

Figures (16) shows the Von Mises stress distribution for the 3D model. The Von Mises stress localized in stones with high stress intensities around contact points between aggregates at aggregate-mastic interface.

Figure (17) shows the mesh for the 30mm x 30mm x 30mm AC geometry. The mesh was generated using Simpleware and contains a total of 254,000 tetrahedral elements. A time-dependent uniaxial displacement was applied at the top of the sample at a rate of 0.001mm/sec and the load displacement was applied for a 10sec period. The total displacement at the top of the sample after 10sec of analysis was 0.01mm which corresponds to the same displacement applied to the geometry in the first uniaxial compression case.

Figure (18) shows the strain distribution in the AC sample. The maximum strain localized in the mastic is 1.2%. Load transfer zones can be observed in Figure (18) which reconfirms the importance of the internal structural arrangement of the AC mix to load response. Figure (19) shows the stress distribution with high stress concentration at the edge and contact between stones.

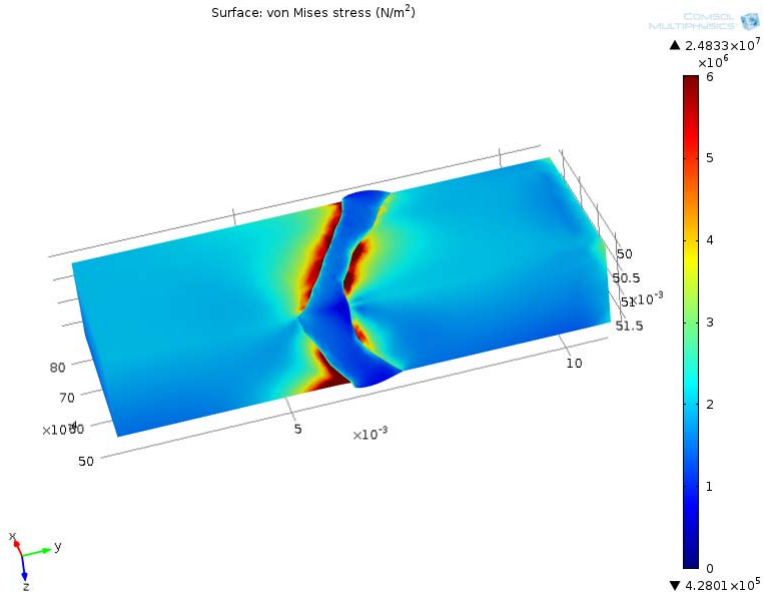

Fig. 16 Von Mises stress distribution in 3D model

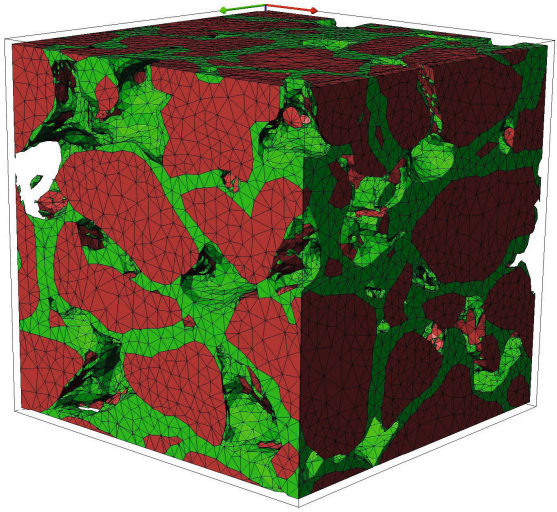

Fig. 17 Mesh of 30mm x 30mm x 30mm AC sample

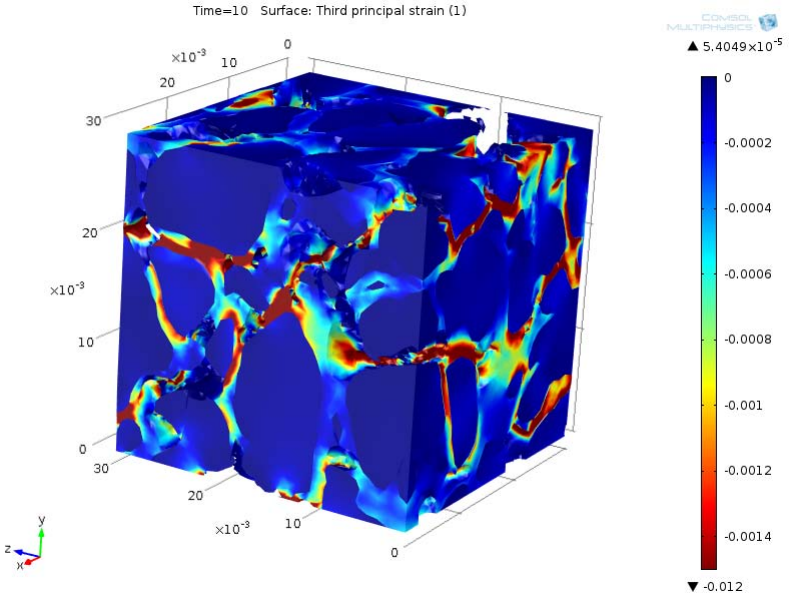

Fig. 18 Compressive strain distribution in 30mm x 30mm x 30mm model

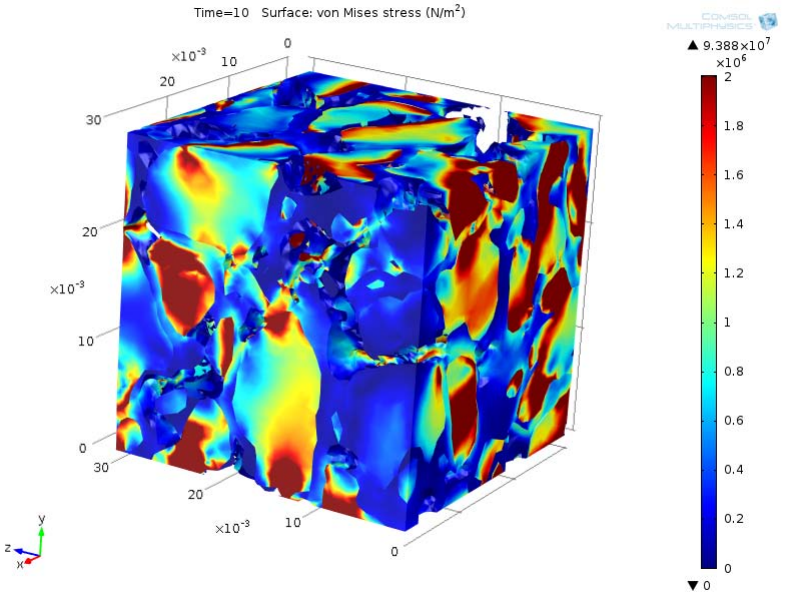

Fig. 19 Von Mises stress distribution in 30mm x 30mm x 30mm model

8 Conclusion

The present study have shown and described the workflow process from image acquisition to micro-mechanical numerical simulation using X-Ray computed tomography and digital image processing techniques. Phase segmentation of the AC micro-structure using thresholding operations does not produce good segmentation results. A non-linear filter together with the distance map based watershed segmentation is used to segment the phases in the AC micro-structure and also to separate adjacent aggregates.

Digital image analysis techniques is used to analyze the phase segmented AC micro-structure. Digital image analysis is used to determine phase volumetric relationships and individual aggregate properties like volume of aggregates, length and width of aggregates, orientation of aggregates and spatial location of aggregates in the AC mix and air-void distribution.

Numerical simulation is used to study the strength and deformation mechanisms in order to characterize the AC micro-structure using a 3D finite element analysis. Load transfer chains can be observed in the micro-structure model with strains localization in the mastic. Further study of the behavior at the aggregate-mastic interface using X-Ray computed tomography and Digital Image Processing can be used to understand the mechanism of debonding and stripping of aggregates so as to mitigate them. This can help to further improve mix performance and reduce permanent deformations in the road pavements.

References

[Avizo, 2009] Avizo: Avizo User's Guide. Visualization Sciences Group, Vordeaux (2009)

[Coleri et al., 2012a] Coleri, E., Harvey, J.T., Yang, K., Boone, J.M.: Development of a micromechanical finite element model from computed tomography images for shear modulus simulation of asphalt mixtures. Construction and Building Materials 30(0), 783–793 (2012a)

[Coleri et al., 2012b] Coleri, E., Harvey, J.T., Yang, K., Boone, J.M.: A micromechanical approach to investigate asphalt concrete rutting mechanisms. Construction and Building Materials 30, 36–49 (2012b)

[Ketcham and Carlson, 2001] Ketcham, R.A., Carlson, W.D.: Acquisition, optimization and interpretation of x-ray computed tomographic imagery: applications to the geosciences. Comput. Geosci. 27(4), 381–400 (2001)

[Masad et al., 2005] Masad, E., Tashman, L., Little, D., Zbib, H.: Viscoplastic modeling of asphalt mixes with the effects of anisotropy, damage and aggregate characteristics. Mechanics of Materials 37(12), 1242–1256 (2005)

[Schlangen and van Mier, 1992] Schlangen, E., van Mier, J.: Simple lattice model for numerical simulation of fracture of concrete materials and structures. Materials and Structures 25, 534–542 (1992)

[Wang, 2010] Wang, L.: Mechanics of Asphalt: Microstructure and Micromechanics. McGraw-Hill (2010)

[Wang et al., 1999] Wang, Z., Kwan, A., Chan, H.: Mesoscopic study of concrete i: generation of random aggregate structure and finite element mesh. Computers and Structures 70(5), 533–544 (1999)

[Wittmann et al., 1985] Wittmann, F., Roelfstra, P., Sadouki, H.: Simulation and analysis of composite structures. Materials Science and Engineering 68(2), 239–248 (1985)

[You et al., 2012] You, T., Al-Rub, R.K.A., Darabi, M.K., Masad, E.A., Little, D.N.: Three-dimensional microstructural modeling of asphalt concrete using a unified viscoelastic viscoplastic viscodamage model. Construction and Building Materials 28(1), 531–548 (2012)

[You et al., 2008] You, Z., Adhikari, S., Dai, Q.: Three-dimensional discrete element models for asphalt mixtures. Journal of Engineering Mechanics 134(12), 1053–1063 (2008)

[Zelelew and Papagiannakis, 2011] Zelelew, H.M., Papagiannakis, A.T.: A volumetrics thresholding algorithm for processing asphalt concrete x-ray ct images. International Journal of Pavement Engineering 12(6), 543–551 (2011)

[Z.P. et al., 1990] Bazant, Z.P., Tabbara, M.R., Kazemi, M.T., Pijaudier-Cabot, G.I.: Random particle model for fracture of aggregate or fiber composites. Journal of Engineering Mechanics 116, 1686–1705 (1990)

Evaluation of Anti-clogging Property of Porous Asphalt Concrete Using Microscopic Voids Analysis

Wei Jiang and Aimin Sha

Key Laboratory for Special Area Highway Engineering of Ministry of Education, Chang'an University, Xi an 710064, Shaanxi, China
jiangwei_029@sina.com, aiminsha64@gmail.com

Abstract. Since the occurrence of voids clogging has an adverse effect on Porous Asphalt Concrete (PAC), an experiment was designed to evaluate PAC's anti-clogging capability with different material compositions. Image processing and X-ray Computer Tomography (CT) were employed to study the characteristics of micro-gap of PAC, such as amount, area, and equivalent diameter of air voids on average. It was found that different PAC material compositions induce large differences on anti-clogging capability. PAC's anti-clogging capability can be improved in different degrees by increasing air voids and nominal maximum aggregate size or using coarse gradation. There was an apparent linear correlation between PAC's voids equivalent diameter and anti-clogging capability: the larger equivalent voids, the better anti-clogging capability. In this research, anti-clogging capability was interpreted, and a new method was put forward for improving the anti-clogging performance of Porous Asphalt Concrete from the perspective of microscopic void geometric features.

Keywords: Road engineering, Porous asphalt concrete, Anti-clogging ability, Void features, CT technology.

1 Introduction

Porous Asphalt Concrete (PAC) is a typical mixture with a skeleton-void structure which provides pavements with additional drainage and noise reduction performance. However, the void of the material could be clogged hindering its normal functionality easily. Therefore, it is important to make additional research efforts on improving anti-clogging capability of PAC.

In recent years, considerable research efforts have been made on the evolution of PAC's clogging and its recovery. Balades and Pratt made experimental studies with four testing methods on PAC's clogging recovery, namely moistening followed by sweeping, sweeping followed by suction, suction alone, and high pressure water jet combined with simultaneous suction[1-3]. Ryuichi investigated the permeability

N. Kringos et al. (Eds.): *Multi-Scale Model. & Charact. of Infrastruct. Mater.,* RILEM 8, pp. 159–172.
DOI: 10.1007/978-94-007-6878-9_12

and durability of the mixtures, and studied the relationship between the traffic and the decrease of permeability[4]. Kurihara studied the anti-clogging ability of PAC with the void content of about 20% and compared the effects of jammer quantity on permeability[5]. Most of the related studies are about the permeability and the recovery of polluted PAC[6-9]. The main objective of this paper is to describe the laboratory pollution tests and the evaluation of anti-pollution ability of different mixtures. The relationship between material properties and void characteristics were studied by 2D image of specimen cross-section through CT and image processing technologies[10-12]. Suggestions were made to improve the anti-pollution property of PAC mixtures from materials design perspective.

2 Materials and Methodology

2.1 Mixture

SK-70 asphalt and diabase aggregates were selected to prepare the PAC mixtures. The mineral aggregate gradations and the air voids of those mixes are shown in Table 1.

Table 1 Gradation of PAC for testing

Mixtures	Passing(by Mass) under different sieve size (mm) /%										Asphalt-aggregate ratio/%	Air voids content /%
	16	13.2	9.5	4.75	2.36	1.18	0.6	0.3	0.15	0.075		
PAC-13a	100.0	90.1	61.5	28.3	20.6	17.4	14.3	10.3	8.2	5.3	5.2	16.1
PAC-13b	100.0	90.1	61.4	25.8	17.7	15.1	12.6	9.3	7.6	5.2	5.0	18.2
PAC-13c	100.0	90.1	61.3	23.4	14.8	12.7	10.8	8.3	7.0	5.0	4.8	20.1
PAC-13d	100.0	90.1	61.2	20.9	11.9	10.4	9.2	7.3	6.3	4.9	4.5	22.7
PAC-13e	100.0	90.1	61.1	18.5	9.0	8.1	7.5	6.3	5.7	4.8	4.2	25.1
PAC-13f	100.0	92.6	70.3	25.2	14.8	12.8	11.0	8.3	7.0	5.1	4.8	19.7
PAC-10	100.0	100.0	97.1	30.8	14.9	12.8	11.0	8.3	7.0	5.1	4.8	20.1

2.2 Test Methodology

The test methods include the anti-clogging, CT, and image processing techniques.

2.2.1 Clogging Experiment

A PAC specimen was prepared in a standard Marshall procedure without removing the cylindrical mold. After measuring its original permeability coefficient, the

surface of the specimen was smeared graded fine grains, then uniformly sprayed with water. After the pollution procedures above, the residual value of the mixture's permeability coefficient was measured. The anti-clogging capability of the mixture was defined as a ratio of the residual value to the initial value of the mixture permeability. The larger the value of residual permeability is, the less impact the "jammer" or fine grains have on the permeability of the mixture, and the higher the anti-clogging capability of the PAC specimen.

The testing procedure is as follows [5]:

① Prepare a Marshall specimen (without removing the mold) and determine the initial permeability coefficient;

② Spread the graded (see Table 2) fine grain (6 g) on the testing specimen surface;

③ Shake the specimen for 30 seconds (note: make sure not losing the fine grains during the test) and then slowly pour some water (about 240 g) on it;

④ Heat the specimen for 6 hours at a temperature of 60 °C, then determine the specimen residual permeability, and calculate the residual permeability(γ) according to previous definition;

⑤ Repeat steps ② ~ ④ for 4 times or until the total mass of fine grains spread is equal to 24 g.

The last residual permeability denoted as $\gamma(24)$ was used to evaluate the anti-clogging ability. Constant head permeability test was used in the experiment to determine the permeability coefficient.

Table 2 Gradation of fine grains used for clogging testing

Grain size /mm	0.15～0.3	0.075～0.15	<0.075
Weight /g	2	2	2

2.2.2 CT Test

As shown in Fig.1, the CT scanner PQ5000 manufactured by PICKER was used to scan the mix specimens. Each specimen was scanned from the bottom to top with an interval of 2 mm, and 25 photos were obtained from scanning each specimen. In the CT tests, the image resolution of 512 pixels × 512 pixels was selected. Fig.2(a) shows an original CT image, and Fig.2(b) is the result after being processed with threshold method[13-14] (the black regions represent air voids). As shown in Fig.2(c), the voids are marked and counted for further analysis.

Fig. 1 CT test equipment and specimens placement

(a) CT image (b) Threshold-processed images (c) Gap fitting & number

Fig. 2 CT images and treatment

3 Anti-clogging Capability

3.1 Void Content

Specimens with different void contents were prepared according to the gradation in Table 1. The test result was shown in Fig.3 and the residual permeability of each specimen was calculated.

The following results were observed that 1) the residual permeability decreased as the fine grains increased; 2) residual permeability decreases more from 0 g to 12 g fine grains than from 12 g to 24 g.

The residual permeability increased with the void content. When the void content of mixture increased from 16.1% to 25.1%, the residual permeability of PAC increased from 38% to 66%, and the anti-clogging ability was enhanced significantly.

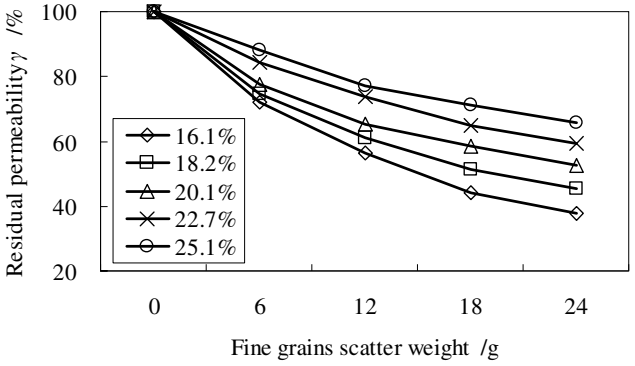

Fig. 3 Influence of air voids on PAC's residual permeability

3.2 Nominal Maximum Aggregate size

For PAC-13c and PAC-10 (Table 1), the test results are shown in Fig.4.

As shown in Fig.4, the nominal maximum aggregate size significantly affected the residual permeability. The residual permeability of PAC-13c was higher than that of PAC-10. Usually, a mixture with a greater nominal maximum aggregate size has better anti-clogging capability.

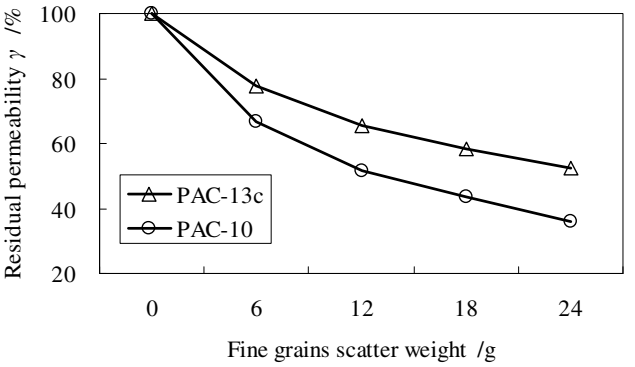

Fig. 4 Nominal maximum aggregate size's influence on PAC's residual permeability

3.3 Gradation

As listed in Table 1, the PAC-13c and PAC-10f mixture had similar void contents but different gradations. The test results of these mixtures are shown in Fig.5.

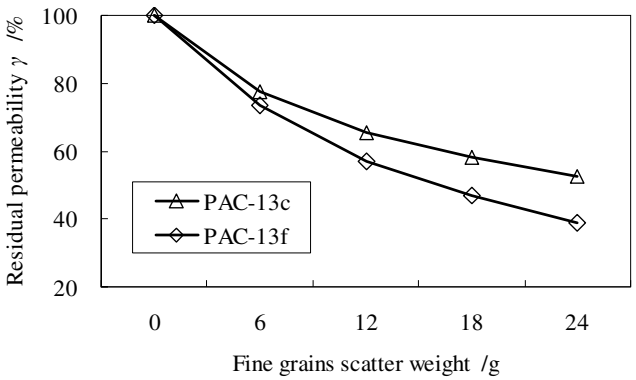

Fig. 5 Gradation's influence on PAC's residual permeability

From Fig.5 it was found that gradation was another important factor affecting the residual permeability. Generally, the PAC-13c specimen which had more course aggregates than PAC-13f specimen did exhibit higher residual permeability. It's proved that when the void content is fixed, PAC mixture with more coarse gradation possesses better anti-clogging capability.

4 Factors Affecting Void Characteristic

In order to further study variation of the anti-clogging capability of PAC mixture, PAC specimens mentioned above were scanned by CT scanner.

The images obtained from CT scanning were processed and analyzed. The following parameters were calculated: (a)average quantity of void, N; (b)average area of a single void, a; (c)average equivalent diameter of a single void, d, and (d)average void ratio of each cross-section, etc. the average quantity of void is the weighted average of void quantity obtained from the threshold-processed CT images of each cross-section (equation 1), while parameters of (b) and (c) are calculated through equation 3 and 4, respectively.

$$\mathrm{N} = \frac{\sum_{i=1}^{n} \mathrm{N}_i}{n} \tag{1}$$

$$\mathrm{A} = \frac{\sum_{i=1}^{n} \mathrm{A}_i}{n} \tag{2}$$

$$a = \frac{A}{N} \tag{3}$$

$$d = 2 \times \sqrt{\frac{a}{\pi}} \tag{4}$$

In the equations above, n is the number of scanned cross-sections and equal to 25 herein; N_i is the quantity of void areas in the i th cross-section; A_i is the total area of void in the i th cross-section. A is the total area of average void.

4.1 Validity of Scanned Average Void Ratio

For validation, comparisons were made between the void contents obtained from scanned images and those obtained from laboratory tests as shown in Table 3. It was found that the air voids from CT Images were very close to those from laboratory tests. It can be used as the representative value of air voids at certain conditions.

Table 3 Air voids measured and VV from CT image

Mixtures / Air voids	PAC-13 a	PAC-13 b	PAC-13 c	PAC-13 d	PAC-13 e	PAC-13 f	PAC-10
Air voids form laboratory test /%	16.1	18.2	20.1	22.7	25.1	19.7	20.1
Connected air voids /%	13.0	14.5	15.5	17.8	19.1	15.8	15.2
Air voids from CT Image /%	16.0	18.0	19.9	22.8	25.0	19.7	20.1

4.2 Air Voids

Fig.6 shows the threshold-processed images of cross-sections with different air voids.

(a) 16.1% (b) 18.2% (c) 20.1% (d) 22.7% (e)25.1%

Fig. 6 Images of cross-sections with different air voids

The void parameters of specimens with different air voids are summarized in Table 4

Table 4 Voids characteristics parameters of cross-sections images with different air voids

Voids characteristics parameters \ Mixtures	PAC-13 a	PAC-13 b	PAC-13 c	PAC-13 d	PAC-13 e
Air voids form laboratory test /%	16.1	18.2	20.1	22.7	25.1
Average void quantity of cross-section /pcs	88.7	86.3	84.5	83.4	82.2
Total void's area of cross-section /mm^2	1290.5	1455.0	1612.9	1852.8	2026.8
Average area of a single void of cross-section /mm^2	14.6	16.9	19.1	22.2	24.7
Void equivalent diameter /mm	4.3	4.6	4.9	5.3	5.6
Air voids from CT Image /%	16.0	18.0	19.9	22.8	25.0

From Table 4, it was found that with the increasing void content, the average void quantity of cross-section decreased while the total area of voids, the average area of a single void, and equivalent diameter increased. For example, the PAC-13e specimen (void content = 25.1%) had an average area (single void) of 25 mm^2, which was almost twice as big as that of PAC-13a specimen (void content = 16.1%).

4.3 Nominal Maximum Aggregate Size

Comparisons were made between the scanned sections of PAC-13c and PAC-10. Those two mixtures had the same void content of 20.1%. Fig.7 showed the threshold-processed images from these specimens. Compared with PAC-10, PAC-13c had much less quantity of voids and larger single void. Table 5 summarized the void characteristic parameters.

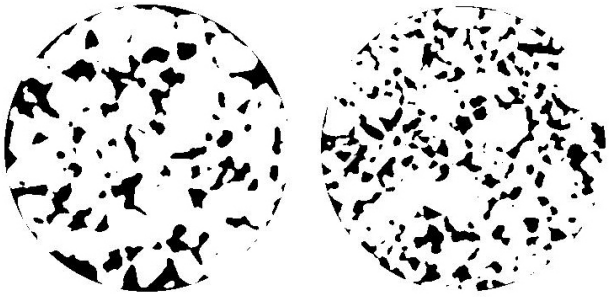

(a) PAC-13 c (b) PAC-10

Fig. 7 Images of cross-sections with different nominal maximum aggregate sizes

Table 5 Voids characteristics with different nominal maximum aggregate sizes

Voids characteristics parameters \ Mixtures	PAC-13c	PAC-10
Air voids form laboratory test /%	20.1	20.1
Average void quantity of cross-section /pcs	84.5	136.6
Total void's area of cross-section /mm^2	1612.9	1628.7
Average area of a single void of cross-section /mm^2	19.1	11.9
Void equivalent diameter /mm	4.9	3.9
Air voids from CT Image /%	19.9	20.1

As shown in Table 5, the one with the less NMAS had more void per area and smaller single void area and equivalent diameter for PAC specimens with same or approximate air voids.

4.4 Gradation

To evaluate how gradation affects the void characteristic, PAC-13c (coarse gradation) and PAC-13f (fine gradation) were compared with each other. The processed images were shown in Fig.8 and the results were summarized in Table 6.

(a) PAC-13 c (b) PAC-13 f

Fig. 8 Images of cross-sections with different gradation

From Table 6, it was observed that PAC-13c had a smaller average quantity of void and a larger average area of a single void compared to PAC-13f. The two specimens had similar air voids and total areas of void.

Table 6 Voids characteristics parameters of cross-sections images with different gradation

Voids characteristics parameters \ Mixtures	PAC-13c	PAC-13f
Air voids form laboratory test /%	20.1	19.7
Average void quantity of cross-section / pcs	84.5	108.6
Total void's area of cross-section /mm^2	1612.9	1591.9
Average area of a single void of cross-section /mm^2	19.1	14.7
Void equivalent diameter /mm	4.9	4.3
Air voids from CT Image /%	19.9	19.7

5 Analysis of Test Results

Based on the laboratory tests and CT imaging analysis, this section herein presents the analysis and the discussion on factors which induce different anti-clogging capabilities of PACs.

Fig.9 to 12 show residual permeability vs. void content, average quantity of void, total area of average void and equivalent void diameter, respectively. The relations between the corresponding parameter and residual permeability were built upon regression.

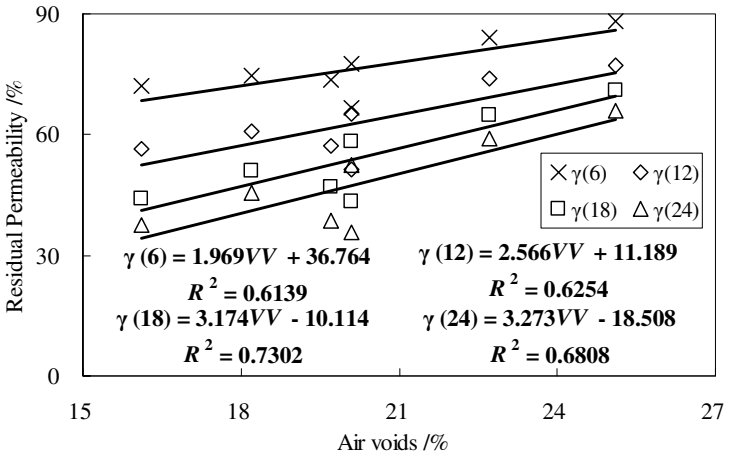

Fig. 9 Relationship between air void and residual permeability

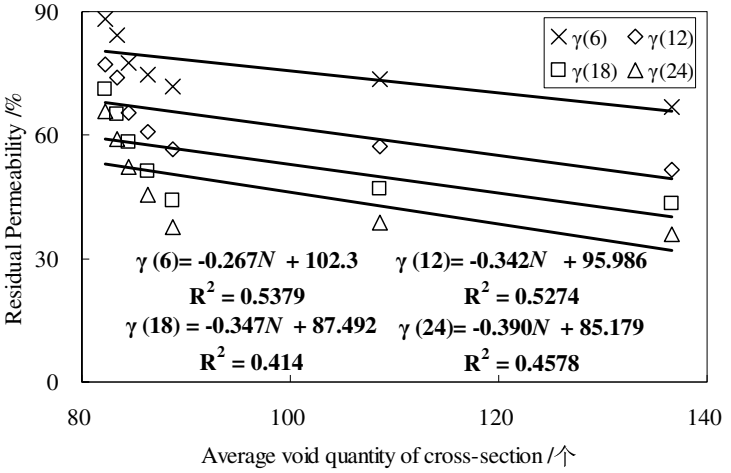

Fig. 10 Relationship between section average voids number and residual permeability

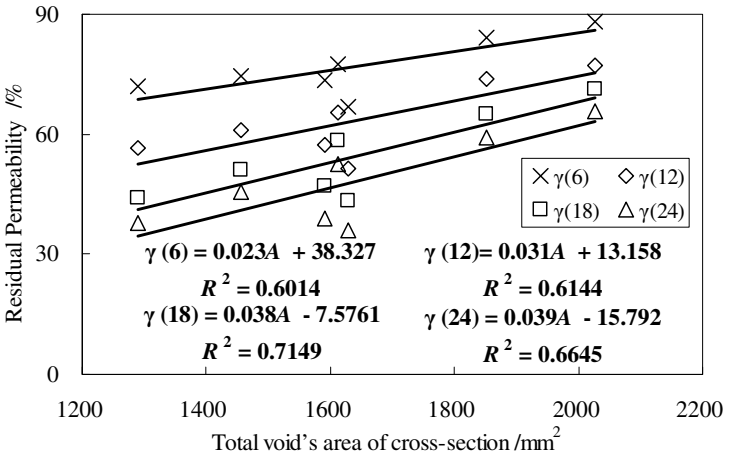

Fig. 11 Relationship between section average voids area and residual permeability

Good linear correlations between the equivalent void diameter and the residual permeability were observed. The correlation coefficient was over 0.96. Therefore, the equivalent void diameter was the important factor that affected the anti-clogging capability of the mixture. This conclusion is reasonable because the possibility for a jammer to pass through the void is higher and the anti-clogging capability is better when the void diameter is larger. Therefore, the fundamental way to improve anti-clogging ability is to increase the equivalent void diameter through increasing the void contents, Nominal Maximum Aggregate Size (NMAS), and the utilization of course gradation.

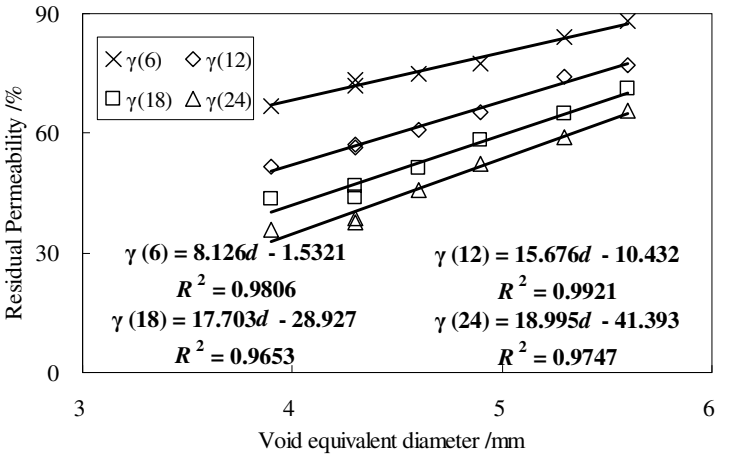

Fig. 12 Relationship between void equivalent diameter and residual permeability

According to the existing research results [15], the performance and durability decreased with the increasing void content. Therefore, design goals and performance requirements should also be met during choosing void content, NMAS and gradation in practice. When used in areas with lower traffic or serious dust issues, PAC with a higher void content is recommended, while those with lower value is recommended when higher performance is required.

The key sizes causing jams are different, depending on the NMAS of PAC. Therefore, the PAC pavement with two-layered structure is often used. The mixture with smaller NMAS is adopted in upper layer (e.g. PAC-5, PAC-10), but larger NMAS in the bottom layer mixtures (e.g. PAC-13, PAC-16). Two-layered structure prevents particles larger than 1.18 mm from passing through the upper layer and reduces the possibility of jams in the bottom layer. Upper jams can be repaired by the special cleaning vehicle.

The testing results indicated that coarse graded mixtures could improve the anti-clogging capability as well as the stabilities of mixture skeleton structures and the high temperature performance.

As Pei had studied through experiments, the void structure slowly changes under cyclic loads [7].. Comparing the rutting test sample before and after tests, it was found that the void content and some of the equivalent void diameter decreased but the quantity of void did not change [16]. Therefore, according to the findings in this paper, the anti-clogging ability should decrease as expected. It is recommended to choose aggregate with high modulus and good adherence to asphalt for keep the stability of the void structure, along with asphalt with high viscosity, high temperature stability and high bonding strength in the mixture. Coarse gradation should be used because skeleton structure is more stable and more un-susceptible to temperature. Besides, the content of flaky particles should be strictly limited to avoid broken particles clogging the voids.

6 Conclusions

(1) The test methods proposed in this paper can be used to evaluate the anti-clogging ability of PAC mixtures. The residual permeability can be used as a criterion for mixture design.
(2) In practice, anti-clogging capability may be effectively improved by increasing the void content and NMAS of mixtures, and utilizing coarse gradation.
(3) The microscopic void features of PAC can be affected significantly by material composition, including void ratio, nominal maximum aggregate size and gradation.
(4) There is a good positive linear correlation between the void equivalent diameter and the residual permeability. The void equivalent diameter is a important parameter affects the anti-clogging ability. But studies by 2D images had some limitations, it would be analyzed by 3D images in subsequent research.

Acknowledgements. This work was supported by the National Natural Science Foundation of China (Grant No. 51208049), China Postdoctoral Science Foundation (Grant No.2012M511964), and Major State Basic Pre-research Development Program of China (973 Program, Grant No. 2012CB626814).

References

[1] Balades, J.D.: Permeable pavements: Pollution management tools. Water Science and Technology 32(1), 49–56 (1995)
[2] Pratt, C.J., Mantle, D.G., Schpfield, P.A.: UK Research into the performance of permeable pavement, reservoir structures in controlling stormwater discharge quantity and quality. Water Science and Technology 32(1), 63–69 (1995)
[3] Pratt, C.J.: Use of permeable, reservoir pavement constructions for stormwater treatment and storage for re-use. Water Science and Technology 39(5), 145–151 (1999)
[4] Ryuichi. Verification of the durability and function of drainage pavement. Kyushu Regional Development Bureau, Japan (2004)
[5] Kurihara, O.: Experimental study on the clogging of voids of porous concrete and porous asphalt. In: Shibaura Institute of Technology Campus Tokyo's: Technical Workshop 35th Kanto Branch Society of Civil Engineers (2008)
[6] Wang, Z.-J., Sha, A.-M., Xiao, J.-J., et al.: Analyses of inner air void characters in composite asphalt concrete based on CT technology. Journal of Shanghai Jiaotong University 45(5), 667–671 (2011)
[7] Pei, J.-Z., Zhang, J.-L., Chang, M.-F.: Influence of mineral aggregate gradation on air void distribution characteristic of porous asphalt mixture. China Journal of Highway and Transport 23(1), 1–6 (2010)
[8] Masad, E., Castelblanco, A., Birgisson, B.: Effects of air void size distribution, pore pressure and bond energy on moisture damage. Journal of Testing and Evaluation 34(1), 15–23 (2006)
[9] Arambula, E., Masad, E., Martin, A.E.: Influence of air void distribution on the moisture susceptibility of asphalt mixes. Journal of Materials in Civil Engineering 19(8), 655–664 (2007)
[10] Wang, L.B., Frost, J.D., Shashidhar, N.: Micro-structure study of WesTrack Mixes from X-ray tomography images. Transportation Research Record (1767), 85–94 (2001)

[11] Tashman, L., Wang, L.B., Thyagarajan, S.: Microstructure characterization for modeling HMA behavior using imaging technology. Road Materials and Pavement Design 8(2), 207–238 (2007)
[12] You, Z.P., Adhikari, S., Emin, K.M.: Dynamic modulus simulation of the asphalt concrete using the X-ray computed tomography images. Materials and Structures 42(5), 617–630 (2009)
[13] Wang, H.-N., Hao, P.-W., Lu, G.-Y.: Distribution properties of internal air voids in asphalt mixtures. Journal of Traffic and Transportation Engineering 9(1), 6–11 (2009)
[14] Masad, E., Jandhyala, V.K., Dasgupta, N., et al.: Characterization of air void distribution in asphalt mixes using X-ray computed tomography. Journal of Materials in Civil Engineering 14(2), 122–129 (2002)
[15] Jiang, W.: Composition Design and Function Evaluation for Materials and Structures of Permeable Asphalt Pavement. Chang'an University, Xi'an (2011)
[16] Pei, J.-Z.: Prediction model of bulk modulus reduction for porous asphalt pavement. Journal of Traffic and Transportation Engineering 9(6), 7–10 (2009)

Representative Volumes for Numerical Modeling of Mass Transport in Hydrating Cement Paste

Neven Ukrainczyk[1,2,*], Eduard A.B. Koenders[1,3], and Klaas van Breugel[1]

[1] Microlab, Faculty of Civil Engineering and Geosciences,
Delft University of Technology, Stevinweg 1, 2628 CN Delft, The Netherlands
n.ukrainczyk@tudelft.nl
[2] Faculty of Chemical Engineering and Technology, University of Zagreb,
Marulicev trg 19, 10000 Zagreb, Croatia
[3] Civil Engineering Department-COPPE, Federal University of Rio de Janeiro,
68506 Rio de Janerio, Brazil

Abstract. Representative elementary volume (REV) has major importance in numerical estimation of effective transport properties of porous materials. The increasing focus on the durability and reliability aspects of cementitious materials, calls for a better understanding of the mass transport phenomenon through their evolving porous microstructure. A multi-scale nature of the cementitious materials imposes a great challenge to modeling efforts. This paper investigates the REV size for numerical modeling of transport in hydrating cement paste. Numerous series of virtual 3D microstructures with different porosities and capillary pore morphologies were generated using Hymostruc platform, a numerical model for cement hydration and microstructure development. Effective diffusion was obtained by using a finite difference scheme. The effect of numerical resolution was also investigated. Based on a statistical analysis, it was concluded that the REV size depends on the complexity of the pore morphology, which further primarily depends on the porosity and employed numerical resolution.

Keywords: Representative elementary volume, Numerical modeling, Effective transport property, Cementitious materials.

1 Introduction

Cement based materials are the most used building materials of modern construction. The long term performance is threatened by the transport of aggressive species through porous microstructure, a mechanism that plays a crucial role in degradation process. The microstructure of cementitious materials is covering multiple scales of sizes, from nanometer-sized pores to centimeter-sized aggregates. Even when considering only a cement paste microstructure, the pore sizes

* Corresponding author.

N. Kringos et al. (Eds.): *Multi-Scale Model. & Charact. of Infrastruct. Mater.*, RILEM 8, pp. 173–184.
DOI: 10.1007/978-94-007-6878-9_13

cross at least four orders of magnitude (10 nm – 100 μm), as shown in Fig 1. Therefore, multi-scale techniques are needed to model the transport properties accurately. A multi-scale analysis in general involves multiple solutions of numerical models with often over 1 million unknowns. Representative elementary volume (REV), together with the homogenization theory, is one of the most employed multi-scale techniques. The REV for (multi-scale) modeling and assessment of effective properties of heterogeneous material, should be large enough to include sufficient information about the microstructure and should be much smaller than the macroscopic body (Hashin 1983).

Rapid developments in numerical modeling have provided novel methods to investigate the influence of microstructure on the evolution of the properties of cement based materials. A virtual 3D porous microstructure created with available hydration models provides a fundamental basis for the analysis of the hydration parameters onto the effective diffusion coefficient. The two main methodological approaches in modeling the microstructural evolution of cement-based systems are: 1) digitalization of the experimental image of the real microstructure, e.g. CEMHYD3D (Garboczi and Bentz (2001), and 2) a particle-based continuous concept of growing spheres, e.g. IPKM (Pignat et al. 2005), Hymostruc (van Breugel 1991, Koenders 1997), μic (Bishnoi and Scrivener 2009). In the hydration models, the resulting microstructure can be simulated as a function of the random distribution of cement particles, degree of hydration, particle size distribution, chemical composition of the cement, morphological development, water to cement ratio, and reaction temperature. Zhang et al. (2011) showed that the simulated value and experimental data for effective diffusion of water are of the same order of magnitude, and the simulated values are about three times higher than the measurement ones. Furthermore, the trend of simulated relationship (diffusivity vs. w/c ratio, and diffusivity vs. curing age) agrees very well with the experiments.

A random nature of distribution of heterogeneities within this material makes the effective transport property a random variable. Generally, transport property of cementitious materials depends on porosity and pore structure morphology, i.e. it's connectivity, tortuosity, constrictivity, and size distribution. Therefore, quantitative determination of REV for this reactive porous multi-scale material is very complex. The RVE concept is widely used today in mechanics, e.g. Gitman et al. (2006) proposed a numerical-statistical method to determine the size of the RVE. Zhang et al. (2010) presented a numerical-statistical approach to determine the REV for transport modelling in cementitious materials.

Therefore, this paper reports an investigation about the REV size for numerical modeling of transport in hydrating cement paste. Virtual microstructures of hydrating cement paste were simulated using the Delft 's Hymostruc, a model for cement hydration and microstructure development. The diffusion properties of the simulated microstructures were analysed by a finite difference 3D transport module implemented within the Hymostruc platform.

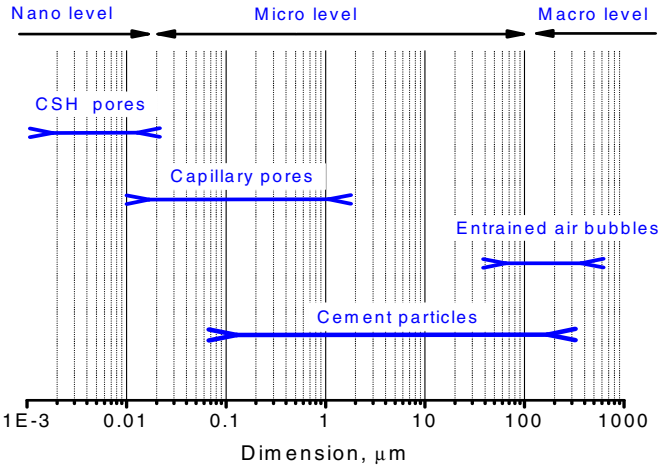

Fig. 1 Multi-scale levels of the cement paste microstructure

2 REV Determination

2.1 Virtual Microstructures Generated by Hymostruc

Hymostruc (van Breugel 1991, Koenders 1997) is a numerical model for cement hydration and microstructure development where the microstructure can be simulated as a function of the random distribution of cement particles, particle size distribution, degree of hydration, chemical composition of the cement, morphological development, water to cement ratio, and reaction temperature. A limited edition of the Hymostruc model is freely available (Koenders 1997). Simulations are done for Portland cement (Blaine 400 m^2 kg^{-1}) with a water to cement mass ratio of w/c = 0.3 at 20 °C. The PSD consisted of around 38 000 particles thrown in an envelope to random positions, ranging from 50-2 µm. First, the cement particles have to be placed in a system to form an initial state of the microstructure. For this, an envelope shape has to be defined and that complies with periodic boundaries. This approach enables filling the envelope while accurately complying with the imposed water/cement ratio.

Particles are stacked in this envelope based on random selection of locations while first placing the larges particles followed by the smaller particles according to the particle size distribution. From this configuration, hydration proceeds, the microstructure evolves and the amounts of the phases change. Volume fractions of reactants, i.e. the non-reacted cement and the free water, decrease, while the total fraction of the formed hydration products increases, during hydration. The solid fraction comprises the fraction of non-reacted cement grains and the formed hydration products (Fig 2): inner and outer hydration product (small gel pores, Fig 1, were disregarded in this paper). The outer expansion of the particles is calculated according to the so-called particle expansion mechanism (van Breugel 1991,

Koenders 1997) accounting for the overlaps. The simulated microstructure of the hydrated cement paste is shown in Fig 2. Location of solid particles is described by six parameters in 3D Cartesian coordinate system, i.e. the centre coordinates of particles (x, y, z), the diameter of non-hydrated cement grain, and the layer thicknesses of inner and outer hydration product. In Hymostruc the size of the developing capillary pore structure (Fig 2) is not limited by any geometrical shape and is represented by the remaining volume of the cementitious system after hydration has ceased. Therefore, theoretically there is no imposing resolution limit on the microstructural formation and pore space representation (Bishnoi and Scrivener 2009).

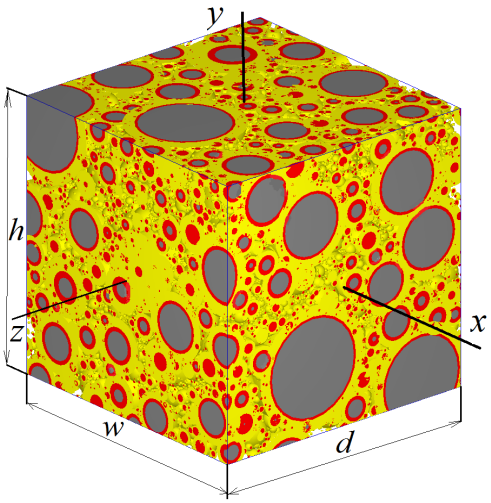

Fig. 2 3D simulated microstructure (grey-cement, red-inner hydration product, yellow-outer hydration product)

As the REV should contain sufficient information on cement paste microstructure, the minimum sample size that may be considered to determine REV is 50 μm. The variations in the effective property of a heterogeneous material are mainly due to differences in the properties of the constituent phases and inconsistencies in the local microstructural configuration (Hashin 1983). The variation in local volume induces variations in the pore structure and volume fraction of each constituent phase. To investigate the REV, a series of cement paste cubic samples with volumes ranging from 50 μm^3 to 110 μm^3 were constructed with Hymostruc. For microstructures with nominal porosities of 11 % and 7% only one sample size of 100 μm^3 was tested. Five realisations (versions) were generated for each sample size and for each porosity. In total 72 different microstructures were generated by Hymostruc.

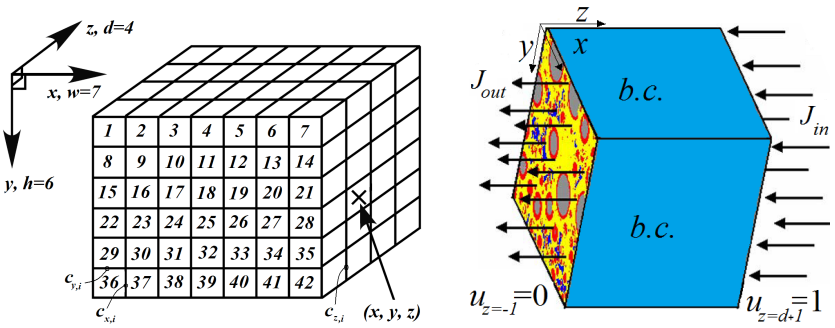

Fig. 3 a FD implementation, position and size of coordinates: width (*x*), height (*y*), and depth (*z*). Each sharing surfaces between neighboring voxels in *x, y,* and *z* directions has an assigned connectivity coefficient c_x, c_y, and c_z, respectively; **b** Steady state flux (*J*) across *z*-axis and adiabatic boundary conditions employed on 4 side faces parallel to the imposed flux.

2.2 *Estimation of Effective Transport Property*

The diffusive transport of species in a fluid is described by the II Ficks law:

$$\partial u / \partial t = -\nabla \left(D_j \nabla u \right) \tag{1}$$

where u is the concentration of the diffusing specie, D_j is the diffusivity in cement paste component j which represents a pore in between or in hydration products or in a cement grain. At the macroscopic length scales, the diffusive transport is generally modeled as:

$$\partial u / \partial t = -D_{eff} \nabla^2 u \tag{2}$$

where u is the average concentration of the diffusing species, and D_{eff} is the effective macroscopic diffusivity in porous media.

In a steady state condition, when the fluxes are steady in time, Fick's II law reduces to Laplace equation. A finite difference (FD) based program for solving the steady state transport problems is written in the C++ programing language within the Hymostruc platform. A virtual 3D microstructure is discretized into a regular 3D mesh (e.g. Fig. 3). Each voxel in a lattice was assigned to be either a capillary pore or a solid according to the particular position in the microstructure. Then, for each sharing surface between the neighboring voxels in *x*, *y*, and *z* directions a connectivity coefficient has to be assigned (c_x, c_y, and c_z, respectively, Fig. 3 **a**) and stored in three **c** vectors (whose lengths correspond to the number of voxels in the system, *N*). Six neighbor connection were used, considering that the central node is connected by the sharing faces of a cube in *x*, *y*, and *z* direction. Connectivity coefficients are obtained from microscopic transport properties of the central FD voxel and neighbor FD voxels according to the series connection of two conductors, Eq. 3.

$$c_i = 1/(0.5\,D_i^{-1} + 0.5\,D_{i+k}^{-1}) \tag{3}$$

where k = 1, w, or (w h) helps to represent a shift of the voxel numbering i to the neighbor voxel in x, y, or z direction (please see Fig. 3 **a**). The FD second order scheme is used to discretize the Laplace's equation. The Laplace's equation is solved by a second order finite difference scheme. Assembling the equations for all (N) FD nodes forms a system of global equations which can be represented in a matrix notation Eq. 4.

$$\mathbf{A}\,\mathbf{u} = \mathbf{b} \tag{4}$$

where u is the voltage vector (size of the total number of voxels in the system, N), **A** is a sparse and symmetric matrix with 7 diagonals (each voxel has 6 nearest neighbors) that contain information about connectivity coefficients of all the bonds among the voxels, and **b** is the vector of knowns (i.e. boundary condition at the top of the last layer: $u_{(x,y,z=d+1)}$= 1, Fig. 3 **b**). The obtained system of equations (3) is solved by a conjugate gradient algorithm with an optimized matrix-vector multiplication. This has been achieved by multiplying only those elements of the matrix that lie on the 7 diagonals while avoiding multiplications of a very large number of zero elements. Furthermore, since the size of the sparse matrix **A** is N times N and can reach huge dimensions, the matrix is not stored explicitly but only implicitly, by means of the vectors $\mathbf{c}_x$, $\mathbf{c}_y$, and $\mathbf{c}_z$ which store the conductivity coefficients of the bonds between voxel faces in the x, y, and z directions, respectively. Hymostruc´s graphical interface was updated to visualize the transport simulation results, Fig. 4.

Next, the flux in z direction at each node i, $J_{i,z}$ was obtained by solving the FD scheme Fick's first law. Then D_{eff} was obtained from the calculated effective flux (normalized to the flux through the same system dimensions without any solid inclusions) according to Eq. 5.

$$D_{eff} \,/\, D_0 = J_{eff} \,/\, J_0 \tag{5}$$

The relative diffusivity is the ratio of the effective diffusivity (D_{eff}) of a diffusing specie in a porous media relative to its value when diffusing in bulk water (D_0), and ranges between 0 and 1.

The simulation of transport properties is implemented in two different ways: 1) transport through capillary pores only; or 2) transport through both capillary pores and hydration products (more precisely through the CSH gel). For those capillary porosities that still exceed the capillary pore percolation threshold, effective diffusion is dominated by the capillary pore space because its diffusion coefficient is about 400 higher than the coefficient of CSH gel (Garboczi and Bentz, 1998 and 2001). Non-hydrated cement grains and portlandite (CH) are considered to be impermeable. Transport is influenced by both transports through capillary pores as well as CSH gel pores. This is because of the layered nature of the CSH gel which connects capillary pores. This paper, however, focuses only on the transport through capillary pores. A multi-scale modeling approach that includes the transport through CSH gel will be further investigated.

Zhang et al. (2011) employed the Hymostruc model and a finite element model, to simulate the diffusivity in concrete samples. The results showed that the simulations and the experimental data were of the same order of magnitude, but that the simulated values overestimated the measurement by about a factor three. The reason for this was attributed to the long measuring times (around three months) needed to achieve steady state measurement condition. However, in general, the simulated results showed similar trend as the experiments (e.g. trends for diffusivity vs. water to cement ratios, and diffusivity vs. curing age) and gave confidence to the modelling approach.

2.3 Statistical Analysis

The REV of a heterogeneous material defines a size of the model to be employed for determining the corresponding effective properties of a homogenised macroscopic model. The REV should be large enough to contain sufficient information about the microstructure in order to be representative, however, it should be much smaller than the macroscopic body, known as micro-meso-macro multi-scale principle (Hashin 1983). Gitman et al. (2006) proposed a numerical-statistical method to determine the size of the REV focusing on the mechanical properties, while Zhang et al. (2010) adapted this approach to determine the REV for transport modelling of cementitious materials. The numerical-statistical method employed here is as follows: a series of numerical experiments (realisations) for increasing sizes of the unit cell is conducted, and for each sample size five different initial cement particle locations (complying with *w*/*c*) are considered for hydration simulation. To find the REV size, the chi-square criterion, Eq. 6, was used to quantify the deviation in the calculated effective property for each nominal microstructure based on the mean value found for the five different numerical realisations.

$$\chi^2 = \sum_{i=1}^{n} \frac{(R_i - \overline{R})^2}{\overline{R}} \tag{6}$$

where R_i is the investigated effective parameter (i.e. a relative diffusivity $R=D_{eff}/D_i$, Eq. 5), $\overline{R}$ is the average of all R_i, and n is the number of numerical realisations performed with different initial cement particle locations for a nominal microstructure (characterised by nominal hydration parameters). Specifically, we apply statistics on results of five numerical realisations (i.e. n = 5). In order to fulfill the dimesionlessness of the chi-square criterion, we employ the approach of Gitman et al. (2006), normalising the R_i with respect to $\overline{R}$, thus rewriting the Eq. 6 as:

$$\chi^2 = \sum_{i=1}^{n} \left(\frac{R_i}{\overline{R}} - 1 \right)^2 \tag{7}$$

Generally, 0.103 is regarded to be an acceptable value for the chi-square coefficient, for a 95 % confidence interval and two degrees of freedom.

3 Simulation Plan

Virtual 3D microstructures were generated by Hymostruc aiming at different nominal porosities and capillary pore morphologies. Simulations are done for ordinary Portland cement (Blaine 400 m^2 kg^{-1}) with a water to cement mass ratio of w/c = 0.3 at 20 ^oC. The PSD consisted of around 38 000 particles thrown in an envelope to random positions, ranging from 50-2 μm. Minimum particle diameter of 2 μm was adopted to speed up simulations (because the lowest fractions have the highest number of particles). Simulations were run to achieve different hydration degrees in order to obtain microstructures with drastically different pore morphologies. In this way four porosities were considered: nominally 30 %, 21 %, 11 % and 7 %.

Five numerical realizations were run for each nominal sample to enable a statistical analysis of the results. Chi-square value was calculated for obtained porosities and effective diffusivities. As said, 72 series of virtual 3D microstructures were generated for this analysis. Moreover, in order to investigate the effect of numerical resolution on transport simulation, the simulated microstructure is digitized to form a 3D matrix of cubic voxels with a number of imposed resolutions. The employed FD numerical resolutions for the transport modelling were: 0.33 μm/pixel, 0.5 μm/pixel, and 1 μm/pixel, that correspond to a FD system size of 300^3, 200^3, and 100^3 voxels, respectively. In total, 150 numerical assessments of effective diffusion were realized.

4 Results and Discussion

The effective diffusion coefficients of a plain molecular diffusion system are obtained for different microstructures aiming at different nominal porosities (P = 30 %, 21 %, 11 %, and 7 %). The values are represented as relative values ranging between 0-1, and show how much the effective transport is reduced, due to the solid inclusions, relative to the diffusion in the bulk water (i.e. 100% pore scenario that has no solid inclusions). Figure 4 depicts a 3D visualization of the internal distribution of the diffusing molecule concentrations in a hydrated cement paste at steady state conditions.

Five numerical realizations were run for each nominal sample to enable a statistical analysis of the results. A random nature of distribution of heterogeneities within the hydrated cement paste was investigated by creating five nominal microstructures with different initial cement particle locations (with nominal values of w/c). This random distribution is a starting point for the hydration simulation, and thus makes the effective transport property also a random variable. The difference in the initial cement particle locations also results in the differences in the final porosities at a pre-fixed degree of hydration. Therefore, the Chi-square value was calculated for both obtained porosities and effective diffusivities. Moreover, investigating also the effect of numerical resolution resulted in a realization of 150 numerical assessments of effective diffusion by the finite difference method.

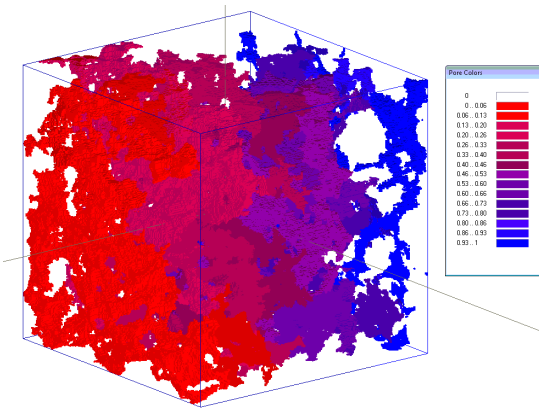

Fig. 4 3D visualizations of the distribution of molecule concentrations in hydrated cement paste at steady state, $P = 11$ % ($w/c = 0.3$)

The mean, and chi-square coefficient of relative effective diffusivity (D_{eff}/D_0) obtained for nominal samples is plotted as a function of the sample size, and shown in Figs 5, **a** and **b**, respectively. Different curves represent results obtained from microstructures with different nominal porosities (P_{nominal} = 30 %, 21%, 11%, and 7 %) as well as from employing different numerical resolutions (0.33 µm/pixel, 0.50 µm/pixel, and 1 µm/pixel). It can be observed that the porosity has a significant effect on the diffusivity (Fig 5 **a**). At lower porosities the pore network is more complex than at higher porosities, the capillary pores being smaller and more tortuous. The mean effective diffusivity for the same nominal simulated samples (same curve) was little affected by the sample size. Moreover, Fig 5 **b** reveals that the porosity and employed resolution could significantly affect the chi-square value for effective diffusivity. Samples with high nominal porosities, namely P = 30 % and 21%, exhibit a very little variability in the diffusivity results. This could be attributed to the complete connectedness of the pore network (low complexity), suggesting that even the smallest sample size, of 50 µm, can be the REV. However, for higher porosities, the chi-square coefficient for effective diffusivity declined significantly and converging as the sample rib size increased from 50 to 110 µm. The REV for microstructures with 11% porosity turned out to be 80 µm, or even better (to be more on the safe side), 90 µm. Generally, employment of finer numerical resolutions yielded lower chi-square coefficients for effective diffusivity. The effect of numerical resolution is increasingly more pronounced with lowering of sample porosity. For 'simple' microstructures with high nominal porosities, 30 % and 21 %, the investigated numerical resolution has negligible influence on the chi-square coefficients for effective diffusivity. For P = 11 %, the effect of numerical resolution becomes visible, while for P = 7%, it is crucial. For the microstructure with 7% porosity, the 100 µm sample size is below acceptable chi-square (95% confidence) level if employing 0.5 µm/pixel resolution, while unacceptable for coarser resolutions. Therefore, the increase in the complexity of the pore morphology (characterized by pore size distribution, tortuosity, constrictivity, and connectivity), requires that the REV size should also increase as the cement hydration evolves. Zhang et al. (2010) investigated the

effect of the water to cement ratio (w/c ranging from 0.30 to 0.60) on the REV of hydrated OPC by keeping the hydration degree at a constant value of 69 %. The conclusion was that the REV for effective diffusivity assessment in cement paste is constant at 100^3 μm^3. In this paper new results are obtained, indicating the strong dependency of the REV on the complexity of the pore morphology. It must be stressed that Zhang et al. (2010) employed initial particle range of 1-50 µm, while the present study was done with 2-50 µm. Bishnoi and Scrivener (2009) observed a finer pore size distribution for hydrated cement paste microstructures obtained from finer cements.

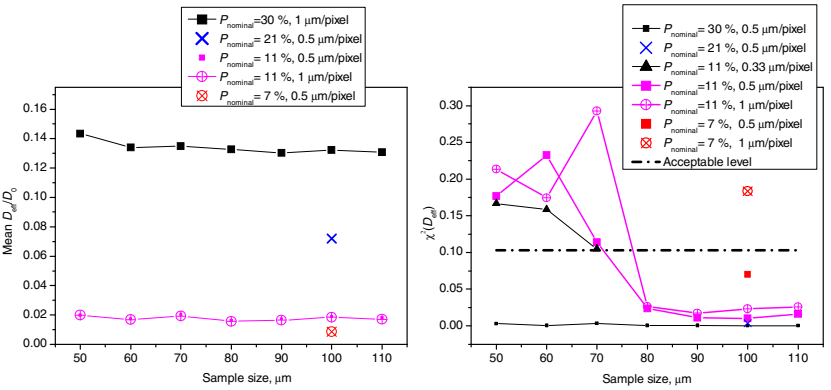

a b

Fig. 5 a Mean relative effective diffusivity vs. sample size, **b** chi-square value of effective diffusivity vs. sample size (obtained for microstructures with different nominal porosities: $P_{nominal}$ = 30 %, 21%, 11%, and 7 %; employing different numerical resolutions: 0.33, 0.50, and 1 µm/pixel)

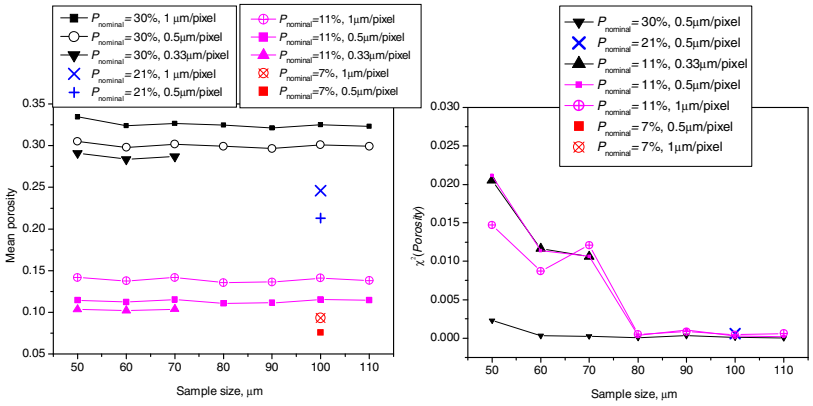

a b

Fig. 6 a Mean porosity vs. sample size, **b** chi-square value of porosity vs. sample size (obtained for microstructures with different nominal porosities: $P_{nominal}$ = 30 %, 21%, 11%, and 7 %; employing different numerical resolutions: 0.33, 0.50, and 1 µm/pixel)

Fig 6, **a** and **b**, depicts the mean and chi-square coefficient of porosity, respectively, obtained for nominal samples with different sizes. Again, different curves represent results obtained for different nominal porosities as well as for employing different numerical resolutions. Fig 6 **a** shows that the refinement of the numerical resolution lowers the calculated porosity of the digitized sample. The mean effective diffusivity for similar (nominal) simulated samples (i.e. the same curve) was affected only a little by the sample size. The investigated difference in the initial cement particle locations, used as a starting point for hydration simulation, results also in the fluctuations of the final porosities at pre-fixed degree of hydration. The chi-square value characterising the variability in obtained porosity, Fig 6 **b**, is increasing with hydration degree (i.e. with decrease in nominal porosities). Samples with high nominal porosities, namely P=30 and 21%, exhibit a very little variability in the porosity, while for low nominal porosities, the variability is higher in general, but decreases with sample size. There is no significant effect of numerical resolution on variability of porosity.

5 Outlook

A short outlook on the future possibilities of the presented approach to investigate other parameters is addressed in this section.

- For cement pastes in particular, and for REV determination in general, a cubic shaped sample is the most reasonable option. This is because the REV theory assumes that the sample can be homogenized at the REV size, so it eliminates the influence of shape. Therefore, the influence of the interface zones between cement paste and aggregates should be investigated at the mortar and concrete level.
- Employing boundary conditions other than adiabatic, such as periodic boundary conditions, indicated a lower variability of the results.
- Micro-cracking, which is commonly observed in real cement pastes, may also be taken into account in mass transport calculations. The influence of these cracks on the REV size should be investigated at the mortar and concrete level. However, this paper is limited to ideal cement paste conditions and neglecting micro-cracking effects on transport.
- External mechanical loadings, temperature gradients and shrinkage may induce additional crack pathways and affect the transport properties. To assess this contribution, a mechanical model for predicting crack distribution and propagation may be required.

6 Conclusion

Numerous series (72) of virtual 3D microstructures with different porosities and capillary pore morphologies were used to investigate the REV size for numerical modeling of transport in hydrating cement paste. Moreover, investigating the effect of numerical resolution resulted in realization of 150 numerical assessments of effective diffusion by the finite difference method. Based on a statistical analysis, it was concluded that the REV size primarily depends on the porosity and

employed numerical resolution. The effect of numerical resolution on the REV is increasingly more pronounced for lowering the sample porosities. The results also showed that a refinement of the numerical resolution lowered the calculated porosity of the digitized sample.

The observed increase in REV size with progress of the hydration process could be attributed to the increase in the complexity of the pore morphology, which is defined by pore size distribution, tortuosity, constrictivity, and connectivity. In future work, besides porosity, emphasis will be on these microstructural parameters that characterize the pore morphology. Among them are the statistical parameters like pore size distribution, tortuosity and constrictivity. In this way the pore morphology can be fundamentally linked to the effective transport properties, and its REV size.

Acknowledgments. The authors acknowledge the support by the Marie Curie Actions EU grant FP7-PEOPLE-2010-IEF-272653-DICEM.

References

Bishnoi, S., Scrivener, K.L.: μic: A new platform for modelling the hydration of cements. Cem. Concr. Res. 39, 266–274 (2009)

van Breugel, K.: Simulation of Hydration and Formation of Structure in Hardening Cement-Based Materials. PhD, Delft University of Technology (1991)

van Breugel, K.: Numerical simulation of hydration and microstructural development in hardening cement paste (I): Theory. Cem. Concr. Res. 25, 319–331 (1995)

Garboczi, E.J., Bentz, D.P.: The effect of statistical fluctuation, finite size error, and digital resolution on the phase percolation and transport properties of the NIST cement hydration. Cem. Concr. Res. 31, 1501–1514 (2001)

Garboczi, E.J., Bentz, D.P.: Multi-scale analytical/numerical theory of the diffusivity of concrete. J. Adv. Cem. Mater. 8, 77–88 (1998)

Gitman, I.M., Askes, H., Sluys, L.J.: Representative volume: Existence and size determination. Eng. Fract. Mech. 74, 2518–2534 (2007)

Gitman, I.M., Gitman, M.B., Askes, H.: Quantification of stochastically stable representative volumes for random heterogeneous materials. Arch. Appl. Mech. 75, 79–92 (2006)

Hashin, Z.: Analysis of composite materials: a survey. J. Appl. Mech. 50, 481–505 (1983)

Koenders, E.A.B.: Simulation of volume changes in hardened cement-based materials. PhD Dissertation, Delft University of Technology (1997), Hymostruc program is available at: `http://www.citg.tudelft.nl/en/about-faculty/departments/structural-engineering/sections/materials-and-environment/chairs/microlab/research/hymostruc/`)

Pignat, C., Navi, P., Scrivener, K.L.: Simulation of cement paste microstructure hydration, pore space characterization and permeability determination. Mater. Struct. 38, 459–466 (2005)

Zhang, M.Z., Ye, G., van Breugel, K.: Microstructure-based modeling of water diffusivity in cement paste. Constr. Build. Mater. 25, 2046–2052 (2011)

Zhang, M.Z., Ye, G., van Breugel, K.: A numerical-statistical approach to determining the representative elementary volume (REV) of cement paste for measuring diffusivity. Materiales de Construción 300, 7–20 (2010)

Exploring the Observed Rheological Behaviour of In-Situ Aged and Fresh Bitumen Employing the Colloidal Model Proposed for Bitumen

Olli-Ville Laukkanen, Terhi Pellinen, and Michalina Makowska

Aalto University, Finland

Abstract. This paper compares in-situ (field) aged road bitumen and fresh paving grade bitumen by presenting various rheological measurements conducted with Dynamic Shear Rheometer (DSR). Performed tests included strain sweeps, frequency sweeps and shear rate sweeps in the linear and nonlinear viscoelastic region of response at temperatures ranging from 2 to 120°C. Some fundamental rheological concepts were utilised to explain the origins of observations employing colloidal model describing bitumen structure. However, additional testing, including chemical analysis techniques like GPC and IR, is needed to validate and maximise output from this single equipment analysis. Testing suggests that Lissajous figures from strain sweep tests could be used to characterise cracking propensity of binders; research revealed ductile like behaviour for aged bitumen in the nonlinear region, which is postulated here to originate from the formation of crazes (microcracks) capable of load transfer.

Keywords: Rheology, DSR, bitumen, ageing, colloidal model.

1 Introduction

The aim of this study was to compare in-situ aged road bitumen with fresh tank bitumen to gain more insight on bitumen's rheology by comparing DSR data with proposed colloidal model in order to provide maximum output from a single equipment analysis. This approach would be valuable since bitumen ageing is one of the principal factors causing deterioration of asphalt pavements due to thermally induced cracking and fatigue combined with loading by traffic.

The rheology of bitumen is affected by irreversible chemical alterations, physico-chemical transformations and reversible processes called steric and physical hardening. Chemical changes had been discussed to include oxidation [1], condensation, polymerisation [2], and cyclisation [3]. In dense graded bituminous mixtures, most physico-chemical changes take place during asphalt mixing in terms of loss of volatile components and exudation or migration of oily components from bitumen into the porous aggregate. From time-dependent, reversible ageing mechanisms, steric hardening is attributed to the association of molecules,

N. Kringos et al. (Eds.): *Multi-Scale Model. & Charact. of Infrastruct. Mater.,* RILEM 8, pp. 185–197.
DOI: 10.1007/978-94-007-6878-9_14

especially asphaltenes, at room temperature, whereas physical hardening is attributed to a molecular structuring towards an optimum thermodynamic state in the vicinity of glass transition temperature [4, 5]. Additionally, oxidative hardening was correlated to the increase of carbonyl and sulfoxide groups' content in bitumen. [1, 6]. As a general trend, rheology of small amplitude oscillatory measurements shows that bitumen moduli, viscosity and relaxation times are increasing as bitumen oxidises.

To characterise straight-run bitumens, both the colloidal model and the Dispersed Polar Fluid (DPF) model have been used by paving industry [7, 8]. The DPF model assumes that bitumen is a single-phase system i.e., a simple homogenous liquid [8] whereas colloidal model presumes that there are two phases present, a continuous, low-polar phase, and a dispersed, highly polar phase.

A new model was proposed in 2000 by Redelius [9], based on mutual solubility of solvents. It incorporates information about cohesion, molecular volume, dispersive and polar interactions as well as hydrogen bonding. Currently, to the best of our knowledge, database of rheological data in connection with this model does not exist that would allow for utilisation of the model in our work.

Nevertheless, the objective of this work is to interpret the ageing mechanisms of straight-run bitumen utilising rheological data in a top to bottom way of approach. As research has shown problems with the DPF model for the waxy bitumens, bitumens with high asphaltene content and bitumens modified with polymers [10, 11, 12] and the majority of analysis presented in this article is valid upon incorporation of a colloidal model [7], therefore such is followed.

According to the colloidal model, bitumen is a mixture of asphaltenes dispersed in an oily medium (maltenes) composed of saturates, aromatics and dispersed part of resins, Figure 1. A part of the resins constitutes a shell around the asphaltene particles forming a temperature and concentration dependent equilibrium between the resins around the asphaltenes and those dissolved in the oily matrix [13]. Due to ageing, asphaltene molecular weight and amount of polar functional groups with oxygen and therefore also abundance of hydrogen bonds are expected to rise. Consequently, increased intermolecular associative interactions and asphaltene aggregation would create a more structured colloidal network in aged bitumen [5, 14, 15]. More information about the manifestations of colloidal structure in the rheological properties of bitumen can be found in [7, 16].

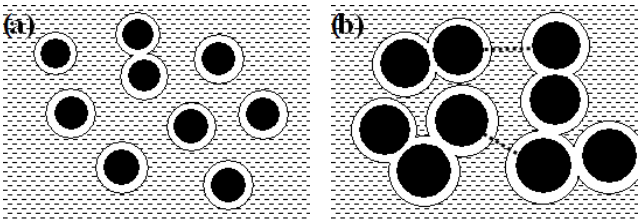

Fig. 1 Simplified colloidal structures of (a) unaged and (b) aged bitumen

2 Materials and Experimental Program

Aged bitumen was extracted from the 10-year-old SMA pavement of Ring Road II, located in the metropolitan area of Helsinki, Finland. Construction records revealed that original binder grade used was 70/100 penetration bitumen, which was then used as the unaged reference bitumen in the study. However, the source of the extracted bitumen could not be confirmed to be the same as that of the unaged one. The possible difference in the crude origin may have some minor effects on the results presented in this paper.

To gain comprehensive understanding of the rheological behaviour of the studied bitumens, various rheological measurements were performed with a stress-controlled Reologica Stresstech rheometer. Frequency sweep measurements were conducted under controlled strain loading conditions. In the measurements, the temperature of the test specimen was treated with an air convection oven.

Summaries of the rheological measurements, measurement geometries and experimental ranges used in this study are presented in Tables 1 and 2. In all the measurements, test specimens were prepared to the rheometer according to the method of direct transfer described in AASHTO standard T315-10. The main steps of specimen preparation procedure are presented in Figure 2.

Table 1 A list of the tests performed and parameters measured in this study

Test	Temperature range (°C)	Parameters	Purpose of testing
Strain sweep	2-70	$G^*(\gamma_0)$, $\delta(\gamma_0)$	LVE strain limits, large strain behaviour
Frequency sweep	2-70	$G^*(\omega)$, $\delta(\omega)$	Crossover points, Black curves
Shear rate sweep	60-120	$\eta(\dot{\gamma})$	Newtonian and non-Newtonian flow behaviour

Table 2 A list of the measurement geometries and experimental ranges used in this study

Test	Temperature range (°C)	Measurement geometry and diameter (mm)	Experimental range
Strain sweep	2-40*	PP 8	0.001-0.3 strain**
	50-70	PP 25	0.001-2.2 strain**
Frequency sweep	2-40*	PP 8	0.01-10 Hz
	50-70	PP 25	0.01-10 Hz
Shear rate sweep	60-80	CP 25	0.001-100 s^{-1}**
	100-120	CP 25	0.001-1000 s^{-1}**

PP parallel plate geometry; *CP* cone-plate geometry

*lower temperature limit was set by the temperature control system of the DSR

**experimental limits were governed by the technical limitations of the DSR

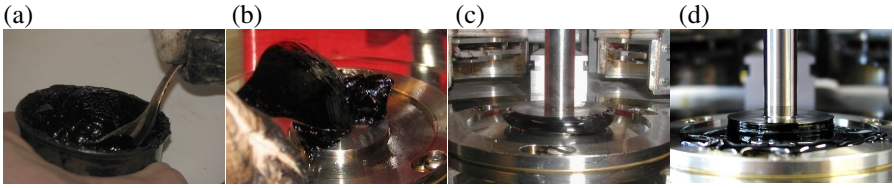

Fig. 2 The main steps of specimen preparation procedure: (a) Curving the specimen from penetration cup with heated spoon; (b) placing the specimen on the lower plate of the DSR (heated to 50°C); (c) the specimen at 1.050 mm gap before trimming; (d) the specimen after it has been trimmed and the gap lowered to 1.000 mm

3 Strain Dependent Behaviour

The strain sweep tests are conducted applying first very small strain amplitude to the sample, which is then continuously increased. These tests are usually done for the sole purpose of determining the limits of the linear viscoelastic (LVE) strain or stress range [17], although here the main emphasis was the nonlinear behaviour of bitumen.

The LVE strain limit represents the deformation where material's molecular structure starts to experience irreversible changes [17]. In the case of the colloidal structure of bitumen, we interpret this onset of strain thinning to be caused by disintegration of aggregated asphaltene micelles and with large strains strain thinning may also be partly due to the reorientation of the micelles in the direction of shear, as is proposed for some viscoelastic materials containing clustered particles [18]. Consequently, this would contribute to the mechanical weakening and more liquid like mechanical response of bitumen in the nonlinear region.

The LVE strain limits in Figure 3 have been calculated as the strain value at which the complex modulus has decreased to 95% of its initial value [8]. Due to ageing, the LVE range has narrowed considerably when compared in the equi-temperature conditions, shown in Figure 3a. However, when temperature is eliminated from the analysis by employing magnitude of the complex modulus calculated from the linear small strain region of the test, differences between aged and unaged binder can barely be seen (Figure 3b).

This suggests that ageing does not change LVE strain limits as a function of stiffness. Hence, for practical purposes, the LVE strain limits of aged straight-run bitumen should be predictable simply by increasing the stiffness (decreasing the temperature or increasing the measurement frequency) of unaged bitumen. Finally, both binders show evidence of a plateauing of the LVE strain limits at high stiffness region (at low temperatures) having an asymptotic limit at approximately 1% strain, which agrees with findings by Airey et al. [19].

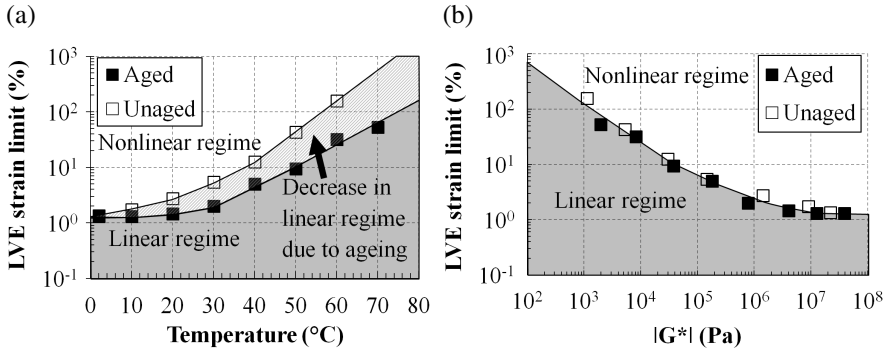

Fig. 3 LVE strain limits as a function of (a) temperature and (b) magnitude of complex modulus at 1 Hz

Also the frequency at which the measurement is conducted is known to have an effect on LVE strain limits. However, in this study, the effect of changing the measurement frequency on LVE strain limits was not studied due to the limited timeframe, but can be found in Airey et al. [19].

The effects of nonlinearity were studied by measuring complex modulus as a function of increasing strain amplitude, γ_0, shown in Figure 4. In addition, Figure 5 shows Lissajous figures [20] of the same data with the trace of norm of complex modulus $|G^*(\gamma_0)|$ computed from the data. In Figure 4, a more gradual decrease in the modulus suggests that the structure of the aged binder does not break down as abruptly as that of the unaged binder. This allows us to assume that the colloidal structure of aged binder has become more structured. It also appears to exhibit more "ductile like" behaviour in the nonlinear strain region (Figure 5a), while the unaged binder exhibits expected liquid like behaviour (Figure 5b) discussed above.

Bitumen could be classified as a glassy thermoplast. This type of material in polymer oriented research (ductile amorphous polymers) is often reported to be subject of brittle cracking or shear dependent deformations, and mechanism of failure is dependent on the stress provided to the system [21]. However, the observation of ductility in macroscopic observation is postulated to be subject to error due to presence of crazes (microcracks), capable of load transfer before the actual brittle damage (cracking) occurs. Similar concept was described for bitumen by Kringos et al. [22].

However, it should be remembered that in this study strain sweep measurements were conducted with a stress-controlled DSR, and the same tests may give divergent results when performed with a strain-controlled DSR.

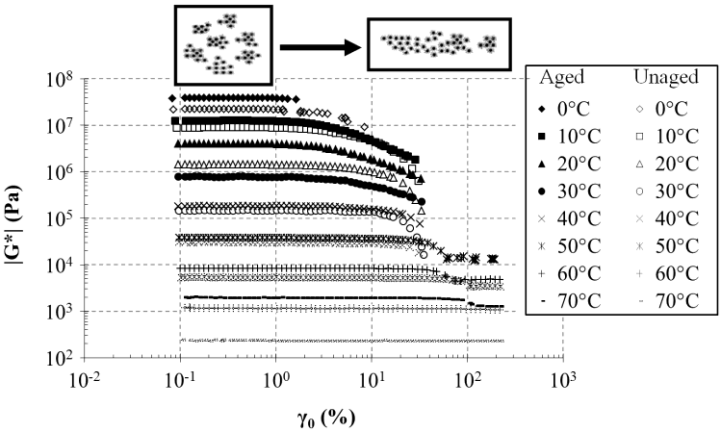

Fig. 4 The norm of complex modulus $|G^*(\gamma_0)|$ as a function of strain amplitude measured at 1 Hz together with schematic pictures of the disintegration and reorientation of asphaltene aggregates

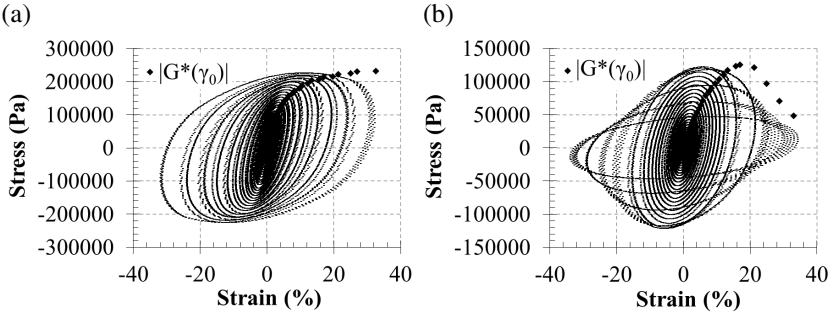

Fig. 5 Lissajous figures and evolution of the norm of complex modulus $|G^*(\gamma_0)|$ for (a) aged and (b) unaged binder at 20°C and 1 Hz

4 Frequency Dependent Behaviour

Frequency sweep data, obtained being in the LVE region, was used to evaluate crossover points, shown in Figure 6. Crossover point is the point where $G'(\omega) = G''(\omega)$ or equivalently $\tan \delta = 1$, and it is defined by two characteristic, material dependent values: crossover frequency ω_c and crossover modulus G_c [17]. At lower frequencies than ω_c material exhibits liquid like character ($G'' > G'$), whereas with higher frequencies it displays gel like behaviour ($G' > G''$). Since both of the studied bitumens produced relatively smooth Black curves (Figure 7a) in the whole experimental range of frequency sweep measurements, the validity of time-temperature superposition (TTS) principle was confirmed [23], thus allowing the construction of master curves (Figure 6) using IRIS Rheo-Hub –software.

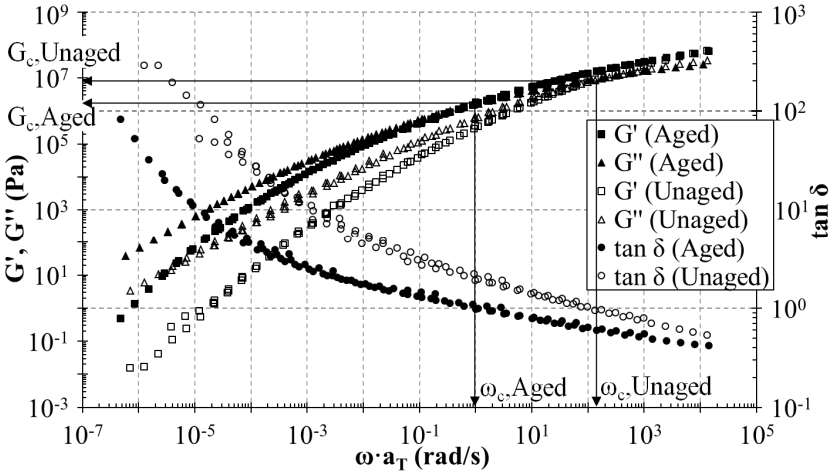

Fig. 6 Storage modulus, loss modulus and loss tangent master curves at the reference temperature of 20°C and the determination of crossover points

Figure 6 shows that the aged bitumen has substantially lower crossover frequency than the unaged binder ($\omega_{c,Aged}$ = 0.928 rad/s, $\omega_{c,Unaged}$ = 121 rad/s) at the reference temperature of 20°C. This suggests that aged binder has higher average molecular mass M [14, 17] as would be expected based on the discussion in Section 1.

In terms of the colloidal approach, a lower crossover frequency or a longer relaxation time, $1/\omega_c$, respectively, relates to larger particles resulting from the aggregation of asphaltenes peptized by resin molecules and, concurrently, to the reduction of the maltenes phase in bitumen's colloidal structure.

In addition, aged binder has lower crossover modulus ($G_{c,Aged}$ = 1.51 MPa) than fresh binder ($G_{c,Unaged}$ = 7.97 MPa). This can be indicative of wider molecular mass distribution (MMD) and increased polydispersity of aged binder [14, 17]. This change in the dispersion of molecular masses may be explained with the fact that a part of lighter molecules have reacted and formed heavier compounds; it is expected that due to ageing some of the aromatics are converted into resins and a part of the resins into asphaltenes [2, 5].

In Figure 7a a semilogarithmic plot of δ vs |G*| – known as Black diagram or Black curve – is shown for both binders. Black curve is a very useful tool for analysing viscoelastic materials since the knowledge of both |G*| and δ allows an overall view on the viscoelastic behaviour of a material. The different shapes of the Black curves in Figure 7a suggest that the colloidal structures of the studied binders are different [24], as would be expected from the analysis above.

It can also be clearly seen that the Black curve of aged binder has shifted downwards in Figure 7a, that is, to the more elastic side of the diagram. Soenen et al. [25] observed this same transition to happen as a result of oxidation and claimed that it could be related to the broadening of relaxation time spectrum.

Indeed, this can be seen from Figure 7b where continuous relaxation time spectra for the studied bitumens have been calculated. In the calculations data from the loss modulus master curves have been exploited using Schwarzl and Staverman approximation, which has been widely used to transform dynamic data into a relaxation one [26]:

$$H(\ln \tau) = 2/\pi * G''[1-(\mathrm{d} \log G''/\mathrm{d} \log \omega)^2+1/2.303*\mathrm{d}^2 \log G''/\mathrm{d} \log \omega^2]_{1/\omega=\tau} \quad (1)$$

where $H(\tau)$ = the relaxation time spectrum at time τ, Pa; G'' = loss modulus, Pa; ω = angular frequency, s^{-1}; and τ = relaxation time, s. Prior to the data conversion, loss modulus data was smoothed with a high-order polynomial fit.

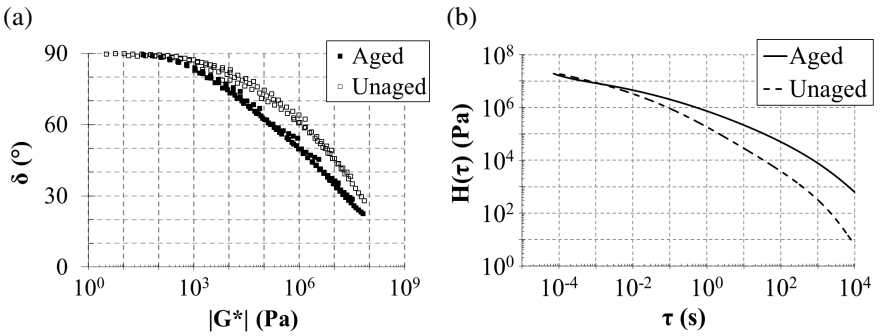

Fig. 7 (a) Black curves and (b) continuous relaxation time spectra (at the reference temperature of 20°C) of aged and unaged binder

Also Ruan et al. [27] observed that oxidative ageing extends binder's relaxation processes to longer times and thus results in a broader relaxation time spectrum. They explained the retardation of relaxation processes to be caused by the shift to more solid like behaviour, as can also be concluded from the shift of Black curve in Soenen et al. [25]. This interpretation seems reasonable also in the light of our test results. Furthermore, the shift in Black curve can be indicative of increased polydispersity [28], and thus of wider MMD, strengthening the conclusion drawn on the basis of the crossover point locations.

5 Steady State Flow Behaviour

The steady state flow behaviour of the tested binders was characterised with shear rate sweep measurements in the high temperature range of 60-120°C, see Figure 8. At low shear rates both binders exhibit Newtonian flow behaviour, but after exceeding the critical shear rate they start to behave as shear thinning fluids. However, the microstructural fundamentals of the shear thinning nature of bitumen are not yet completely understood. The simplest explanation would be that the imposed shear stress reaches a critical value where aggregated asphaltene micelles are dissociated, thus deteriorating the colloidal structure of the bitumen [29].

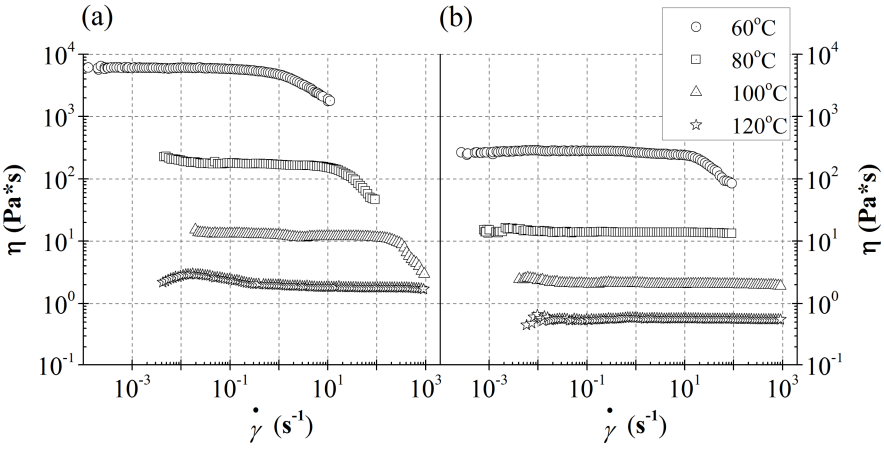

Fig. 8 Viscous flow curves for (a) aged and (b) unaged binder

This type of non-Newtonian flow behaviour can be described fairly well with the Cross equation [30]:

$$(\eta(\dot{\gamma})-\eta_\infty)/(\eta_0-\eta_\infty) = 1/(1+(\lambda_c\dot{\gamma})^m) \quad (2)$$

where $\eta(\dot{\gamma})$ = shear rate dependent viscosity, Pa*s; η_∞ = the infinite shear viscosity, Pa*s; η_0 = the Zero Shear Viscosity (ZSV), Pa*s; λ_c = the characteristic time, s; $\dot{\gamma}$ = shear rate, s^{-1}; and m = the Cross rate constant (related to the degree of dependence of viscosity on shear rate in the shear thinning region). The reciprocal of the characteristic time, $1/\lambda_c$, gives us the critical shear rate, $\dot{\gamma}_c$, which proves a useful indicator of the onset shear rate for shear thinning. The Cross model was fitted to the measured viscosity data to obtain the values of Cross model parameters shown in Table 3.

As can be seen from Figure 8, the maximum shear rate was not high enough to capture non-Newtonian flow behaviour of the studied binders at all the temperatures. At these temperatures, the ZSV values are calculated as an average of all the measurement points in each temperature in order to minimise experimental errors.

Due to ageing, ZSVs have increased by a factor of 3.2-21.5 depending on the temperature, having the highest factor in the lowest temperature and vice versa. Since higher ZSVs correspond to higher average molecular masses (M) [17], this result suggests an increase in M of aged binder, which agrees with the lower crossover frequency, ω_c, discussed in Section 4. Viscosity of bitumen has also been proven to depend on asphaltene content [1]. However, maltenes viscosity would need to be additionally established as supplementary data for the correlation to be exact, and thus is outside of the scope of this paper.

Table 3 Cross model parameters, critical shear rates and flow activation energies defined from shear rate sweep measurements

	Aged bitumen				Unaged bitumen			
Temperature (°C)	60	80	100	120	60	80	100	120
η_0 (Pa*s)	6070.62	173.53	12.32	1.82	274.25	13.92	2.07	0.58
η_∞ (Pa*s)	0.0001	0.0001	0.0001	-	0.0008	-	-	-
λ_c (s)	0.2626	0.0245	0.0021	<0.001*	0.0237	<0.010*	<0.001*	<0.001*
M	0.88	1.37	1.77	-	1.22	-	-	-
$\dot{\gamma}_c$ (s^{-1})	3.81	40.76	465.63	>1000*	42.22	>100*	>1000*	>1000*
E_a (kJ/mol)	148				112			

*values are outside of the measuring range

For both binders, ZSV values are merging as the temperature increases. Consequently, the thermal susceptibility of the binders is reduced at high temperatures. This is probably due to a simpler colloidal structure, as then most of the resins stand dissolved into the maltenic matrix [7, 13]. From Table 3 and Figure 8 it can also be seen that characteristic times, λ_c, have increased and critical shear rates, $\dot{\gamma}_c$, decreased due to ageing. This observed increase in the shear dependence of aged binder agrees with the decreased LVE strain limits discussed in Section 3.

The temperature dependence of the ZSV (denoted here as η_0) may be described by an Arrhenius-type equation [17]:

$$\eta_0 = A\exp(E_a/RT) \tag{3}$$

where A = a pre-exponential constant, Pa*s, which represents the ZSV of the binder, η_0, at infinite temperature; E_a = the activation energy for viscous flow, J/mol; R = the universal gas constant (= 8.314 J/(mol*K)); and T = absolute temperature, K. The flow activation energies for aged and unaged binder calculated from shear rate sweep measurements are presented in Table 3.

The flow activation energy is considerably higher for the in-situ aged binder (148 kJ/mol) than for the unaged binder (112 kJ/mol), as expected assuming that the average molecular mass M has increased (see Section 4). Similarly, increase in the abundance of functional groups might have contributed to this change. Furthermore, an increasing content of polar oxygen-containing functional groups, especially in aged asphaltenes, have probably increased polarity, aromaticity and intermolecular associative interaction among functional groups in aged binder, resulting in a higher flow activation energy [6, 31, 32]. Also, flow activation energy has been shown to correlate with the amount of asphaltenes [32], and thus higher flow activation energy might also be indicative of the higher abundance of asphaltenes in aged bitumen.

6 Conclusions

As literature reveals and our own measurements corroborate, the mechanical properties of bitumen seem to be dependent not only upon the relative abundance of dispersed and continuous phases, but as well the magnitude and dispersion in both molecular masses and intermolecular forces. On the basis of rheological analysis, we postulate, as well as many others, that the aged binder exhibits higher average molecular mass M and broader molecular mass distribution MMD which indicates a shift towards higher abundance of asphaltenes and resins in aged bitumen. However, supplementary testing methods, for example GPC and IR, are needed to quantify the observations of this study. Also, crude source dependence of bitumen behaviour should be quantified in further work for a more rigorous comparison of in-situ aged and fresh bitumens.

Based on our test results, LVE strain limits of the aged straight-run bitumen should be predictable simply by increasing the stiffness (decreasing the temperature or increasing the measurement frequency) of the unaged bitumen. Testing in nonlinear region revealed ductile like behaviour for aged bitumen, which is postulated here to originate from the formation of crazes (microcracks) capable of load transfer. For the unaged binder, expected behaviour in terms of evolution towards a liquid like behaviour was observed in the nonlinear region. Testing suggests that Lissajous figures from strain sweep tests could be used to characterise cracking propensity of binders. However, further research is needed to validate and maximise output from this single equipment analysis.

References

[1] Petersen, J.C.: A Review of the Fundamentals of Asphalt Oxidation: Chemical, Physicochemical, Physical Property, and Durability Relationship. Transportation Research Circular E-C140 (October 2009)

[2] Siddiqui, M.N., Ali, M.F.: Investigation of chemical transformations by NMR and GPC during the laboratory aging of Arabian asphalt. Fuel 78(12), 1407–1416 (1999)

[3] Quddus, M.A., Sarwar, S.N., Khan, F.: The chemical composition of catalytic air blown asphalt. Fuel 74(5), 684–689 (1995)

[4] Masson, J.F., Polomark, G.M., Collins, P.: Time-dependent microstructure of bitumen and its fractions by modulated differential scanning calorimetry. Energy & Fuels 16(2), 470–476 (2002)

[5] Lu, X., Isacsson, U.: Effect of ageing on bitumen chemistry and rheology. Construction and Building Materials 16(1), 15–22 (2002)

[6] Ruan, Y., Davison, R.R., Glover, C.J.: Oxidation and Viscosity Hardening of Polymer-Modified Asphalts. Energy & Fuels 17(4), 991–998 (2003)

[7] Lesueur, D., Gérard, J.F., Claudy, P., Létoffé, J.M., Planche, J.P., Martin, D.: A structure related model to describe asphalt linear viscoelasticity. Journal of Rheology 40(5), 813–836 (1996)

[8] Anderson, D.A., Christensen, D.W., Bahia, H.U., Dongre, R., Antle, C.E., Sharma, M.G.: Binder Characterization and Evaluation. SHRP-A-370, National Research Council, Washington, DC (1994)
[9] Redelius, P.G.: Solubility parameters and bitumen. Fuel 79(1), 27–35 (2000)
[10] Soenen, H., De Visscher, J., Vanelstraete, A., Redelius, P.: Influence of thermal history on rheological properties of various bitumen. Rheologica Acta 45(5), 729–739 (2006)
[11] Airey, G.D.: Rheological evaluation of ethylene vinyl acetate polymer modified bitumens. Construction and Building Materials 16(8), 473–487 (2002)
[12] Da Silva, L.S., De Camargo-Forte, M.M., De Alencastro Vignol, L., Cardozo, N.S.: Study of rheological properties of pure and polymer-modified Brazilian asphalt binders. Journal of Materials Science 39(2), 539–546 (2004)
[13] García-Morales, M., Partal, P., Navarro, F.J., Martínez-Boza, F., Mackley, M.R., Gallegos, C.: The rheology of recycled EVA/LDPE modified bitumen. Rheologica Acta 43(5), 482–490 (2004)
[14] Scarsella, M., Mastrofini, D., Barre, L., Espinat, D., Fenistein, D.: Petroleum Heavy Ends Stability: Evolution of Residues Macrostructure by Aging. Energy & Fuels 13(3), 739–747 (1999)
[15] Moschopedis, S.E., Speight, J.G.: The effect of air blowing on the properties and constitution of a natural bitumen. Journal of Materials Science 12(5), 990–998 (1977)
[16] Lesueur, D.: The colloidal structure of bitumen: Consequences on the rheology and on the mechanisms of bitumen modification. Advances in Colloid and Interface Science 145(1), 42–82 (2009)
[17] Mezger, T.G.: The rheology handbook: For users of rotational and oscillatory rheometers, 1st edn. Vincentz Verlag, Hannover (2002)
[18] Marcovich, N.E., Reboredo, M.M., Kenny, J., Aranguren, M.I.: Rheology of particle suspensions in viscoelastic media. Wood flour-polypropylene melt. Rheologica Acta 43(3), 293–303 (2004)
[19] Airey, G., Rahimzadeh, B., Collop, A.: Linear Viscoelastic Perfomance of Asphaltic Materials. Road Materials and Pavement Design 4(3), 269–292 (2003)
[20] Melito, H.S., Daubert, C.R., Foegeding, E.A.: Validation of a large-amplitude oscillatory shear protocol. Journal of Food Engineering 113(1), 124–135 (2012)
[21] Kuriyama, T., Narisawa, I.: Fracture behaviour of ductile polymer under mixed mode loading. Technical Papers of the Annual Technical Conference - Society of Plastics Engineers 52(3), 3235–3240 (1994)
[22] Kringos, N., et al.: A finite element based chemo-mechanics model to simulate healing of bituminous materials. In: Kringos, N. (ed.) Chemo-Mechanics of Bituminous Materials, Delft, pp. 69–75 (2009) ISBN/EAN 978-94-90284-04-9
[23] van Gurp, M., Palmen, J.: Time-temperature superposition for polymeric blends. Rheology Bulletin 67(1), 5–8 (1998)
[24] Giavarini, C., Mastrofini, D., Scarsella, M., Barre, L., Espinat, D.: Macrostructure and Rheological Properties of Chemically Modified Residues and Bitumens. Energy & Fuels 14(2), 495–502 (2000)
[25] Soenen, H., De La Roche, C., Redelius, P.: Fatigue behaviour of bituminous materials: from binders to mixes. Road Materials and Pavement Design 4(1), 7–27 (2003)
[26] Schwarzl, F., Staverman, A.J.: Higher approximation methods for the relaxation spectrum from static and dynamic measurements of visco-elastic materials. Applied Scientific Research 4(2), 127–141 (1953)

[27] Ruan, Y., Davison, R.R., Glover, C.J.: The effect of long-term oxidation on the rheological properties of polymer modified asphalts. Fuel 82(14), 1763–1773 (2003)
[28] Trinkle, S., Friedrich, C.: Van Gurp-Palmen-plot: a way to characterize polydispersity of linear polymers. Rheologica Acta 40(4), 322–328 (2001)
[29] Polacco, G., Berlincioni, S., Biondi, D., Stastna, J., Zanzotto, L.: Asphalt modification with different polyethylene-based polymers. European Polymer Journal 41(12), 2831–2844 (2005)
[30] Sybilski, D.: Non-Newtonian viscosity of polymer-modified bitumens. Materials and Structures 26(1), 15–23 (1993)
[31] Lu, X., Isacsson, U.: Artificial aging of polymer modified bitumens. Journal of Applied Polymer Science 76(12), 1811–1824 (2000)
[32] Mastrofini, D., Scarsella, M.: The application of rheology to the evaluation of bitumen ageing. Fuel 79(9), 1005–1015 (2000)

Effect of Film Thickness of Asphalt Mixture in Compression Test

Ying Li[1], Dong Wang[2], Linbing Wang[3,*], Lei Zhang[4], and Xudong Wang[5]

[1] Department of Civil and Environmental Engineering,
Virginia Polytechnic Institute and State University,
Blacksburg, VA 24061
liy86317@vt.edu
[2] Virginia Tech Transportation Institute,
Blacksburg, VA 24061
wangd@vt.edu
[3] Department of Civil and Environmental
Engineering, Virginia Polytechnic Institute and State University;
Director, Center for Smart Infrastructure and Sensing Technology,
Virginia Tech Transportation Institute (VTTI),
Virginia Polytechnic Institute and State University,
Blacksburg, VA 24061
wangl@vt.edu
[4] Research Institute of Highways (RIOH), China
[5] Research Institute of Highways (RIOH), China

Abstract. Discrete element modeling was used to investigate the effect of film thickness of asphalt mixture in compression test. Compressive tests of asphalt mixtures with different film thicknesses were conducted and the axial stress responses of the specimens were documented. The peak axial stress of the mixture was found to be as a power-law function of film thickness. The internal geometry of asphalt mixture was modeled using PFC3D code and cracking within the structure was modeled by allowing bond breakage between adjacent particles. The effect of random variations in internal sample geometry, the distribution of bond strengths between adjacent particles and the coefficient of friction between particles where the bond were broken were investigated. A simple viscoelastic model was applied to contacts between asphalt binder and aggregates. By using the cabinet X-ray tomography system, the displacement and resistant force of a group of particles bonded by a thin layer of asphalt binder are measured. A reasonable agreement between experiments results and simulation results is obtained combined with parametric analysis.

Keywords: Discrete element modeling; Asphalt mixtures; Visco-elastic model; Compression tests; X-ray tomography.

* Corresponding author.

N. Kringos et al. (Eds.): *Multi-Scale Model. & Charact. of Infrastruct. Mater.,* RILEM 8, pp. 199–218.
DOI: 10.1007/978-94-007-6878-9_15

1 Introduction

Asphalt mixture is a composite material which consists of interspersed aggregates, asphalt binder and air voids. The constitutive behavior of the material depends largely on the interaction between the aggregates and asphalt binder (*1*). The aggregate skeleton determines the load carrying mechanism and the asphalt binder serves as an adherent which enables the mixture to hold tensile and shear stresses (*2*). To study the constitutive behavior of an aggregate-binder system, the contact between aggregates coated with asphalt binder is the key problem to solve. A contact model which properly shows the relationship between the contact force and relative movement is needed. Combined with the mechanical model, numerical tools could be incorporated into the study. Discrete Element Method (DEM) based on the discrete approach can be used to analyze the individual characteristic effects of each component in the asphalt mixture, such as the influence of shape, gradation and relative slippage of aggregates. The proper representation of internal structure of asphalt mixture is possible through the use of X-ray tomography analysis. These techniques are utilized to accurately capture the actual microstructure of the asphalt mixture (*3*). Given the proper internal structure and constitutive contact models, the simulation could avoid huge amount of sample preparation work in the lab and provide reliable results in the research of the asphalt mixtures.

DEM was developed by Cundall and Strack for simulating movement and interaction of assemblies of rigid particles (*4*). In their original BALL model, the movement and interaction of unbounded assemblies of rigid spherical particles subjected to external stress was simulated. Later developments of this approach were implemented in PFC3D software (Itasca Consulting Group Inc. 2003). Although DEM was applied to model the behavior of soils and granular materials it wasn't widely used to investigate the behavior of asphaltic materials.

The response of materials to load is defined by the stress-strain behavior. Elastic material shows time-independent behavior and can be characterized by its elastic modulus. Viscous material behaves time-dependently and exhibits non-zero strain after the stress is removed. Asphalt binder exhibits both elastic and viscous behaviors; hence it is considered visco-elastic materials. A contact model called Normal Compliance Model which was developed by Zhu was reviewed and compared with the simulation and experiment results in this paper (*5*). This model described a visco-elastic binder layer which is bonding two contact aggregates. Simulations of Asphalt mixture in compression tests were presented in this paper. A simple visco-elastic model was applied to contacts in PFC3D. A cabinet X-ray tomography system was used to build a particle-binder system which matches the geometry of the model, the relative normal displacement and resistant force of the system under compression were documented during the test. Major works in this paper include: investigating relationship between film thickness and important parameters of asphalt mixture, such as resistant force, stress, pressure, and displacement, etc.; simulating asphalt mixture under compressive load and applying visco-elastic contact model through DEM in PFC3D; validating numerical analysis and DEM simulations by experiments based on X-ray tomography technology.

2 Method

2.1 Normal Compliance Model

Zhu developed a contact model called Normal Compliance Model in 1996 (*5*). The model analyzes a system with two elastic particles bonded by a thin viscoelastic binder layer. The configuration of this axi-symmetric system is defined in Figure 1.

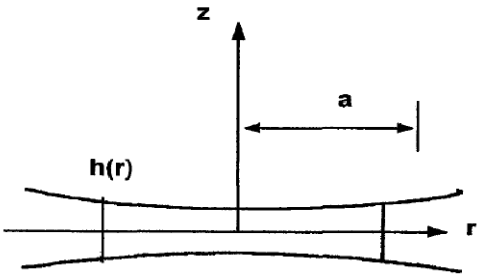

Fig. 1 Binder-particle system (*6*)

The function $z = h(r)$ represents the geometry of interfacial boundary between the particles and the binder, given by

$$h_r = h_0\left(1 + d\frac{r^2}{a^2}\right) \tag{1}$$

where a is the radius of contact area, h_0 is the thickness of the binder at $r = 0$, and d is the dimensionless shape parameter related to the curvature of particle surface, which is limited in a range $0 < d < 1$. For a planar surface, d is zero. For a spherical particle, d is given by

$$d = \frac{a^2}{2Rh_0} \tag{2}$$

where R is the radius of the spherical particles.

Zhu defined the constraint modulus $E_1$and E_2 and Poisson's ratio υ_1, and υ_2 for the particles and the binder respectively (*5*), where the constraint modulus E_1, and E_2 are defined as

$$E_i = \frac{2G_i(1-v_i)}{1-2v_i}, i = 1,2 \tag{3}$$

and G_1, and G_2 are the shear modulus of the particles and the binder respectively.

For Maxwell binder, the normal stress-strain relationship in the thin layer of binder is given by

$$\dot{\varepsilon}_2(r,t) = \frac{1}{E^2}\,\dot{p}(r,t) + \frac{1}{\eta_\varepsilon}p(r,t) \tag{4}$$

or in its integral representation

$$\varepsilon_2(r,t) = \frac{p(r,t)}{E_2} + \frac{1}{\eta_\varepsilon}\int_0^t p(r,\tau)d\tau \tag{5}$$

where, ε_2 (r, t) denotes the normal strain and $p(r, t)$ denotes the normal stress in the binder. η_ε is the coefficient of viscosity.

The relative normal approach δ_z (t) for the two particles is separated into two components, both are time dependent: the normal displacement at the binder-particle interface relative to the particle's centroid, $w_1(r, t)$; and the normal displacement at the binder-particle interface (i.e., at $z = h(r)$ relative to the $z = 0$ plane), $w_2(r, t)$, given by

$$\delta_z(t) = w_1(r,t) + w_2(r,t) \tag{6}$$

It is approximated that the normal strain is uniform in the z direction across the thin layer of binder. Thus the normal displacement $w_2(r, t)$ can be expressed as follows

$$w_2(r,t) = h(r)\frac{p(r,t)}{E_2} + \frac{h_r}{\eta_\varepsilon}\int_0^t p(r,\tau)d\tau \tag{7}$$

where $p(r, t)$ is the interfacial normal pressure between the particle and the binder. The method assumed that the characteristic dimension of the particle is much larger than that of the particle-binder contact area. So $w_1(r, t)$ is pursued based on a halfspace premise. Using the well-known Boussinesq equation, $w_1(r, t)$ can be related to $p(r, t)$ by:

$$w_1(r,t) = \frac{1-v_1^2}{\pi E_1}\int_0^a p(\rho,t)\frac{I(\rho,r)}{\sqrt{\rho^2+r^2}}d\rho \tag{8}$$

where $I(\rho, r)$ is defined as

$$I(\rho,r) = I(k) = \int_0^{2\pi}\frac{d\theta}{\sqrt{1-k\cos\theta}} \tag{9}$$

$$k = \frac{2r\rho}{r^2 + \rho^2} \tag{10}$$

By summing up the two components $w_1(r, t)$ and $w_2(r, t)$, the relative normal approach $\delta_z(t)$ for the two contact bodies is

$$\begin{aligned}\delta_z(t) = h(r)\frac{p(r,t)}{E_2} \\ + \frac{h(r)}{\eta_\varepsilon}\int_0^t p(r,\tau)d\tau \\ + \frac{1-v_1^2}{\pi E_1}\int_0^a p(\rho,t)\frac{I(\rho,r)}{\sqrt{\rho^2+r^2}}d\rho\end{aligned} \tag{11}$$

Integration of the interfacial pressure function, $p(r, t)$, over the contact area gives the resultant normal contact force $P_z(t)$

$$P_z(t) = 2\pi\int_0^a p(r,t)rdr \tag{12}$$

Equations (11) and (12) govern the magnitude and distribution of interfacial pressure. The compliance relationship is a time-dependent function that relates the relative normal approach $\delta_z(t)$ and the contact force $P_z(t)$.

Equations above derived time-dependent relationships between the contact forces and the relative particle/binder movement. They also indicate the time-dependent interfacial contact pressure distribution between the elastic particle and the visco-elastic binder. The rate-dependent compliance relationship can be determined by simultaneously solving Equation (11) and (12). This model is chosen because a visco-elastic binder layer was used to bond the two contact particles in both simulations and experiments. The boundary conditions described by the model could be perfectly satisfied by our experiment devices.

This numerical method is also supported by other literatures. Chang simplified relationship of film thickness and resistant force in Equation (13) (*6*). From Equation (13), distance between two particles (*L*) keeps constant. When radius of the contact area (*a*) and compression applied to system is fixed, all parameters have same values except film thickness. Resistant force (*F*) will decrease when film thickness (*h*) increase. And this resistant force could be represented by axial normal stress.

$$P = \frac{F}{\pi a^2} * \frac{h}{LX} \tag{13}$$

where P is normal contact force; F is resistant force; h is film thickness; L is distance between two particles; a is contact area; X is a constant value relative to particle diameter. It's calculated by $X=(ln^{(1+d)})/d$, d is particle diameter.

Relationship of F and h is plot in Figure 2. Along with film thickness decreasing, resistant force increases. Other parameters may have different value, but keep constant.

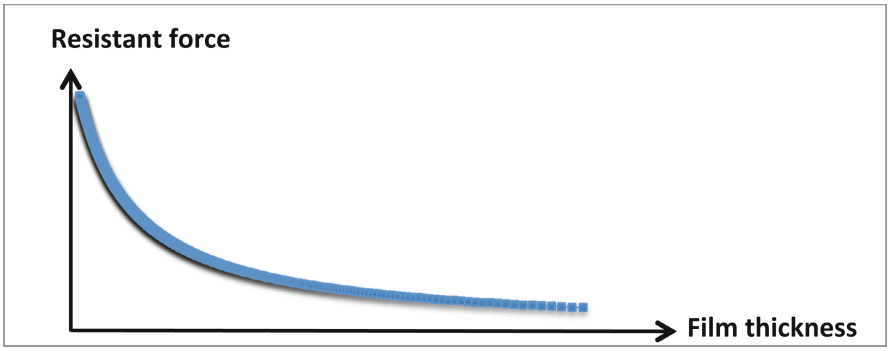

Fig. 2 Relationship between film thickness and resistant force

2.2 DEM Simulation of Compression Tests of Asphalt Mixture in PFC3D

Several methodologies were used to represent particle geometry and the mechanical interaction between particles. For example, particle geometry has been represented using image based models (*7-8*), and elastic, visco-elastic and cohesive models have been used to represent mechanical behaviors. How the user-defined contact model especially simple visco-elastic model represented particular materials and contact properties in PFC3d were introduced in following sections.

2.2.1 User Defined Contact Model in PFC3D

Figure 3 plots the flowchart of DEM simulation using User-defined contact model (UDM) in PFC3D (*9*). The input is done via the PFC interface, but the UDM dictates the behavior of all interactions within specific models. The UDM calculates the fore-displacement law each timestep. During each timestep relative motion of particles and contact forces are extracted from different models and applied in these models to dictate the force-displacement behavior between two particles in contact (*10*). The procedure is achievable by using a coding langue called "FISH".

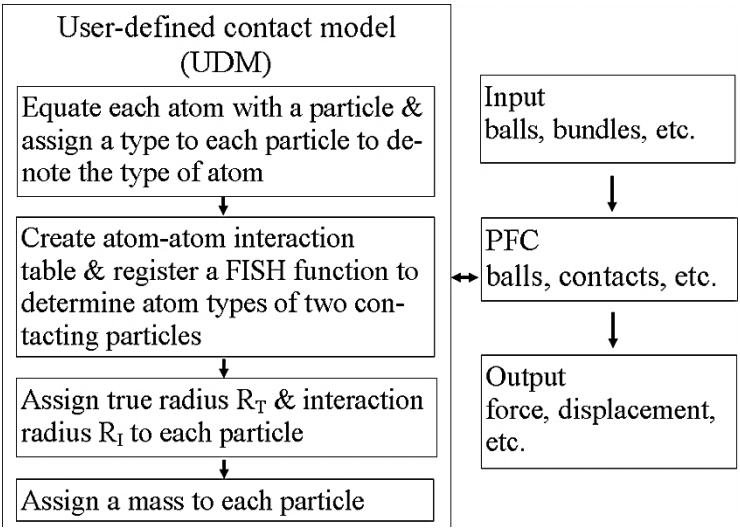

Fig. 3 Flowchart of a PFC3D Program Code Using UDM (*9*)

The constitutive model used in PFC3D comprises three parts:

- a contact model;
- a bond model;
- a friction slip model.

The contact model is described in terms of a normal secant contact stiffness K_n and a shear tangent contact stiffness K_s between the two contacting entities either wall-particle or particle-particle. Note that the in-plane and out-of-plane shear parameters are assumed to be the same. PFC3D allows particles to be bonded together at contacts. If the value of the tensile normal contact force equals or exceeds the normal contact bond strength, the bond breaks, and both the normal and shear contact forces are set to zero. If the value of the shear contact force equals or exceeds the shear contact bond strength, the bond breaks and the slip model is activated. Parameters which were defined in PFC3D are the normal and shear contact stiffness K_n, K_s, the normal and shear bond strengths Pb_n, Pb_s and the coefficient of friction between contacting particles.

Discrete element modeling was used to simulate compressive tests of asphalt mixtures with different film thicknesses. Figure 4 shows a model represent an asphalt mixture. The mixture includes two aggregates and asphalt binder. Each aggregate is covered by thousands small particles which represent asphalt binder around aggregates. Between the two aggregates, several layers made of even smaller blue balls represent film. Each layer of film in the model contains 60*60=3600 particles with size:

- radius of big aggregate = 500μm;
- radius of yellow balls = 15~30μm;
- radius of blue balls in film layers = 5μm.

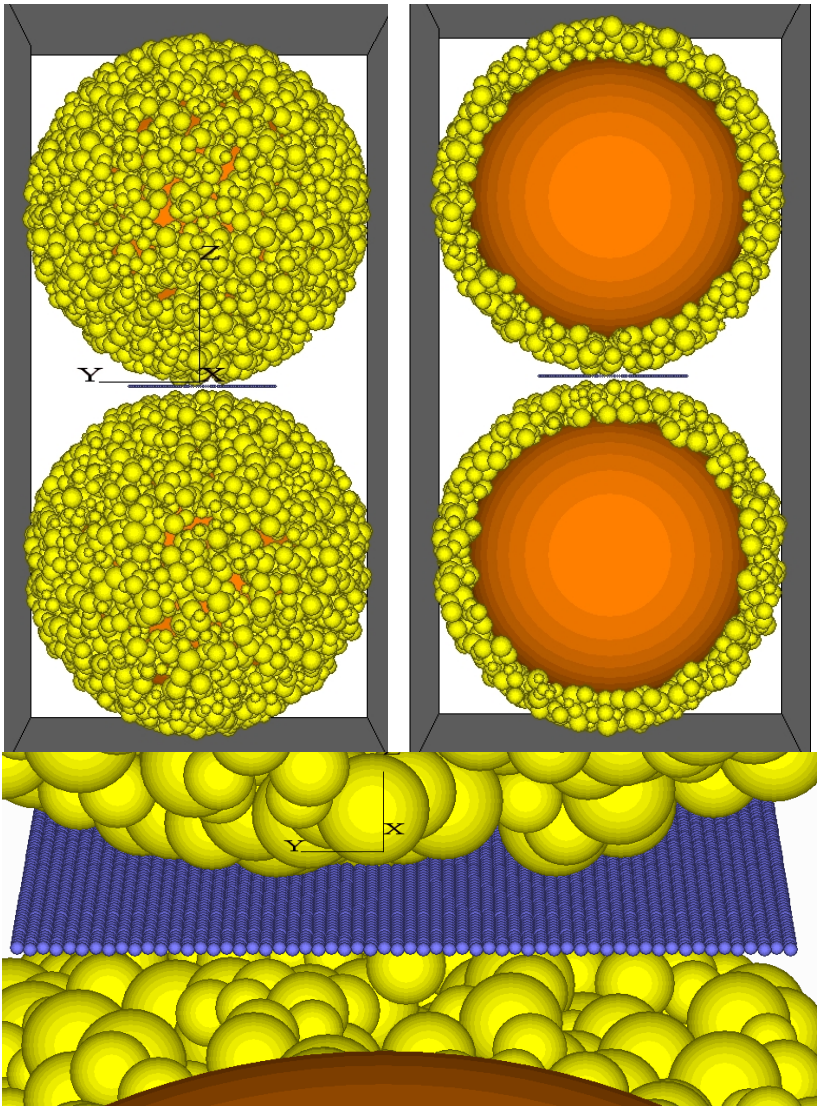

Fig. 4 Asphalt mixture includes two aggregates and asphalt binder

2.2.2 Simple Viscoelastic Model

Asphalt mixture was modeled in PFC3D. Material properties were specified by applying corresponding values of relative parameters. Such as normal stiffness, shear stiffness, friction ratio, etc. Parallel bonds were built between adjacent particles. Cracking within the structure was modeled by allowing bonds breakage. Elastic contact properties were used to investigate the effect of random variations

in internal sample geometry. A simple viscoelastic model was used to introduce time dependent shear and normal contact stiffness and an elastic contact were assumed for normal contact.

Consider a simple viscoelastic model in which the shear behavior consists of a spring in series with a dashpot (*11*). The total shear velocity, $\dot{u}_s$, can be decomposed into elastic and viscous parts: Viscoelastic properties had been applied to film clump.

$$\dot{u_s} = \dot{u_s}^e + \dot{u_s}^v \tag{14}$$

For the two-dimensional case, the shear velocities and forces can be taken as scalars. In Equation (15), Δt is the change of timestep. Taking $F_s°$ and F_s' as the shear forces before and after one timestep, respectively, we can express the components of shear velocity as

$$\dot{u_s}^e = -\frac{F_s' - F_s°}{k_s \Delta t} \tag{15}$$

and

$$\dot{u_s}^v = -\frac{F_s' + F_s°}{2\eta} \tag{16}$$

where k_s is the shear stiffness and η is the viscosity. Substituting these expressions into Equation (14) and rearranging:

$$F_s' = \frac{F_s°\left(\frac{1}{k_s} - \frac{\Delta t}{2\eta}\right) - \dot{u_s}\Delta t}{\frac{1}{k_s} + \frac{\Delta t}{2\eta}} \tag{17}$$

For the three-dimensional case, the shear force and relative shear velocity are both vectors, and the constitutive equation becomes

$$F_{si}' = \frac{F_{si}°\left(\frac{1}{k_s} - \frac{\Delta t}{2\eta}\right) - \dot{u_{sl}}\Delta t}{\frac{1}{k_s} + \frac{\Delta t}{2\eta}} \tag{18}$$

Equation (18) is encoded into a contact model accessed with the “model viscous” command. The required properties are as follows. Parameters of the contact model used in simulations are summarized in Table 1.

- *vis* k_n: viscoelastic normal stiffness
- *vis* k_s: viscoelastic shear stiffness
- *vis viscosity*: shear viscosity

Table 1 Properties Applied in Simulations

Properties for parallel bonds:	**Properties for viscoelastic contact model:**
Normal stiffness=$30*10^{15}$ Nm^{-3}; Shear stiffness=$30*10^{15}$ Nm^{-3};	*vis* $k_n = 0.36*10^6$ N/m
Normal strength=190 MPa; Shear strength=190MPa;	*vis* $k_s = 0.12*10^6$ N/m
Radius multiplier = real parallel bond radius/radius $= 30*10^{-9}$	*vis viscosity* $= 0.414*10^6$ N/m

2.3 Experiment

The Skyscan 1174 cabinet X-ray tomography system was used in the experiment to verify the normal compliance model introduced before. The Skyscan 1174 system, shown in Figure 5, is a compact, cost efficient micro x-ray scanner for nondestructive three-dimensional microscopy. It's supplied with software for system control, X-ray radiography, three-dimension (3D)-reconstruction, two-dimensional (2D) /3D image analysis and 3D realistic visualization. The SkyScan-1174 scanner supports variable magnification (6 to 30mm field of view), adjustable source energy (20 to 50KV) and flexible image format. The material testing stage of Skyscan system, shown in Figure 6, can perform compression, tension and torsion test. The loading-displacement or the stress-strain curve can be saved as an image or text file. The testing sample can be held under specific loading for scanning. The testing stage applies displacement to the top and bottom of the sample in equal amount but in opposite directions. This keeps the central part of the sample relatively static for scanning purpose.

Fig. 5 Skyscan 1174 system

Fig. 6 Testing stage of the microscopy system (*12*)

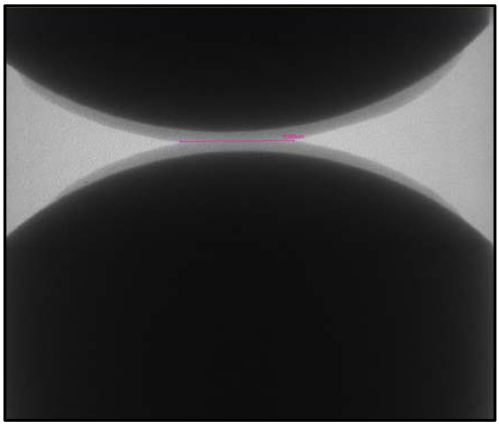

Fig. 7 Test image and measurement

Samples were tested under uniaxial compression loads applied on top and bottom stage. With the help of x-ray scanner, the parameters needed in the compliance model were measured by the tools provided by the software. The testing stage (Figure 7) is displacement controlled. The displacement speed was set at 17.5μm/s, chosen according to the allowable range of the testing device, and was set at 17.5μm/s. The resistant force was monitored and recorded during the loading. When the force reaches the maximum allowable value of the testing stage, the displacement application will stop. For the sample in this study, the application of displacement was stopped when two elastic particles started to contact to each other through the asphalt layer. Prior to each test, the testing stage was calibrated according to the procedure recommended by the manufacturer. Force displacement data was stored as a text file for each sample. The

specification of asphalt binder is PG 64-22 coming from the lab of the Virginia Tech Transportation Institute and the temperature at which the experiments are conducted is around 25-27C^{o} given by thermometer. The specifics of the experiment are listed in the Table 2.

Table 2 Experiment Specifics

Inner diameter of the chamber	10mm
Diameter of particle	12.7mm
Column diameter	9mm
Material of particle	Polyvinyl Chloride (E=2400-4100 MPa, υ = 0.41)
Asphalt binder	PG 64-22
Test temperature	Room Temperature
Loading speed	17.5 μm/s

3 Results

3.1 Simulation Results

The model analyzes a system with two elastic particles bonded by a thin viscoelastic binder layer. The only difference in comparison is film thickness. Figure 9 to Figure 13 show models simulated in PFC3D with varied thickness from 10μm to 20μm, 30μm, 40μm, 50μm, and axial stress of each case. Peak axial stresses are summarized in Figure 8. The peak stress of asphalt mixture was found to be as a power-law function of film thickness. As Figure 8 shows, peak stress decreases with the increase of film thickness. From relationship of axial stress and film thickness shows in Figure 8, it's clearly that simulation results agree reasonably with theoretical analysis.

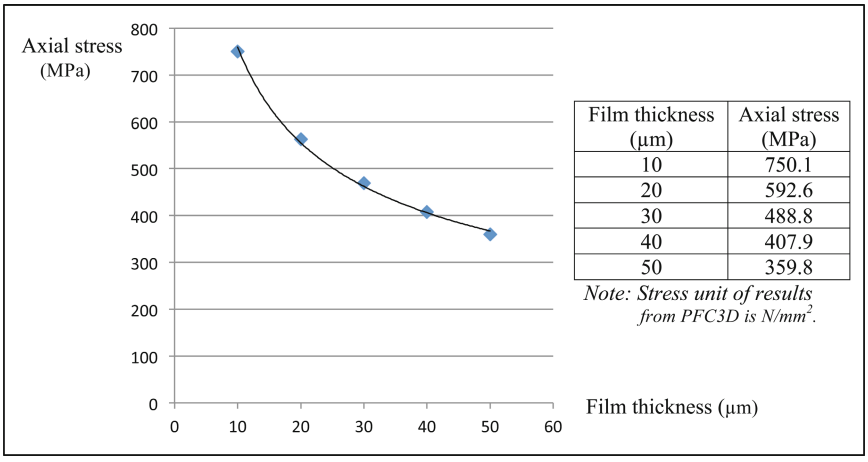

Film thickness (μm)	Axial stress (MPa)
10	750.1
20	592.6
30	488.8
40	407.9
50	359.8

Note: Stress unit of results from PFC3D is N/mm^2.

Fig. 8 Summary of Peak Axial Stresses

Case 1, Film Thickness = 10μm

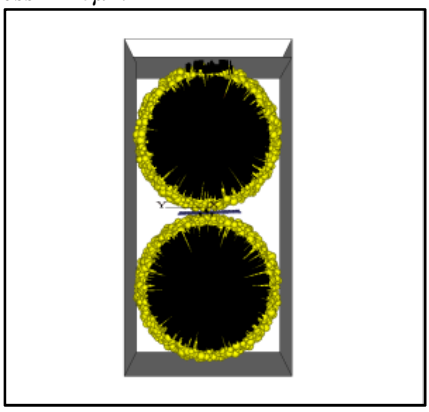

Fig. 9 (a) 10μm film and two aggregates under compressive load

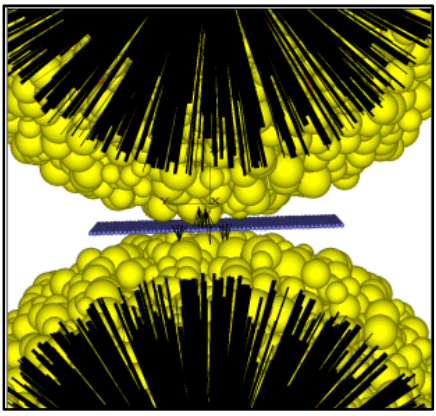

Fig. 9 (b) Detailed view of film layer (blue layer), film thickness = 10μm

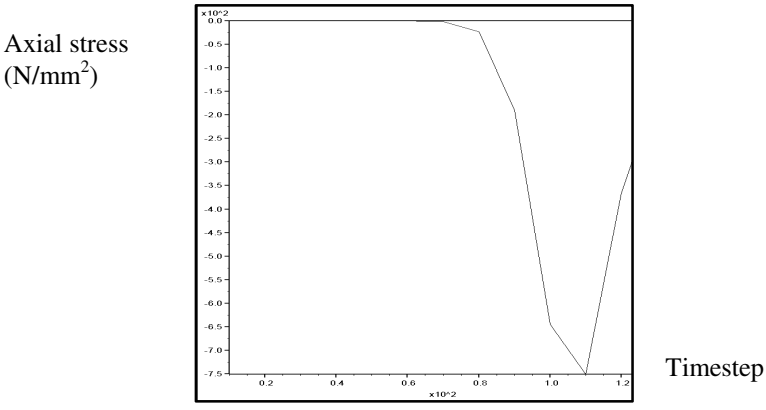

Fig. 9 (c) Axial stress under compressive load (10μm)

Case 2, Film Thickness = 20μm

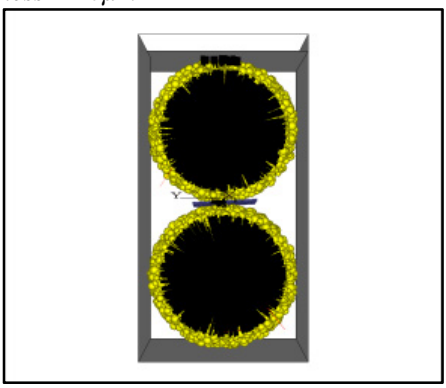

Fig. 10 (a) 20μm film and two aggregates under compressive load

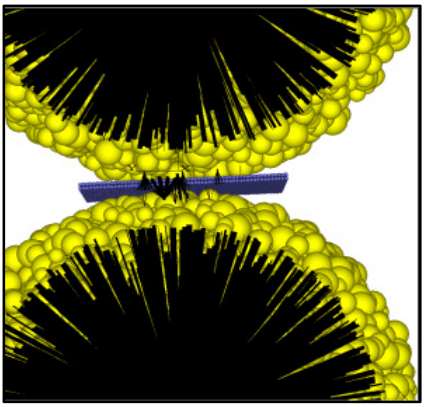

Fig. 10 (b) Detailed view of film layer (blue layer), film thickness = 20μm

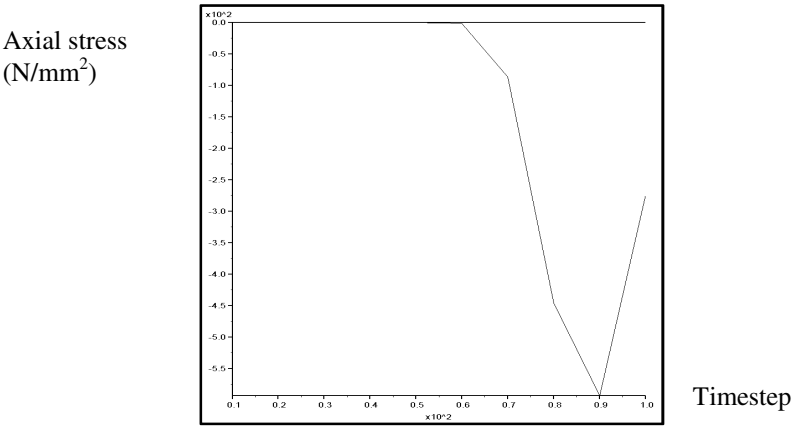

Fig. 10 (c) Axial stress under compressive load (20μm)

Case 3, Film Thickness = 30μm

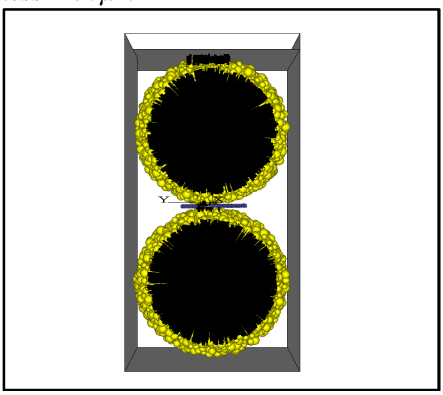

Fig. 11 (a) 30μm film and two aggregates under compressive load

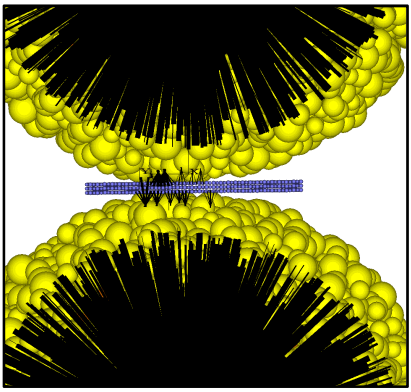

Fig.11 (b) Detailed view of film layer (blue layer), film thickness = 30μm

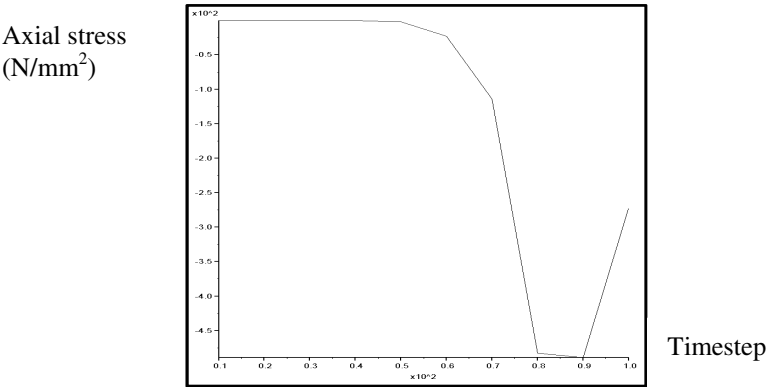

Fig. 11 (c) Axial stress under compressive load (30μm)

Case 4, Film Thickness = 40μm

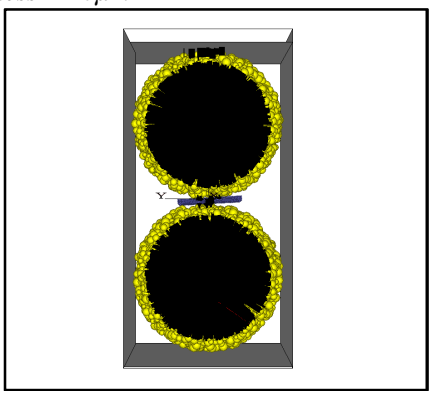

Fig. 12 (a) 40μm film and two aggregates under compressive load

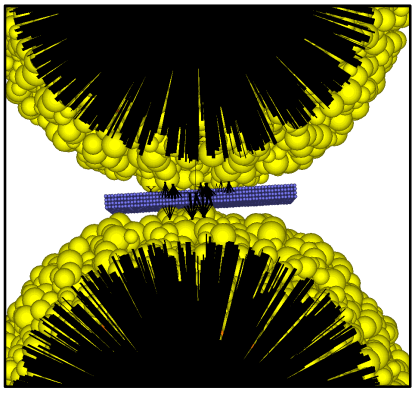

Fig. 12 (b) Detailed view of film layer (blue layer), film thickness = 40μm

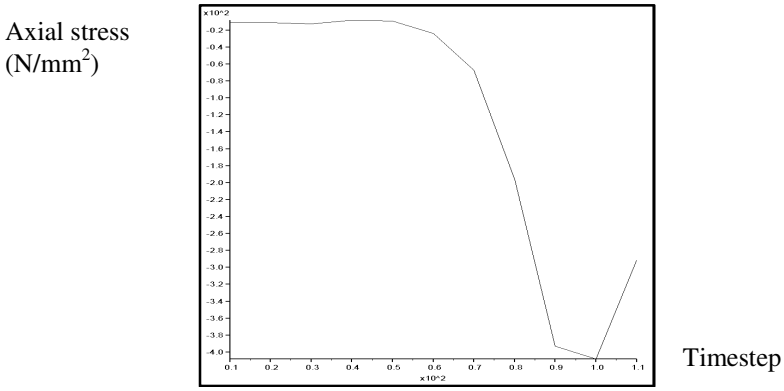

Fig. 12 (c) Axial stress under compressive load (40μm)

Case 5, Film Thickness = 50μm

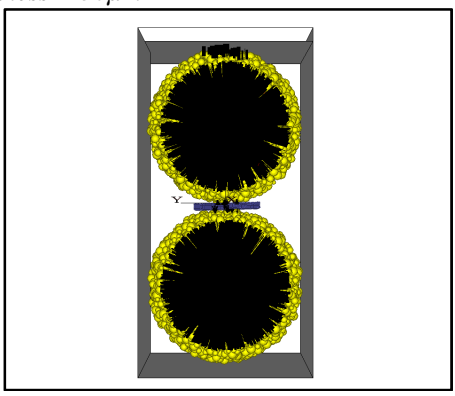

Fig. 13 (a) 50μm film and two aggregates under compressive load

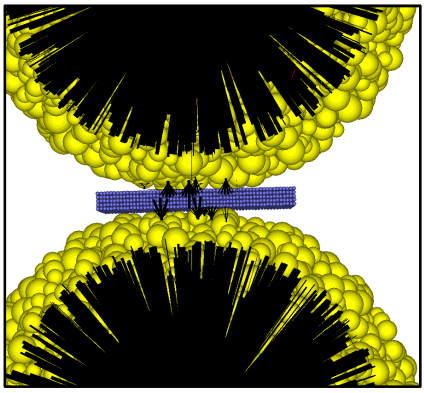

Fig. 13 (b) Detailed view of film layer (blue layer), film thickness = 50μm

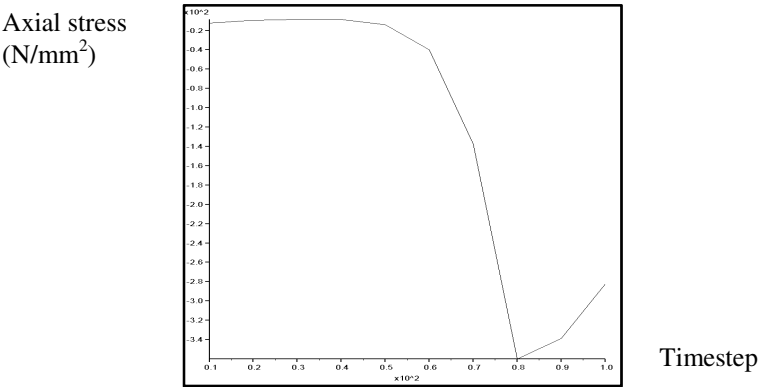

Fig. 13 (c) Axial stress under compressive load (50μm)

3.2 *Experiment Results*

In order to investigate the thickness effect of the asphalt binder to the contact behavior of aggregates, three compression tests were conducted using samples with different binder film thicknesses. Figure 14 provides changing of displacement dependent resistance force when asphalt mixture under a compressive load. Number 0.252mm, 0.238mm and 0.399mm in Figure 14 denote asphalt binder film thickness in there specimens.

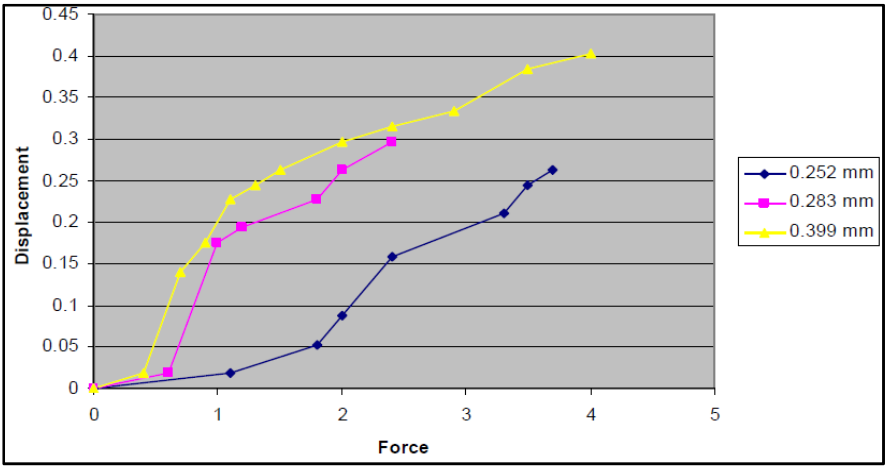

Fig. 14 Test results: resistant force (N) vs. displacement (mm)

Table 3 Parameters and Results of Test

Parameters used	**Film thickness (*h*) mm**		
	0.252	0.283	0.399
Complex modulus of the binder (G^*) MPa	4.3	4.3	4.3
Phase angle of the binder (δ)^o	53	53	53
Elastic modulus of the particle (E) MPa	4100	4100	4100
Particle Radius (R) mm	12.7	12.7	12.7
Results calculated			
Constraint Modulus of the particles (E_1) MPa	9531	9531	9531
Shape parameter of the particle (d)	0.636	0.554	0.540
Constraint Modulus of the binder (E_2) Mpa	11.21	11.21	11.21
Viscosity of the binder (η) Mpa	1.28	1.28	1.28

Due to limitation of experiment equipment, size of samples in the experiments are much bigger than models in simulations. But the relationship between asphalt binder film thickness and resistant force are similar. Results in Table 3 show that, moving same displacement, the resistant force of thinner binder film system is larger than the mixture with thicker binder film. Numerical analysis and simulation results were validated by experiment results.

4 Conclusions

Zhu and Chang derived time-dependent relationships between the contact forces and the relative particle/binder movement (*5-6*). They also indicate the time-dependent interfacial contact pressure distribution between the elastic particle and the visco-elastic binder. By simultaneously solving govern equations of normal complacent model time-dependent compliance relationship were determined. Based on numerical analysis of their derivation, a reciprocal relationship was found between film thickness and axial stress.

DEM has been used to simulate the behavior of an idealized asphalt mixture with different film thicknesses under compressive load. Aggregates and asphalt binder were simulated by balls generated in PFC3D. Corresponding behaviors were achieved by applying properties to different clumps and contacts in PFC3D. These clumps represent aggregates, surrounding asphalt binder, and asphalt film layer. UDM associated with material properties provides a plate for performing visco-elastic behavior. A simple linear visco-elastic model was introduced to give time dependent shear and normal contact stiffness. Asphalt binder of asphalt mixture was successfully simulated using simple viscoelastic contact model. Results of axial stresses of models simulated in PFC3D with varied thickness from 10μm to 20μm, 30μm, 40μm, 50μm showed peak stress of asphalt mixture is a power-law function of film thickness. Peak stress decreases with the increase of film thickness.

Three compression tests which is a validation of numerical analysis and DEM simulations were conducted using samples with different binder film thicknesses. The Skyscan 1174 cabinet X-ray tomography system was used in the experiments. Samples were tested under uniaxial compression loads. With the help of x-ray scanner, the parameters needed in the compliance model were measured. Compression tests were done by applying displacement to the top and bottom of the sample in equal amount but in opposite directions. This displacement controlled testing stage output displacement vs. resistant force results. Based on the experiment results, it's clearly that moving same displacement, the resistant force of thinner binder film system is larger than the mixture with thicker binder film.

Both simulation results and experiment results agree reasonably with theoretical analysis. When compressive load keeps constant and all asphalt mixtures move same displacement, the one with thinnest asphalt film had highest axial stress and resistant force. That means the mixture includes aggregates and binder will become stiffer if the film thicknesses decrease.

References

1. Abbas, A., Papagiannakis, A.T., Masad, E.: Linear and Non-LinearViscoelastic Analysis of the Microstructure of Asphalt Concretes. Journal of Materialsin Civil Engineering, ASCE 16, 133–139 (2004)
2. Alar, A.: Simulation of the micromechanical behavior of asphaltmixtures using the discrete element method. Doctoral dissertation submitted to the Department of Civil and Environmental Engineering of Washington State University (2004)
3. Bahia, H.U., Zhai, H., Bonnetti, K., Kose, S.: Non-LinearViscoelastic and Fatigue Properties of Asphalt Binders. Journal of the Association of Asphalt Paving Technologists, AAPT 68, 1–34 (1999)
4. Cundall, P.A., Strack, O.D.L.: A discrete numerical model for granular assemblies. Geotechnique, 47 (1979)
5. Zhu, H., Chang, C., Ching, S., Rish, J.W.: Normal and tangential compliance for the conforming binder contact II: visco-elastic binder. International Journal of Solids Structures 33(29), 4351–4363 (1996b)
6. Chang, C.S., Shi, Q., Zhu, H.: Micro-mechanical Modeling for Elastic Moduli of Bonded Granules. Journal of Engineering Mechanics, ASCE Publication 125(6), 648–653 (1999)
7. Buttlar, W.G., You, Z.: Discrete element modelling of asphalt concrete: A microfabric approach. Journal of Transportation Board, 111–118 (2001)
8. Adhikari, S., You, Z.: 3D microstructural models for asphaltmixtures using X-ray computed tomography images. International Journal of Pavement Research and Technology, 94–99 (2008)
9. Anderson, T., Balakrishnan, H., Parulkar, G., Peterson, L.: Integrated OpenFlow–GMPLS control plane: an overlay model for software defined packet over optical networks. Optics Express 19(26), B421–B428 (2011)
10. Cleland, H., Suzuki, M., Ito, N.: Efficient Implementations of Molecular Dynamics Simulations for Lennard-Jones Systems. Progress of Theoretical Physics 126(2), 203–235 (2010)
11. Itasca, PFC3d 4.0 Manual: Background and Theory
12. Skyscan 1174 X-ray microtomograph – user guides

Insulating Pavements to Extend Service Life

Rajib B. Mallick[1], Aaron Sakulich[1], Bao-Liang Chen[1], and Sankha Bhowmick[2]

[1] Worcester Polytechnic Institute, 100 Institute Road, Worcester, MA 01609, USA
rajib@wpi.edu
[2] University of Massachusetts Dartmouth, 285 Old Westport Road, North Dartmouth, MA 02747, USA
sbhowmick@umassd.edu

Abstract. Temperature fluctuations in asphalt pavements can increase the potential for rutting and cracking distresses. One way of countering this problem is to insulate a pavement from the extremes of air temperature and to also use a high reflectivity surface in warmer climates to reduce the absorption of solar radiation. This paper presents modeling and simulation results of the application of these concepts. Pavements with and without insulation layers were modeled in low temperature (Juneau, AK) and high temperature (Houston, TX) cities. A high reflectivity surface was also modeled in Houston. Temperature and solar radiation data for an entire year were analyzed for each city and the data corresponding to lowest and highest temperature (respectively) were utilized in the low and high temperature city pavement models. Results indicate that high temperatures were significantly reduced and that low temperatures were increased, depending on the thermal conductivity and thickness of the insulation layer. The presence of a highly reflective layer was also found to be very effective in reducing high temperatures in pavements. The positive effects of high temperature reduction on the service life of pavements was found to be significant, and the use of conventional materials of sufficient thickness was found to be feasible. Based on these findings, an ideal pavement section is suggested as one with an insulation layer near the surface, which could also serve as a moisture prevention layer; with a high reflectivity surface; and which is economical, durable, and capable of retaining its properties.

1 Introduction

High quality roads are critical for the smooth functioning of our society, as they constitute the primary mode of transportation of people and freight. The performance of roads or pavements (including those used at airports) is primarily affected by two factors: loading and environmental effects, such as temperature fluctuations and moisture due to rain or snow. A pavement is designed and constructed such that the effects of the environment can be mitigated, therefore the cost of a pavement generally increases with an increase in the range of temperature fluctuation. In this context, the increased cost generally coincides

N. Kringos et al. (Eds.): *Multi-Scale Model. & Charact. of Infrastruct. Mater.,* RILEM 8, pp. 219–236.
DOI: 10.1007/978-94-007-6878-9_16

with an increased environmental impact in the form of energy consumed and gases emitted during the construction of the pavement [Sakulich, 2011]. Furthermore, the ability of the pavement to resist the effects of the environment is not always guaranteed because of the enormous variability in the prediction of the factors, the stochastic nature of the design process, and the unavoidable variations in material properties and construction quality.

In a conventional asphalt pavement, higher ambient temperatures generally increase the likelihood of rutting in the hot mix asphalt (HMA) layer, whereas lower temperatures increase the risk of cracking due to thermal contractions [Van de Loo, 1978, Brown and Cross, 1992, Monismith et al, 1994, Vinson et al, 1989, Schmidt, 1966]. Repairing cracks or ruts consumes a significant amount of time (resulting in wasted time and fuel as vehicles move inefficiently) and energy (most of which comes from non-renewable resources). Therefore, if the service life of a pavement can be extended, avoiding such repairs (or at least making them less frequent), then a significant amount of energy, driver time, and fuel could be saved while reducing CO_2 emissions. That is, extending the life of the pavement is a step towards achieving true sustainability. Reducing temperature fluctuations in the pavement will therefore extend service life.

One way in which the temperature fluctuations in a pavement can be reduced is to impregnate the pavement with phase change materials (PCMs) [Bentz and Turpin, 2007]. These are materials that have a relatively high enthalpy of change; as temperatures drop to the phase change temperature of a particular PCM, the PCM exothermically solidifies. The energy released during this process (in the form of heat) can keep the local pavement warm, preventing damage due to freezing. Similarly, as the ambient temperature increases to the phase change temperature of a PCM, the PCM will endothermically melt; the energy absorbed during this process prevents a buildup of heat in the local area and keeps the pavement cool.

Two older studies [Miyamoto and Takeuchi, 2002, Stoll et al, 1996] investigated placing metal pipes full of PCM beneath bridge decks and sidewalks with the goal of keeping the system from freezing; though they showed that the concept was technically feasible, the added cost and complexity of placement meant the systems were not practical. A more recent set of studies [Bentz and Turpin, 2007, Sakulich and Bentz, 2012a, 2012b] used PCM embedded in lightweight aggregate as an incorporation method, which showed significant improvements in practicality. To deal with both high and low temperatures, the incorporation of two different PCMs with different transition temperatures could possibly be used, but has yet to be investigated.

In this study, the use of an insulating layer near the surface of the pavement has been investigated. Examples of available insulation materials are polypropylene (commonly used in geotextiles; K=0.2 W/mK) and polystyrene (K=0.03 W/mK) (The Engineering Toolbox, 2013). Other materials that are being researched include nano-insulation materials(K= 0.002 W/mK, Jelle et al, 2010). Similar to the PCM method, this insulating layer ‘smooths’ the temperature profile of the pavement – the lows become less low, and the highs become less high. A direct

comparison between this insulation system and the PCM systems, which to our knowledge is the only other work attempting to increase service life by altering thermal properties, cannot be directly made, as all of the extant PCM work focuses on bridge decks. At the same time, to our knowledge, work with insulation layers in the asphalt mix layer part of asphalt pavements have not been conducted. However, researchers have investigated the use of thermal insulation to prevent frost damage in soils (for example, Kestler and Berg, 1992, Wen et al, 2007, Humphrey and Blumenthal, 2010,and Field et al, 2011,) and the useof asphalt mix layer as insulation over concrete pavements (Khazanovich et al, 2012).

1.1 Objective

The objective of this paper is to present the results of a theoretical simulation evaluating the concept of extending the functional life of a pavement by reducing temperature fluctuations via the help of an insulating layer.

1.2 Scope

The scope of work consists of modeling and simulating the effects of temperature (due to ambient air temperature, solar radiation, etc.) on a full depth asphalt pavement with and without insulation, and determining the effect of the variation in insulation and insulation layer thickness.

1.3 Analysis of High and Low Temperatures of Two Selected Cities

Two US cities were selected for case studies – Juneau, Alaska, and Houston, Texas (experiencing low and high average temperatures, respectively). The hourly air temperature for Juneau was obtained from NOAA National Climatic Data Center (NOAA, 2012)for the most recent year (2005). The data were analyzed to determine the lowest temperature in the entire year; next, the time/day at which the temperature was last observed to be above 0°C prior to falling to the minimum was determined. The dataset starting from this point to the end of the day at which the lowest temperature was observed was selected for use in the pavement analysis and simulation. This temperature range was selected to help evaluate the effect of insulation during the coldest part of the year.

Houston, TX, was selected as a case study of a locale with average temperatures on the other end of the temperature spectrum. The hourly air temperature for the most recent year for which data is available (2007) was extracted and the highest temperature was determined. Next, data were analyzed to determine the last time at which the temperature was recorded as 25 °C – data starting from this point to the end of the day at which the maximum temperature occurred were then extracted for further analysis. Next, solar radiation data

(the total amount of statistically modeled average direct and diffuse solar radiation received on a horizontal surface during the 60-minute period ending at the timestamp) were obtained for the latest year available (2005) from the National Solar Radiation Database from the National Renewable Energy Laboratory (NREL) site (NREL, 2012). Radiation data relevant to the period of time in question were extracted. Radiation and temperature data were used for the modeling and simulation of the pavement in the next step.

1.4 Modeling and Simulation

One rectangular layer (sub-domain) was created for the control HMA only model (Table 1). The HMA layer contains 462 triangular mesh elements and 979 degrees of freedom. Three rectangular layers (sub-domains) were created for the HMA with insulation model with the relevant thermal properties (Table 1). The insulation layer was inserted and placed between two HMA layers. The entire geometry contains 1,047 triangular mesh elements and 2,174 degrees of freedom.

Table 1 Thermal properties of the materials (Chen *et al*. 2008)

	Thermal conductivity k, W/m^2	Heat Capacity C, J/kg	Density ρ, kg/m^3
HMA	1.2	1200	2350
Insulation #1	0.17	904	1963.5
Insulation #2	0.02	904	1963.5
Insulation #3	0.002	904	1963.5

In the ambient and external temperature condition model (Juneau), only the top boundary of the HMA layer is exposed to the temperature function and the other three boundaries are assumed to be thermally insulated. The emissivity of HMA and surface radiation absorptivity were assumed to be 0.9 and 0%, respectively. The initial temperature of the HMA layer was assumed to be 4°C and the model was run for the transient condition for 435 hours with a time step of 1 hour. The time was selected to simulate the effect of temperature for the exact time for which the actual air temperature data was utilized for Juneau, and the time step was selected to complete the analysis within a reasonable amount of time.

In the radiation condition model (Houston), only the top boundary of the HMA layer is exposed to the radiation and ambient temperature function, and the other three boundaries of the HMA layer are assumed as thermally insulated. The emissivity of HMA is assumed as 0.9 and the surface radiation absorptivity of HMA is assumed as 100% for all the cases, except the models with high reflectivity surface condition where the absorptivity is assumed as 50%.The initial

temperature of the HMA layer is assumed as 25°C and the model is run for the transient condition for 160.6 hours with time step of 0.5 hours. In this case also, the time of analysis was selected to simulate the effect of solar radiation for the exact amount of time for which the actual data was utilized, and the time step was selected to complete the analysis within a reasonable amount of time; in this case the time step is smaller than in the time step in the case of the low temperature simulation since the overall time of analysis is less.

1.5 FEM Equations

The boundary condition is defined by:

$$(-k_p \nabla \mathrm{T}) = \alpha \cdot q_0 + h_{ave}\left(T_{inf} - T\right) + \varepsilon\sigma(T_{amb}^4 - T^4)$$

where k_p is thermal conductivity of asphalt pavement, ∇T is temperature gradient, α is the absorptivity, q_0 is the heat flux, h_{ave} is the heat transfer coefficient, T_{inf} is the external temperature, ε is the emissivity of asphalt pavement, σ is the Stefan Boltzmann constant, T_{amb} is the ambient temperature, and T is the temperature.

The natural heat transfer coefficient (based on COMSOL multiphysics approach) for the top of a horizontal surface, is defined by:

$$h_{ave} = 0.54 F_{lam} \left(\frac{\Delta T}{L}\right)^{0.25}$$
$$F_{lam} = 6.3126 - 1.4322 \log\left(T\right)$$

where F is the air flow in laminar characteristic, ΔT is the temperature difference between surface of HMA and ambient temperature, and L is the length scale in meters,.

The sub-domain condition of the HMA is defined by:

$$\rho_p C_p \, {}^{\partial T}/_{\partial t} + \nabla \cdot \left(-k_p \nabla T\right) = Q + q_s T$$

where ρ_p is the density of HMA, C_p is the specific heat of HMA, t is the time, ∇ is the gradient, Q is the heat source, and q_s is the production/absorption coefficient.

In the insulation, the sub-domain condition is defined by:

$$\rho_g C_g \, {}^{\partial T}/_{\partial t} + \nabla \cdot \left(-k_g \nabla T\right) = Q + q_s T$$

where ρ_g is the density of insulation material, C_g is the specific heat of insulation material, and k_g is the thermal conductivity of material.

1.6 Evaluation of the Effect of Temperature

Low Temperature

First, a full depth asphalt pavement was modeled using the finite element modeling (FEM) technique (using COMSOL Multiphysics 'general' and 'heat transfer' modules, COMSOL, 2012). All sides except the top were considered to be insulated. The air temperature was used in the model as a time-dependent parameter.The temperature of the surface and at different depths upto 100 mm wassimulated for a total of 435 hours (approximately 18 days). Thissimulation over a relatively long period of time enabled the observation of the effect of falling air temperatures, specifically below freezing, on the temperature of the pavement. A model was next created for a pavement with insulation, and identical FEM analysis and simulation were conducted. The model consisted of a 6 mm layer of HMA over one of three different insulation layers, ranging in thickness from 2.4 mm (typical thickness of a geosynthetic layer) to 24 mm, atop a standard HMA pavement. The three insulation materials examined had thermal conductivities of 0.17 W/mK (polypropylene), 0.02 W/mK (polystyrene) or 0.002 W/mK (nano insulation materials, NIM, Jelle et al, 2010).

1.7 Observations

A comparison oftemperatures at different depths of the modeled pavements and air temperatures(Fig. 1) shows thatwithin a time span of 435 hours the air temperature dropped (not steadily) to a low of -20 °C for the Juneau case study. The pavement temperature at the surface and different layers are affected by the change in air temperature - the predicted values are shown for five cases: HMA only, HMA with 2.4 or24 mm insulations (K=0.17 W/mK), and with 24 mm insulations of K=0.02 or 0.002 W/mK, respectively. The minimum temperature during this time period was significantly greater for the cases with the insulations of 24 mm of K=0.02 or 0.002 W/mK, as compared to those with 2.4 or24 mm of insulation with K=0.17 W/mK. The increase in thickness of the insulation layer from 2.4 to 24 mm did not have any significant effect for a K value of 0.17 W/mK.For the lower values of K (0.02W/mK and 0.002 W/mK) the minimum temperatures were increased significantly (-12 °Cand -3 °C compared to -16 °C for K=0.17) for the same thickness. Furthermore, the change in temperature versus time for the case with the insulation of K=0.17W/mK is significantly affected by the daily fluctuations in temperature, whereas the changes for the cases with insulation of K=0.02or 0.002W/mK are relatively unaffected. The surface temperatures for the pavements with the different thermal conductivities do not differ significantly.

The minimum temperatures do not occur at the same time at different depths(Fig. 2). For the cases in which 24 mm insulation layers are used, the 25 mm depth indicates the depth just below the insulation layer, whereas 12.5 mm depth is within the insulation layer itself. Insulation layers with thermal conductivities of K=0.02or0.002 W/mK are therefore seen to be effective in reducing the effect of low air temperatures on the pavement layers.

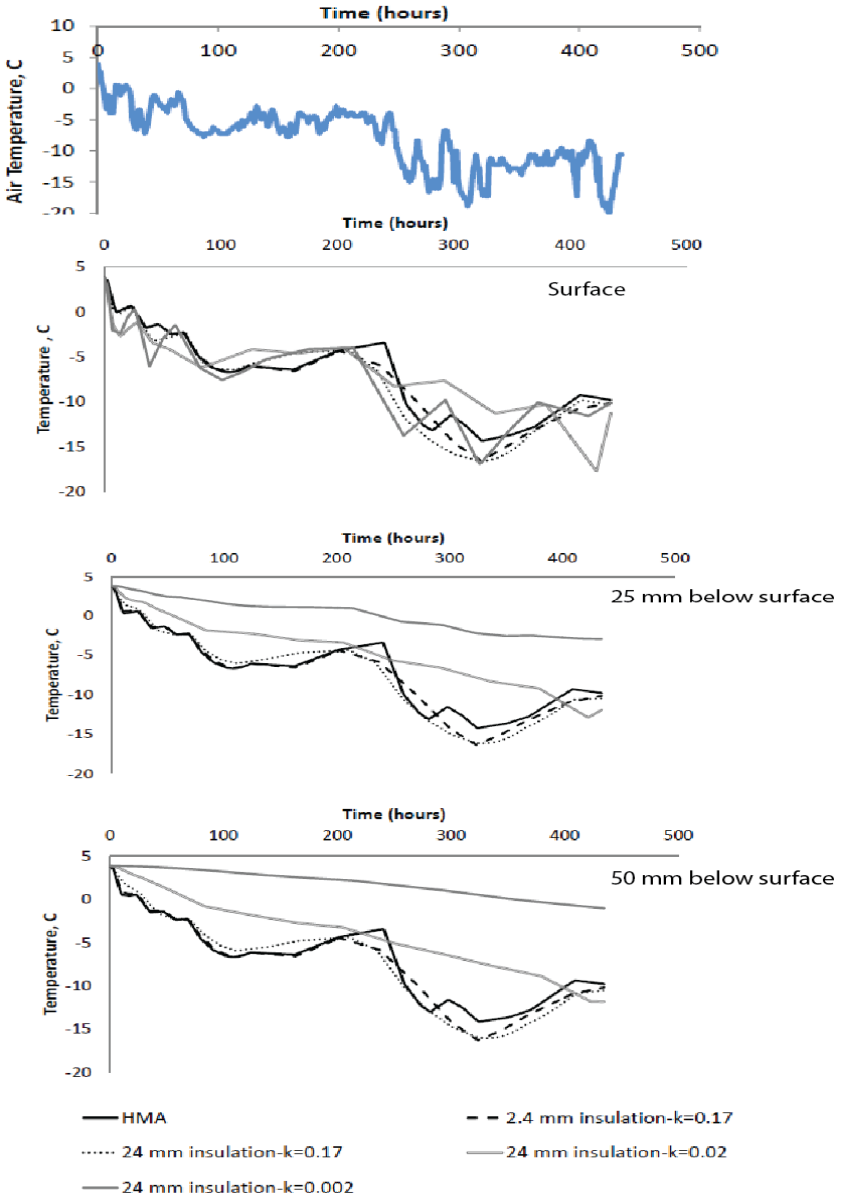

Fig. 1 Air temperature and results of simulation for Juneau

High temperature and solar radiation

The HMA models as indicated in the low temperature analysis werereutilized in this step, except that a surface layer of relatively high reflectivity (50%) was used in this step along with the environmental data from Houston. Both solar radiation

and high temperature were utilized for simulation, which was conducted for a total time period of 161 hours (approximately 7 days). Temperatures vary at different depths of the pavements (Fig. 3), whereas the maximum temperatures (Fig. 4)do not occur at the same timeat the different depths.

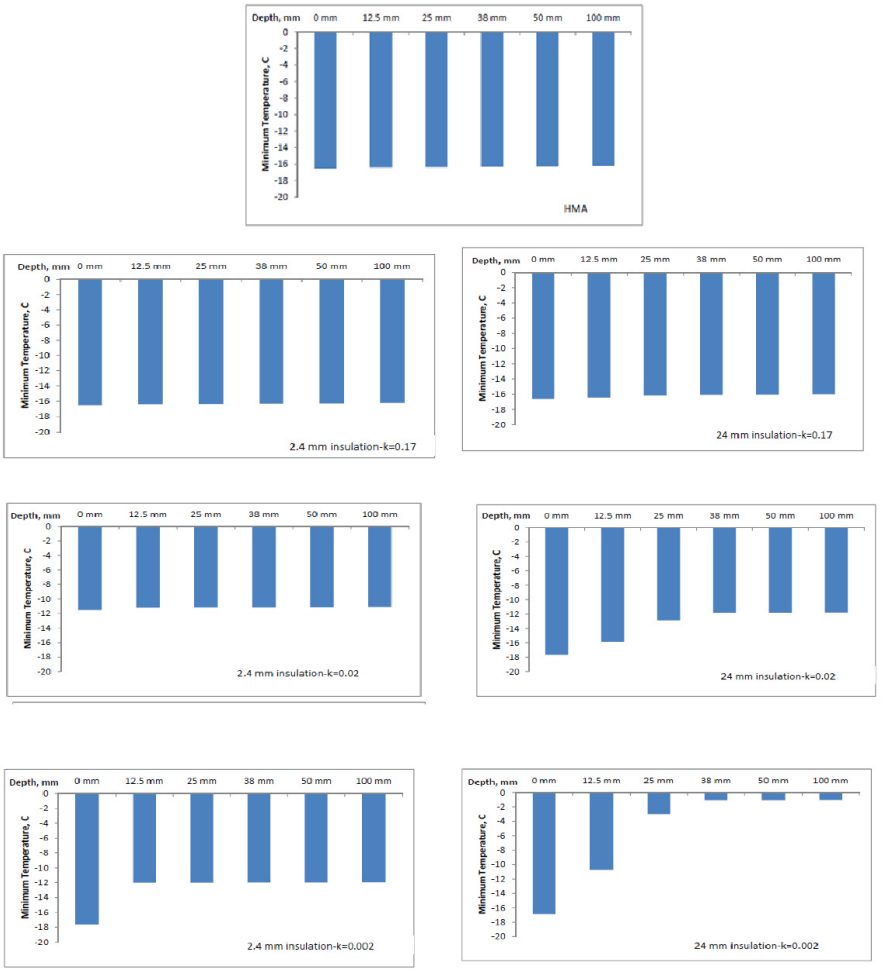

Fig. 2 Predicted minimum temperatures at different depths for different cases; Juneau

1.8 Observations

The simulation shows the presence of insulation to be effective in lowering the temperature at the lower layers to different extents. The 2.4 mm thick insulation layer of K=0.17W/mK is marginally effective; however, the change in thickness from 2.4 mm to 24 mm seems to have a significant effect on the reduction in

temperature. The insulation layers with K=0.02or 0.002 W/mK reduce the temperatures significantly, although at the cost of also significantly increasing the surface temperature. The best result seems to be from the 2.4 mm thick insulation layer with K=0.17 W/mK and a highly reflectivity surface – temperatures at all layers including the surface are reduced significantly, obviously due to the effect of the high reflectivity, and hence low absorption of heat.

The presence of a high reflectivity surface by itself is highly effective in reducing the temperature of all layers (Fig. 5). Such a highly reflective surface could be achieved with the use of a thin or ultra-thin layer of fresh portlandcement concrete for example.

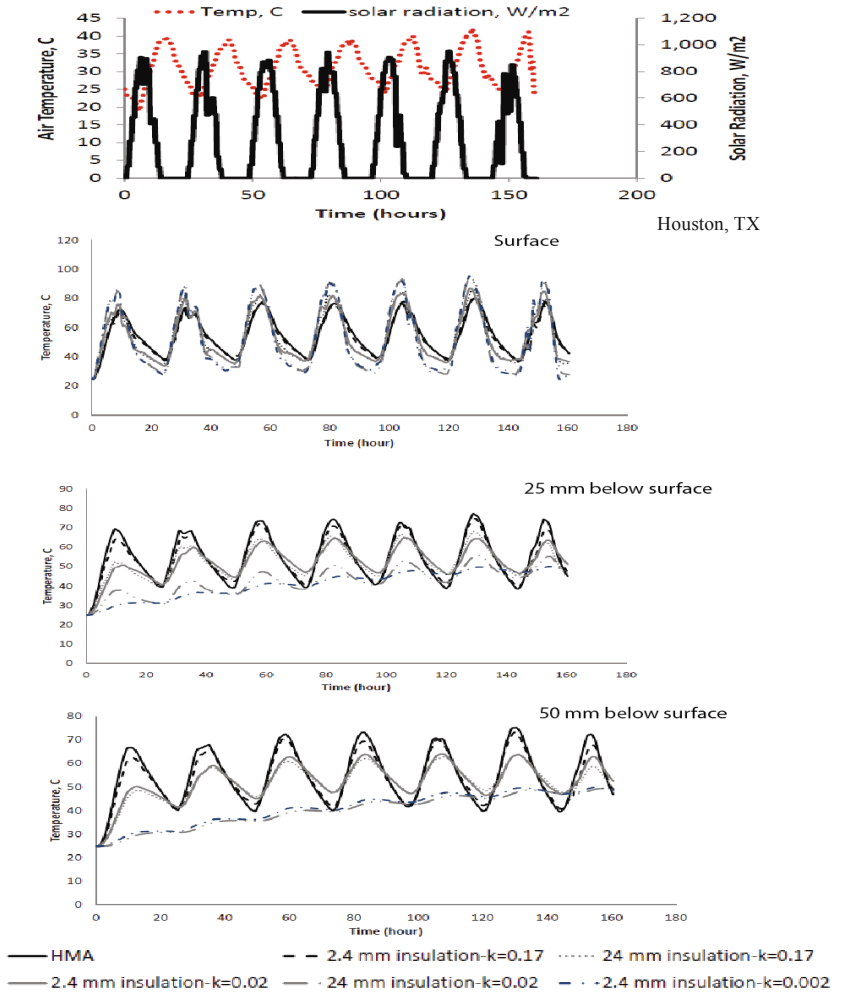

Fig. 3 Air temperature and solar radiation, and results of simulation for Houston

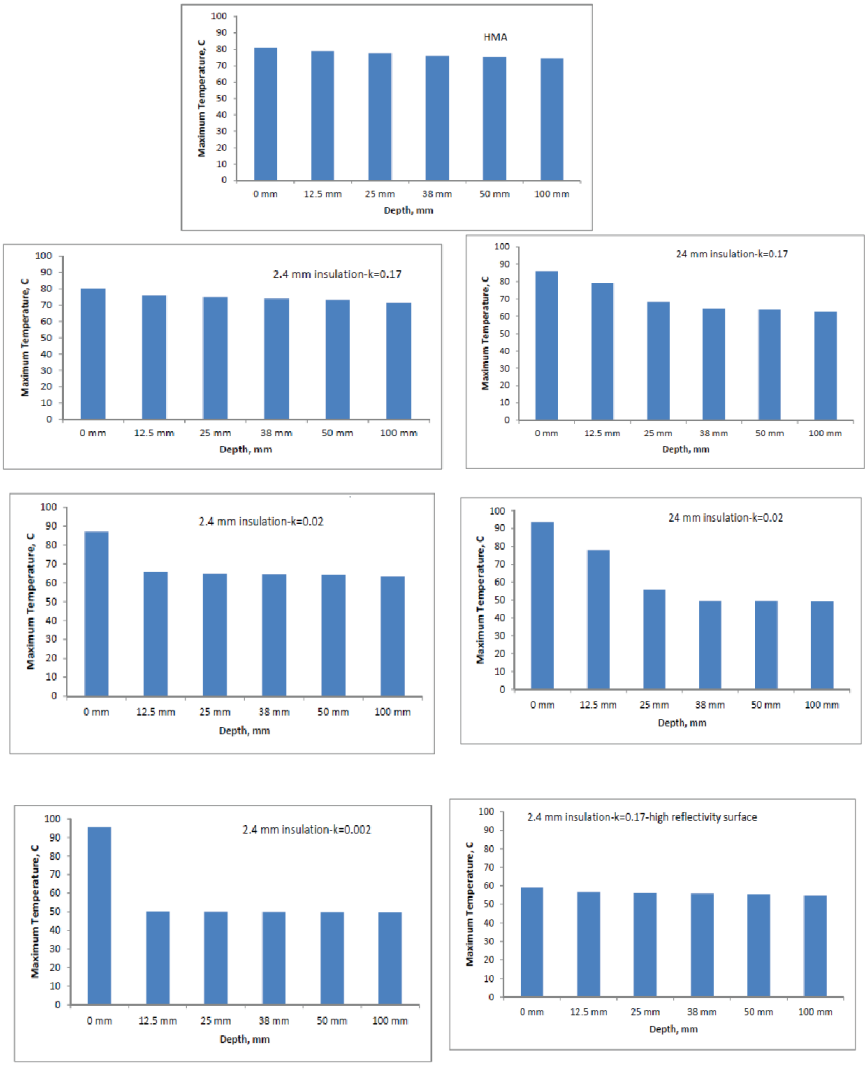

Fig. 4 Predicted maximum temperatures at different depths for different cases

1.9 Discussion

The use of an insulation layer can be effective in reducing temperature extremes in asphalt pavements, and hence extending service life by reducing the impact of the environment. The use of a highly reflective surface is also feasible; however, such layers could lose the reflectivity over time, and may not be cost effective. Some issues with the durability of ultrathin portland cement concrete (PCC) layers have

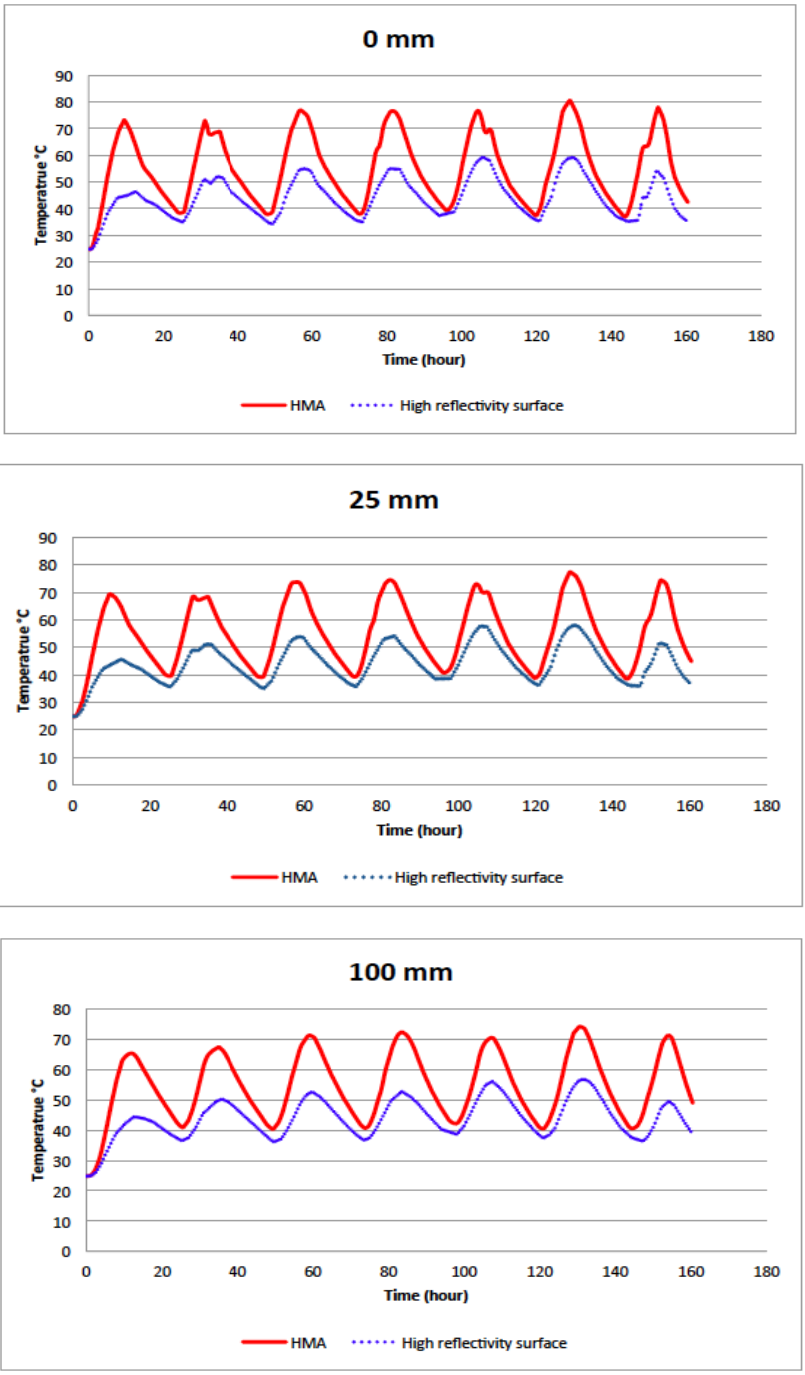

Fig. 5 Effect of high reflectivity surface on the temperature

also been noted in the literature. Furthermore, the presence of an insulation layer (such as in the form of a geosynthetic layer) could contribute as a protective membrane against moisture ingress. Table 1 shows the reduction in maximum temperature that can be achieved with different insulations. While a very low thermal conductivity could be achieved only through the use of specialized products such as the nanoinsulation materials, it is quite possible to use existing polypropylene geosynthetic layers to achieve a significant reduction in maximum temperature (such as 9 °C for a thickness of 24 mm).

To determine the effect of this reduction of temperature fluctuations on service life, the MEPDG/MEPDS(MEPDG, 2007) software can be used to predict rutting damage of conventional and insulated pavement systems. To do this, the weather database in the MEPDS was utilized. For this example, four cities were selected to consider a range of maximum pavement temperatures, from 70^{o}C to 52^{o}C. These are, in decreasing average temperatures:Houston, TX, Raleigh-Durham, NC, Chicago, IL, and Portland, ME. A pavement located in Houston was simulated, using the climatic information for the above four cities, to determine the rutting damage over the years, and the years to failure, for the range of temperatures from 70^{o}C to 52^{o}C. It can be seen (Fig. 6) that for the same traffic loading and the same materials, the life of the pavement can be extended by 5 years for a5^{o}C drop in maximum temperature. The drop in temperature is more effective in extending the life of the pavement at higher temperatures. It is evident from the data presented earlier that such extension in service lives is quite feasible with the use of insulation layers with K=0.17 W/mK (for example, polypropylene/geosynthetic layers).

The increase in minimum temperature (during cooling), however, requires a layer with K value of the order of 0.02W/mK, which is possible through the use of polystyrene materials (Table 2).

The surface layer that is above the insulation layer will experience a higher temperature for warmer climates and lower temperature for cooler climates. It will therefore need to be of such a nature that its load bearing capabilities remain relatively unaffected by changesin temperature. For example, a thin polymer modified binder layer (6- 12 mm thick) or a polymer modified chip seal would be ideal for warmer climates. Such thin layers are not likely to fail by rutting. Similarly, highly modified polymer binder layers can also be utilized for the surface layer in the case of cooler climates; the presence of layers such as geosynthetics underneath the surface layer will most likely be more forgiving of thermal cracking potential than a conventional base layer. The use of a high reflectivity surface is also another option, provided that it is durable, can retain the reflectivity for sufficient length of time, does not cause visual distress to drivers, and is cost effective.

Table 1 Reduction in maximum temperature (at a depth of 25 mm)

Case	Maximum temperature, C	Reduction in temperature, C
HMA	77.5	---
HMA + 2.4 mm K=0.17 W/mK	74.8	2.7
HMA + 24 mm K=0.17 W/mK	68.1	9.4
HMA + 24 mm K=0.02 W/mK	55.8	21.7
HMA + 24 mm K=0.002 W/mK	34.5	43.0

Table 2 Increase in minimum temperature (at a depth of 25 mm)

Case	Maximum temperature, C	Increase in temperature, C
HMA	-16.4	---
HMA + 2.4 mm K=0.02 W/mK	-11.2	5.2
HMA + 24 mm K=0.002 W/mK	-3	13.4

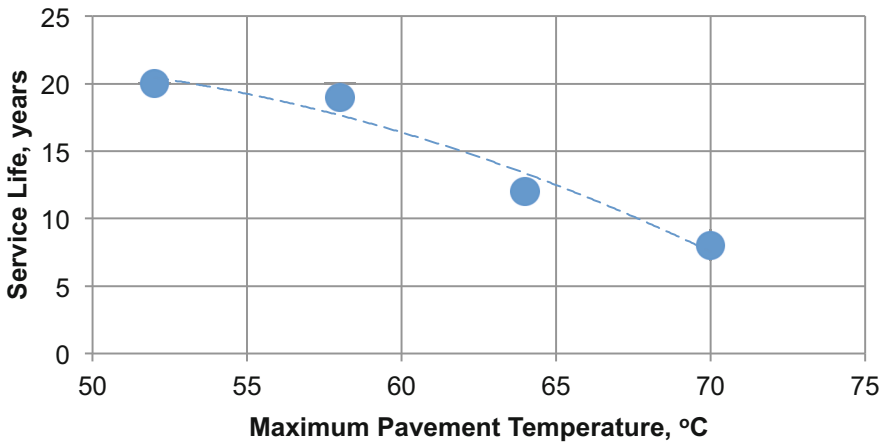

Fig. 6 Service life versus maximum pavement temperature

Therefore, the most desirable cross section of a pavement is one with insulation and a moisture-resistant layer near the top, with a highly durable surface (and preferably one with high to moderate reflectivity, such as a chip seal or an ultrathin PCC layer, Fig. 7). Also, at this time, with the existing insulation materials that are currently available, it seems that this application is more appropriate for hot than for cold climatic conditions.

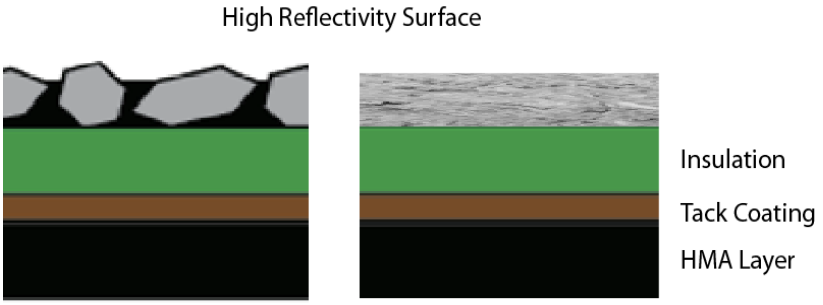

Fig. 7 Desirable combination of high reflectivity surface and insulation near the surface

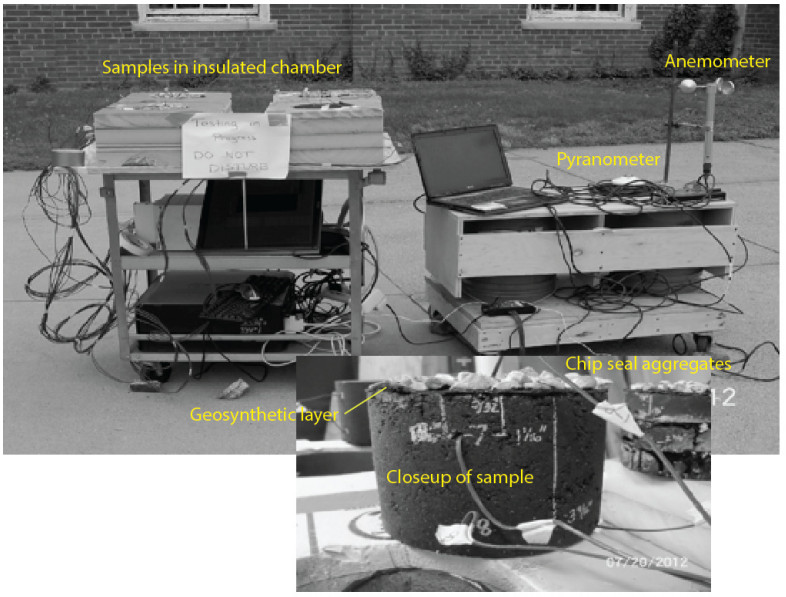

Fig. 8 Close-up of HMA sample with geosynthetic layer and chip seal aggregates, and test set-up

2 Validation of the Concept with Laboratory Experiments

Experiments were carried out with samples of HMA with and without geosynthetic reinforced chip seals with light colored aggregates(Fig. 8). The samples consisted of Massachusetts Highway Department 12.5 mm nominal maximum aggregate size (NMAS) gradation with 6% PG 64-28 asphalt binder. The conditions during the tests were as follows:Air temperature: 19.7-37.84 °C; Solar radiation: 41-887 kW/m^2, and wind speed: 0.2 - 12.7 km/h. The samples were subjected to solar radiation outdoor, and temperatures at different depths

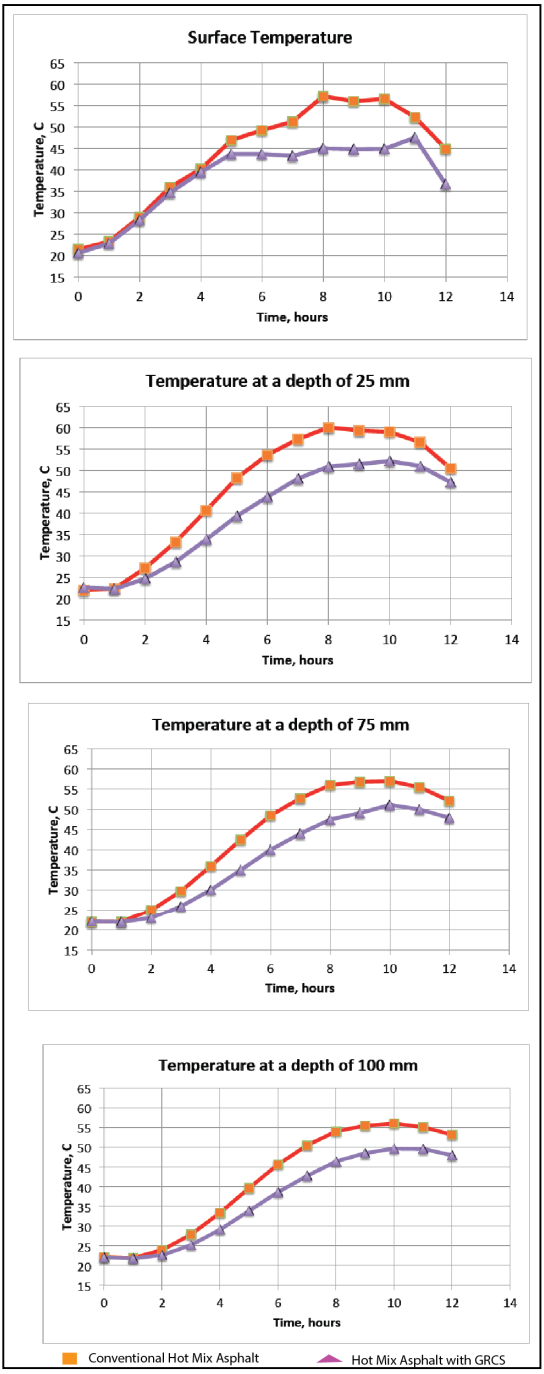

Fig. 9 Plot of temperature versus time data from experiment

were collected over a time period of 12 hours during the day time. It is evident that the temperatures are significantly reduced at different depths. To separate the effects of the light colored aggregate s in the chip seal and the geosynthetic layer, similar experiments were carried out with a geosynthetic layer with and without aggregates, as well as a control sample (air temperature: 24 - 29 °C, solar radiation: 74-1007 kW/m^2, wind speed: 2 - 9 km/h). It can be seen (Fig. 9) that the both the geosynthetic layer and the light colored aggregates are separately contributing towards the reduction in temperature.Furthermore, experiments with one (2 mm) and three (6 mm) geosynthetic layers also show the positive effect of increasing the layer thickness (Fig. 10; air temperature: 23 - 28 °C, solar radiation: 166 - 930 W/m^2, windspeed: 3 - 12.5 km/h).

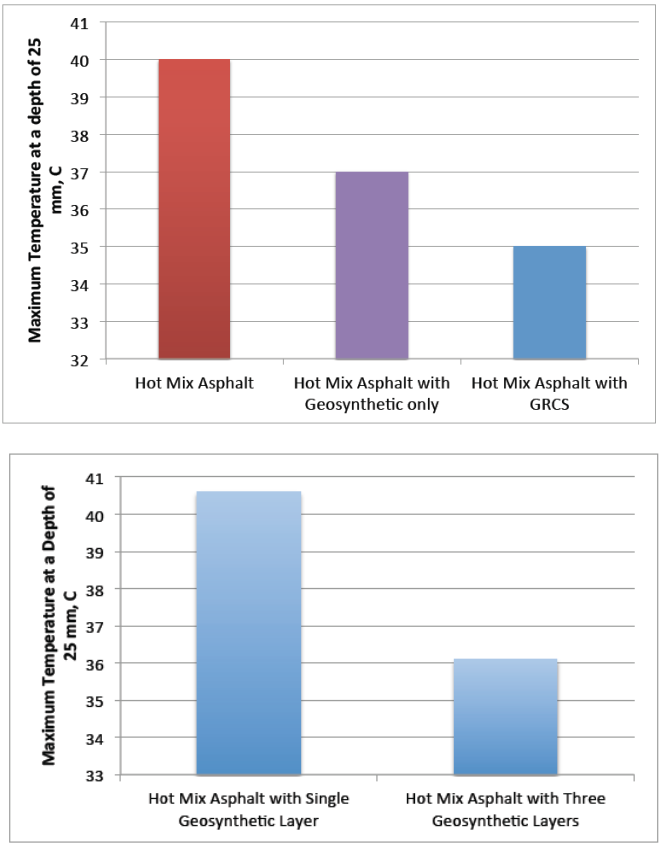

Fig. 10 Results of experiments showing effect of chip seal and geosynthetic layer and thickness of geosynthetic layers

2.1 Practical Application

The concept of geosynthetic reinforced chip seal (GRCS) is not new, but its application for reducing pavement temperature is new.GRCS is used in many areas (for example, Myers, 2012), as a pavement preservation treatment. However, the temperature reduction potential opens up a new application of this treatment, and should be researched further.

References

1. Bentz, D.P., Turpin, R.: Potential applications of phase change materials in concrete technology. Cement and Concrete Composites 29 (2007)
2. Brown, E.R., Cross, S.A.: A National Study of Rutting in Hot Mix Asphalt (HMA) Pavements. NCAT Report 92-5, National Center for Asphalt Technology, Auburn, Alabama (1992)
3. Field, D., Ruban, T., Johnston, A., Dixon, D., Lewycky, D.: Edmonton Experience with Bottom Ash and Other Insulating Materials for Mitigation of Frost Heave Induced Damage in Pavements. In: Proceedings of the 2011 Conference and Exhibition of the Transportation Association of Canada - Transportation Successes. Let's Build on Them, Edmonton, Canada (2011)
4. Humphrey, D., Blumenthal, M.: The Use of Tire-Derived Aggregate in Road Construction Applications. In: Proceedings of the 2010 Green Streets and Highways Conference, Denver, CO (2010)
5. Jelle, B.P., Gustavsen, A., Baetens, R.: The High Performance Thermal Building Insulation Materials and Solutions of Tomorrow. ASHRAE (2010), `http://www.ornl.gov/sci/buildings/2010/B11%20papers/132_Jelle.pdf` (accessed October 2012)
6. Kestler, M.A.: Performance of Insulated Pavements at Newton Field, Jackman, Maine. CRREL Report 92-9, US Department of Transportation, Federal Aviation Administration (May 1992)
7. Khazanovich, L., Balbo, J.T., Johanneck, L., Lederle, R., Marasteanu, M., Saxena, P., Tompkins, D., Vancura, M., Watson, M., Harvey, J., Santero, N.J., Signore, J.: Design and Construction Guidelines for Thermally Insulated Concrete Pavements. Center for Transportation Studies. University of Minnesota (Augusta 2012)
8. MEPDG Version 1.003, developed for projects NCHRP 1-37a, NCHRP 1-40d (2003-2007)
9. Miyamoto, S., Takeuchi, M.: Snow-melting and de-icing system on road using natural thermal energy sources. In: New Challenges for Winter Road Service XIth International Winter Road Congress. World Road Association - PIRAC, Sapporo, Japan (2002)
10. Monismith, C.L., Hicks, R.G., Finn, F.M., Sousa, J., Harvey, J., Weissman, S., Deacon, J., Coplantz, J., Paulsen, G.: Permanent Deformation Response of As-phalt Aggregate Mixes. SHRP-A-415, Strategic Highway Research Program, TRB, National Research Council, Washington, D.C. (1994)
11. Myers, R.: Geosynthetic reinforced chip seals. California Pavement Preservation Center, CP2 Center News (March 2012)

12. NOAA. National Climatic Data Center, http://www.ncdc.noaa.gov/oa/climate/climatedata.html#hourly (accessed October 2012)
13. NREL. National Solar Radiation Database, http://rredc.nrel.gov/solar/old_data/nsrdb/ (accessed October 2012)
14. Sakulich, A.R.: Reinforced geopolymer composites for enhanced material greenness and durability. Sustainable Cities and Society 1 (2011)
15. Sakulich, A., Bentz, D.P.: Incorporation of phase change materials in cementitious systems via fine lightweight aggregate. Construction and Building Materials 35 (2012)
16. Sakulich, A., Bentz, D.P.: Increasing the service life of bridge decks by incorporating phase-change materials to reduce freeze-thaw cycles. Journal of Materials in Civil Engineering 24 (2012)
17. Schmidt, R.J.: The Relationship of the Low Temperature Properties of Asphalt to the Cracking of Pavements. In: Proceedings of the Association of Asphalt Paving Technologists, vol. 35 (1966)
18. Stoll, F., Drake, M.L., Salyer, I.O.: Use of phase change materials to prevent overnight freezing of bridge decks. IDEA project final report (1996)
19. The Engineering ToolBox, http://www.EngineeringToolBox.com (accessed February 1, 2013)
20. Van de Loo, P.J.: The creep test, a key tool in asphalt mix design and in the prediction of pavement rutting. In: Proceedings of the Association of Asphalt Paving Technologists, vol. 47 (1978)
21. Vinson, T., Janoo, V., Hass, R.: Summary Report on Low Temperature and Thermal Fatigue Cracking. SHRP A/IR-90-001, Transportation Research Board, Washington, D.C. (1989)
22. Zhi, W., Yu, S., Wei, M.: Numerical Evaluation of Insulation Application to Embankment of Qinghai–Tibetan Highway. Journal of Cold Regions Engineering 21(2) (2007)

Prediction of Linear Viscoelastic Behaviour of Asphalt Mixes from Binder Properties and Reversal

Quang Tuan Nguyen, Hervé Di Benedetto, and Cédric Sauzéat

University of Lyon/Ecole Nationale des Travaux Publics de l'Etat (ENTPE)
Laboratoire de Tribologie et Dynamique des Systèmes - CNRS 5513
Département Génie Civil et Bâtiment
Rue Maurice Audin, 69518 Vaulx en Velin, France
{quangtuan.nguyen,herve.dibenedetto,
cedric.sauzeat}@entpe.fr

Abstract. The linear viscoelastic (LVE) behaviour of bituminous materials (observed in the small strain domain) is considered for road design. The objective of this paper is to investigate the links between the LVE properties of binders and asphalts mixes. Complex modulus tests were carried out to determine the LVE behaviours of a bituminous binder and two mixes produced with this bitumen. Dynamic Shear Rheometer (DSR) tests and tension-compression tests (using a Métravib device) were performed on the bitumen. Complex modulus E^* and complex Poisson's ratio ν^* of mixes which characterize the (LVE) properties in 3 Dimension (3Dim) were measured using tension-compression tests. The experimental results show the dependence between mixes and associated bitumen behaviours. The prediction of LVE behaviour of bituminous mixes from bitumen properties was carried out using the SHStS (Shift-Homothety-Shift and time-Shift) transformation developed at ENTPE.

1 Introduction

Mechanical behaviour of bituminous materials is complex. This paper focuses on the linear viscoelastic (LVE) properties of bituminous materials which can be considered as a first approximation for loadings up to a few hundred cycles and in small strains domain [Di Benedetto et al. 2001, Airey and Behzad 2004]. The objective of this paper is to investigate the links between the LVE properties of binders and asphalts mixes. Firstly, the LVE behaviour of bituminous binder and mixes is characterized and secondly, the correspondence of LVE behaviours of related binder and mixes is verified. To fulfil the objective of the study, complex modulus tests were carried out on both bituminous binder and mixes. Tests on bituminous binder were conducted using Dynamic Shear Rheometer (DSR) and Métravib device (tension-compression). To characterize the LVE properties in 3D of bituminous mixes, measurements of complex modulus E^* and complex

N. Kringos et al. (Eds.): *Multi-Scale Model. & Charact. of Infrastruct. Mater.,* RILEM 8, pp. 237–248.
DOI: 10.1007/978-94-007-6878-9_17

Poisson's ratio ν^* were carried out using tension-compression tests. From the obtained results, the dependence of the properties of mixes with binder one is studied. The 2S2P1D (2 Springs, 2 Parabolic elements, 1 Dashpot) model, developed at the "Ecole Nationale des Travaux Publics de l'Etat" (ENTPE), was used to fit the experimental results. Then, the SHStS (Shift-Homothety-Shift and time-Shift) transformation (developed at ENTPE) was applied to obtain VEL properties of mix from bitumen data.

2 Materials

The tested materials are provided by EIFFAGE Travaux Publics Company. Two bituminous mixes, called GB3 and GB5® (GB stands for "Grave Bitume" in French), were produced with the same pure bitumen (35-50 penetration grade). The bitumen content in total weight of both GB3 and GB5® is 4.5% by weight of the aggregate. The 0/14mm grading curve is either continous (GB3) or gap-graded (GB5®). Aggregate nature is diorite (from "La Noubleau" quarry, France). Grading curves are presented in Fig. 1. The tested specimens are 2.1% (GB3) and 0.7% (GB5®) of air void. Unfortunately, it is noteworthy that the respective air void content of the studied GB3 and GB5® mixes does not strictly corresponds to in-situ values. Indeed, typical air void content of GB3 (resp. GB5®) is between 6 and 9% (resp. 3 and 6%) [Olard 2012].

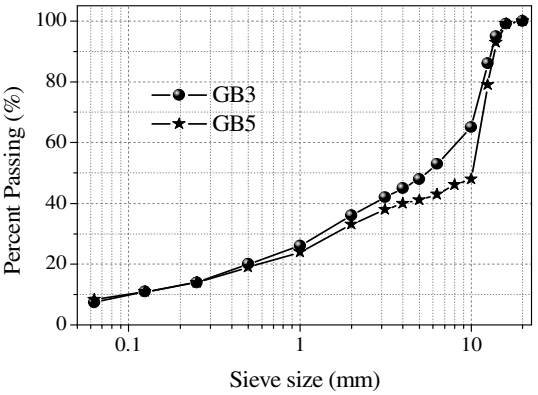

Fig. 1 Aggregates grading curves of tested bituminous mixture

3 Experimental Campaign

3.1 Complex Modulus Tests on Binder

The complex modulus tests on bituminous binder were conducted using the Dynamic Shear Rheometer (DSR) and Métravib devices at EIFFAGE Travaux Publics research centre (Corbas, France).

DSR apparatus is a 8 mm diameter plate-plate configuration (2 mm gap). Temperatures ranging from 10°C to 70°C and frequencies ranging from 0.01 Hz to 30 Hz were applied during DSR test. Complex modulus E^* (norm $|E^*|$ and phase angle ϕ_E) of bitumen was calculated from measured shear complex modulus G^* by applying an arbitrary Poisson's ratio equal to 0.5 ($E^* = 3G^*$).

The test using Métravib apparatus is tension-compression test. The cylindrical specimen is 20 mm long and 10 mm diameter. The sample was loaded at temperatures ranging from -30°C to 10°C and at frequencies ranging from 0.01 Hz to 30 Hz. Métravib test gives directly the complex modulus E^* of bitumen.

From the DSR and Métravib test, the LVE behaviour of bitumen (norm and phase angle of complex modulus E^*) is obtained for a very large range of temperatures (-30°C to 70°C) and of frequencies (0.01 Hz to 30 Hz).

3.2 Complex Modulus Tests on Bituminous Mixes

Fig. 2 presents a general view of the test equipment used to apply sinusoidal loading in tension and compression on bituminous mixtures. This tension-compression test creates a homogenous stress and strain field in the middle part of the cylindrical specimen. The tested sample is 74 mm in diameter and 140 mm high. The specimens were cored and sawn from slabs made with a French LPC ("Laboratoire des Ponts et Chaussées") wheel compactor, according to the European standard [EN 12697-33:2003+A1:2007]. Tension and compression loading is applied in direction 1. The measurement of radial strain is realised in material directions 2 and 3. The material directions (1, 2, 3) are indicated in Fig. 3. Axial strain is measured in the middle part of the specimen (Fig. 4) using three extensometers. They are located at 120° around the specimen with an initial length of 75 mm. Radial strain is measured in direction 2 and direction 3 using 4 non-contact sensors. For each direction, two sensors are fixed oppositely on a sample diameter and aim at two targets glued on the sample (Fig. 4).

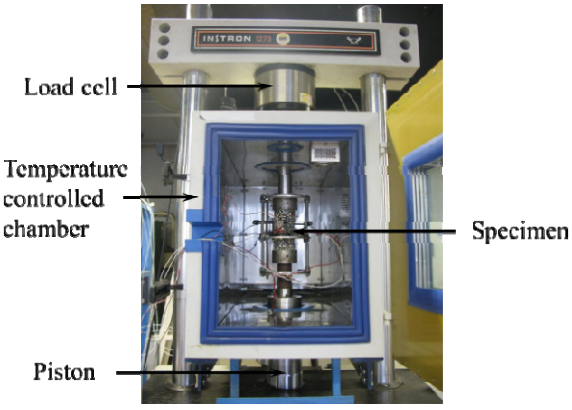

Fig. 2 General view of the test equipment

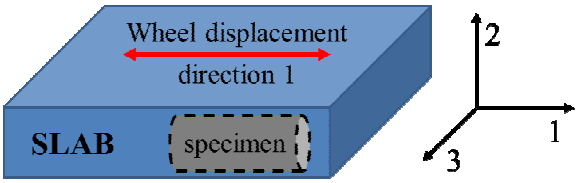

Fig. 3 The material directions

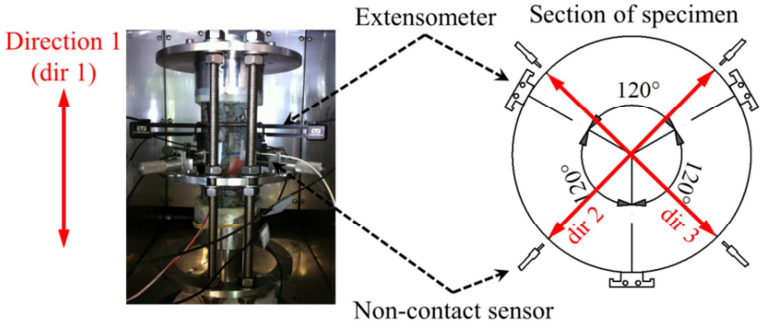

Fig. 4 Specimen and devices used to measure axial strain, radial strain

Complex modulus tests on GB3 and GB5® mixes are a part of an international research project in the framework of TG3 of RILEM TC 237 – SIB. Temperatures ranging from -25°C to 40°C and frequencies ranging from 0.03 Hz to 10 Hz were applied. Sinusoidal axial strain (ε_1) (average of three extensometers) is used for monitoring. The number of cycles applied at each frequency is small (less than 80), then heating problems due to viscous dissipation [Di Benedetto et al. 2011, Nguyen et al. 2012a] are negligible. Sinusoidal axial stress (σ_1) is obtained from load cell signal and sinusoidal radial strains (ε_2 and ε_3) is deduced from the two non-contact output. Sinusoidal curves of strains and stress were then fitted to the experimental data and used to calculate the norm and phase angle of complex modulus (E^*) and complex Poisson's ratios (ν_2^* and ν_3^*) using the equations (1) to (5), where ε_{01}, ε_{02}, ε_{03} and σ_{01} are respectively the axial strain amplitude, the radial strain amplitude in directions 2, 3 and the axial stress amplitude. ϕ_E is the phase angle between axial strain and axial stress, and ϕ_{v2}, ϕ_{v3} are the phase angles between the axial strain and the opposite of radial strains in directions 2 and 3. $|E^*|$, $|\nu_2^*|$ and $|\nu_3^*|$ are respectively the norm of complex modulus and complex Poisson's ratios. j is the complex number defined by $j^2 = -1$. Fig. 5 presents an example of axial stress, axial strain and radial strains measurements at T = 12.5°C and f = 0.1 Hz on GB5® mix.

$$\varepsilon_1(t) = \varepsilon_{01}\sin(\omega t) \quad (1)$$

$$\sigma_1(t) = \sigma_{01}\sin(\omega t+\phi_E) \quad (2)$$

$$\varepsilon_i(t) = -\varepsilon_{0i}\sin(\omega t+\phi_{vi}) \ (i = 2, 3) \quad (3)$$

$$E^* = \frac{\sigma_{01}}{\varepsilon_{01}} e^{j\phi_E} = \left|E^*\right| e^{j\phi_E} \quad (4)$$

$$\nu_i^* = \frac{\varepsilon_{0i}}{\varepsilon_{01}} e^{j\phi_{vi}} = \left|\nu_i^*\right| e^{j\phi_{vi}} \ (i = 2, 3) \quad (5)$$

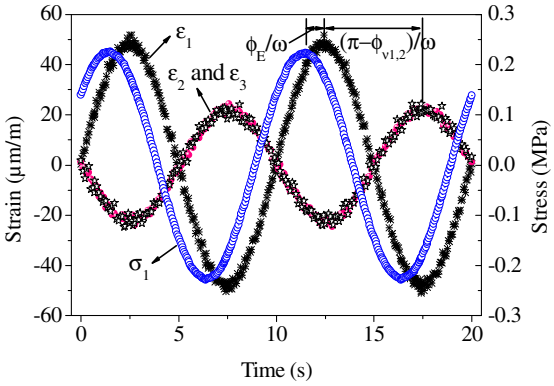

Fig. 5 Example of stress and strains measurements (2 cycles at f = 0.1 Hz and T = 12.5°C on GB5® mix)

3.3 Test Results on Bitumen

Fig. 6 presents the complex modulus test results on bitumen in the Black diagram. The Black curve is unique that means the Time Temperature Superposition Principle (TTSP) [Ferry 1980, Olard 2003, Di Benedetto et al 2007, Pouget et al. 2010a, Nguyen et al. 2012b, among others] is verified. This specific property of bituminous materials allows plotting a master curve at any chosen reference temperature (T_{ref}). The norm of E^* master curve is built in Fig. 7 using the shift factor a_T presented in Fig. 10.

The experimental results are fitted using 2S2P1D (2 Springs, 2 Parabolic elements, 1 Dashpot) model, developed at ENTPE. Due to the limited space in this paper, the details of this model are not presented. Readers can consult the references [Olard et al. 2003, Di Benedetto et al. 2004, 2007] for more explanation.

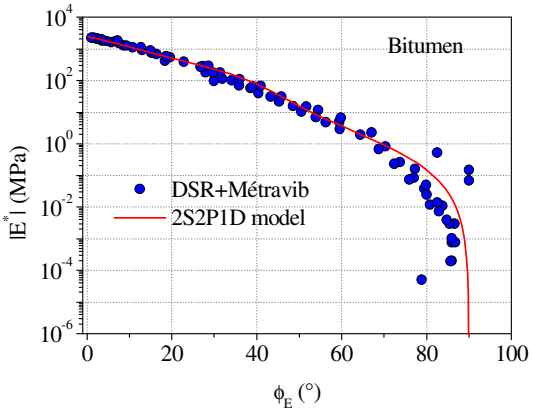

Fig. 6 Black diagram of studied 35/50 pure bitumen

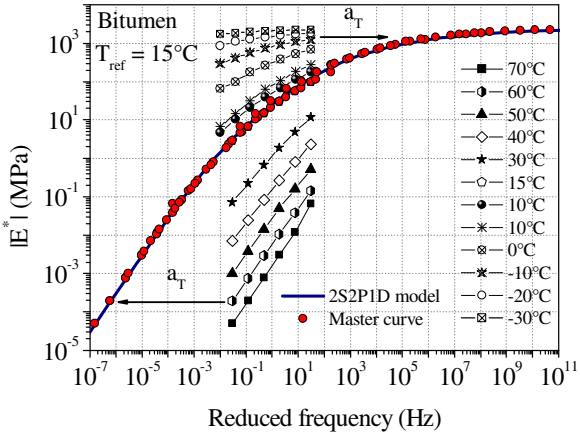

Fig. 7 Values of $|E^*|$ and master curve of bitumen at the reference temperature T_{ref} = 15°C

3.4 Test Results on Bituminous Mixes

The Black diagram of GB3 mix is presented in Fig. 8. The master curves for the norm of E^* and the norm of ν^* are plotted in Fig. 9. The results show that the TTSP is verified in 3 Dim for tested mixes. The obtained values of complex Poisson's ratio ν^* are very close in the two directions 2 and 3. A good simulation of 3Dim LVE behaviour can be obtained using the 2S2P1D model (plotted in Fig. 8 and 9).

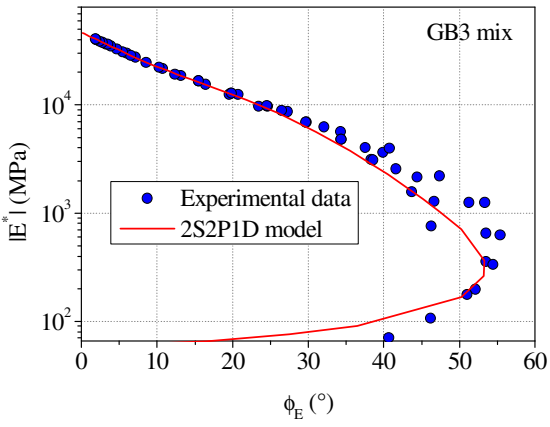

Fig. 8 Black diagram of GB3 mix

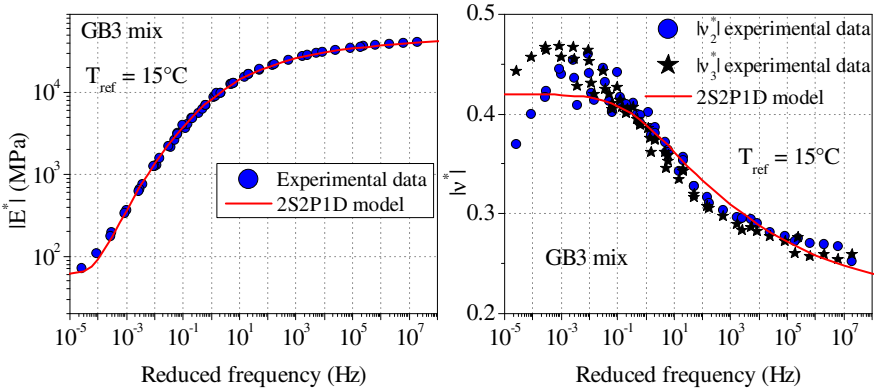

Fig. 9 Master curve for GB3 mix at the reference temperature T_{ref} = 15°C (left: norm of E^* and right: norm of ν^*)

It should be noted that the master curves of E^* and ν^* were built with the same shift factor a_T (Fig.10). This result is confirmed by other recent studies [Di Benedetto et al. 2007, Nguyen HM et al. 2009, Pouget et al. 2010b, Nguyen et al. 2011].

3.5 Prediction of Mechanical Behaviour of Asphalt Mixes from Binder Properties and Vice Versa

Fig. 10 presents the values of shift factors a_T of bitumen and mixes. The shift factors a_T of mixes are very close to the shift factors of the incorporated bitumen. Then, the thermal sensitivity for mixes can be considered as given by the binder. The classical WLF law (William, Landel and Ferry) [Ferry 1980] is used to fit the shift factor values a_T.

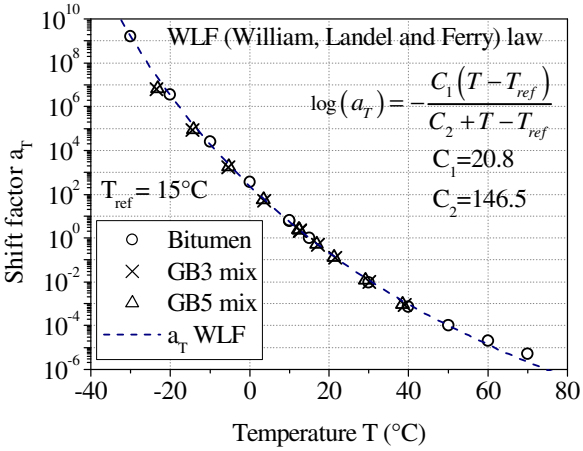

Fig. 10 Shift factors a_T of bitumen, GB3 mix, GB5® mix and WLF law fitting

The normalized complex modulus (E^*_{norm}) and normalized complex Poisson's ratio (ν^*_{norm}) are introduced in equations 6 and 7 where E_{00} and E_0 (ν_{00} and ν_0) are asymptotic values of the norm of complex modulus (the norm of complex Poisson's ratio, respectively) when the frequency tends towards 0 and infinity. These values of E_{00}, E_0, ν_{00} and ν_0 obtained from the complex modulus tests on bitumen and mixes are given in Table 1.

$$E^*_{norm} = \frac{E^* - E_{00}}{E_0 - E_{00}} \tag{6}$$

$$\nu^*_{norm} = \frac{\nu^* - \nu_{00}}{\nu_{00} - \nu_0} \tag{7}$$

When plotted in a Cole-Cole diagram (Fig. 11), the normalized complex modulus curves of the bitumen, GB3 and GB5® mixes superimpose. This confirms that the TTSP originates from the bitumen used to produce the bituminous mixtures. In 3Dim, it is interesting that the normalized master curves of E^*_{norm} and ν^*_{norm} for mixes are very close together as can be observed in Fig. 12.

From the observed superimposition between the binder and the asphalt mixtures curves (Fig. 11 and 12), it is possible to predict mechanical behaviour of asphalt mixes from binder one and vice versa. The SHStS (Shift-Homothety-Shift and time-Shift) transformation developed at ENTPE [Olard et al. 2003, 2005, Di Benedetto et al. 2004, Pouget et al. 2010a] is considered in this paper. This transformation does not need using a rheological model and is valid over a wide range of temperatures and frequencies on both norm and phase angle of complex modulus and Poisson ratios. In the case of complex modulus, equation 8 gives the

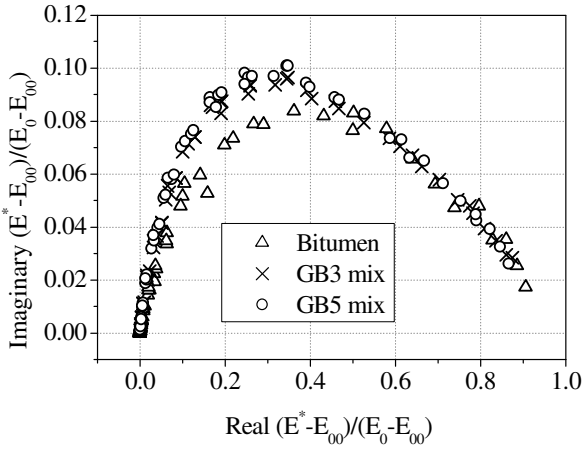

Fig. 11 Normalized complex modulus curves in Cole-Cole diagram of the bitumen and GB3, GB5® mixes

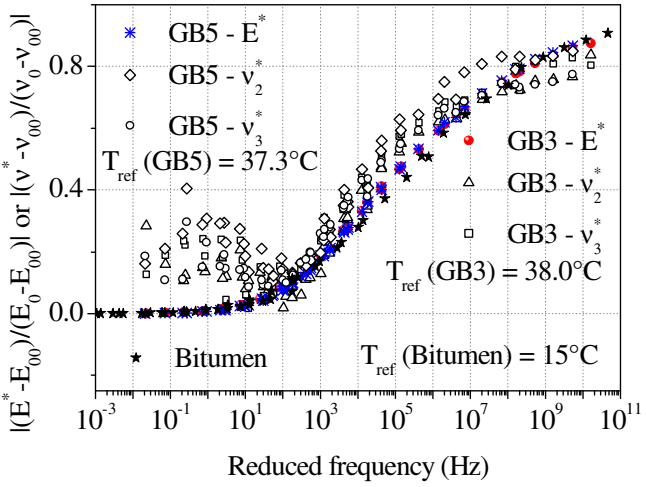

Fig. 12 Normalised master curves for E^* and ν^* of bitumen, GB3 and GB5 mixes

ENTPE SHStS transformation relationship**,** where constant α depends on the considered mix design. The values of α is given in Table 1.

$$E^*_{mix}(\omega,T)=E_{00,mix}+\left[E^*_{binder}(10^{\alpha}\omega,T)-E_{00,binder}\right]\frac{E_{0,mix}-E_{00,mix}}{E_{0,binder}-E_{00,binder}} \quad (8)$$

As most of binders have a nil (or negligible) value for E_{00}, equation 8 can be simplified and becomes equation 9**:**

$$\mathrm{E}^{*}_{mix}\left(\omega,T\right)=\mathrm{E}_{00,mix}+\mathrm{E}^{*}_{binder}\left(10^{\alpha}\omega,T\right)\frac{\mathrm{E}_{0,mix}-\mathrm{E}_{00,mix}}{\mathrm{E}_{0,binder}} \tag{9}$$

Fig. 13 presents the results for SHStS predictions. As can be seen on this figure, SHStS transformation successfully predicts mixes LVE behaviour from binder LVE behaviour. It can also be applied in the reverse way very easily.

Table 1 Values used for the normalized curves and SHStS transformation

	E_{00} (MPa)	E_0 (MPa)	ν^{*}_2		ν^{*}_3		α
			ν_{00}	ν_0	ν_{00}	ν_0	
Bitumen	0	2480					
GB3 mix	40	46400	0.42	0.22	0.42	0.22	2.67
GB5® mix	40	49500	0.48	0.18	0.48	0.2	2.58

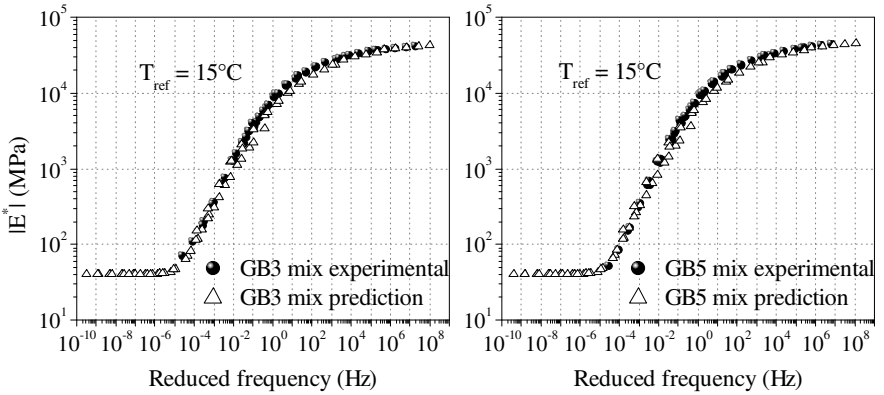

Fig. 13 The SHStS prediction results for GB3 and GB5® mixes using the experimental data on 35/50 bitumen (equation 9), at the reference temperature T_{ref} = 15°C

4 Conclusions

The aim of our research was to characterize the links between the LVE properties of binders and of asphalts mixes. From the obtained results, the following conclusions can be drawn:

- The LVE behaviour of bitumen and two types of mixes are obtained experimentally. The TTSP is verified in the 1D case for bitumen and 3D case for mixes. An identical shift factor a_T for complex modulus and complex Poisson's ratio is obtained for bitumen and mixes. This shift factor is fixed by the bitumen.

- The 2S2P1D model simulates correctly the LVE behaviour of the three tested materials.
- The experimental results show the dependence of the behaviour of mixes on that of used bitumen. The thermal sensitivity and the TTSP of mixes can be considered as given by the binder.
- Proposed ENTPE transformation "SHStS" gives a successful prediction of mixes LVE behaviour from binder LVE behaviour. It can also easily be applied in the reverse side to obtain properties of binder from mix ones. This geometrical transformation in the complex plane needs only 3 constants and is independent of any model.

Acknowledgments. This work was carried out as part of TG3 of RILEM TC 237 – SIB. We would like to acknowledge EIFFAGE Travaux Publics Company for providing the materials and performing the complex modulus tests on bitumen.

References

Airey, G.D., Behzad, R.: Combined bituminous binder and mixture linear rheological properties. Construction and Building Materials 18, 535–548 (2004)

Di Benedetto, H., Delaporte, B., Sauzéat, C.: Three-dimensionnal linear behavior of bituminous materials: experiments and modelling. International Journal of Geomechanics (ASCE) 7(2), 149–157 (2007)

Di Benedetto, H., Olard, F., Sauzéat, C., Delaporte, B.: Linear viscoelastic behavior of bituminous materials: from binders to mixes. International Journal of Road Materials and Pavement Design 5(Special Issue), 163–202 (2004)

Di Benedetto, H., Partl, M.N., Francken, L., De la Roche, C.: Stiffness testing for bituminous Mixtures. Journal Materials and Structures 34, 66–70 (2001)

Di Benedetto, H., Nguyen, Q.T., Sauzéat, C.: Nonlinearity, Heating, Fatigue and Thixotropy during Cyclic Loading of Asphalt Mixtures. Road Materials and Pavement Design 12(1), 129–158 (2011)

EN 12697-33:2003+A1:2007 standard, Bituminous mixtures – Test methods for hot mix asphalt – Part 33: Specimen prepared by roller compactor (2007)

Ferry, J.D.: Viscoelastic Properties of Polymers, 642 p. John Wiley & Sons (1980)

Nguyen, H.M., Pouget, S., Di Benedetto, H., Sauzéat, C.: Time-Temperature Superposition Principle for bituminous mixtures. European Journal of Environmental and Civil Engineering, 1095–1107 (2009)

Nguyen, Q.T., Di Benedetto, H., Sauzéat, C.: Determination of Thermal Properties of Asphalt Mixtures as Another Output from Cyclic Tension-Compression Test. Road Materials and Pavement Design 13(1), 85–103 (2012a)

Nguyen, Q.T., Di Benedetto, H., Sauzéat, C.: 3D Viscoelastic Linear and Nonlinear Behavior of Asphalt Mixtures. In: 5th International Conference Bituminous Mixtures and Pavements, Thessaloniki, Greece, pp. 471–480 (2011)

Nguyen, Q.T., Di Benedetto, H., Sauzeat, C., Tapsoba, N.: Time temperature superposition principle validation forbituminous mixes in the linear and nonlinear domains. J. Mater. Civ. Eng. (2012b), doi:10.1061/(ASCE)MT.1943-5533.0000658

Olard, F., Di Benedetto, H.: General 2S2P1D model and relation between the linear viscoelastic behaviors of bituminous binders and mixes. Journal of Road Materials and Pavement Design 4(2), 185–224 (2003)

Olard, F.: Comportement thermomécanique des enrobés bitumineux à basses températures. PhD. ENTPE-INSA Lyon. Mecanique, Energétique, Acoustique et Génie Civil, 221p. (2003) (in French)

Olard, F.: GB5 mix design: high-performance and cost-effective asphalt concretes by use of gap-graded curves and SBS modified bitumens. Road Materials and Pavement Design 13(suppl. 1), 234–259 (2012)

Olard, F., Di Benedetto, H., Dony, A., Vaniscote, J.-C.: Properties of bituminous mixtures at low temperatures and relations with binder characteristics. Materials and structures 38(1), 121–126 (2005)

Pouget, S., Sauzeat, C., Di Benedetto, H., Olard, F.: From the behavior of constituent materials to the calculation and design of orthotropic bridge structures. Road Materials and Pavement Design 11(SI EATA), 111–144 (2010a)

Pouget, S., Sauzéat, C., Di Benedetto, H., Olard, F.: Numerical simulation of the five-point bending test designed to study bituminous wearing courses on orthotropic steel bridge. Materials and Structures 43(3), 319–330 (2010b)

A 3D/2D Comparison between Heterogeneous Mesoscale Models of Concrete

Filip Nilenius[1,2,⋆], Fredrik Larsson[2], Karin Lundgren[1], and Kenneth Runesson[2]

[1] Department of Civil and Environmental Engineering, Chalmers University of Technology, Göteborg, Sweden
[2] Department of Applied Mechanics, Chalmers University of Technology, Göteborg, Sweden

Abstract. A model for 3D Statistical Volume Elements (SVEs) of mesoscale concrete is presented and employed in the context of computational homogenization. The model is based on voxelization where the SVE is subdivided into a number of voxels (cubes) which are treated as solid finite elements. The homogenized response is compared between 3D and 2D SVEs to study how the third spatial dimension influence the over-all results. The computational results show that the effective diffusivity of the 3D model is about 1.4 times that of the 2D model.

1 Introduction

Computational homogenization is a well known technique to account for material heterogeneities while keeping computational costs at a moderate level. One benefit of this technique is that it enables to determine bulk properties of a material *a priori* in the case of linear subscale properties. This is beneficial if the macroscopic behaviour of a material is sought and the subscale features is highly complex. In case of non-linear material behaviour the subscale response needs to be determined concurrently during the computations in a nested fashion using a FE^2-approach. Furthermore, the technique opens up to "virtual testing" of new materials.

Concrete has a highly heterogeneous and random material structure at multiple length scales. Thus, considerable computational work on the effects of its heterogeneity has been done for this material, see eg. Kim and Al-rub [10], Idiart et al. [9] and Wang and Ueda [13].

However, most computational work reported in the literature deals with 2D models of concrete and any 3D feature that might be of importance is naturally not accounted for in these instances. A natural evolution in the development of computational homogenization is thus to account for all three spatial dimensions to obtain numerical results that potentially better reflect the real material behaviour.

⋆ Corresponding author.

N. Kringos et al. (Eds.): *Multi-Scale Model. & Charact. of Infrastruct. Mater.*, RILEM 8, pp. 249–259.
DOI: 10.1007/978-94-007-6878-9_18

This paper presents a 3D heterogeneous mesoscale model of concrete and compares computational homogenization between 2D and 3D models to study how the third spatial dimension contributes to the homogenized results. This is done in the context of mass diffusion; thus, the effective diffusivity of concrete is the studied material property in this work.

2 Mesoscale SVE

The concept of Statistical Volume Element (SVE) is fundamental to computational homogenization techniques as it is the foundation on which all computational work is built. The SVE is expected to contain all material heterogeneities in a statistical manner and tends to become an Representative Volume Element (RVE) only when it is sufficiently large, i.e. when the influence of boundary conditions are sufficiently small, see Ostoja-Starzewski [12]. The RVE, in turn, is used to extract the sought macroscopic material properties.

In this work, the mesoscale material constituents are the cement paste matrix, aggregates and Interfacial Transition Zone (ITZ). The aggregates are modelled as spheres with random spatial distribution enfolded by an interface layer of ITZ. The cement paste matrix is considered homogeneous, i.e. cracks are not accounted for.

2.1 Sieve Curve

The aggregates in the SVE can be of arbitrary size and quantity. The volume fraction of aggregates is defined as

$$n_{\mathrm{a}} = \frac{V_{\mathrm{a}}}{V_{\mathrm{SVE}}} \qquad n_{\mathrm{a}} \in [0,1], \tag{1}$$

where $V_\bullet$ is the volume and sub-index 'a' denotes aggregate. The SVE model implementation allows for any realistic n_{a} to be used as input. Any sieve curve is possible to have as input for the SVE realization and we have the requirement that

$$\sum_{i=0}^{N} n_{\mathrm{a},i} = n_{\mathrm{a}}, \tag{2}$$

where $n_{\mathrm{a},i}$ denotes the volume fraction of aggregate size i and N denotes the total number of particles sizes included in the specified sieve curve. Both N and $n_{\mathrm{a},i}$ can be chosen freely given that the constraint in Eq. (2) is fulfilled.

2.2 Algorithm for Generating SVEs

The algorithm for generating SVEs is given below as pseudo-code and has been implemented in MATLAB. The algorithms assures that no aggregates

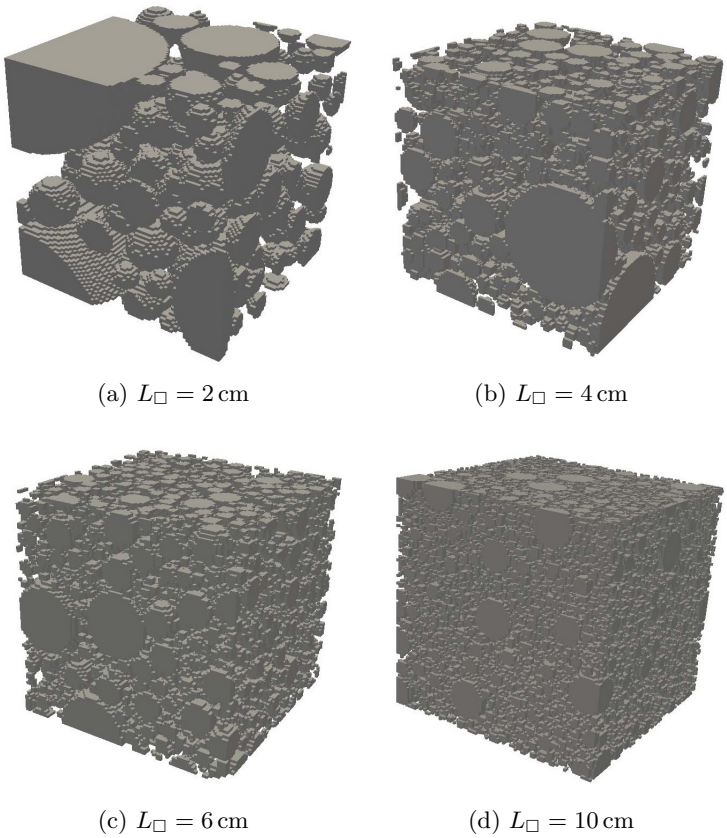

(a) $L_\square = 2\,\text{cm}$ (b) $L_\square = 4\,\text{cm}$

(c) $L_\square = 6\,\text{cm}$ (d) $L_\square = 10\,\text{cm}$

Fig. 1 Example SVEs all having the same sieve curve with $n_\text{a} \approx 0.45$. $L_\square$ refers to the side lenght of the SVE.

Algorithm 1 Generating SVE

```
while the volume fraction of aggregate inside Ω□ [1] < n_a do
    Generate aggregate from given sieve curve
    Place the new aggregate at a random point in Ω□
    if new particle overlap already existing particle then
        Remove the new aggregate
    end if
    add area of the new aggregate to the accumulated aggregate volume
end while
```

overlap once the algorithm has completed. In Figure 1, four example SVEs produced by the algorithm are show.

[1] The SVE domain is denoted $\Omega_\square$.

3 FE Discretization of SVE

The spatial discretization technique is based on voxelization to create a structured grid of equally sized voxels. The concept is to subdivide a cubic body into a number of smaller cubes (voxels) which are considered solid finite elements. This approach was used by Bentz et al. [2] and Garboczi [5] in the context of analytical homogenization of heterogeneous concrete and later adapted by Hain and Wriggers [6, 7] for elasticity problems and computational homogenization. Other discretization approaches for 3D domains have been devised in the literature: both Caballero et al. [4] and Asahina and Bolander [1] used Voronoi tessellation where the aggregates were based on a polyhedron representation to generate 3D SVEs.

Material properties of the finite elements are determined by looping over all elements and for each element measure its distance to the center of all aggregates (spheres). If the distance is greater that the radius of any of the aggregates then the elements is located in the cement paste matrix and can be assigned its proper material property. If the distance is smaller than the radius then the element sits inside an aggregate.

4 ITZ Implementation

Experimental results by Hedenblad [8] indicate that the effective, or volume average, diffusivity of concrete slightly increase with increasing aggregate content, alternatively remains unchanged. This fact implies that the ITZ has a non-negligible effect on the diffusivity of concrete.

As the SVEs are discretisized into a structured grid, a certain number of voxels end up right at the interface between the cement paste matrix and aggregate, see Figure 2.

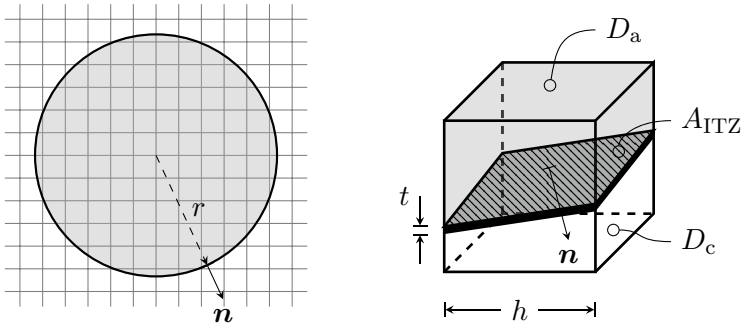

(a) 2D analogy: circle discretisized into a structured grid.

(b) Interface voxel.

Fig. 2 Interface voxel (right) containing all three mesoscale constituents located at the surface of an aggregate (left)

Consequently, these interface voxels will contain all three mesoscale materials; cement paste, aggregate and ITZ. For these voxels, we employ an anisotropic Voigt assumption on the over-all diffusivity, expressed as

$$\bar{\boldsymbol{D}} = \frac{V_\mathrm{a} D_\mathrm{a} + V_\mathrm{c} D_\mathrm{c}}{V_\mathrm{a} + V_\mathrm{c}} \boldsymbol{I} + \frac{A_\mathrm{ITZ} D_\mathrm{ITZ} t}{V_\mathrm{a} + V_\mathrm{c}} \left(\boldsymbol{I} - \boldsymbol{n} \otimes \boldsymbol{n} \right), \tag{3}$$

where $D_\bullet$, are material diffusivities[1]. Generally, we have that $D_\mathrm{a} \ll D_\mathrm{c} \ll D_\mathrm{ITZ}$ and for this work we assume that $D_\mathrm{a} = 0\,\mathrm{cm}^2/\mathrm{s}$ and we set $D_\mathrm{c} = 1\,\mathrm{cm}^2/\mathrm{s}$. The unknown parameters in Eq. (3) are the thickness, t, and diffusivity, D_ITZ, of the ITZ. Computationally, it is the product of these two, $D_\mathrm{ITZ} \times t$, that become the model parameter.

There are several ways in which the aggregate interface surface, A_ITZ, can cut through the voxel and the intersection points between the surface and the line segments of the voxel can range from 3 to 6. The gray and white aggregate and cement paste volumes in Figure 2b become convex hulls, see Berg et al. [3], spanned by these intersection points and corner nodes, and are computed by utilizing this geometrical property. The interface area, A_ITZ, is determined in a similar fashion.

5 First Order Homogenization

We wish to determine the difference between 3D and 2D SVEs in terms of homogenized response. This is done by starting from the fully resolved, stationary, boundary value problem

$$\boldsymbol{\nabla} \cdot \boldsymbol{J} = 0 \quad \forall \boldsymbol{x} \in \Omega, \tag{4}$$

for which all material heterogeneities are embedded in $\Omega \subset \mathbb{R}^3$. Here, $\boldsymbol{\nabla}$ is the nabla operator and $\boldsymbol{J}(\boldsymbol{x})$ is the flux of some generic physical quantity. The corresponding weak form reads

$$\int_\Omega \boldsymbol{\nabla} \delta\phi \cdot \boldsymbol{J} = \int_{\Gamma_\mathrm{N}} \delta\phi \boldsymbol{J} \, \mathrm{d}\Gamma, \tag{5}$$

for suitable test function $\delta\phi$ that is sufficiently regular.

Homogenization implies that the integrands of the volume integrals in Eq. (5) are replaced by space-averages on RVEs, i.e.

$$\int_\Omega \boldsymbol{\nabla} \delta\phi \cdot \boldsymbol{J} \, \mathrm{d}\Omega \longrightarrow \int_\Omega \langle \boldsymbol{\nabla} \delta\phi \cdot \boldsymbol{J} \rangle_\square \, \mathrm{d}\Omega, \tag{6}$$

where $\langle \bullet \rangle_\square$ denotes the volume average

$$\langle \bullet \rangle_\square \overset{\mathrm{def}}{=} \frac{1}{|\Omega_\square|} \int_{\Omega_\square} \bullet \, \mathrm{d}\Omega_\square, \tag{7}$$

[1] "a" = aggregate, "c" cement paste

on the RVE that occupies the domain $\Omega_\square$ centered at the macroscale position $\bar{\boldsymbol{x}} \in \Omega$; hence, $\langle \boldsymbol{x} - \bar{\boldsymbol{x}} \rangle_\square = 0$.

We assume first order homogenization defined by the split of a scalar field ϕ within $\Omega_\square$ into the macroscale and fluctuation parts[2] as follows:

$$\phi(\boldsymbol{x}; \bar{\boldsymbol{x}}) = \phi^{\mathrm{M}}(\boldsymbol{x}; \bar{\boldsymbol{x}}) + \phi^{\mathrm{s}}(\boldsymbol{x}). \tag{8}$$

The macroscale part varies linearly as

$$\phi^{\mathrm{M}}(\boldsymbol{x}; \bar{\boldsymbol{x}}) = \bar{\phi}(\bar{\boldsymbol{x}}) + \bar{\boldsymbol{g}}_\phi(\bar{\boldsymbol{x}}) \cdot [\boldsymbol{x} - \bar{\boldsymbol{x}}] \quad \forall \boldsymbol{x} \in \Omega_\square, \tag{9}$$

with $\bar{\boldsymbol{g}} \overset{\mathrm{def}}{=} \bar{\boldsymbol{\nabla}} \bar{\phi}$. Hence, we obtain $\boldsymbol{\nabla} \phi^{\mathrm{M}}(\bar{\boldsymbol{x}}; \bar{\boldsymbol{x}}) = \bar{\boldsymbol{g}}(\bar{\boldsymbol{x}})$ constant within $\Omega_\square$. We then obtain for any macroscale point $\bar{\boldsymbol{x}} \in \Omega$ the identity

$$\langle \boldsymbol{\nabla} \delta\phi \cdot \boldsymbol{J} \rangle_\square = \delta \bar{\boldsymbol{g}} \cdot \bar{\boldsymbol{J}} \quad \text{with} \quad \bar{\boldsymbol{J}}_\phi = \langle \boldsymbol{J} \rangle_\square. \tag{10}$$

In order to compute the homogenized flux quantity $\bar{\boldsymbol{J}}$, it is necessary to compute the fluctuation field ϕ^{s} as well as the spatial gradient on the subscale: $\boldsymbol{g}^{\mathrm{s}} \overset{\mathrm{def}}{=} \boldsymbol{\nabla} \phi^{\mathrm{s}}$. This is done on each RVE with given prolongation conditions. Here, we choose Dirichlet boundary conditions , i. e. $\phi^{\mathrm{s}} = 0$ on $\Gamma_\square$, whereby the pertinent RVE-problem becomes: For given values of the macroscale variables $\bar{\phi}$ and $\bar{\boldsymbol{g}}$, compute the subscale field ϕ^{s} that satisfy the system

$$\langle \boldsymbol{\nabla} (\delta\phi^{\mathrm{s}}) \cdot \boldsymbol{J} \rangle_\square = 0, \tag{11}$$

for all possible $\delta\phi^{\mathrm{s}}$ that are sufficiently regular and which vanish on $\Gamma_\square$. We note that the macroscale prolongations ϕ^{M} are completely defined (varies linearly) on $\Omega_\square$.

Our objective is to determine the mapping

$$L_\square \mapsto \langle \boldsymbol{J} \rangle_\square (L_\square) \tag{12}$$

and to study how this mapping differs between 3D and 2D SVEs of mesoscale concrete models. This is done by solving Eq. (12) given a macroscale gradient $\bar{\boldsymbol{g}} = [-1\ 0\ 0]^{\mathrm{T}}$ for SVEs of varying $L_\square$.

6 2D SVEs

The 2D SVEs are generated from cutting a 3D SVE into a number of 2D slices, see Figure 3. The same boundary conditions are applied to the 3D and 2D SVEs. The mean values of all slices are then compared to the single result obtained for the corresponding 3D SVE. In this way, the 2D/3D comparison becomes meaningful since comparison is made on the same topology.

[2] Superscripts M denotes macroscale, whereas s denotes subscale.

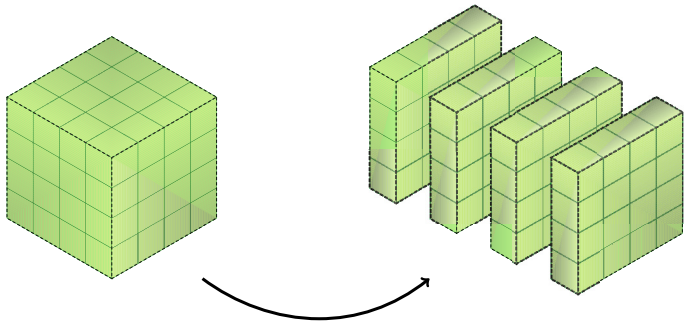

Fig. 3 3D SVE cut into 2D slices

7 Numerical Examples

7.1 3D/2D Comparison

The numerical example compares the first component of the homogenized flux tensor, $\langle \boldsymbol{J} \rangle_1$, as a function of the SVE size[3] denoted $L_\square$. The RVE size based on the numerical results becomes $L_{\text{RVE}} \overset{\text{def}}{=} 10\,\text{cm}$ since convergence has been reached for this value of $L_\square$. The cement paste was assigned a unit diffusivity of $D_\text{c} = 1\,\text{cm}^2/\text{s}$, for simplicity, and $D_\text{a} = 0\,\text{cm}^2/\text{s}$. The ITZ layer is omitted in the example.

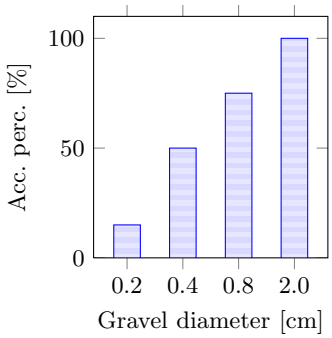

Fig. 4 Sieve curve SVEs used in the numerical example

Forty 3D SVEs were generated for each $L_\square$ all having an aggregate volume fraction, n_a, of 0.45 with the sieve curve shown in Figure 4. Each 3D SVE was cut into 69 2D slices. Thus, μ_{2D} is the mean value of $40 \times 69 = 2760$ SVE slices for each $L_\square$.

[3] "size" refers to side length of the cube.

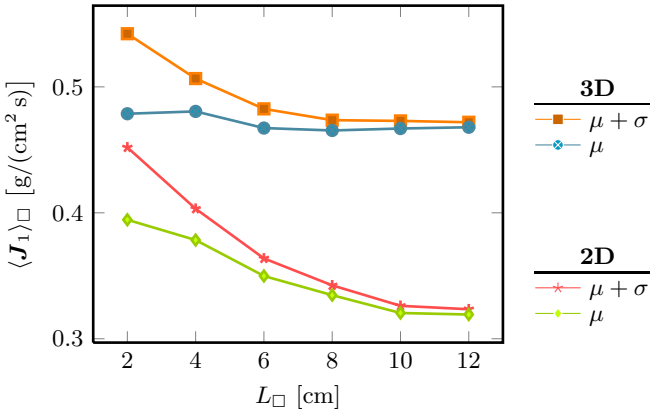

Fig. 5 Homogenized flux versus size of SVE. Average values denoted μ and corresponding standard deviations denoted σ.

The results are shown in Figure 5; they show that the 2D results in general are lower than the corresponding ones for 3D. The reason for this is probably that the out of plane solution in the 2D case is locked; hence, for the 2D case the diffusion substance has only two directions (over or under) to bypass an aggregate but in the 3D case a third direction (around) is enabled. For $L_\square = 10\,\text{cm}$, $\mu_{2D} \approx 0.7\mu_{3D}$; i.e. the 2D SVE homogenized diffusivity is about 70 % of the corresponding 3D value.

7.2 The Effect of ITZ

The same computations as —●— and —■— in Figure 5 were carried out again now including the ITZ in the mesoscale model and the results are shown in Figure 6.

The results in Figure 6 show that it is possible to increase the effective diffusivity by utilizing the ITZ implementation as a model parameter. The results also show the robustness of the implementation as the mean values, -■-, in practice become independent of the SVE size, $L_\square$. Only the spread in results, -●-, varies and decreases with increasing $L_\square$, as expected.

The value $D_{\text{ITZ}} \times t = 0.15 D_{\text{c}}$ has manually been calibrated such that $\langle \boldsymbol{J}_1 \rangle_\square$ gets close to a value of $1\,\text{g}/(\text{cm}^2\,\text{s})$, i.e. corresponding to a diffusivity of pure cement paste. The outcome of this numerical example is that the over-all effect of the aggregates is that they do not change the diffusivity of the bulk material. This is achieved by the implementation of ITZ in the model. In this way, the product $D_{\text{ITZ}} \times t$ becomes a useful tool for calibrating the model with experimental data.

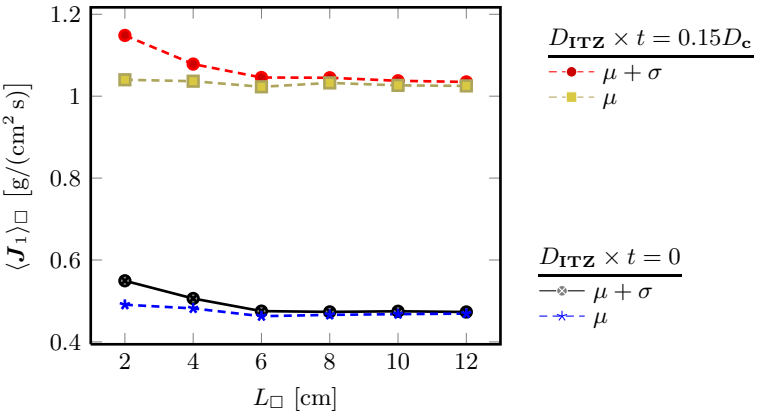

Fig. 6 Numerical results with ITZ included in the SVEs. The results for $D_{\mathrm{ITZ}} \times t = 0$ are the same as those presented in Figure 5. $\langle \boldsymbol{J}_1 \rangle = 1\,\mathrm{g/(cm^2\,s)}$ corresponds to an effective diffusivity equal to that of pure cement.

7.3 Computational Time

The computational work for this paper has been carried out on a standard laptop machine having 4 GB of RAM with a dual-core processor running Windows 7. The implementation is made in MATLAB and is parallelized to reduce computational time.

The average computational time for one 3D SVE is approximately 20 min, and approximately 0.5 min for one 2D SVE, but since the multiple SVEs can be run in parallel the total time is governed by the number of processors available.

8 Conclusions and Outlook

A 3D model of heterogeneous mesoscale concrete was presented and employed in the context of computational homogenization. The algorithm on which the model is based generates a random structure of aggregates embedded in cement paste. Any sieve curve is possible as input for the algorithm and any (realistic) aggregate content is possible to obtain.

The numerical examples presented in the paper shows that the difference between a 3D and 2D model in terms of effective diffusivity differ approximately by a factor 0.7. The numerical results further show that the ITZ implementation is robust and can be used to calibrate/adjust the effective diffusivity of cement with embedded aggregates in it, i.e. concrete. With the ITZ included in the model, it is possible to increases the effective diffusivity of concrete in an easy and consistent manner.

The next step is to use 3D SVEs to determine effective material properties as a function of aggregate volume fraction, as was done in previous work (in

2D), see Nilenius et al. [11]. The effect of ITZ on the numerical results will further be investigated so that the model can be calibrated with experimental data. Additionally, both Dirichlet and Neumann boundary conditions will be applied to obtain upper and lower bounds, respectively, on the effective material properties.

References

[1] Asahina, D., Bolander, J.E.: Voronoi-based discretizations for fracture analysis of particulate materials. Powder Technology 213(1-3), 92–99 (2011) ISSN 00325910, http://linkinghub.elsevier.com/retrieve/pii/S0032591011003330, doi:10.1016/j.powtec.2011.07.010 252

[2] Bentz, D.P., Garboczi, E.J., Snyder, K.A.: National Institute of Standards, and Technology (U.S.). A hard core/soft shell microstructural model for studying percolation and transport in three-dimensional composite media. U.S. Dept. of Commerce, Technology Administration, National Institute of Standards and Technology (1999) 252

[3] de Berg, M., Cheong, O., van Kreveld, M., Overmars, M.: Computational Geometry: Algorithms and Applications, 3rd edn. Springer-Verlag TELOS, Santa Clara (2008) ISBN 3540779736, 9783540779735 253

[4] Caballero, A., Lopez, C., Carol, I.: 3D meso-structural analysis of concrete specimens under uniaxial tension. Comput. Methods Appl. Mech. Engrg. 195(52), 7182–7195 (2006) ISSN 00457825, doi:10.1016/j.cma.2005.05.052 252

[5] Garboczi, E.: Multiscale Analytical/Numerical Theory of the Diffusivity of Concrete. Adv. Cem. Based Mater. 8(2), 77–88 (1998) ISSN 10657355, doi:10.1016/S1065-7355(98)00010-8 252

[6] Hain, M., Wriggers, P.: Numerical homogenization of hardened cement paste. Computational Mechanics 42(2), 178–7675 (2007) ISSN 0178-7675, doi:10.1007/s00466-007-0211-9 252

[7] Hain, M., Wriggers, P.: Computational homogenization of micro-structural damage due to frost in hardened cement paste. Finite. Elem. Anal. Des. 44(5), 233–244 (2008) ISSN 0168874X, doi:10.1016/j.finel.2007.11.020 252

[8] Hedenblad, G.: Moisture permeability of mature concrete, cement mortar and cement paste. PhD thesis, Div. of Building Materials LTH, Lund university (1993) 252

[9] Idiart, A.E., López, C.M., Carol, I.: Chemo-mechanical analysis of concrete cracking and degradation due to external sulfate attack: A meso-scale model. Cement and Concrete Composites 33(3), 411–423 (2011) ISSN 09589465, http://linkinghub.elsevier.com/retrieve/pii/S0958946510001939, doi:10.1016/j.cemconcomp.2010.12.001 249

[10] Kim, S., Al-rub, R.K.A.: Meso-scale computational modeling of the plastic-damage response of cementitious composites. Cement and Concrete Research 41(3), 8–8846 (2011) ISSN 0008-8846, doi:10.1016/j.cemconres.2010.12.002 249

[11] Nilenius, F., Larsson, F., Lundgren, K., Runesson, K.: Macroscopic diffusivity in concrete determined by computational homogenization. Int. J. Numer. Anal. Meth. Geomech. (2012), doi:10.1002/nag.2097 258

[12] Ostoja-Starzewski, M.: Material spatial randomness: From statistical to representative volume element. Probabilistic Engineering Mechanics 21(2), 112–132 (2006) ISSN 02668920, http://linkinghub.elsevier.com/retrieve/pii/S0266892005000433, doi:10.1016/j.probengmech.2005.07.007 250

[13] Wang, L., Ueda, T.: Mesoscale modeling of water penetration into concrete by capillary absorption. Ocean Engineering 38(4), 519–528 (2011) ISSN 00298018, doi:10.1016/j.oceaneng.2010.12.019 249

Meso-Scale Analysis Considering Effect of Fiber Inclination in Fiber Reinforced Cementitious Composites

Hiroki Ogura[1], Minoru Kunieda[2], and Hikaru Nakamura[2]

[1] Shimizu Corporation,
Institute of Technology, Tokyo, Japan
ogura_h@shimz.co.jp
[2] Nagoya University,
Dept. of Civil Engineering, Nagoya, Japan

Abstract. This paper introduces meso-scale modeling of fiber reinforced cementitious composites, which can consider the effect of fiber inclination. Fibers and matrix are modeled separately in this model, and each fiber is randomly arranged within the specimen models. The feature of this analytical model is to evaluate fiber resistance by calculating the pullout angle and the pullout displacement of each fiber. In order to investigate the effect of the pullout angle of the fibers on the load carrying capacity, fiber pullout analysis and bending analysis was conducted. It was confirmed that bending tests were more adequately represented by the modeling taking into consideration the pullout angle than by one without considering the pullout angle.

1 Introduction

There are a wide variety of short fiber reinforced cement composites. One of the materials is Strain Hardening Cementitious Composites (SHCC) that exhibit strain hardening and multiple cracking in tension. Quantitative material design methods considering the properties of matrix, fiber and their interface should be established. In addition, numerical models to simulate the fracture process including crack width and crack distribution for the material are needed.

Bolander & Saito [1], for instance, conducted 2-D parametric analysis in which short fibers were discretized as beam elements to examine the effect of the fiber distribution on the mechanical performance of the resulting composite. The authors have also proposed a numerical model for 3-D analysis of SHCC tensile fracture, in which the salient features of the material meso-scale (i.e. matrix, fibers and their interface) are discretized [2-3]. This model has the following characteristics: (1) the fibers with a specific length are randomly arranged as discrete entities within the specimen models; (2) crack patterns can be estimated in addition to the improvement of mechanical response due to fiber bridging. It has

N. Kringos et al. (Eds.): *Multi-Scale Model. & Charact. of Infrastruct. Mater.,* RILEM 8, pp. 261–272.
DOI: 10.1007/978-94-007-6878-9_19

been confirmed that the proposed model can adequately simulate the tensile failure of SHCC including crack patterns [2].

This paper describes the aforementioned meso-scale modeling, which can consider the effect of fiber inclination. In order to investigate the effect of pullout angle of the fiber on load carrying capacity, fiber pullout analysis and bending analysis was conducted.

2 Outline of Rigid-Body-Spring Model (RBSM)

In this study, the concrete matrix (hereinafter, matrix) is represented by a 3-D RBSM [4]. Fig. 1 shows an example of a pair of Voronoi cells composing the element stiffness matrix in the RBSM. These Voronoi cells are assumed to be rigid bodies with 6 degrees of freedom. Six springs are placed on each boundary plane of each cell, in the normal (1 spring) and tangential (2 springs) directions to the boundaries, and rotational direction (3 springs).

The material properties (tensile strength, elastic modulus, and fracture energy) of the matrix are adopted as the mechanical properties of the normal and tangential springs, whereas the mechanical properties of the rotational springs are assumed based on the literature [5]. As the tensile model of the normal spring, a linear elastic model is employed up to the tensile strength, and a bilinear softening branch in accordance with a 1/4 model is considered after cracking. Tensile fracture energy is taken into consideration in the model. For the tangential springs, the Mohr-Coulomb fracture criterion is applied to represent the shearing behavior of concrete [6].

When using a RBSM, the onset and propagation of cracks are strongly affected by the mesh size and shape. Therefore, such dependence is minimized by adopting Voronoi discretization based on randomly placed seed points.

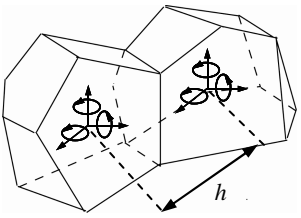

Fig. 1 Voronoi cells and defined freedom degree

3 Modeling of Fiber Action after Cracking

3.1 Outline of Modeling

Short fibers are arranged in elements assuming the specimen size to be analyzed, as shown in Fig. 2(a). Random numbers are used for the arrangement to decide

first vertex and angle. As shown in Fig. 2(b), a zero-size spring is placed on a point where a fiber crosses a boundary of two Voronoi cells, and the force transfer by fibers across a crack plane (hereinafter, fiber bridging force) acts on the spring. The embedment length l_e is also calculated for each fiber. Note that the embedment length l_e should be defined on the short side, as it is assumed that pullout behavior of the fiber will prevail at shorter embedment lengths.

A model based on pullout behavior that includes the pullout angle of the fibers is proposed. One of the characteristics is to calculate the fiber length between the crack planes l_c shown in Fig. 2(c). l_c is used to assume the length of fiber pullout displacement. With this method, fiber resistance can be analyzed, even if only shear deformations are excessive without crack opening. In addition, the pullout angle θ_f of each fiber is calculated in each analytical step to consider the change in θ_f depending on the direction of the shear deformation. θ_f is calculated from P and P' (Fig. 2(c)), where P and P' are points where a fiber crosses a boundary of two cells after deformation.

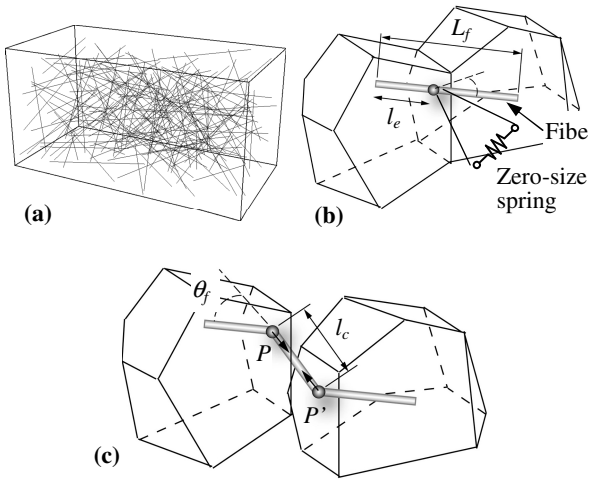

Fig. 2 **(a)** Discretized fiber; **(b)** fiber location and zero-size spring; **(c)** modeling fiber bridging force against shear deformation

In this model, the fiber bridging force is calculated by the steps shown in Fig. 3. Half of l_c is assumed to be the length of fiber pullout displacement before softening of the fiber bridging force-displacement relationship. After softening, pullout displacement is assumed to be equal to l_c. The shape of slip distribution is determined through the analysis of single fiber pullout tests. If the shape of slip distribution is known, then the bond stress distribution is determined from the bond stress-slip relationship. The fiber bridging forces across cracks can then be calculated by integrating the bond stress distribution in the direction of the fiber axis.

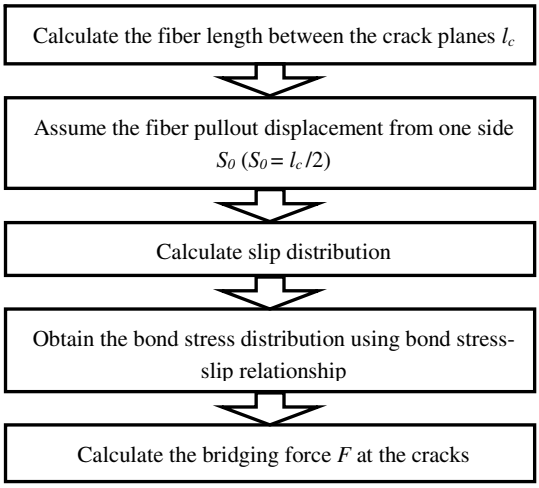

Fig. 3 Procedure for calculation of fiber bridging force

At this stage, the slip distribution of a fiber and the bond stress-slip relationship are necessary. These are identified in the same manner as the existing method [3], by conducting analysis of single fiber pullout bond testing [7] as stated in the following chapter.

3.2 Effect of the Pullout Angle

Li et al. [8] revealed the increase of pullout resistance in the inclined fiber pullout test. It has also been experimentally confirmed that the strength of the inclined fiber itself was decreased due to surface damage during the pullout process. Therefore, in this study, the effect of the pullout angle θ_f is calculated using the following equations [8]:

$$F = F^n e^{f \cdot \theta_f} (\theta_f \leq 45°) \tag{1}$$

$$\sigma_{f_u} = \sigma^n_{f_u} e^{-f' \theta_f} \tag{2}$$

where F = pullout load (N), F^n = pullout load at pullout angle of 0° (N), f = snubbing coefficient (0.4), θ_f = pullout angle of fiber (rad), σ_{fu} = rupture strength of fiber (MPa), σ^n_{fu} = rupture strength at pullout angle of 0° (MPa), f'= strength reduction factor (0.3).

The effect of improvements in pullout resistance is not considered in cases with a pullout angle 45° or more, because reduction of maximum pullout loads is confirmed in the case of polypropylene (PP) fiber used in this study. This was caused by the matrix spalling at the fiber exit point as reported in [7].

4 Analysis of Fiber Pullout Behavior

In this chapter, the pullout behavior of fibers embedded in the matrix is verified, through an analysis using the modeling described in Sect. 3.

4.1 Pullout Behavior of a Single Fiber

As shown in Fig. 4(a), tensile analysis was conducted for a uniaxial tension test using specimens containing fibers [7]. While this test conducted by Dong et al. used a specimen containing five strings of fiber, this analysis applied the model with a single embedded fiber, as shown in Fig. 4(b). The entire body of the matrix is divided into two elements and the fiber is arranged, so that a predetermined embedment length and pullout angle are given. In order to represent the separator in the test (Fig. 4(a)), 1MPa is used for the physical properties of the concrete elastic modulus in the analysis, to prevent matrix from being loaded. Table 1 shows the characteristics of the short fiber and fiber-concrete interface used for the analysis. Note that the rupture strength varies depending on the pullout angle, as shown in Equation 2. The properties of the interface are identified by a similar method in an existing study [3].

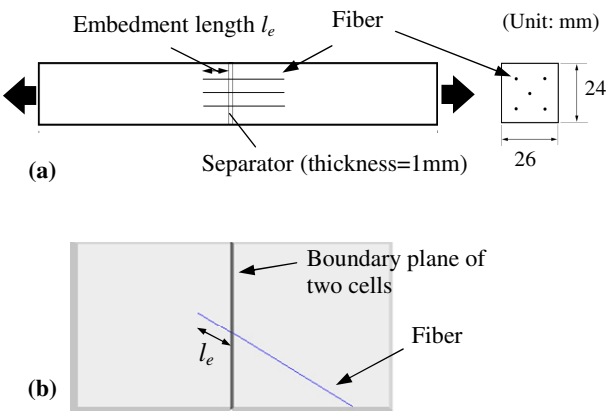

Fig. 4 (a) Outline of fiber pullout test (Dong et al.); (b) analysis model

The fiber bridging force-crack width curves in the case of θ_f = 0° and the deformation are as shown in Figs. 5(a) and 5(b), respectively. Once the loads reach a peak, the fiber is found to be pulled out with a moderate reduction of loads. In the case of embedment length l_e = 15mm, the value of displacement at complete pullout is 15mm. As mentioned above, the results from this model are controlled by the pullout behavior of the shorter embedment length on each fiber.

Fig. 6 shows the relationship between the bridging force per fiber and the crack width in the case of pullout angle $\theta_f > 0°$. In the case of $l_e = 24$mm, fiber rupture was observed before the pullout process. Since the maximum load in these curves depends on the rupture strength σ_{fu} calculated from Equation 2, the maximum load of $\theta_f = 75°$ was lower than that of $\theta_f = 30°$.

Table 1 Material properties for the analysis

Fiber (PP)	Length L_f (mm)	48
	Diameter d_f (mm)	0.8
	Strength at pullout angle of 0° σ^n_{fu} (MPa)	308
	Elastic modulus E_f (GPa)	9.8
Fiber/concrete interface (bond)	Frictional bond strength τ_i (MPa)	1.8
	Chemical bond strength τ_s (MPa)	4.0
	Bond stiffness G (MPa/mm)	60

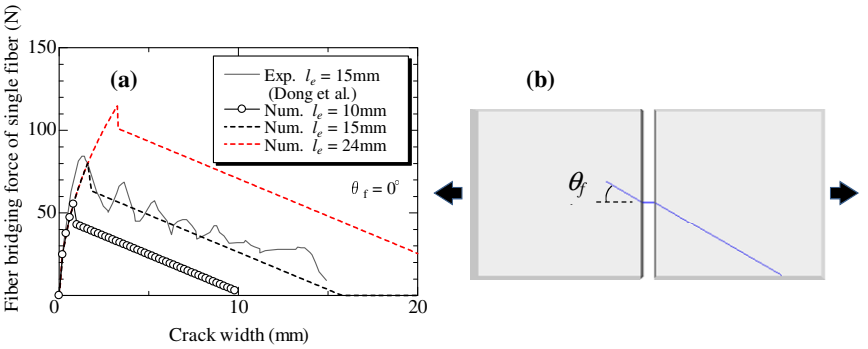

Fig. 5 (a) Fiber bridging force-crack width curves ($\theta_f = 0°$); **(b)** deformation in analysis

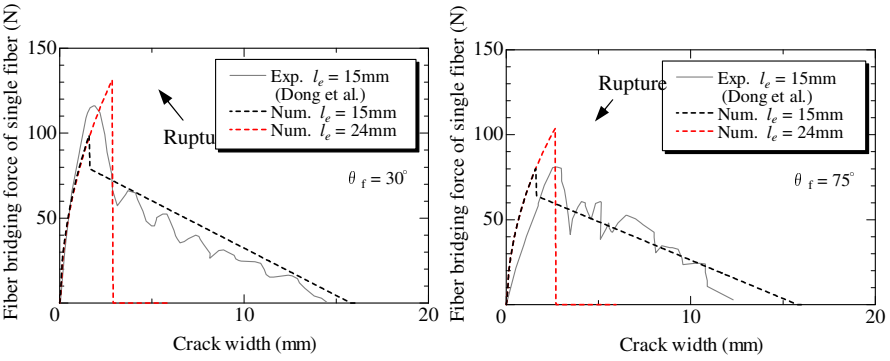

Fig. 6 Fiber bridging force-crack width curves ($\theta_f > 0°$)

In the case of $\theta_f = 75°$, the initial stiffness is smaller in the experimental results than the analytical results. This is assumed to be because a deceptive pullout displacement was increased by the matrix spalling at the exit point in the experiments, once the angle becomes $\theta_f > 45°$, as reported in [7]. The effect of this phenomenon is not considered in this modeling. As a result, the initial stiffness of the fiber bridging force-crack width curves in the case of $\theta_f > 45°$ is overestimated.

4.2 Pullout Behavior of Multiple Fibers

The authors conducted uniaxial tensile analysis and shear analysis to verify the fiber pullout behavior of a specimen containing multiple fibers. Fig. 7 shows the analysis model. The fibers are placed in the specimen using random numbers. The fiber volume fraction V_f is 1.0%. The fibers shown in Table 1 are used in the same as the analysis in Sec. 4.1, and 1MPa is used for the physical properties of the concrete elastic modulus, so that the concrete would not resist stress. Forced displacement is given to reach mode I and mode II fracture. Moreover, two snubbing coefficients f (Equation 1) and two strength reduction factors f' (Equation 2) were adopted with the same specimen, as shown in Table 2.

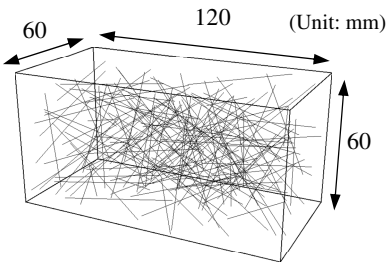

Fig. 7 Discretized fibers (V_f = 1.0%)

Table 2 Analysis cases of fiber pullout behavior simulations

Case	Fracture mode	Snubbing coefficient f	Strength reduction factor f'
Case 1	Mode I	0.4	0.3
Case 2			0.0
Case 3		0.0	0.3
Case 4	Mode II	0.4	0.3

The deformation results taken from the analysis are shown in Fig. 8. The bridging fibers appear blue in the figure, while the ruptured fibers and the pulled-out fibers appear red and green, respectively. Some ruptured fiber is observed in the figures, and the ratio of ruptured fibers in bridging fibers at the displacement = 3mm is tabulated in Table 3.

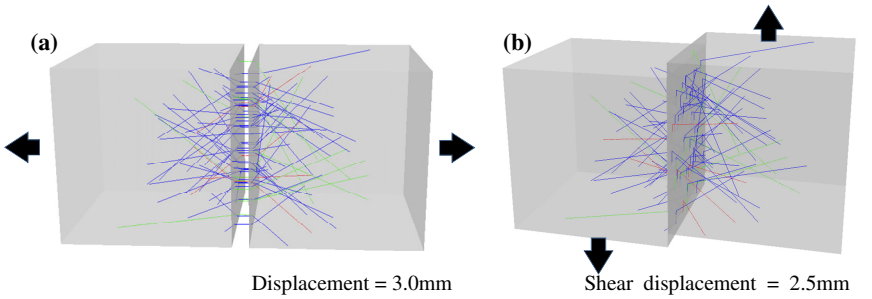

Fig. 8 Deformation **(a)** Case 1 (tensile analysis); **(b)** Case 4 (shear analysis)

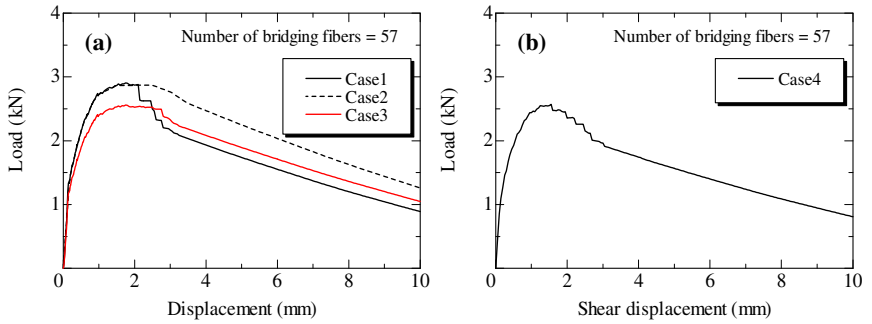

Fig. 9 Load-displacement curves **(a)** tensile analysis; **(b)** shear analysis

The load-displacement curves are shown in Fig. 9. For all cases, the load reaches a peak until displacement reaches 2mm. After that, the fibers are found to be pulled out with moderate reduction of loads, from the results of both tensile analysis and shear analysis. In case 1, the maximum load is higher than case 3 as shown in Table 3. It is noted that the load at displacement = 5mm is smaller than case 3 due to larger softening behavior. The reason is that the number of ruptured fibers is larger due to fiber bridging force increased by considering the snubbing coefficient. On the other hand, in case 2, the rupture strength of the inclined fiber is not decreased because adopted strength reduction factors f is equal to zero.

Table 3 Analysis results of fiber pullout behavior simulations

Case	Number of ruptured fibers / number of bridging fibers (%)	P_{max} (kN)	P_{dis5} (kN)
Case 1	8.8	2.88	1.74
Case 2	0.0	2.88	2.25
Case 3	1.8	2.53	1.89
Case 4	10.5	2.57	1.56

P_{max}: maximum load, P_{dis5}: load at displacement = 5mm

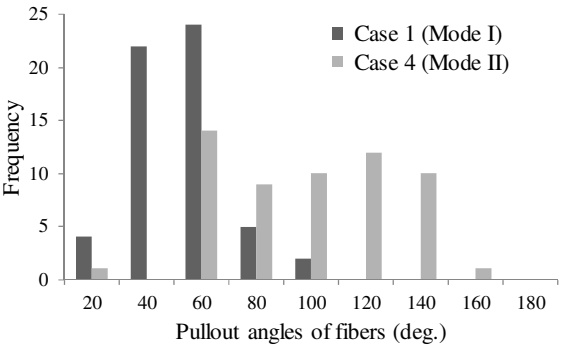

Fig. 10 Frequency distribution of pullout angles of fibers

Therefore, the load at displacement = 5mm is higher because fiber rupture does not occur, as shown in Table 3.

Fig. 10 shows the frequency distribution of pullout angles of fibers. In the tensile analysis, the fibers are pulled out in vertical directions against cracks. Therefore, the pullout angle θ_f is less than 90°. On the other hand, the result showed that the pullout angle of the shear analysis is distributed from acute angles to obtuse angles.

5 Analysis of Bending Behavior

In this chapter, analysis is conducted on bending tests to investigate the effect of pullout angle of the fiber on load carrying capacity.

5.1 Outline of Bending Analysis

Fig. 11(a) shows the outline of the bending test. Experiments were conducted by changing the volume fraction V_f of PP fiber to 0.71 and 1.18%. The fibers were 30mm in length, 1.0mm in diameter.

The analysis model is shown in Fig. 11. Short fibers of the specified length are randomly arranged in the elements assuming the specimen size. As for the boundary conditions, forced vertical displacement is given to the elements located in loading plate. The material properties of concrete for the analysis are given as elastic modulus 31.0GPa based on the results of the material test. The properties of the fiber and the interface between fibers and concrete are identical to Table 1 in Sect. 4.1. The rupture strength at a pullout angle 0° is 70% of the nominal value, as confirmed in the previous tests that the value should be less than the nominal value disclosed by the manufacturer [8]. In the case of V_f = 1.18%, two snubbing coefficients f (Equation 1) were also adopted.

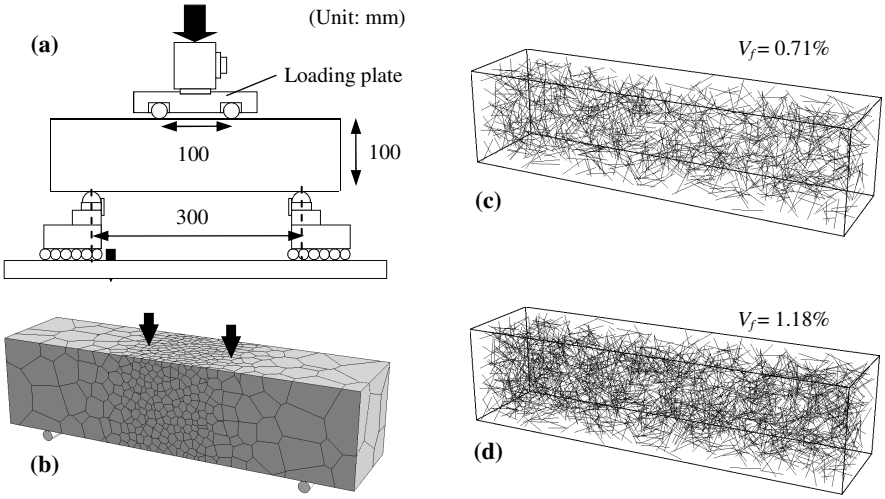

Fig. 11 **(a)** Overview of the bending test; **(b)** modeling of discretized concrete; **(c)**, **(d)** fiber distribution

5.2 Results of Analysis

Fig. 12 shows the simulated crack pattern, and Fig. 13 shows the load-deflection curves of the bending analysis, as well as experimental results. In the case of V_f= 1.18%, the results of f = 0.4 and 0.0 are included. The figure reveals that the analysis reproduced the load decrease after the crack onset and load increase again due to the fiber bridging force. In the case of f = 0.4, the load-displacement relationships obtained by the analysis adequately express the experimental results. On the other hand, the load after the crack onset in the case of f = 0.0 is underestimated in comparison with the experimental result.

Fig. 14 shows the relative frequency distribution of pullout angles of fibers. This result is similar to the trend of case 1 in Fig. 10, so that this suggests the fracture behavior of this bending analysis is close to mode I fracture.

From the results of the experiment and analysis, the proposed analysis method is verified to be sufficient to capture the principal aspects of the reinforcing effects of fibers. Moreover, these results suggest bending tests were more adequately represented by the modeling taking into consideration the pullout angle of the fibers than by one without considering the pullout angle.

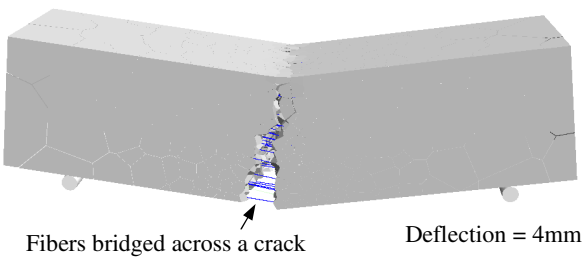

Fig. 12 Crack pattern in bending analysis ($V_f = 0.71\%$)

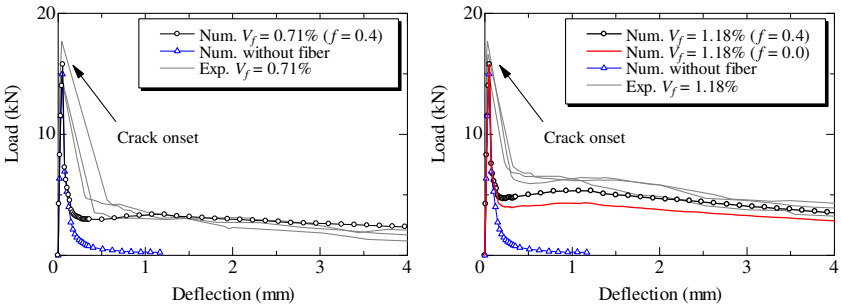

Fig. 13 Load-deflection curves in simulated bending test

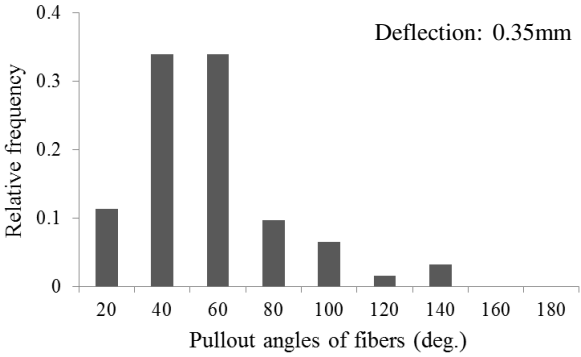

Fig. 14 Relative frequency distribution of pullout angles of fibers ($V_f = 0.71\%$)

6 Conclusions

This paper has introduced the meso-scale modeling for fiber reinforced concrete. The findings obtained include the following:

(1) By the analysis conducted on bending tests of fiber reinforced concrete, this model adequately simulated the mechanical response represented by the load-displacement relationships.

(2) By the modeling taking into consideration the pullout angle of the fibers, bending tests were more adequately represented than using the modeling without considering the pullout angle.
(3) A pullout angle of each fiber can be evaluated in addition to the macro mechanical responses by the use of this analysis.

References

1. Bolander, J.E., Saito, S.: Discrete modeling of short-fiber reinforcement in cementitious composites. Advanced Cement Based Materials 6, 76–86 (1997)
2. Kunieda, M., Ogura, H., Ueda, N., Nakamura, H.: Tensile fracture process of Strain Hardening Cementitious Composites by means of three-dimensional meso-scale analysis. Cement & Concrete Composites 33, 956–965 (2011)
3. Ogura, H., Kunieda, M.: Analysis for flexural failure behavior of PET fiber rein-forced cementitious composites by means of 3-D meso-scale analysis. In: Proc. of 33rd IABSE Symposium, pp. 272–273. CD-ROM (full paper) (2009)
4. Kawai, T.: New discrete models and their application to seismic response analysis of structures. Nuclear Engineering and Design 48, 207–229 (1978)
5. Bolander, J.E., Berton, S.: Cohesive zone modeling of fracture in irregular lattices. Proc. of Fracture Mechanics of Concrete Structures FraMCoS-5, 989–994 (2004)
6. Saito, S.: Fracture analyses of structural concrete using spring network with random geometry. Doctoral thesis, Kyushu University (1999)
7. Dong, H., Okubo, S., Fukui, K.: The bond characteristics with concrete and the effects of embedding angle and length of polyolefin fibers. Journal of MMIJ 126, 654–659 (2010)
8. Kanda, T., Li, V.C.: Interface property and apparent strength of high-strength hydrophilic fiber in cement matrix. Journal of Materials in Civil Engineering, ASCE 10(1), 5–13 (1998)

Development of an Adherence Energy Test via Force-Displacement Atomic Force Microscopy (FD-AFM)

Troy Pauli*, Will Grimes, Mengxi Wang, Peng Lu, and Shin-Che Huang

Western Research Institute, University of Wyoming, 365 North 9th Street, Laramie, WY 82072, USA
{tpauli,rgrimes1,shuang,mwang1,plu1}@uwyo.edu

Abstract. Significant progress has been made in regard to scientific and engineering investigations to understand the influence of material composition and mechanical properties of bituminous binder on damage and self-healing behavior associated with pavement fracture. It is well known that visco-elastic materials tend to exhibit rate and temperature dependant behavior in terms of fracture energy. As a representative of this class of materials, rate-dependant fracture should be expected for bituminous binders. Preliminary results are reported regarding a study using an atomic force microscopy (AFM) technique developed to determine if rate dependence is a factor in micro-scale adhesive fracture of bitumen thin-films. The technique involves creating then fracturing a standardized adhesive contact between bitumen and glass by application of a direct tensile force to the contact at various rates. The work required to fracture the standard contact is measured and recorded as a function of temperature and separation rate. The results of this study show that bitumen fracture energy is indeed rate and temperature dependant. The study also shows that bitumen derived from different crude sources exhibit differing fracture rate (and temperature) dependencies.

1 Introduction

Bituminous binder is a vital component in the composition of a majority of roads and highways constructed worldwide. Furthermore, the composition, which dictates the mechanical properties of bitumen, has a direct impact on the durability of roads and highways. A typical bitumen pavement structure is effectively a composite of bituminous binder, aggregate and aggregate fines constructed at a predetermined thickness on top of a rigid base. Compared to gravel pavements, the

* Corresponding author.

N. Kringos et al. (Eds.): *Multi-Scale Model. & Charact. of Infrastruct. Mater.,* RILEM 8, pp. 273–284.
DOI: 10.1007/978-94-007-6878-9_20

stability of an asphalt pavement is greatly enhanced due primarily to the adhesive nature of the bituminous binder portion of the composite structure. Atomic force microscopy (AFM) is a technique capable of studying material properties such as the "adhesiveness" of bituminous binders at a scale that is relevant considering the size of fine filler particles in the bitumen-aggregate fines mastic. AFM is a specific type of scanning probe microscopy that has been used to provide insight into surface topography and phase composition of bituminous binder films. This technique can also provide insight into the mechanical and adhesion properties of bituminous binders.

Many publications have reported on the use of AFM imaging techniques to characterize topographic and phase structuring in bitumen films (Pauli et al. 2011). One focus of these works has concentrated on AFM imaging and subsequent compositional characterization of peculiar microstructural features that are commonly detected in some bitumen, colloquially referred to as "bee" structures (Pauli et al. 2011; Jäger et al. 2004; De Moraes et al. 2010; Schmets et al. 2010; Zhang et al. 2011; Sourty et al. 2011; Dourado et al. 2012). Other researchers also report on the utilization of nano-mechanical AFM techniques, including force-distance, colloidal probe and nano-indentation AFM to investigate bituminous binder mechanical and physicochemical properties (Jäger et al. 2004; Dourado et al. 2012; Tarefder and Zaman 2010; Tarefder et al. 2010; Allen 2010). In the present paper the development of a test procedure is reported to investigate adherence energy of bitumen thin-films utilizing force-displacement AFM. This technique utilizes a glass micro-bead colloidal tip cantilever as the test probe. These studies were undertaken to quantify surface energy of bituminous binder as it relates to fatigue and self healing behavior compounded by moisture intrusion in bitumen-mastic systems and pavements (Pauli et al. 2003; Wang 2012; Lu 2012; Hefer and Little 2005).

Adherence energy is defined by the reversible or equilibrium work of adhesion, $\mathcal{G}_0$, and energy lost due to dissipative processes $\mathcal{W}_{diss}$, including plastic flow (Shull 2002; Packham 1996), where

$$\mathcal{G} = \mathcal{G}_0 + \mathcal{W}_{diss} \tag{1}$$

To accommodate for rate υ and temperature T dependence in $\mathcal{G} \equiv \mathcal{G}(\upsilon, T)$, $\mathcal{W}_{diss}$ is further defined in terms of a viscoelastic loss function Ψ, expressed by

$$\mathcal{W}_{diss} = \mathcal{G}_0 \Psi(\upsilon / \upsilon^*, a_T) = \left[\mathcal{G}_0 (\upsilon / \upsilon^*)^n \right]_T \tag{2}$$

given a characteristic crack speed υ^* and a rate-temperature dependent shift factor a_T (Ahn and Shull 1996; Crosby and Shull 1999).

2 Experimental Approach

2.1 Equipment and Apparatus

A Quesant Q-Scope 250 AFM was modified to perform the experiments conducted in this study (Figure 1). The main components of the system are an AFM-microscope, which includes a piezo-scanner/controller, probe/tip and laser/detector. In addition the system also includes a nano-positioning stage (Mad City Labs, Inc.) with a peltier thermal stage heater and an environmental chamber. The cantilevers used for FD-AFM experiments reported here were custom fabricated by NovaScan Technologies and are reported by the manufacturer to have a nominal spring constant of 14 N/m and a nominally spherical glass micro-bead tip with radius of approximately 5000 nm.

The AFM controller in this system provides a voltage to a piezo-scanner to initially establish contact between the cantilever tip and sample surface. A laser and quadphoto detector monitor the deflection signal of the cantilever. The AFM electronics and feedback loop are used to establish a controlled preloading of an adhesive contact. The nano-positioning stage controller and software package (NanoRoute-3D®) is used to retract the sample from the cantilever at a controlled rate, thus rupturing the contact. A National Instruments® data acquisition module and associated PC programmed with LabVIEW are used to monitor signals for the stage position, feedback loop and cantilever deflection as a function of time.

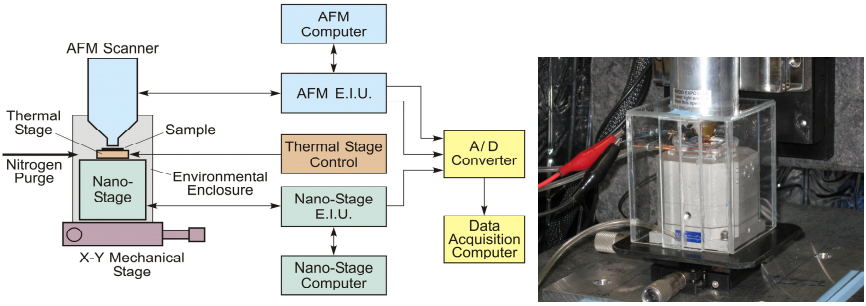

Fig. 1 Schematic diagram of AFM stress-strain system [left] and photograph [right] of the AFM-scanner, nano-stage, thermal stage and environmental enclosure assembly

2.2 Cantilever Calibration and Sample Preparation

A calibration procedure was performed for each cantilever used in the study. A different cantilever was used for each of the asphalt samples investigated. Duplicate investigations, using the same cantilever, were conducted for some of the samples considered in this study. Calibration was performed on a non-compliant surface (a glass microscope slide in this case).

Calibration involves engaging the probe on the glass surface, locking the AFM feedback loop, moving the nano-stage a specified distance and recording the cantilever deflection as a voltage signal. The stage motion divided by the cantilever deflection voltage gives the cantilever calibration factor.

The experiments involve forming an adhesive contact between the AFM tip and a glass surface using a bitumen sample as the 'glue' and subsequently measuring the work required to rupture this contact as a function of temperature and separation rate. A procedure entailing an engage and loading step, performed with the AFM piezo-scanner is used to create a reproducible adhesive contact. The contact formation and loading step is followed by a pull-off and re-contact step, performed using the nano-positioning stage. Values of stage and cantilever offset, hold time, rate of stage motion and voltage-vs.-time slopes $\xi_s = \Delta V_s / \Delta t_s$ and $\xi_c = \Delta V_c / \Delta t_c$, respectively, are used to convert raw signal data to force curves.

SHRP asphalt-bitumen AAA-1, AAD-1 and AAM-1 (Jones 1993), selected for their diverse compositional and rheological properties, were prepared as thin-films on glass microscope slides (borosilicate glass). Films ranging in thickness from 100-nm to 2-µm (Figure 2) were prepared for experiments in which film thickness was used as a controlled variable. It should be pointed out that other methods of sample preparation including heating and smearing bitumen were found to be inadequate for achieving the precision of film thickness sought for this test protocol. Findings from this study will be reported elsewhere. Solutions for spin casting were prepared by dissolving 0.083 ± 0.002-g of sample in 1.00 ± 0.01-mL of toluene. Prior to spin casting, sample solutions were allowed to stand for approximately 24 hours to assure complete dissolution of the asphalt material. For spin-cast films a 1.0-µL "drop" of the solution was deposited on a spinning glass microscope slide, using an ICL (International Crystal Laboratories) Roto-film™ Rotational Casting Thin Film Maker fitted with a custom fabricated robotic arm that controlled a precision syringe pump (Harvard Apparatus). Samples were spin-cast at a revolution speed of 500-RPM.

Freshly spin-cast samples were annealed in an oven for approximately 5 hours at 120℃. This practice results in a stiffened material assumed to be free of any

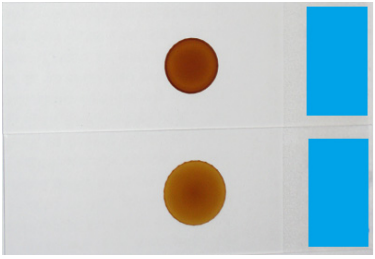

Fig. 2 Solvent spin cast bitumen films (2±0.1-µm [top] and 1±0.1-µm [bottom])

residual solvent potentially retained after spin-casting and better represents a mix plant aged bitumen binder. All materials tested were prepared under identical conditions for consistency but future testing will likely involve the influence of sample conditioning on adherence energy properties. After cooling samples to room temperature in air, sample thickness was determined using a Filmetrics F20 instrument. The measured film thicknesses for the spin-cast samples was generally in good agreement with the thickness as calculated based on the measured dimensions of the film and the film's mass and density.

2.3 FD-AFM Testing Procedure

FD-AFM experiments were conducted employing the following protocol: A sample film was placed on the thermal stage, which is affixed to the nano-positioning stage. The nano-positioning/thermal stage and AFM scanner with calibrated cantilever are enclosed within an environmental chamber and purged with inert gas. A test temperature is selected and the sample is heated/cooled and equilibrated for 10 minutes. Once the test temperature is attained the cantilever is then engaged with the sample with the AFM in Z-height imaging mode using the engage routine supplied with the AFM to apply and maintain a compressive contact load of approximately 2.5-μN. The compressive loading is maintained for 1-minute after which the AFM feed-back signal is deactivated and the test is initiated by retracting the nano-positioning stage down and away from the cantilever at a pre-selected rate. The actual motion of the stage is a linear retract, hold, then approach back into contact with the sample. This protocol is repeated 5 or more times, each at a new randomly selected location on the sample surface.

3 Results and Discussion

3.1 Theory and Data Analysis

Determination of adherence energy in the present case actually involves the rupture of a cohesive contact between a glass micro-bead affixed to the end of an AFM micro-cantilever initially in contact with a thin bitumen film plated on a glass microscope slide. The total potential energy involved in the contact-ruptured AFM cantilever–substrate system (Cappella et al. 1997; Cappella and Dietler 1999) may be expressed as the sum of potentials

$$U_{tot} = U_c(\delta_c) + U_s(\delta_s) + U_{cs}(\delta_{cs}) \tag{3}$$

relating to the forces which act over displacements D, δ_c and δ_s, where the sum of these three distances defines the total displacement of the cantilever/piezo-scanner system,

$$Z = D + \left(\delta_c + \delta_s\right) \tag{4}$$

Each energy potential is defined in terms of a force, where the Hookian force exerted (compressive or tensile) on or by the cantilever is defined by (with minus sign denoting tensile force)

$$F_c = -k_c \delta_c \tag{5}$$

The Hookian force which describes (tensile) deformation of the sample is further defined by

$$F_s = -k_s \delta_s \tag{6}$$

Finally, an "action-at-a-distance" attraction/repulsion force exists during approach between the cantilever tip and substrate surface, defined by

$$F(D) = -\partial U_{cs} \big/ \partial D = -C \big/ D^n \tag{7}$$

In this set of equations k_c and k_s define the force constants of the cantilever and the deforming sample material, respectively, and D defines the distance over which "action-at-a-distance forces act, where n and C both depend on the type of interaction (e.g., van der Waals forces, polar interactions, Hydrogen bonding, etc.). The total potential energy of a contact-rupture system is expressed by

$$U_{tot} = \int \left(F_c + F_s + F(D)\right) dZ \tag{8}$$

For a glass micro-bead/glass substrate system which exhibits virtually no sample deformation $Z = D + \delta_c \approx \delta_c$. For a glass micro-bead-bitumen thin-film system $Z \approx \delta_s + \delta_c$. Thus, for tests involving a bitumen film, the total potential energy term is simplified to

$$U_{tot} = \int \left(F_c + F_s\right) dZ \tag{9}$$

The potential energy specifically associated with the "work to break contact" $\mathcal{W}$, is derived by integrating force-displacement curves (Grierson et al. 2005; Maugis 1992; Schwarz 2003), over the distance $\left(Z_1 - Z_0\right)$. Figure 3 depicts a force-displacement (distance) curve denoting limits of integration.

Work to break contact versus reduced rate data are then fit to an energy dissipation function identical in form to the adherence energy expression presented in Eqs. 1 and 2.

$$\mathcal{W} = \mathcal{W}_0 \left[1 + (\upsilon / \upsilon^*)^n\right]_T \tag{10}$$

Given the results from regression analyses for work to break contact versus reduced rate data, where $\mathcal{W}_0$ and n represent regression coefficients, adherence energies are reported in a plot as a function of reduced rate. Here equilibrium work of adhesion values, $\mathcal{G}_0$, are calculated from the pull off force $|F_c| = k_c |\delta_c|$, where

$$\mathcal{G}_0 = k_c \delta_c / 2\pi R \tag{11}$$

Thus, adherence energy $\mathcal{G}_T(\upsilon)$ determined at a given temperature as a function of rupture rate is derived as

$$\begin{aligned} \mathcal{G}_T &= \left\{ \left(\mathcal{W}_0 / \mathcal{A} \right) \left[1 + (\upsilon / \upsilon^*)^n \right] \right\}_T = \left\{ \mathcal{G}_0 \left[1 + (\upsilon / \upsilon^*)^n \right] \right\}_T \\ &= \left[\mathcal{G}_0 + \mathcal{G}_0 \Psi(\upsilon / \upsilon^*) \right]_T \end{aligned} \tag{12}$$

In Eq. 12 $\mathcal{A} = \mathcal{W}_0 / \mathcal{G}_0$ is a yet undefined contact area of the probe tip with sample just prior to adhesive (or cohesive) failure.

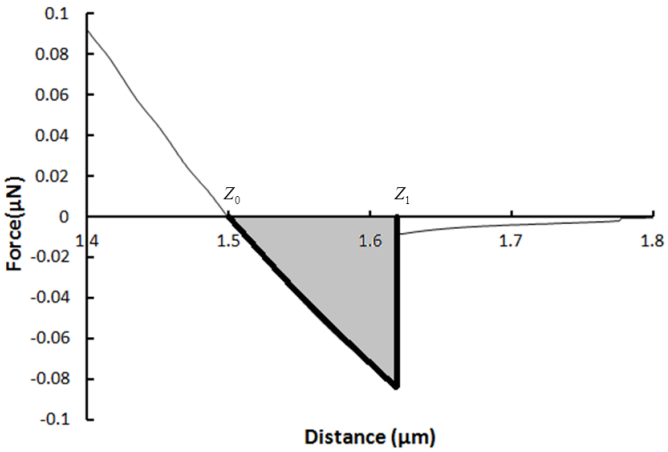

Fig. 3 Force-displacement (distance) curve denoting limits of integration

3.2 Work to Break Contact

Work to break contact values are evaluated by numerically integrating a rate dependent set of forces curves employing a trapezoidal technique,

$$U_{tot}(test) \approx \mathcal{W} = \int_{Z_0}^{Z_1} FdZ = \int_{Z_0}^{Z_1} \left(F_c + F_s\right) dZ$$
$$\approx \left(\left(Z_1 - Z_0\right)/2N\right) \sum_{i=1}^{n} \left[F(Z_{i+1}) + F(Z_i)\right] \tag{13}$$

Work to break contact values for a given temperature are plotted as a function of reduced rate (i.e., stage velocity υ per critical crack speed υ^*) where the critical crack speed in this analysis is taken to be the slowest stage velocity for a given set of test measurements. Figure 4 depicts a set of FD-AFM deflection-distance curves measured at different rupture rates for SHRP asphalt AAA-1 at 2°C. Here, the change in displacement of the piezo scanner-cantilever assembly at increasing rate $\Delta Z(\upsilon)$ becomes much greater than the average in the cantilever deflection $\overline{\delta}_c(\upsilon)$. This is observed because the material is stretched or elongated (referred to as necking) to a much greater extent with increasing rupture rate compared to the deflection of the cantilever, where $\delta_c(\upsilon = 20\mu m/s) \ll \delta_s(\upsilon = 20\mu m/s)$. The deflection averaged over all rate and temperature data is used to calculate $\overline{\mathcal{G}}_0$, where $\overline{\mathcal{G}}_0 = k_c \overline{\delta}_c / 2\pi R$, which represents the equilibrium work of adhesion based on the DMT contact model (Grierson et al. 2005; Maugis 1992; Schwarz 2003), assumed to be a nearly constant-value material property over this narrow temperature range.

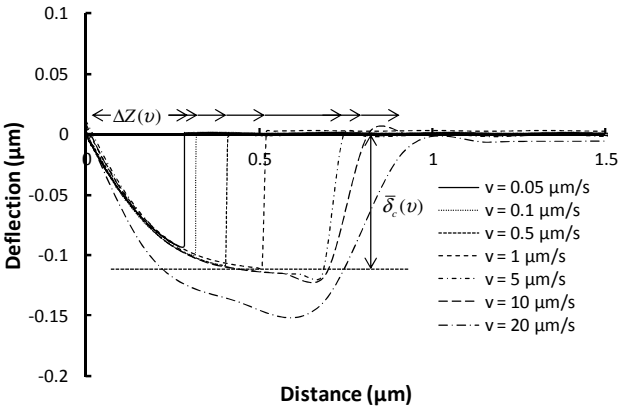

Fig. 4 FD-AFM deflection-distance curves measured at different rupture rates for SHRP asphalt AAA-1 at 2°C

3.3 Adherence Energy (Rate and Temperature Dependence)

Table 1 lists regression coefficients $\overline{\mathcal{U}}_0$ (μN · μm) and *n*, contact areas, equilibrium work of adhesion and adherence energies reported at $\upsilon / \upsilon^* = 200$, determined for SHRP asphalt-bitumen AAD-1 (film thickness of ~1000-nm), measured at three different temperatures. Figure 5 depicts adherence energy versus reduced rate plots corresponding to data listed in table 1.

A shift function $n(T)$, where

$$n(T) = \left[\beta_1 + \beta_2 \left(T/T^*\right)\right] / \left[1 + \beta_3 \left(T/T^*\right)\right] \tag{14}$$

based on the regression coefficients *n* and reduced temperatures T/T^*, where $T^* = 2°C$ may be calculated to relate the temperature dependence to $\mathcal{G}(\upsilon, T)$ for a given film thickness

$$\mathcal{G}(\upsilon, T) = \mathcal{G}_0 \left[1 + \Psi(\upsilon / \upsilon^*)^{n(T)}\right] \tag{15}$$

Here $\beta_1 = 0.1005$, $\beta_2 = -0.0007$ and $\beta_3 = -0.0285$ for this particular set of data.

Table 1 Regression coefficients $\mathcal{U}_0$ and n, cross-sectional area of the neck $\mathcal{A}_0$ and equilibrium and adherence energy $\overline{\mathcal{G}}_0$ and $\mathcal{G}$, respectively, reported for SHRP asphalt-bitumen AAD-1 (1-μm thick film), determined at different temperatures

T (°C)	$\mathcal{U}_0$ (μN · μm)	n	$\overline{\mathcal{G}}_0$ (mJ/m^2)	$\mathcal{A} = \mathcal{W}_0 / \mathcal{G}_0$ (μm^2)	$\mathcal{G}(\upsilon / \upsilon^* = 200)$ (mJ/m^2)
2.0	0.6013	0.5138	(54.0)	9.51	147
26.7	0.6455	0.4736		8.77	172
42.0	0.7065	0.3904		7.23	221

The data presented here strongly suggests that rupture of the bond occurs in the bitumen film where the material deforms as an elongated neck prior to loss of contact and not at a glass-bitumen interface. This assumption is based on observed values in $\overline{\mathcal{G}}_0$ which are typical of cohesive energies of organic compounds and polymers. It is observed that adherence energy increases with increasing temperature, where it is assumed that with increasing temperature the bitumen exhibits more plastic flow, and hence stretches more prior to rupture of the adhesive/cohesive bond. This trend in adherence energy also corresponds with decreasing cross-sectional neck area $\mathcal{A} = \mathcal{W}_0 / \mathcal{G}_0$. It is also noted that small

differences in $\overline{\mathcal{G}}_0$ values occur for data sets measured for the same bitumen material. It is well documented in FD-AFM testing that test variables including cantilever properties (e.g., reported spring constants and bead diameter), calibration procedures, instrument thermal drift, and a host of other potential test condition variables may contribute to experimental error, thus, it should be understood that the reported values are not necessarily exact. However, the trends exhibited by the various bitumen samples, particularly rate dependencies, are real.

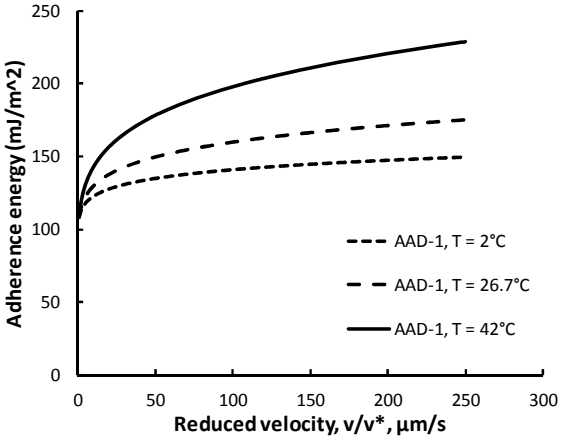

Fig. 5 Adherence energy versus reduced rate plots for SHRP asphalt AAD-1 (1-µm thick film) measured at three different temperatures

Adherence energy determined as a function of temperature and rate was also measured for SHRP core asphalt-bitumen AAA-1 and AAM-1 in this preliminary study. These materials exhibited similar material response to the type of testing reported here, but also differed from each other in terms of the magnitude adherence energy suggesting that adherence energy is a crude source dependant property of the material. Results of this work will to be reported elsewhere. Another part of this preliminary study investigated the effect of film thickness on adherence energy. The results of the complete study including film thickness dependency, sample conditioning and testing conditions will be reported elsewhere.

4 Conclusion

In this paper preliminary results were presented from a study using an atomic force microscopy (AFM) technique developed to determine if rate dependence is a factor in bituminous finder fracture at a nano-scale. The technique involves creating and subsequently fracturing a standardized adhesive contact between

bitumen and glass by application of a direct tensile force to the contact at various rates. The work required to fracture the standard contact is measured and recorded as a function of temperature and separation rate. The results of this preliminary study show that bitumen adherence energy is indeed a rate dependant phenomenon. The study also shows, and will be reported on in a future publication, that bituminous binders derived from different crude sources exhibit differing rate and temperature dependent adherence energy.

Acknowledgements. The authors gratefully acknowledge the Federal Highway Administration, U. S. Department of Transportation, for their financial support: Contract No. DTFH61-07-D-00005 and DTFH61-07-H-00009.

References

Ahn, D., Shull, K.R.: JKR Studies of Acrylic Elastomer Adhesion to Glassy Polymer Substrates. Macromolecules 29(12), 4381–4390 (1996)

Allen, R.G.: Structural characterization of micromechanical properties of asphalt using atomic force microscopy. Master of Science Thesis, Civil Engineering, Texas A&M University (2010)

Cappella, B., Dietler, G.: Force-Distance Curves by Atomic Force Microscopy. Surface Science Reports 34, 1–104 (1999)

Cappella, B., Baschieri, P., Frediani, C., Miccoli, P., Ascoli, C.: Force-Distance Curves by AFM: A Powerful Technique for Studying Surface Interactions. IEEE Engineering in Medicine and Biology, 58–65 (1997)

Crosby, A.J., Shull, K.R.: Adhesive Failure Analysis of Pressure-Sensitive Adhesives. Journal of Polymer Science: Part B: Polymer Physics 37, 3455–3472 (1999)

De Moraes, M.B., Pereira, R.B., Simão, R.A., Leite, L.F.M.: High temperature AFM study of CAP 30/45 pen grade bitumen. Journal of Microscopy 239(Pt. 1), 46–53 (2010)

Dourado, E.R., Simao, R.A., Leite, L.F.M.: Mechanical properties of asphalt binders evaluated by atomic force microscopy. Journal of Microscopy 245(Pt. 2), 119–128 (2012)

Grierson, D.S., Flater, E.E., Carpick, R.W.: Accounting for the JKR–DMT Transition in Adhesion and Friction Measurements with Atomic Force Microscopy. J. Adhesion Sci. Technol. 19(3-5), 291–311 (2005)

Hefer, A., Little, D.: Adhesion in bitumen-aggregate systems and quantification of the effects of water on the adhesive bond. Research Report ICAR-505-1 (2005)

Jäger, A., Lackner, R., Eisenmenger-Sittner, C., Blad, R.: Identification of four material phases in bitumen by atomic force microscopy. Road Materials and Pavement Design, EATA, 9–24 (2004)

Jones, D.R.: SHRP Materials Reference Library, Asphalt Cements: A Concise Data Compilation. Technical Report SHRP-A-645, Strategic Highway Research Program, National Research Council, Washington DC (1993)

Lu, P.: Development of an AFM-based fracture test for asphalt film thickness dependence of viscoelastic fracture. Master of Science, Thesis, Chemical Engineering, University of Wyoming (2012)

Maugis, D.: Adhesion of Spheres: the JKR-DMT Transition using a Dugdale Model. Journal of Colloid and Interface Science 150(1), 243–269 (1992)

Packham, D.E.: Work of adhesion: contact angles and contact mechanics. Int. J. Adhesion and Adhesives 16, 121–128 (1996)

Pauli, A.T., Grimes, R.W., Beemer, A.G., Turner, T.F., Branthaver, J.F.: Morphology of Asphalts, Asphalt Fractions and Model Wax-doped Asphalts Studied by Atomic Force Microscopy. International Journal of Pavement Engineering 12(4), 291–309 (2011)

Pauli, A.T., Grimes, W., Huang, S.C., Robertson, R.E.: Surface energy studies of asphalts by AFM. American Chemical Society Division of Fuel Chemistry Preprints 48(1), 14–18 (2003)

Schmets, A., Kringos, N., Pauli, T., Redelius, P., Scarpas, A.: On the existence of wax induced phase separation in bitumen. International Journal for Pavement Engineering 11(6), 555–563 (2010)

Schwarz, U.D.: A generalized analytical model for the elastic deformation of an adhesive contact between a sphere and a flat surface. Journal of Colloid and Interface Science 261, 99–106 (2003)

Shull, K.R.: Contact mechanics and the adhesion of soft solids. Materials Science and Engineering 36, 1–45 (2002)

Sourty, E.D., Tamminga, A.Y., Michels, M.A.J., Vellinga, W.-P., Meijer, H.E.H.: The microstructure of petroleum vacuum residua for bituminous concrete: a microscope approach. Journal of Microscopy 241(Pt. 2), 132–146 (2011)

Tarefder, R.A., Zaman, A.M., Uddin, W.: Determining hardness and elastic modulus of asphalt by nanoindentation. International Journal of Geomechanics, 106–116 (May/June 2010)

Tarefder, R.A., Zaman, A.M.: Nanoscale evaluation of moisture damage in polymer modified asphalts. J. Mater. Civ. Eng. 22, 714–725 (2010)

Wang, M.: Development of an AFM-based fracture test for bituminous materials: rate-dependence of viscoelastic fracture. Master of Science, Thesis, Chemical Engineering, University of Wyoming (2012)

Zhang, H.L., Wang, H.C., Yu, J.Y.: Effect of aging on morphology of organo-montmorillonite modified bitumen by atomic force microscopy. Journal of Microscopy 242(Pt. 1), 37–45 (2011)

Towards a Multi-scale Framework to Optimize Ageing Resistance of Asphaltic Materials

Prabir Kumar Das*, Niki Kringos, and Björn Birgisson

Division of Highway and Railway Engineering, KTH Royal Institute of Technology, Stockholm, Sweden
prabir.kumar@abe.kth.se

Abstract. This paper describes an ongoing research project that is aiming at developing a comprehensive multi-scale approach to optimize the ageing resistance of asphaltic mixtures. In this, ageing has been focused on oxidative ageing, but allows future extension to other ageing mechanisms. The developed framework considers three different scales: the nano, micro and meso-scale which are defined as the bitumen phase, the mastic phase and the mixture phase, respectively. In nano-scale, atomic force microscopy and calorimetry are coupled to each other to give insight into how bitumen phase separation evolves and the mobility of microstructure changes with temperature and ageing. On the micro-scale, the energy dissipation as a function of ageing is measured and coupled to the phase behavior information from the nano-scale. On the meso-scale a morphology framework is defined, capable of identifying the dominant mixture morphology parameters that control mixture performance under ageing conditions. By coupling the three scales, the dominant parameters that control ageing of asphaltic mixtures can be defined, modeled and analyzed and as such a tool is created that has the potential of enhancing the sustainability of asphaltic mixtures.

Keywords: Ageing, Multi-scale framework, Microstructure, Dissipated energy, Mixture morphology.

1 Introduction

Asphalt concrete is today still the most commonly used material for the top layer of pavements. The material's ability to provide the necessary stiffness and strength via its strong aggregate skeleton, while at the same time offering a damping and self-restoring ability via its visco-elastic bituminous binder, makes it a uniquely qualified material for increased driving comfort and flexible maintenance. This flexibility is, however, dependent on the material's long term performance and changes due to ageing and other environmental-mechanical processes will have a significant impact. Age hardening of asphalt mixtures is an irreversible process,

* Corresponding author.

N. Kringos et al. (Eds.): *Multi-Scale Model. & Charact. of Infrastruct. Mater.,* RILEM 8, pp. 285–295.
DOI: 10.1007/978-94-007-6878-9_21

which starts as soon as the mixture is heated during its production and paving phase and continues over time during the pavement's service life due to chemical changes and environmental interactions. Since ageing of asphalt mixtures leads to a reduction of the durability and an increase in maintenance cost of pavements, having a better handle on this process could have significant economic and environmental benefits.

Age hardening of asphalt mixture will depend on design variables that operate in different scales, for example: the chemical and mechanical properties related to the source of bitumen and mineral filler, the mastic (i.e. the asphalt cement) film thickness, air void size of the mixture, interconnectivity and distribution of airvoids, aggregate gradation and volumetric properties. From the existing literature in this field, it has been observed that most research efforts often only investigate the ageing behavior of one or two individual parameters [e.g 1-3]. Since ageing of the asphalt mixtures is a combined results of material, mixture, construction and environmental parameters, a clear understanding of ageing on the different scales and how these are coupled could lead to enhanced mix design, novel material selections procedures and enhanced long-term performance.

In this paper, a multi-scale framework to capture the ageing process in asphalt mixtures to optimize design that is currently being developed is presented. The framework is mainly based on oxidative ageing, but will enable the inclusion for other type of ageing in the future, such as UV ageing or ageing due to intrinsic chemical changes. As such, the framework is currently focusing on air diffusion by considering a feedback loop on three different scales.

2 Multiscale Ageing Framework Description

In the developed multi-scale framework, the effects on the nano, micro and meso-scale due to ageing are considered, Fig. 1. In this, the *nano-scale* behavior has been investigated utilizing atomic force microscopy (AFM) and differential scanning calorimetry (DSC) on the bitumen level. As the physical properties of bitumen are influenced by the behavior of microstructure at this scale, the prediction of the performance of asphalt pavements is also directly related to this. A detailed knowledge of the microstructure is needed to understand the physico-chemistry of bitumen, which can serve as the direct link between the molecular structure and the rheological behavior [4-5]. Since the AFM has the advantage of imaging almost any type of surface, it opens a window for investigating different variables at the surface, such as different types of aging phenomena, presence of wax or the effect of light or temperature.

On the *micro-scale* level the effects of ageing on the mastic (i.e. the mixture of bitumen with mineral fillers and additives) is investigated by measuring the change of energy dissipation. At this scale it is also possible to investigate the effect of the presence of wax, the source of the bitumen, filler type and temperature on the age hardening and linking it to the nano-scale observations.

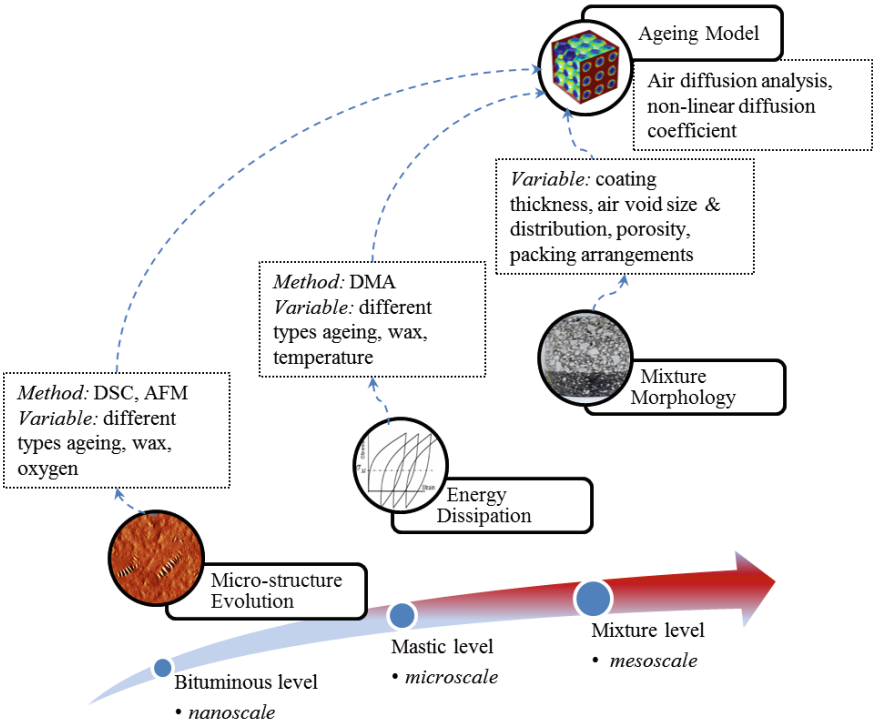

Fig. 1 Schematic depiction of multi-scale ageing framework

On the *meso-scale* level, the parameters that are related to asphalt mixture morphology are being investigated. These are parameters related to the structure or form (i.e. morphology) of the mixtures, such as the airvoid distribution, the aggregate skeleton and the mastic distribution. The meso-scale observations can therefore be easily coupled into this scale via the mastic related parameters. Since the mixture morphology also determines the availability of air within the mixture that can then influence the micro scale processes, the framework couples all the scales in both directions.

The multi-scale framework can thus be used to couple the fundamental phenomena that are active at the lower scales, to the mechanisms on the higher scales and, as such, be utilized to optimize the asphalt mixture design and material selection to diminish deterioration due to ageing.

2.1 Micro-structure Evolution

It is important to understand the fundamental mechanisms that drive the bitumen phase behavior and that cause the microstructure appearance we can observe from surface investigations using, for instance, AFM [6-7]. From

mechanical considerations, interfaces between two materials with different stiffness properties serve as natural stress inducers. This means that when the material is exposed to mechanical and or environmental loading, these interfaces will attract high stresses and are prone to cracking. It is therefore of interest to understand the conditions under which this phase behavior occurs and the speed, or mobility, at which it evolves. For this, bitumen was investigated using AFM in contact mode in which both topography and relative surface stiffness can be obtained simultaneously. The imaging was done at temperatures from 30°C to 60°C, where the heating rate was 1°C/min and rest periods were 10 minutes before starting scanning at each temperature. The same bitumen was then also investigated using differential scanning calorimetry (DSC), to investigate how the thermodynamic behavior would correlate to the observed behavior under the temperature controlled AFM. One reason for combining these two methods is to overcome the limitations that AFM has, being a tool that can only observe surface phenomena. A detail description of the test procedure and the motivations can be found in Das et al. [6].

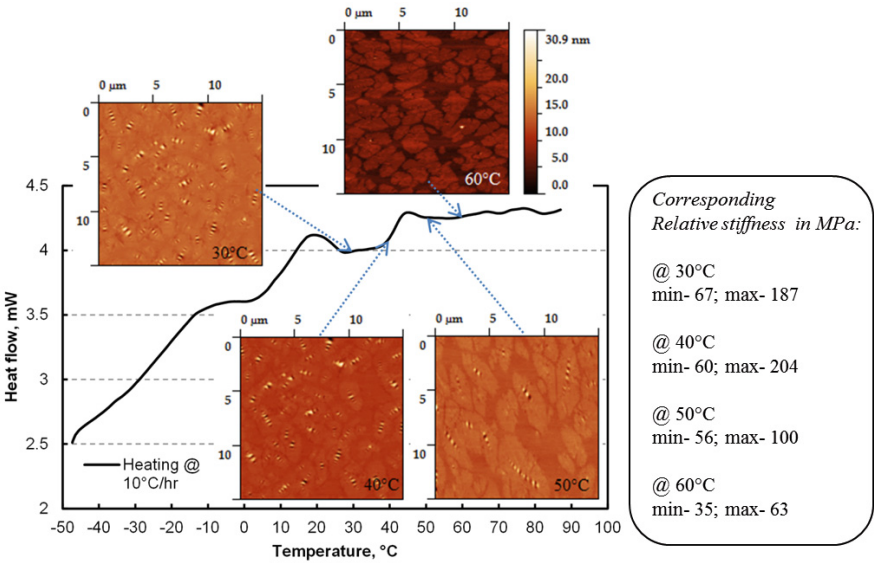

Fig. 2 Investigation of phase separation behavior by using AFM and DSC

From the experiments it became clear that the change of the micro-structures in the bitumen surfaces, observed under the AFM due to a temperature increase, correlated directly with the DSC test results: the appearance of micro-structures is always in the crystallization temperature range of that specific bitumen and the dissolution of these micro-structures is directly related with the melting temperature range (Fig. 2). Since AFM scanning was conducted in contact mode, the reduced modulus was also measured simultaneously with the topographic

image. This modulus reflects the relative stiffness of the bitumen surface. As expected, it was found that with the temperature increasing the average modulus value was decreasing (Fig. 2). Thus based on this, the observed phase separation was related to the wax fraction of the bitumen, as was also concluded by earlier research.

The evolution of these microstructures due to laboratory aging was also investigated using AFM. For this, the bitumen was subjected to both short term (RTFOT, EN 12607) and long term (PAV, EN 14769) aging. Physically, the RTFOT procedure is intended to resemble the ageing of bitumen that happens when the mixture is heated initially, to create enough workability for compaction of the mixture in the field. The PAV is then intended to represent the long-term ageing of bitumen that will happen over time during the pavement's service life. One can of course argue that especially in the latter type of ageing, temperature may create a similar hardening as time would, but is not representing the actual physical phenomenon of oxidative ageing. Nevertheless, these methods are today used to represent the ageing phenomenon and are therefore relevant to investigate further. The corresponding topographic images are shown in Fig. 3. As can be seen from the graphs (a-c), there is a change of microstructures size, shape and quantity changing due to the aging procedure. As mentioned in earlier research, ageing seems to increase the amount of bee structure (Fig 3b) in the case of the RTFOT ageing. In the case of the RTFOT and PAV ageing, not much conclusions can be drawn when comparing the unaged with the aged (Fig 3c). It should also be noted that more extensive research on various bitumen sources has also shown that the phase behavior is very variable depending on the bitumen source, its history and its treatment.

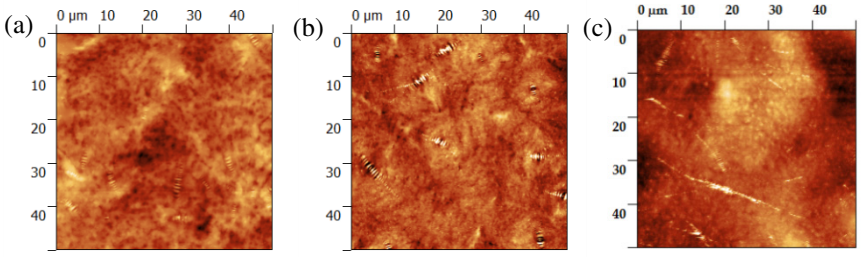

Fig. 3 AFM Topographic image of (a) un-aged, (b) RTFOT aged and (c) RTFOT+PAV aged bitumen at 25°C

2.2 Energy Dissipation

One could generally argue that the more mastic surfaces in an asphalt mixture are exposed to a supply of air, the greater the rate of oxidative ageing would be. Due to ageing, mastic is generally known to become stiffer and less able to dissipate

energy visco-elastically. As discussed in the paper by Hesami et.al in this book, mastic energy dissipation can be measured by performing fatigue testing in a direct tension set up. One example of such accumulated dissipated creep strain energy (DCSE) is shown in Fig. 4. In this test the mastic was prepared with 70/100 penetration grade bitumen uniformly mixed with 20% filler (fly ash in the depicted case). The test was done at 15°C using a dynamic mechanical analyzer from TA Instrument in a stress controlled cyclic load. The load sequence was 1 second loading followed by 9 seconds unloading, repeated for 100 times, during which consequently the force or displacements were measured. From these, the DSCE values can be calculated for each loading cycle. From the figures it can be seen that a steady accumulation of the creep strain is build up inside the material. It is also interesting to see from the overlapping force-displacement cycles that after a large number of cycles the material is no longer able to store much visco-elastic energy and will thus become more brittle and less and less flexible to absorb stresses, making it more susceptible for damage generation. By performing the energy dissipation tests on the same materials as investigated under the AFM, a link can be made between the bitumen phase behavior and the energy dissipation potential of the material. Linking this to the creation of interfaces due to bitumen phase separation and bitumen-filler interphases, the nano- and meso can be linked and the effect of ageing can be seen on both scales.

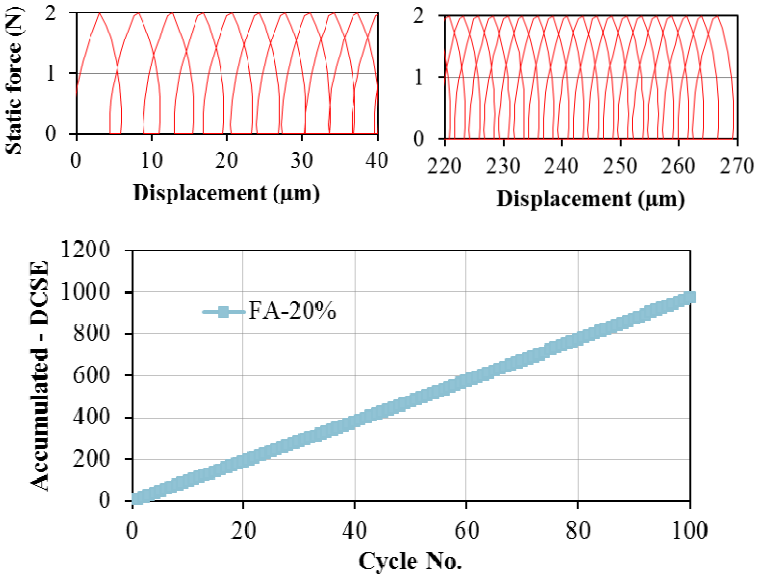

Fig. 4 Accumulated DSCE under repeated creep test

2.3 Asphalt Mixture Morphology Framework

Recently, a new asphalt mixture morphology framework to evaluate the effect of the mix design on the performance has been developed at KTH Royal Institute of Technology in Sweden for both unbound granular materials and asphalt mixtures [8-9]. By modeling the contact between the particles and their interactions, the morphology framework is able to analyze and model different aggregate packing arrangements and its function to the load carrying capacity. It is also able to analyze and model the porespace and mastic distribution based on asphalt design parameters. The framework identifies four different aggregate size groups: oversized structure (OS), primary structure (PS), secondary structure (SS) and filler particles. The latter, together with the bitumen form the mastic, which coats the secondary structure. The mixture of mastic and secondary structure then flow around the primary structure, coating it with the so called 'coating thickness', as shown in Fig. 5. To be able to quantify mixtures in this structured way allows for a direct analysis of the effect of the morphological (design) parameters on the overall mixture performance. Linking the information from this level to the material information from micro- and nano-scales can thus provide a powerful, yet easy to handle framework to optimize asphalt mixtures.

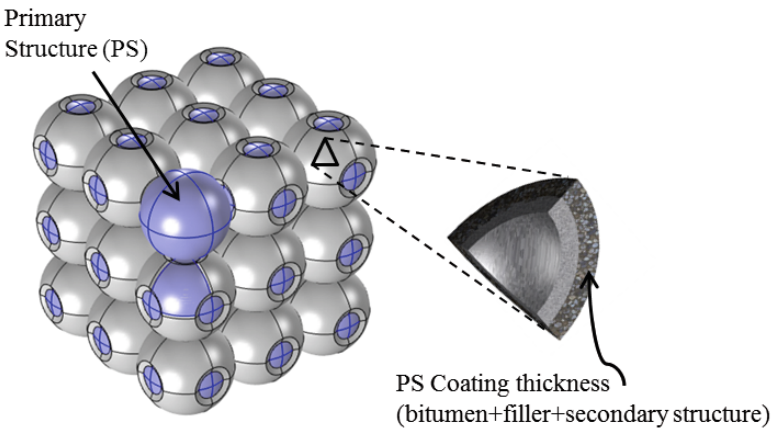

Fig. 5 Illustration of the coating thickness of primary structure

In the case of ageing analysis, earlier the statement was made that accessibility of air to the mixture will affect the ageing risk of the mixture. Yet asphalt mixtures that have the same air void content, can still have different ageing performance [3, 10]. Hence, besides material properties of the components, age hardening of asphalt mixtures is significantly affected by the mixture morphology parameters such as: voids distribution, their interconnectivity and the average size of air voids. The asphalt morphology framework can thus be utilized to investigate the

interplay between the coating thickness around the primary structure, the average air void size in the mixture, the porosity and level of compaction and relate this to ageing propensity.

In [10] a detailed demonstration and validation is given of the asphalt mixture morphology framework for identifying ageing performance. In this, a large dataset of asphalt mixtures from different sources were studied to investigate the effect of degree of mix compaction, bitumen content, average air void size, porosity and aggregate gradation on ageing performance. The relationship between PS coating thickness and age hardening of asphalt mixture with varying material properties was investigated and the dominant effect of the mixture morphology was demonstrated. It was also shown that the developed framework can be successfully utilized to design mixtures with reduced ageing susceptibility. Since mixture morphology is controllable, having insight into how the various morphological parameters influence the mixture's long-term behavior can be of great value to optimize its design, regardless of the individual material properties. By linking this framework into the micro- and nano-scale characterization and modeling efforts as described in this paper, a comprehensive approach can be used to focus attention on the dominant parameters.

2.4 Ageing Model

Bitumen is known to slowly react with the atmospheric oxygen, in which temperature plays an important role as a catalyst. This reaction eventually leads to an overall stiffening of the mixture and reduces its durability under traffic and environmental loading. Several researchers have performed studies to explain the phenomenon of the oxygen diffusion-reaction in bitumen films [11-14]. In the multi-scale framework, the asphalt morphology framework is utilized to analyze air diffusion in the PS coating thickness using the Finite Element Method. The framework opens the window to understand the age hardening effects due to different variables (e.g packing arrangements, porosity, PS coating thickness, temperature).

As an example, a simulation is shown for an idealized aggregate packing in which a constant diffusion coefficient of 1.828E-10 m^2/sec [14] was used to simulate the diffusion, Figure 6. In this case, a simple cubic packing arrangement of primary structures with 10 mm diameter and 0.5 mm coating thickness was employed in a cubic box with full access to air on the outside boundaries. The assumption in this system was that air can diffuse into the mastic coating but not into the primary structure and the air flow is continuous, Fig. 6. By coupling the morphology framework to diffusion analyses, that affect the properties of the mastic (in terms on energy dissipation) that is affecting to the phase behavior of the bitumen, the developed framework allows for a multi-scale characterization of oxidative ageing of asphalt mixtures.

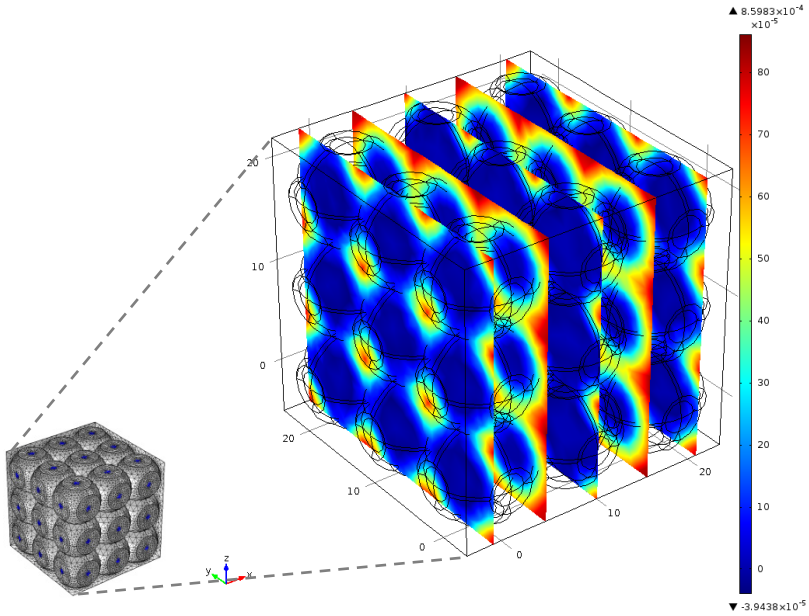

Fig. 6 Oxygen diffusion through PS coating thickness

3 Discussion and Further Research

In this paper a newly developed multi-scale framework has been presented that is coupling bitumen phase behavior at the nano-scale, to its energy dissipation properties on the micro-scale and the mixture morphology properties on the meso scale. As such, the framework can link the in-time changes to the mastic as a function of the airvoid distribution, the mastic film thickness and the diffusion properties to the changes of the physical properties of the material due to loss of flexibility in absorbing energy without damage generation to the bitumen phase behavior, which, in its turn, is an effect of the bitumen refinery and source. As such, the framework has great potential to enhance the understanding of the dominant phenomenon that cause ageing in asphaltic mixtures.

On the nano-scale, AFM and DSC tests are employed to understand how the phase separation in bitumen surface evolves and the mobility of microstructure changes with temperature and ageing. On the micro level, which is here defined as the mastic, the energy dissipation can be measured and links the bitumen phase-behavior to the filler effects. On the meso-scale level, here defined as the mixture level, the mixture morphology parameters are defined, determined and linked to a diffusion analyses.

In the continuation of this research, the developed multi-scale framework will be employed and further coupled via experimental and numerical analyses to demonstrate the practical application of it to enhance mixture design. From these analyses, direct guidelines will be developed that can help material producers and pavement engineers to optimize their procedures. Since in current practice these scales are not linked to each other in any fundamental way, the new framework can contribute to a new multi-scale approach to enhance the sustainability of the future infrastructure.

Acknowledgments. The authors would like to kindly acknowledge the Swedish Transport Administration (Trafikverket) for providing financial support for the project under which this research was performed.

References

[1] Petersen, J., Harnsberger, P.: Asphalt aging: dual oxidation mechanism and its interrelationships with asphalt composition and oxidative age hardening. J. Transport. Res. Rec. 1638(1), 47–55 (1998)
[2] Lu, X., Isacsson, U.: Effect of ageing on bitumen chemistry and rheology. J. Constr. Build. Mater. 16(1), 15–22 (2002)
[3] Nukunya, B., Roque, R., Tia, M., Birgisson, B.: Evaluation of VMA and other volumetric properties as criteria for the design and acceptance of superpave mixtures. J. Asso. of Asphalt Paving Tech. 70, 38–69 (2001)
[4] Lesueur, D., Gerard, J.-F., Claudy, P., Létoffé, J.M., Planche, J.-P., Martin, D.: A structure-related model to describe asphalt linear viscoelasticity. J. of Rheol. 40(5), 813–836 (1996)
[5] Loeber, L., Sutton, O., Morel, J., Valleton, J.-M., Muller, G.: New direct observations of asphalts and asphalt binders by scanning electron microscopy and atomic force microscopy. J. Microsc. 182(1), 32–39 (1996)
[6] Das, P.K., Kringos, N., Wallqvist, V., Birgisson, B.: Micromechanical investigation of phase separation in bitumen by combining atomic force microscopy with differential scanning calorimetry results. Int. J. Road Mater. Pavement Des. (2013), doi:10.1080/14680629.2013.774744
[7] Schmets, A., Kringos, N., Pauli, T., Redelius, P., Scarpas, T.: Wax Induced Phase Separation in Bitumen. Int. J. Pavement Eng. 11(6), 555–563 (2010)
[8] Tatek, F.Y., Birgisson, B., Jelagin, D., Guarin, A.: Packing theory-based framework to evaluate permanent deformation of unbound granular materials. Int. J. Pavement Eng. 14(3), 309–320 (2013)
[9] Lira, B., Jelagin, D., Birgisson, B.: Gradation-based framework for asphalt mixture. Mater. Struct. (2013), doi:10.1617/s11527-012-9982-3
[10] Das, P.K., Kringos, N., Jelagin, D., Birgisson, B.: Investigation of the asphalt mixture morphology influence on its ageing propensity. Mater. Struct. (submitted 2013)
[11] Dickinson, E.J.: The diffusion-controlled reaction of oxygen with films of bituminous binders. Aust. Road Res. 14(3), 121–132 (1984)

[12] Tuffour, Y.A., Ishai, I.: The diffusion model and asphalt age-hardening. J. Asso. of Asphalt Paving Tech. 59, 73–92 (1990)
[13] Dickinson, E.J.: Prediction of the hardening of the bitumen in pavementsurfacings by reaction with atmospheric oxygen. Int. J. Road Mater. Pavement Des. 1(3), 255–280 (2000)
[14] Herrington, P.R.: Diffusion and reaction of oxygen in bitumen films. Fuel 94, 86–92 (2012)

Effects of Nano-sized Additives on the High-Temperature Properties of Bituminous Binders: A Comparative Study

Ezio Santagata*, Orazio Baglieri, Lucia Tsantilis, and Giuseppe Chiappinelli

Department of Environmental, Land and Infrastructure Engineering,
Politecnico di Torino, 24, corso Duca degli Abruzzi, 10129 Turin, Italy
{ezio.santagata,orazio.baglieri,lucia.tsantilis,
giuseppe.chiappinelli}@polito.it

Abstract. In this paper the effects of different nano-sized additives on the high temperature properties of bituminous binders are evaluated and compared. Single wall carbon nanotubes (CNTs) and two different types of nanoclay (NC) were employed in combination with a single base bitumen. Two percentages of CNTs (0.5 and 1%) and three percentages of NCs (1, 3 and 6%) were used. The investigation included viscosity, oscillatory shear loading and multiple stress creep-recovery tests performed at different temperatures. Experimental results indicate that CNTs and one type of NC at high dosages may have beneficial effects on the high temperature properties of bituminous binders.

Keywords: Carbon nanotubes, nanoclays, bituminous binders, rheology, rutting.

1 Introduction

It is well recognized that modification of bituminous binders may provide significant improvements to the performance of asphalt pavements. For this reason the use of modified binders has seen a widespread diffusion in road construction and rehabilitation in the last decades [1, 2]. In addition to traditional modifiers such as polymers, in recent years various alternative materials have been considered and in particular the emergence of nano-technologies in many engineering fields [3] has motivated a number of researchers in evaluating the use of nano-materials for such a purpose. Among the commonly available nano-sized products, carbon nanotubes (CNTs) and nanoclays (NCs) currently represent the most promising nano-modifiers for the enhancement of performance characteristics of bituminous materials.

Xiao et al. [4, 5] indicated that carbon nano-particles can enhance the rheological properties of bituminous binders after short-term and long-term aging

* Corresponding author.

N. Kringos et al. (Eds.): *Multi-Scale Model. & Charact. of Infrastruct. Mater.,* RILEM 8, pp. 297–309.
DOI: 10.1007/978-94-007-6878-9_22

treatments. Santagata et al. [6] showed that when added in a sufficiently high percentage, CNTs lead to a significant improvement in terms of stiffness and elasticity at low frequencies and high temperatures, thus providing beneficial effects to potential rutting resistance. In their studies on unaged binders, Amirkhanian et al. [7, 8] also recommended the use of a relatively high percentage of carbon nano-particles (> 1%) to increase resistance to permanent deformation at high temperatures. Khattak et al. [9] found that modification of neat bituminous binders with carbon nano-fibres improves fatigue and rutting resistance to an extent which depends on the mixing procedure employed for the dispersion of nano-fibres.

Jahromi and Khodaii [10] observed that nanoclay modification can enhance stiffness and aging resistance of bituminous binders, also indicating that nanoclays can have a significant effect on the internal structure of bituminous blends. You et al. [11] employed different nanoclays with variable percentages finding that modified binders are significantly more viscous and stiffer. Polacco et al. [12] investigated the use of nanoclay as the third component in polymer modified binders, showing that final rheological properties are influenced by the adopted mixing procedure. Results obtained by Ghile [13] indicate that mechanical properties of asphalt mixtures such as indirect tensile strength, creep and fatigue resistance, can be improved by modification with cloisite.

The study presented in this paper focused on the rheological characterization at high temperatures of nano-modified bituminous binders obtained by combining a single base bitumen and three different types of nano-sized additives (one CNT and two NCs). On the basis of the obtained experimental results, effects of the different nano-additives on material properties were analyzed and compared.

2 Materials

A single base binder and three different nano-sized additives were used in the experimental investigation.

The base bitumen (70/100 penetration grade) was provided by a refinery located in North-Western Italy. Results of its preliminary characterization are given in Tables 1 and 2, which respectively refer to SUPERPAVE performance grading (AASHTO M 320) and to chemical analysis carried out by means of the combined use of Thin Layer Chromatography and Flame Ionization Detection [14, 15].

The nano-sized additives were commercially available products. Multiwall carbon nanotubes (CNTs) were produced by means of the Catalyzed Chemical Vapour Deposition (CCVD) technique, while the two nanoclays (NC_A and NC_B) originated from natural montmorillonites modified with different quaternary ammonium salts. Main characteristics of the additives, based on manufacturers' technical specifications, are reported in Tables 3 and 4.

Table 1 Rheological characterization of base bitumen

PG58-22		
Aging condition	Temperature [°C]	Rheological characteristic
Original	135.0	η = 0.375 Pa·s
	63.2	$G^*/\sin\delta$ = 1 kPa
RTFO	64.0	$G^*/\sin\delta$ = 2.2 kPa
PAV	19.9	$G^*\cdot\sin\delta$ = 5000 kPa
	-16.6	m = 0.300
	-17.6	S = 300 MPa

Table 2 Chemical analysis of base bitumen

Saturates [%]	Aromatics [%]	Resins [%]	Asphaltenes [%]
5.5	38.1	42.0	14.4

Table 3 Main properties of multiwall CNTs

Average diameter [nm]	Average length [μm]	Surface area [m^2/g]	Density [g/cm^3]	Carbon purity [%]	Metal oxide [%]
9.5	1.5	250-300	0.0427	90	10

Table 4 Main properties of NCs

NC type	Organic modifier	Anion	Basal spacing [nm]	Cation Exchange Capacity (CEC) [meq/100g]	Density [g/cm^3]
NC_A	Dimethyl, dihydrogenatedtallow, quaternary ammonium	Chloride	3.15	125	1.66
NC_B	Methyl, tallow, bis-2-hydroxyethyl, quaternary ammonium	Chloride	1.85	90	1.98

Several bitumen-additive blends were prepared in the laboratory by combining the base bitumen with the nano-sized materials at various dosages. As indicated in Table 5, different percentages (by weight of the base bitumen) were adopted for CNTs and NCs due to their different density values which reflect in great differences in terms of added volumes.

A simple shear mixing technique was employed to incorporate nano-additives into the base bitumen not only because it is very convenient in laboratory operations, but also because it has the potential of being easily transferred to the industrial scale in hot mix asphalt plants. Following preliminary attempts in which different mixing times and temperatures were considered, the final mixing protocol used in the study consisted in two subsequent phases: a first phase in which nano-sized products were added and manually blended to the bitumen, and a second phase in which the bitumen-additive blends were mixed with a mechanical stirrer, operating at a speed of 1,550 rpm for a total time of 90 minutes at a mixing temperature of 150°C, kept constant by a thermostatic oil bath.

All blends were tested both in the unaged condition and after short-term aging, simulated by means of the Rolling Thin Film Oven test (RTFOT).

Table 5 Composition of the bitumen-additive blends

Additive type	Percentage by weight of base bitumen			
	0.5%	1%	3%	6%
CNT	X	X	-	-
NC_A	-	X	X	X
NC_B	-	X	X	X

3 Testing Program

Rheological characterization at high temperatures of the bitumen-additive blends was based on Oscillatory Shear Loading (OSL) and Multiple Stress Creep-Recovery (MSCR) tests. In both cases, measurements were carried out by means of a Dynamic Shear Rheometer (Physica MCR 301 DSR from Anton Paar Inc.) equipped with parallel plates (25 mm diameter, 1 mm gap).

OSL tests were performed according to AASHTO T 315-10, at a frequency of 10 rad/s over a temperature range comprised between 58 and 70°C for unaged blends and between 58 and 76°C for RTFO-aged blends, with 6°C increments between each measurement step.

MSCR tests were performed according to AASHTO TP 70-10 only on short-term aged blends, at the same temperatures used for OSL tests (from 58 to 76°C).

In order to obtain supplementary information related to mixing and compaction issues, viscosity tests were also performed by means of a Brookfield rotational viscometer in accordance to AASHTO T 316-10, at temperatures of 135 and 165°C on all unaged blends.

A minimum of two replicates were run for each test and average data were used in the analysis. The specimen to specimen variability was found to be quite low, with maximum relative variations generally not exceeding 5%.

4 Experimental Results

4.1 OSL Tests

On the basis of the experimental data gathered from OSL tests, values of SUPERPAVE rutting parameter G*/sinδ were calculated for the base bitumen and all the blends considered in the study. Results obtained for unaged and short-term aged materials are summarized in Figure 1 and Figure 2, respectively.

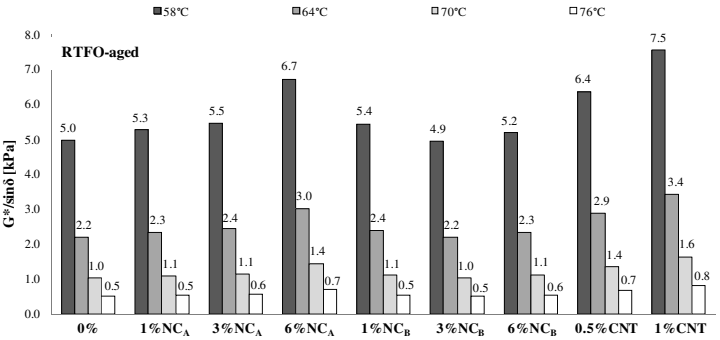

Fig. 1 G*/sinδ values of unaged bitumen-additive blends

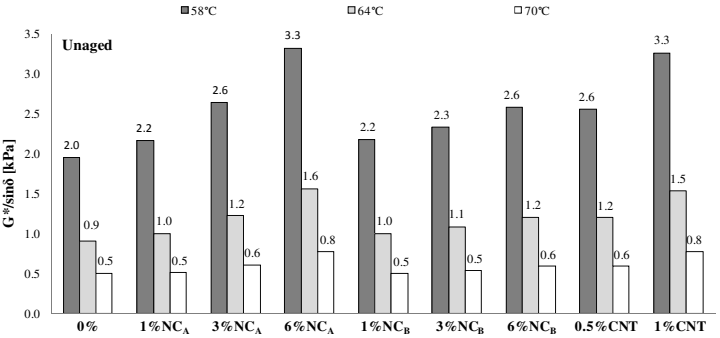

Fig. 2 G*/sinδ values of short-term aged bitumen-additive blends

In agreement with the findings of several investigations described in literature [7-9, 16], an increase of G*/sinδ with the increase of additive dosage is observed at any given temperature for each additive type and aging condition. The only exception to this general trend is constituted by the case of NC_B blends tested after RTFOT. For these binders, G*/sinδ values at 1% dosage exceed the values obtained at higher dosages (3 and 6%), probably as a result of problems which may have occurred during the dispersion of nanoclay in the base bitumen and of deterioration phenomena caused by the high temperature aging treatment. Similar

observations were made by Jasso et al. [16] during a laboratory study which focused on the effects of montmorillonite clay and other additives on the viscoelastic properties of asphalt binders.

As clearly pointed out by other authors [12, 17], effectiveness as bitumen modifiers of nano-sized additives is strongly dependent both on the volume occupied within the blends (due to a simple filling effect) and on the interactions which can arise with the continuous bituminous matrix (dependent upon specific surface and compatibility). Consequently, both factors need to be taken into account while comparing the effects on binder rheology caused by CNTs and NCs characterized by different physical and chemical properties.

Results obtained from OSL tests carried out on unaged binders show that CNT and NC_A blends exhibit a very similar behavior in terms of rutting resistance, provided that they are compared by rescaling their dosage appropriately. In particular, a correspondence can be found between 0.5% CNT and 3% NC_A and between 1% CNT and 6% NC_A. Such an occurrence can be partially explained by referring to the different densities of the two additives (Tables 3 and 4) which at a given dosage by weight lead to significantly different volume fractions. However, interaction effects have a non negligible importance and it can be hypothesized that in the case of the considered materials CNTs have a greater compatibility with the employed base bitumen.

The observations and deductions reported above need to be slightly changed when considering the experimental results obtained on RTFO-aged binders. In particular, the comparison between CNT and NC_A blends performed with a rescaled additive dosage does not highlight an equivalent performance-related response. CNTs are more effective in modifying the rheological properties of the base bitumen, probably as a result of a more efficient surface interaction with aged bitumen and/or as a consequence of partial deterioration of NC particles. This explanation is supported by the observation that CNTs apparently are not affected by RTFO treatment: in fact, the ratio between the $G^*/\sin\delta$ values obtained after and before short-term aging for the base bitumen and for CNT blends at both dosages is almost the same (approximately equal to 2.0-2.5).

Given that the two nanoclay additives considered in the study are characterized by different chemical and physical characteristics (Table 4), NC_A and NC_B blends show a different behavior in terms of rutting parameter $G^*/\sin\delta$. More specifically, at the same weight dosage NC_B provides a performance-related improvement to the base bitumen which in both aging conditions is lower than that of nanoclay NC_A. Thus, equivalencies similar to the ones discussed for CNTs and NC_A can be identified only if a different rescaling is considered in the analysis.

4.2 MSCR Tests

Experimental results retrieved from MSCR tests carried out on the unaged binders were analyzed in order to obtain information on various aspects of their response under repeated loading, including non-recoverable creep compliance (parameters $J_{nr0.1}$ and $J_{nr3.2}$), elasticity ($R_{0.1}$ and $R_{3.2}$) and stress sensitivity (J_{nrdiff} and R_{diff}).

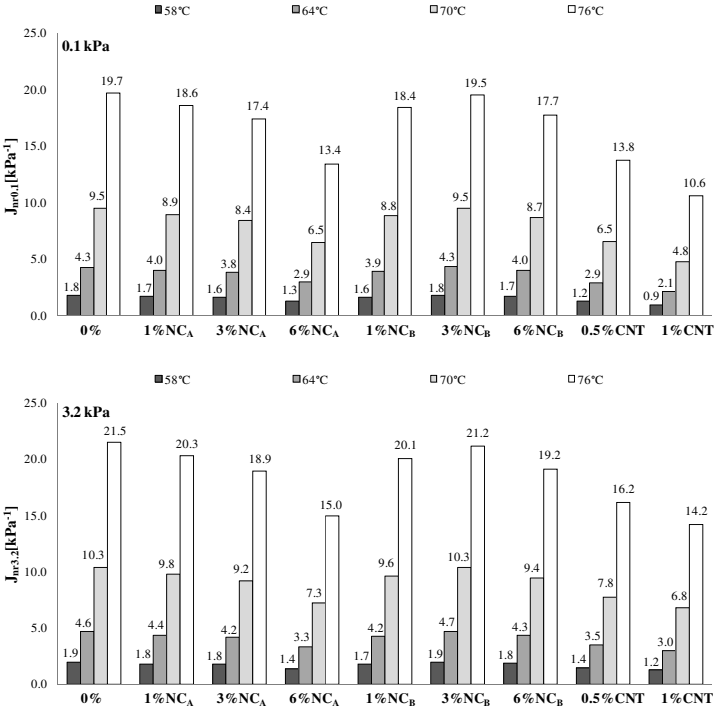

Fig. 3 Non-recoverable creep compliance values at 0.1 and 3.2 kPa

Values of non-recoverable creep compliance determined from MSCR tests at 0.1 kPa ($J_{nr0.1}$) and 3.2 kPa ($J_{nr3.2}$) are reported in Figure 3.

As expected, presence of the nano-sized additives enhances the resistance to permanent deformation of the base bitumen with a corresponding reduction of both $J_{nr0.1}$ and $J_{nr3.2}$. As in the case of parameter G*/sinδ derived from OSL tests, the extent of such an effect depends upon additive type and dosage. However, the previously discussed equivalency correspondence between CNT and NC_A blends requires a further rescaling. In particular, from the viewpoint of creep compliance the 6% NC_A blend exhibits a response under repeated loading which is very similar, for all temperatures and stress levels, to that of the 0.5% CNT blend. Analysis of the data represented in Figure 3 also shows that the blend containing 1% CNTs has the highest anti-rutting performance and that, as already observed from OSL test results, NC_A provides superior properties than NC_B at any given dosage, test temperature and stress level.

While the discussion of creep compliance ($J_{nr0.1}$ and $J_{nr3.2}$) data are coherent with the results of OSL tests, quite different observations can be drawn from the analysis of average percent strain recovery at 0.1 and 3.2 kPa ($R_{0.1}$ and $R_{3.2}$) which provide a quantitative measure of elastic properties (Figure 4). In fact, it can be

observed that modification of the base bitumen may lead to an enhancement or reduction of the elastic response under repeated loading depending upon the type of nano-sized additive.

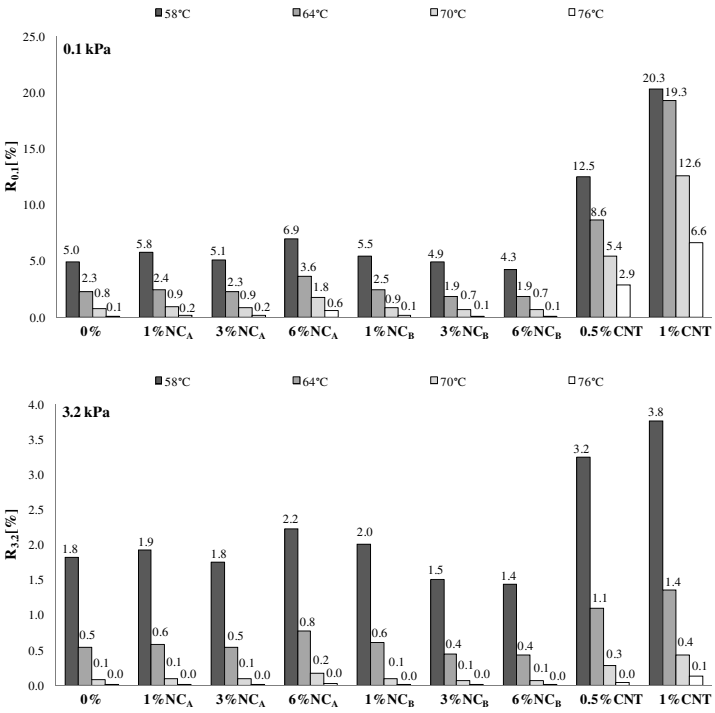

Fig. 4 Average percent strain recovery values at 0.1 and 3.2 kPa

By increasing additive dosage, in the case of both CNTs and NC_A the degree of elasticity tends to increase. However, additive-bitumen interactions seem to be substantially higher in the former case since equivalent values of percent strain recovery cannot be reached even in the case of the highest considered NC dosage.

Due to its peculiar characteristics, nanoclay NC_B does not provide any benefit to the elastic response of the base binder. With the exception of the lowest dosage, at which NC_B is almost uneffective, for the higher dosages (3 and 6%) the strain recovery capability of the base bitumen is reduced. These observations seem to indicate that the analysis of the response under repeated loading in terms of strain recovery can be a useful tool to discriminate between additives which mainly provide a filling effect (such as NC_B) and those which also effectively interact with the bituminous matrix (such as CNT and NC_A).

Further information on the rheological and performance-related effects of the considered nano-sized additives can be retrieved from the analysis of parameters J_{nrdiff} and R_{diff}. These are given by the relative difference in non-recoverable creep

compliance or average percent strain recovery between 0.1 and 3.2 kPa, thus providing a quantitative measure of stress dependency of the materials.

From the results displayed in Figures 5 and 6, it is apparent that both parameters are marginally influenced by the modification with nanoclays (either NC_A or NC_B), whereas a significant increase of stress dependency is exhibited by blends containing carbon nanotubes. In this last case, in particular, the increase of applied stress results in a remarkable increase of the non-recoverable creep compliance and in a non negligible decrease of the average percent strain recovery.

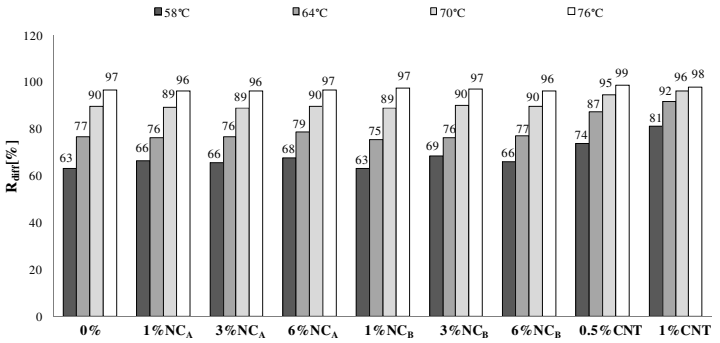

Fig. 5 Percent difference in strain recovery between 0.1 and 3.2 kPa

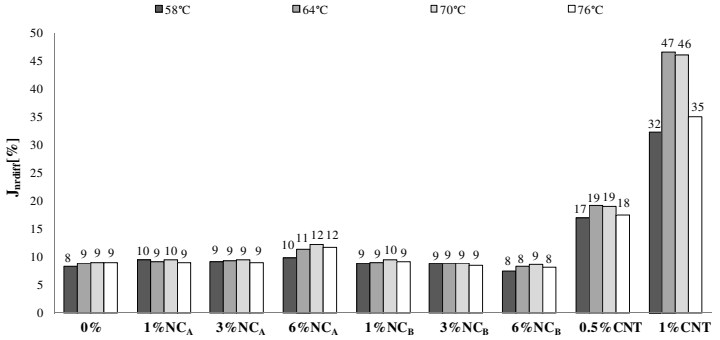

Fig. 6 Percent difference in non-recoverable creep compliance between 0.1 and 3.2 kPa

4.3 Limiting Performance Grade Temperatures

The experimental data obtained by carrying out the two previously described rheological tests (OSL and MSCR) were combined in order to determine the limiting values of the high performance grade temperature (T_{HL}) according to the criteria established by AASHTO M 320-10 and MP 19-10 (Table 6).

Table 6 Criteria used for the determination of high temperature limiting values

Specification	Aging condition	Controlling parameter	Limit
AASHTO M 320-10	Unaged	G*/sinδ	1.0 kPa
	RTFO	G*/sinδ	2.2 kPa
MP 19-10	Unaged	G*/sinδ	1.0 kPa
	RTFO	$J_{nr3.2}$	4.0 kPa^{-1}

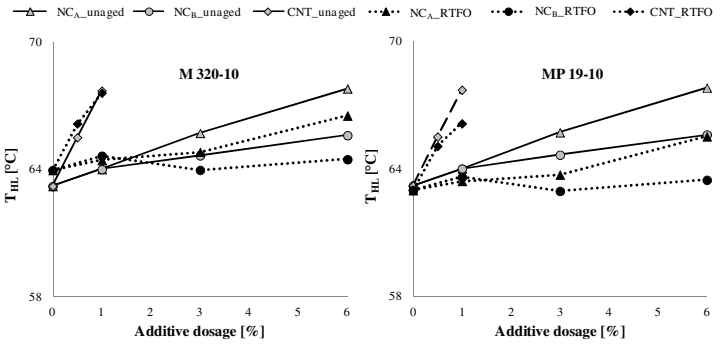

Fig. 7 Limiting temperature values calculated on the basis of different criteria

In Figure 7, limiting temperatures calculated by referring to the above mentioned criteria are plotted as a function of additive dosage. It can be observed that the adoption of the $J_{nr3.2}$ limit for RTFO-aged materials leads to T_{HL} values which are lower than those determined on the basis of the G*/sinδ criterion. In any case, increase of additive dosage results in an increase of the limiting temperatures except for the case of NC_B which shows an opposite trend passing from 1% to the higher additive dosages.

Based on the analysis of T_{HL} values it can be concluded once again that CNTs exhibit a superior anti-rutting potential than those modified with NCs. In the case of nanoclays, only a 6% dosage of NC_A leads to results which are comparable to 0.5% CNT blends.

4.4 Viscosity Tests

Figure 8 contains viscosity (η) values determined at 135 and 165°C by means of a Brookfield viscometer. As expected, viscosity decreases with increasing temperature. Moreover, it can be noticed that viscosity increases with the increase of additive percentage, reaching a growth of the order of 100% in the case of 1% CNT and 6% NC_A.

For the production and laying of bituminous mixtures containing nano-sized additives incorporated into the base bitumen it is necessary to increase mixing and

compaction temperatures. This is shown in Figure 9, which contains reference mixing and compaction temperatures calculated by considering standard viscosities respectively equal to 170 and 280 mPa·s. In both cases, a temperature increase of up to 20°C may be required for the higher additive dosages. Nevertheless, it should be underlined that viscosity of all the materials used in the present study does not exceed that of polymer modified binders commonly used in road pavements [1, 18].

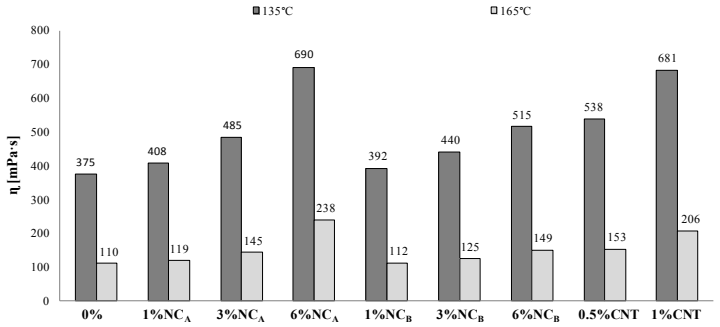

Fig. 8 Viscosity values at 135 and 165°C

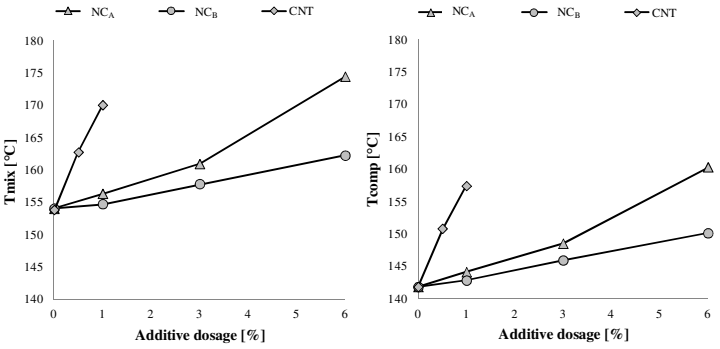

Fig. 9 Reference mixing and compaction temperatures

5 Conclusions

Based on the experimental results presented in this paper, it can be concluded that nano-sized additives such as single wall carbon nanotubes (CNTs) and montmorillonite nanoclays (NCs) can affect the high temperature rheological and flow properties of bituminous binders. However, additive effectiveness is strongly dependent upon type and dosage since the combination of these two factors influences both the volume occupied by the nano-sized products in the blends and their interactions with base bitumen.

With respect to anti-rutting potential, by considering the values of several performance-related parameters ($G^*/\sin\delta$, $J_{nr,}$ R and T_{HL}) it was observed that CNTs provide improvements which are higher than those associated to the use of NCs. Moreover, effects produced by nanoclay modification were found to be extremely sensitive to variations of the physical and chemical properties of the employed NCs. Finally, it was shown that it is crucial to consider percent strain recovery values derived from multiple stress creep-recovery (MSCR) tests in order to identify the possible existence, or absence, of true interactions between the employed additives and the surrounding bituminous matrix.

As expected, modification with nano-sized additives caused, in all considered cases, a remarkable increase of viscosity. This inevitably leads to an increase of required mixing and compaction temperatures (T_{mix} and T_{comp}), which needs to be taken into account from a technical and economical point of view in the case of full-scale paving applications.

Acknowledgments. The study reported in this paper is part of the FIRB research project on "Innovative nano-structured and polymer modified bituminous materials" funded by the Italian Ministry of Education, University and Research (MIUR).

References

[1] Bahia, H.U., Hanson, D.I., Zeng, M., Zhai, H., Khatri, M.A., Anderson, R.M.: Characterization of modified asphalt binders in Superpave mix design. NCHRP Report 459, National Cooperative Highway Research Program, Washington, D.C. (2001)

[2] Santagata, E., Baglieri, O.: Experimental evaluation of modified bituminous binders for heavy duty applications. In: 3rd International SIIV Congress, Bari, Italy (2005)

[3] Bergman, C.P., Jung de Andrade, M.: Nanostructured materials for engineering applications. Springer (2011)

[4] Xiao, F., Amirkhanian, A.N., Amirkhanian, S.N.: Influence on rheological characteristics of asphalt binders containing carbon nanoparticles. Journal of Materials in Civil Engineering 23, 423–431 (2011)

[5] Xiao, F., Amirkhanian, A.N., Amirkhanian, S.N.: Long-term ageing influence of carbon nanoparticles on the rheological characteristics of short-term aged asphalt binders. International Journal of Pavement Engineering 12(6), 533–541 (2011)

[6] Santagata, E., Baglieri, O., Tsantilis, L., Dalmazzo, D.: Rheological characterization of bituminous binders modified with carbon nanotubes. In: SIIV - 5th International Congress on Procedia - Social and Behavioral Science, vol. 53, pp. 546–555 (2012)

[7] Amirkhanian, A.N., Xiao, F., Amirkhanian, S.N.: Characterization of unaged asphalt binder modified with carbon nano particles. International Journal of Pavement Research and Technology 4(5), 281–286 (2011)

[8] Amirkhanian, A.N., Xiao, F., Amirkhanian, S.N.: Evaluation of high temperature rheological characteristics of asphalt binders with carbon nano particles. Journal of Testing and Evaluation 39(4), 1–9 (2011)

[9] Khattak, M.J., Khattab, A., Rizvi, H.R., Zhang, P.: The impact of carbon nano-fiber modification on asphalt binder rheology. Construction and Building Materials 30, 257–264 (2012)

[10] Jahromi, S.G., Khodaii, A.: Effects of nanoclay on rheological properties of bitumen binder. Construction and Building Materials 23, 2894–2904 (2009)
[11] You, Z., Mills-Beale, J., Foley, J.M., Roy, S., Odegard, G.M., Dai, Q., Goh, S.W.: Nanoclay-modified asphalt materials: Preparation and characterization. Construction and Building Materials 25, 1072–1078 (2011)
[12] Polacco, G., Kriz, P., Filippi, S., Stastna, J., Biondi, D., Zanzotto, L.: Rheological properties of asphalt/SBS/caly blends. European Polymer Journal 44, 3512–3521 (2008)
[13] Ghile, D.B.: Effects of nanoclay modification on rheology of bitumen and on performance of asphalt mixtures. Delft University of Technology, Delft (2005)
[14] Lesueu, D.: The colloidal structure of bitumen: Consequences on the rheology and on the mechanisms of bitumen modification. Advances in Colloid and Interface Science 145(1-2), 42–82 (2009)
[15] Santagata, E., Baglieri, O., Dalmazzo, D., Tsantilis, L.: Rheological and chemical investigation on the damage and healing properties of bituminous binders. Journal of the Association of Asphalt Paving Technologists 78, 567–596 (2009)
[16] Jasso, M., Bakos, D., MacLeod, D., Zanzotto, L.: Preparation and properties of conventional asphalt modified by physical mixtures of linear SBS and montmorillonite clay. Construction and Building Materials 38, 759–765 (2013)
[17] Merusi, F., Giuliani, F., Polacco, G.: Linear viscoelastic behaviour of asphalt binders modified with polymer/clay nanocomposites. In: SIIV - 5th International Congress on Procedia - Social and Behavioral Science, vol. 53, pp. 335–345 (2012)
[18] West, R.C., Watson, D.E., Turner, P.A., Casola, J.R.: Mixing and Compaction Temperatures of Asphalt Binders in Hot-Mix Asphalt. NCHRP Report 648, National Cooperative Highway Research Program, Washington, D.C. (2010)

Differential Scanning Calorimetry Applied to Bitumen: Results of the RILEM NBM TG1 Round Robin Test

Hilde Soenen[1], Jeroen Besamusca[2], Lily D. Poulikakos[3], Jean-Pascal Planche[4], Prabir K. Das[5], Niki Kringos[5], James Grenfell[6], and Emmanuel Chailleux[7]

[1] Nynas NV, Bitumen Research, Noorderlaan 183, 2030 Antwerp, Belgium
[2] Kuwait Petroleum R&T, Moezelweg 251, Europoort (RT), The Netherlands
[3] Empa, Swiss Federal Laboratories for Materials Science and Technology, Überlandstrasse 129, 8600 Dübendorf, Switzerland
[4] Western Research Institute, 365 North 9th Street, Laramie, WY 82072, USA
[5] Highway and Railway Engineering, KTH Royal Institute of Technology, Brinellvägen 23, 10044 Stockholm, Sweden
[6] Nottingham Transportation Engineering Centre, University of Nottingham, University Park, Nottingham, NG7 2RD, United Kingdom
[7] Ifsttar, Centre de Nantes, Département Matériaux / Groupe Matériaux pour les Infrastructures de Transports, Route de Bouaye CS4 44344 Bouguenais, France

Abstract. The application of Differential Scanning Calorimetry (DSC) has been proven useful in characterizing bituminous binders, distillates and crude oils. In this paper, results of the round robin test, organized by the Rilem TC 231 Nanotechnology-based Bituminous Materials (NBM) TG1 group are reported. The purpose is to investigate the repeatability and reproducibility of standard DSC measurements when applied to bituminous binders. In the full test program of the Rilem NBM group, DSC measurements are further compared to observations made in atomic force microscopy (AFM), AFM measurements are reported in a separate paper. Seven laboratories have participated in this round robin test. Four bituminous binders were investigated, containing various amounts of natural or added wax. The test program consisted of a well-defined isothermal annealing procedure, followed by a first heating and cooling scan, and afterwards followed by a second heating scan. At this stage, the data, as they were reported by the different participants, were compared. For the glass transition (Tg), mid temperatures, can be defined with a reasonable reproducibility, which improves if natural wax is not present. Regarding melting and crystallization, the shape of the melting curve is highly dependent on the thermal history of the samples. Peak temperatures of melting and crystallization phenomena were reported with a good reproducibility, while the reproducibility of melting enthalpies (or surface area's under the melting and crystallization signals) was not satisfactory. Different reasons for this and recommendations for improving the results are discussed in the paper.

N. Kringos et al. (Eds.): *Multi-Scale Model. & Charact. of Infrastruct. Mater.,* RILEM 8, pp. 311–323.
DOI: 10.1007/978-94-007-6878-9_23

1 Introduction

Natural wax in petroleum is very often defined as the amount of material that precipitates at a certain temperature or upon cooling. Waxes in crude oils can be subdivided into two types, paraffin wax and micros crystalline wax [1, 2]. Paraffin wax consists mainly of normal alkanes (C20-C40) and after a distillation process it will be distributed over several of the distillates, depending on the boiling points. Micro crystalline wax, on the other hand, is after the distillation process collected in the residue or in the bitumen fraction. It consists of molecules with a higher boiling point, it crystallizes in micro-sized crystals, and contains considerable amounts of iso- and cyclo alkanes, unsaturated compounds, and it may even contain some aromatic compounds. This subdivision does however not mean that waxes in bitumen are always of the micro crystalline type, since paraffin waxes may also be formed afterwards by processes like visbreaking or cracking.

In literature Differential Scanning Calorimetry (DSC) has been used to investigate wax in bitumen and in crude oil [3-8]. Typically, for bitumen DSC transitions show on very broad temperature ranges. They are related to glass transitions, melting and crystallization. DSC scans of different bitumen types appear to have different shapes and variations in intensity of the melting peaks or shifts of the peak positions to higher or lower temperatures. Most investigations also report that DSC scans are strongly influenced by the thermal history of the samples. Annealing at a certain temperature can induce an extra melting signal slightly higher compared to the annealing temperature. Annealing below the glass transition temperature, can result in an enthalpy relaxation, in the subsequent heating scan. In the heating scan, an exotherm has been reported, and has been interpreted as a cold crystallization of material, which upon cooling could not crystallize. In ref. 5 DSC measurements on fractions separated from bitumen have been reported. Fractions were obtained, using solvent de-asphalting, and elution-adsorption chromatography. The authors concluded that napthene aromatics contribute heavily to the endothermic effect of the parent asphalt. And also polar aromatics showed a small endothermic effect at similar temperature ranges.

In ref 5 reproducibility numbers of DSC measurements on bitumen are reported but without information regarding the number of participating labs or the number of repeats. The authors report a fairly good reproducibility for Tg onset and Tg mid points, these temperatures were varying within ±2°C. Melting maxima were not very reproducible for samples with weak and broad endothermic peaks; but for samples with relatively large and well-defined peaks these values varied within ± 2°C. For melting enthalpy (ΔH), a fluctuation between ± 10% and ±15% was reported, depending on the size of the melting peaks, small melting signals having a larger fluctuation.

In a second study [8] the results of four laboratories are compared on four bitumen samples, each laboratory using two to three repeats. In this study, the onset temperature of the melting signal seen on heating varied a lot (between 7°C to 15°C), the variation in the end temperature of this melting signal was much less

(between 0 and 5°C). For the enthalpy, the reproducibility varied considerably, between ±15% to ±30%. This variation was higher as the value of ΔH was lower.

If melting enthalpies are divided by the melting enthalpy of a 100% crystalline material (ΔH_0) (with no border effects) it is possible to calculate a crystallinity percentage: various values of ΔH_0 were found in literature: In ref 3 and 8 a value of 200J/g was used, in ref 4, it was 180 J/g and 121 J/g in ref 9.

The effects of natural wax on the performance of bituminous binders are not fully understood [9]. Probably the influence depends on whether the crystals act as a filler (only stiffening the bitumen) or act as a cross-linker. This could for example be the case if crystals incorporate linear paraffinic side chains from molecules with other functional groups or aromatic ring structures, as reported in ref 5. The effects on performance certainly also depend on the amount of crystallinity, especially the fraction of material that is crystallized at the temperature and time of interest, and the strength of cross-linking points if these are formed. Rheological tests have shown a tendency for a more elastic behavior, especially at low frequencies, when natural waxes are present in bitumen [10]. This effect is larger after isothermal annealing. But, stress sweeps indicate that these small network points seem to break quickly when strain or stress is increased. [11]. For example for rutting, the melting temperature as well as the fraction that is molten at the highest service temperature is probably most important. A negative influence at low service temperatures has not been observed in asphalt fracture tests [12] but a correlation between physical hardening at low temperatures and the formation of crystalline material at the same temperature has been reported [13]. And a correlation between physical hardening and low temperature cracking in field sections has also been reported.

In literature, several other test methods have been used to evaluate waxes and the morphology of wax crystals, examples are microscopic techniques including confocal laser microscopy and AFM. Other methods like x ray diffraction, or test methods looking at CH2 sequences (NMR, or FT-IR) have also been used [15-16]

2 Experimental Plan

Four binders were selected based on their expected wax content, Bit-A was expected to be wax-free, Bit-B and C contained natural wax, and Bit-D contained added wax. A summary can be found in table 1. The wax content, determined by EN 12606-1, is included in table 1. Until the publication of the new EN 12591 in 2009, this wax content was part of the European bitumen specification for road paving with a maximum value depending on the bitumen grade and on the test method selected. All laboratories were asked to calibrate their equipment and to report the calibration procedure. An overview of the equipment used in this round robin test is given in table 2.

Table 1 Summary of investigated binders

Code	Supplier	Bitumen	Pen, dmm	R&B, °C	Wax content acc. to EN 12606-1
Bit-A	Nynas	70/100	91	46.2	0.3*
Bit-B	Nynas	70/100	86	46.4	1.7
Bit-C	Q8	70/100	82	45.8	1
Bit-D	Nynas	Bit-A +3% sasobit	50	78	-

* The EN 12606-1 method will give a result even with non-waxy bitumen. Bitumen D was not investigated with EN 12606-1.

Table 2 Overview of participating labs and their equipment

code	DSC equipment
Lab-1	Mettler Toledo DSC1
Lab-2	TA DSC Q200 V24.9
Lab-3	Mettler Toledo DSC1
Lab-4	Netzsch 204
Lab-5	DSC 8000 Perkin Elmer
Lab-6	TA DSC Q2000 V24.9
Lab-7	TA DSC Q2000

A detailed testing procedure was prepared. The main points are represented here: Take a small binder amount (15 to 30 mg) and place this in a measuring pan. It was advised to have a small opening in the sample pan to prevent pressure build up during the test. After filling the sample pans, these should be homogenized at 110°C – 130°C for 15 minutes. Then samples should be kept in a horizontal position for 24 hour at 25°C. After this preparation and annealing step, the samples are placed in the DSC equipment. In a first period the sample is cooled to a low temperature (to – 80°C or –100°C) at -10°C/min (no heat flow recording required in this step). Afterwards a first heating scan at 10°C/min is recorded, heating continuously up to 140°C, this scan is followed by a recorded cooling scan at -10°C/min, back to the low temperature used in the first run. And this test is again followed by a second heating, exactly the same as the first one. The thermal history is depicted schematically in Figure 1. In total, it was requested to repeat this complete set of sample preparation, annealing and heating -cooling scans twice for each binder. But, only two labs made these repeats, and therefore, the analysis will mainly focus on reproducibility and not on repeatability. And not all labs followed the requested temperatures, for example lab 3 and 5 recorded the heating scans only up to 100°C.

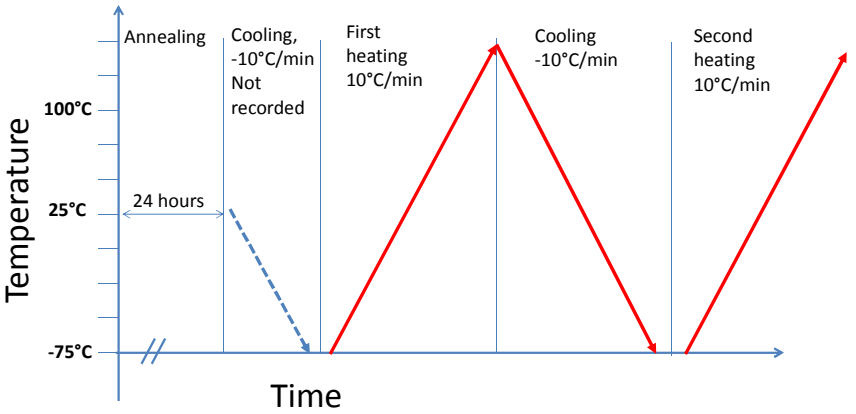

Fig. 1 Schematic of the requested DSC procedure, red are the recorded measurements, the blue dotted line is the cooling after 24h annealing. Heating and cooling rates are at 10°C/min.

3 Results

3.1 Curve Shapes and Baselines

In figures 2 and 3, heat flow/mass curves of Bit-A and Bit-C, respectively, are represented for the different labs and equipment. From figure 2, it is clear that Bit-A only displays a glass transition while in figure 3 glass transition and melting phenomena are observed.

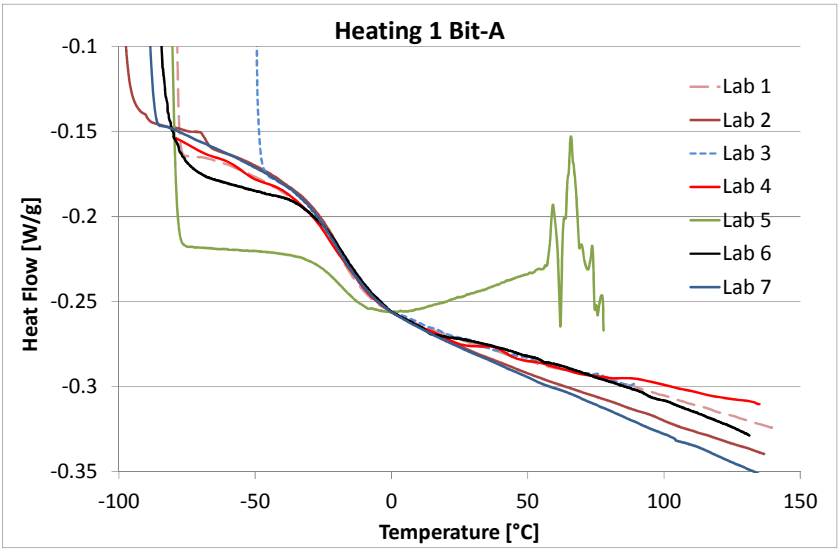

Fig. 2 Heating curves of Bit-A (first heating). The Y-axis represents the heat flow divided by the sample weight, and is normalized, all curves are shifted to the same point at 0°C.

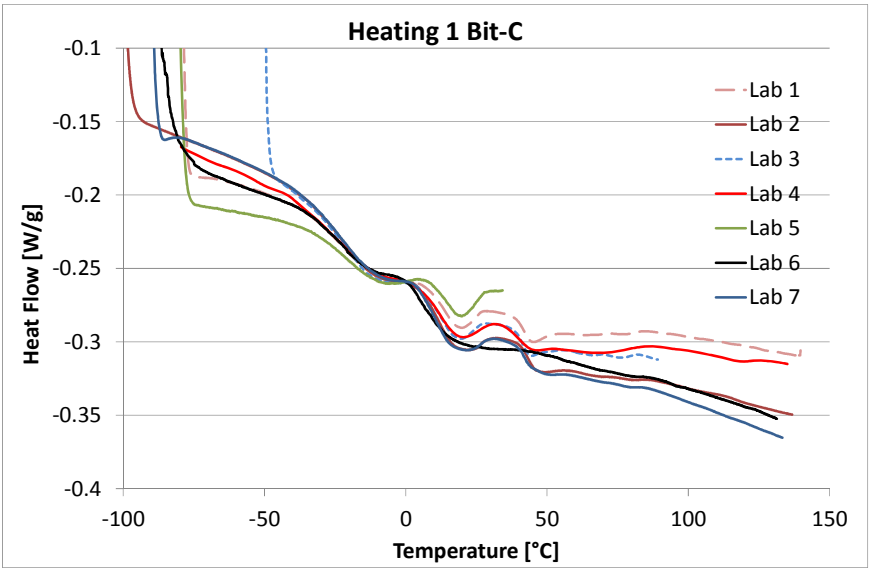

Fig. 3 Heating curves of Bit-C (first heating). The Y-axis represents the heat flow divided by the sample weight, and is normalized, all curves are shifted to the same point at 0°C.

It is also clear that in order to evaluate the transitions accurately, a temperature scan over a wide temperature range is needed. Some labs used a reduced temperature range, for example in figure 2, lab 3 starts measurement at a rather high temperature, so that the baseline before the glass transition becomes very short. In figure 3, lab 5 missed part of the melting signal, the measurement was stopped below 50°C, while lab 3 stops the measurement directly after the melting signal. In this case the baseline from the melt, when all crystallinity is molten, is difficult to observe and to use. Depending on the pan size and the amount of bitumen used, some labs reported expansion of the bitumen outside of the pan resulting in disturbances of the signal depicted in the results of lab 5 in figure 2. Reduction of the mass to ca. 15 mg improved this aspect.

Equipment with the option to calibrate “tau lag”, can prove advantageous. Tau lag is an adjustment factor to compensate for temperature differences between the furnace and the reference temperature, and is heating rate dependent. Calibrating this factor should have an effect on the baseline, and can therefore also influence the glass transition and enthalpy determination. In this study, slight differences are observed between the results of labs with this adjustment, but at this stage too little data are available to draw firm conclusions.

3.2 Evaluation of the Glass Transition Temperature

In DSC scans the glass transition is observed as a shift in baseline. ASTM E1356-08 describes several temperatures for determining the glass transition, these definitions are repeated here:

- The extrapolated end temperature, (Tg e), °C—the point of intersection of the tangent drawn at the point of greatest slope on the transition curve with the extrapolated baseline following the transition.
- The extrapolated onset temperature, (Tg f), °C—the point of intersection of the tangent drawn at the point of greatest slope on the transition curve with the extrapolated baseline prior to the transition.
- The inflection temperature, (Tg i), °C—the point on the thermal curve corresponding to the peak of the first derivative (with respect to time) of the parent thermal curve. This point corresponds to the inflection point of the parent thermal curve.
- The midpoint temperature, (Tg mid), °C—the point on the thermal curve corresponding to 1⁄2 the heat flow difference between the extrapolated onset and extrapolated end.
- The temperature of first deviation, (Tg o), °C—the point of first detectable deviation from the extrapolated baseline prior to the transition.
- The temperature of return to baseline, (Tg r), °C—the point of last deviation from the extrapolated baseline beyond the transition.

In this study, Tg midpoints, extrapolated onsets, ends and inflection points were asked, from first and second heating scans, and also from the cooling scan. Most labs only delivered the three first temperatures.

In literature, Tg midpoints are mostly used, and in figure 4, average Tg mid temperatures are shown, from first as well as from second heating scans. Figure 4 includes the temperatures obtained from all the labs. In this figure, the standard deviation (between all labs) is half the total length of the error bar. Figure 4 shows that this standard deviation of Tg mid is quite good for all the samples, and is slightly better for Bit-A and Bit-D, the two binders that do not contain natural wax. The DSC scans for Bit-A were already represented in figure 2, where it is also obvious that the position of the glass transition overlaps quite well for all the participating labs. The reason why reproducibility decreases when natural wax is present, is because Tg end becomes difficult to determine, due to an overlap with recrystallization and melting phenomena, as will be discussed in the next section. Comparing glass transition temperatures taken in first and second heating scans can reveal the influence of thermal history. It is clear, from figure 4, that there is no significant difference in glass transition temperature between first and second heating scans. Obviously, the annealing procedure used in this study, and for these binders did not affect the glass transition temperature. Longer annealing times, or other temperatures may still have an influence. For materials where thermal history is important on the Tg temperature, it is common to report Tg values in a second heating scan, since then the thermal history is controlled.

Figure 4 also indicates that the position of the glass transition is not influenced by the addition of 3% synthetic wax. And there are indications that binders containing natural wax have, for the same penetration grade, a lower glass transition temperature. This could be attributed to a stiffening effect of natural wax, when measuring the penetration at 25°C. At 25°C, natural wax is partly crystalline and stiffens the binder, so in fact without wax, the same binder would belong to a higher penetration grade, which is more likely to have a lower glass transition temperature.

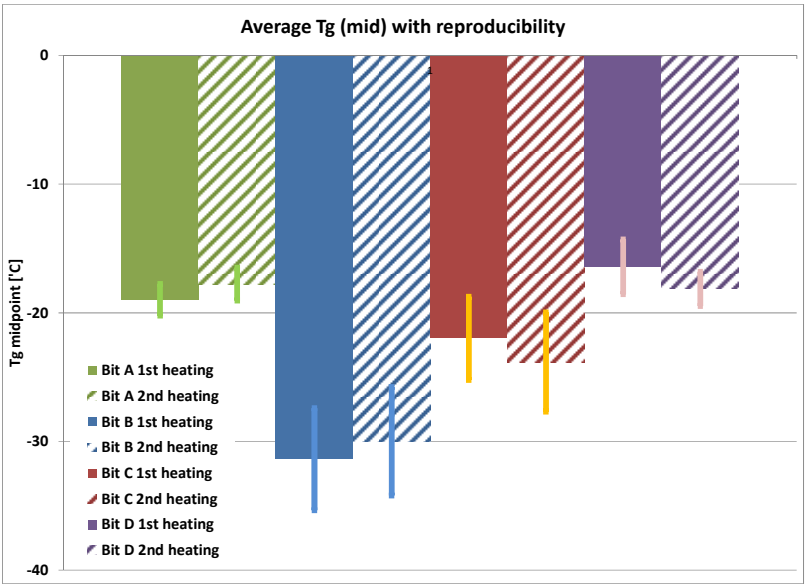

Fig. 4 Overview of average Tg mid temperatures, determined for all binders from first and second heating scans. The standard deviation is half the length of the total error bar.

Regarding Tg temperatures from the cooling scans, these scans were very often complicated by the occurrence of small spikes (or peaks) appearing in the curves. These were attributed to differences in contraction, and loss of contact between the sample and the aluminium sample pan. These peaks made it often impossible to determine the Tg temperature. An example is shown in figure 5.

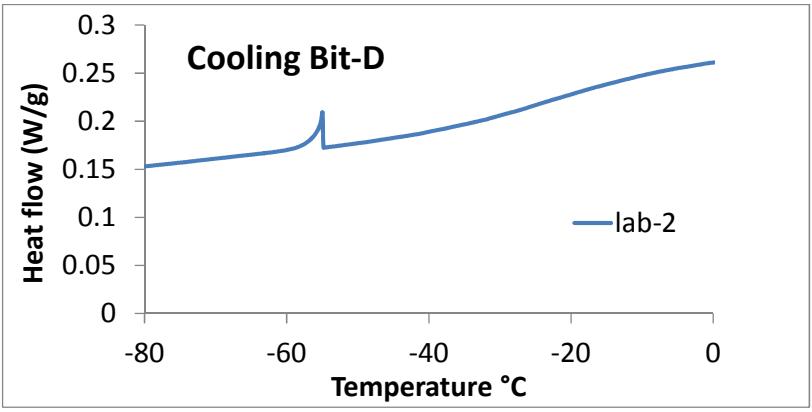

Fig. 5 Illustration of a cooling scan showing the small vertical peak

3.3 Melting, Crystallization and Enthalpy Evaluation

Melting and crystallization are observed in a DSC scan as an upward or downward peak, the sign of the signals depends on the type of DSC (endotherm or exotherm). The enthalpy is derived from the area under the melting or crystallization signals. Similar to the glass transition, different temperatures can be defined for melting or crystallization, according to ASTM E 2253:

- Tm peak °C—the peak temperature of the melting signal.
- Tm extrapolated onset °C—the point of intersection of the tangent drawn at the point of greatest slope on the melting transition when reaching the peak temperature, with the extrapolated baseline prior to the transition.
- Tm extrapolated end °C—the point of intersection of the tangent drawn at the point of greatest slope on the melting transition after reaching the peak temperature, with the extrapolated baseline prior to the transition.
- Similar definitions can be used for the crystallization temperatures (Tc).

Heating scans (first and second ones) for Bit-C and Bit-D are respectively represented in figure 6 and 7. Bit-B, is not represented separately, since it is very similar to Bit-C. It is clear that melting phenomena are very broad, and that the shape of the curves is very dependent on the thermal history before recording the scans. This corresponds to literature observations. For Bit-C, it seems that after isothermal annealing (24h at 25°C) the melting signals consists of two peak temperatures. For this bitumen, the signal can be interpreted in various ways; it seems that upon heating through the glass transition, there is a small exothermal signal, which can be due to a cold crystallization, or a liquid phase separation, while upon further heating, a melting signal is observed. It is apparent that this small exotherm complicates the drawing of a baseline, and therefore also the enthalpy determination. For Bit-D, where only Sasobit is present, the thermal history before the test is again important, but the effect is different compared to the two samples that contain natural wax. Drawing of the baseline seems to be more straightforward for Bit-D compared to Bit-C.

Regarding the melting and crystallization temperatures, average values and standard deviations, which measure reproducibility, are shown in table 3. This table shows that in a cooling scan, the peak crystallization temperatures can be defined with a reasonable reproducibility, except for Bit-B. But, the crystallization onset and end-temperatures are hard to define for all the binders. There is no difference between natural or added wax. Upon heating, again only the peak temperature can be defined with a good reproducibility; also the end melting temperature of Bit-D can be defined quite well.

Enthalpies, as delivered by the various labs are represented in figure 8. As expected, crystallization and melting enthalpies do not have a good reproducibility, since onset and end temperatures are hard to define. For Bit-D the enthalpy determination is somewhat better.

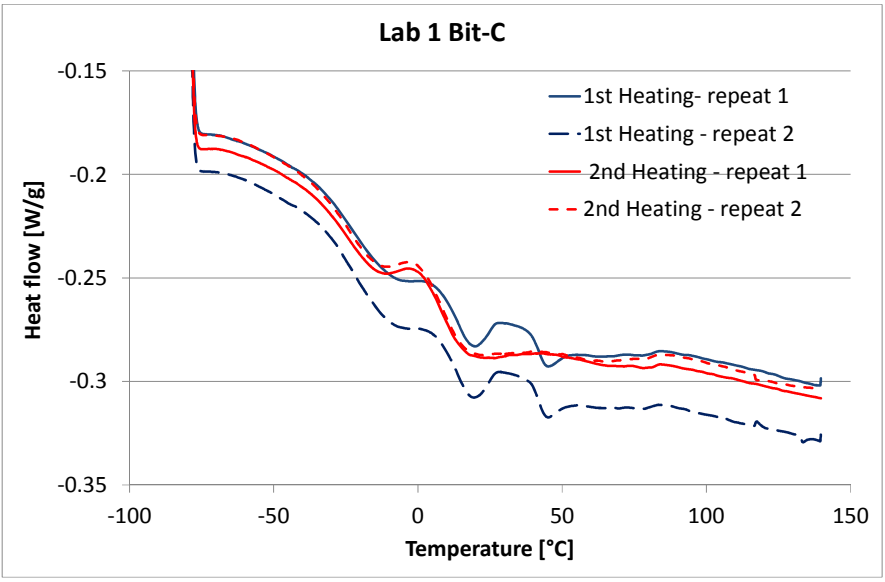

Fig. 6 Heating scans of Bit-C, data by lab 1

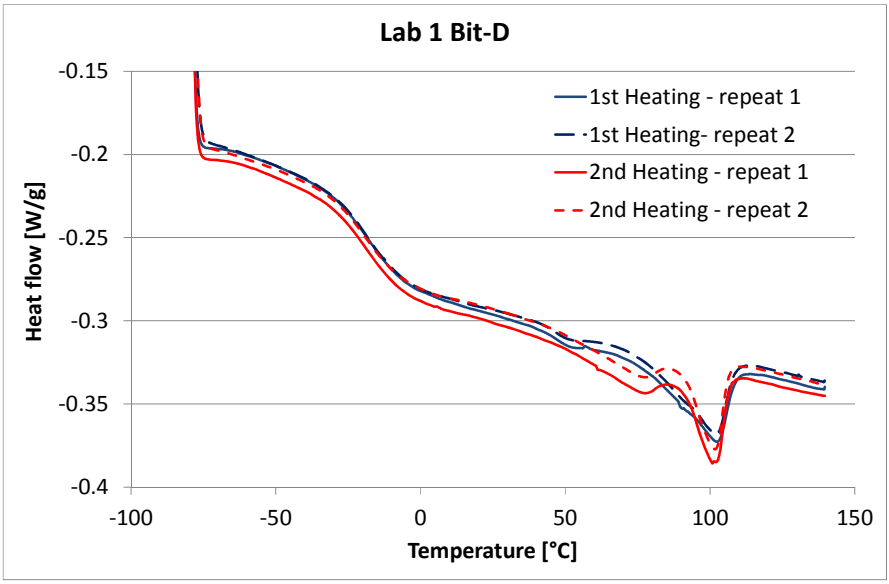

Fig. 7 Heating scans of Bit-D taken by lab 1

Table 3 Summary of melting and crystallization temperatures (all labs are included)

sample	DSC scan	Tm peak		Tm extrap.onset		Tm extrap. end	
		average	stdev	average	stdev	average	stdev
Bit-B	**1st heating**	51.8	2.8	0.1	14.4	91.0	17.5
	2nd heating	52.2	6.6	0.1	13.2	98.3	23.4
Bit-C	**1st heating**	28.1	13.7	6.9	5.2	98.2	16.8
	2nd heating	21.8	2.7	4.4	4.3	87.2	26.3
Bit-D	**1st heating**	100.6	1.4	51.2	27.4	119.6	7.4
	2nd heating	101.4	0.9	55.4	30.5	117.7	8.2
		Tc peak		**Tc extrap. onset**		**Tc extrap. end**	
		average	stdev	average	stdev	average	stdev
Bit-B	**cooling**	31.3	1.5	42.9	5.5	8.1	11.1
Bit-C	**cooling**	19.9	10.0	43.5	33.3	9.8	20.8
Bit-D	**cooling**	71.6	3.0	73.0	25.6	40.4	33.8

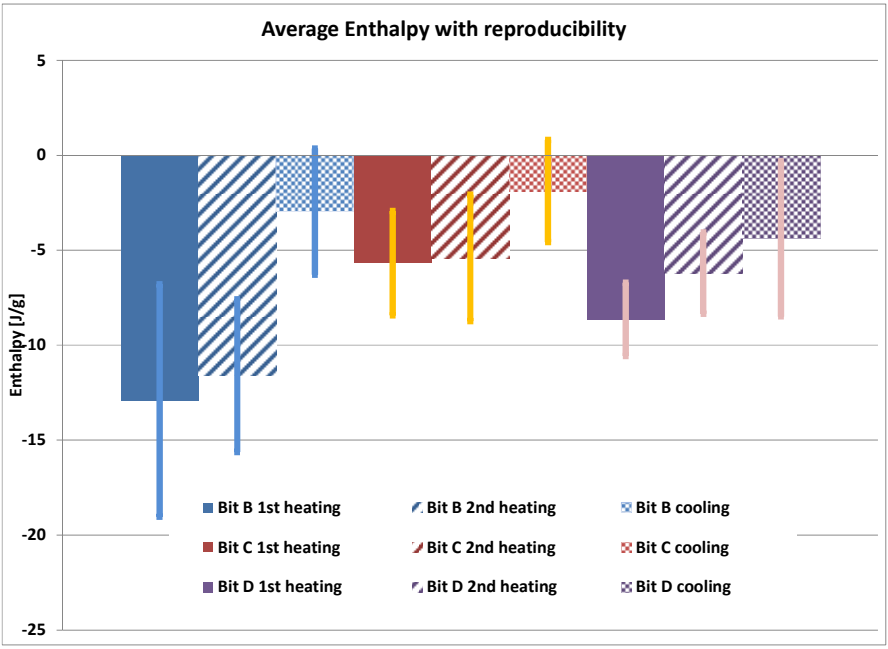

Fig. 8 Average enthalpies, determined in first and second heating scan and upon cooling. The standard deviation is half the total length of the error bar.

4 Conclusions

The conclusions are subdivided into observations related to the glass transition, and observations related to endo- and exothermal effects:

Regarding the glass transition: Tg-mid temperatures, can be determined in the heating scans with a good reproducibility. This reproducibility was best for Bit-A and Bit-D, the two binders that do not contain natural wax. If natural wax was present the Tg-end became difficult to determine exactly. If synthetic wax was present, Tg-end could still be determined from the heating scans. Glass transitions were more difficult to determine from the cooling scans, since small spikes were observed during cooling, these were attributed to differences in contraction between the sample and the aluminium sample pan. It was also observed that adding 3% of synthetic wax did not influence the glass transition. And for the conditions used here, the thermal history had little effect on the glass transition temperature.

Regarding exo- and endothermal effects: The shape of the endotherm in the heating scan is clearly dependent on the annealing procedure before recording this scan. This was observed for natural, and for the synthetic wax. Regarding the temperatures, only peak temperatures can be defined with a good reproducibility. And regarding enthalpies of melting and crystallization, these did not have a good reproducibility. Because of the broad signals, the combination of exo- and endothermal effects, and the occurrence of double endotherms, it becomes difficult to determine the position of the baseline, and small differences in drawing this baseline result in large differences in the enthalpy determination.

The results obtained so far, were obtained by directly comparing the data as they were received by the various labs. Sample preparation and testing instructions were provided, as well as the respective definitions of various temperatures that were asked. But there were no instructions on for example how to draw the baseline under the signals, or how to perform the enthalpy calculation. In addition, some labs did not follow the test instructions, and used a smaller temperature interval. This has serious consequences upon the visualization of the base-line in those temperature regions where no transitions take place. In a further follow-up, it is the intention to include additional instructions upon estimating the baseline, for example by measuring empty pans and subtracting these of the measured scans. It is also the intention to investigate modulated DSC. A number of papers have been published in this area [17], and with this technique it should be possible to separate first order transitions, like melting and (re)- crystallization, from second order transitions, like the glass transition temperature. This should improve the temperature and enthalpy determination.

Acknowledgments. The authors would like to thank all people involed in this study, in particular; Hartmut Fischer, from TNO, Pär Wedin from Nynas, Cynthia Nijssen-Wester from KPR&T, Beatrice Fischer from EMPA, Jerry Forney and Fred Turner from Western Research Institute and Cédric Petiteau from IFSTTAR.

References

1. Meyer, G.: Thermal Properties of Micro-crystalline Waxes in Dependence on the Degree of Deoiling. SOFW Journal 135(8), 43–50 (2009)
2. Edwards, Y.: Influence of Waxes on Bitumen and Asphalt Concrete Mixture Performance. Doctoral Thesis in Highway Engineering, KTH, Sweden (2005)
3. Claudy, P.M., Létoffé, J.-M., Martin, D., Planche, J.-P.: Thermal behavior of asphalt cements. Thermochimica Acta 324, 203–213 (1998)
4. Michon, L.C., Netzel, D.A., Turner, T.F.: A C^{13}NMR and DSC study of the amorphous and crystalline phases in Asphalts. Energy & Fuels 13, 602–610 (1999)
5. Harrison, I.R., Wang, G., Hsu, T.C.: SHRP-A/UFR-92-612, A Differential Scanning Calorimetry Study of Asphalt Binders, Strategic Highway Research Program, National Research Council, Washington, DC (1992)
6. Kok, M.V., Létoffé, J.-M., Claudy, P., Martin, D., Garcin, M., Vollet, J.-L.: Comparison of wax appearance temperatures of crude oils by differential scanning calorimetry, thermomicroscopy and viscometry. Fuel 75(7), 787–790 (1996)
7. Lesueur, D.: Propriétés mécaniques des liants routiers. Thèse de Doctorat, Institut National Des Sciences appliquées de Lyon, France (1996)
8. Lesueur, D., Planche, J.-P., Dumas, P.: Détermination de la teneur en paraffines des bitumes. Bulletin des Laboratoires des Ponts et Chausseés 229, 3–11 (2000)
9. Lu, X., Redelius, P.: Effect of bitumen wax on asphalt mixture performance. Construction and Building Materials 21, 1961–1970 (2006)
10. Planche, J.P., Claudy, P.M., Létoffé, J.-M., Martin, D.: Using thermal analysis methods to better understand asphalt rheology. Thermochimica Acta 324, 223–227 (1998)
11. Soenen, H., De Visscher, J., Vanelstraete, A., Redelius, P.: The Influence of Thermal History on Binder Rutting Indicators. IJRMPD 6(2), 217–238 (2005)
12. Lu, X., Soenen, H., Redelius, P.: Impact of Bitumen Wax on Asphalt Performance – Low Temperature Cracking. In: E&E Conference (2004)
13. Claudy, P., Letoffe, J.M., Rondelez, F., Germanaud, L., King, G., Planche, J.P.: A new interpretation of time-dependent physical hardening in asphalt based on DSC and optical thermoanalysis. ACS 92, 1408–1426
14. Evans, M., Hesp, S.A.M.: Physical Hardening Effects on Stress Relaxation in Asphalt Cements and Implications for Pavement Performance transportation research board (2011)
15. Lu, X., Kalman, B., Redelius, P.: A new test method for determination of wax content in crude oils, residues and bitumens. Fuel 87, 1543–1551 (2008)
16. Lu, X., Langton, M., Olofsson, P., Redelius, P.: Wax morphology in bitumen. J. Mat. Sci. 40, 1893–1900 (2005)
17. Masson, J.-F., Polomark, G.M.: Bitumen microstructure by modulated differential scanning calorimetry. Thermochimica Acta 374, 105–114 (2001)

Review of Multiscale Characterization Techniques and Multiscale Modeling Methods for Cement Concrete: From Atomistic to Continuum

Wenjuan Sun[1,*], Ya Wei[2], Dong Wang[3], and Linbing Wang[4]

[1] Department of Civil and Environmental Engineering,
Virginia Polytechnic Institute and State University, Blacksburg, VA 24061
sunwj@vt.edu
[2] Department of Civil Engineering, Tsinghua University, China
[3] Virginia Tech Transportation Institute (VTTI), Blacksburg, VA 24060
wangd@vt.edu
[4] Department of Civil and Environmental Engineering,
Virginia Polytechnic Institute and State University; Director, Center for Smart Infrastructure and Sensing Technology, Virginia Tech Transportation Institute (VTTI)
Virginia Polytechnic Institute and State University, Blacksburg, VA 24061
wangl@vt.edu

Abstract. Due to the heterogeneous composite nature of cement concrete, it is vital to understand the structure and mechanical properties from nanoscale to macroscale. Therefore, it is essential to utilize microscopy techniques to characterize the microstructure of cement concrete and to develop low-cost and computational effective multiscale modeling methods. This paper presents a brief review of different microscopy techniques for the microstructure characterization of cement concrete, and then three widely used multiscale modeling methods are discussed, including quasi-continuum method, coarse-grained molecular dynamics (CGMD) method and hand-shake method. Finally, a short discussion on multiscale failure modeling of cement concrete is presented as an example for the multiscale failure modeling of cement concrete.

1 Introduction

Stone-based materials are granular materials that contain natural stones and/or crushed stones, such as asphalt concrete, cement concrete, and crushed stone base material, etc. Failure in stone-based materials may present in different modes, such as localized failure, and diffuse failure, etc. Macroscopic detection of failure is relatively well understood with numerous models using the finite element method, discrete element method, etc. However, the underlying

* Corresponding author.

N. Kringos et al. (Eds.): *Multi-Scale Model. & Charact. of Infrastruct. Mater.,* RILEM 8, pp. 325–341.
DOI: 10.1007/978-94-007-6878-9_24

microstructure and interactions between particles and molecules are yet to be well modeled. Consequently, there is an urgent need to simulation the failure of stone-based materials using the multiscale characterization method to establish the multiscale models.

Both asphalt concrete and cement concrete is inherently a type of heterogeneous composite materials with multiscale phases (*1-2*). For instance, the microstructure of cement concrete could be discretized into four scales, from calcium silicate hydrate (C-S-H) solid phase at level 0 (10^{-9}-10^{-10} m), low density and high density C-S-H phases at level I (10^{-6}-10^{-9} m), C-S-H matrix and calcium hydroxide (CH) crystals at level II (10^{-6}-10^{-3} m), up to cement paste and sand at level III (>10^{-3} m) (*3*). Fig. 1 plots the schematic view of the multiscale nature of asphalt concrete and cement concrete.

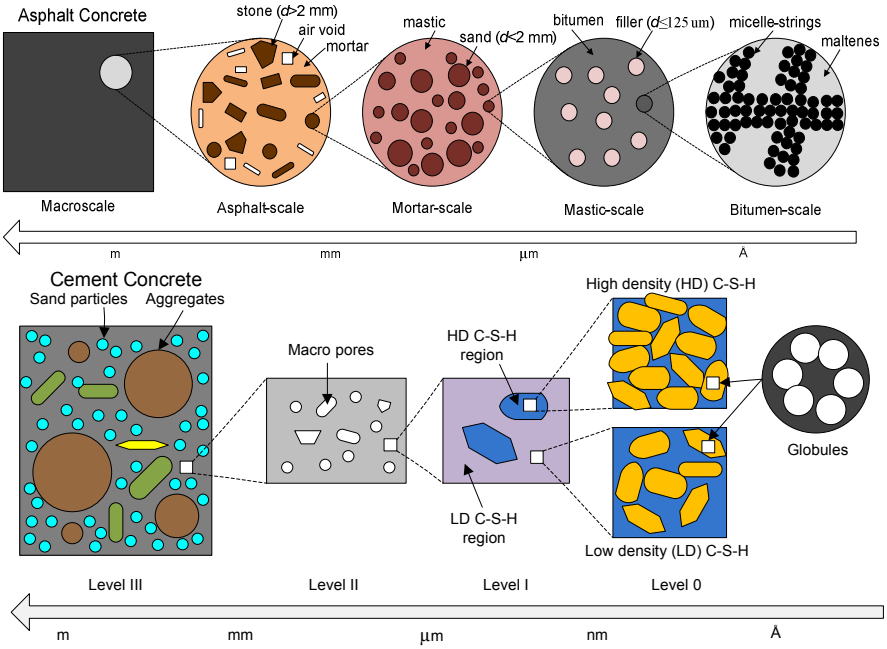

Fig. 1 Multiscale nature of cement concrete (*2-3*)

Due to the complexity nature of stone-based materials, it is essential to investigate the fundamental mechanisms of mechanical failures in stone-based materials from different scales. Both multiscale characterization techniques and multiscale modeling methods are expected to provide a convenient means to better understand the microstructure and mechanical properties. This paper presents a brief review of microscopy techniques for the characterization of stone-based materials, followed by three widely used multiscale modeling methods. The multiscale failure modeling methods for both asphalt concrete and cement concrete are further discussed in the end.

2 Multiscale Characterization of Cement Concrete

2.1 Microscopic Technique

The molecular structure of stone-based materials could be determined from different scales by using microscopic techniques. To elucidate how the microscopic techniques are applied to analyze the microstructure, cement concrete is taken as an example. Table 1 tabulates the cement structures at different scales and corresponding microscopy techniques. The available microscopic techniques include transmission electron microscopy (TEM), X-ray absorption spectroscopy (XAS), and energy dispersive X-ray analysis (EDX), scanning electron microscopy (SEM), nuclear magnetic resonance spectroscopy (NMR), and Raman spectroscopy, etc.

TEM experiments image hydrates and determine spatially resolved chemical compositions of the main hydration products of cement pastes. TEM experimental results reveal that the microstructure of C-S-H is in disk shape with a thickness of 5 nm in long axis in the 60 nm range (*4*). Two types of C-S-H gel at the scale of μm are found during hydration process: HD C-S-H and LD C-S-H. Extensive TEM studies show that the composition of C-S-H in hardened cement paste varies with age, and the Ca-Si ratio ranges from 0.6 to 2.1 (*5*). In 2002, Richardson summarized TEM techniques and their applications to cementitious materials, also pointed out that the misinterpretation of images and chemical data can happen due to serious electron-beam damages in TEM experiments (*6*).

XAS, including both extensive X-ray absorption fine structure (EXAFS) and X-ray absorption near edge structure (XANES), can be used to characterize the local environment of aluminum and calcium in phases formed in the hydrated cement (*7*). Scheidegger et al. investigated the chemical speciation of traced element in cementitious materials using XAS experiments to evaluate the mobility and the fate of radionuclides and contaminants (*8*).

EDX is usually used with SEM together. Samples in EDX are usually epoxy impregnated, polished, and carbon coated. SEM experiments of hydrated Portland cement show the information about sample surface topography, composition and other microstructural properties. There are ASTM standards for the examination of hardened cement concrete using SEM combined with EDX (*9*). Bentz et al. evaluated the microstructure, specifically capillary pore structure, of hydrated pastes with the water-cement ratio of 0.35 and 0.435, respectively (*10*).

NMR provides a unique insight into chemical bonds in hydrated cement pastes. In solid-state NMR, the sample is spinning at frequencies of 1-35 kHz around an axis oriented 54.7° to the magnetic field (*11*). For example, ^{29}Si NMR presents the ^{29}Si chemical shift representing the degree of condensation of SiO_4 tetrahedra (*12*), with distinction of resonances from alite, belite, and C-S-H phases (*13*). Consequently, ^{29}Si NMR is used to example the polymerization of a silicate tetrahedron in synthesized C-S-H, and the polymerization of C-S-H depends on its Ca-Si ratio and the humidity within the interlayer water (*12, 14-16*). Kim et al.

found that packing density of C-S-H might increase if the cement paste is hydrated under high temperature and pressure, according to the investigation of microstructure using nanoindentation and NMR (*17*).

Raman spectroscopy is a vibrational spectroscopic technique and provides structural and dynamic information with spatial resolution of micrometers (*13*). It characterizes local environment of sulphate anions and hydrogen bonds in hydrated cement paste (*178*). Raman spectra of C-S-H phases are dominated by the symmetrical silicate bending bands around 670 cm^{-1} and the stretching bending bands at 800-1050 cm^{-1} (*13, 19-21*). According to Renaudin et al., wet ettringite structure is similar as ettringite dried to 35% relative humidity, and ettringite does not form a high-hydrate polymorph in equilibrium with alkaline solution, whereas AFm phases lose water on drying (*18*).

Table 2 tabulates the characteristics of different microscopy techniques. The analyzed area in is on the scale of μm^2 to mm^2. Based on microscopic experimental results, the ratios between different atoms within the molecular structure are determined with various molecular models proposed (*23-31*). The diversity of different molecular models is due to the following reasons: all these microscopy techniques only provide fragments of the molecular structure information; consequently, the proposed molecular structure only represents the structure located at the measured area.

Table 1 Structures of Cement Concrete and Microscopy Techniques

Scales	Compositions	Features	Microscopy technique
Globules $<5.6\times10^{-9}$ m	○ basic building block	○ 18% nanoporosity ○ structural water	○ AFM ○ TEM
Level 0 10^{-9}~10^{-10} m	○ C-S-H solid ○ Gel porosity	○ LD C-S-H 37% gel porosity ○ HD C-S-H 24% gel porosity	○ TEM ○ EDX ○ EXAFS ○ In-situ SPM
Level I 10^{-6}~10^{-9} m	○ C-S-H matrix ○ two types of C-S-H	○ ultimate building blocks of C-S-H	○ SEM ○ EDX
Level II 10^{-4}~10^{-6} m	○ C-S-H matrix ○ clinker phases ○ CH crystals ○ macroporosity	○ inclusions embedded in porous C-S-H matrix	○ SEM ○ Raman ○ NMR
Level III $\geq10^{-3}$ m	○ cement paste ○ sand ○ aggregate ○ interfacial transition zone (ITZ)	○ porous cement matrix & sand particle inclusions ○ ITZ between inclusions and matrix	○ OM ○ Raman ○ NMR

Note: AFM=Atomic force microscopy, EDX=Energy dispersive X-Ray analysis, NMR=Nuclear magnetic resonance spectroscopy, OM=Optical microscopy, Raman=Raman spectroscopy, SEM=Scanning electron microscopy, SPM=Scanning probe microscopy, TEM=Transmission electron microscopy. (After *22*)

Table 2 Characteristics of Different Microscopy Techniques

Microscopy technique	Resolution	Scale range	Advantage	Disadvantage
AFM	lateral: <1 nm height: <1 Å (MEE-Inc., 2012)	analyzed area: $150\times150\ \mu m^2$ depth: 20 μm	o 3D surface profile o no special treatment to samples o high resolution in three dimensions o can be combined to optical microscopy techniques	o slow rate of scanning may lead to thermal drift in the image o affected by nonlinearity, hysteresis, and creep of piezoelectric material cross-talk between *x*, *y* and *z* axes
SANS	1 nm ~ 1 μm	analyzed area: $1\times1\ \mu m^2$	o sensitive to light element o possible isotope labeling o strong scattering by magnetic moments	o costly neutron source o low neutron flow o large samples are required due to weak interaction with neutron
SAXS	5 nm ~ 150 nm	1 nm ~ 1 μm	o no need to crystalline sample	o loss of information due to spatial averaging compared to crystallography
TEM	0.5 Å (> ×500 million magnification)	5 nm ~ 500 μm	o composition and crystallographic information can be obtained o 3D imaging	o High vacuum environment (1×10^{-9} ~ 1×10^{-4} Torr) o 2D project of sample o <100 nm thick o complex sample preparation: plat polished sample, carbon/gold coated
SEM	Lateral: 0.1 μm ~ 1 μm	50 nm ~ 1 cm	o high magnification (>100,000×) o near real-time (fast scanning rate) o low vacuum environment (<1×10^{-5} Torr)	o complex sample preparation: polished sample, metal/carbon coating o costly equipment
EDX		analyzed area ~ μm^2		

Table 2 (*continued*)

SPM	~ pm	-	o can be observed in air at standard temperature and pressure	o difficult to determine the shape of the scanning tip o very small image size
NMR	~ mm	-	o non-invasive o no contrast media required o 3D structure reconstruction	o too complex information requires great resolving power o bulk sample of a few milligrams contained in NMR tubes o costly equipment
Raman	lateral: 250 nm depth: 1.7 µm	-	o can be used with solids and liquids o no sample preparation needed o non-destructive quick acquisition of Raman spectra	o cannot be used for metals or alloys o sensitive and highly optimized instrumentation o great influence due to the fluorescence of impurities

2.2 Micro-mechanical Properties

To understand the mechanical properties of cement-based materials from multiscale, experimental methods are widely adopted, including destructive and non-destructive methods. In the destructive category, there are four types of experimental methods, including static methods, dynamic methods, indentation methods, and atomic force acoustic microscopy. In the nondestructive category, three types of ultrasonic methods are usually used to measure the elastic properties of cement, including pulse-echo method, V(z) curve method, and resonance ultrasonic microscopy (RUS). Table 3 tabulates the measured mechanical properties in the aforementioned experimental methods.

There are two types of static methods for measuring the elastic properties of stone-based materials, i.e., static tension/compression test and static bending test. In the static tension/compression test, the elastic constant could be determined by means of measuring the displacement as a linear response to the applied force, i.e., a small tensile/compressive load. In the static bending test, the elastic constant could be calculated from the applied bending moment, and the corresponding radius of curvature, as well as the moment of inertia. In Kurtz et al.'s paper, static mechanical test was performed on Acrylic bone cement to compare with the fatigue test results, and the comparison results indicate that bone cement can be designed with barium sulfate level sufficiently high to both retaining overall mechanical properties and permitting fluoroscopic visualization (*32*).

Table 3 Available Methods for the Measurement of Mechanical Properties

Category	Method		Measured properties
Destructive	Static methods	Static tension/compression test	o elastic modulus
		Static bending test	o elastic modulus
	Dynamic methods	Dynamic longitudinal vibration	o dynamic modulus of elasticity o the modulus of elasticity in shear o dynamic Poisson's ratio
		Dynamic flexural vibration	
	Indentation methods	Macro-indentation	o mechanical properties at macroscale
		Micro-indentation	o mechanical properties at microscale
		Nano-indentation	o mechanical properties at nanoscale
	Atomic force acoustic microscopy		o elastic modulus at atomic scale
Nondestructive	Ultrasonic methods	Pulse-echo method	o elastic modulus o shear modulus
		V(z) curve method	o elastic modulus o shear modulus
		Resonance ultrasound spectroscopy (RUS)	o elastic modulus o Poisson's ratio

After (*36-38*)

The dynamic elastic properties, such as dynamic modulus of elasticity, dynamic modulus of elasticity in shear, and dynamic Passion's ratio, could be determined using dynamic vibration methods (*33*). In the dynamic longitudinal vibration test, the specimen is clamped at middle point and free at both ends. On the contrary, in dynamic flexural vibration test, the specimen is clamped at one end and loaded with mass at the other end. On average, dynamic modulus is known to be higher than static modulus, as cement concrete is subjected to very small strain in dynamic test. According to Popovics (*34*), the value of dynamic modulus depends on measurement methods, and the longitudinal vibration test gives a lower prediction value.

Indentation method at macroscale could be used to determine the mechanical properties and fracture toughness of cement. Chou et al. used indentation-strength method to investigate the fracture toughness of a macro-defect free cement, validated using fracture surface analysis (*35*). Micro-indentation method could be utilized to determine micro-mechnical properties of cement matrices in cementitious composites (*36*). Tritik et al. performed the micro-indentation test on cement concrete to quantitatively compare the micro-properties of the interfacial transition zone (ITZ) with those of the bulk cement matrix by characteristics, such as elastic modulus and creep (*36*). Indents within 30 μm distance from the interface are considered as ITZ, whereas indents outside of this distance are

considered as bulk matrix. It was found that elastic modulus within ITZ was about 25 % lower than that of bulk matrix (*36*). Sonebi had successfully used the depth-sensing nano/micro-indentation method to determine the elastic modulus and micro-hardness of the ITZ between aggregates and the paste of underwater concrete and evaluate the extent of the ITZ around the aggregate-matrix interface (*37*). Kurumisawa et al. evaluated the micro-elastic modulus of the C-S-H phases using micro-indentation and then calculated the porosity of C-S-H from the micro-elastic modulus using Jennings' packing model (*38-39*).

Among all the indentation methods, nanoindentation experimental techniques can be used to determine the local mechanical properties of individual constituents. For instance, in hydrated cement paste, the phase mixtures and the short-term creep behaviors of C-S-H phases are be detected using the nanoindentation test (*43-48*). Constantinides et al. confirmed the existence of two types of C-S-H, i.e., HD and LD C-S-H, and investigated the distinct role played by two phases on the elastic properties of cement-based materials (*49*). On the other hand, the application of nanoindentation to the determination of hardness and elastic modulus of asphalt concrete is proved to have great potential for realistic characterization of asphalt mixture components (*50*).

Unlike the aforementioned methods, ultrasonic resonance method is a nondestructive technique that could measure an elastic vibration in a propagating wave (*51*). The most commonly used method is pulse-echo method, determining the elastic constants of materials by measuring the time of flight of sound pulses within bulk materials. The pulse frequency used for testing cementitious materials range from 20 kHz to 250 kHz with 50 kHz being appropriate for field testing of cement concrete (*52*). In 1989, Keating et al. investigated ultrasonic longitudinal (P) wave propagation in fresh cement pastes (*53*). Different from pulse-echo method, V(z) curve method utilizes surface acoustic wave traveling on the surface. Zhu et al. utilized V(z) curve method to investigate the air content in early age cement pastes (*54*). RUS is applicable to a wide range of sample sizes, from micrometers to centimeters, with the advantage of determining elastic constant of a small sample from one spectrum (*55*). RUS measures the natural frequency of elastic vibration for a number of a sample's normal modes along with the shape and mass of the sample, and then process the measured signal using a computer (*51*). At mesocale, elastic properties of cement can be measured using RUS with high precision and great efficiency (*55-57*). Besides mechanical properties, RUS is also capable to measure the temperature-induced phase transition, internal friction and attenuation, as well as the detection of internal flaws and cracks (*55*).

All these techniques have their own advantages to determine the nanostructures and microstructures of stone-based materials. Mechanical properties and/or microstructures of stone-based materials can be determined from microscopic analysis, and then further used as inputs in microstructural modeling for upscaling.

3 Multiscale Modeling of Stone-Based Materials

3.1 Multiscale Modeling Methods for Atomistic-to-Continuum

The atomistic-to-continuum coupling is essential due to the following two reasons. First, a continuum model may not be capable to simulate singular phenomenon, such as dislocations and cracks at microscale; second, simulation of the bulk structure using atomistic model at nanoscale or microscale throughout the whole region is computationally too expensive due to large number of atoms or particles (*58*). Consequently, by considering computational effectiveness, atomistic-continuum coupling models are widely used with atomistic model in the vicinity of singularity regions and continuum model in the other regions.

There are three methods are widely used for the atomistic-to-continuum coupling: quasi-continuum method, Coarse-Grained Molecular Dynamics (CGMD) method and hand-shake method. Quasi-continuum method was firstly developed by Tadmor et al. in 1996. In quasi-continuum method, domain decomposition uses the same physical description, that is to say the same type of governing equation is applied throughout the whole domain (*59-60*). The continuum model is refined down to atomic dimensions where necessary. The energy of each refined mesh is computed from atomistic calculation by calculating a representative portion of each mesh. Deformation gradient is defined at the nodes of the mesh and the atomistic energy is computed for a representative atom embedded in the mesh according to the nodal deformation gradient. A weighted sum of the representative energies determines the energy of the system. The number of degrees of freedom is dramatically reduced from the atomistic model to the continuum model. Its unique advantage is that it avoids common assumptions in continuum models so that the number of degree of freedom is significantly reduced, and its disadvantage is that governing equations at macroscale might not be true at microscale, sometimes leading to unrealistic results.

Coarse-Grained Molecular Dynamics (CGMD) method was proposed by Rudd and Broughton in 2000 (*61*). It is used in cases where the atomistic/continuum coupling is more accurate. The need for a higher quality coupling may be due to the physics of the system under study, like center portion of crack tip. In these cases, CGMD controls the errors introduced by the atomistic/continuum coupling. CGMD provides a consistent treatment of the short wavelength modes which are missing from the coarse finite element mesh. The short wavelength part of the spectrum is relevant to the behavior of the system when the system is sufficiently small or when there is a strong high frequency elastic wave like cracking process. CGMD provides a way to reduce the atomistic coordinates to a much smaller set of degrees of freedom associated with the displacement field at the nodes of the coarse mesh, and the equations of motion for this mean displacement field. The major advantage of CGMD is that the coupling is derived from the atomistic scale.

Hand-shaking method proposed by Abraham et al. in 1998 provides a convenient means to determine how the displacement field on the finite element

mesh coincides with the positions of atoms in the atomistic model and how the forces are determined to satisfy the consistent dynamics and thermodynamics (*62-63*). There are typically three components in the whole simulation region: a finite element model representing for continuum subdomain where the deformation field is smooth and homogeneous, a molecular model representing atomistic subdomain where bond breaking is expected, and a hand-shaking region that somehow couple these two subdomains (*64*). In the hand-shaking region, displacements and forces/energy are usually tied together as constraints (*58, 65*), as shown in Fig. 2. The internal finite element nodes are corresponding to atoms. The equations of motion for the internal nodal fields are not derived from continuum models, but from the underlying atomistic model. The nodal fields represent the average properties of the underlying atoms, and the equations of motion are constructed to describe the mean behavior. Many degrees of freedom are eliminated in the process based on quasi-continuum technology and the calculated displacement and/or force are transferred between nodes based on principles of hand-shaking method. For example, within a distance equal to the range of the inter-atomic potential, finite element nodes in continuum model are placed at the equilibrium position of atoms in the atomistic model, and the displacement field can be viewed as motion of an atom away from its equilibrium position.

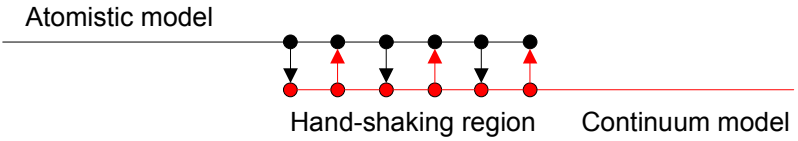

Fig. 2 Hand-shaking region

According to the coupled parameters within the hand-shaking region, there are two types of hand-shaking methods: force-based blending method and energy based blending method. In the first method, displacement field and forces are coupled in the hand-shake region. A force-based blending method was proposed by Badia et al. for coupling atomistic and continuum models, and preliminary one-dimensional computational examples in were presented with the validation of some simple patch tests (*58*). This atomistic-to-continuum coupling method accounts forces acting at nodes in the hand-shaking region; however, the particle displacements are only slaved to displacements in the continuum model in an average sense using Lagrange multipliers to reduce the number of constraints. Besides coupling atomistic and continuum models at the force level, the two models can also be coupled at energy level using Arlequin method with the assumption that energy of the system is shared between the two co-existing models (*66-67*). Seleson et al. proposed an energy blending method for the one-dimensional atomistic-to-continuum blended model, and the equilibrium configuration of the whole system was determined according to the minimization of the blended potential energy (*68*).

3.2 An Example of Multiscale Failure Modeling of Stone-Based Materials

The following content gives an example of multiscale failure modeling of stone-based materials. In this example, cement concrete is chosen as the modeled stone-based material. Cement paste with low tensile strength is more likely to exhibit cracks, consequently reducing durability of cement-based materials. As shown in Fig. 3, failure cracks could occur either within a bulk of cement concrete or along an interface between two different materials; the former crack failure is termed as cohesive crack, and the latter is named as adhesive (or interfacial) crack (*69*). For cohesive cracks, homogenization can be used in a finite element model to represent the bulk material around the crack region; conversely, a micro model can be established to simulate the adhesive layer for adhesive cracks (*69*).

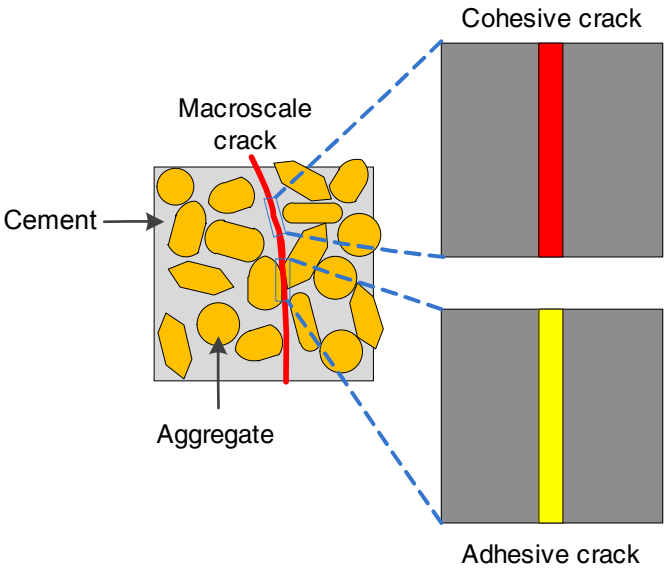

Fig. 3 Cohesive crack and adhesive crack in cement concrete

Nguyen et al. proposed a macro-micro two scales failure model for hydrated cement concrete materials (*1*). At microscale, a numerical cement hydration model was used to simulate the microstructure of cement paste and mechanical behaviors of hardening cement paste. Standard homogenization method was utilized to obtain effective elastic properties of hydrated cement for upscaling. The microstructure was then discretized into a finite element model to perform mechanical simulations at macroscale. Macroscopic failure was represented using cohesive cracks, whose behavior was determined based on finite element simulations realized on microscopic samples. Fig. 4 shows the two-scale finite element failure analysis of mortar under the uniaxial tension test, and a reasonable

force-displacement relationship was achieved. However, there are some unresolved problems in this model: (*i*) inelastic properties of hardening cement are somehow arbitrarily selected in the microscale model without inverse analysis from macroscale experiments; (*ii*) the bridging between microscale and macroscale is not well established yet (*1*).

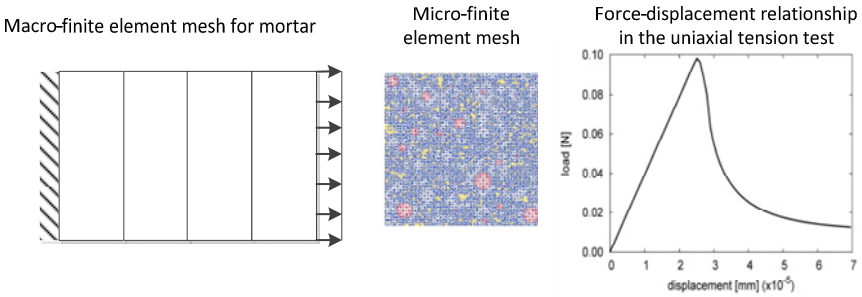

Fig. 4 Two-scale finite element analysis of the uniaxial tension test for mortar (*1*)

4 Conclusions

Based on this investigation, the following conclusions can be drawn.

(*i*) The molecular structure of cement can be determined from different scales by using microscopic techniques, including TEM, XAS, EDX, SEM, NMR, and Rama microcopy, etc. All these techniques have their own advantages to understand the nanostructures and microstructures of hydrated cement pastes/concrete, depending on which mechanical properties and/or microstructures of cement paste can be determined on the scale from μm to nm. However, there are a great variety of molecular models for stone-based materials. The diversity of molecular models is due to the following reasons: all these microscopy techniques only provide fragments of the molecular structure information; consequently, the proposed molecular structure only represents the structure located at the measured area.

(*ii*) There are three widely used methods for the atomistic-to-continuum coupling: Quasi-continuum method, CGMD method and hand-shake method. In quasi-continuum method, the same type of governing equation is applied throughout both microscale and macroscale. Its unique advantage is that common assumptions are avoided in continuum models so that the number of degree of freedom is significantly reduced, and its disadvantage is that governing equations at macroscale might not be true at microscale, leading to unrealistic results. CGMD method usually provides better accuracy than quasi-continuum method. The advantage of CGMD method is that coupling is originated from atomistic scale, therefore, microstructure of simulated materials is well represented. In handshaking method, there are mainly three components: a finite element model

representing for continuum subdomain, a molecular model representing atomistic subdomain, and a hand-shaking region that somehow couple these two subdomains. Handshaking method is recommended, because both microstructure and macrostructure could be well represented.

(*iv*) There are two types of failure cracks in cement-based materials: cohesive cracks and adhesive crack. In Nguyen et al.'s macro-micro two-scale failure simulation of cement concrete, cohesive cracks are simulated using a numerical hydration model at microscale and a finite element model at macroscale. This model is capable to analyze uniaxial tension failure of cement concrete in two-dimension. Further efforts should be made to improve the selection of inelastic properties in the microscale model and the bridging between two scales.

References

1. Nguyen, V.P., Stroeven, M., Sluys, L.J.: Multiscale failure modeling of concrete: Micromechanical modeling, discontinuous homogenization and parallel computations. Computer Methods in Applied Mechanics and Engineering 201-204, 139–156 (2012)
2. Aigner, E., Lackner, R., Pichler, C.: Multiscale prediction of viscoelastic properties of asphalt concrete. Journal of Materials in Civil Engineering 21, 771–780 (2009)
3. Jennings, H.M., Bullard, J.W., Thomas, J.J., Andrade, J.E., Chen, J.J., Scherer, G.W.: Characterization and modeling of ores and surfaces in cement paste: correlations to processing and properties. Journal of Advanced Concrete Technology 6, 5–29 (2008)
4. Selvam, R.P., Subramani, V.J., Murray, S., Hall, K.: Potential application of nanotechnology on cement based materials. Publication MBTC DOT 2095/3004. Arkansas Highway and Transportation Department (AHTD) and Mack-Blackwell Rural Transportation Center, MBTC (2009)
5. Richardson, I.G.: The nature of C-S-H in hardened cements. Cement and Concrete Research 29, 1131–1147 (1999)
6. Richardson, I.G.: Electron microscopy of cements. In: Bensted, J., Barnes, P. (eds.) Structure and Performace of Cements, 2nd edn. Spon Press, London (2002)
7. Richard, N., Lequeux, N., Boch, P.: EXAFS study of refractory cement phases: $CaAl_2O_{14}H_{20}$, $Ca_2Al_2O_{13}H_{16}$, and $Ca_3Al_2O_{12}H_{12}$. Journal of Phys. 5, 1849–1864 (1995)
8. Scheideger, A.M., Vespa, M., Grolimund, D., Wieland, E., Harfouche, M., Bonhoure, I., Dahn, R.: The use of (micro)-X-RAY absorption spectroscopy in cement research. Waste Management 26, 699–705 (2006)
9. ASTM C1723 - 10 Standard guide for examination of hardened concrete using scanning electron microscopy. In: ASTM International, West Conshohocken, PA (2010), doi:10.1520/C1723-10
10. Bentz, D.P., Stutzman, P.E.: Curing, hydration, and microstructure of cement paste. ACI Materials Journal 103, 348–356 (2006)
11. Macomber, R.S.: A complete introduction to modern NMR spectroscopy. Wiley, New York (1998)
12. Lippmaa, E., Magi, M., Samoson, A., Engelhardt, G., Grimmer, A.R.: Structural studies of silicates by solid-state high-resolution ^{29}Si NMR. Journal of the American Chemical Society 102, 4889–4893 (1980)

13. Richardson, I.G., Skibsted, J., Black, L., Kirkpatrick, R.J.: Characterization of cement hydrate phases by TEM, NMR and Raman spectroscopy. Advances in Cement Research 22, 233–248 (2010)
14. Wieker, W., Grimmer, A.-R., Winkler, A., Tarmak, M., Lippmaa, E.: Solid-state high-resolution 29Si NMR spectroscopy of synthetic 14 Å, 11 and 9 Å tobermorites. Cement and Concrete Research 12, 333–339 (1982)
15. Bell, G.M.M., Benstedm, J., Glasser, F.P., Lachowski, E.E., Roberts, D.R., Taylor, M.J.: Study of calcium silicate hydrate by solid state high resolution ^{29}Si nuclear magnetic resonance. Advances in Cement Research 3, 23–27 (1990)
16. Cong, X., Kirkpatrick, R.J.: ^{29}Si MAS NMR study of the structure of calcium silicate hydrate. Advances in Cement Based Materials 3, 144–156 (1996)
17. Kim, J.J., Rahman, M.K., Taha, M.M.R.: Examining microstructural composition of hardened cement paste cured under high temperature and pressure using nanoindentation and ^{29}Si MAS NMR. Journal of Applied Nanoscience (2012), doi:10.1007/s13204-012-0058
18. Renaudin, G., Filinchuk, Y., Neubauer, J., Goetz-Neunhoeffer, F.: A comparative structural study of wet and dried ettringite. Cement and Concrete Research 40, 370–375 (2010)
19. Kirkpatrick, R.J., Yarger, J.L., McMilan, P.F., Yu, P., Cong, X.D.: Raman spectroscopy of C-S-H, tobermorite, and jennite. Advanced Cement Based Materials 5, 93–99 (1997)
20. Black, L., Breen, C., Yarwood, J., Garbev, K., Stemmermann, P., Gasharova, B.: Structural features of C-S-H(I) and its carbonation in air – A Raman spectroscopic study. Part II: Carbonated phases. Journal of the America Ceramic Society 90, 908–917 (2007)
21. Garbev, K., Stemmermann, P., Black, L., Breen, C., Yarwood, J., Gasharova, B.: Structural features of C-S-H(I) and its carbonation in air – A Raman spectroscopic study. Part I: Fresh phases. Journal of the American Ceramic Society 90, 900–901 (2007)
22. Ulm, F.-J., Constantinides, G., Heukamp, F.H.: Is concrete a poromechanics materials? - A multiscale investigation of poroelastic properties. Materials and Structures 37, 43–58 (2004)
23. Feldman, R.F., Sereda, P.J.: A new model for hydrated Portland cement and its practical implications. Engineering Journal of Canada 53, 53–59 (1970)
24. Jennings, H.M.: A model for the microstructure of calcium silicate hydrate in cement paste. Cement and Concrete Research 30, 101–116 (2000)
25. Jennings, H.M., Thomas, J.L., Gevrenov, J.S., Constantinides, G., Ulm, F.-J.: A multi-technique investigation of the nanoporosity of cement paste. Cement and Concrete Research 37, 329–336 (2007)
26. Jennings, H.M.: Refinements to colloid model of C-S-H in cement; CM II. Cement and Concrete Research 38, 275–289 (2008)
27. Mondal, P., Shah, S.P., Marks, L.: A reliable technique to determine the local mechanical properties at the nanoscale for cementitious materials. Cement and Concrete Research 37, 1440–1444 (2007)
28. Pellenq, R.J.-M., Kushima, A., Shahsavari, R., Van Vliet, K.J., Buehler, M.J., Yip, S., Ulm, F.-J.: A realistic molecular model of cement hydrates. Proceedings of the National Academy of Science (PNAS) 106, 16102–16107 (2009)

29. You, T., Abu Al-Rub, R.K., Darabi, M.K., Masad, E.A., Little, D.N.: Three-dimensional microstructural modeling of asphalt concrete using a unified viscoelastic-viscoplastic-viscodamage model. Construction and Building Materials 28, 531–548 (2012)
30. You, Z.P., Adhikari, S., Dai, Q.L.: Three-dimensional discrete element models for asphalt mixtures. Journal of Engineering Mechanics 134, 1053–1063 (2008)
31. Öchsner, A., Murch, G.E., Shokuhfar, A., Delgado, J.M.P.Q.: Microstructure and properties of nanoclay reinforced asphalt binders. Defects in Solids and Liquids V 297-301, 579–583 (2010)
32. Kurtz, S.M., Villarraga, M.L., Zhao, K., Edidin, A.A.: Static and fatigue mechanical behavior of bone cement with elevated barium sulfate content for treatment of vertebral compression fractures. Biomaterials 26, 3699–3712 (2005)
33. ASTM C215-08 Standard Test Method for Fundamental Transverse, Longitudinal, and Torsional Frequencies of Concrete Specimens. In: ASTM International, West Conshohocken, PA (2008), doi:10.1520/C0215-08
34. Popovics, J.S.: A study of static and dynamic modulus of elasticity of concrete. ACI-CRC Final report (2008)
35. Chou, Y.-S., Mecholsky Jr., J.J., Silsbee, M.R., Roy, D.M., Adair, J.H., Heiland, P.: Indentation fracture of macro-defect free (MDF) cements. In: 1989 MRS Proceeding, vol. 179, p. 123 (1998), doi:10.1557/PROC-179-123
36. Tritik, P., Bartos, P.J.M.: Micromechnical properties of cementitious composites. Materials and Structures 32, 388–393 (1999)
37. Sonebi, M.: Utilization of micro-indentation technique to determine the micromechanical properties of ITZ in cementitious material. In: Proceedings of ACI Session on "Nanotechnology of Concrete: Recent Development and Future Perspectives", Denver, USA (November 2006)
38. Kurumisawa, K., Nawa, T., Owada, H.: Prediction of the diffusivity of cement-based materials using a three-dimensional spatial distribution model. Concrete and Cement Research 34, 408–418 (2011)
39. Jennings, H.M., Thomas, J.J., Gevrenov, J.S., Contantinides, G., Ulm, F.-J.: A multi-technique investigation of the nanoporosity of cement paste. Cement and Concrete Research 37, 329–336 (2007)
40. Kim, N., Kim, H.-J., Oh, S.-W., Hozumi, H., Lee, C.-K., Hong, M.: Ultrasonic measurement of elastic properties of nanostructural alumina. Key Engineering Materials 321-323, 1711–1714 (2006)
41. Wu, W.: Multiscale modeling and simulation of concrete and its constituent materials: from nano to continuum, PhD Dissertation, University of Mississippi (2008)
42. Kim, J.H., Balogun, O., Shah, S.P.: Atomic force acoustic microscopy to measure nanoscale mechanical properties of cement pastes. Transposration Research Record: Journal of Transportation Research Board, No. 2141, 102–108 (2010)
43. Constantinides, G., Ulm, F.-J., Van Vliet, K.: On the use of nanoindentation for cementitious materials. Materials and Structures 36, 191–196 (2003)
44. Hughes, J.J., Trtik, P.: Micro-Mechanical properties of cement paste measured by depth-sensing nanoindentation: A preliminary correlation of physical properties with phase type. Materials Characterization 53, 223–231 (2004)
45. Ulm, F.-J., Vandamme, M., Bobko, C., Ortega, J.A., Tai, K., Ortiz, C.: Statistical indentation techniuqes for hydrated nanocomposites: concrete, bone and shale. Journal of the American Ceramic Society 90, 2677–2692 (2007)

46. Sorelli, L., Constantinudes, G., Ulm, F.-J., Toutlemonde, F.: The nano-mechanical signature of ultra-high performance concrete by statistical nanoindentation techniques. Cement and Concrete Research 38, 1447–1456 (2008)
47. Chen, J.J., Sorelli, L., Vandamme, M., Ulm, F.-J., Chanvillard, G.: A coupled nanoindentation/SEM-EDS study on low water/cement ratio Portland cement paste: evidence for C-S-H/$Ca(OH)_2$ nanocomposites. Journal of the American Ceramic Society 93, 1484–1493 (2010)
48. Jones, C.A., Grasley, Z.C.: Short-term creep of cement paste during nanoindentation. Cement and Concrete Composites 33, 12–18 (2010)
49. Constantinides, G., Ulm, F.-J.: The effect of two types of C-S-H on the elasticity of cement-based materials: Results from nanoindentation and micromechanical modeling. Cement and Concrete Research 34, 67–80 (2004)
50. Tarefder, R.A., Zaman, A.M., Uddin, W.: Determining hardness and elastic modulus of asphalt by nanoindentaiton. Internaitonal Journal of GeOMECHANICS 10, 106–116 (2010)
51. Maynard, J.D.: Resonant ultrasound spectroscopy. Phys. Today 49, 26–31 (1996)
52. Tesinova, P.: Advances in composite materials – analysis of natural and man-made materials. InTech (2011)
53. Keating, J., Hannant, D., Hibbert, A.: Comparison of shear modulus and pulse velocity techniques to measure the buildup of structure in fresh cement pastes used in oil-well cementing. Cement and Concrete Research 19, 554–566 (1989)
54. Zhu, J., Kee, S.-H., Han, D., Tsai, Y.-T.: Effects of air voids on ultrasonic wave propagation in early age cement pastes. Cement and Concrete Research 41, 872–881 (2011)
55. Wu, W., Al-Ostaz, A., Gladden, J., Cheng, A.H.-D.: Measurement of mechanical properties of hydrated cement paste using resonant ultrasonic spectroscopy. Journal of ASTM International 7, 2657–2665 (2010)
56. Maynard, J.D.: The use of piezoelectric film and ultrasound resonance to determine the complete elastic tensor in one measurement. Journal of the Acoustic Society of America 91, 1754–1762 (1992)
57. Ulrich, T.J., McCall, K.R., Guyer, R.A.: Determination of elastic moduli of rock samples using resonant ultrasound spectroscopy. Journal of the Acoustic Society of America 111, 1667–1674 (2002)
58. Badia, S., Bochev, P., Fish, J., Gunzburger, M., Lehoucq, R., Nuggehally, M., Parks, M.L.: A force-based blending model for atomistic-to-continuum coupling. International Journal for Multiscale Computational Engineering 5, 387–406 (2007)
59. Tadmor, E.B., Ortiz, M., Philips, R.: Quasicontinuum analysis of defects in solids. Philosophical Magazine 73, 1529–1563 (1996)
60. Knap, J., Ortiz, M.: An analysis of the quansicontinuum method. Journal of the Mechanics and Physics of Solids 49, 2001 (1923)
61. Rudd, R.E., Broughton, J.Q.: Concurrent Coupling of Length Scales in Solid State Systems. Physica Status Solidi (b) 217, 251–291 (2000)
62. Abraham, F.F., Broughton, J.Q., Berstein, N., Kaxiras, E.: Spanning the length scales in dynamic simulation. Computer in Physics 12, 538–546 (1998)
63. Abraham, F.F., Broughton, J.Q., Berstein, N., Kaxiras, E.: Spanning the continuum to quantum length scales in a dynamic simulation of brittle fracture. Europhysics Letters 44, 783–787 (1998)

64. Zhang, S., Khare, R., Lu, Q., Belytschko, T.: A bridging domain and strain computation method for coupled atomistic-continuum modeling of solids. International Journal for Numerical Methods in Engineering 70, 913–933 (2007)
65. Xiao, S.P., Belytschko, T.: A bridging domain method for coupling continua with molecular dynamics. Computer Methods in Applied Mechanics and Engineering 193, 1645–1669 (2004)
66. Dhia, H.B.: Multiscale mechanical problems: the Arlequin method. Comptes Rendus de l'Academie des Sciences Series IIB 326, 889–904 (1998)
67. Prudhomme, S., Dhia, H.B., Bauman, P.T., Elkhodja, N., Oden, J.T.: Computational analysis of modeling error for the coupling of particle of particle and continuum models by the Arlequin method. Computer Methods in Applied Mechanics and Engineering 197, 3399–3409 (2008)
68. Seleson, P., Gunzburger, M.: Bridging methods for atomistic-to-continuum coupling and their implementation. Communications in Computational Physics 7, 831–876 (2010)
69. Nguyen, V.P.: Multisclae failure modeling of quasi-brittle materials. PhD Dissertation, Delft University of Technology, Delft, Netherland (2011)

Effects of Various Modifiers on Rheological Property of Asphalt

Guo Meng and Tan Yiqiu

School of Transportation Science and Engineering, Harbin Institute of Technology, Harbin 150090, Heilongjiang, P.R. China

Abstract. The effects of different modifiers on rheological properties of asphalt were studies by dynamic shear tests. Seven kinds of asphalt binders were used to study the viscoelastic effects based on the hysteresis loop analysis from the following aspects: accumulation of deformation, elastic stored energy, viscous dissipative energy, viscoelastic ratio and complex modulus. Another two kinds of modified asphalts were used to verify the previous results and to describe performance of composite modified asphalt by conventional dynamic sweep tests. The results show that it is practicable and effective to use energy method to evaluate viscoelastic properties of asphalt; Aromatic oil can increase residual strain dramatically; Combination of rubber powder (or SBS) and aromatic oil can increase elastic stored energy greatly; Both rubber powder and SBS can increase viscoelastic ratio dramatically, followed by SBR; Composite modified asphalt has an excellent performance on road engineering.

Keywords: Asphalt, Modifier, Rheology, Hysteresis loop, Dynamic shear rheometer.

1 Introduction

Asphalt is used widely in pavement construction because of its superior qualities, such as readily adhesive, highly waterproof, and durable, etc. The polymer modified asphalt used in the road construction has more advantages including lower susceptibility to daily and seasonal temperature variations, higher resistance to deformation at elevated pavement temperature, better adhesion between aggregate and binder, higher fatigue life of mixes, delay of cracking including reflective cracking, overall improved performance in extreme climatic conditions, and heavy traffic conditions. The performance of asphalt modified by various polymers including polyethylene (PE), crumb rubber (CR), styrene–butadiene–styrene (SBS), ethylene vinyl acetate (EVA), styrene–butadiene rubber (SBR), and starch have been described (Singh et al. 2013; Moren et al. 2013; Al-Hadidy and Tan 2010; Zhang and Yu 2010; Sengoz and Isikyakara 2008). These modifiers can improve the high and low temperature characteristics of asphalt compositions, as

N. Kringos et al. (Eds.): *Multi-Scale Model. & Charact. of Infrastruct. Mater.,* RILEM 8, pp. 343–356.
DOI: 10.1007/978-94-007-6878-9_25

well as to improve their toughness and durability. Materials in this paper include neat asphalt binder, rubber powder, SBS, SBR and aromatic oil.

Substantial benefits can be achieved by designing longer lasting asphalt pavements which are less susceptible to common distresses. Major hot mix asphalt (HMA) pavement distresses such as rutting, raveling, and stripping can be assessed by using the rheological characteristics of asphalt binders (Soleymani et al. 2004). Dynamic shear modulus (G*) and phase angle (δ) are two key rheological parameters to characterize Performance Grade (PG) asphalt binders introduced in the Superpave (Superior Performing Asphalt Pavements) binder specifications (Roberts et al. 1996). SHRP specification properties rutting factor (G*/sinδ) and fatigue factor (G*sinδ) can reflect rutting and fatigue resistances of asphalt, respectively. But viscoelastic behaviors of different modified asphalts can't be described and distinguished exactly only by these parameters.

The purposes of doing the present research work are to: (1) find indexes which can distinguish the effects of different modifiers on rheological properties of asphalt clearly. (2) compare the effects of mixing various modifiers to neat asphalt binder in terms of viscoelastic property, temperature susceptibility, fatigue life, etc;

2 Materials and Test Methods

2.1 Experimental Materials

Asphalt

As the basic raw material, the property of asphalt undoubtedly plays a vital role in preparation. The asphalt binder used in this paper is with the penetration grade 90 produced in liaohe of china, which is more extensive in production and use. The basic properties of asphalt are shown in Table 1.

Table 1 Physical properties of neat asphalt binder

Property	Unit	Engineering requirements	Test result	Test method
		AH-90	AH-90	
Penetration (100g, 5s, 25°C)	0.1mm	80~100	83.1	ASTM D-5
Ductility (5cm/min, 10°C)	cm	_	>100	ASTM D-113
Ductility (5cm/min, 15°C)	cm	≥100	>140	ASTM D-113
Softening point	°C	42~52	46.2	ASTM D-36
Solubility (Triclene)	%	99.0	99.4	ASTM D-2042
Flash point (COC)	°C	230	320	ASTM D-92
Density (15°C)	g/cm^3	actual measurement	1.008	ASTM D-1298
Wax content (Distillation method)	%	≤3	1.5	UOP46-85

SBS Powder

SBS used in this study is linetype-3411 produced in Taiwan, which technical data is shown in Table 2. The contents of all additives used in this paper were determined by referring the work of Tan et al. (Tan et al. 2012).

Table 2 Physical properties of SBS

Test item	Proportion	Hardness (shore A)	Volatile matter content (%)	Butadiene/styrene	Ash content (%)	25% toluene solution viscosity (mPa•s)
Test data	0.94	80	0.25	70/30	0.1	20000

SBR Powder

SBR powder used in this paper grafted the SBR styrene monomer in butadiene styrene rubber, whose technical specifications are shown in Table 3.

Table 3 Quality standards of SBR

Test item	Particle size (mesh)	Molecular weight (thousand)	Combination of styrene (%)	Raw rubber Mooney viscosity [M/(1+4)100℃]
Quality indicators	≤40	200~300	21.5~35	47~66

Rubber Powder and Aromatic Oil

The rubber powder of 50-100 mesh was obtained by sieving with standard square holes sieve. Aromatic oil is a kind of light oil.

2.2 Laboratory Testing

Determination of Processing Technic

The processing technic is shown in Fig. 1 by referencing the results of Al-Hadidy and Tan (Al-Hadidy and Tan 2007). The stirring speed was 4000 circles/min.

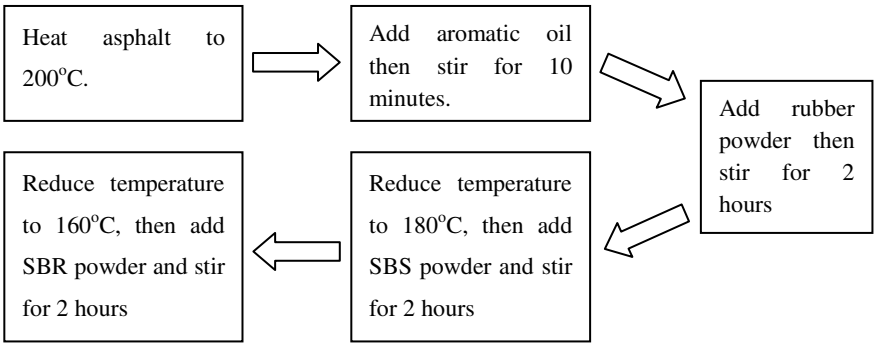

Fig. 1 Preparation process of sealant

Dynamic Shear Rheometer Test

The dynamic shear rheometer (DSR) applies a shearing force to a thin sandwiched between two plates (Fig. 2); the lower plate is fixed, and the upper plate oscillates back and forth across the asphalt sample at a fixed frequency and strain (or stress) amplitude to create the shearing action.

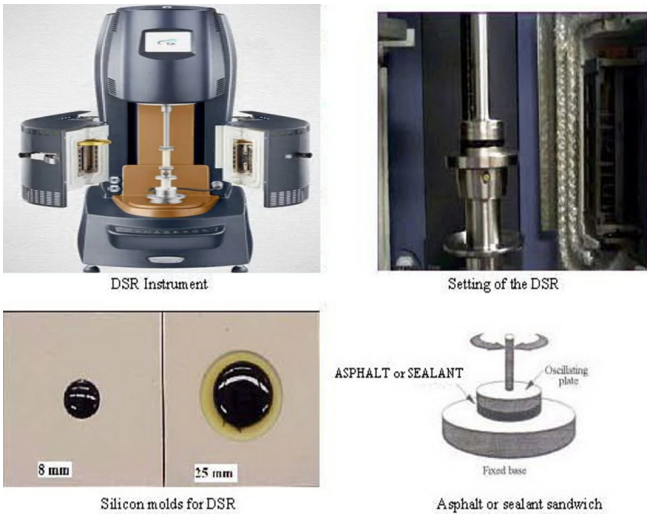

Fig. 2 DSR apparatus

The conventional DSR tests were performed in the light of the AASHTO T315-2 under the following test conditions:

- Strain sweep: mode of loading: controlled-strain (0.1%--100%).
  temperature: 25°C.
  frequency: 1.59Hz.
- Temperature sweep: mode of loading: controlled-strain (2%).
  temperatures: 10°C, 20°C, 30°C, 40°C, 50°C, 60°C.
  frequency: 1.59Hz.
- Time sweep: mode of loading: controlled-strain (12%).
  temperature: 25°C.
  frequency: 1.59Hz.
  time: 600s.

Hysteresis Loop Test

One hysteresis loop could be obtained by using DSR to make a cyclic load on the specimen once (Fig 3). Loss energy can be described as the area surrounded by the loop (red area in Fig 3, ω_1). Storage energy can be described as the area surrounded by restore strain curves (green area in Fig 3, ω_2). Elastic proportion is defined as the following formula: $\omega_2/(\omega_1+\omega_2)$. Residual strain ($\varepsilon'$) is used to describe the deformation after some load circles. Complex modulus is defined as the following formula: $\sigma_{max} / \varepsilon_{max}$. This paper tested neat asphalt binder and six different kinds of modified asphalt, and analyzed the indicators in fifty load circles. Stress-controlled log-type torsional shear cyclic tests were conducted at stress level of 500Pa at 25 °C and 8.33×10^{-3} Hz. The total loading cycles were 50 and the viscoelastic parameters were calculated by the 50th loading.

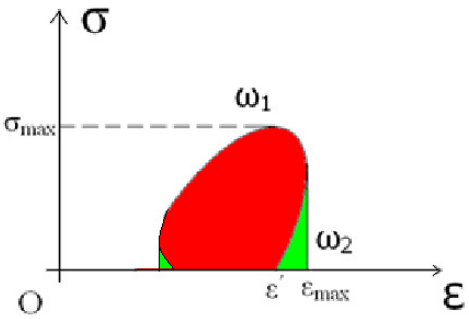

Fig. 3 Schematic of hysteresis loop analysis

3 Results and Discussion

3.1 Analysis of Hysteresis Loop Test

Residual strain can be used to characterize the permanent deformation resistance of modified asphalt. The smaller the residual strain is, the stronger the resistance ability of permanent deformation is.

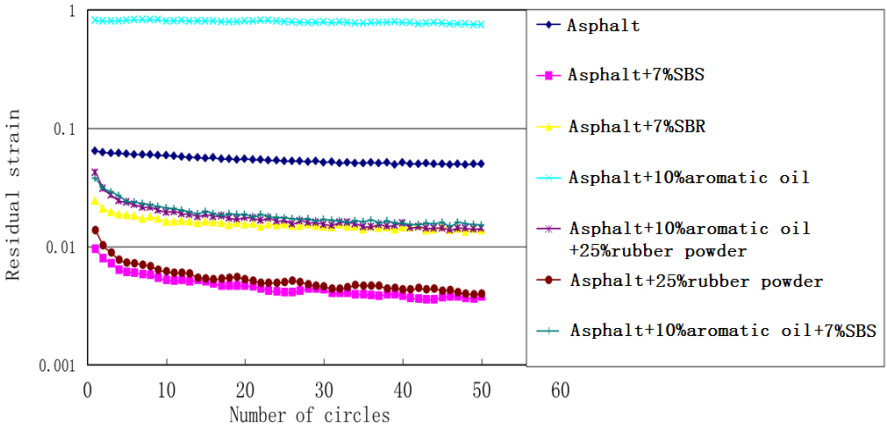

Fig. 4 Relationship between residual strain and number of load circles

Fig. 4 shows that in terms of reducing residual strain, the effects of rubber powder and SBS are the same (nearly 92%), and are larger obviously than SBR. Addition of aromatic oil will make the residual strain increase dramatically. The combined effects of aromatic oil and rubber powder (or SBS) make the same contribution to the decrease of residual strain with the individual influence of SBR (nealy 70%).

Complex modulus is used to characterize the stiffness of modified asphalt.

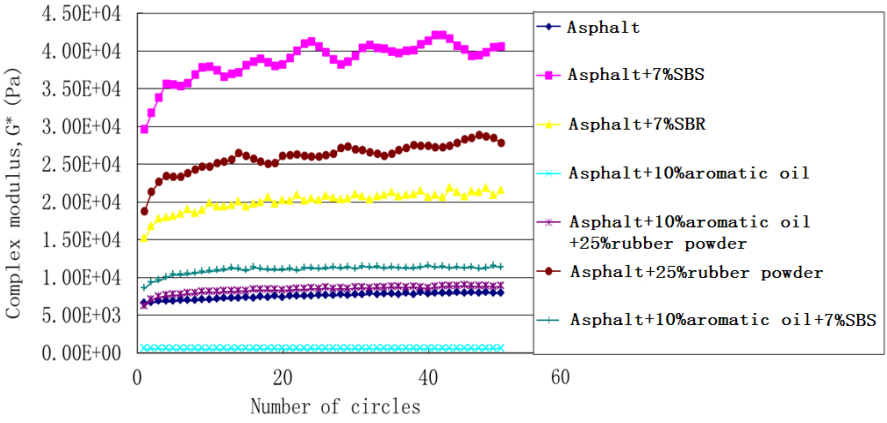

Fig. 5 Relationship between complex modulus and number of load circles

Fig. 5 shows that complex modulus is most sensitive to the additions of aromatic oil and SBS (increasing by more than three times), while rubber powder and SBR effect less. So when the softness of modified asphalt needed to be changed dramatically, aromatic oil and SBS could be added, and when the softness of modefied asphalt is close to the optimum value, SBR and rubber powder can be used to change it slightly. In addition, it can be seen from Fig. 15 that the curve of the asphalt modified by aromatic oil and rubber powder is nearly the same as neat asphalt binder, which indicates that the effects of rubber powder and aromatic oil on complex modulus just cancel each other out.

Storage energy is used to characterize elastic behavior of modified asphalt under the repeated loading. The more modified asphalt storage energy is, the stonger deformation recoverability of modified asphalt is.

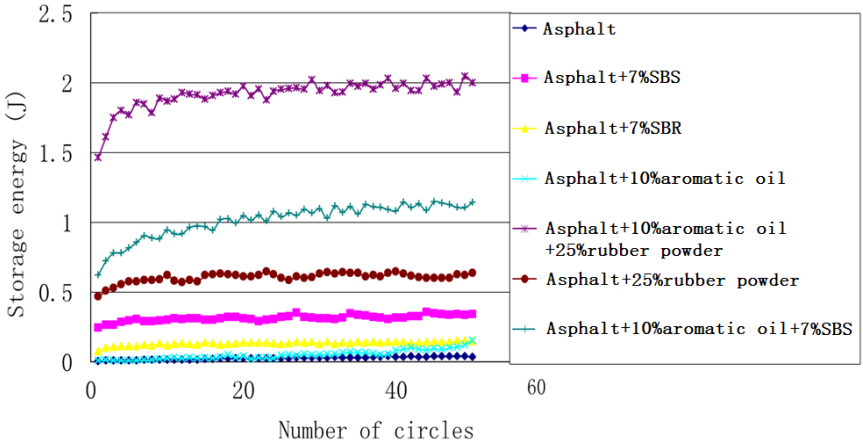

Fig. 6 Relationship between storage energy and number of load circles

Fig. 6 shows that when only one factor is considered, rubber powder can improve the elasticity of modified asphalt the most, and SBS comes second (accounting for half of the rubber powder), then followed by SBR, and aromatic oil effects the least. But the interaction of aromatic oil and rubber powder (or SBS) can make a substantial increase (by three times of single additive) in elastic energy storage capacity, which indicates that aromatic oil can play a role of helping rubber powder (or SBS) dissolve, swelling, and decentralize.

Loss energy is used to characterize the energy making modified asphalt flow viscously under repeated loading, which is unrecoverable.

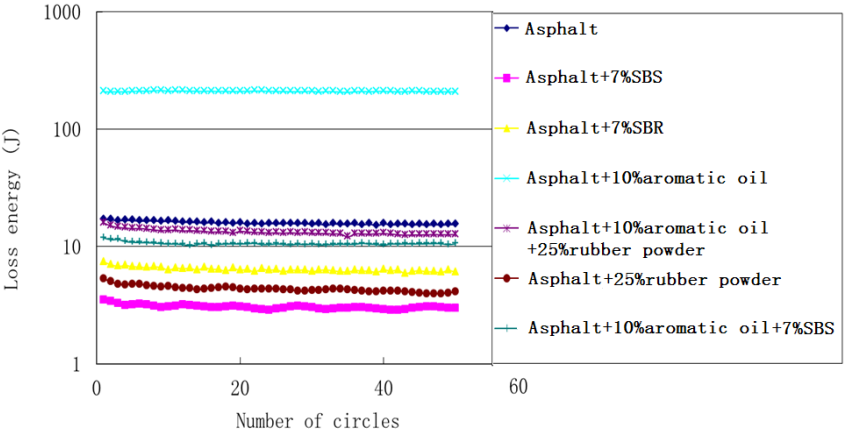

Fig. 7 Relationship between loss energy and number of load circles

Fig. 7 indicates that the addition of aromatic oil can increase loss energy rapidly, and can make the viscous flow of modified asphalt become easier. In contrast, SBS, rubber powder and SBR can increase the viscosity of modified asphalt, so as to decrease loss energy, whose rank are in the following order: SBS > rubber powder > SBR. When aromatic oil and rubber powder (or SBS) work together, the effect is not obvious.

Elastic proportion is used to characterize relationgship between elasticity and viscosity of modified asphalt. The lager elastic proportion value is, the more the recoverable part of modified asphalt deformation is, that is, the stronger its ability of resisting permanent deformation is.

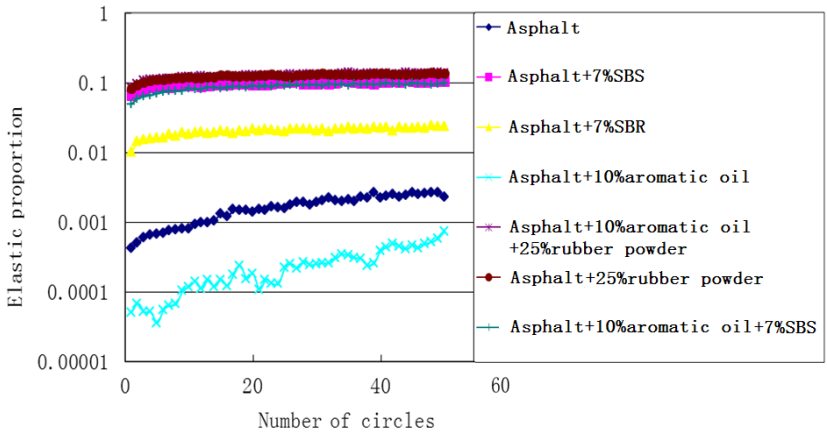

Fig. 8 Relationship between elastic proportion and number of load circles

Fig. 8 shows that when only one factor is considered, aromatic oil can decrease elastic proportion, while rubber powder, SBS, and SBR can increase it. The capacities of proportion rubber powder and SBS for increasing elastic are nearly the same, both stronger than SBR. It can be seen that when aromatic oil and rubber powder (or SBS) work together, the addition of aromatic oil has no impact on the elastic proportion of specimens, which result from that aromatic oil increases the elastic storage energy and viscous dissipated energy at the same time.

3.2 Conventional Dynamic Sweep Tests

In order to study the effects of strain, temperature and loading time on the rheological property of composite modified asphalt and verify the previous conclusions, neat asphalt binder and PMA-A (asphalt+25%rubber powder+5%SBR+7%aromatic oil) were tested by strain sweep, temperature sweep and time sweep methods. In order to verify the elastic enhancing effect of SBS in composite modified asphalt, PMA-B (asphalt+25%rubber powder+5%SBS+3%SBR+10%aromatic oil) were tested by time sweep method.

Strain Sweep Test

The strain sweep results of PMA-A and neat asphalt binder are shown in Figs. 9 and Figs. 10.

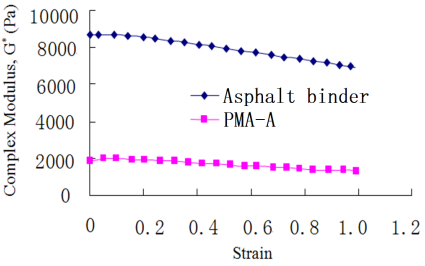

Fig. 9 Relationship between complex modulus and strain

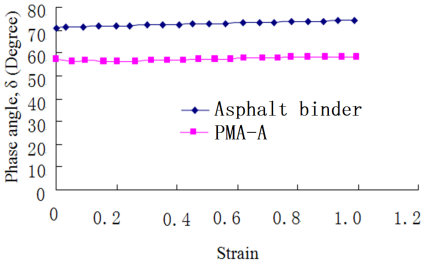

Fig. 10 Relationship between phase angle and strain

Fig. 9 shows that complex modulus decreases gradually with strain increasing, and initial data indicates the linear viscoelastic range for neat asphalt binder is 35%, and PMA-A is 38%. Fig. 9 also indicates that PMA-A is not sensitive to strain change compared with neat asphalt binder. Fig. 10 indicates that PMA-A has more elastic proportion than neat asphalt binder, that is, PMA-A is better at resisting permanent deformation than neat asphalt binder.

Temperature Sweep Test

The temperature sweep results of PMA-A and neat asphalt binder are shown in Figs. 11 ~ Figs. 14.

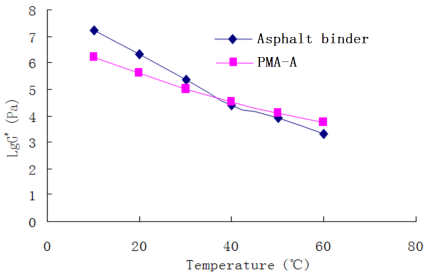

Fig. 11 Relationship between lg G* and temperature

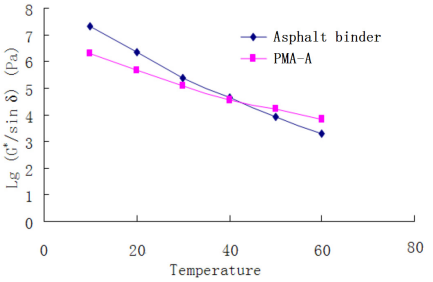

Fig. 12 Relationship between rutting factor and temperature

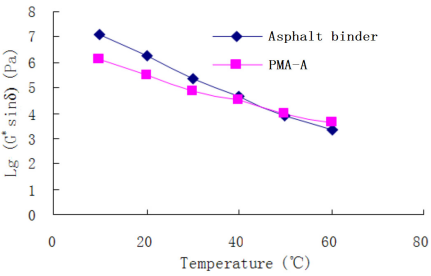

Fig. 13 Relationship between fatigue factor and temperature

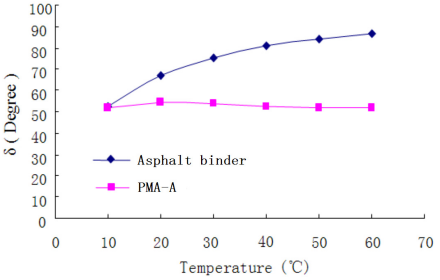

Fig. 14 Relationship between phase angle and temperature

Fig. 11-13 indicate that both PMA-A and neat asphalt binder are sensitive to temperature, and the lower the temperature is, the faster the speed of change is, and the temperature susceptibility of PMA-A is better than neat asphalt binder. Fig. 12 shows that the permanent deformation resistant capacity of PMA-A and neat asphalt binder decrease dramatically with temperature increasing. When the temperature is more than 40°C, the rutting factor (G*/sinδ) of PMA-A is larger than neat asphalt binder, that is, the resistant capacity of permanent deformation of PMA-A is stronger than neat asphalt binder when the temperature is higher than 40°C. Fig. 13 indicates that anti-fatigue performance of PMA-A and neat asphalt binder become better with the temperature increasing. When the temperature falls down below 40°C, the fatigue factor of PMA-A is smaller than neat asphalt binder, which indicates that the anti-fatigue performance of PMA-A is stronger than neat asphalt binder when temperature is lower than 40°C.

Fig. 14 shows that phase angle of neat asphalt binder is very sensitive to temperature, while PMA-A changes little with temperature changing. When the temperature is between 10°C and 60°C, the phase angle of PMA-A is smaller than neat asphalt binder, which indicates that elastic proportion of PMA-A is larger than the neat asphalt binder. When the temperature increases to more than 60°C, the phase angle of neat asphalt binder is nearly 90 degrees, and it goes into viscous flow state with the loss of its elasticity.

Time Sweep Test

The time sweep results of PMA-A, PMA-B and neat asphalt binder are shown in Figs. 15 ~ Figs. 18.

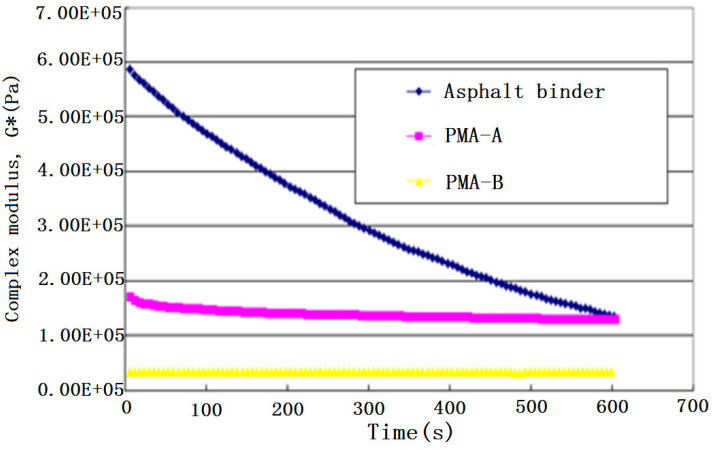

Fig. 15 Relationship between complex modulus and time

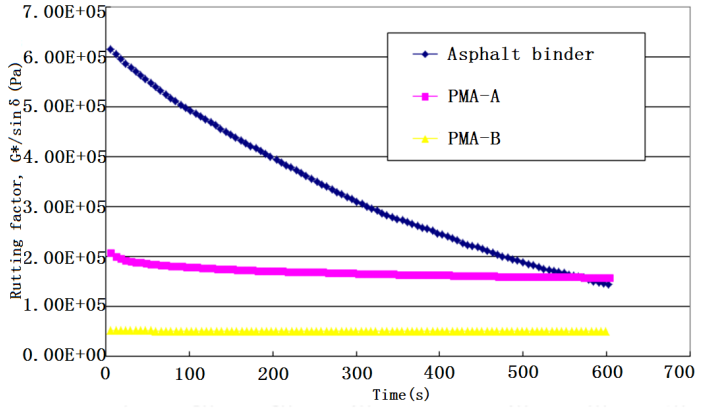

Fig. 16 Relationship between rutting factor and time

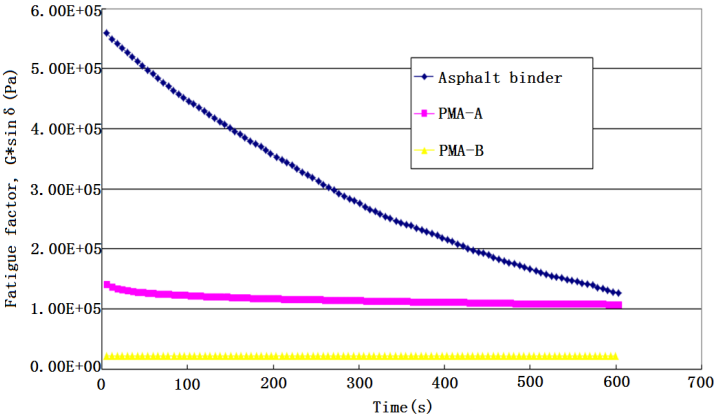

Fig. 17 Relationship between fatigue factor and time

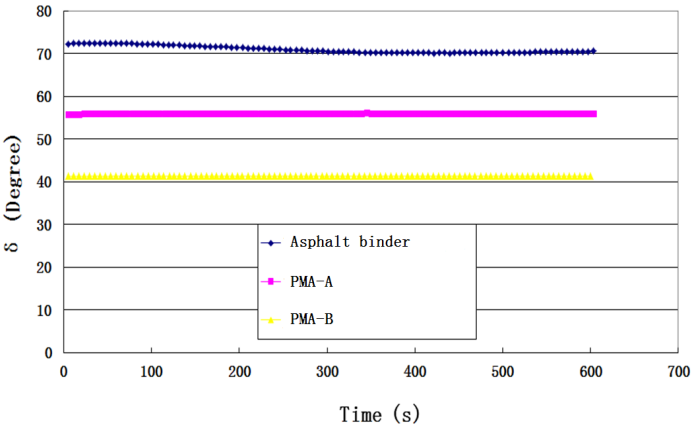

Fig. 18 Relationship between phase angle and time

Fig. 15~Fig. 17 show that many indicators of neat asphalt binder decrease rapidly with time increasing, while PMA-A decrease slightly only in the initial stage, soon entere into a stable state, and PMA-B changes little, which indicates that anti-fatigue performance of PMA-A and PMA-B is better than neat asphalt binder. Fig. 15 and Fig. 16 show that complex modulus and rutting factor of PMA-B are both smaller than PMA-A, and Fig. 17 shows that fatigue factor of PMA-B is smaller than that of PMA-A, which indicate PMA-B has weaker rutting resistance and stronger anti-fatigue properties than PMA-A. It can be seen from Fig. 18 that phase angles ranking of three samples are in following order: neat asphalt binder > PMA-A > PMA-B, which indicates that PMA-A and PMA-B have more elastic behavior than neat asphalt binder under repeated loading. Improved elasticity is

potentially beneficial for resisting deformation, and PMA-B is better than PMA-A in this regard, which results from the previous conclusion, i.e. SBS can increase the elastic proportion more than SBR.

4 Conclusions and Recommendations

Based on the testing and analysis presented herein, the conclusions of the study are summarized as follows:

(1) Five indicators including residual strain, complex modulus, elastic storage energy, viscous loss energy and elastic proportion are proposed to evaluate viscoelastic behavior of modified asphalt. The testing results of neat asphalt binder and six kinds of modified asphalt indicate that the five inidicators can characterize the modification effects well from different angles, and the distinguish effects of residual strain and elastic proportion are most obvious.

(2) Rubber powder and SBS are good choices for increasing the resistance ability of permanent deformation. Rubber powder or the composition of rubber powder and aromatic oil can increase the elastic ratio effectively. The combination of rubber powder and aromatic oil can enhance the elastic stored energy as well. SBS can reduce the viscous loss energy and increase the complex modulus, while aromatic oil can reduce the complex modulus dramatically.

(3) Compared with neat asphalt binder, PMA-A has smaller complex modulus, stronger deformation ability, lower temperature susceptibility, higher elastic proportion. The complex modulus of PMA-A and PMA-B change slowly with time growing, which indicate their anti-fatigue performance is very strong.

However, limited experiments were performed due to the limited funding and lab conditions. Further research can be processed, including mechanism analysis by various microcosmic tests (such as DSC tests, FTIR tests, and SEM analyses), effects of more extensive additives and synergistic effects exsiting among different additives.

References

Al-Hadidy, A.I., Yi-qiu, T.: New technical method for production homogenous and storage stable polymer modified asphalt. In: Proceedings of the 7th International Conference of Chinese Transportation Professionals (ICCTP 2007), May 21-22, pp. 799–810 (2007)

Al-Hadidy, A.I., Yi-qiu, T.: Comparative performance of the SMAC made with the SBS- and ST-modified binders. J. Mater. Civ. Eng. 22(6), 580–587 (2010)

Moreno, F., Sol, M., Martín, J., Pérez, M., Rubio, M.C.: The effect of crumb rubber modifier on the resistance of asphalt mixes to plastic deformation. Mater. Design 47, 274–280 (2013)

Roberts, F.L., Kandhal, P.S., Lee, D., Kennedy, T.W.: Hot mix asphalt materials, mixture, design, and construction, 2nd edn. Napa Education Foundation, Lanham (1996)

Sengoz, B., Isikyakara, G.: Evaluation of the properties and microstructure of SBS and EVA polymer modified bitumen. Constr. Build. Mater. 22(9), 1897–1905 (2008)

Singh, B., Kumar, L., Gupta, M., Chauhan, G.S.: Polymer-modified bitumen of recycled LDPE and maleated bitumen. J. Appl. Polym. Sci. 127(1), 67–78 (2013)

Soleymani, H.R., Zhai, H., Bahia, H.: Role of modified binders in rheology and damage resistance behavior of asphalt mixtures. Transp. Res. Record 1875, 70–79 (2004)

Tan, Y., Guo, M., Cao, L., Li, X., Xu, H.: Performance optimization method of composite modified asphalt sealant. Journal of Highway and Transportation Research and Development 29(1), 11–17 (2012)

Zhang, F., Yu, J.: The research for high-performance SBR compound modified asphalt. Constr. Build. Mater. 24(3), 410–418 (2010)

Coupled Creep and Damage Model for Concrete at Moderate Temperatures

Minh-Quan Thai[1,2], Benoît Bary[1,*], and Qi-Chang He[2]

[1] CEA, DEN, DPC, SECR, Laboratoire d'Etude du Comportement des Bétons et des Argiles, F-91191 Gif-sur-Yvette, France
[2] Université Paris-Est, Laboratoire de Modélisation et Simulation Multi Echelle, MSME UMR 8208 CNRS, 77454 Marne-la-Vallée Cedex, France

Abstract. We develop in this study a coupled creep-damage model for concrete subjected to moderate temperatures. The coupling procedure relies on the concept of pseudo-strains introduced by Schapery [1], which allows to reformulate the initial viscoelastic problem as an equivalent elastic one by using a correspondence principle. The creep model is based on a micromechanical approach where a simplified representation of the material as a composite made of a linear viscoelastic matrix with distributed elastic inclusions and pores is adopted. One interesting feature is that analytical expressions for both bulk and shear moduli in the time space are derived in simpler cases when a limited number of Maxwell elements are involved to describe the matrix behavior. The well-known macroscopic isotropic damage model due to Mazars [2] is adopted to reproduce the cracking effects. The evolution of the damage variable is governed by an equivalent strain calculated from the pseudo-strains. The model is further extended to the case of moderate temperature increases with the aid of the equivalent time method. It is then applied to the simulation of concrete basic creep tests at different temperatures ranging from 20 to 80°C. The results are compared to experimental data and show a good agreement provided an adequate identification of the model parameters. The model response tends to show that the creep strains result mainly from the viscous characteristics of the material, and to a lesser extent to the damage growth. This conclusion holds for both ambient and moderate temperatures.

1 Introduction

Concrete is a very common construction material, in particular in the context of nuclear waste storage structures. For these applications, its durability and long-term performance are essential to ensuring the protection against radionuclide migration. Among the important mechanisms to be accounted for, the differed deformations are known to considerably alter the long-term response of structures and their service life due to the resulting redistributions of strains and stress which

* Corresponding author.

N. Kringos et al. (Eds.): *Multi-Scale Model. & Charact. of Infrastruct. Mater.,* RILEM 8, pp. 357–368.
DOI: 10.1007/978-94-007-6878-9_26

may lead to damage initiation and growth. The precise knowledge of creep phenomenon and related induced damage appears then of particular importance regarding such structures. Creep models for concrete are generally developed at the macroscale, and include for the most sophisticated ones variables and parameters aiming to capture in a simple way the effects of particular mechanisms occurring at the micro and nanoscale (see e.g. [3–6]). By contrast, few models are based on micromechanical approaches and associated upscaling techniques, whose advantages are to incorporate more rigorously the main characteristics of the elementary phases composing the material. It is nonetheless well-known that cementitious materials exhibit a heterogeneous and hierarchical microstructure, and that their main phases behave differently (viscoelastic behavior for the cement paste, linear elastic for the aggregates). The reason is probably that classical homogenization methods are not directly applicable to the case of viscoelastic materials without the recourse for instance of the Laplace-Carson (LC) transform and related correspondence principle (see e.g. [7–9]). The problem is even more complicated when cracking is considered, since damage growth becomes also time-dependant and its coupling with strain or stress rate difficult to describe. In most cases this time dependency is captured by introducing relevant parameters in the evolution law of the damage variables (e.g. [10,11]).

We present in this paper a coupled basic creep-damage model based on the pseudo-strain approach due to Schapery et al. [1,12] and the use of the isotropic damage model of Mazars [2]. The application of an equivalence principle allows obtaining a particularly simple formulation. Another characteristic of the proposed model resides in the application of analytical upscaling techniques to obtain the evolution of the linear viscoelastic bulk and shear moduli of the concrete. This procedure relies on the description of the material as a linear viscoelastic matrix in which are randomly distributed spherical elastic inclusions representing aggregates, and pores. The Mori-Tanaka (MT) scheme is applied in the LC space to estimate the mechanical parameters, and it is shown that the analytical inversion of these parameters into the time space can be achieved provided the calculation of the roots of polynomials. The model is further extended by making use of the equivalent time method to the cases of variable moderate temperatures. In this paper simulations of basic creep tests on concrete (recovery is not dealt with in this first attempt) subjected to various temperatures ranging from 20 to 80°C are carried out and the results are discussed and confronted to experimental data.

2 Creep-Damage Model

We describe in this section the coupled creep-damage model proposed for concrete materials. As already mentioned in the introduction, a key feature of this model is the use of the pseudo-strains concept introduced in [1,12]. This approach is extended here to the 3D isotropic case such that the viscoelastic creep model is written in a form equivalent to the Hooke's law via an elastic-viscoelastic correspondence principle:

$$\boldsymbol{\sigma} = 3k_R \boldsymbol{L} : \boldsymbol{\varepsilon}^R + 2\mu_R \boldsymbol{J} : \boldsymbol{\varepsilon}^R \tag{1}$$

where $\boldsymbol{\sigma}$ is the stress tensor, k_R et μ_R are the reference elastic bulk and shear moduli, respectively, $\boldsymbol{L}$ et $\boldsymbol{J}$ are the projection operators defined by $\boldsymbol{L} = 1/3\boldsymbol{I} \otimes \boldsymbol{I}$ and $\boldsymbol{J} = \boldsymbol{I} \underline{\otimes} \boldsymbol{I} - \boldsymbol{L}$ with $\boldsymbol{I}$ the second-order identity tensor, and $\boldsymbol{\varepsilon}^R$ is the tensor of pseudo-strains incorporating all the loading history and defined by:

$$\mathrm{tr}\left[\boldsymbol{\varepsilon}^R(t)\right] = \frac{1}{3k_R}\int_0^t k(t-\tau)\,\mathrm{tr}\left(\frac{d\boldsymbol{\varepsilon}}{d\tau}\right)d\tau \text{ and } \boldsymbol{\varepsilon}^R_{dev}(t) = \frac{1}{\mu_R}\int_0^t \mu(t-\tau)\frac{d\boldsymbol{\varepsilon}_{dev}}{d\tau}d\tau \tag{2}$$

in which $k(t)$ and $\mu(t)$ are the isotropic bulk and shear moduli, $\mathrm{tr}(\cdot)$ designates the trace, $\boldsymbol{\varepsilon}_{dev}$ and $\boldsymbol{\varepsilon}^R_{dev}$ are the deviatoric part of the tensors of strains and pseudo-strains, respectively. Note that the above approach can be applied when a linear or nonlinear creep model is concerned. Besides, we consider isotropic viscoelastic materials with potentially different time functions for $k(t)$ and $\mu(t)$, i.e. the Poisson ratio may also be time-dependant. The formulation of Eq. (1) is particularly simple, and allows a direct coupling with damage mechanics in the same way as elastic-damage models. We choose for representing the effects of cracking the well-known damage approach proposed by Mazars [2] due to its simplicity and robustness. Introducing the scalar damage variable D into Eq. (1)-(2), we get:

$$\boldsymbol{\sigma} = \left(1 - D(\tilde{\varepsilon}^R)\right)\left(k_R\,\mathrm{tr}\left(\boldsymbol{\varepsilon}^R\right)\boldsymbol{I} + 2\mu_R\boldsymbol{\varepsilon}^R_{dev}\right) \tag{3}$$

with $\tilde{\varepsilon}^R$ the equivalent strain whose definition is obtained from [2] by replacing the strains by the pseudo-strains expressed in Eq. (2) as:

$$\tilde{\varepsilon}^R = \sqrt{\sum \left\langle \varepsilon_i^R \right\rangle_+^2} \tag{4}$$

where ε_i^R stands for the eigenvalues of $\boldsymbol{\varepsilon}^R$ and $\langle\cdot\rangle_+$ designates the Macauley brackets, i.e. whose result equals the argument if positive, and zero otherwise. The evolutions of the damage variable are then controlled by the pseudo-strains, and the following law initially proposed by Mazars in the context of time independency is retained:

$$D(\tilde{\varepsilon}^R) = 1 - \frac{\varepsilon_d(1-A_{t,c})}{\tilde{\varepsilon}^R} - A_{t,c}\exp\left[-B_{t,c}(\tilde{\varepsilon}^R - \varepsilon_d)\right] \tag{5}$$

in which A and B are adjusting parameters, with the subscripts *t* and *c* indicating tension and compression states of stresses, respectively, and ε_d is the initial damage threshold. It is important to notice that with this law depending on the equivalent pseudo-strains, the evolution of the damage variable is implicitly time-dependant.

We briefly describe now the model developed for estimating the linear viscoelastic bulk and shear moduli of the concrete. As already discussed, this model is based on the application of the MT scheme in the LC space to the heterogeneous material defined by an isotropic linear viscoelastic matrix with distributed spherical isotropic elastic inclusions and voids representing aggregates and pores, respectively. The bulk $k^m(t)$ and shear $\mu^m(t)$ moduli of the matrix are assumed to be described by a generalized Maxwell model with 4 elements (one with only a spring), so that they can be expressed by:

$$k^m(t) = k_\infty^m + \sum_{i=1}^{3} k_i^m e^{-\frac{t}{\tau_i^{m,k}}} \quad \text{and} \quad \mu^m(t) = \mu_\infty^m + \sum_{i=1}^{3} \mu_i^m e^{-\frac{t}{\tau_i^{m,\mu}}} \tag{6}$$

where k_∞^m, k_i^m, μ_∞^m and μ_i^m are the elastic moduli in the Maxwell models and $\tau_i^{m,k}$ and $\tau_i^{m,\mu}$ are the relaxation times. In the following, we assume that $\tau_i^{m,k} = \tau_i^{m,\mu} = \tau_i^m$, i.e. the relaxation times for both bulk and shear moduli are equal. Eq. (6) then defines the matrix properties at the microscale. We showed that in the LC space, the homogenized (or effective) properties of the composite material estimated with the MT scheme can be expressed in the form [13]:

$$\tilde{k}^{hom}(s) = \frac{\sum_{i=0}^{3} A_i^k s^i \sum_{i=0}^{6} C_i^k s^i}{\sum_{i=0}^{3} B_i^k s^i \sum_{i=0}^{6} D_i^k s^i} \quad \text{and} \quad \tilde{\mu}^{hom}(s) = \frac{\sum_{i=0}^{3} A_i^\mu s^i \sum_{i=0}^{9} C_i^\mu s^i}{\sum_{i=0}^{3} B_i^\mu s^i \sum_{i=0}^{9} D_i^\mu s^i} \tag{7}$$

in which A_i^κ, B_i^κ, C_i^κ and D_i^κ with $\kappa \in \{k, \mu\}$ are coefficients calculated from the microscopic mechanical properties of the matrix and of the aggregates, and the volume fractions of the aggregate and pore phases ϕ_a and ϕ_p, respectively. Provided the calculation of the roots of the polynomial denominators appearing in the previous relations, i.e.:

$$\sum_{i=0}^{3} B_i^k s^i \sum_{i=0}^{6} D_i^k s^i = 0 \quad \text{and} \quad \sum_{i=0}^{3} B_i^\mu s^i \sum_{i=0}^{9} D_i^\mu s^i = 0 \tag{8}$$

it is also demonstrated that the inversion of k^{hom} and μ^{hom} expressed in the LC space and defined in Eq. (7) may be expressed by the following analytical formulae in the time space (see [13] for more details):

$$k^{hom}(t) = k_\infty + \sum_{i=1}^{9} k_i e^{-\frac{t}{\tau_i^k}} \quad \text{and} \quad \mu^{hom}(t) = \mu_\infty + \sum_{i=1}^{12} \mu_i e^{-\frac{t}{\tau_i^\mu}} \tag{9}$$

In these equations, k_∞, k_i, μ_∞ and μ_i are the coefficients derived explicitly in function of the mechanical parameters and volume fractions of the different

phases composing the material; τ_i^k and τ_i^μ are the relaxation times which are also calculated from the microscopic phase characteristics, but as they are the solutions of Eqs. (8), they are evaluated numerically (there is no general algebraic solution in radicals for polynomial equations of degree greater than 4). Note that the analytical relations (9) are a key feature of our creep model. We observe that the number of relaxation times defining the macroscale behavior is much higher than that at microscale, indicating an enrichment of the relaxation spectra due to the homogenization procedure.

Eqs. (2), (3) and (9) then define the macroscopic creep-damage behavior of the material. The extension of this formulation to non isothermal cases with moderate temperature increases is achieved by applying the equivalent time method consisting in replacing in Eq. (2) the time variable t by an equivalent one $t_e(t)$ expressed by:

$$t_e(t) = \int_0^t \exp\left[-\frac{Q}{R}\left(\frac{1}{T(\tau)} - \frac{1}{T_{ref}} \right) \right] d\tau \tag{10}$$

with T and T_{ref} the current and initial temperatures, Q the activation energy of the process and R the gas constant. This method has been successfully applied for similar phenomena by a number of authors, e.g. [3,14]. Note that the use of $t_e(t)$ for modifying the dashpot viscosities (and then the relaxation times) at the macroscale is equivalent here to introducing it directly at the microscale in the Maxwell model for the matrix.

The response of the creep-damage model is analyzed in the next section through the simulation of basic creep tests on concrete at different temperatures.

3 Applications

We apply here the model presented in the previous section to the simulation of the tests performed by Arthanari and Yu [15]. They consist in classical axial basic creep tests on ordinary CEM I concrete specimens at different constant temperatures ranging from 20 to 80°C, and without moisture exchange with the environment (the specimens are assumed initially saturated). The Table 1 gathers the main data regarding the concrete used, with an estimation of the volume fractions of both aggregate and pore phases. The compressive stress applied during the creep tests is σ_f = 6.9 MPa and represents 30% of the material strength. In this Table are also indicated the parameters of the Mazars model, which have been adjusted on a standard static compression test. The first step of the simulation relates to the identification of the viscoelastic parameters of the model. This is done by making use of the experimental longitudinal creep strains at 20°C and by applying the standard least-square method to minimize the differences between numerical results and test data. Since the creep model assumes two different time

functions for the bulk and shear moduli, the identification process also requires a priori two distinct experimental time-dependant data. Typically this consists of the measured values of both longitudinal and transversal strain evolutions. However in the creep tests by Arthanari and Yu [15], as in most published experimental works, only the longitudinal strains were monitored. We then make the hypothesis that the Poisson ratio of the material evolves as experimentally reported in the study by Parrott [16] on a cement paste, which is a material relatively close the one considered in this study. This allows defining the time evolutions of both mechanical moduli of the model. The microscopic parameters identified with this method are listed in Table 2. The macroscopic parameters calculated from all these coefficients (see Eq. (9)) are given in Table 3.

Table 1 Main parameters of concrete and of damage model

Parameter	E (GPa)	ν	ϕ_p	ϕ_a	σ_f (MPa)	A_c	B_c	ε_d
value	28	0.25	0.12	0.62	6.9	0.8	1289	10^{-4}

Table 2 Microscopic parameters of the Maxwell models at 20°C (Eq. (6))

Elements	∞	1	2	3
k_i^m (GPa)	4.86	5.60	3.98	2.94
μ_i^m (GPa)	3.09	4.48	2.24	1.50
τ_i (days)		1	5	20

Table 3 Macroscopic parameters of the creep model at 20°C (Eq. (9))

Elements	∞	1	2	3	4	5	6	7	8	9	10	11	12
k_i (GPa)	6.68	3.60	1.02	1.11	3.63	1.02	0.937	3.70	0.57	0.40			
μ_i (GPa)	4.79	1.60	0.11	0.051	0.011	1.86	0.54	0.65	0.173	2.00	0.60	0.963	0.251
τ_i^k (days)		1.0	1.24	1.52	5.0	5.79	7.33	20.	22.5	32.5			
τ_i^μ (days)		1.0	1.29	1.47	1.50	5.0	6.01	7.31	7.33	20.0	23.3	33.0	33.4

Once the model parameters are identified at 20°C, the activation energy Q can be adjusted by appealing to the experimental creep strains measured at another temperature. We then chose the results at 40°C to obtain the value Q = 50803 J/mol. The Fig. 1 reports both experimental (symbols, [15]) and numerical (curves) creep strains at different temperatures. As the transversal strains were not measured during the tests, only the simulated curves are shown. Notice that to ease comparison, we have chosen to exclude the thermal strains from this figure and the next ones. Also, the usual convention consisting in representing creep

compressive strains as positive is adopted, albeit the real values are negative. We observe a good concordance between experimental and numerical longitudinal strains for all the considered temperatures, indicating that the proposed model is able to correctly reproduce the concrete behavior. The Fig. 2 presents the evolutions of longitudinal (left) and transversal (right) pseudo-strains. We note that the relative variations with both time and temperature of the pseudo-strains are comparatively less marked than those of the strains in Fig. 1.

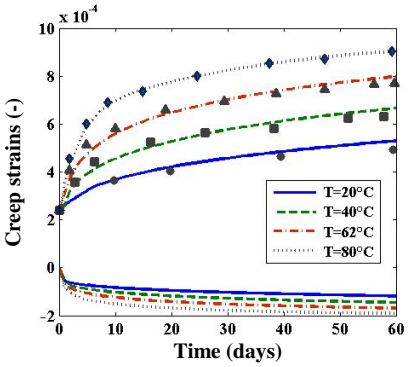

Fig. 1 experimental (symbols, [15]) and numerical (curves) creep strains at different temperatures. The longitudinal strains are positive and the transversal ones are negative.

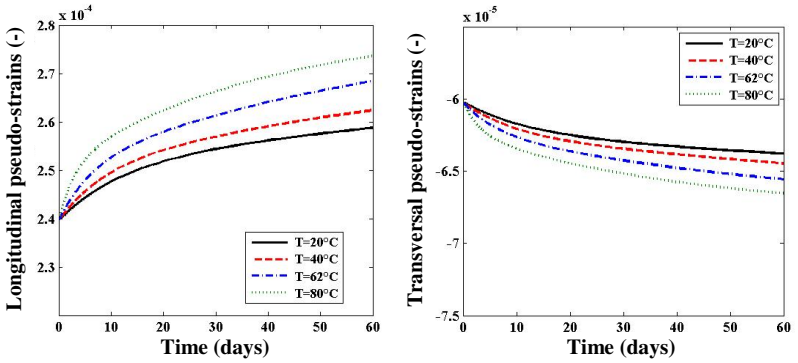

Fig. 2 evolutions of longitudinal (left) and transversal (right) pseudo-strains at different temperatures

This is confirmed on Fig. 3 showing the evolutions of the damage variable D (which are controlled by the pseudo-strains): at 20°C the damage increases from about 0.15 due to the instantaneous loading at $t = 0$ to 0.175 at 60 days, while at 80°C it reaches 0.195. We can conclude from the model response to the considered creep tests that the damage growth is not very sensitive to moderate temperature increases, and that at ambient temperature its evolution is limited.

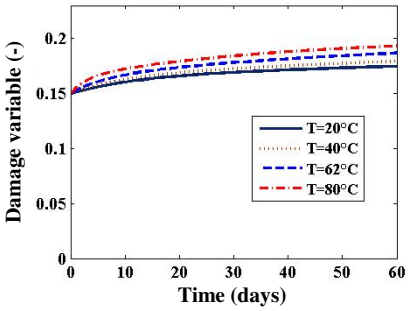

Fig. 3 Evolutions of the damage variable at different temperatures

The Fig. 4 shows the evolutions of bulk (left) and shear (right) moduli at different temperatures. We remark that both parameters decrease rapidly the first 10-20 days, then more slowly. We also notice that, in accordance with Eq. (10), an elevation of the temperature accelerates the decrease of the moduli. Indeed, for constant temperatures Eq. (10) indicates that t_e is proportional to t; thus, we obtain $t_e \approx 3.79t$, $t_e \approx 13.64t$ and $t_e \approx 34.57t$ at 40, 62 and 80°C, respectively. To complete the study, the Fig. 5 shows the evolutions of the Poisson ratio for the various temperatures. We observe that this parameter is significantly affected by an increase of temperature, as it decreases at 60 days from 0.25 to 0.212 at 20°C, and from 0.25 to 0.183 at 80°C.

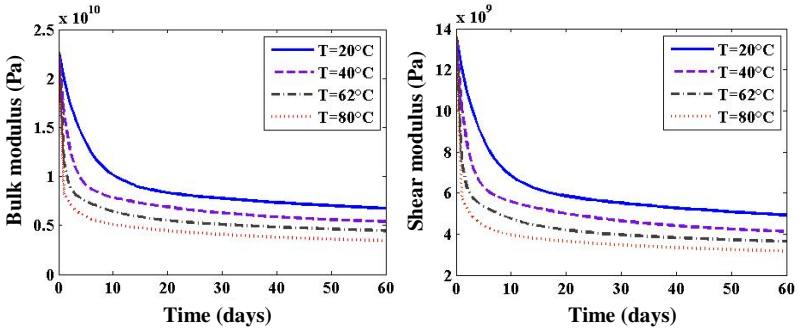

Fig. 4 Evolutions of bulk (left) and shear (right) moduli at different temperatures

From these results, we conclude that the simulated creep strains are mainly due to the viscoelastic characteristics of the homogenized material, and to a lesser extent to the damage growth. Indeed, the time evolutions of damage (Fig. 3) are small compared to the ones of the bulk and shear moduli (Fig. 4). The conclusions are similar for an elevation of temperature, i.e. the corresponding amplification of

the creep strains results principally from the viscous behavior of the material and for a minor part from damage increases. Finally, we consider now the case of variable temperatures. To take into account these variations, Eq. (10) is simply discretized by assuming that the temperature is constant within each time interval $[t_i, t_{i+1}]$, which gives:

$$t_e(t_{i+1}) \approx \sum_{k=1}^{i+1} \exp\left[-\frac{Q}{R}\left(\frac{1}{T_k}-\frac{1}{T_{ref}}\right)\right]\Delta t_k \tag{11}$$

with $\Delta t_{i+1} = t_{i+1} - t_i$.

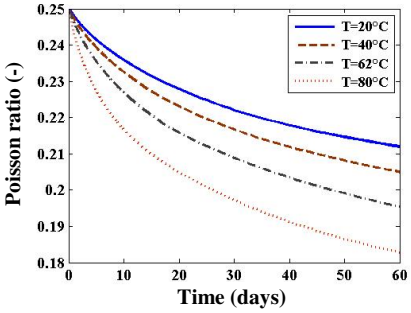

Fig. 5 Evolutions of the Poisson ratio at different temperatures

Without loss of generality and to illustrate the model response in this case, we suppose in the following that the temperature varies linearly from 20 to 80°C and we consider the two different heating rates of 1°C and 2°C per day (designated with the unit °C/d in the figures). We present on Fig. 6 the corresponding simulation results for the creep tests in terms of creep strains (left) and damage variable (right) evolutions. On this figure are also reported the curves obtained with constant temperatures of 20 and 80°C. The time interval is set to $\Delta t = 10^4$ s.

We observe as expected a significant influence of the temperature variations on the creep strains. In fact the strain curves depend not only on the maximum temperature reached, but also on its evolutions, i.e. the temperature history. Indeed, at any time, we note that the strain magnitudes are greater for larger heating rates, the limit case being the result with $T = 80$ °C kept constant during the test. The Fig. 7 shows the corresponding evolutions of the bulk and shear moduli for the variable temperature cases. Again, important differences are observable, and the moduli values appear to coincide with the ones obtained at constant $T = 80$ °C when this maximum temperature is reached, whatever the loading path.

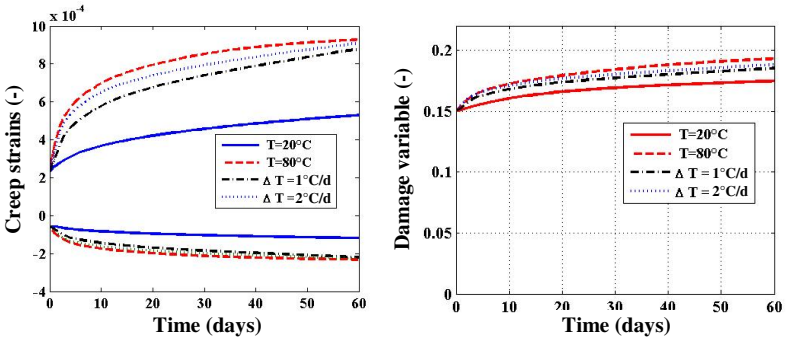

Fig. 6 Evolutions of creep strains (left) and damage (right) for linearly variable temperatures

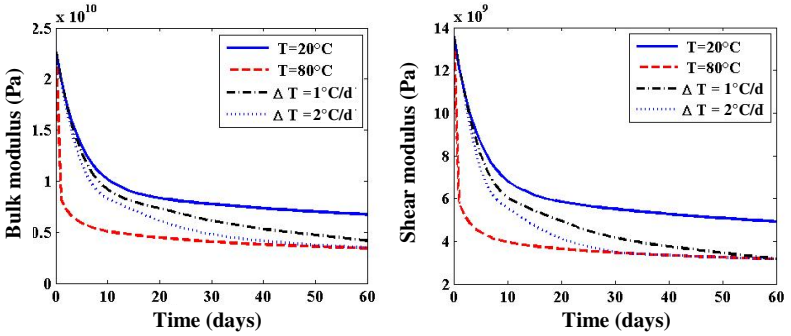

Fig. 7 Evolutions of bulk (left) and shear (right) moduli for linearly variable temperatures

In a subsequent contribution, the effects of the relative humidity will also be investigated through the use of a simplified approach based on the equivalent time method. Then the simulation of concrete subjected to drying creep will be carried out via the proposed model, and its response will be analyzed and discussed.

4 Conclusions

We have presented in this study a creep-damage model based on the pseudo-strain approach of Schapery coupled with the isotropic damage model of Mazars. A simple formulation analogous to a damage-elastic model is obtained. Further, the MT scheme is applied in the LC space to estimate the evolutions of the linear viscoelastic bulk and shear moduli of the concrete. This procedure relies on the material representation as a composite consisting in spherical elastic aggregates and voids embedded in a linear viscoelastic matrix. Analytical expressions of the time-dependant effective mechanical properties are then derived. The model is

extended to the case of moderate heating by making use of the equivalent time method. It is then applied to the simulation of standard creep tests at different temperatures ranging from 20 to 80°C. A good agreement is obtained between experimental and numerical results of creep strains, after an adequate identification of the model parameters. The model response tends to show that the creep strains result mainly from the viscous characteristics of the material, and to a minor extent to the damage growth. This conclusion is valid for ambient as well as for moderate temperatures.

The perspectives of this work are manifold. A study in progress takes advantage of the viscoelastic multi-scale model to investigate the effects of the shape and volume fraction of the aggregates and pores on the macroscopic properties of the material. Another one deals with the influence of the relative humidity on the estimated mechanical properties and with the explicit introduction of the capillary pressure so as to extend the approach to the case of coupled thermo-hydro-mechanical problems. In this context, the effects of thermal expansion mismatch between aggregates and matrix on the internal stresses and strains due to different thermal expansion coefficients will be investigated. Finally, some issues as the existence of permanent strains at unloading and the response model to higher creep loads will also be addressed in the future.

Acknowledgments. ANDRA is gratefully acknowledged for its financial support.

References

[1] Schapery, R.A.: Correspondence principles and a generalized J integral for large deformation and fracture analysis of viscoelastic media. International Journal of Fracture 25, 195–223 (1984)
[2] Mazars, J.: A description of micro-and macroscale damage of concrete structures. Eng. Fracture Mech. 25, 729–737 (1986)
[3] Bazant, Z.P., Chern, J.C.: Concrete creep at variable humidity: constitutive law and mechanism. Mater. Struct. 18, 1–20 (1985)
[4] Bažant, Z.P., Xi, Y.: Drying creep of concrete: constitutive model and new experiments separating its mechanisms. Mater. Struct. 27, 3–14 (1994)
[5] Benboudjema, F., Meftah, F., Torrenti, J.M.: Interaction between drying, shrinkage, creep and cracking phenomena in concrete. Eng. Struct. 27, 239–250 (2005)
[6] Sellier, A., Buffo-Lacarriere, L.: Towards a simple and unified modelling of basic creep, shrinckage and drying creep of concrete. Eur. J. Environ. Civ. Eng. 13, 1161–1182 (2009)
[7] Le, Q.V., Meftah, F., He, Q.-C., Le Pape, Y.: Creep and relaxation functions of a heterogeneous viscoelastic porous medium using the Mori-Tanaka homogenization scheme and a discrete microscopic retardation spectrum. Mech. Time-Depend Mater. 11, 309–331 (2008)
[8] Scheiner, S., Hellmich, C.: Continuum microviscoelasticity model for aging basic creep of early-age concrete. J. Eng. Mech.-ASCE 135, 307–323 (2009)
[9] Gu, S.-T., Bary, B., He, Q.-C., Thai, M.-Q.: Multiscale poro-creep model for cement-based materials. Int. J. Numer. Anal. Methods Geomech. (2012)

[10] Mazzotti, C., Savoia, M.: Nonlinear creep damage model for concrete under uniaxial compression. J. Eng. Mech.-ASCE 129, 1065–1075 (2003)
[11] Briffaut, M., Benboudjema, F., Torrenti, J.M., Nahas, G.: Numerical analysis of the thermal active restrained shrinkage ring test to study the early age behavior of massive concrete structures. Engineering Structures 33, 1390–1401 (2011)
[12] Park, S.W., Richard Kim, Y., Schapery, R.A.: A viscoelastic continuum damage model and its application to uniaxial behavior of asphalt concrete. Mechanics of Materials 24, 241–255 (1996)
[13] Thai, M.-Q.: Modélisation micromécanique et simulation numérique du fluage des bétons avec prise en compte de la microfissuration et des effets thermohydriques, PhD thesis, Université de Marne-La-Vallée (2012) (in French)
[14] Bazant, Z.P., Cusatis, G., Cedolin, L.: Temperature effect on concrete creep modeled by microprestress-solidification theory. J. Eng. Mech. 130, 691–699 (2004)
[15] Arthanari, S., Yu, C.W.: Creep of concrete under uniaxial and biaxial stresses at elevated temperatures. Mag. Concr. Res. 19, 149–156 (1967)
[16] Parrott, L.J.: Lateral strains in hardened cement paste under short-and long-term loading. Mag. Concr. Res. 26, 198–202 (1974)

Mitigating Resolution Problems in Numerical Modeling of Effective Transport Properties of Porous Materials

Neven Ukrainczyk[1,2,*], Eduard A.B. Koenders[1,3], and Klaas van Breugel[1]

[1] Microlab, Faculty of Civil Engineering and Geosciences, Delft University of Technology, Stevinweg 1, 2628 CN Delft, The Netherlands
n.ukrainczyk@tudelft.nl
[2] Faculty of Chemical Engineering and Technology, University of Zagreb, Marulicev trg 19, 10000 Zagreb, Croatia
[3] Civil Engineering Department-COPPE, Federal University of Rio de Janeiro, 68506 Rio de Janerio, Brazil

Abstract. Generating a realistic microstructure for a computational grid, which accurately represents heterogeneities while maintaining a computational efficiency, is still an unsolved problem. This paper presents a novel multi-scale approach to mitigate the resolution problems in numerical methods for calculating effective transport properties of porous materials using 3D digital images. The method upscales sub-voxel information of the fractional occupancy of interface voxels (i.e. voxels containing phase-boundary) in order to increase the accuracy of the pore schematization and hence the accuracy of the numerical transport calculation as well. The method is validated on a simple periodic arrangement of mono-sized particles. The numerical algorithm is implemented within the Hymostruc platform (numerical model for cement hydration and microstructure development) and backed up with a 3D graphics visualization. The new approach significantly reduces computational efforts, is easy to implement, and improves the accuracy of the transport property estimation.

Keywords: Resolution refinement, Multi-scale modelling, Effective transport property, Porous materials, Cementitious materials.

1 Introduction

When it comes to the description of transport processes in porous media, a parameter that is of paramount importance is the effective transport (e.g. diffusion) coefficient. Transport processes in cementitious materials play a crucial role in both the degradation process of building materials as well as in the containment of

* Corresponding author.

N. Kringos et al. (Eds.): *Multi-Scale Model. & Charact. of Infrastruct. Mater.,* RILEM 8, pp. 369–381.
DOI: 10.1007/978-94-007-6878-9_27

hazardous wastes. Challenges include difficulties in the overall description of the multiple scales that characterize the random structure of this porous media, covering a wide range of sizes, i.e. from nanometer-sized pores to centimeter-sized aggregates. Even when only considering a cement paste microstructure, the pore sizes cross at least four orders of magnitude (10 nm – 100 μm).

A representative starting point for the numerical analysis of transport properties in cement based microstructures can be obtained by either using: 1) advanced 3D simulation models; or 2) experiments, e.g. by X-ray computed tomography (CT) (Zhang et al 2012, Koster et al. 2006). In the numerical hydration models, the resulting microstructure can be simulated as a function of the degree of hydration, the particle size distribution, the chemical composition of the cement, the water/cement ratio, and the reaction temperature. The two main methodological approaches in modeling the microstructural evolution of cement-based systems are: 1) digitalization of the experimental image of the real microstructure, e.g. CEMHYD3D (Garboczi and Bentz (2001), and 2) a particle-based continuous concept of growing spheres, e.g. IPKM (Pignat et al. 2005), Hymostruc (van Breugel 1991, Koenders 1997), μic (Bishnoi and Scrivener 2009). CEMHYD3D as well as novel NIST model HydratiCA (Bullard 2007) simulate hydration and microstructure evolution based on the (cellular automata) movement and phase change of each discrete voxel. The model is limited to represent the microstructure of hydrated cement paste at levels smaller than the voxel size used, which also affects the ability to describe the pore structure into a small detail. Refining the resolution of these systems is often desirable but this directly increases the simulation computing time significantly. On the other hand, the particle-based models have a vector approach and the size of the developing pore structure is not limited by any geometrical shape (as there are no basic building blocks) and is represented by the remaining volume of the cementitious system after hydration has ceased. Therefore, theoretically there is no imposing resolution limit (Bishnoi and Scrivener 2009) on the microstructural formation and pore space representation by growing spheres models. However, for calculating the effective properties of 3D images requires meshing, generally regular lattice voxelisation with a uniform spacing. Numerical modelling, then, is based on a 3D digital image built up from voxels, where each voxel is identified by a phase flag that indicates which phase is represented by a certain voxel volume. The size of the system volume, as well as the resolution, have an exponentially increasing effect on the computation cost for finite element (FEM) or finite difference (FD) numerical transport calculation.

In this paper we propose an efficient numerical method to mitigate the resolution problems in numerical determination of the transport properties of porous materials from 3D digital images effectively. From a conceptual point of view, the method includes information of the fractional occupancy of interface voxels

(a voxels containing a phase-boundary as depicted in Fig. 1) in order to increase the accuracy and efficiency of the pore schematization and hence of the numerical transport calculation as well. The sub-micro level information of each of the FD voxels is quantified by increasing the pre-procesing resolution. The proposed method is validated by means of an effective transport calculation on a simple periodic arrangement of mono-sized particles. The method is general in nature that should be applicable to a diverse range of investigated porous medias (e.g. microstructures obtained by different numerical or experimental methods).

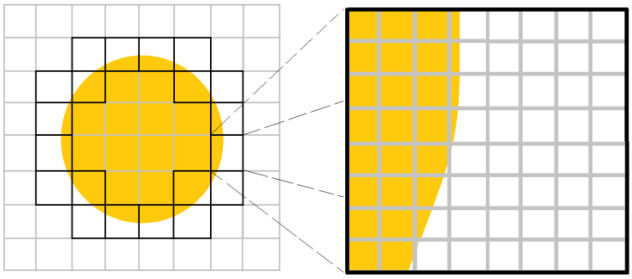

Fig. 1 Schematic of a disc discretization: **a** FD regular mesh (pixels having a pore-solid interface are embolden as black); **b** pre-processing refinement to capture arbitrary shapes more accurately (porosity=(64-22)/64)

2 Analytical Solutions

For random porous material structures there are, in general, numerous boundaries representing all kinds of irregular shapes. The analytical calculation of the effective transport properties from these random systems does not exist. Therefore it is not possible to exactly assess the accuracy of their numerical solutions. However, exact solutions can still be used to thoroughly assess a numerical method. Most effective are theoretical solutions that are originally established for the electrical conductivity of a composite medium, but due to their mathematical analogy, these models are also valid for diffusion processes (Torquato 2002). Cheng and Torquato (1997) presented an analytical model for calculating effective property of periodic arrangement of monosized spheres. The uncertainty of the Cheng and Torquato model solution is estimated by a solid volume fraction of the 9^{th} potential (estimation of error is f^{9}). Therefore, the uncertainty of the theoretical model for each unit cell rises with decrease of the system porosity. In this paper the FD steady state transport implementation is validated against the theoretical solution of a simple cubic periodic arrangement.

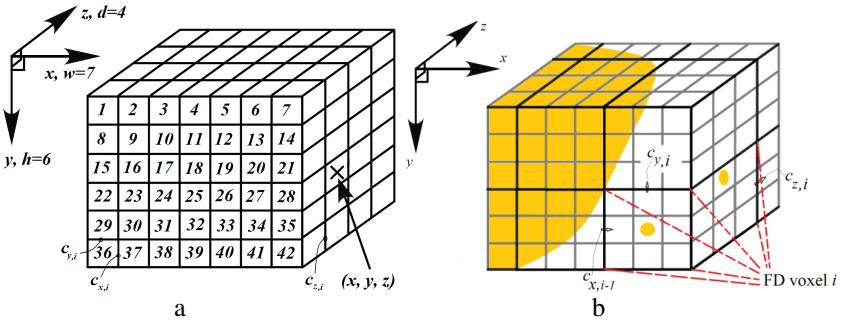

Fig. 2 a Example of numbering of the voxel nodes for FD implementation, position and size of coordinates: width (x), height (y), and depth (z)**, b** pre-processing refinement: each sharing surfaces between neighboring FD voxels in x, y, and z directions has an assigned connectivity coefficients c_x, c_y, and c_z, respectively. $c_{j,i}$ are calculated (Eq. 1) considering porosity information of the FD voxels (as detailed in Sect. 3.2)

3 Numerical Implementation

In a steady state condition, when the fluxes are steady in time, Fick's II law reduces to Laplace equation. A finite difference (FD) based program for solving the steady state transport problems is written in the C++ programing language within the Hymostruc platform. Hymostruc´s graphical interface was updated to visualize the transport simulation results. Implementation of the FD transport model without employing pre-processing multi-scale algorithm is described first. A virtual 3D microstructure is discretized into a regular 3D mesh (e.g. Fig. 1). Each voxel in a lattice is assigned to be a capillary pore or solid according to the particular position in the microstructure. Then, for each sharing surface between the neighbouring voxels in x, y, and z directions a connectivity coefficient has to be assigned (c_x, c_y, and c_z, respectively, Fig. 2) and stored in three **c** vectors (whose lengths correspond to the number of voxels in the system, N). Six neighbour connection were used, considering that the central node is connected by the sharing faces of a cube in x, y, and z direction. Connectivity coefficients are obtained from microscopic transport properties of the central FD voxel and neighbour FD voxels according to the series connection of two conductors, Eq. 1.

$$c_i = 1/(0.5 D_i^{-1} + 0.5 D_{i+k}^{-1}) \tag{1}$$

where $k = 1$, w, or (w h) helps to represent a shift of the voxel numbering i to the neighbour voxel in x, y, or z direction (please see Fig. 2 **a**). The FD second order scheme is used to discretize the Laplace's equation. The Laplace's equation in finite difference form, at each node i is given by Eq. 2.

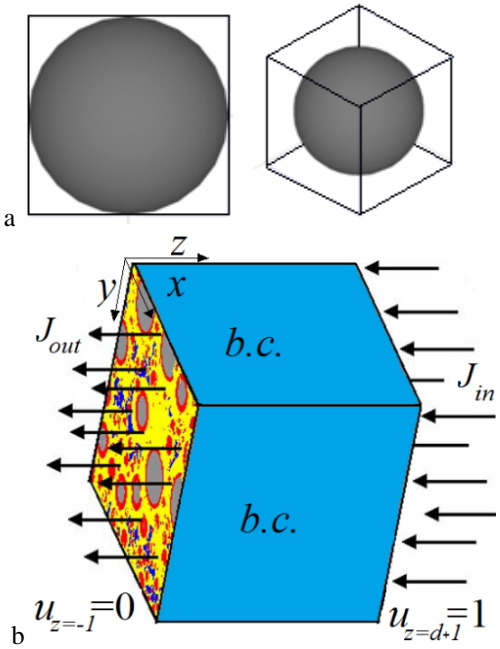

Fig. 3 a Unit cell of simple cubic lattice structure (dense packing) used for testing of the numerical method, **b** steady state flux (J) across z-axis and adiabatic boundary conditions employed on 4 side faces parallel to the imposed flux

$$\begin{aligned} &c_{x,i-1}u_{i-1} + c_{y,i-w}u_{i-w} + c_{z,i-wh}u_{i-wh} + \\ &-\left(c_{x,i} + c_{x,i-1} + c_{y,i} + c_{y,i-w} + c_{z,i} + c_{z,i-wh}\right)u_i + \\ &+c_{x,i}u_{i+1} + c_{y,i}u_{i+w} + c_{z,i}u_{i+wh} = 0 \end{aligned} \tag{2}$$

Assembling all these N equations (Eq. 2) for all the FD nodes forms a system of global equations which can be represented in a matrix notation Eq. 3.

$$\mathbf{A}\,\mathbf{u} = \mathbf{b} \tag{3}$$

where u is the voltage vector (size of the total number of voxels in the system, N), **A** is a sparse and symmetric matrix with 7 diagonals (each voxel has 6 nearest neighborings) that contain information about connectivity coefficients of all the bonds among the voxels, and **b** is the vector of knowns (i.e. boundary condition at the top of the last layer: $u_{(x,y,z=d+1)}= 1$, Fig. 3). The obtained system of equations (3) is solved by a conjugate gradient algorithm with an optimized matrix-vector multiplication. This has been achieved by multiplying only those elements of the matrix that lie on the 7 diagonals while avoiding multiplications of a very large number of zero elements. Furthermore, since the size of the sparse matrix **A** is N times N and can reach huge dimensions, the matrix is not stored explicitly but only

implicitly, by means of the vectors $\mathbf{c}_x$, $\mathbf{c}_y$, and $\mathbf{c}_z$ which store the conductivity coefficients of the bonds between voxel faces in the x, y, and z directions, respectively.

Next, the flux in z direction at each node i, $J_{i,z}$ was obtained by solving the Fick's first law. The FD scheme used for this is:

$$J_{i,z} = 0.5\left((u_{i-wh} - u_i)\, c_{z,i-wh} + (u_i - u_{i+wh})\, c_{z,i}\right) \tag{4}$$

The effective steady state flux J_{eff} is calculated by averaging the fluxes in the total system volume (total number of nodes $N = w\ h\ d$).

$$J_{eff,z} = \left(\sum_i J_{i,z}\right) \Big/ (whd) \tag{5}$$

Then D_{eff} was obtained from the calculated effective flux (normalized to the flux through the same system dimensions without any solid inclusions) according to eq. (6).

$$D_{eff} \,/\, D_0 = J_{eff} \,/\, J_0 \tag{6}$$

The relative diffusivity is the ratio of the effective diffusivity (D_{eff}) of a diffusing specie in a porous media relative to its value when diffusing in bulk water (D_0), and ranges between 0 and 1.

3.1 Multi-scale Algorithm

The proposed multi-scale algorithm consists of the following steps:

1. FD (coarse) meshing of the microstructure
2. Refine mesh by n^3 times (multi-scale resolution)
3. Calculate the volume fractions of the FD voxels
4. Calculate the effective properties of the FD voxels
5. Return to the FD (coarse) mesh
6. Assemble eq. 3
7. Go to conjugate gradient solver

A virtual 3D microstructure is discretized into a regular 3D mesh (e.g. Fig. 1). Steps 1-5 are a part of the pre-processing algorithm. In step 2, the FD lattice resolution is increased n times in each of the three spatial directions. In that way every FD voxel consists of a sub mesh of n^3 sub-voxels. A schematic impression of a fractional quantification of the FD interface voxels is depicted as an example in Figure 1. Each sub-voxel in a lattice is assigned to be a capillary pore or solid according to the particular position in the microstructure. The sub-voxel's state (solid or pore) is determined from the state of the center point at of the sub-voxel. In step 3, the fractional composition of each of the FD voxel is quantified by n^3 sub-voxels. The fractional occupancy within a FD voxel is calculated by counting the number of pore sub-voxels. For the example shown in Fig. 1 **b**) there are 22

solid voxels so the porosity is P = (64-22)/64. In this approach, the very small particles (Fig. 2 **b**), as well as the boundaries of the bigger particles, are now schematized with a much higher accuracy.

In step 4, the effective properties, determined with the higher resolution sub-voxels algorithm (steps 1-4), are assigned to the FD (coarser) voxels. Next, connectivity coefficients are calculated from the microscopic transport properties of the neighbour FD voxels according to and the eq. 3 is assembled (step 6). Therefore, for the interface voxels the connectivity coefficients (c) are calculated more accurately by considering their fractional compositions. Moreover, it may be argued that the morphology of the interface voxels is also somewhat considered as an average with its nearest-neighbour voxels (Eq. 1); e.g. the connection to the completely solid voxel has again a zero connectivity (Fig. 1, discussed further in Sect. 5).

The multi-scale resolution pre-processing algorithm (steps 1-5) is done in a loop invoking each sub-voxel only once. After this, the calculation of the transport properties in step 6 and 7 is done on a coarser (FD) mesh which now includes the sub-voxel information. The bottleneck of the transport calculation by FD scheme (eqs. 2 and 3) is a conjugate gradient algorithm that requires numerous (thousands) of iterations until converging. Therefore, the main contribution to the efficiency of the multi-scale resolution approach is by using the refinement sub-voxel information in the FD voxels, according to a pre-processing algorithm that requires only one iteration.

4 Validation Plan

The proposed method is validated for an effective transport calculation on a simple periodic arrangement of mono-sized particles. In order to test the FD program, a single particle is placed in a cubic cell to form a unit cell arrangement with a specific porosity (Fig. 3 **a**). The effective transport property was investigated for a densely packed simple cubic periodic structure with porosity P = 0.4764, and $D_{eff,theor}$ = 0.34363 ± 0.003. This was achieved by assigning a particle radius of 50 μm within the 100^3 μm^3 unit cell. The employed FD numerical resolutions were: 0.25, 0.33, 0.5, 1, 2, and 5 μm/pixel, corresponding to FD system sizes of 400^3, 300^3, 200^3, 100^3, 50^3 and 20^3 voxels, respectively. Furthermore, the effect of pre-processing multi-scale resolution refinement (for obtaining fractional volumes for the boundary pixels and transferring this information for FD property assignment) is also investigated. The finest pre-processing resolution used was 83.3 nm/pixel, resulting in a system with a size of 1200^3 voxels (took <150 sec. to run).

5 Results and Discussion

This paper proposes a resolution scaling approach by introducing fractional values for properties of the interface voxels, Fig. 1. For example, in this approach interface voxels are not only considered to express binary behaviour such as fully

solid or fully pore, but instead, they behave like intermediate voxels with a certain fraction of solid and pore. The values of occupancy of these interface voxels are then used to ascribe the properties to these 'interface' voxels. The easiest and still very efficient way to obtain the occupancy of these interface voxels is by increasing the pre-processing resolution. This paper shows how the information from as low as 0.083 μm can be used in calculations of transport properties in cement paste systems (of size 100 μm^3). The 83 nm limit is due to the computer resource limitation of 6GB RAM memory.

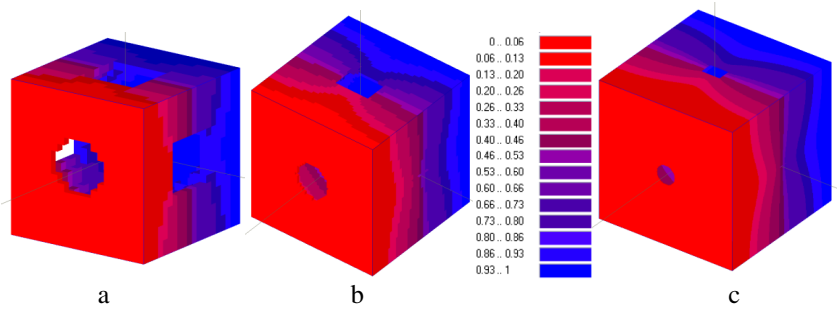

Fig. 4 Influence of resolution on solution of concentration distribution for densely packed simple cubic arrangement of mono-sized spheres: **a** 5 μm/pixel, **b** 2 μm/pixel, and **c** 0.5 μm/pixel

For computers that have more memory resources as well as a higher number of processors, the presented method can be employed to yield simulations that have even much better resolution limits while exhibiting only a small increase in the computation time. The sub-micro information of each of the FD voxels is quantified by increasing the pre-procesing resolution by down to 83.3 nm. In this way, very small particles as well as phase boundaries with bigger particles can now be tracked with a much higher accuracy. It must be noted that the information on pore morphology within FD voxel resolution scale was not considered. In this first approach only the porosity within the interface voxels is considered. Therefore, the sub-(FD-)voxel pore morphology with (closed) pores that disconnect in certain directions cannot yet be predicted correctly. This is because this first approach uses only fractional porosity information and does not consider the morphology (e.g. connectivity) within the sub-micro voxel level. To fully capture the sub-voxel morphological effect one requires a full multi-scale approach which will be investigated and implemented in future developments for further improvement of the transport model. However, by averaging the connectivity with the neighbouring voxels (eq. 1) the discontinuous nature can still be approximated and captured on this (nearest neighbour) scale approximation (e.g. see Fig. 1). For example, the interface voxels that surround a big solid inclusion have the fraction of pore volume accurately quantified by the refined pre-processing resolution. The FD voxels in the direction of a solid should have a zero flux because this voxels depercolate in this direction. However, the transport property of these interface voxels are given a value equal to the value of its fractional porosity. But, Eq. 1

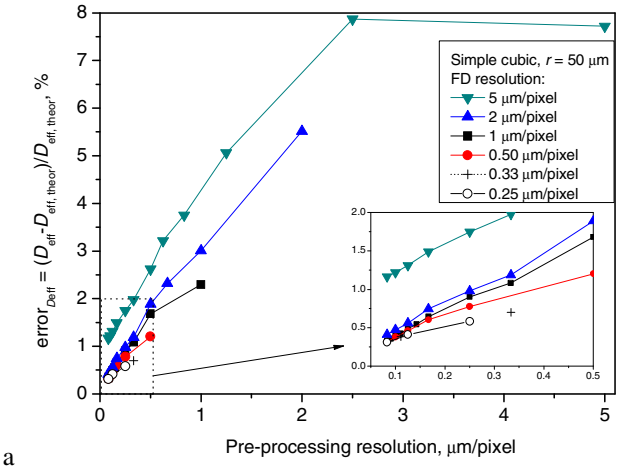

a

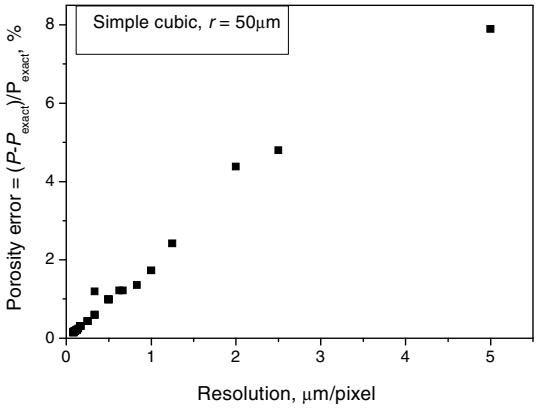

b

Fig. 5 Effect of pre-processing resolution and FD resolution on accuracy of calculated results for simple cubic periodic structure ($D_{eff,theor}$= 0.34363±0.003, P_{exact} = 0.4764): **a** effective transport property, **b** porosity

uses the diffusivity coefficient of the neighbour voxel, which is all-solid, and therefore finally yields a correct estimate of the zero connectivity.

Exact solution on simple periodic inclusion of mono-sized spheres was employed to thoroughly assess the accuracy of the numerical method. The numerical method was tested on a simple cubic periodic structure, which has a known analytical solution (Sect. 2) in the densely packed (P = 0.4764) case. The simulated microstructures of a simple cubic structure with a 3D visualization of the molecular concentrations (relative values 0-1) at steady state are shown in Fig. 4. The red parts show the high concentrations and the blue parts show the low concentrations of species. Figure 4 shows that the resolution effects the applied system boundary

condition. The effective diffusion coefficients of a plain molecular diffusion are obtained. The values are represented as relative values ranging between 0-1, and show how much the effective transport is reduced due to the solid inclusions relative to the diffusion in the bulk water (i.e. 100% pore scenario that has no solid inclusions). Figure 5 **a** depicts the effect of pre-processing and the effect of the FD resolution on the accuracy of the calculated effective transport property for a densely packed simple cubic periodic structure with (porosity) $P = 0.4764$ and $D_{eff,theor} = 0.34363 \pm 0.003$. It can be observed that for the FD model, the predictions calculated without employing the pre-processing refinement algorithm, the error declines with increase of the FD resolution. These results are represented by the right end point of each curve. Each curve corresponds to a different FD resolution used to calculate the effective transport property. With increasing refinement of the pre-processing resolution up to 1/12 μm (i.e. 83 nm), the error of the predictions decline sharply. Figure 5 **a** also shows that the calculated effective property values converge. The most interesting finding in Fig. 5 **a** is that it is possible to obtain a high accuracy prediction by using a very small FD resolution, e.g. 2 μm/pixel, if the high resolution pre-processing information is incorporated in the transport model. In this simple periodic structure the effective transport property depends on the porosity but as well on the influence of the pore morphology which is characterised only by constrictivity and tortuosity, while the connectivity is 1. In other words, there is only one big pore which is connected in flow direction from the back to the front Dirichlet boundary face of the cube system (Figs. 3 and 4). The effect of resolution on the accuracy of the calculated porosity for a simple cubic periodic structure is given in Fig. 5 **b**). It can be seen that the calculated porosity (as well as the error) declines with enhancing the resolution.

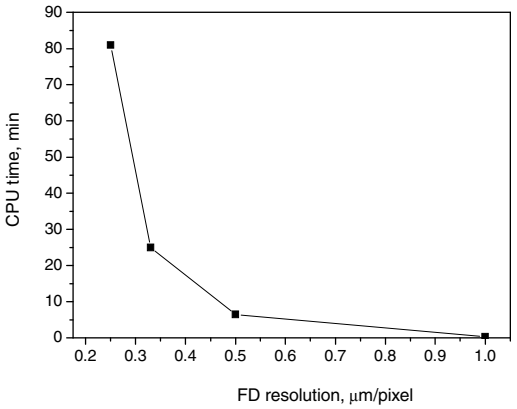

Fig. 6 CPU time requirement for calculations of effective property on simple cubic microstructure (for details on computer and used parameters for calculations please see text)

The method is currently being tested on a more complex microstructures generated by the Hymostruc, a numerical model for simulating cement hydration and microstructure development.

5.1 Performance of the Numerical Algorithm

The simulations reported in this paper were run on a multi core processor Intel(R) Core(TM) i7 CPU 950 @ 3.07GHz, with 6GB of installed RAM memory using 64-bit operating system. The norm error tolerance of the conjugate gradient solver was set to 10^{-8}, which assured a very high accuracy for the conjugate gradient solver (but more computational cost). The CPU time requirement for the calculations for a simple periodic microstructure is depicted in Fig. 6. An exponential CPU time is observed with increased resolution. The time for solving the effective transport largely depends on the complexity of the microstructure. For complex microstructures, such as generated by Hymostruc model or CT experiment, the time for running the numerical model can be about 10 times higher. The sub-micro level resolution used in the reported calculations was up to 83.3 nm/pixel, yielding a system with a size of 1200^3 voxels. The pre-processing in this finest resolution took less than 150 seconds to run. As said, the promising finding (in Fig. 5 **a**) is that it is possible to obtain a high accuracy prediction by using 'coarse' FD resolution, e.g. 2 μm/pixel, if high resolution pre-processing information is incorporated in the transport model. Therefore, a simulation that would normally take many hours is now possible to run in less than a minute, with a similar accuracy. This demonstrates the powerful capability of the presented multi-scale resolution method and its efficiency.

5.2 Muli-scale Modelling Outlook

The presented approach is a multi-scale resolution refinement approach. It obtains information on a lower (sub-micro) scale, i.e. 0.01-0.5 μm, and then passes the information (e.g. porosity) to the micro-scale level (0.5-100 μm). The digital images obtained experimentally, e.g. by means of X-ray computed tomography or microscopy imaging, or by means of modelling tools such as Hymostruc or CEMHYD3D, should also be evaluated with the presented multi-scale resolution refinement method in order to assess the accuracy of the calculated transport properties. The multi-scale transport modelling can be further employed, e.g. by inputting the effective transport properties of CSH gel, obtained from nano scale modelling (Bentz et al. 1995, Garboczi and Bentz 1998), and by applying the presented approach to quantify fractional occupation of each phase in a sub-FD-voxel level. The next step in the planned research is to investigate such an integrated multi-scale modelling system and also to try to include the morphological influence on the transport properties when passing the information from sub-FD to FD-voxel level. Furthermore, the application and extension of the method to higher (e.g. mortar and concrete) scales will be studied next.

6 Conclusion

In this article, a new multi-scale approach is proposed to mitigate a resolution problem in the effective transport property calculation of porous materials in

general, acquired from 3D digital images. The proposed method is validated for an effective transport calculation on a simple periodic arrangement of mono-sized particles.

From the findings of this study, the following conclusions can be drawn:

- The proposed multi-scale resolution refinement method maintains the simplicity of structured grids, while extending the resolution limit and keeping the calculations both more accurate and efficient.
- The calculated digitized porosity of porous media is decreasing with increased resolution.
- Both the accuracies of the calculated porosity and the estimated effective transport coefficient are significantly decreasing with increase in the pre-processing resolution (Fig. 5) for the proposed multi-scale method.

Further improvements of the method would be to include the morphological influence of transport properties when up-scaling the information from sub-voxel level. Moreover, further research will focus on an extension of the method towards an integrated multi-scale model that combines nano and micro level (i.e. to include the CSH gel pores), as well as up-scaling to higher (e.g. mortar and concrete) scales.

Acknowledgments. The authors acknowledge the support by the Marie Curie Actions EU grant FP7-PEOPLE-2010-IEF-272653-DICEM, and thank Fred Schilperoort for assistance with programming.

References

Bentz, D.P., Quenard, D.A., Baroghel-Bouny, V., Garboczi, E.J., Jennings, H.M.: Modelling drying shrinkage of cement paste and mortar Part 1. Structural models from nanometres to millimeters. Mater. Struct. 28, 450–458 (1995)

Bishnoi, S., Scrivener, K.L.: μic: A new platform for modelling the hydration of cements. Cem. Concr. Res. 39, 266–274 (2009)

Bullard, J.W.: A three-dimensional microstructural model of reactions and transport in aqueous mineral systems. Model. Sim. Mat. Sci. Eng. 15, 711–738 (2007)

Cheng, H., Torquato, S.: Effective conductivity of periodic arrays of spheres with interfacial resistance. Proc. R. Soc. Lond. A 453, 145–161 (1997)

Garboczi, E.J., Bentz, D.P.: Multi-scale analytical/numerical theory of the diffusivity of concrete. J. Adv. Cem. Mater. 8, 77–88 (1998)

Garboczi, E.J., Bentz, D.P.: The effect of statistical fluctuation, finite size error, and digital resolution on the phase percolation and transport properties of the NIST cement hydration. Cem. Concr. Res. 31, 1501–1514 (2001)

Koenders, E.A.B.: Simulation of volume changes in hardened cement-based materials. Dissertation, Delft University of Technology (1997)

Koster, M., Hannawald, J., Brameshuber, W.: Simulation of water permeability and water vapor diffusion through hardened cement paste. Comput. Mech. 37, 163–172 (2006)

Pignat, C., Navi, P., Scrivener, K.L.: Simulation of cement paste microstructure hydration, pore space characterization and permeability determination. Mater. Struct. 38, 459–466 (2005)

Torquato, S.: Random Heterogeneous Materials. Springer Science & Business Media, New York (2002)

van Breugel, K.: Simulation of Hydration and Formation of Structure in Hardening Cement-Based Materials. Dissertation, Delft University of Technology (1991)

Zhang, M.Z., He, Y., Ye, G., Lange, D.A., van Breugel, K.: Computational investigation on mass diffusivity in Portland cement paste based on X-ray computed microtomography (μCT) image. Constr. Build. Mat. 27, 472–481 (2012)

A 3D Image Correlation Algorithm for Tracking Movement of Aggregates in X-ray CT Images of Asphalt Mixtures Captured during Compaction

M. Emin Kutay[1], Nelson Gibson[2], and Xinjun Li[3]

[1] Michigan State University
Department of Civil and Environmental Engineering
East Lansing, Michigan, 48824-1226
kutay@egr.msu.edu
[2] Federal Highway Administration
Turner-Fairbank Highway Research Center
McLean, Virginia 22101
nelson.gibson@dot.gov
[3] SES Group & Associates, Inc.
Turner-Fairbank Highway Research Center
McLean, Virginia 22101
xinjun.li@dot.gov

Abstract. The current state of knowledge on development of asphalt mixtures' microstructure during compaction is very limited. Such knowledge can lead to better understanding of the differences and similarities between the laboratory and field compactors and the internal structure of HMAs they produce. This paper presents a 3D image correlation algorithm that computes the 3D displacements of aggregates in an asphalt sample during compaction. Microstructural evolution of aggregates in asphalt mixtures during compaction were tracked by using X-ray CT images that were acquired at different compaction levels in the Superpave gyratory compactor. The procedure involved compaction of the asphalt sample to a specified compaction level, cooling down and scanning using X-ray CT. This process was repeated at different compaction levels. The x-, y- and z-direction displacements at various points inside the asphalt mixture were calculated using the 3D image correlation algorithm. It was observed that, in addition to downward movement of aggregates within the HMA, the displacement vectors also showed torsional movement in the tangential and radial direction with respect to the center of the specimen. It was also observed that the strain in z-direction was approximately constant within the sample during compaction between the gyrations 8 and 30. However, as the number of the gyrations increased, strain in z-direction became non-uniform with depth, where higher strain was observed at the top and bottom plates as compared to the central portion.

N. Kringos et al. (Eds.): *Multi-Scale Model. & Charact. of Infrastruct. Mater.,* RILEM 8, pp. 383–393.
DOI: 10.1007/978-94-007-6878-9_28

1 Introduction

Internal structure characteristics of hot mix asphalt (HMA) pavements significantly affect their durability (Stephens and Sinha, 1978; Kalcheff and Tunnicliff, 1982; Tashman et al., 2001; Hunter et al. 2004). These characteristics include air void content (and distribution), orientation, segregation and aggregate contact points. Effect of internal structure characteristics on the overall performance of asphalt pavements has been well documented in the literature. Prowell et al. (2005) showed that the flat and elongated (F&E) particles tend to breakdown during compaction, which leads to weak zones susceptible to moisture damage (because of uncoated fractured aggregate faces). Vavrik et al. (1999) showed that large percentages of F&E particles in asphalt mixtures lead to increased air void levels in the Superpave gyratory compactor. They also observed that the gyratory compaction slope is increased with increased levels of F&E particles. Shashidhar (1999) utilized X-Ray Computed Tomography (CT) imaging technique to study the internal structure of laboratory compacted specimens and field cores. They showed that air void distribution and aggregate interlock are related to mixture performance. Kutay et al. (2007a and 2007b) showed that water flow through the air voids of HMAs (which affects the moisture susceptibility) are significantly affected by the aggregate gradation, mix type and compaction levels. Coleri et al. (2012a) developed an X-ray CT-based micromechanical finite element model (FEM) to study the shear behavior of asphalt mixtures. In another study, Coleri et al. (2012b) utilized X-ray CT images of asphalt samples extracted from a Heavy Vehicle Simulator (HVS) site to study the movement of aggregates because of plastic deformation. In that study (Coleri et al. 2012b), authors used a particle tracking algorithm similar to the one presented in this paper.

Another factor affecting the final microstructure of HMA is the compaction procedure. There are several laboratory asphalt mixture compaction methods such as the Superpave Gyratory, Marshall, Hveem, French Roller and German Sector compactors. These methods simulate field compaction and produce a representative sample for mix design and/or performance testing in the laboratory. Several studies have compared the compacted mixture density, air voids, and mechanical properties achieved by different compaction methods (Buchanan and Brown 2001; Masad et al. 2002; Peterson et al. 2004; Saadeh et al. 2002; Tashman et al. 2002). Hunter et al. (2004) observed circumferential particle orientation in specimens compacted by gyratory and vibratory compaction. Partl et al. (2007) studied the effect of different compaction methods on the generation of internal microstructure of asphalt mixtures using their X-ray Computed Tomography images. The literature indicates that variability exists within the results of the same compaction protocol performed in different laboratories as well as between different compaction methods (Khan et al. 1998). Thus, depending on the compactor and protocol of choice, this variability could yield to different estimates of the expected performance of the asphalt pavement. Therefore, there is a need for developing techniques that can characterize the internal structure of compacted asphalt mixtures.

This is important for understanding the difference between various compaction methods and their effect on mixture performance.

While there is extensive research on the internal structure characteristics of compacted HMAs, current state of knowledge on what happens to the microstructure during compaction is very limited. Such knowledge can lead to better understanding of the differences and similarities between the laboratory and field compactors and the internal structure of HMAs they produce. This paper to presents a methodology to quantify the evolution (rotation, translation and densification) of the aggregates in an HMA during the process of compaction in the Superpave gyratory compactor. The method involves a 3D image correlation algorithm that computes the 3D displacements of aggregates in an asphalt sample during compaction. The algorithm uses X-ray Computed Tomography (CT) images of asphalt specimens captured at different compaction levels.

2 3D Image Acqusition Using X-ray Computed Tomography

In order to better understand the microstructural evolution of aggregates in an asphalt sample during compaction, X-ray CT images were captured at different compaction levels in the Superpave gyratory compactor. X-ray Computed Tomography (CT) images of the mixture were acquired at the Turner Fairbank Highway Research Center (TFHRC) of the Federal Highway Administration (FHWA). First, the asphalt sample was compacted to 8 gyrations then cooled down and taken to the X-ray CT equipment chamber for 3D imaging. Once the 3D image was obtained at 8 gyrations, the same sample was re-heated to the compaction temperature, further compacted to 30 gyrations (additional 22 gyrations applied after the CT scanning). Then, the sample was cooled down and scanned using the X-ray CT. This procedure was repeated at 61 and 75 gyrations. Then the 3D images obtained at 8, 30, 61 and 75 gyrations were analyzed using the 3D image correlation algorithm developed as part of this study.

3 3D Image Correlation Algortihm

A 3D optical flow (also known as 3D image correlation) algorithm was developed for analysis of X-ray CT images of the asphalt specimens compacted at different gyrations in the Superpave gyratory compactor. First, image processing on the raw X-ray CT images were performed. These included rotation, translation, cropping and Gaussian smoothing of the images to align images of different specimens and prepare them for 3D optical flow analysis. Then, the 3D optical flow algorithm was run on these images and the displacement vectors within the X-Ray CT images in x-, y- and z- direction were computed.

Figure 1 shows the evolution of 3D X-ray CT images of an HMA specimen. As shown, as the number of gyrations increase, overall brightness of the features within the image (aggregates, mastic, air voids etc.) increases. The increase in the overall brightness of the X-ray CT image slices is an evidence of the densification

of the specimen. It should be noted that the pixel intensity in an X-ray CT image is based on density (or atomic number) of the material located at that location. Therefore, air voids (with negligible density as compared to the rest of the medium) are shown as pure black (intensity of zero (0)) in the X-ray CT image. As shown in Figure 1, the amount of the air voids decrease with increasing gyrations (as expected).

3.1 3D Optical Flow: Sum of Squared Differences (SSD) Method

The term "optical flow" is commonly used in computer science for problems related to pixel matching in two consecutive images captured at different times. The movement of a pixel (or an object represented by a pixel) from one image to another is termed as "optical flow". There are various methods to compute this movement. One method is the Normalized Cross Correlation (NCC) and another is Sum of Squared Distances (SSD) method. Since many optical flow algorithms use the NCC, this technique has been called "Image Correlation", in lieu of the term "optical flow". The implementation used the SSD method instead of NCC. It can mathematically be shown than SSD and NCC produces identical results and this derivation is available in image processing textbooks (Trucco and Verri 1998).

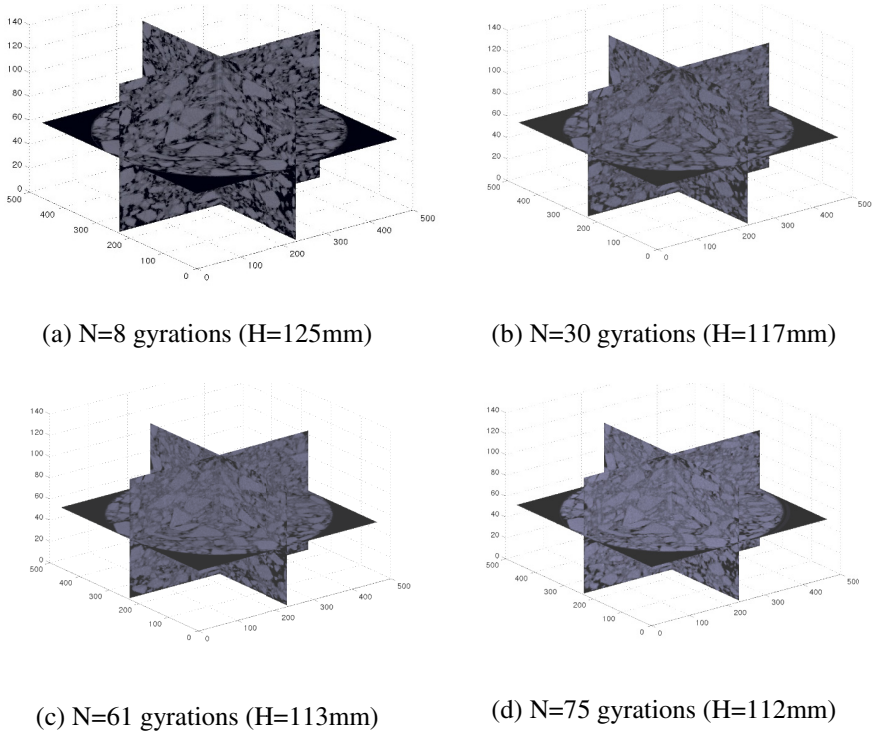

(a) N=8 gyrations (H=125mm)

(b) N=30 gyrations (H=117mm)

(c) N=61 gyrations (H=113mm)

(d) N=75 gyrations (H=112mm)

Fig. 1 X-ray CT images compaction levels of an HMA specimen

Figure 2 illustrates how the 3D displacement vectors are computed using the two consecutive 3D X-ray CT images. Fundamentally, the algorithm searches for a block of constant size between successive image frames based on a matching criterion. Similar patterns are tracked sequentially from one image to the next and the amount of movement is directly related to the movement of selected patterns. The amount of displacement is calculated for each block, which produces the "optical flow" for the entire image. The reference block and search window sizes are two important parameters that need to be selected appropriately to improve the performance of the matching algorithm. The reference block is a block of voxels used to match similar patterns between successive 3D images. The search window is essentially a region of voxels that defines the locus of the reference block in the current 3D image during the search operation. The algorithm has the capability to change both the aspect ratio of reference blocks and the search window size depending on the dimensions of individual image frames and the rate of deformation visualized within image frames during testing. The algorithm uses Sum of Squared Differences (SSD) method, which is given in the following form:

$$\text{SSD}\ (\hat{d}_x, \hat{d}_y, \hat{d}_z) = \sum\sum\sum \left(E_t(x, y, z) - E_{t+\Delta t}(x + \hat{d}_x, y + \hat{d}_y, z + \hat{d}_z) \right)^2 \quad (1)$$

$$(d_x, d_y, d_z)_{\min} = \arg\ \text{minimum SSD}\ (\hat{d}_x, \hat{d}_y, \hat{d}_z) \quad (2)$$

where $(d_x, d_y, d_z)_{\min}$ is the 3D displacement vector corresponding to the minimum of the sum of the differences between the reference image block and scan image block, $E_t(x,y,z)$ is the gray scale pixel intensity at location (x, y, z) at time t, and $E_{t+\Delta t}(x+d_x, y+d_y, z+d_z)$ is the gray scale pixel intensity at location at time $t+\Delta t$. Typical size of a search cube was 20 x 20 x 10 voxels.

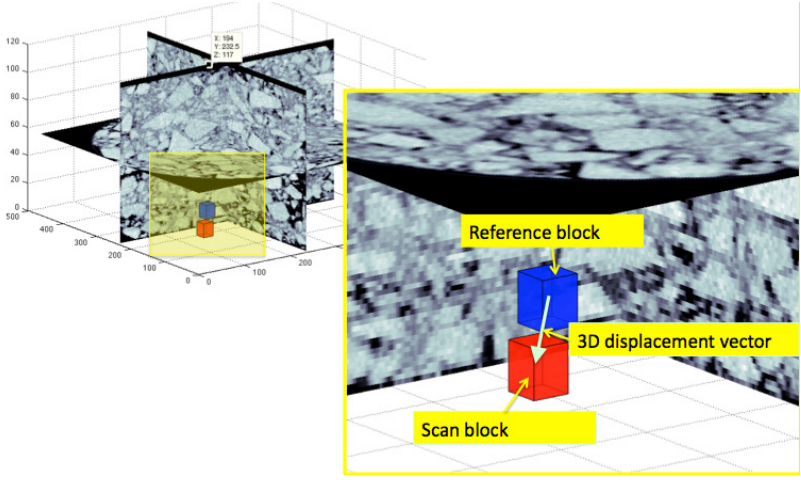

Fig. 2 Illustration of the 3D Optical Flow Method

4 Analysis of Results

Figure 3 shows the 3D displacement vectors computed using the 3D optical flow algorithm. While displacement vectors clearly show the downward movement of the points within the HMA, the vectors also show torsional movement in the tangential direction with respect to the center of the specimen. This is an evidence of the effect of gyration motion and shear on the movement of the aggregates within the mixture. This torsional movement phenomenon is clearer and more pronounced in Figure 3c, which shows the movement from 61 gyrations to 75 gyrations.

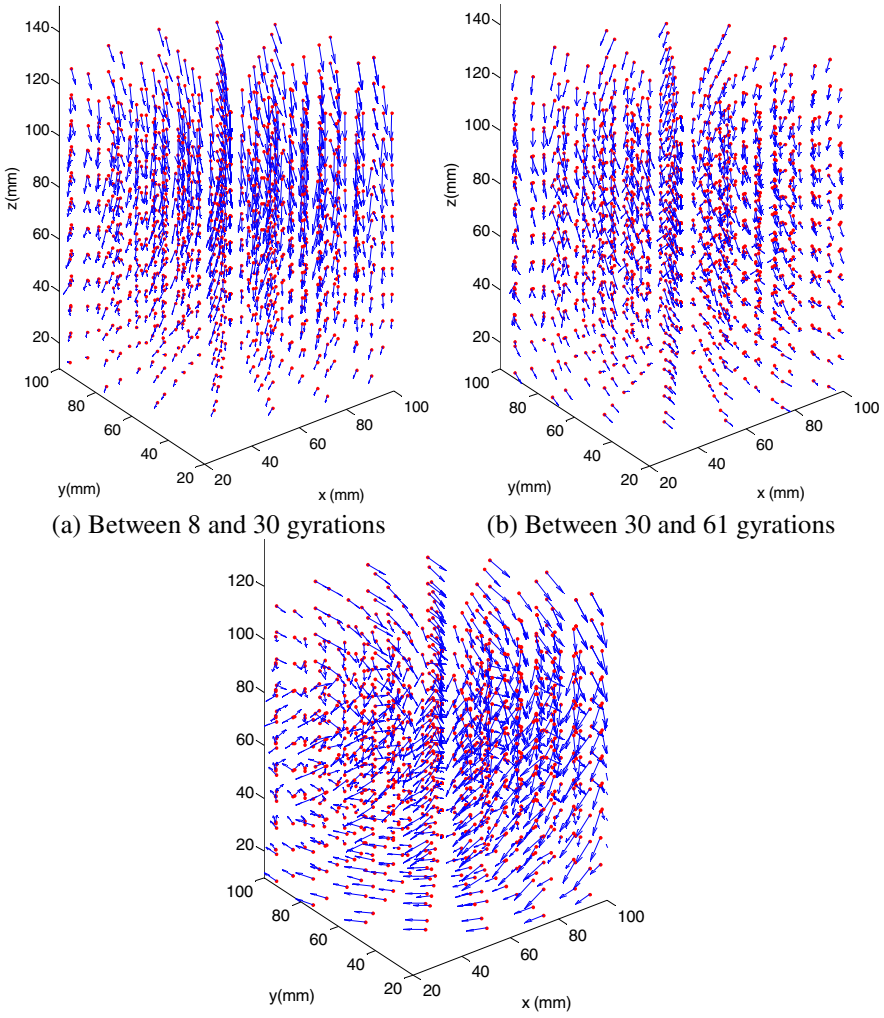

(a) Between 8 and 30 gyrations

(b) Between 30 and 61 gyrations

(c) Between 61 and 75 gyrations

Fig. 3 Visualization of 3D displacement vectors

Possible explanation for this could be that since the aggregates are closer to each other at 61 gyrations (as opposed to the state in lower gyrations), the gyratory shear motion causes the aggregates to move in the tangential direction, rather than moving downwards. Figure 4a through c show the displacement distribution (contours) for the movement in the z-direction (i.e., d_z in Equation 2). The color bar indicates units of displacement in mm. The Figure 4a and Figure 4b show that the z-displacement is slightly more in the center than the edges of the specimen. This is a somewhat reasonable since the core of the asphalt specimen stays warm at longer periods of time as compared to the edges. As a result, more localized movement is expected. The same phenomenon was not seen in Figure 4c, possibly because of the fact that at this gyration level, the mixture is already dense and difference in movement between the center and the edges is minimal.

In order to quantify the torsional (i.e., spinning) and radial movement (movements from center to outer edge or vice versa) that occurs on the x-y plane, the magnitude of the 3D displacement vector projected on the x-y plane was computed as follows:

$$d_{xy} = \sqrt{(d_x^2 + d_y^2)} \tag{3}$$

Figure 4d, Figure 4e and Figure 4f show the distribution of d_{xy} within the asphalt sample during compaction. As shown, the d_{xy} of the aggregates is more pronounced at the edges as compared to the central portion of the asphalt specimen. This is an indication of aggregates rotating/translating more at the edges than the center because of the gyratory shear forces. It should be noted that this is not necessarily an indication of better compaction at the edges since the aggregates may rotate/translate but not get closer to each other. In addition, the overall magnitude of movement is less than 2 mm (please see the colorbar in Figure 4d through f), whereas, the magnitude of d_z (as shown in Figure 4a through c) is a lot higher (as much as 8 mm).

In order to illustrate the variation of displacements with depth, average of the d_z and d_{xy} values at different depths was computed. This was done by taking the average of d_z (and d_{xy}) values of all points located at a certain depth (i.e., points on an X-ray CT slice). Figure 5a through f show the variation of average d_z with depth. It can be observed from Figure 5a that the displacement in z-direction changes linearly with depth. The slope of this line actually corresponds to the average strain in z-direction, i.e., $\varepsilon_z = \partial d_z / \partial z$. Therefore, Figure 5a indicates that the vertical strain (ε_z) is approximately constant within the sample during compaction between the gyrations 8 and 30. On the other hand, as the number of the gyrations increases (see Figure 5c and Figure 5e) the d_z curve becomes nonlinear. As a result, at these gyration levels, the vertical strain (ε_z) is higher at the top and bottom portions of the sample as compared to the center. This is perhaps an indication of rapid densification of the central portion (core) of the asphalt sample at early stages during compaction. Whereas, because of the proximity of top and bottom to the gyrating plates, aggregates at these two ends of the sample continuously rotate/translate. A clear trend was not observed in the variation of d_{xy} with depth as shown in Figures 5b, d and f.

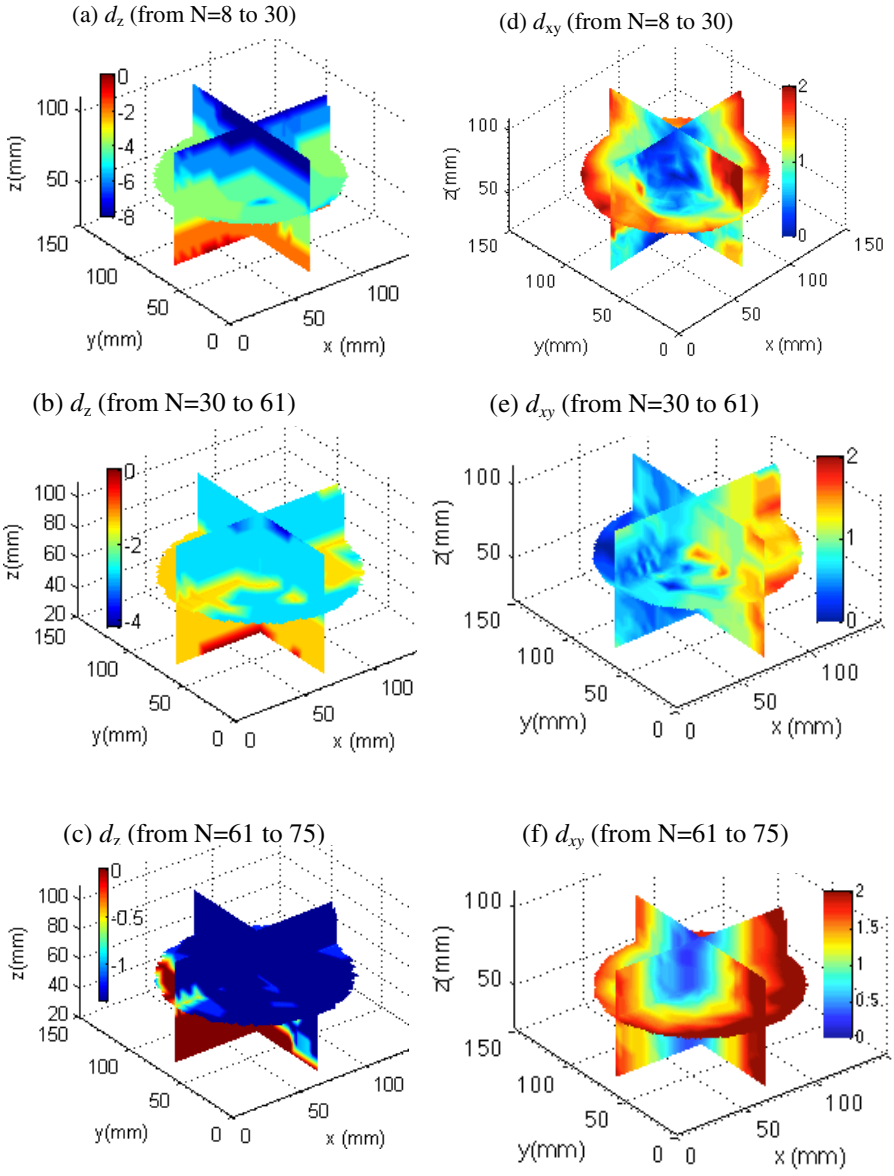

Fig. 4 (a through c): Displacement contours in z-direction for (a) N=8 to 30, (b) N=30 to 61 and (c) 61 to 75 gyrations. (d through f): Displacement contours in r-direction for (d) N=8 to 30, (e) N=30 to 61 and (f) 61 to 75 gyrations.

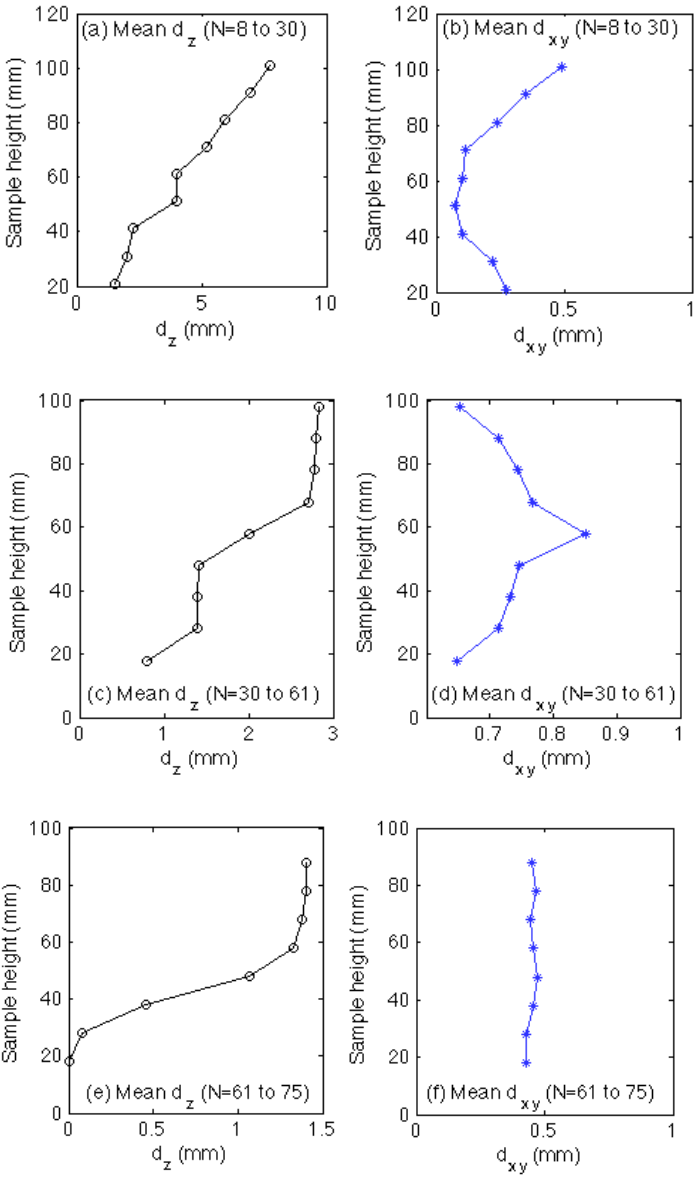

Fig. 5 Variation of average d_z and d_{xy} with depth: (a) &(b) N=8 to 30, (c) &(d) N=30 to 61 and (e)&(f) N= 61 to 75 gyrations

5 Conclusions

A 3D image correlation algorithm was developed to compute 3D displacements of aggregates in asphalt samples. The algorithm uses X-ray Computed Tomography (CT) images of asphalt specimens captured at different compaction levels. While the algorithm was developed for the asphalt mixtures, it can be used in analyzing time-series X-ray CT images of any material (e.g., concrete), provided that there is good contrast between different constituents. The analysis procedure included compaction of an asphalt sample to a specified compaction level, and scanning using X-ray CT. Once the X-ray CT images were obtained at a compaction level, the mold was taken to oven, heated up and compacted to a higher gyration level. This process was repeated several times at different compaction levels. The displacements in x-, y- and z-directions at various points inside the asphalt mixture were calculated using the 3D image correlation algorithm. Based on the analyses, following major conclusions were drawn:

- In addition to downward movement of aggregates within the HMA, the displacement vectors showed torsional movement in the tangential and radial direction with respect to the center of the specimen.
- The strain in z-direction was approximately constant within the sample during compaction between the gyrations 8 and 30. However, as the number of the gyrations increased, strain in z-direction became non-uniform with depth. Higher strain was observed at locations close to the top and bottom plates as compared to the central portion.
- At low gyration levels, more z-displacement was observed in the central portion of the sample as compared to the edges of the specimen.

References

Buchanan, M.S., Brown, E.R.: Effect of Superpave gyratory compac-tor type on compacted hot-mix asphalt density. Transportation Research Record: Journal of the Transportation Research Board, No. 1671, 50–60 (2001)

Coleri, E., Harvey, J.T., Yang, K., Boone, J.M.: Development of a micromechanical finite element model from computed tomography images for shear modulus simulation of asphalt mixtures. Construction and Building Materials 30, 783–793 (2012a)

Coleri, E., Harvey, J.T., Yang, K., Boone, J.M.: A micromechanical approach to investigate asphalt concrete rutting mechanisms. Construction and Building Materials 30, 36–49 (2012b)

Hunter, A.E., Airey, G.D., Collop, A.C.: Aggregate Orientation and Segregation in Laboratory-Compacted Asphalt Samples. Transportation Research Record: Journal of the Transportation Research Board, No. 1891, 8–15 (2004)

Kalcheff, I.V., Tunnicliff, D.G.: Effects of Crushed Stone Aggregate Size and Shape on Properties of Asphalt Concrete. Journal of the Association of Asphalt Paving Technologists 51, 453–483 (1982)

Khan, Z.A., Wahab, H.I.A.-A., Asi, I., Ramadhan, R.: Comparative study of asphalt concrete laboratory compaction methods to simulate field compaction. Construction and Building Materials 12, 373–384 (1998)

Kutay, M.E., Aydilek, A.H., Masad, E.: Estimation of Directional Permeability of HMA Based on Numerical Simulation of Micro-scale Water Flow. Transportation Research Record: Journal of the Transportation Research Board, No. 2001, 29–36 (2007b)

Kutay, M.E., Aydilek, A.H., Masad, E., Harman, T.: Computational and Experimental Evaluation of Hydraulic Conductivity Anisotropy in Hot Mix Asphalt. International Journal of Pavement Engineering 8(1), 29–43 (2007a)

Masad, E., Jandhyala, V.K., Dasgupta, N., Somadevan, N., Shashidhar, N.: Characterization of air void distribution in asphalt mixes using x-ray computed tomography. Journal of Materials in Civil Engineering 4(2), 122–129 (2002)

Partl, M.N., Flisch, A., Jönsson, M.: Comparison of Laboratory Compaction Methods Using X-ray Computer Tomography. RMPD 8(2) (2007)

Peterson, R.L., Mahboub, K.C., Anderson, R.M., Masad, E., Tashman, L.: Comparing Superpave gyratory compactor data to field cores. Journal of Materials in Civil Engineering 16(1), 78–83 (2004)

Prowell, B.D., Zhang, J., Brown, E.R.: Aggregate Properties and the Per-formance of Superpave-Designed Hot Mix Asphalt. Transportation Research Board, NCHRP Report 539 (2005)

Saadeh, S., Tashman, L., Masad, E., Mogawer, W.: Spatial and directional distribution of aggregates in asphalt mixes. Journal of Testing and Evaluation 30(6), 1–9 (2002)

Stephens, J.E., Sinha, K.C., Tashman, L., Masad, E., Peterson, B., Saleh, H.: Internal Structure Analysis of Asphalt Mixes to Improve the Simulation of Superpave Gyratory Compaction to Field Conditions. Journal of the Association of Asphalt Paving Technologists 70, 605–645 (1978, 2001)

Tashman, L., Masad, E., D'angelo, J., Bukowski, J., Harman, T.: X-ray tomography to characterize air void distribution in Superpave gyratory compacted specimens. The International Journal of Pavement Engineering 3(1), 19–28 (2002)

Tashman, L., Masad, E., Peterson, B., Saleh, H.: Internal Structure Analysis of Asphalt Mixes to Improve the Simulation of Superpave Gyratory Compaction to Field Conditions. Journal of the Association of Asphalt Paving Technologists 70, 605–645 (2001)

Trucco, E., Verri, A.: Introductory Techniques for 3-D Computer Vision, 343 p. Prentice Hall, New Jersey (1998)

Research into Applications of Acrylic Fibres in Porous Asphalt: Laboratory, Numerical and Field Study

Milliyon Fekade Woldekidan[1], Jan Voskuilen[2], Dave Vliet[3], and Greet A. Leegwater[3]

[1] Delft University of Technology, Delft, The Netherlands
[2] Rijkswaterstaat, Dutch Ministry of Infrastructure and Environment, The Netherlands
[3] TNO, Delft, Schoemakerstrrat 97, The Netherlands

Abstract. A laboratory and numerical study were conducted to gain insight into the performance of a short fibre containing Porous Asphalt (PA) mixture. Laboratory works include microscopy analysis and mechanical tests using Dynamic Shear Rheometer (DSR). From microscopic analysis it was observed that the fibre serve as a good drainage inhibitor. The DSR test results showed the fibre has stiffening effect to the mastic and improved fatigue behaviour. Numerical work performed to evaluate winter performance showed that the fibre containing PA mixture has comparable performance with other good-performing PA layers in literature. Field performance data that was obtained from test sites constructed on Dutch motorways showed the fibre-containing PA is performing very well. The results from the laboratory and numerical investigations were found consistent with the performance data obtained from field observations. The methods used in this study demonstrated the possibility of utilizing the lab and numerical methods for evaluating expected performances of newly designed PA mixtures. Based on the obtained results on the use of acrylic fibres, the good performance of the fibre containing PA mixtures potentially indicate a new route to PA layer design without the use of polymer modified bitumen.

1 Introduction

The Netherlands is a very densely populated country (more than 400 people per km^2) and as a consequence has an extensive infrastructure. Since many of its inhabitants live near motorways, noise generated by traffic is a serious environmental issue. Hence, since 1990 the government policy dictates the use of silent pavements on motorways. This has resulted to the current situation that almost 90% of all Dutch motorways now have single-layer Porous Asphalt as a wearing course but if more noise reduction is needed, Two-Layer Porous Asphalt (TLPA) is laid. TLPA consist of a 25 mm top-layer PA 4/8 mm with an air voids content of 20% and a bottom-layer of 45 mm PA 11/16 mm with an air void content of 25%. The noise reduction of TLPA in comparison to Dense Asphalt

N. Kringos et al. (Eds.): *Multi-Scale Model. & Charact. of Infrastruct. Mater.,* RILEM 8, pp. 395–406.
DOI: 10.1007/978-94-007-6878-9_29

Concrete and single layer PA is 6 and 3 dB(A), respectively. However this large improvement in traffic noise performance is known to compromise the wearing course's durability. The average service life of the top layer in TLPA, which in the Netherlands always contains PMB as a binder, is therefore only 8 years [1].

The challenge for researchers is to improve the functional performance, extend the service life and improve the cost-effectiveness of TLPA. One of the initial problems of TLPA after construction was the poor skid resistance and brake deceleration. In order to improve this, the standard TLPA top-layers were modified by special additives. In 2005 six different test sites of TLPA structures were laid on the Dutch motorway A15, nearby Leerdam, to improve the early skid resistance and early brake deceleration [2]. In Table 1 the coarse materials, the special additives and bitumen contents of the TLPA top-layers are given. The bottom-layer for all TLPA structures was the same. Glanzkies is fine broken glass, EUF 1 is a coarser angular filler, fine sand is finer than the normally used coarser crusher sand and Panacea (PAN) is an acrylic fibre obtained from Lambda Furtherance, the Netherlands with length of 3.2 or 6.4 mm. Based on results obtained from tests on-site after construction of the various wearing courses, only the top-layer DV improved both the early skid resistance and early brake deceleration.

Table 1 Mix compositions parameters of the top-layers of TLPA

	DV	BAM	H1	H2	R1	R2
Coarse material	Bestone 4/8		Gres d'Ardennes 2/6	Gres d'Ardennes 2/6 + Andesit 4/8	Gres d'Ardennes 2/6 + Andesit 4/8	Gres d'Ardennes 2/6 + Andesit 4/8
Additives	Glanzkies 0/1	EUF 1	fine sand	-	PAN 6.4	PAN 3.2
Bitumen 70/100	-	-	-	-	-	6.1
PMB	5.5	5.5	6.5	6.1	6.1	-

The six test sites were subsequently monitored in time to determine the long term effects of the additives on PA performance. Despite the fact that the top-layer of DV performed best in terms of early skid resistance and break deceleration, the DV site together with the BAM site had to be replaced by a new top-layer in 2010 due to significant ravelling. This premature damage appeared to be caused by poor bonding of Glanzkies and EUF 1 to the PMB. The behaviour of the other four top-layers (H1, H2, R1 and R2) was inspected in 2010 and they all were found in good condition. Recently in 2012 the sections were again monitored. Whereas R1 and H2 show light ravelling damages, R2 and H1 are still in good condition [3]. Especially the predicted long rest service life of top-layer R2 is surprising, since it is a TLPA without PMB. Until present however the common consensus in in the Netherlands is that a TLPA top-layer, for durability reason, always has to contain a PMB. To understand why this TLPA top-layer with pen grade bitumen 70/100

and PAN fibres behaves so well, a research was carried out on PA mortars containing PAN fibres. The investigation was focussed on microscopy analysis, laboratory research into stiffness and fatigue behaviour and numerical computations to evaluate ravelling resistance. In this paper the results of this research are presented and discussed.

2 Experimental

The experimental work consisted of two parts: Microscopy analysis and mechanical testing, which consists of fatigue characterization and response testing. Besides the laboratory research, the field behaviour of the TLPA test sites was also monitored. The Microscope analysis was performed to obtain insight on the distribution of the fibres in the mortar domain and the time dependant processes. Mechanical tests were performed to obtain insight on the response and fatigue characteristics of the mortars. Response results were used as an input for numerical computations. The numerical computations were performed for evaluating the mixture performance for winter weather conditions. Available PA design tool, the Lifetime Optimisation Tool (LOT) [4, 5] was utilized for this purpose.

2.1 Microscopy Analysis

Polarization and fluorescence microscopy (PFM) are microscopic techniques to study the morphology of a material in detail. In this research these techniques were used to both study the interaction between fibres and the asphalt matrix and the time dependant physical processes. PFM samples were made out of cores from actual road surfaces, from new laid test sites (A2) in 2010 (just after laying) and aged test sites (A15) laid in 2005 with and without fibres [6-8]. The most obvious effect of the fibre, as could be observed using PFM, is the drainage inhibition effect. This results in thicker mortar layers in the top section of the TLPA top-layer, which will improve the resistance to ravelling. A thicker mortar film is known to age slower and can handle larger strains. The binder drainage inhibition effect can also be seen from the shape of the pores with fibres, as demonstrated in Figure 1. The shape of the bitumen film is influenced by the fibres as can be seen from them sticking out in the air voids just after placement. The binder drainage inhibition effect was found stronger for fibres compared to samples made with PMB as a binder drainage inhibitor. With respect to the homogeneity, the PAN fibres show a good dispersion throughout the mortar. The synthetic fibres additionally have good adhesion with the bitumen and no degradation of the fibres was observed, not even after 6 years of service. Based on visual assessment the fibres do not influence the interaction between the mortar and the aggregates.

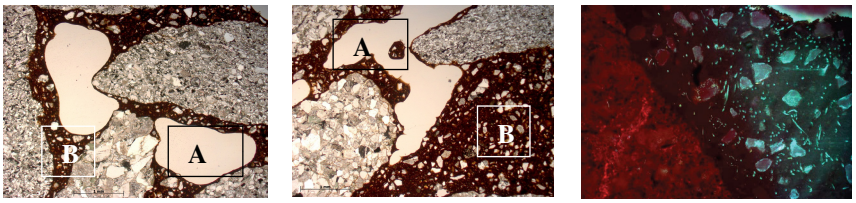

Fig. 1 Left and Middle: Air voids (A) shape and bitumen (B) surface in young asphalt with 0.1 % and 0.3% PAN fibres respectively, Right: distribution of fibre

The microscopic investigation may provide three major signs of degradation of the TLPA morphology. These are the degradation of the mastic surface, the detachment of the aggregate grains from the mastic and clogging of the air-voids. However, none of these three signs of degradation appear to be related to the presence of PAN fibres, since the same phenomena were observed, to a comparable extent, for the TLPA top-layers without fibres. From these observations it can therefore be concluded that the fibres do not appear to have a negative effect on the visible degradation phenomena.

2.2 Fatigue Tests

For the mortar fatigue tests two types of mortar were made in the laboratory, one reference mortar (Mortar R) and one with PAN fibres (Mortar P). The bitumen used for preparing the asphalt mortars was a standard Q8 pen grade 70/100 bitumen. Before further use the bitumen was artificially aged according to the RTFOT standard; EN 12607-1. Filler material (<63 µm) and fine sand (< 500 µm) were of standard road-construction grade and were subsequently used without any further treatment. The length of the dried PAN fibres was 3.2 mm. To produce mortar the aged binder was hand-mixed with the filler and the fine sand at approximately 180°C. Utilized ratios for bitumen, filler and fine sand were according the requirements for single-layer PA16+ as shown in Table 2. The fibres were added to the mortar and mixed by hand to produce homogeneous fibre reinforced mortar. Then, the hot mortar was cast in the molds for further testing.

Table 2 Composition of (fibre reinforced) asphalt mortars R and P

Components (wt. fraction)	Reference (R)	Panacea (P)
Bitumen 70/100	0.38	0.38
Filler (<63 µm)	0.38	0.37
Fine sand (<500 µm)	0.24	0.23
PAN fibres	0	0.020

DSR fatigue testing were then performed on the mortar columns (length: 20mm, diameter: 6mm) in a sinusoidal torque mode at 10°C and -10°C at 10rad/s. The applied strain level was varied between 0.4 and 1.5%. Failure was defined as

the moment when the measured stiffness of the column was below 50% of the initial stiffness. The results performed at 10°C and strain between 0.8 and 1.5% are illustrated in Figure 2. Similar results were obtained at -10°C. The tests demonstrated that the presence of fibres significantly increases the fatigue resistance. This effect is even more pronounced at lower levels of strain.

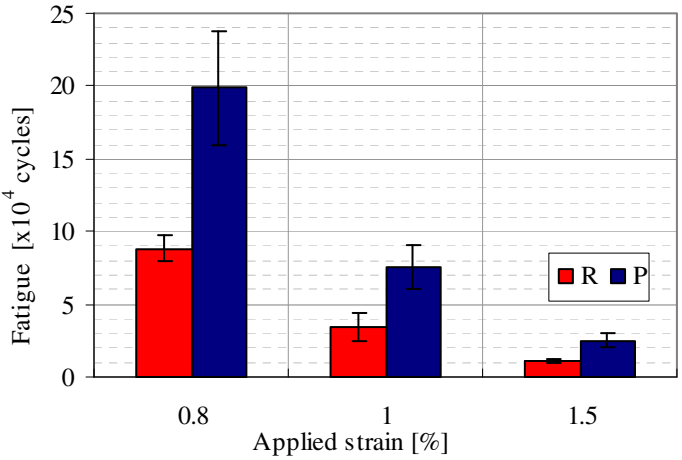

Fig. 2 Combined results of DSR fatigue tests for all investigated asphalt mortars at 10°C and a frequency of 10 rad/s

2.3 Response Characterization

For the response characterization, mortar materials were extracted from field cores taken from the A15 motorway. In order to compare fibre containing mortar to PMB mortar, cores from the R2 and H1 test sections were used (see Table 1 for abbreviations). The mortars are labelled as R2 and H1. In the extraction process, the cores were first cleaned and then pulverized at elevated temperature (60°C to 80°C). Pulverization was performed using a manually operated hydraulic machine. To obtain the mortar from the pulverized PA mixture, the material was placed in a pan and heated to a temperature of 190°C. The heated material was then mixed with a spatula. The mortar sticking to the bottom of the pan and the spatula were then collected. The collected mortar was finally used to produce DSR test samples.

The sample preparation and mounting to the DSR setup is illustrated in Figure 3. DSR frequency sweep tests were conducted at 9 different temperatures, ranging from -10°C to 70°C at 10°C increment. The results of the tests were then used to construct master curves using Time-Temperature-Superposition principle. In obtaining each master curve, results from two test specimens were used. The test setup provided very high result repeatability that in all cases the master curve fits has R-squared (R^2) values greater than 0.99 for both the phase angle and the complex modulus.

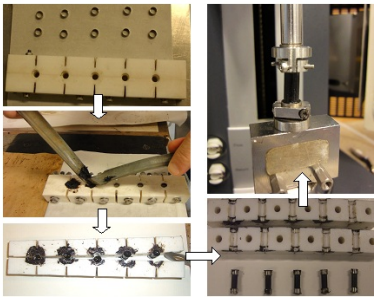

Fig. 3 DSR sample preparation and test setup

In Figure 4, the master curve comparison between the two mortars is presented. The test data from two test specimens are also plotted on the master curve to illustrate the good result repatability.

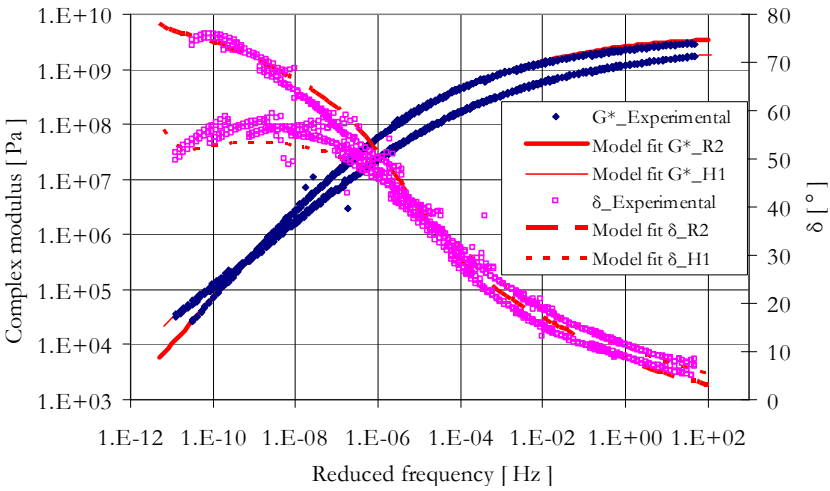

Fig. 4 Master curve comparisons of R2 and H1 mortars, Tref= -10°C

Master curve description was performed using the MHS model [9] and the shift factors were described using the WLF formula. The relevant model parameters for the master curve are given in Table 3. For details on the model reference is made to available literature [9]. Master curve comparison from Figure 4 shows that the PAN containing mortar (R2) is relatively stiffer than H1 mortar for a wide range of temperatures. This can be seen from the higher $G\infty$ value for R2 mortar in Table 3. Only at very high temperature, R2 mortar shows somewhat softer behaviour in Figure 4. This is also depicted by the lower η_3 value (viscous behaviour) in Table 3.

Table 3 WLF and MHS model parameters for mortars at T_{ref}=-10^{0}C

	WLF		MHS model parameters						
Mortar	C1	C2	m_1	m_2	δ_1	τ	G_∞	G_0	η_3
	-	-	-	-	-	s	MPa	MPa	MPa.s
H1	28.3	144	0.6	0.22	0.02	0.13	2460	0.02	1.07E+09
R1	24.8	125	0.7	0.26	1.00	1.83	3860	0.01	2.27E+08

3 Numerical

To evaluate the winter performances of the H1 and R2 TLPA layers, numerical computations were made using the LOT tool. LOT is a meso-scale PA design tool that allows mixture performance computations taking into account the meso-scale geometry of the PA, mixture component material properties, traffic loading and temperature fluctuation effects. For detailed information on the model the reader is referred to available literature [4, 5]. With this tool insight can be obtained in the ravelling performance of mixtures. Computed performance results can be compared with available field-and-numerically validated performance data for various PA mixtures. Below, an overview of the required inputs is briefly discussed and numerical results are presented.

3.1 Input Parameters

The input parameters for the LOT model are the meso-scale geometry of the mixture, the mechanical behaviour of the mixture component materials and the loading. In addition, the effect of the underlying pavement deflection on the PA surface can also be taken into account by specifying deflection profiles as a boundary condition in the PA model. The meso-scale geometry is defined based on the mixture volumetric composition of the existing PA layer. For this reason air void, binder and aggregate content and equivalent grain diameter were determined after pulverization and extraction process (Table 4). In defining mechanical property of materials, the corresponding viscoelastic model parameters for the mortar were determined based on a Prony series model fit on the master curve data. Matlab tools were utilized for the regression fitting [10].

Table 4 LOT geometrical input

	R1	H1
Average stone diameter (mm)	5.31	5.31
Bitumen density (kg/m³)	1030	1030
Density mineral in mortar (kg/m³)	2700	2700
Density stone (kg/m³)	2743	2743
% stone	84.3	84.0
% bitumen on 100% aggregate	6.02	6.16
% air voids	22.21	22.53

The loading applied to a PA surfacing comprises traffic and temperature loadings. In addition, the effect of deflection coming from the supporting pavement structure is taken into account by specifying deflection profile of the pavement as a boundary condition in the PA model.

Traffic loading: For the simulations in this work a standard axle load of 100 kN and a speed of 75 km/hr was used. Based on similar works performed in the past, an estimated total equivalent axle load of 11450 per day was considered.

Pavement deflection: The pavement deflection profile at different temperatures was obtained using the multi-layer program BISAR. The thicknesses and properties of the pavement layers corresponding to the PA sections are given in Table 5. Deflection profiles up to 15 m from the wheel load were computed.

Table 5 Thickness and layer properties used in BISAR

Layers	Thickness (mm)	Poissons' ratio	Stiffness [MPa]			
			-10°C	0°C	10°C	20°C
PA	70	0.35	14000	9500	5250	2750
AC bind	40	0.35	18200	18200	14400	6330
AC base	120	0.35	28000	19000	10500	5500
Sand	350	0.4	1000	1000	1000	1000
Sub grade	∞	0.4	55	55	55	55

Temperature fluctuation: Temperature fluctuation causes expansion and shrinkage which results in temperature-related stresses in the PA layer. In the LOT tool, these effects are taken into account by specifying the temperature-related displacements as a boundary condition. Linear thermal expansion coefficients of 6.6E-6 and 2.5E-5 were used for the stone and mortar, respectively. By applying the temperature-related displacements as a load, the resulting thermal stresses were obtained using FE models. Aggregate size and the mortar film thickness from Table 4 were used.

3.2 LOT Damage Model

With the input parameters discussed in the previous section, the LOT tool provides stress and strain signals in the stone-stone contact areas for a passing wheel load. The stress and strain signals from the tool are fed to the adhesive and cohesive damage models. In investigating winter-related damage the adhesive damage model is of key interest. The adhesive damage model that is used for translating the stress signals into damage is given as:

$$\dot{D} = \left(\frac{\sigma_{et}}{\sigma_0} \right)^{n_0} \text{ for } \sigma_{et} > 0, \quad \dot{D} = 0 \text{ for } \sigma_{et} < 0 \quad \text{with } \sigma_{et} = \sigma_n + \frac{\tau}{\tan \phi} \qquad (2)$$

where D denotes the rate of damage accumulation, σ_{et} is the equivalent tensile stress (MPa), σ_n is the adhesive zone normal stress (MPa), τ is the adhesive zone shear stress (MPa), ϕ is the friction angle in degrees and, σ_0 (MPa) and n_0 are model parameters. The adhesive zone model parameters determined for Greywacke and Bestone (sandstone), two commonly used stones in the Netherlands, are available in the literature [11]. Table 6 presents the damage model parameters for various temperatures. Since adhesive parameter data for Gres d'Ardenne is not available, the average parameter values from Tale 6 is used for the LOT computations performed in this work.

Table 6 Damage model parameters for adhesive zone [11, 13]

	Bestone			Greywacke		
Temp (°C)	σ_0 (MPa)	n	ϕ (°)	σ_0 (MPa)	n	ϕ (°)
-10	18.91	2.57	74.2	22.34	2.9	66.2
0	13.75	4.33	27.1	11.93	5.36	24
10	14.89	3.01	32.6	8.18	3.83	32.4
20	7.51	3.33	38.2	9.98	2.77	39.6

3.3 LOT Performance Results

LOT calculations were made for mean temperatures of -10, 0, 10 and 20 °C. At each temperature, the effect of temperature fluctuation was investigated. The following procedure was followed in performing the computations:

- Determine input parameters, viscoelastic parameters for the mortar, deflection profiles and temperature stresses, at each temperature.
- Run LOT computations, 100 kN axle load with a speed of 75 km/hr.
- Obtain the stress in the adhesive zone of the idealized model.
- Analyze the stress history together with the temperature stresses to compute the resulting damage in the adhesive zone.

Stresses were translated to damage using the adhesive damage model. Once the damage resulting from a single wheel pass is known, available axle load spectrum for Dutch traffic [13] was used to compute the total damage from 11450 equivalent axle loads in a 24 hour period. Figure 5 shows the 24 hour damage distribution for mortar R2 at a mean daily temperature of -10°C and a daily temperature fluctuation of 3°C. It can be seen from this figure that, significant damage occurs during the night when the temperature drops to a minimum.

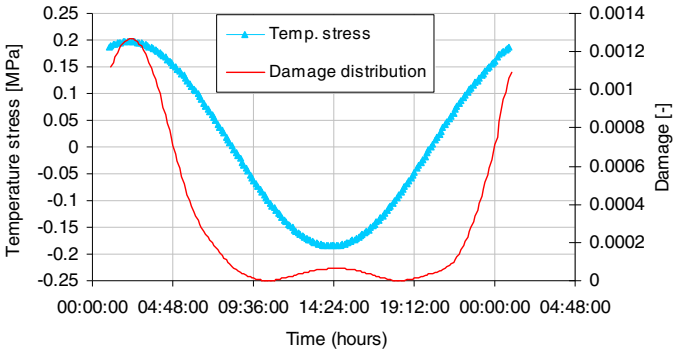

Fig. 5 Damage spectrum within 24 hour period, R2 mortar at -10 °C

The total damage for the 24 hour period is obtained by summing the damages calculated for each hour. At each mean daily temperature, temperature fluctuations with various amplitudes varying from ΔT = 1 °C to ΔT = 10 °C were considered, and the resulting performances were calculated. For ΔT = 3°C at a mean temperature of -10°C the relative damages computed for H1 and R2 mixtures are presented in Figure 6. In Figure 6, performance data from literature for other existing PA sections that were constructed in the period of 1995 to 2006 were also included [12-13]. Data points marked with 2 represent sections that showed severe ravelling while those marked with 0 represent the best performing sections during the severe winter of 2008/2009 in the Netherlands. From Figure 6 the performance data of R2 and H1 mixtures are both within the good performing mixture category.

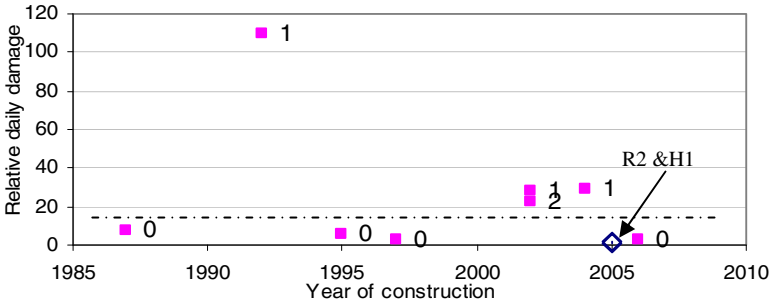

Fig. 6 H1 and R2 mix performance comparisons with available PA performance data from literature; ΔT = 3°C

The field observation for these mixtures has also shown consistent results. Since in the Netherlands application of PMB is thought necessary in the top layer of TLPA, the good performance of PAN-fibre containing mixture, based on numerical computations and field observation, is encouraging. However, this does not necessarily imply the PAN-fibres can replace PMB. In fact, in relative terms the mixture performance for PMB binder (relative daily damage = 0.96) is better

than the PAN-fibre containing mixture (relative daily damage=1.96). Whether this relative difference in computational performance translates to significant field performance results will be seen in the future from the long term field monitoring.

4 Discussions

In this article microscopic, mechanical testing and numerical study were used to gain insight into the performances of the fibre-containing PA mixtures. Microscopic study showed that an acrylic fibre has served as a good binder drainage inhibitor in time. The fatigue result has also shown that the acrylic fibre improved the fatigue performance of the mortar in general. These findings in part may explain the good performance in practice of the fibre-containing mortar based on standard pen grade binder analogue to TLPA layers constructed with PMB. The LOT simulation results additionally indicate that the two PA mix performances lie in the good performing category for severe winter weather conditions. The consistency between the field and the laboratory-and- numerical investigation results are encouraging to utilize the described methods in the future in order to rank and evaluate expected performances of new or innovative PA mixtures.

In recent field monitoring survey, the 6.2 mm fibre containing PA section, R1, shows light to moderate ravelling while the 3.2 mm fibre, R2, is still good performing [3]. The light to moderate ravelling observed for R1 could imply there might be an optimum fibre length in relation to the maximum diameter of the used coarse material in PA. It could also be due to the possible difficulty in obtaining uniform fibre distribution within PMB due to the longer fibre length. Performing similar microscopic, laboratory and numerical investigation for the R1 mixture could give more insight on the possibilities of using acrylic fibres in PA.

5 Conclusions and Recommendations

From field observation very good performance was obtained for PA with acrylic fibre. Microscopy analysis showed a homogeneous distribution of fibre in the mortar, and a good adhesion existed between the PAN fibre and the mortar. The anti-dripping effect of PAN fibres was also present and stronger compared to PMB. Based on the laboratory investigation, the presence of fibres did not seem to affect the aging of the mortar. For the mechanistic investigation, tests carried out on mortar extracted from PA cores showed relatively stiffer behaviour for the fibre mortar. However, numerical computations performed for winter performance have shown both the PMB and fibre containing PA lie in a good performing category. Results from the laboratory and numerical investigations are all in agreement with the field observations. In relation to the investigation methods, this implies the future possibility of utilizing the lab and numerical methods for ranking expected performances of newly designed PA mixtures. In regard to the use of acrylic

fibres, the good performance of the PAN containing PA mixtures could especially lead to a new possibility of designing PA layers without polymer modifications. For the follow-up, it is recommended to carry out further investigation into the performance of the 6.2 mm fibre containing mixture so as to understand the possible relation between the PA performance with the fibre length, aggregate size and the selected binder combinations, i.e., binder with or without polymer.

References

[1] Reisen van, F., Erkens, S., Ven van der, M., Voskuilen, J., Hofman, R.: Verbetering levenduur tweelaags ZOAB. Report DVS-2008-020, The Netherlands (2008)
[2] IPG Report, Tweelaags ZOAB Proefvakken A15 te Leerdam, Dutch Minstry of Transport, DWW-2005-086, The Netherlands (2005)
[3] KOAC-NPC, Monitoring restlevensduur A15 Leerdam (II), Report, e120133401-04, Nieuwegein, The Netherlands (2012)
[4] Huurman, M., Mo, L., Woldekidan, M.F.: Overview of the LOT meso mechanical research into porous asphalt ravelling. Adv. Testing and Characterisation Bituminous Mater. 1, 2, 507–518 (2009)
[5] Huurman, M., Mo, L., Woldekidan, M.: Mechanistic Design of Silent Asphalt Mixtures. International Journal of Pavement Research and Technology 3(2), 56–64 (2010)
[6] Mookhoek, S.D., Van Vliet, D.: Thermo-mechanical properties of fibre reinforced porous asphalt mortars, 060-DTM-2012-01789,TNO,The Netherlands (2012)
[7] Valcke, S.L.A.: Microscopic observations of young and aged fibre reinforced porous asphalt, 060-DTM-2012-01791, TNO, The Netherlands (2012)
[8] Mookhoek, S.D.: Fibre reinforced porous asphalt, TNO, R10140, The Netherlands (2012)
[9] Woldekidan, M.F., Huurman, M., Pronk, A.C.: A modified HS model: Numerical applications in modelling the response of bituminous materials. Finite Elements in Analysis and Design 53, 37–47 (2012)
[10] Woldekidan, M.F.: Response Modelling of Bitumen, Bituminous Mastic and Mortar. PhD Dissertation, Delft University of Technology, The Netherlands (2011)
[11] Mo, L.: Damage Development in the adhesive zone and mortar of porous asphalt concrete. PhD Dissertation, Delft University of Technology, The Netherlands (2010)
[12] Huurman, M., Mo, L.T., Woldekidan, M.F.: Mechanistic Design of Silent Asphalt Mixtures and its Validation. Journal of the Association of Asphalt Paving Technologists 79, 365–401 (2010)
[13] Huurman, M., Mo, L.T., Woldekidan, M.F.: Porous asphalt Raveling in Cold Weather Conditions. International Journal of Pavement Research and Technology 3(3), 110–118 (2010)

Finite Element Modeling of Rejuvenator Diffusion in RAP Binder Film – Simulation of Plant Mixing Process

Martins Zaumanis and Rajib B. Mallick

Worcester Polytechnic Institute, 100 Institute Road, Worcester, MA 01609, USA
{mzaumanis,rajib}@wpi.edu

Abstract. In order to sustain the needs of the 21st century civil infrastructure, we need a paradigm shift in recycling – from current 20-40% to 100% (zero waste). The main hindrance to successful recycling of high Reclaimed Asphalt Pavement (RAP) content mixes is the lack of confidence which stems from a lack of understanding of the rejuvenation and diffusion process that is supposed to occur when a recycling agent is added to an aged asphalt mix. This research presents finite element simulation of rejuvenator diffusion into an aged asphalt binder film. Five different rejuvenators and aged RAP binder were tested to obtain the required input data for simulation – viscosity at different temperatures and molecular weight. The simulation was run assuming 100% RAP mixture and three different temperatures were simulated for three rejuvenator dosages. The final viscosity for complete diffusion and the required time to reach this state was determined. The results show significant differences in the softening potential of different rejuvenators and helps in the estimation of temperature range to reach homogeneous rejuvenator concentration within the binder film before the production process is completed. The simulation results are compared with mechanical tests of binder penetration and mixture creep compliance to confirm the softening effect.

1 Introduction

The use of non-renewable materials needs to be replaced by recycling in order to sustain the needs of the 21st century civil infrastructure. Although recycling of asphalt materials, which make up most of our pavements, is a top priority for all state departments and other transportation agencies, we need a paradigm shift in recycling – from the current 20-40% to 100 % (zero waste). The main hindrance to successful recycling of high Reclaimed Asphalt Pavement (RAP) content mixes is the lack of confidence which stems from a lack of understanding of the rejuvenation and diffusion process that is supposed to occur when a recycling agent is added to an aged asphalt mix.

The use of rejuvenators in hot mix asphalt plant production process is picking up. Different types of rejuvenating agents are available, including bio-based and different products that are manufactured from renewable resources (Zaumanis,

N. Kringos et al. (Eds.): *Multi-Scale Model. & Charact. of Infrastruct. Mater.,* RILEM 8, pp. 407–419.
DOI: 10.1007/978-94-007-6878-9_30

2013). In conventional HMA production process the RAP is mixed together with virgin aggregates, and fresh asphalt or rejuvenator. A critical aspect of the use of rejuvenators is the diffusion of the different products into aged RAP binder. It is expected that during the short mixing time the aged asphalt attains necessary viscosity so that RAP and virgin aggregates receive a homogeneous film thickness. At the same time sufficient diffusion of the rejuvenator is required in the aged asphalt to restore its properties to the required level. The diffusion is a function of temperature, viscosity, mixing, transportation and storage time, and it may continue in the pavement during the service period. Therefore, until equilibrium is reached, the outer layer of the asphalt film may have relatively lower viscosity which can lead to increased probability of developing permanent deformations.

The in-plant addition of rejuvenator involves three main interaction mechanisms between the aged binder and rejuvenator – dispersion, diffusion and mechanical mixing. Dispersion is the phenomenon of distribution of the rejuvenator on the RAP, diffusion occurs from the intermingling of the rejuvenator with the RAP binder, and mechanical mixing is caused by the friction between aggregate particles. At a drum plant the rejuvenator is usually added after drum heating and there is mechanical interaction between mix aggregates in the silo/elevator and during transportation. At a batch plant the rejuvenator would be introduced before the pugmill and therefore there would be even more contact between the mix aggregates when the RAP undergoes the mixing process in the pugmill. The dispersion and mechanical mixing are therefore defined by the technology and equipment at the specific plant and would be unrealistic to simulate. The simulation study reported in this paper concerns the diffusion process only.

1.1 Approach to the Study

The goal of the study is to develop a simulation process of the diffusion of recycling agents into the aged RAP binder in order determine the softening efficiency, optimum mixing time and temperature range.

The diffusion process was simulated with the help of finite element (FE) modeling, analysis and simulation using COMSOL "Multiphysics" software. The analysis was conducted with heat transfer module. The specific tasks of the modeling included:

- evaluate the softening performance of five different rejuvenators at three different dosages on the aged RAP binder,
- compare the time of "equilibrium" (end of diffusion) after adding a predefined dosage of each of them,
- evaluate the changes in equilibrium time and softening performance at different temperatures within the common mixing and compaction range.

Five different rejuvenators and aged RAP binder were utilized in this study. The rejuvenators include refined tallow, paraffinic base oil, waste vegetable oil (brown grease), waste frying oil (yellow grease), as well as a softer asphalt binder. The

required parameters for diffusion simulation were tested or obtained from manufacturers of the products.

The softening effect of rejuvenators was tested on extracted binder by means of penetration tests at two different temperatures. The effect on low temperature mixture performance was verified at minus 10ºC by means of Creep compliance for a 12.5mm Superpave mixture that was prepared with 100% RAP and different rejuvenators.

2 Theoretical Basis for Diffusion Simulation

The diffusion process has been modeled using Stoke-Einstein's equation (Eq. 1) and Fick's Law (Eq.2), on the basis of the fact that their applicability have been proven by several researchers in the past (for example, Karlsson and Issacsson (2003) and Oliver (1975)). The model was validated with the use of closely controlled laboratory experiment and is discussed in the previous paper of the authors (Mallick (2012)).

$$D = \frac{K_B T}{6\pi\mu(R)} \tag{1}$$

D is rate of diffusion (m^2/s), R is the mean molecular radius, μ is dynamic viscosity (Pa·s), K_BT is the internal heat energy, K_B is Boltzmann's constant ($1.3807 \cdot 10^{-23}$ J/K), and T is absolute temperature (K).

$$J = -D\frac{\sigma c}{\sigma x} \tag{2}$$

J is diffusion flux ($mol/m^2 \cdot s$), D is diffusion coefficient, C is concentration (mol/m^3), and x is distance (m).

It is hypothesized that the diffusion of the rejuvenator changes the viscosity of the aged binder, and as the process continues, more and more of the aged binder is "rejuvenated" – which is reflected by the change (lowering) of viscosity, until equilibrium is attained. The mixing of two materials of different viscosities to produce a mix with a specific viscosity was modeled by Eq. 3.

$$\ln\mu_{mix} = c_1 \cdot \ln\mu_1 + c_2 \cdot \ln\mu_2 + c_1 \cdot c_2 \cdot G_{12} \tag{3}$$

Index 1 and 2 denote two different liquids or binder and c_1 and c_2 denote volume, mass or molar fraction of liquid/binders 1 and 2. The parameter G_{12} considers the effect of the intermolecular interaction between different sets of binders– this parameter has not been considered in the analysis.

The diffusion process was modeled using finite element simulation. The following are the sequence of steps used by the FE software calculation and result expression.

- Run the diffusion process for time interval of Δt seconds; readjust the viscosity of the layers, based on the concentration of the rejuvenator in the layers at Δt, according to Eq. 3 (mixing model); run the diffusion process for another Δt seconds; repeat for the entire time t_{end} that is allowed for mixing. The selection for the Δt seconds was made on the basis of two things – 1) how fast the diffusion is occurring; 2) what is the smallest time that can be considered without having excessive computation time.
- The concentration of the rejuvenator and the viscosity of the resultant binder at each Δt time intervals throughout the thickness of the RAP binder were determined.
- The total time of the simulation t_{end} was chosen in order to reach homogeneous concentration (and viscosity) throughout the binder film thickness. This balance must be maintained at the aggregate and binder interface for least $10 \cdot t_1$ intervals which shows that further changes in concentration will not occur.
- Time of reaching homogeneous distribution of the rejuvenator in the entire film is reported as $t_{balance}$. It is calculated as the viscosity at time t_{end} minus 1%.

3 Parameters Used for Modeling and Simulation

The formulation of the diffusion problem with respect to asphalt mix recycling in plant recycling is demonstrated in figure 1. The simulation was run assuming 100% RAP recycling with the use of rejuvenator; there is no virgin binder or aggregates.

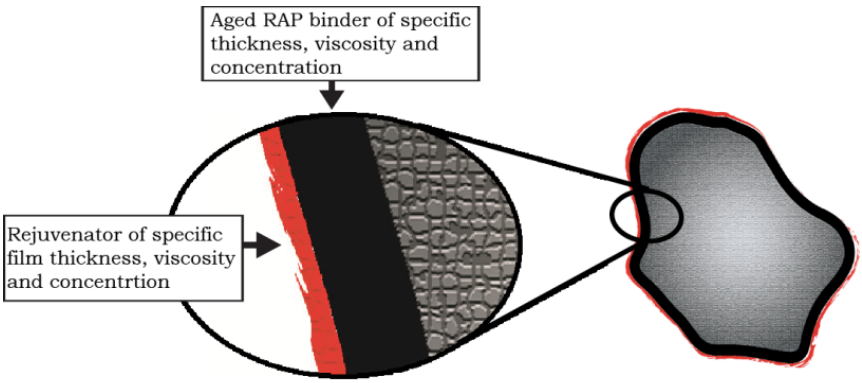

Fig. 1 Aggregate, binder and rejuvenator interface

Plant Mixing Process and Temperature. The asphalt mixture production in the plant involves two main characteristics - temperature and time of heating. The rejuvenator diffusion into the aged RAP binder film strongly depends on both of

these factors. In a drum plant the rejuvenator is usually added after the RAP has been heated in the drum to the required temperature as illustrated in figure 2. The RAP temperature at this point was obtained from field data and in this case it was 145ºC. After addition of the rejuvenator the material is transported by elevator to the storage silo and hauled to the construction site. Through the first phase of this process the temperature remains relatively stable, therefore simulations were performed to determine the required time at this constant temperature for the rejuvenator to have maximum efficiency (to reach balance within the binder film).

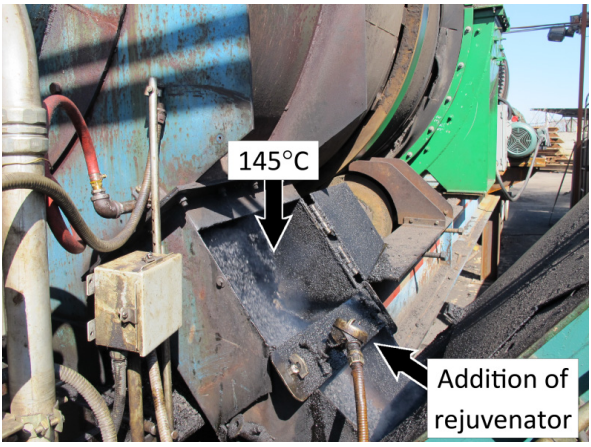

Fig. 2 Rejuvenator addition to the mixture (Courtesy: Bob Frank, RAP Technologies, LLC)

To analyze the effect of temperature on the diffusion time, diffusion at two more temperatures (120ºC and 95ºC) was simulated. Different temperature may be used based on local circumstances (weather, RAP condition, binder grade, etc.) or the mix (for example, when some warm mix technology is utilized (Zaumanis, 2012).

Viscosity of Rejuvenators and Binders. A range of rejuvenators were tested for kinematic viscosity using capillary tube viscometers at two different temperatures – 95ºC and 145ºC. Bitumen was extracted from RAP and tested for penetration at 25ºC and kinematic viscosity at 135ºC. The penetration data was converted to viscosity using the procedure by Davis (1981). Log-log viscosity versus log temperature regression was used to express the viscosity of rejuvenators and binder at the required temperate range that is typically used for production and compaction of asphalt. The density of the products (listed in Table 2 and Table 3) was obtained from the manufacturers in order to calculate the dynamic viscosity as presented in table 1.

Table 1 Viscosity of rejuvenators and bitumen

Product	Viscosity, Pa·s				
	60ºC	95ºC	120ºC	135ºC	145ºC
Extracted RAP binder	344.71*	14.92	4.12	2.31*	1.65
Virgin AC-20 binder**	198.44*	3.50	0.78	0.40*	0.28
Refined Tallow	0.0277	0.0055*	0.0033	0.0027	0.0025*
Paraffinic base oil	0.0529	0.0054*	0.0029	0.0023	0.0021*
Brown Grease	0.0438	0.0085*	0.0049	0.0040	0.0035*
Yellow Grease	0.4326	0.0092*	0.0058	0.0048	0.0043*

*Test temperatures

**Viscosity obtained from source (Houston 2006)

Rejuvenator Parameters. Film thickness, volume and concentration of the rejuvenators are required for FE calculation. The concentration depends on molecular weight, while the film thickness and volume depends on rejuvenator dosage.

The molecular weight of the materials was obtained using Gel Permeation Chromatography (GPC) technique and in some cases from the information provided from producers of the rejuvenators.

The film thickness of the rejuvenators was calculated according to Eq. 4 (Read and Whiteoak 2003), where the surface area factor was calculated for the mixture that was used for the experimental study of this research. The rejuvenator mass (Eq. 5) in the mixture is required to calculate volume and a 2500g sample that was used in experimental study was utilized for this purpose. The specific gravity of the rejuvenators was provided by the producers of the products. The calculation of concentration (Eq. 8) requires the number of moles for each rejuvenator (Eq. 7). The calculations of required parameters were performed for three different dosages of rejuvenators – 1%, 2%, and 3% by the weight of mixture. The sequence of results for all the rejuvenators at 1% dosage are summarized in table 2.

$$FT_{rejuvenator} = \frac{b}{100 - b} \cdot \frac{1}{\rho_b} \cdot \frac{1}{SAF} \tag{4}$$

Where FT – film thickness, mm ; b – rejuvenator content, %; ρ_b – specific gravity ; SAF – surface area factor, m^2/kg (10.35 m^2/kg was used).

$$Mass\ of\ rejuvenator = rejuvenator\ dosage * sample\ mass \tag{5}$$

$$Volume\ of\ rejuvenator = \frac{Mass}{Density} \tag{6}$$

$$Number\ of\ moles = \frac{Mass\ or\ rejuvenator}{Molecular\ weight} \tag{7}$$

$$Concentration = \frac{Number\ of\ moles}{Volume} \tag{8}$$

Table 2 Rejuvenator parameters

Product description	Specific gravity	Dosage, %	Film thickness, μm	Mass in 2500g sample, g	Molecular weight, g/mole	Volume, m3	Number of moles, mole	Concentration, mol/m^3
Refined Tallow	0.90*	1.0	1.14	25	283*	2.8E-05	8.9E-02	3186
Paraffinic base oil	0.88*	1.0	1.16	25	395*	2.8E-05	6.3E-02	2228
Brown Grease	0.92*	1.0	1.11	25	771	2.7E-05	3.2E-02	1193
Yellow Grease	0.92*	1.0	1.11	25	2442	2.7E-05	1.0E-02	377
AC-20	1.02*	1.0	1.00	25	730	2.5E-05	3.2E-02	1320

*Provided by the producer material data sheets

Binder Parameters. The parameters of the aged RAP bitumen that were used in the simulation are provided in table 3. A film thickness (9 μm) was considered on the basis of the recommendations found in literature for dense graded mixes of 9-10 μm, in terms of VMA, (Campen et al. 1995; Goode and Lufsey 1965; Kandhal et al. 1996). The molecular radius was obtained from Karlsson and Isacsson (2003).

Table 3 Parameters of the aged binder

Parameter	Value
Specific gravity	1.02
Film thickness, μm	9.00
Molecular weight, g/mole	877.2
Thermal conductivity, W/m·K	1.0
Specific heat capacity, J/kg·K	1006
Molecular radius, m	3e-10

4 Simulation Results

The change in viscosity at the aggregate and bitumen interface is illustrated in figure 3. For the first few seconds the rejuvenator has not reached the bitumen and aggregate interface and the viscosity is constant; in the next phase through diffusion process the rejuvenator softens the bitumen; at around 205 to 215 seconds the viscosity is found to be stable for 10 seconds which suggests that no further softening is possible with increased time or temperature. A tolerance of 1% is deducted from the end viscosity and the time to reach this viscosity level is defined

as the time to reach homogeneous rejuvenator concentration through the film. The illustration shows this process for 1% brown grease rejuvenator at a temperature of 145ºC.

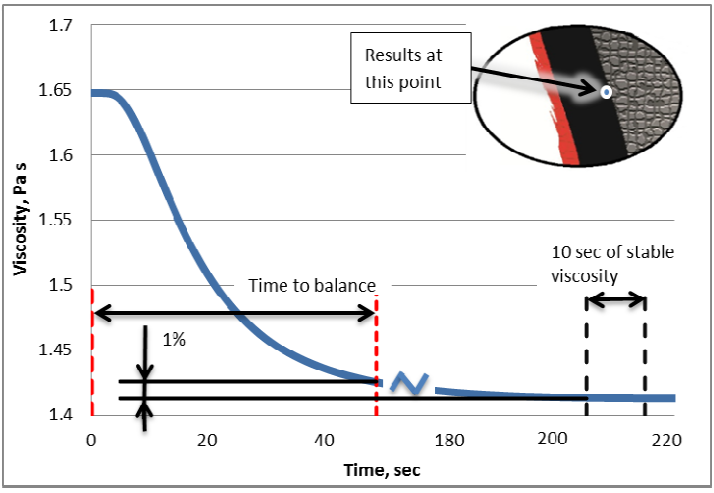

Fig. 3 The viscosity at different times for 1% Brown Grease

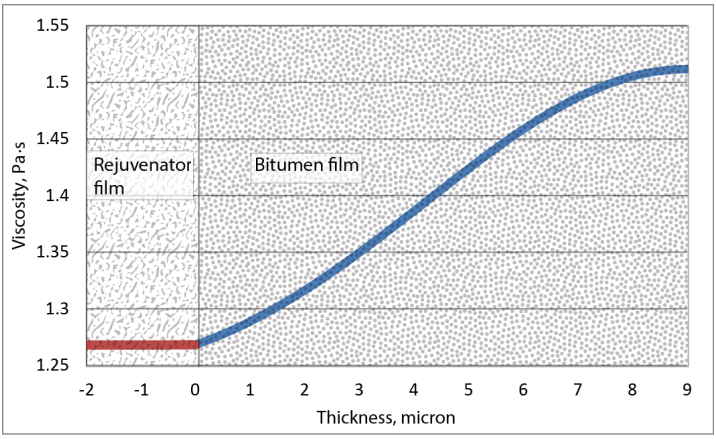

Fig. 4 Viscosity at 145ºC through film thickness at 20 sec for yellow grease rejuvenator

In the diffusion process the rejuvenator penetrates in the bitumen film gradually reducing the viscosity starting from the outer layer of the binder film and continuing throughout the film thickness until equilibrium is reached. If the process is interrupted by, for example reducing the temperature, the equilibrium will not be reached. The viscosity of the film will remain lower at the surface of the film and

higher at the interface of bitumen and aggregate. This is potentially dangerous situation and may cause permanent deformations to the pavement. The viscosity through the rejuvenator and bitumen film for a simulation of 145ºC at 20 seconds is illustrated in figure 4. The negative thickness represents rejuvenator film while the positive is the binder. It is clear that this time interval is too short for yellow grease rejuvenator to reach homogeneous distribution.

The changes of aged binder viscosity from adding different dosages of rejuvenators at 145ºC are illustrated in figure 5. It is evident that the refined tallow and paraffinic base oil has to highest softening performance, while the yellow grease and virgin binder has the lowest. The difference is significant and refined tallow can be up to four times more efficient than addition of virgin asphalt. Potentially such approach can be used to determine the dosage of rejuvenator to reach target viscosity, for this purpose viscosity of virgin AC-20 binder is illustrated in the figure.

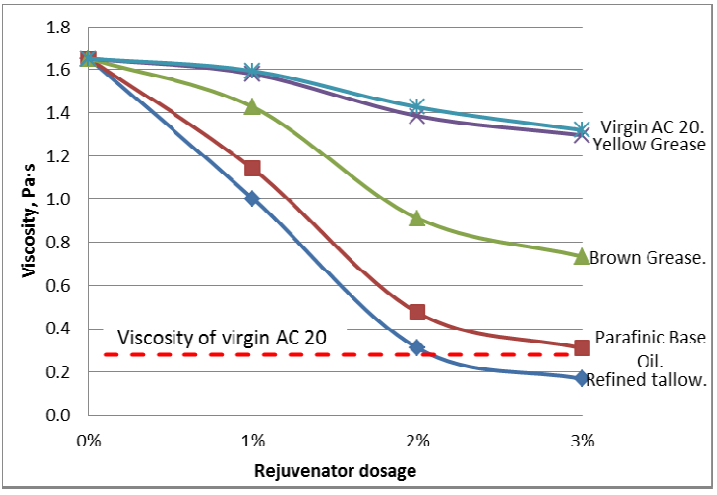

Fig. 5 Viscosity at different dosages

The time to reach the viscosity illustrated in figure 5 can be very different when using different rejuvenators. Figure 6 shows minimum period of time that is required to reach balanced viscosity at entire film thickness for three different rejuvenator dosages. It is evident that the time to reach equilibrium depends on the type of rejuvenator. By changing the dosage of rejuvenator the relative comparison between the different rejuvenators also changes. This is due to the fact that the weight of parameters that influence the viscosity changes as described by mixing model (Eq. 3). While the concentration and viscosity remains constant, the volume and mass of the samples changes. For example the concentration of yellow grease is significantly lower compared to the other samples, which causes increase in the required time to reach equilibrium.

In absolute numbers the required time at this temperature seems to be significant to reach homogeneous rejuvenator distribution within the binder film. This is somewhat contradictory to the reports in literature about "black rock" effect and suggests that some other mechanisms are involved in this process. Perhaps two staged rejuvenation as reported by Huang et al (2005) would simulate the process more realistically. According to this theory the rejuvenator first dissolves the outer layer of the binder while the remaining bitumen part forms a stiff coating around the aggregate particles in which the solution penetrates through diffusion.

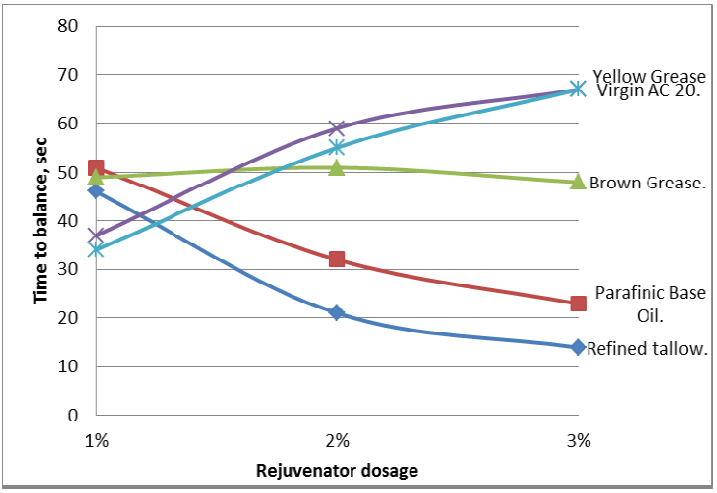

Fig. 6 Required time to reach equilibrium at different rejuvenator dosages

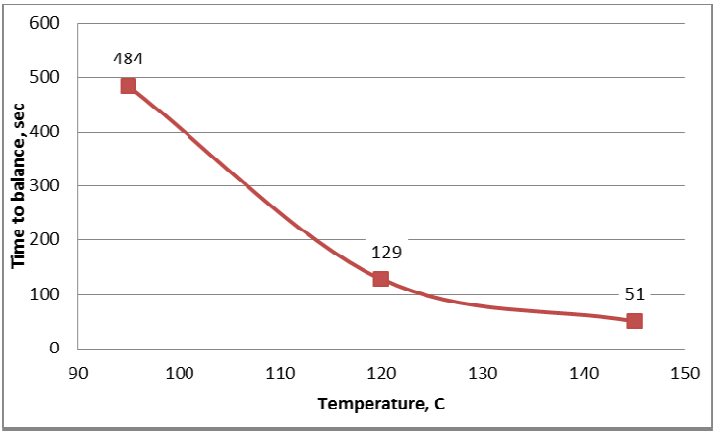

Fig. 7 Time of equilibrium at different temperatures for 1% paraffinic base oil

Figure 7 illustrates the required time to reach balance at different temperatures for 1% paraffinic base oil. The increase in time is significant and there is a large chance that the diffusion process will not be finalized before construction if lower than recommended temperature is chosen. This extension of time is caused by the viscosity increase of both – the binder and the rejuvenators.

5 Mechanical Testing Results

Penetration at 25ºC results of extracted binder and virgin binder as well as the rejuvenated samples are summarized in table 4. It can be assumed that equilibrium of rejuvenator has been reached in these samples. Note that the dosages of rejuvenator are different from the simulation and between the rejuvenators. This was done to have the penetration results in a reasonable range for given climate. All of the rejuvenators have increased the penetration (reduced viscosity) of the aged RAP binder. The virgin binder has been the least effective and the brown grease has the best performance per 1% of rejuvenator dosage. These results support the fact the rejuvenators are more efficient than virgin binder in reducing the viscosity but at the same time the softening performance ranking is not the same as for FE simulation. The reasons for that probably being the different test temperatures (145ºC VS 25ºC) and fact that the simulation considers diffusion, but the rejuvenators were added to the binder by mechanical mixing of the two substances.

Table 4 Bitumen Test results

Binder type	Rejuvenator dosage, % from binder mass	Penetration @ 25°C, 1/10mm
RAP extracted binder	-	16
Virgin AC–20 binder	-	76
RAP binder + Refined tallow	9	84
RAP binder + Paraffinic base oil	18	91
RAO binder + Yellow grease	12	90
RAP binder + Brown grease	9	89
RAP binder + Virgin AC-20 binder	18	21

The RAP mixture was mixed together with three from the above mentioned five rejuvenators and tested for creep compliance at -10ºC. Creep compliance is a way of characterizing the stiffness of material. The higher the creep compliance the more is the ability of the material to flow at low temperature and the smaller is the possibility of thermal cracking. Therefore this is a good illustration of binder stiffness at low temperature. The results (Figure 8) rank the three rejuvenators in

the same sequence of softening performance relative to their dosage as the FE simulation where the paraffinic base oil and refined tallow are much more effective than yellow grease.

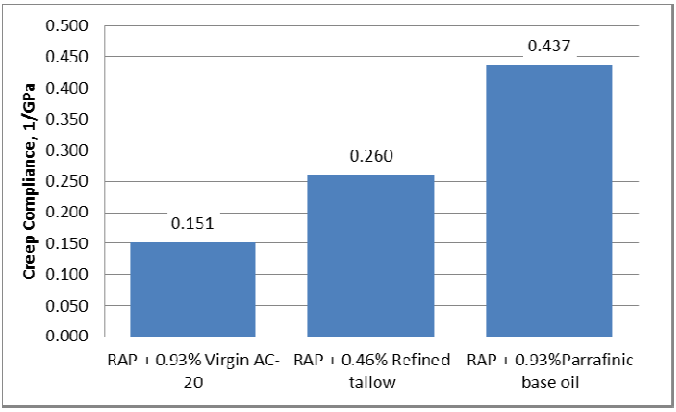

Fig. 8 Creep compliance at -10ºC of aged RAP plus select rejuvenators

6 Conclusions

1. The softening level of the aged binder depends on the parameters of rejuvenators which include, but is not limited to viscosity. Refined tallow was up to four times more effective than the virgin binder.
2. The dosage of the rejuvenator changes the time to reach equilibrium in the binder. However, total diffusion time at 145ºC according to simulation is sufficient for complete diffusion. Simulation of staged diffusion, considering "black rock" effect may give more realistic results.
3. If the diffusion process has not been complete before opening to traffic because of insufficient time or low temperature, the outer layer of the film will have lower viscosity which can lead to lower stiffness and instability under traffic.
4. The simulation results only partly correlate with the bitumen and mix testing data, suggesting that diffusion is only one of the processes taking place. The others include mechanical mixing and homogeneous dispersion of the rejuvenator.
5. The testing of penetration after addition of rejuvenators and the mechanical tests of asphalt mixture confirm that rejuvenators are much more effective in improving the performance of aged binder compared to addition of softer binder.

References

Campen, W., Smith, J., Erickson, L., et al.: The Relationships Between Voids, Surface Area, Film Thickness and Stability In Bituminous Paving Mixtures. J. Assoc. Asphalt Pav. 28, 149–178 (1959)

Goode, J., Lufsey, L.: Voids, Permeability, Film Thickness vs. Asphalt Hardening. J. Assoc. Asphalt Pav. Association 34, 430–463 (1965)

Houston, W., Mirza, W., Zapata, C.: Environmental effects in pavement mix and structural design systems. NCHRP report No.9-23 (2006), http://onlinepubs.trb.org/onlinepubs/nchrp/docs/NCHRP09-23_Part2_FR.pdf (accessed November 10, 2012)

Huang, B., Guoquiang, L., Dragan, V., et al.: Laboratory Investigation of Mixing Hot-Mix Asphalt with Reclaimed Asphalt pavement. Transport. Res. Rec. 1929, 37–45 (2005), doi:10.3141/1929-05

Kandhal, P., Chakraborty, S.: Evaluation of Voids in the Mineral Aggregate for HMA Paving Mixtures. NCAT Report No. 96-4 (1996), http://ntl.bts.gov/lib/6000/6300/6362/rep96-4.pdf (accessed October 3, 2013)

Karlsson, R., Isacsson, U.: Application of FTIR-ATR to Characterization of Bitumen Rejuvenation Diffusion. J. Mater. Civ. Eng. 15(2), 157–165 (2003), doi:10.1061/(ASCE)0899-1561

Mallick, R., Chen, B., Daniel, S.: Heating and its Effect on Hot In-Place Recycling of Asphalt Pavements with Rejuvenator. International J. Pavement Res. Technol. 5(6) (2012)

Oliver, J.: Diffusion of Oils in Asphalts. Ind. Eng. Chem. Prod. Res. Dev. 13(1), 65–70 (1975), doi:10.1021/i360049a013

Read, J., Whiteoak, D.: The Shell Bitumen Handbook. Thomas Telford Publishing, London (2003)

Davis, R.: The ASTM Penetration Method Measures Viscosity (With Disclosure and Closure). In: Skok Jr., E. (ed.) Association of Asphalt Paving Technologists Proceedings (1981)

Zaumanis, M., Olsen, E., Haritonovs, V., Brencis, G., Smirnovs, J.: Laboratory evaluation of organic and chemical warm mix asphalt technologies for SMA asphalt. Balt. J. Road Bridge E. 7(3), 191–197 (2012), doi:10.3846/bjrbe.2012.26

Zaumanis, M., Mallick, R., Frank, R.: Evaluation of Rejuvenator's Effectiveness with Conventional Mix Testing for 100% RAP mixtures. In: Proceedings of Transportation Research Board 92nd Annual Meeting, Washington, DC (2013)

Micromechanical Simulation of the Permanent Deformation Properties of Asphalt Concrete Mixtures

Habtamu Zelelew[1,*], Enad Mahmoud[2], and A.T. Papagiannakis[3]

[1] ESC INC, FHWA Office Pavement Technology
1200 New Jersey Ave., SE, Washington, DC 20590
habtamu.zelelew.ctr@dot.gov
[2] Civil Engineering & Construction
Bradley University, Peoria, IL 61625
emahmoud@fsmail.bradley.edu
[3] Department of Civil and Environmental Engineering
University of Texas-San Antonio, San Antonio, TX 78249
at.papagiannakis@utsa.edu

Abstract. This paper presents simulation results of Asphalt Concrete (AC) Flow Number (FN) properties. It utilizes the Discrete Element Method (DEM) technique to simulate the microstructure of three ACs captured using X-ray Computed Tomography (CT). These three mix designs (coarse-graded, gap-graded, and fine-graded) prepared with hard limestone aggregate and a PG 76-22 modified binder were included in the study. Advanced digital image processing techniques were utilized to process the X-ray CT images and to suitably input their microstructure into the DEM model. The viscoelastic rheological properties of the asphalt mastics were defined by fitting Burger model parameters on frequency sweep test data conducted at 60 °C. The DEM simulation, in two-dimensions, involved modeling the unconfined FN tests under a repeated stress of 690 kPa. The simulation loading was applied for 0.1 second followed by a 0.9 seconds rest period until 10,000 load cycles or 5 % accumulated strain was reached. The 2D DEM simulation results appear to capture the significant differences in FN properties between these three AC mixtures and hence can be used to compare their rutting susceptibility.

Keywords: Asphalt Mixtures, Mastics, Image Analysis, Discrete Element, Flow Number, and Permanent Deformation.

1 Introduction-Objective

Asphalt concrete (AC) mixtures are uniquely complex heterogeneous materials composed of air voids, mastic and aggregates. Mastics are blends of asphalt binder

* Corresponding author.

N. Kringos et al. (Eds.): *Multi-Scale Model. & Charact. of Infrastruct. Mater.,* RILEM 8, pp. 421–432.
DOI: 10.1007/978-94-007-6878-9_31

and fines, typically considered as particles passing sieve No. 200 (i.e., sizes finer than 75 μm). The distribution of these three phases and their interaction defines the mechanical properties of ACs and contributes significantly to their rutting resistance, load carrying capacity and durability. Pavement rutting consists of surface depressions along the wheel paths caused by the plastic deformation of the AC and the underlying granular layers. The AC plastic deformation properties are greatly influenced by the mastic rheology, aggregate properties, and the microstructure of mixture constituents.

The AC behavior is dominated by the interaction between mastics and distinct aggregate particles. The micromechanics-based Discrete Element Method (DEM) has been commonly used to simulate the large-strain behavior of granular materials such as ACs. The DEM technique is ideally suited to describe particle contact interaction (Cundall and Strack, 1979). The literature to date provides valuable insight into the modeling of the microstructure of ACs. Previous studies on modeling the AC mixture behavior using the micromechanical modeling approach include Shashidhar, 2000; Rothenburg *et al.,* 1992; Chang and Meegoda, 1997; Buttlar and You, 2001; You and Buttlar, 2004; Abbas *et al.,* 2005; Collop *et al.,* 2006; and Zelelew and Papagiannakis 2010.

The objective of this paper is to simulate the unconfined cyclic Asphalt Mixture Performance Test (AMPT) and focus on the estimated Flow Number (FN) of ACs using the DEM method in two-dimensions. The number of load cycles corresponding to the minimum rate of change of permanent axial strain during a repeated load test defines FN (AASHTO TP 79). The microstructure of the AC mixtures was captured using X-Ray Computed Tomography (CT) and advanced digital image processing techniques were utilized to process the microstructure and input into the 2D DEM model. Moreover, the viscoelastic mastic rheological properties were captured using Burger models fitted to Dynamic Shear Rheometer (DSR) frequency sweep data.

2 Materials and Methods

Three AC mix designs were considered in this study:

- A coarse-graded Coarse Matrix High Binder Type C (CMHB) mix,
- A gap-graded Porous Friction Course (PFC) mix, and
- A fine-graded Superpave Type C (Superpave) mix.

Each of these mix designs was prepared with a hard limestone aggregate type and a PG 76-22 modified binder meeting the Texas DOT specifications. The aggregate gradations for each of the mix designs are shown in Figure 1 while the volumetric properties are presented in Table 1. Detailed mix design data and experimental test plan as well as numerical modelling of creep performance can be found elsewhere (Zelelew 2008).

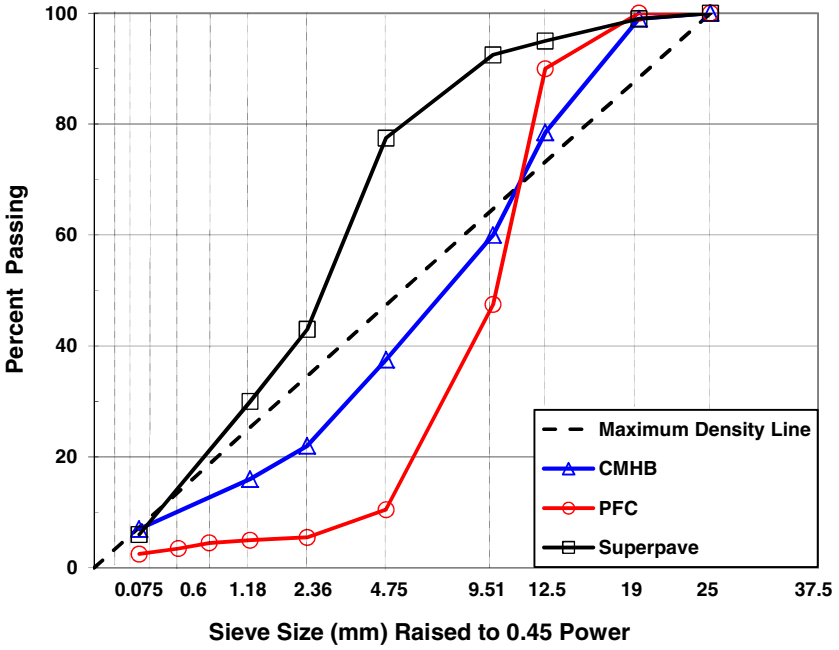

Fig. 1 Mix design aggregate gradations

Table 1 Asphalt concrete mix design data

Parameter	CMHB	PFC	Superpave
Binder Grade	PG 76-22		
P_b (%)	4.2	5.1	4.0
V_a (%)	7.3	19.5	7.4
VMA (%)	12.7	27.2	12.7
VFA (%)	70.2	26.4	68.5

P_b = percent binder content, V_a= percent air voids, VMA= percent voids in mineral aggregates, and VFA= percent voids filled with asphalt.

3 X-ray Computed Tomography Scanning and Image Processing

The AC performance test specimens were fabricated by coring the 150 mm diameter Superpave gyratory compacted (SGC) specimens to a diameter of 100 mm. The cored samples were also trimmed to a height of 150 mm. The X-ray CT scanning of AC performance specimens was conducted by the Advanced Characterization of Infrastructure Materials Laboratory (ACMI) of the Texas Transportation Institute (TTI). Each of the three AC specimens was scanned perpendicular to their vertical axis at 1 mm distance interval to yield 150 2D image slices with an image resolution of 0.195 mm/pixel. Digital image processing techniques were then applied to effectively analyse the AC microstructure.

The X-ray CT images of the ACs were processed utilizing the Volumetric-based Thresholding Algorithm (VTA) developed by Zelelew and Papagiannakis (2011). The VTA algorithm provides a quantitative means of establishing a unique grayscale threshold for the boundaries between air-mastic and mastic-aggregate. Moreover, it allows visualizing the microstructure of these three phases in 2D and 3D. An example of the resulting 2D rectangular sections is shown in Figure 2. The white objects (grayscale = 255) in these figures represent mixture constituents. The watershed image segmentation technique was also utilized to separate the connected or/and overlapped aggregate particles.

4 Mastic Burger Model Parameters

The aggregate finer than 0.075 mm and binder proportions used in preparing the mastics were obtained from the volumetric properties of the AC mixtures. The PG 76-22 binder (RTFO-aged) was used to prepare the mastic specimens. Frequency sweep tests were conducted using a test temperature of 60 °C using a wide range of frequencies (i.e., from 0.01 to 100 rad/sec). The Burger model consisting of a Maxwell and Kelvin-Voigt element coupled in series was used to describe mastic viscoelastic rheological models. Several researchers have implemented Burger model to describe the viscoelastic behavior of mastics (Abbas *et al.,* 2005; Kim and Little, 2004; and Yu *et al.,* 2007). The Burger models were fitted to the frequency sweep test data by minimizing the squared differences between modeled and observed storage and loss shear moduli (Papagiannakis *et al.,* 2002; and Baumgaertel and Winter, 1989). The Burger model yielded a fairly good fit to the observed mastic behavior, although a higher number of Kelvin units would probably improve it. The constants of the Burger model for the mastic specimens are shown in Table 2.

Table 2 Burger model parameters; 60 °C

Mastic ID	Maxwell Element		Kelvin Element	
	E_M (kPa)	η_M (kPa.sec)	E_K (kPa)	η_K (kPa.sec)
CMHB	225.0446	45.4928	13.1130	10.5862
PFC	220.0117	20.4781	12.9337	6.7759
Superpave	260.0253	40.3797	13.7607	10.3791

E_M and η_M denote the spring and dashpot constants of Maxwell element, respectively; E_K and η_K denote the spring and dashpot constants of Kelvin element, respectively.

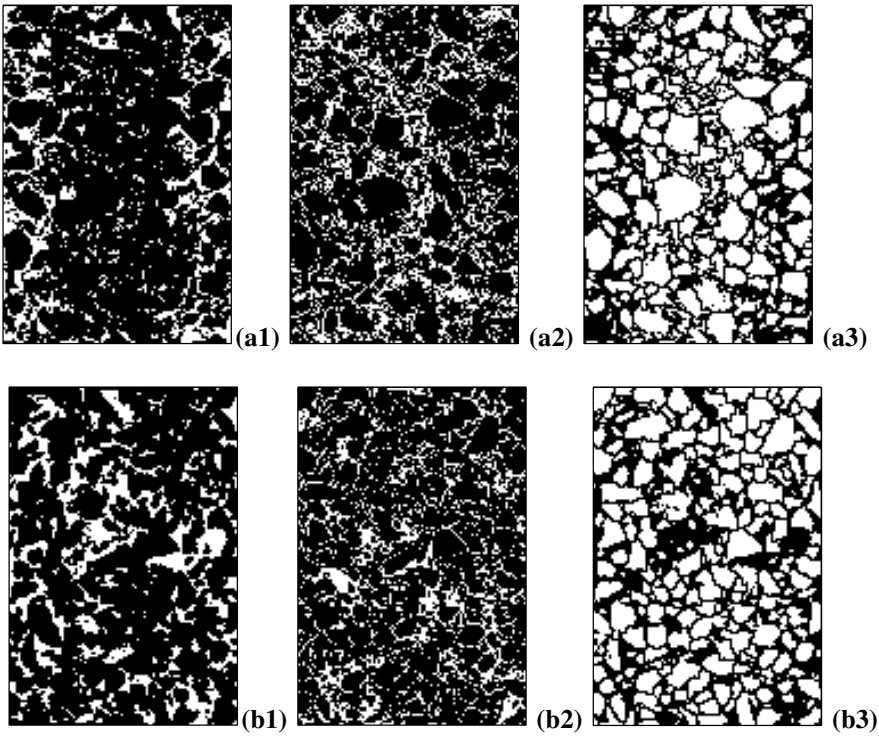

Fig. 2 VTA processed rectangular images; (a1) CMHB air, (a2) CMHB mastic, (a3) CMHB aggregate; (b1) PFC air, (b2) PFC mastic, (b3) PFC aggregate; (c1) Superpave air, (c2) Superpave mastic, and (c3) Superpave aggregate; white objects denote mixture constituents

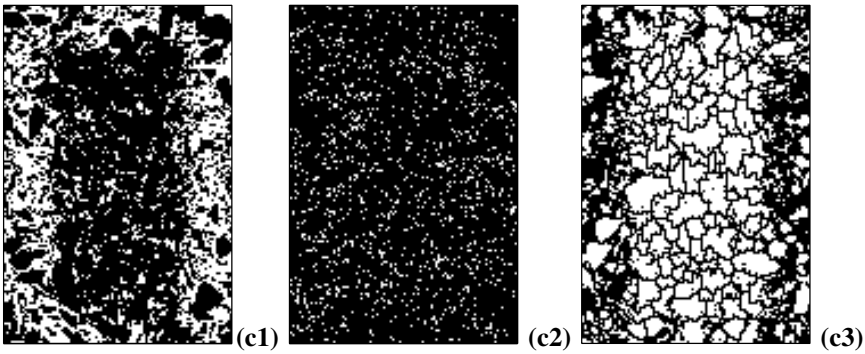

Fig. 2 (*continued*)

5 Flow Number Data

The use of the Flow Number (FN) obtained through unconfined or confined cyclic AMPT test has gained acceptance as a means of evaluating the permanent deformation resistance of AC mixtures. The AMPT involves applying a cyclic load for 0.1 second followed by a 0.9 second rest period. The number of load cycles and accumulated axial strains are continuously recorded. The FN test termination criteria is either 10,000 load cycles or the accumulation of 50,000 microstrain (i.e., 5% strain), whichever occurs first. The number of load cycles corresponding to the minimum rate of change of permanent axial strain during a repeated load test defines FN. The FN test temperature is typically determined through *LTPPBind* software using the closest weather station to the project location.

6 DEM Simulation of FN Test

The study utilized the Particle Flow Code in two-dimensions (PFC^{2D}) version 3.1 software (Itasca, 2004). The methods described here can be readily extended to a three-dimensional DEM modeling approach, which should produce more accurate results. The first step in the DEM simulation process is to input the AC microstructure (shown in Figure 2 a3, b3 and c3) obtained as described above into the PFC^{2D} input module. The built-in *BALL* command generates particles and can assign mastic or aggregate attributes to them through their Cartesian coordinate locations identified from the processed images. An advantage of the PFC^{2D} is that it allows "clumping" similar adjacent particles together using the *FISH* clump function and thus, avoids force-displacement calculations between them. The combinations of mastic and aggregate particles producing a realistic representation of the AC microstructure suitable for DEM modeling is shown in Figure 3 for the PFC mixture.

Four rigid walls were defined as the boundary constraining the AC microstructural models. For the unconfined FN test, the upper wall was used to load the AC model by specifying a wall velocity, while fixing the lower platen. The DEM simulation of unconfined FN tests was conducted using an axial deviator stress of 690 kPa. Before applying the wall velocity corresponding to 690 kPa, a contact stress of 35 kPa (i.e., 5% of the axial deviator stress) was used to obtain uniform initial stress distribution within the DEM specimen model. The AC model was loaded in a stress-controlled fashion by specifying the upper wall velocity. A numerical "servo-mechanism" implemented via the *FISH* function was devised to monitor the amount of stress generated by the displacement of the upper boundary. The stresses were computed by dividing the total force acting on upper wall by the wall area.

Contact models describe the force-displacement interaction between particles. For the AC microstructure, the primary contacts include mastic-to-mastic, mastic-to-aggregate, and aggregate-to-aggregate. These interactions were defined using two contact models, namely a linear contact model (frictional law) and a linear viscoelastic model. The linear elastic contact model was used to define the aggregate-to-aggregate contacts. Previous studies showed that an elastic modulus value of 30 GPa is appropriate for aggregates (Abbas *et al.,* 2005). In addition to this model, slippage in the aggregate-to-aggregate contact was allowed by means of the contact friction coefficient. The Burger model was used to describe the mastic-to-mastic and the mastic-to-aggregate contacts (Table 2). The elastic constants for the Burger model in the normal direction were obtained from those in the shear direction.

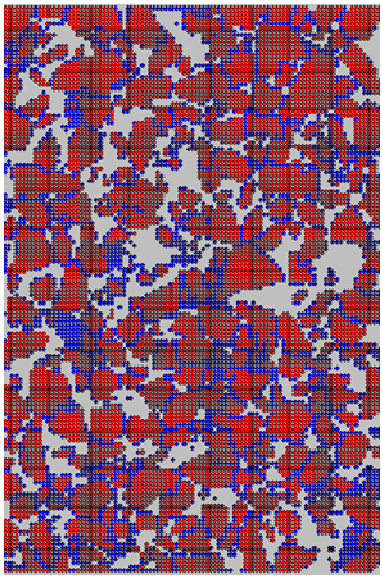

Fig. 3 AC DEM model; PFC mix (Red and blue elements represent aggregates and mastics, respectively)

7 DEM Simulation Results

The DEM simulations included a time step of 0.05 second for a total of 10,000 calculation cycles, to simulate the full length of the FN tests. The results were in the form of vertical strain using a virtual gauge length of 100 mm centered at the mid-height of the sample. Consequently, the vertical locations (y coordinates) of discrete elements on the two sides of the model at the two ends of the virtual gauge were tracked and monitored. The DEM simulations included an aggregate-to-aggregate friction of 0.5 and the normal to shear stiffness ratio of 2.8.

An example of the DEM simulation results in the first fifty loading cycles is shown in Figure 4. This figure includes the computed axial strain at each load cycle and the accumulated strain as a function of the number of load cycles. A summary of the DEM simulation results for the AC mixtures analyzed is shown in Figure 5. As it can be seen, the DEM simulation was terminated at 10,000 load cycles for each of the three mixtures analyzed (i.e., none measured the 50,000 microstrain limit). The plots of axial strain versus number of loading cycles exhibited two distinct regions:

- a primary region where the strain rate decreased and
- a secondary (or steady state) region where the strain rate was constant (i.e., accumulated strain curve was linear).

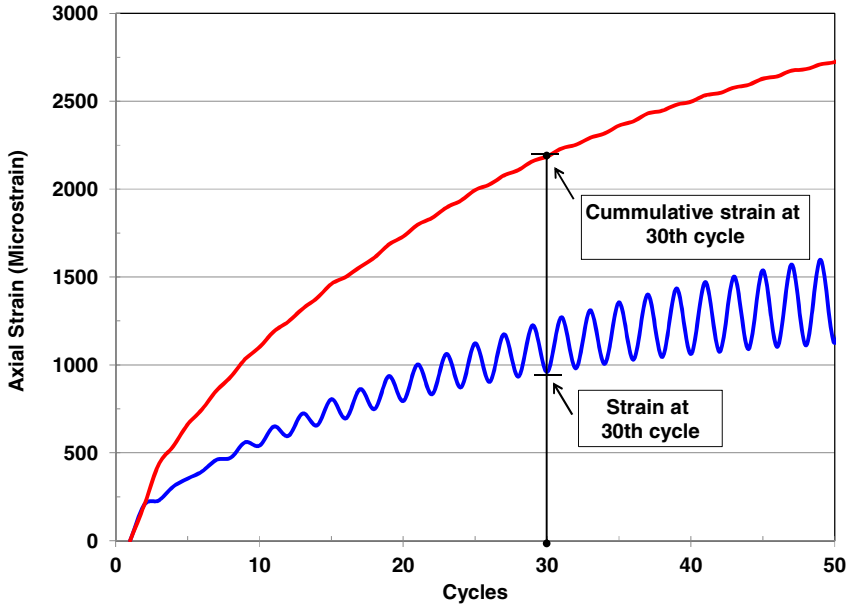

Fig. 4 DEM results example; Axial strain versus load cycles

None of these plots exhibited a tertiary region (i.e., a range beyond which the strain rate significantly increased) suggesting that their FNs are larger than 10,000. On the other hand, the shape/magnitude of the accumulated plastic strains was significantly different between the three ACs simulated. A summary of the intercept and slope of the accumulated plastic strain versus the number of cycle curves is given in Table 3. It is concluded that the rutting propensity of the PFC is much higher than that of the CMHB and the Superpave mixtures. Higher intercept and slope values suggest lower resistance to permanent deformation.

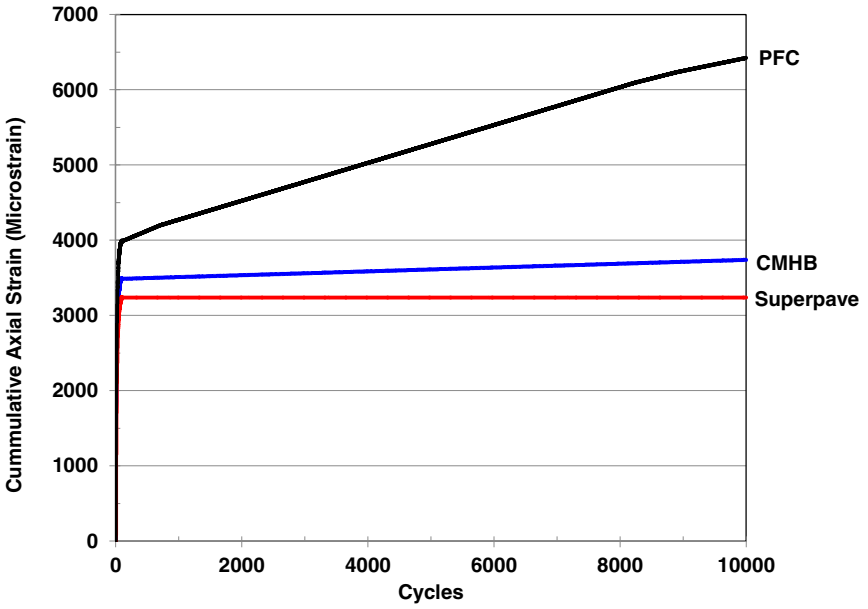

Fig. 5 DEM simulation results

Table 3 DEM simulation results

Parameter	Units	Mix		
		CMHB	PFC	Superpave
Flow Number (FN)	cycles	>10,000	>10,000	>10,000
Intercept	microstrain	3,484	4,021	3,238
Slope	microstrain/cycle	0.025	0.252	0.000

In addition, the cumulative axial strain at 5,000 cycles was used as a surrogate measure of plastic deformation propensity for these AC mixtures (Figure 6). Overall, the Superpave mix yielded much lower rate of deformation followed by the CMHB mix and then the PFC mix. Zelelew (2008) also reported similar findings when these mixes were tested and modeled (2D DEM) under monotonic creep loading conditions (i.e., unconfined Flow Time, FT). For the mixes tested, the FT performance index exceeded 10,000 seconds which agrees with the FN simulation results presented in this paper.

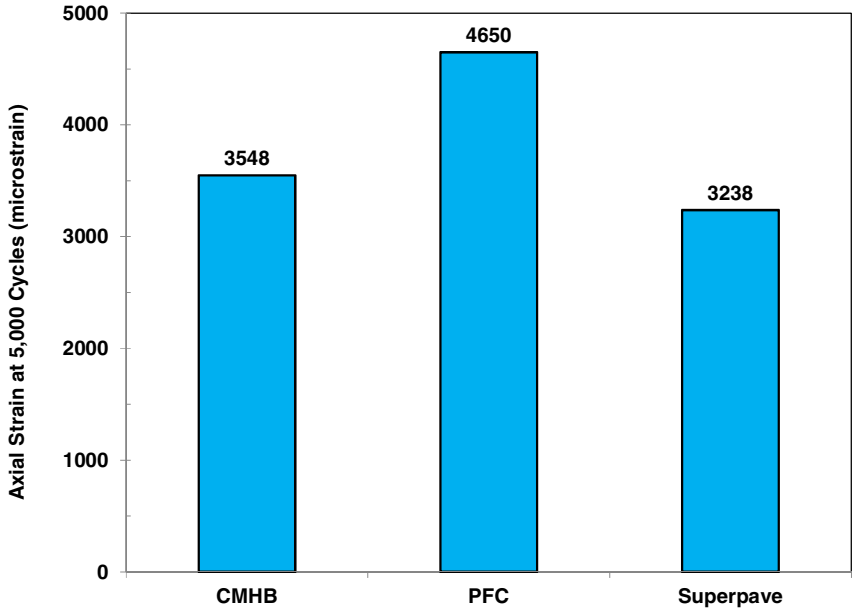

Fig. 6 DEM simulation results; Accumulated axial strain at 5,000 cycles

8 Summary and Conclusions

This paper presented a Discrete Element Method (DEM) approach for modeling the permanent deformation properties of asphalt mixtures. A 2D DEM was used to simulate the unconfined Asphalt Mixture Performance Tester (AMPT) with a focus on the simulated Flow Number (FN) estimates using the PFC^{2D} software package. The microstructure of the AC mixtures was captured using X-Ray Computed Tomography (CT). Advanced digital image processing techniques were then utilized to process the microstructure and input into the DEM model. Three AC mix designs were included; a coarse-graded Coarse Matrix High Binder Type C (CMHB) mix, a gap-graded Porous Friction Course (PFC) mix, and a fine-graded Superpave Type C (Superpave) mix. Each of these mix designs was

prepared with a hard limestone aggregate type and a PG 76-22 modified binder. The viscoelastic mastic rheological properties were captured using the Burger model fitted to the frequency sweep data tested at a temperature of 60°C. The 2D DEM simulation resulted identical FN values (i.e., 10,000 cycles) for all AC mixtures. The steady state regression parameters (i.e., slope and intercept) as well as the strain at 5,000 cycles were used to rank the permanent deformation performance of the AC mixtures included in the study. Overall, the Superpave mix measured lower rate of deformation followed by the CMHB mix. The PFC mix demonstrated the lowest resistance to permanent deformation. In conclusion, DEM estimates of FN appear capable of differentiating between the plastic deformation resistance of asphalt concrete mixtures.

References

1. Abbas, A., Papagiannakis, A.T., Masad, E., Shenoy, A.: Modeling asphalt mastic stiffness using discrete element analysis and micromechanics-based models. The International Journal of Pavement Engineering 6(2), 137–146 (2005)
2. AASHTO TP 79, Standard method of test for determining the dynamic modulus and flow number for Hot Mix Asphalt (HMA) Using the Asphalt Mixture Performance Tester (AMPT), American Association of Highway and Transportation Officials (AASHTO), Washington D.C. (January 2012)
3. Baumgaertel, M., Winter, H.H.: Determination of discrete relaxation and retardation time spectra from dynamic mechanical data. Rheological Acta 28, 511–519 (1989)
4. Buttlar, W.G., You, Z.: Discrete element modeling of asphalt concrete: a micro-fabric approach. Transportation Research Record 1757, Transportation Research Board, National Research Council, Washington, D.C., pp. 111-118 (2001)
5. Chang, K.G., Meegoda, J.N.: Micromechanical simulation of hot mix asphalt. Journal of Engineering Mechanics 123(5), 495–503 (1997)
6. Collop, A.C., McDowell, G.R., Lee, Y.W.: Modeling dilation in an idealized asphalt mixture using discrete element modeling. Granular Matter 8, 175–184 (2006)
7. Cundall, P.A., Strack, O.D.: Discrete numerical model for granular assemblies. Geotechnique 29(1), 47–65 (1979)
8. Itasca Consulting Group, Particle flow code in two-dimensions (PFC2D) manual version 3.1, Itasca Consulting Group, MN (2004)
9. Kim, Y., Little, D.: Linear viscoelastic analysis of asphalt mastics. Journal of Materials in Civil Engineering 16(2), 122–132 (2004)
10. Papagiannakis, A.T., Abbas, A., Masad, E.: Micromechanical analysis of viscoelastic properties of asphalt concrete. Transportation Research Record 1789, Transportation Research Board, National Research Council, Washington, D.C., pp. 113-120 (2002)
11. Rothenburg, L., Bogobowicz, A., Haas, R., Jung, F.W., Kennepohl, G.: Micromechanical modelling of asphalt concrete in connection with pavement rutting problems. In: Proceedings of the 7th International Conference on Asphalt Pavements, pp. 230–245 (1992)
12. Shashidhar, N., Zhong, X., Shenoy, A.V., Bastian, E.J.: Investigating the role of aggregate structure in asphalt pavements. In: 8th Annual Symposium Proceedings on Aggregates, Asphalt Concrete, Base, and Fines, Denver Co. (2000)

13. You, Z., Buttlar, W.G.: Discrete element modeling to predict the modulus of asphalt concrete mixtures. Journal of Materials in Civil Engineering 16(2), 140–146 (2004)
14. Yu, L., Shi-Feng, R., Guang-Hu, X.: Discrete Element Simulation of Asphalt Mastics Based on Burgers Model. Journal of Southwest Jiaotong University Journal of Southwest Butler University 1(15), 20–26 (2007)
15. Zelelew, H.: Simulation of the permanent deformation of asphalt concrete mixtures using discrete element method (DEM). PhD Dissertation, Department of Civil and Environmental Engineering, Washington State University, Pullman, WA (2008)
16. Zelelew, H., Papagiannakis, T.: Micromechanical modeling of asphalt concrete uniaxial creep using the discrete element method. International Journal of Road Materials and Pavement Design 11(3), 613–632 (2010)
17. Zelelew, H., Papagiannakis, T.: A Volumetrics thresholding algorithm for processing asphalt concrete X-Ray CT images. International Journal of Pavement Engineering 12(6), 543–551 (2011)

Author Index